Lecture Notes in Electrical Engineering 892

Manish Tiwari
Yaseera Ismail
Karan Verma
Amit Kumar Garg *Editors*

Optical and Wireless Technologies

Proceedings of OWT 2021

Springer

Lecture Notes in Electrical Engineering

Volume 892

The book series *Lecture Notes in Electrical Engineering* (LNEE) publishes the latest developments in Electrical Engineering - quickly, informally and in high quality. While original research reported in proceedings and monographs has traditionally formed the core of LNEE, we also encourage authors to submit books devoted to supporting student education and professional training in the various fields and applications areas of electrical engineering. The series cover classical and emerging topics concerning:

- Communication Engineering, Information Theory and Networks
- Electronics Engineering and Microelectronics
- Signal, Image and Speech Processing
- Wireless and Mobile Communication
- Circuits and Systems
- Energy Systems, Power Electronics and Electrical Machines
- Electro-optical Engineering
- Instrumentation Engineering
- Avionics Engineering
- Control Systems
- Internet-of-Things and Cybersecurity
- Biomedical Devices, MEMS and NEMS

For general information about this book series, comments or suggestions, please contact leontina.dicecco@springer.com.

To submit a proposal or request further information, please contact the Publishing Editor in your country:

China

Jasmine Dou, Editor (jasmine.dou@springer.com)

India, Japan, Rest of Asia

Swati Meherishi, Editorial Director (Swati.Meherishi@springer.com)

Southeast Asia, Australia, New Zealand

Ramesh Nath Premnath, Editor (ramesh.premnath@springernature.com)

USA, Canada:

Michael Luby, Senior Editor (michael.luby@springer.com)

All other Countries:

Leontina Di Cecco, Senior Editor (leontina.dicecco@springer.com)

**** This series is indexed by EI Compendex and Scopus databases. ****

More information about this series at https://link.springer.com/bookseries/7818

Manish Tiwari · Yaseera Ismail · Karan Verma ·
Amit Kumar Garg
Editors

Optical and Wireless Technologies

Proceedings of OWT 2021

Springer

Editors
Manish Tiwari
Electronics and Communication Engineering
Manipal University Jaipur
Jaipur, India

Karan Verma
Computer Science and Engineering
National Institute of Technology Delhi
Delhi, India

Yaseera Ismail
Quantum Research Group
University of KwaZulu-Natal
Durban, South Africa

Amit Kumar Garg
Electronics and Communication Engineering
Indian Institute of Information Technology Kota
Jaipur, India

ISSN 1876-1100 ISSN 1876-1119 (electronic)
Lecture Notes in Electrical Engineering
ISBN 978-981-19-1644-1 ISBN 978-981-19-1645-8 (eBook)
https://doi.org/10.1007/978-981-19-1645-8

This Springer imprint is published by the registered company Springer Nature Singapore Pte Ltd.
The registered company address is: 152 Beach Road, #21-01/04 Gateway East, Singapore 189721, Singapore

Preface

Optical and wireless technologies are advancing at an accelerating rate recently. The traditional approaches to providing high data rates to the masses are transforming and expanding in a way that is beyond our imagination. The challenges in providing uninterrupted data and broadband communications have not changed. Our mission as a technical community is to understand these challenges and find ways to mitigate them. This includes the development and management of appropriate channels, novel devices, new protocols, efficient networks, and their integration. Keeping in view the amalgamation of these issues, the proceedings of 5th International Conference on Optical and Wireless Technologies (OWT 2021) is being presented herewith.

Due to outbreak of COVID-19 pandemic, the conference (OWT 2021) was organized online during October 09–10, 2021, as per guidelines of GOI. A total of 160 participants including the invited speakers, contributing authors, and attendees participated in the conference. The participants were explored to broad range of topics critical to our society and industry in the related areas. The conference provided an opportunity to exchange ideas among global leaders and experts from academia and industry in topics like optical materials, optical signal processing and networking, photonic communications systems and networks, all-optical systems, microwave photonics, optical devices for optical communications, nonlinear optics, nanophotonics, software-defined and cognitive radio, signal processing for wireless communications, antenna systems, spectrum management and regulatory issues, vehicular communications, wireless sensor networks, machine-to-machine communications, cellular-WiFi integration, etc.

Apart from high-quality contributed paper presented by delegates from all over the country and abroad, the conference participants also witnessed the informative demonstrations and technical sessions form the industry as well as invited talks from renowned experts aimed at advances in these areas. Overall response to the conference was quite encouraging. A large number of papers were received. After a rigorous editorial and review process, 52 papers were invited for presentation during the conference. Among the presented papers, 51 papers were selected for inclusion in the conference proceedings. We are confident that the papers presented in this

proceeding shall provide platform for young as well as experienced professionals to generate new ideas and networking opportunities.

The editorial team members would like extend gratitude and sincere thanks to all contributed authors, reviewers, panelist, local organizing committee members, and the session chair for paying attention to the quality of the publication. We are thankful to our sponsors for generously supporting this event. In the last, we pay the highest regard to the Irisworld Science & Technology Education and Research (IRISWORLD), a "Not for Profit" society from Jaipur for extending support for financial management of the OWT 2021.

Best Wishes from:

Manish Tiwari
Yaseera Ismail
Karan Verma
Amit Kumar Garg

Acknowledgments

The editors wish to extend heartfelt acknowledgment to all contributing authors, esteemed reviewers for their timely response, members of various organizing committee, and production staff whose diligent work put shape to the OWT 2021 proceedings. We especially thank our dedicated reviewers for their volunteering efforts to check the manuscript thoroughly to maintain the technical quality and for useful suggestions.

We also pay our best regards to the faculty members from institutional partners (MNIT Jaipur and Manipal University Jaipur) for extending their enormous assistance during the conference-related assignments especially to Dr. Dinesh Yadav from Manipal University Jaipur, Dr. Ashok Kumar, Jitendra Deegwal from Government Women Engineering College Ajmer, Mr. Nidhish Tiwari from MNIT Jaipur, Mr. Ramesh Dewanda, Executive Member, Irisworld Society, Jaipur, and Sh. Narendra Godara from MNIT Jaipur.

In last, we extend our sincere thanks to Springer for agreeing to be our publishing partner. Specially, the efforts made by Swati Meherashi, Senior Editor, Kamiya Khatter, Editor, and Sushmitha Shanmuga Sundaram, Project Coordinator—Total Service, Books Production are highly appreciable.

Manish Tiwari
Yaseera Ismail
Karan Verma
Amit Kumar Garg

Conference Committee Members

Organizing Committee

General Chairs

Ghanshyam Singh	MNIT Jaipur, India
Manish Tiwari	Manipal University Jaipur, India
J. K. Deegwal (Principal)	GWEC Ajmer, India
Moustafa Hussein	AASTMT, Egypt

Organizing Chairs

Ravi Kumar Maddila	MNIT Jaipur
Amit Kumar Garg	IIIT, Kota
Sanjeev Kumar Metya	NIT Arunachal Pradesh
Nikhil Deep Gupta	VNIT Nagpur
Ashok Kumar	GWEC Ajmer

Organizing Secretaries

Rakesh Ranjan	NIT Patna
Mukesh Gupta	MBM Jodhpur
Ashish Kumar	JECRC Jaipur
Arjun Kumar	Bennett University
Dinesh Yadav	Manipal University Jaipur

IETE Oversight Committee

Deepak Bhatnagar	FIETE
S. K. Bhatnagar	FIETE
K. M. Bajaj	FIETE

Media and Publicity Committee

Karan Verma (Chair)	NIT Delhi
Arjun Kumar (Co-chair)	Bennett University
Ankur Saharia	Manipal University Jaipur
Nitesh Mudgal	MNIT Jaipur

Sponsorship Committee

Ashok Kumar (Chair)	GWEC Ajmer
Pankaj Verma (Co-chair)	NIT Kurukshetra
Dinesh Yadav	Manipal University Jaipur
Monika Mathur	SKIT Jaipur
Rakesh Ranjan	NIT Patna

Registration Committee

Ankur Saharia (Chair)	Manipal University Jaipur
Ravi Kumar Maddila	MNIT Jaipur
Nidhish Tiwari	CITM Jaipur
Nitesh Mudgal	MNIT Jaipur
Shweta Mittal	Manipal University Jaipur

Publication Committee

Amit Kumar Garg	IIIT, Kota
Nikhil Deep Gupta	VNIT Nagpur
Ashish Kumar	JECRC Jaipur
Kamal Kishore Choure	MNIT Jaipur

Hospitality Committee

Kapil Saraswat (Chair)	Central University Rajasthan
Mukesh Kumar Gupta	MBM Jodhpur
Narendra Kumar Godara	MNIT Jaipur
Ankit Agrawal	SKIT Jaipur
Bipin Kumar Saw	MNIT Jaipur

International Advisory Committee

Hiroyuki Tsuda	Keio University, Japan
Ali Gharsallah	University of Tunis E. M., Tunisia
Buryy Oleh Anatolievyach	LPNU, Ukraine
Ajoy Kar	HW University Edinburgh UK
Suchandan Pal	CEERI Pilani, India
Jagannath Malik	SB Solutions Inc., Gangnam, Seoul, South Korea
Kolin Poul	IIT Delhi, India
Konstantin Kozadaev	BSU, Minsk, Belarus
Mário F. S. Ferreira	University of Aveiro, Portugal
Miklos Veres, HAS	Budapest, Hungary
Sergii Ubizskii	LPNU, Ukraine
Ashwini Kumar Arya	Kyung Hee University, Gyeonggi, South Korea
Yuri Shpolyanskiy	University of Saint Petersburg, Russia
Yaseera Ismail	UKZN Durban, South Africa
Aulia M. T. Nasution	ITS Surabaya, Indonesia
Agus Muhamad Hatta	ITS Surabaya, Indonesia

Technical Program Committee

Akshay Kr. Rathore	Concordia University, Canada
Takasumi Tanabe	Keio University, Japan
Toshiharu Saiki	Keio University, Japan
Ratnajit Bhattacharya	IIT Guwahati
Fazal Talukdar	NIT Silchar
Bishnu Prasad Gautam	WAKHOK, Japan
Reza Abdi-Ghaleh	University of Bonab, Iran
Kalpana Dhaka	IIT Guwahati, India
Upena D. Dalal	SVNIT, Surat
Manish Mathew	CEERI Pilani, India
Preetam Kumar	IIT Patna

C. Periasamy	MNIT Jaipur
Seema Verma	Banasthali University
Narendra Kumar Yadav	Manipal University Jaipur
Rekha Mehra	GEC Ajmer
Bramha P. Pandey	MMMUT Gorakhpur
Sanyog Rawat	Manipal University Jaipur
Lokesh Tharani	RTU, Kota
Girish Parmar	RTU, Kota
Anil Yadav	Amity University Gurgaon
Nagesh Janrao	Government Polytechnic, Pune

Our Reviewers

Surendra Agarwal	Government Women Engineering College, Ajmer
Ashwini Arya	Kyung Hee University
Ramesh Battula	Malaviya National Institute of Technology Jaipur
Sudhir Bhaskar	Indian Institute of Technology BHU, Varanasi
Jaiverdhan Choudhary	Jaipur Engineering College and Research Center
Ajay Dadhich	Government Engineering College Ajmer
Jitendra Deegwal	Government Engineering College Ajmer, Rajasthan
Tarun Dubey	Manipal University Jaipur
Mukesh Gupta	MBM Engineering College Jodhpur
Nikhil Deep Gupta	Visvesvaraya National Institute of Technology, Nagpur
Tawfik Ismail	Cairo University
Sheilza Jain	YMCA University of Science and Technology
Anshul Jaiswal	Indian Institute of Technology Roorkee
Nagesh Janrao	Technical Education
Amit Joshi	Malviya National Institute of Technology
Arshpreet Kaur	National Institute of Technology, Delhi
Arjun Kumar	Bennett University, Greater Noida
Trivesh Kumar	Indian Institute of Information Technology, Design and Manufacturing
Ravi Maddila	Malaviya National Institute of Technology Jaipur
Saurabh Maheshwari	Government Women Engineering College Ajmer
Sandeep Mandia	Government Mahila Engineering College, Ajmer
Abhilash Mandloi	S.V. National Institute of Technology Surat
Manish Mathew	CEERI Pilani
Monika Mathur	Rajasthan Technical University
Arka Prokash Mazumdar	Malaviya National Institute of Technology
Sanjeev Metya	National Institute of Technology Arunachal Pradesh
Satyasai Jagannath Nanda	Malaviya National Institute of Technology Jaipur
Malaya Nath	National Institute of Technology Puducherry
Ankit Pandey	Bennett University, Greater Noida

Pravin Prajapati	Gujarat Technological University
Sanyog Rawat	Manipal University
Ankur Saharia	Malviya National Institute of Technology
Sourabh Sahu	Jabalpur Engineering College
Kapil Saraswat	Central University of Rajasthan, Ajmer
Indra Bhooshan Sharma	Malviya National Institute of Technology Jaipur
Jankiballabh Sharma	Rajasthan Technical University
Saurabh Shukla	Indian Institute of Technology Kanpur
Hardeep Singh	Thapar Institute of Engineering and Technology, Patiala
Mandeep Singh	NIT Karnataka
Satyanand Singh	Fiji National University
Sukwinder Singh	NIT, Jalandhar
Sarthak Singhal	Malaviya National Institute of Technology Jaipur
Manisha Upadhyay	Nirma University
Karan Verma	Universiti Teknologi Petronas
Pankaj Verma	National Institute of Technology, Kurukshetra
Seema Verma	University Banasthali Vidyapith
Anurag Vidyarthi	Graphic Era University, Dehradun
Rajesh Vishwakarma	Jaypee University of Engineering and Technology (JUET)
Kirti Vyas	ACEIT, Kuaks, Jaipur
Sandeep Vyas	Jaipur Engineering College & Research Centre
Ajay Yadav	Bennett University
Dinesh Yadav	Manipal University Jaipur
Menka Yadav	MNIT Jaipur

Invited Speakers

Exotic Wave-Matter Interactions in Metamaterials Based on Broken Symmetries

Andrea Alù
CUNY Advanced Science Research Center

Biography: Andrea Alù is Founding Director and Einstein Professor at the Photonics Initiative, CUNY Advanced Science Research Center. He received his Laurea (2001) and Ph.D. (2007) from the University of Roma Tre, Italy, and, after a postdoc at the University of Pennsylvania, he joined the faculty of the University of Texas at Austin in 2009, where he was Temple Foundation Endowed Professor until January 2018. Dr. Alù is Fellow of NAI, MRS, AAAS, IEEE, AAAS, OSA, SPIE, and APS and has received several scientific awards, including the Blavatnik National Award in Physical Sciences and Engineering, the AAAFM Heeger Award, the Dan Maydan Prize in Nanoscience, the IEEE Kiyo Tomiyasu Award, the Vannevar Bush Faculty Fellowship from DoD, the ICO Prize in Optics, the NSF Alan T. Waterman award, the OSA Adolph Lomb Medal, and the URSI Issac Koga Gold Medal.

Compact Antenna for High-Speed Communications

Jagannath Malik
Ulsan National Institute of Science and Technology

Biography: Dr. Jagannath Malik obtained his doctoral degree from IIT Roorkee, India. He is currently Team Lead (sensor development) at SB Solutions Inc., Seoul, South Korea. He is involved in developing RF-based biosensors for biomedical applications. Prior to this, he was associated with UNIST, South Korea, for the development of near-field wireless power transfer systems and communication systems. He has contributed toward the developed of state-of-the-art antenna solutions for enabling communications in RF shielded environments and marine ships.

A Network of Cooperative Routers to Distribute Live Multimedia Content over the Internet

Leandro Melo de Sales
Federal University of Alagoas, Brazil

Biography: Leandro Melo de Sales received his Ph.D. (2014) and Master Degree (2008) in Computer Science, Federal University of Campina Grande (UFCG), and BSc (2006) in Computer at Federal University of Alagoas (UFAL), Brazil. He is currently Adjunct Professor of the Computing Institute at Federal University of Alagoas, Brazil. His research interests include computer networks, distributed systems, cloud computing, and scalable systems.

Optically Transparent Antennas- An Overview

Edgar Colín-Beltrán
INAOE in Puebla, Mexico

Biography: He obtained his bachelor in Electronics Engineering and the medal Ignacio M. Altamirano given by the UAEM to the highest grade in each department in 2004. He obtained his M.Sc. in Electronics and his Ph.D. in Astronomical Instrumentation in 2007 and 2013, respectively, at INAOE in Puebla, Mexico. During his Ph.D., Edgar was Visitor Researcher at UCLA in 2011 working with Prof. Tatsuo Ito. In 2013, he occupied a postdoctoral position at University of Cambridge, UK, working in the antenna design for the mid-Freq instrument of the SKA. In 2015, Edgar joined the industry at Intel Labs in Guadalajara working in communications component development. And from 2017, he has been assigned by the CONACYT to the Large Millimeter Telescope group at the Astrophysics Department in INAOE for developing new astronomical instrumentation in the millimeter range. Edgar interests are mainly in passive component design and implementation from microwave to millimeter ranges.

Advances in Plasmonic Sensors for Biomedical Applications

Santosh Kumar
Liaocheng University, China

Biography: Santosh Kumar received the Ph.D. degree from IIT (ISM) Dhanbad, Dhanbad, India. He is currently Associate Professor with the School of Physics Science and Information Technology, Liaocheng University, Liaocheng, China. He has received an international travel grant from SERB-DST, Government of India, in 2016. He has guided seven M.Tech. dissertations and six Ph.D. candidates. He has published more than 140 research articles in national and international SCI journals and conferences. He has presented many articles at conferences held in Belgium and USA. He has published two books entitled Fibre Optic Communication: Optical Waveguides, Devices and Applications (University Press, 2017), India, and another book entitled 2D Materials for Surface Plasmon Resonance-Based Sensors (CRC Press, Taylor & Francis Group, 2021). He has reviewed more than 600 SCI journals of IEEE, Elsevier, Springer, OSA, SPIE, and Nature. His current research interests include optical fiber sensors, nano and biophotonics, terahertz sensing and spectroscopy, and waveguide and interferometer. He is Life Fellow Member of the Optical Society of India (OSI) and Senior Member of IEEE, OSA, and SPIE. He is also Traveling Lecturer of OSA. Recently, he has nominated for Chief-Elect of OSA Optical Biosensors Technical Group. He has delivered many invited talks and serves as Session Chair of IEEE conferences. He is also Associate Editor of the IEEE SENSORS JOURNAL, IEEE ACCESS, IEEE TRANSACTIONS ON NANOBIOSCIENCE, and Biomedical Optics Express.

Power Estimation for On-Chip Network

Mushtaq Ahmed
MNIT Jaipur, India

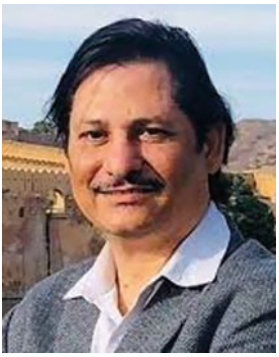

Biography: Dr. Mushtaq Ahmed is Faculty for past 22 years in Computer Science and Engg. Department. He did Ph.D. from MNIT in 2012. He is teaching various courses like computer networks, advanced microprocessors, computer architecture, embedded system design, operating systems, VLSI algorithms digital logic design, etc. His research areas are network of chip, wireless networks, cloud computing, embedded system design, and image processing. Presently, he is guiding research in network on chip and other areas of interest such as high-speed overlay networking, fault-tolerant systems, wireless sensor networks, and multi-core and cloud computing. Dr. Mushtaq is Member IEEE, Member IEANG, and Life Member of ACM.

Contents

About the Editors

Dr. Manish Tiwari 2020 OSA Ambassador, IEEE Rajasthan Subsection Chairperson, and SPIE Community Champion, Dr. Manish Tiwari received Ph.D. in ECE in the field of Photonics from MNIT Jaipur. Presently, he is Professor and Head of Department of ECE at Manipal University Jaipur. He has more than 22 years of professional experience in various colleges and universities of repute. He has published more than 100+ research papers in reputed journals and conferences and more than 15 chapters. He has also authored and edited more than around a dozen of books. He has also supervised more than 29 projects sponsored by DST Rajasthan. He is Principal Investigator in a BRICS project on Quantum Satellite and Fiber Communication (QuSaF) along with research partners in UKZN, Durban; PSUTI, Samara; and USTC, Shanghai. He has also served on panel of experts and Editor in various workshops by CSTT, MHRD, Govt. of India.

He has been Visiting Researcher to City University, London, under UKIERI project in Microstructured Optical Fibers during 2010 and 2011 and Tsinghua University, Beijing, during 2016. Dr. Tiwari has presented talks in PIERS at NTU, Singapore; APMP at PolyU, Hong Kong; TJMW at KMUT, Bangkok; and Kasetsart University, Bangkok; City University, London, and several UKIERI workshops. He is on the panel of Traveling Lecturer Program of reputed societies like SPIE (USA) and OSA (USA) under which he has delivered invited talks in USTC, Shanghai; UESTC, Chengdu; Tsinghua University, Beijing; ITS Indonesia, and University of KwaZulu-Natal, Durban

(SA) on photonics technologies and career development. He has been Technical Program Committee Member of many IEEE conferences and Reviewer of IEEE/Elsevier/OSA/Springer/T&F journals.

He is Senior Member of IEEE Photonics Society, Communication Society, Broadcast Technology Society, Antenna and Propagation Society; Life Fellow of the Optical Society of India (OSI-India); Senior Member of OSA; Member of SPIE; and Fellow of Institution of Electronics and Telecommunication Engineers (IETE), India. His current research interest includes micro/nanostructure photonic devices, photonic ICs, fiber optics, numerical modeling, nonlinear optics, and photonic crystal fibers.

Dr. Yaseera Ismail is Senior Lecturer of Physics within the School of Chemistry and Physics at the University of KwaZulu-Natal, South Africa, and leads the experimental activities within the Quantum Research Group. She obtained her MSc Cum Laude based at the CSIR National Laser Centre and holds a Ph.D. in Quantum Physics from the University of KwaZulu-Natal, South Africa. Dr. Ismail is a 2016 TechWomen Emerging Leader awarded by the United States Department of States, and in 2018, she was chosen as the Optical Society of America (OSA) Ambassador, which is a lifetime achievement award for young researchers excelling in photonics. Dr. Ismail was awarded in 2020 the DHET Future Professor Fellow, which recognizes the top young researchers in South Africa. Dr. Ismail's research is based on the advancement of quantum technology, specializing in improving optical techniques for quantum communication.

Dr. Karan Verma is working as Assistant Professor in Computer Science and Engineering Department, NIT Delhi, as well worked as Assistant Professor in Computer Science and Engineering Department, Central University of Rajasthan in December 2015 to March 2018. He received his B.E and M.Tech. degrees in Information Technology and Computer Science & Engineering, respectively, from the University of Rajasthan, in 2008, and Indian Institute of Technology Roorkee, in 2010. He received his Ph.D. degree from Department of Computer and Information Science at the Universiti Teknologi PETRONAS, Malaysia, in 2015 and Postdoc (PDF) in Computer Science & Engineering from University of Californian, Davis, USA. Dr. Verma received 3 times IETF, one time IEEE-IETF, one time ICANN fellowship, and one time DAAD fellowship. He has completed six projects and two are ongoing. Dr. Verma has supervised four PhD and 20 master students. His research interests include information security, wireless sensor networks, and VANET.

Dr. Amit Kumar Garg is Assistant Professor in Dept. of Electronics & Comm. Engineering, Indian Institute of Information Technology, Kota, India. He obtained his Ph.D. from the Department of Electronics and Communication Engineering at Malaviya National Institute of Technology (MNIT), Jaipur, India, in 2018. He received B.E. and M.Tech. in ECE from the University of Rajasthan and MNIT Jaipur in 2009 and 2013, respectively. His current research interest includes fiber optics and photonics including smart, flexible, energy-efficient, and latency-aware optical access networks and high-speed gigabit passive optical networks. He also works on the latest information and communication technologies for developing smart cities, buildings, etc. He is Active Member of SPIE and OSA. He is Recipient of SPIE officer travel grant. He has been associated with the previous OWT conferences OWT 2018, OWT 2019, and OWT 2020 in various capacities such as Organizing Secretary, Convener, and Editor. He also coordinated, AICTE ATAL Sponsored One Week Online FDP on ***Advanced Optical Access Networks and its Role in Smart Cities*** during November 23–27, 2020, at IIIT, Kota (virtual mode).

Design and Analysis of All-Optical Universal Logic Gates Using 2D Silicon Photonic Crystal Structures

Anushka Lucas, R. Narayanan, and Nikhil Deep Gupta

Abstract With the continuous increase in the demand for higher computational speeds, photonics-based Integrated Circuits (ICs) are becoming more vital for future computational technologies. For designing Photonic ICs there is a requirement to have logic gates that can work in all-optical domain. The proposed work presents the design and numerical analysis of All-Optical universal logic gates including NAND, NOR, and NOT gates that are realized using 2-D Silicon periodic nanophotonic structures through light beam interference-effect. 2D Photonic crystals through photonic bandgap optimization, make it possible to reduce the losses incorporated during the propagation of light. The structures are designed to operate at 1.55 μm. The present work demonstrates an unpretentious but effective approach for designing the all-optical universal logic gates. The design has shown good transmission efficiency for all the input combinations of the logic gates and thus can be used to design other forms of logic gates and circuits, further.

Keywords Photonic crystals · Optical logic gates · Silicon photonics · Universal logic gates

1 Introduction

Conventionally, from past several decades, electrons are the preferred choice to make information flow from one place to another through semiconductor transistor-based devices, but as they are reaching the pinnacle of their performances in terms of limitations such as power dissipation, input power requirement, and delay, one has to look for the alternatives. To overcome the mentioned limitations, photonics-based designs can come to the rescue. There are a lot of concentrated efforts going on

A. Lucas
Centre for Nanoscience and Genomics, Karunya Institute of Technology and Sciences, Coimbatore, India

R. Narayanan · N. D. Gupta (✉)
Centre for VLSI and Nanotechnology, Visvesvarya National Institute of Technology, Nagpur, India
e-mail: nikhildeepgupta@cvn.vnit.ac.in

M. Tiwari et al. (eds.), *Optical and Wireless Technologies*, Lecture Notes in Electrical Engineering 892, https://doi.org/10.1007/978-981-19-1645-8_1

all around the globe to design all-optical Photonic Integrated Devices and circuits [1]. In that regard, all-optical logic gates (AOLGs) have to compulsorily evolve and required to make its mark for the development of futuristic technologies like optical computers, optical networks etc.

On the other hand, Photonic crystal (PhC), a periodic dielectric nanophotonic sub-wavelength structure, in the past decade or so has shown its immense potential to manipulate light beyond fundamental principles [2]. PhC structures are also known as semiconductors of light as they can control the propagation of light. 3D PhCs can allow full control over the photons transmission in all directions. PhC structure has a periodic arrangement of two different materials of a particular refractive index. Due to the periodic arrangement, they lead to the generation of photonic band gaps that implies that the device does not allow a certain range of wavelengths to travel through it [3]. Many insects such as butterflies and peacock's feathers have naturally occurring PhC structures due to which we can see beautiful colours in their wings and feathers.

The PhC-based AOLGs have numerous advantages [4–9]. Because of their remarkable ability to manipulate the density of states for photons at particular wavelengths, these structures give the freedom to open photonic bandgaps as per the requirement of application and can be a perfect ingredient for the realization of integrated all-optical devices. AOLGs based on these periodic sub-wavelength structures are thus realistically promising for practical on-chip applications.

In the present paper, we are presenting the design and analysis of a 2-D Silicon PhC based Universal AOLGs i.e. NAND, NOR and NOT gate based on light beam interference-effect. The devices are designed on the Si platform to make it compatible with Si photonic integrated circuits. The design has been realized with Si based PhC waveguide having optimized defects created in it that make these AOLGs simple and at the same time easy to design practically. The results have demonstrated the good transmission efficiency for all the input combinations and thus it is predicted that it can be a good option to fit in with the Si-based photonic integrated circuits. It has also been observed that for the operation of these AOLGs, high power excitation is not required.

2 Structure Design and Numerical Analysis

In the projected design, All-optical Universal Logic Gates i.e. NAND, NOR and NOT gates are realised based on waveguide defects created by light beam interference effect [7]. The 2D PhC are preferred over 3D designs because of the owning to the bigger chances of their replication for mass productions. The schematic structure of the proposed 2-D PhC is shown in Fig. 1(a). The structure is composed of hexagonal lattice arrays of cylindrical Si rods considered to be placed in the air as a background medium. The structure is optimized on the premise of the band diagram as given in Fig. 1(b).

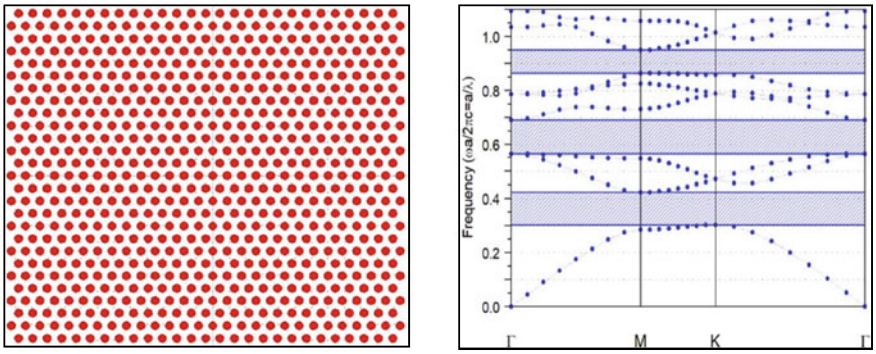

(a) (b)

Fig. 1 **a** Schematic diagram of 2-D PhC taken as a base for the proposed AOLGs designs; **b** Photonic band diagram for the structure shown in 1(a)

The optimized lattice constant for the structure is then taken as 0.875 um and the Si rods radius is considered as 0.2475 um as it suits the design requirement to work at 1550 nm. The area of PhC calculated is 1.4051 μm^2. As the design is set to work at 1550 nm, the Si relative permittivity is set at 11.56 [7]. A continuous-wave (CW) light source at a wavelength of 1550 nm is used as an input. The parameters of the optimized structure are listed in Table 1.

There are various numerical modelling techniques that has been used over the years for the modelling of photonic devices such as Finite-Difference Time-Domain (FDTD) Method, Plane Wave Expansion (PWE) Method, Beam Propagation Method, Finite-Element Method, etc. [10]. Although, all the different techniques are having their own advantages, out of them few techniques have shown more adaptability on account of their applicability for numbers of applications and those techniques involved FDTD and PWE method [9]. In the present work, FDTD and PWE methods are getting used for the optimization of the design and its analysis. During this research work, commercially available Synopsys Rsoft CAD tools has been used, which are supported by the concepts of FDTD and PWE algorithms [11].

The PWE technique is commonly used to obtain dispersion relation and mode profiles for PhC structures. PWE is traceable to analytical formulations and is useful in calculating Maxwell's modal alternatives over an inhomogeneous or regular geometry, it is a technique of the frequency domain in which Bloch principle is employed

Table 1 Parameters used for the design of proposed basic 2-D Si PhC platform for the design of AOLGs

S. no	Parameters	Value
1	Background medium index	1 (Air)
2	Rod index at 1550 nm	11.56 (Si)
3	Lattice constant or period	875 nm
4	Radius of rods	247.5 nm

to deal with the issues of its own value and answers are acquired as a plane wave superposition. The FDTD method, which is one of the most reliable and rigorous method to provides a solution to Maxwell's equations, has been used in the present case as it does not have any approximations or theoretical restrictions and is reliable being used throughout the optics and photonics research community.

3 Design Procedure and Optimization

The section discusses about the design aspects specific for the particular logic gate. The universal optical gates that we are going to discuss, are NOT, NAND and NOR gates. The input source is taken as continuous wave (CW) source at 1550 nm with input launch power of 1 W for all the cases. Defects are created in the structure shown in Fig. 1(a) to create a Y-shape junction, which is in the proposed logic gate designs taken as a basic building block and modified to get different operations. The Y-shaped structure is shown in Fig. 2.

3.1 NOT Gate

The study and analysis of an optical NOT logic gate is realized by modifying the Y-shape junction such that the reference light (RC) waveguide would become longer than the input waveguide (AC) as shown in Fig. 3. A CW reference light of 1550-nm wavelength is given at into the port R to travel through waveguide RC, whereas the input is applied at port A.

At first, when there is no input signal at port A, this allows the reference beam introduced through port R to propagate through RC and the output, then, produced

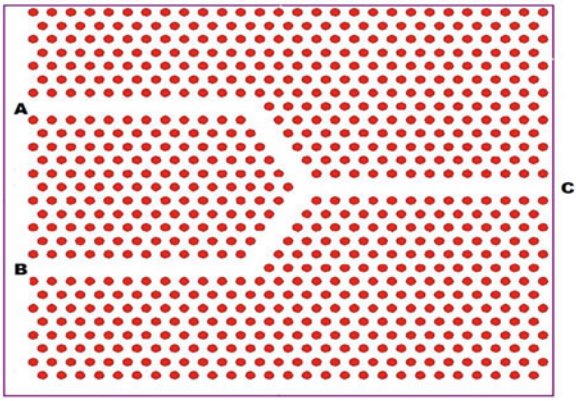

Fig. 2 Schematic diagram of basic Y-shaped junction waveguide used to design AOLGs

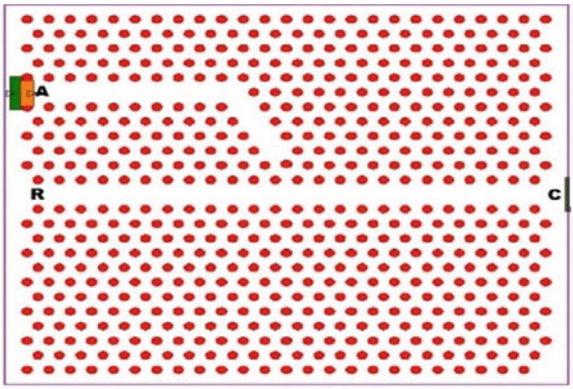

Fig. 3 Schematic diagram of proposed NOT gate

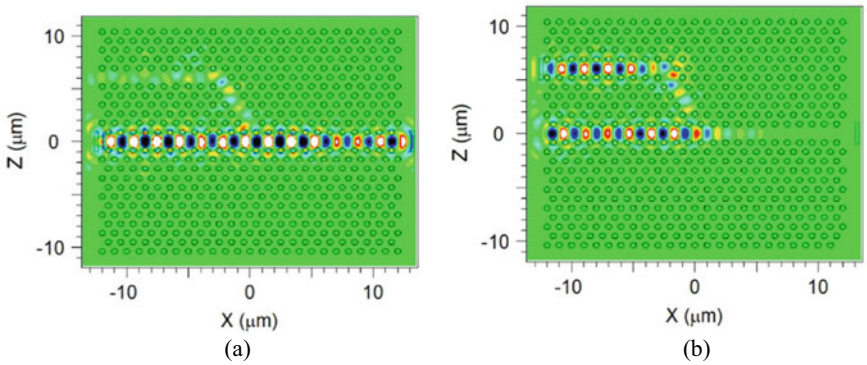

Fig. 4 Observed field distributions for the proposed NOT AOLG at steady state, **a** when no signal applied at port A, **b** when the input beam injected into port A

at port C, as shown in Fig. 4(a), corresponds to the logical operation of "0 NOT = 1". The transmission percentage observed at port C is around 85%. The transmission percentage has been calculated as the percentage of input received as compared to the input launch. Next, when an input signal is fed to port A, leads to destructive interference between the signals given at port A and port R that occurs due to the as such designing of the structure, as they travel toward the output port across defect waveguide. There is, then, no signal received at the output port that can be seen from Fig. 4(b) and corresponds to the logical operation "1 NOT = 0". From the two operations mentioned above, it can be said that the proposed design can work reasonably well as NOT AOLG. The transmission percentage calculated at output port for low logic is only 0.11%. The truth table with transmission ratio for the proposed NOT AOLG is given in Table 2.

Table 2 Truth table for realized NOT AOLG with transmission percentage

Input (A)	Output (C)	Transmission %
0	1	85
1	0	0.11

3.2 NAND Gate

To design and study the 2 input NAND AOLG function, the path length for the input optical signal in waveguide AC is made larger than that in RC, whereas the signal in waveguide BC is made to travel less than that in RC by one lattice constant (period of PhC structure). The design is used to make sure that there are sufficient constructive and destructive interferences to take place to achieve required logic operations. In this case too, A CW at 1550-nm wavelength is fed into the reference port R to travel through RC. The reference beam fed to port R has double the power as that of the input signals fed at port A and B, separately. The proposed schematic of the NAND AOLG is shown in Fig. 5.

When there is no input given at ports A and B, then the reference signal fed at port R can propagate across RC and the output signals are observed at port C, as shown in the Fig. 6(a) that resembles the logical operation "0 NAND 0 = 1". Very small back reflections are observed at port A and B. The transmission percentage calculated for the corresponding logic operation at output is 85%. Now, when the optical signal is fed at input port A with no signal at port B (A = 1 and B = 0), then input signal while propagating through the waveguide lead to the destructive interference when interacts with reference beam. However, as the reference signal given at port R has double the power as that of signal, the output signal with sufficient transmission percentage is observed at port C, as shown in Fig. 6(b). This process is equivalent to the logical operation "1 NAND 0 = 1". The transmission percentage calculated for the corresponding logical operations is 86%.

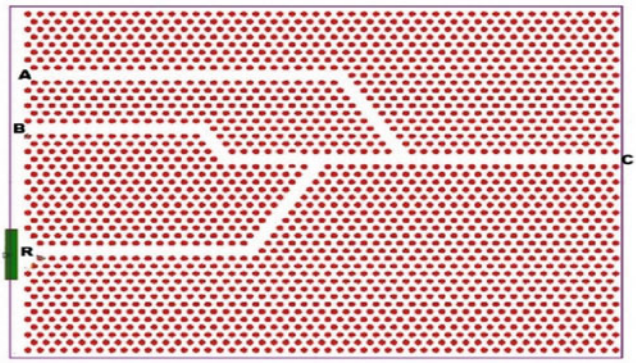

Fig. 5 Schematic diagram of proposed NAND Gate

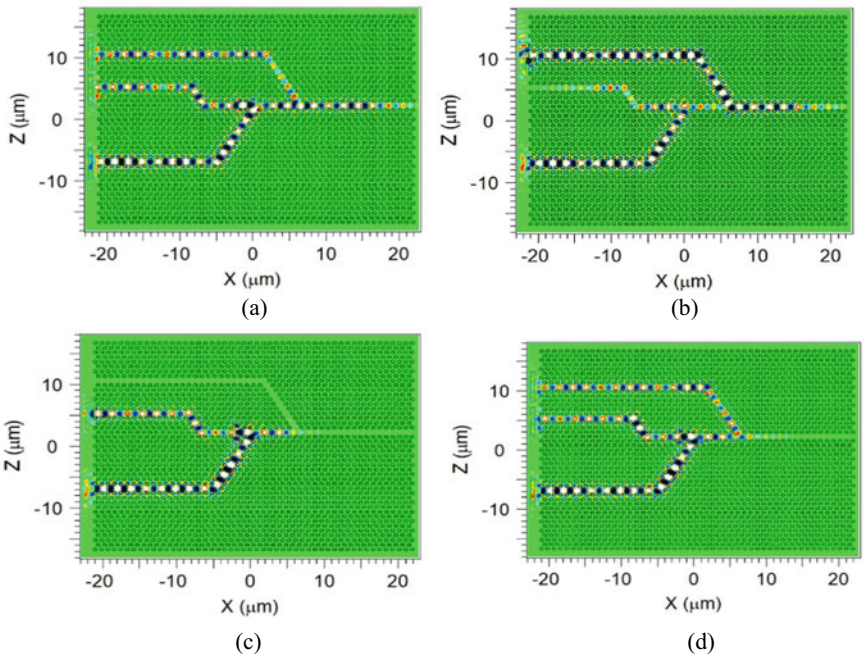

Fig. 6 Observed field distributions for the proposed NAND AOLG at steady state, **a** when both A = B = 0; **b** when A = 1 and B = 0; **c** When, A = 0 and B = 1; **d** When, A = 1 and B = 1

Now, for the case, when B = 1 and there is no signal at port A. In that case, destructive interference takes place between the signal fed at port B and reference fed at port R as they interact with each other during forward propagation, as discussed above.

However, as the feed at port R has double the power that of the input at port B, the high output is observed at port C, as observed in Fig. 6(c), which is equivalent to the logical operation "0 NAND 1 = 1". The transmission percentage calculated is 86%. Lastly, for the case when signal is applied at both port A and B, then the three signals (two input and one reference) when interact with each other during forward propagation undergo destructive interference due to the as such design of the device. However, in this case, as the reference beam power is equal to the summation of the power of two input signals, there's no output observed at port C, as observed in Fig. 6(d). The entire process resembles to the logical operation of "1 NAND 1 = 0". The truth table for the proposed NAND AOLG with transmission values are given in Table 3.

Table 3 Truth table for realized NAND AOLG with transmission percentage

Input A	Input B	Output C	Transmission %
0	0	1	85
1	0	1	86
0	1	1	86
1	1	0	0.1

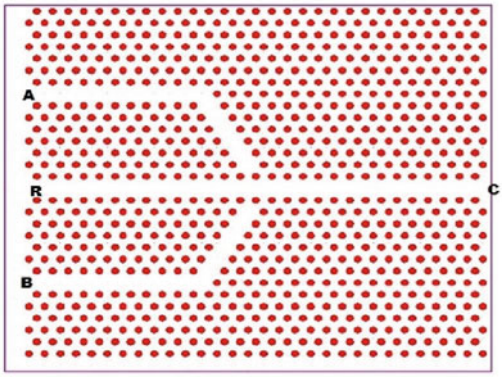

Fig. 7 The proposed schematic diagram of the NOR AOLG

3.3 NOR Gate

A 2 input NOR AOLG is realized by modifying the Y-shape junction (Fig. 2) such that the reference light waveguide (RC) is longer than the input waveguides (AC, BC). Here also, 1550-nm CW is used as the reference signal that is fed at port R. The reference signal fed at port C is fed with double the power than the signal fed at port A and B, separately. The proposed NOT AOLG schematic is shown in Fig. 7.

When there is no input signal at port A and B (A = 0 and B = 0), the reference fed at port R can propagate through waveguide RC and output is observed at port C, as shown in the Fig. 8(a), which resembles the logical operation "0 NOR 0 = 1". Now, when the light is fed at port A only (A = 1 and B = 0), without any signal at port R, the output signal received is approximately negligible, as shown in Fig. 8(b). The process is equivalent to the logical operation "1 NOR 0 = 0". The transmission percentage calculated for the corresponding logic operations is 0.11% only. Next, when there is signal applied at input port B without any input at port A and R. Again, the output signal observed is negligible, as observed in Fig. 8(c), and matches with the logical operation "0 NOR 1 = 0". The transmission percentage in this case is also only around 0.11%. Finally, when signals are fed at both the input ports together with signal at port R, destructive interference is observed among the signals in the output waveguide and as a result there is no significant signal output observed at port C, as can be seen from Fig. 8(d) that matched with the logical operation "1 NOR

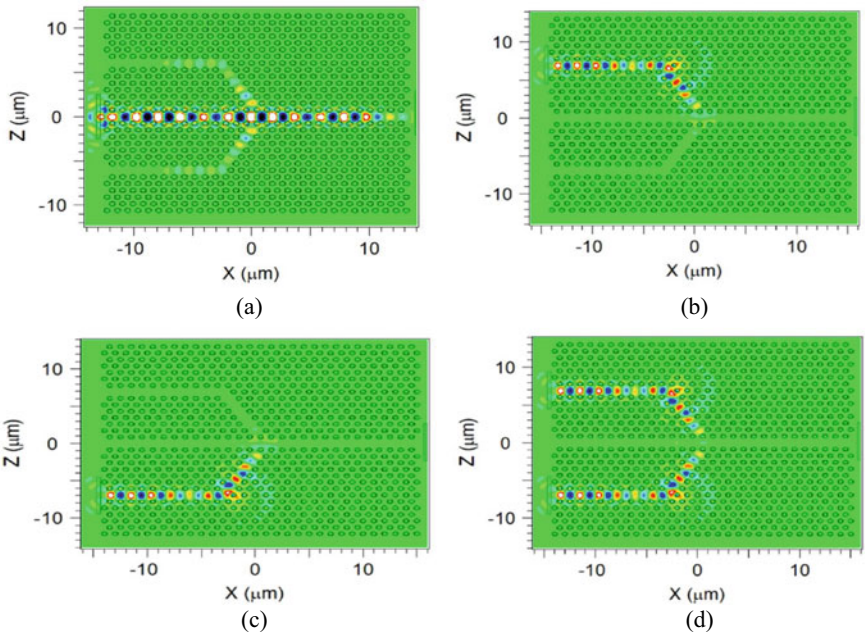

Fig. 8 Observed field distributions for the proposed NOR AOLG at steady state. **a** When both A = B = 0; **b** When A = 1 and B = 0; **c** When, A = 0 and B = 1; **d** When, A = 1 and B = 1

Table 4 Truth Table for realized NOR AOLG with transmission percentage

Input A	Input B	Output C	Transmission %
0	0	1	80
1	0	0	0.1
0	1	0	0.1
1	1	0	0.1

1 = 0". The proposed design can perform all the required operations for the NOR gate using light, thus can be termed as NOR AOLG. The transmission percentage calculated for the corresponding logic operations in this case is also less than 0.2%. The truth table for the proposed 2-input NOR AOGL operation is given in Table 4.

4 Conclusion

The presented work has demonstrated a simple but effective design for a universal all-optical gate including NAND, NOR, and NOT gates. The transmission losses are controlled through the incorporation of the subwavelength structures designed with 2D PhC structures. The numerical simulation studies are done for the different input

signals and the transmission percentage is calculated. For all the three logic gates operations, the observed transmission percentages have shown good contrasts for the logic high and low output. For 'OFF' or '0', the output transmission percentage observed is less than even 1% and for 'ON' or '1' it is in all the cased is more than 80%. The used 2D PhC structures in the proposed designs are supposed to be done over the Si platform and therefore, has a realistic potential for Si photonics-based on-chip applications, that can be designed with current microfabrication techniques, including electron-beam lithography processes etc.

References

1. Pirzadi M, Mir A, Bodaghi D (2016) Realization of ultra-accurate and compact all-optical photonic crystal or logic gate. IEEE Photonics Technol Lett 28(21):2387–2390
2. De Tommasi E, Esposito E, Romano S et al (2021) Frontiers of light manipulation in natural, metallic, and dielectric nanostructures. Riv Nuovo Cim 44:1–68
3. Noda S, Mahi FT, Zappe H (2016) Photonic crystal in reference module in materials science and materials engineering
4. Joannopoulos JD et al (2011) Photonic crystals: molding the flow of light. Princeton University Press, Princeton
5. Singh BR, Rawal S (2015) Photonic crystal based all-optical NOT logic gate. J Opt Soc Am A 32(12):2260–2263
6. Mehdizadeh F, Soroosh M, Alipour-Banaei H (2017) A proposal for 4-to-2optical encoder based on photonic crystals. IET Optoelectron 11(1):29–35
7. Fu Y, Hu X, Gong Q (2013) Silicon photonic crystal all-optical logic gates. Phys Lett A 377:329–333
8. Jianga YC, Liua SB, Zhanga HF et al (2014) Reconfigurable design of logic gates based on a two-dimensional photonic crystals waveguide structure. Opt Commun 332:359–36, 53
9. Notomi M, Tanabe T, Shinya A, Kuramochi E, Taniyama H, Mitsugi S, Morita M (2007) Nonlinear and adiabatic control of high-Q photonic crystal nanocavities. Opt Exp 15(26):17458
10. Scarmozzino R, Whitlock BK, Heller EK, Osgood Jr RM (2000) Numerical methods for modeling photonic devices and systems. In: SPIE proceedings volume 3944, physics and simulation of optoelectronic devices VIII
11. Gupta ND, Janyani V (2014) Dense wavelength division demultiplexing using photonic crystal waveguides based on cavity resonance. Optik 125(19):5833–5836

Effect of Super Gaussian Parameter on Soliton Interaction Length in Highly Nonlocal Media

Mohit Sharma, Sandeep Kumar Kajala, Brajraj Singh, and Manoj Mishra

Abstract This article investigates the collision dynamics of two super-Gaussian (SG) beams in a highly nonlocal nonlinear media by numerically simulating the governing nonlocal nonlinear Schrödinger equation (NNLSE). The NNLSE will be simulated by the use of the split-step-Fourier method to find the collision distance between two co-propagating beams. The effect of the SG parameter will be highlighted in the conclusion.

Keywords Highly non-local media · NNLSE · Split-step-Fourier method · Accessible soliton

1 Introduction

The self-trapped optical beam in nonlocal nonlinear media has attracted great attention by the theoretician and the experimentalist owing to potential technological advancement in the area of Nematic liquid crystals, Bose-Einstein condensate, etc. [1–12]. The order of nonlocality is defined on the basis of the width of response function in comparison with beam width, and they are named as local, weakly nonlocal, generally nonlocal, and highly nonlocal [3–10]. In a highly nonlocal case, the response function width is much greater than the beam width, whereas in the case of local it is opposite. The weakly nonlocal, generally nonlocal cases are lying between the local and highly nonlocal. The response of the nonlocal media can be modeled by many types of response functions, but theoreticians have opted mainly the Gaussian-type response function [5] and the exponential-decay response function [6]. An extensive investigation on weakly nonlocal spatial solitons [7], generally nonlocal spatial solitons [8], and strongly nonlocal spatial solitons [9, 10] were performed.

M. Sharma · S. K. Kajala · B. Singh · M. Mishra (✉)
Department of Physics, SLAS, Mody University of Science and Technology, Lakshmangarh, Sikar 332 311, Rajasthan, India
e-mail: manoj2712@gmail.com

M. Tiwari et al. (eds.), *Optical and Wireless Technologies*, Lecture Notes in Electrical Engineering 892, https://doi.org/10.1007/978-981-19-1645-8_2

In 1997, Snyder et al. [11] converted NNLSE into a simplified model for the highly nonlocal media, which is called an accessible soliton (AS). The investigation on AS has revealed a bunch of new phenomena like large phase shift [9], an attraction between out-of-phase solitons [6, 11–13], an attraction between dark solitons [14], and long-range interaction between solitons [15], etc., which are not found in local solitons.

The AS has a stationary Gaussian shape exact solution. There are several other shapes have been investigated, namely Hermite-Gaussian (HG) form [16], cosh-Gaussian form [17], Gaussian forms [9, 11], Laguerre-Gaussian and Hermite-Gaussian forms [16, 18], Ince-Gaussian form [19], complex-variable-function Gaussian form [20], super-Gaussian (SG) [21–23], in the highly nonlocal media.

The beam governing equations of a Gaussian beam propagating in highly nonlocal media has been discussed [21]. The two-beam dynamics of an SG beam have been investigated in a highly non-local media analytically and numerically [22]. Further, the multiple beam collision dynamics of the SG beam have been elaborated [23]. The SG beams are known for the narrow tail and flat-top peak, hence they are easy to detect. Also, the SG beams contain lesser energy than the Gaussian beam of the same beam width [24]. The order of the SG beam has been decided by the parameter n (Eq. 4) and as the value of n increases, the SG beam becomes flattered (Fig. 1). To the best of our knowledge, no one has studied the effect of the SG parameters on the collision dynamics yet, hence, this article presents the numerical study of the effect of SG beam parameter n on the collision dynamics in highly nonlocal media. The article is structured as: Mathematical model is presented in Sect. 2, a numerical investigation is discussed in Sect. 3 and the result is summarized in Sect. 4.

2 The Mathematical Model

The modeling of optical beam propagation through the nonlocal nonlinear medium is done by the NNLSE of the form

$$i\,\frac{\partial u}{\partial z} + \mu\frac{\partial^2 u}{\partial x^2} + \rho u\int_{-\infty}^{\infty} R(x-x')\,I(x',z)\,dx' = 0 \tag{1}$$

where $u(x,z)$ is a beam envelop, $\mu = 1/2k$, $\rho = k\eta$, and k is the wavenumber. The investigation has assumed a quasi-monochromatic partially incoherent beam propagating through nonlocal media produces a Gaussian response function as,

$$R(x) = \frac{1}{\sqrt{\pi}\sigma} \exp\left(-\frac{x^2}{\sigma^2}\right), \tag{2}$$

where σ is the response function length. For the case of highly nonlocal media the Eq. (1) reduced to [9, 11],

$$i\,\frac{\partial u}{\partial z} + \mu\frac{\partial^2 u}{\partial x^2} + \rho u \frac{P_0}{\sqrt{\pi}\sigma}\left(1 - \frac{x^2}{\sigma^2}\right) = 0. \tag{3}$$

The intensity profile of the SG beam has been shown in Fig. 1, for the different values of SG parameters i.e. $n = 1, 2, 3, 5$ and 8. Obviously, for $n = 1$, it is a Gaussian beam. It can be clearly seen that as the value of n increases the beam's edge becomes steeper and its top becomes flatter. Such beam profile can be obtained from directly modulated lasers [24]. The Fig. 2 shows the profile of material response function for the various cases of nonlocality, namely, highly nonlocal ($\sigma = 10.0$), generally nonlocal ($\sigma = 4.0$), weakly nonlocal ($\sigma = 1.0$) and local ($\sigma = 0.1$) with blue color, whereas the profile of Gaussian beam is shown with black color.

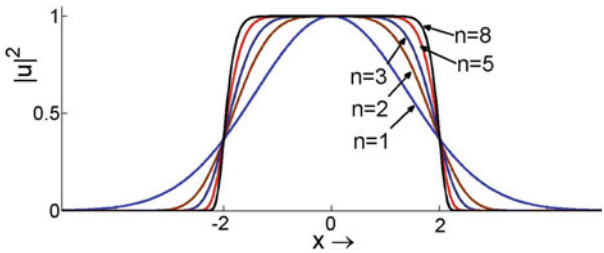

Fig. 1 The profile of the SG beam for $n = 1, 2, 3, 5$ and 8.

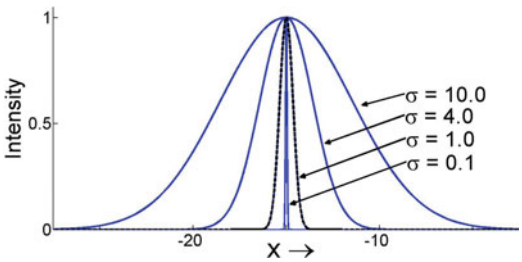

Fig. 2 Profile of response function for $\sigma = 0.1,\ 1.0,\ 4.0$ and 10.0 (in blue color) and the profile of the Gaussian beam (in black color).

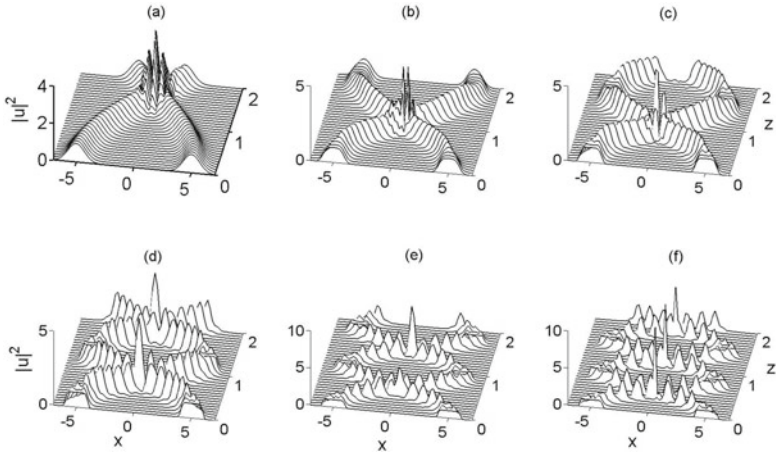

Fig. 3 The collision of two solitons beams for SG parameters $n = 1, 2, 3, 5, 8$ and 12

3 Soliton Interaction

The interaction of optical beam in highly local Media is well documented [6, 11–13]. Hence it becomes important to study the interaction of the SG beams in highly nonlocal media for the change in the SG parameter. The numerical simulation is carried out by split-step-Fourier method [24] by taking two SG beams with an initial peak to peak separation of $2d = 8$, for which the typical parameters are fixed as $\sigma = 10$, $w_0 = 1$, $\mu = 1/2$, and $\rho = 1/6$. The launching beam profile is,

$$u(x,z) = \sqrt{\frac{n\,P_0}{w_0}\Gamma\left(\frac{1}{2n}\right)}\left[\exp\left(-\frac{1}{2}\left(\frac{x-d}{w_0}\right)^{2n}\right) + \exp\left(-\frac{1}{2}\left(\frac{x+d}{w_0)}\right)^{2n}\right)\right] \tag{4}$$

where $w_0(z)$ is beam width, $c(z)$ is the phase front curvature of beam, $2d$ is the separation of peaks of two beams, and P_0 is the beam energy. Here n is the SG parameter that controls the degree of edge sharpness. The collision of two Gaussian or SG beams in the nonlocal media are depicted in Fig. 3. It is clear from Fig. 3 that, as the value of the SG parameter increases the beam collision distance decreases. This is due to the increase in oscillatory behavior of beam on the increase of n. Interestingly, the SG beam recovers its original shapes during the propagation distance periodically. The Fig. 4 show the variation of collision distance with the parameter n. Hence it can be concluded that the higher-order SG beams are detrimental for beam propagation.

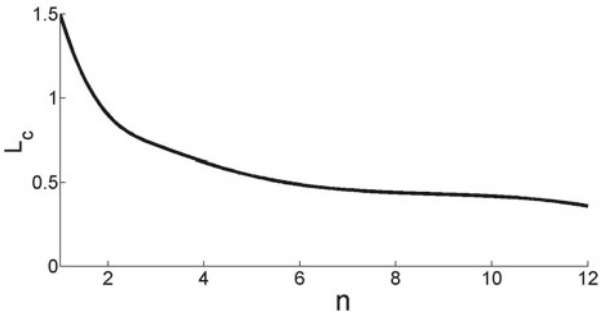

Fig. 4 The variation of collision distance with the parameter *n*

4 Conclusion

The article investigated the collision dynamics of two SG beams in a highly nonlocal nonlinear media by numerically simulating the governing nonlocal nonlinear Schrödinger equation (NNLSE). It is revealed that the propagation of the Gaussian beam is stable, whereas it is oscillatory for the SG beam. Further, on the increase in SG parameter '*n*' the collision distance between two beams decreases. Also, it is seen that the shape of the SG beam converts into a Gaussian beam in propagation and it recovers to an SG shape periodically. It is concluded that the shape of the laser beam in highly nonlocal media should be close to Gaussian for the longer interaction length.

Acknowledgement The author MM is thankful to DST-SERB for the fast track project grant (***FTP/PS-211/2012***).

References

1. Dong L, Huang C, Qi W (2019) Nonlocal solitons in fractional dimensions. Opt Lett 44(20):4917–4920
2. Yang Z-J, Yang Z-F, Li J-X, Dai Z-P, Zhang S-M, Li X-L (2017) Interaction between anomalous vortex beams in nonlocal media. Results Phys 7:1485–1486
3. Zhang H, Chen M, Yang L, Tian B, Chen C, Guo Q, Shou Q, Wei H (2019) Higher-charge vortex solitons and vector vortex solitons in strongly nonlocal media. Opt Lett 44(12):3098–3101
4. Song L, Yang Z, Li X, Zhang S (2018) Controllable Gaussian-shaped soliton clusters in strongly nonlocal media. Opt Express 26(15):19182–19198
5. Krolikowski W, Bang O, Rasmussen JJ, Wyller J (2001) Phys Rev E 64(1):016612
6. Rasmussen PD, Bang O, Królikowski W (2005) Phys Rev E 72(6):066611
7. Królikowski W, Bang O (2000) Phys Rev E 63(1):016610
8. Ouyang S, Guo Q, Hu W (2006) Phys Rev E 74(3):036622
9. Guo Q, Luo B, Yi F, Chi S, Xie Y (2004) Phys Rev E 69(1):016602
10. Xie Y, Guo Q (2004) Opt Quant Electron 36(15):1335–1351

11. Snyder AW, John Mitchell D (1997) Science 276(5318):1538–1541
12. Peccianti M, Brzdakiewicz KA, Assanto G (2002) Opt Lett 27(16):1460–1462
13. Hu W, Zhang T, Guo Q, Xuan L, Lan S (2006) Appl Phys Lett 89(7):071111
14. Dreischuh A, Neshev DN, Petersen DE, Bang O, Krolikowski W (2006) Phys Rev Lett 96(4):043901
15. Rotschild C, Alfassi B, Cohen O, Segev M (2006) Nat Phys 2(11):769–774
16. Deng D, Zhao X, Guo Q, Lan S (2007) JOSA B 24(9):2537–2544
17. Yang Z, Daquan L, Wei H, Zheng Y, Gao X, Guo Q (2010) Phys Lett A 374(39):4007–4013
18. Buccoliero D, Desyatnikov AS, Krolikowski W, Kivshar YS (2007) Phys Rev Lett 98:053901
19. Deng D, Guo Q (2007) Opt Lett 32(21):3206–3208
20. Deng D, Guo Q, Wei H (2009) Opt Lett 34(1):43–45
21. Mishra M, Paltani PP, Singh B, Singh K (2013) Int J Pure Appl Math 83(5):673–677
22. Mishra M, Hong W-P (2011) Progress Electromagn Res B 31:175–188
23. Acharya N, Mishra M (2019) In laser science, pp JTu3A-60. Optical Society of America
24. Agrawal GP (1995) Nonlinear fiber optics. Academic Press, San Diego

Simulation of Optical FBG Based Sensor for Measurement of Temperature, Strain and Salinity

Mohd. Ashraf and Mainuddin

Abstract This paper presents simulation results of optical fiber sensors based on Fiber Bragg Grating (FBG). The selection of proper grating is done on the basis of comparative analysis between different grating shapes and apodization. The simulation results show the variation of Bragg wavelength with respect to change in strain, temperature and salinity. The sensitivities of Strain, temperature and salinity sensor are found to be 1.2 pm/microstrain, 13.8 pm/°C and 0.6 pm/ (% change in concentration) respectively.

Keywords Fiber Bragg Grating · Strain sensor · Temperature sensor · Salinity sensor

1 Introduction

Measurement and control [1, 2] of various parameters such as chemical [3, 4, 5], physical [6] and biological [7] are of critical significance for the protection and monitoring of ecosystems. The most essential parameters in these applications, particularly in physical oceanography, are salinity and temperature. Optical methods [8, 9, 10] of parameters detection have proved their superiority over conventional methods. Sensors based on Fiber Bragg Gratings (FBG) have received a lot of attention in this field, owing to the fact that the measurand-induced modulation is over an absolute parameter wavelength. Furthermore, FBG sensors have an inherent nature and provide varied benefits in contrast to conventional electrical sensors viz. compactness, immunity to electromagnetic interference and capability to function in extreme conditions [11, 12]. FBG sensor can be used for measuring temperature and/or strain. Wang. J et al. [13] conducted experiments on a pipeline leakage test platform for

Mohd. Ashraf (✉) · Mainuddin
Department of Electronics and Communication Engineering, Jamia Millia Islamia, New Delhi, India
e-mail: mohd.ashraf@gmail.com

Mainuddin
e-mail: mainuddin@jmi.ac.in

M. Tiwari et al. (eds.), *Optical and Wireless Technologies*, Lecture Notes in Electrical Engineering 892, https://doi.org/10.1007/978-981-19-1645-8_3

system performance verification by employing an FBG-based approach. Final results depict that pressure change trends can be accurately determined using this approach which helps to calculate the negative pressure width (NPW) velocity. T. J. Ashik et al. [14] presented the analysis of different combinations of FBG. H.B Liu et al. [15] demonstrated a sensor scheme comprised of a polymer fibre Bragg grating and a silica fibre Bragg grating that worked well and provided an excellent temperature and strain sensor.

Earlier degree of water salinity was determined by the presence of chlorine ions in the water solution which depicted its electrical conductivity [16]. However, for measuring the salinity, the standard optical technique is to measure the optical refractive index with the help of a refractometer [17]. To improve the accuracy and lower its temperature sensitivity, the refractometers have undergone various changes for numerous applications unbounded by the salinity measurement [18]. D. Luo et al. measured salinity concentrations and its refractive index (RI) by a prism coupler at 1550 nm and 20 °C for NaCl liquid [19]. Chiang et al. presented an excellent method for measuring the salinity sensor transducer for monitoring the salinity of the ocean environment and aquaculture [20]. Ajay Yadav et al. measured sugar and salt concentration using a polyimide (PI-2525)-coated fiber Bragg grating and a hydrogel (agarose)-coated long period grating [21].

However, to the best of our knowledge, no paper has reported the measurement of salinity, temperature and strain using the same FBG sensor. This paper reports the simulation results for FBG based optical sensor for strain, temperature and salinity of the water. The Paper is divided into four sections. In Sect. 2, system design and mathematical modelling have been presented. The simulation results have been discussed in Sect. 3. Section 4 concludes the work along with the future scope.

2 Design and Mathematical Modelling

Single-mode fiber consists of a periodic modulation of refractive index to form fiber Bragg grating. For single-mode profiles, important parameters are core diameter, core refractive index (RI), clad diameter, clad RI, photosensitivity profile and central wavelength. Single-mode fiber (SMF) has a small diameter of the core due to which only one mode of light propagates through the core. The number of reflections, in this case, decreases which results in low attenuation of light signal and hence it travels long distance along with the fiber.The reflected spectrum is of major interest while analyzing spectral information for FBG. In the reflected spectrum, Bragg wavelength (λ_b) is the wavelength at the point of maximum reflectivity, which is dependent on the grating period and the core effective refractive index. The operation of the FBG sensor is based on the principle of the wavelength shift of the reflected Bragg signal with changes in the environment such as temperature, strain and can be expressed mathematically as [22]

$$\lambda_b = 2n_{eff}\Lambda \tag{1}$$

where, $\boldsymbol{\lambda_b}$ is the Bragg wavelength, Λ is grating period and n_{eff} is the effective refractive index. Therefore, the sensitivity of FBG sensor with respect to temperature is obtained by the partial derivative of Eq. (1)

$$\frac{\Delta\lambda_b}{\Delta T} = 2n_{eff}\frac{d\Lambda}{dT} + 2\Lambda\frac{dn_{eff}}{dT} \tag{2}$$

where, ΔT is the change in temperature. On substituting Eq. (1) in Eq. (2), we get

$$\frac{\Delta\lambda_b}{\Delta T} = \frac{1}{\Lambda}\frac{d\Lambda}{dT}\lambda_b + \frac{1}{n_{eff}}\frac{dn_{eff}}{dT}\lambda_b \tag{3}$$

Equation (3) can be re-written as

$$\frac{\Delta\lambda_b}{\lambda_b} = \frac{1}{\Lambda}\frac{d\Lambda}{dT}\Delta T + \frac{1}{n_{eff}}\frac{dn_{eff}}{dT}\Delta T \tag{4}$$

Since, FBG system design parameters can be divided into four major parts namely strain optic parameters, thermo-optic parameters, micro strain and temperature. Therefore, $\frac{\Delta\lambda_b}{\lambda_b}$ can be written in terms of thermo-optic coefficient and thermal expansion coefficient as

$$\frac{\Delta\lambda_b}{\lambda_b} = (\alpha + \eta)\Delta T \tag{5}$$

where, α is a thermal expansion coefficient of silica and η is thermo-optic coefficient. Also, the sensitivity of FBG sensor corresponding to strain can be calculated by the partial derivative of Eq. (1) w.r.t displacement as

$$\frac{\Delta\lambda_b}{\Delta L} = 2n_{eff}\frac{d\Lambda}{dL} + 2\Lambda\frac{dn_{eff}}{dL} \tag{6}$$

On substituting Eq. (1) in Eq. (6), we get

$$\frac{\Delta\lambda_b}{\lambda_b} = \frac{1}{\Lambda}\frac{d\Lambda}{dL}\Delta L + \frac{1}{n_{eff}}\frac{dn_{eff}}{dL}\Delta L \tag{7}$$

Equation (7) may be simplified in terms of ρ_e is a photoelastic Coefficient of fiber and ε is an applied strain. [23] as follows:

$$\frac{\Delta\lambda_b}{\lambda_b} = (1 - \rho_e)\varepsilon \tag{8}$$

3 Simulation Results

Two application software Opti-grating and Opti-systems have been used to model this sensor setup. The Opti-grating has been used to develop various forms of gratings. These files are then exported to Opti-system 15.2 to simulate the spectrum and monitor the parameters of the designed FBG sensor. A comparative analysis of the various grating types and Grating shapes has been done. The comparison has been made based on reflectivity, sidelobes power, delay and bandwidth parameters that have been listed in Table 1. The Uniform Grating Structure with positive only index change and Gaussian apodization have been used in this design (Fig. 1).

The rectangular shape Gaussian apodized grating has been selected for sensors application as it provides the least delay, thereby providing fast response time. The side lobes power is also very less. The reflective power of the FBG sensor can be improved by increasing index modulation or taper's parameter [24].

Table 1 Comparative results of different gratings

Parameters	Reflected power (dB)	Left side lobe power (dB)	Right side lobe power (dB)	Delay (ps)	Bandwidth (nm)
Rectangular shape gaussian apodized	−10.0551	−0.00103915	−0.00103949	25.7123	0.205
Rectangular shape uniform apodized	−24.3302	−1.97562	−1.97314	91.02556	0.2225
Sine shape gaussian apodized	−6.91069	−0.00071	−0.00070	28.5317	0.1825
Sine shape uniform apodized	−17.8463	−1.31927	−1.31989	72.0808	0.185

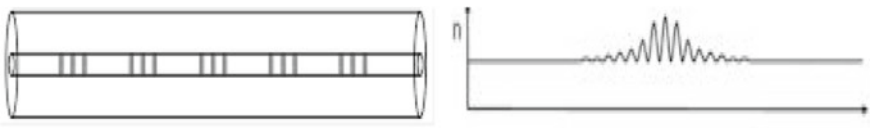

(a) (b)

Fig. 1 Grating structure **a** Uniform with positive only index change **b** Gaussian apodized

3.1 Strain Sensor

On applying uniform strain on FBG, the change in the grating period occurs which leads to a shift in Bragg wavelength. The FBG sensor has been characterized on the basis of its sensitivity and linear response to the applied physical measurand. Table 2 shows the observed reflected wavelengths and intensity for different applied strain values.

The variation of Bragg wavelength with respect to applied strain has been shown in Fig. 2 for a central wavelength 1550 nm at reference temperature 25 °C. From the simulation results, it is evident that a 0.12 nm shift in wavelength has been observed on every 100 micro-strains. The designed FBG sensor has been found to be linear from 20 to 430 με applied strain with an R square value of 0.9999. The output of FBG sensors is dependent on variation in the strain as well as on temperature. These changes will lead to sensitivity drift and zero drift of the sensor. Figure 3 shows the sensitivity drift and zero drift due to ambient temperature variation.

It is clearly evident from Fig. 3 that both the strain measurements and temperature can be done simultaneously using the FBG sensor. Good linearity between the strain and wavelength shift has been obtained at different temperature values. During the entire measurement, constant sensitivity has been observed. The strain sensitivities for the proposed FBG sensor have been found to be 1.2 pm/microstrain. The FBG sensor parameters have been shown in Table 3.

Table 2 Reflected wavelength and intensity at different applied strain

Strain applied (με)	Reflected wavelength (nm)	Reflection intensity (dB)
20	1556.2942	−10.0549
40	1556.3176	−10.0547
60	1556.3428	−10.0545
80	1556.368	−10.054
100	1556.3914	−10.0539
120	1556.4166	−10.0538

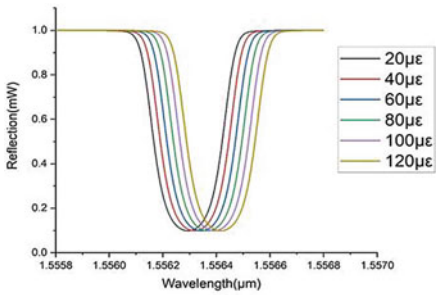

Fig. 2 Reflection spectrum at different applied strain values

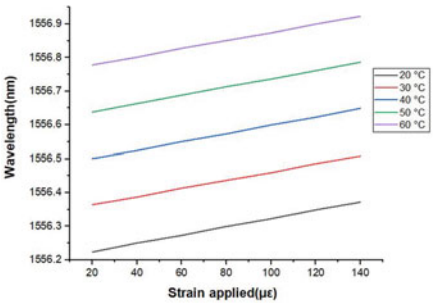

Fig. 3 Effects of disturbance; zero drift plus sensitivity drift

Table 3 FBG sensor parameters

Parameters	Value
Sensitivity	1.2 pm/με
Linearity (R-square method)	0.9999
Resolution	4 micro-strain (με)
Offsets	0.013 nm/°C
Uncertainty	9.26617×10^{-7}
Range	20–430 με
Delay	25.714 pico-sec

Table 4 Reflected wavelength and intensity of FBG sensor at different temperatures

Temperature (°C)	Reflected wavelength (nm)	Reflection intensity (dB)
10	1556.0625	−10.0573
20	1556.2	−10.0558
30	1556.3375	−10.0539
40	1556.4775	−10.0525
50	1556.615	−10.0517
60	1556.7525	−10.0505
70	1556.89	−10.0491

3.2 Temperature Sensor

On applying uniform temperature on FBG, the grating period changes which in turn leads to a shift in Bragg wavelength. The sensor has been characterized on the basis of its sensitivity and linear response to the applied physical measurand i.e., temperature. The variation of wavelength and intensity of simulated FBG sensor with respect to temperature has been illustrated in Table 4. It is evident from the simulated results

that the observed sensitivity has been found to be 13.8 pm/°C. The central wavelength of 1550 nm has been selected and it has also been found that sensors exhibit linear characteristics from −10 to 150 °C with an R square value of 1.

The variation of Bragg wavelength for different values of temperature has been shown in Fig. 4. The increase in Bragg wavelength has been observed to increase with an increase in temperature and the amount of reflected power also varies with a very slight difference.

3.3 Salinity Sensor

The measurement of the salinity of the water is important for the characterization of seawater for different applications. The salinity environment has been simulated by creating a relative refractive index to the surrounding medium. The salinity sensor design is based on providing an extra region to the outer covering of the sensor which includes the different RI values ranging from 1.3159 to 1.3591 which corresponds to the RI of pure water to the RI of a saline solution (NaCl solution). The change in Bragg wavelength has been observed at different concentrations of salinity in water as shown in Table 5. Figure 5 shows the variation of reflected signal and wavelength

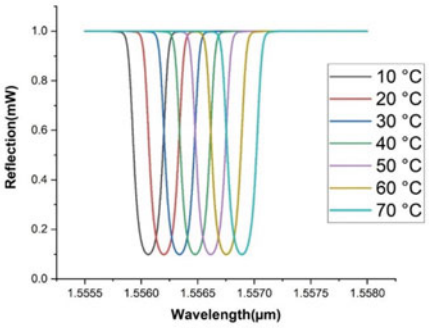

Fig. 4 Reflection spectrum of temperature sensor

Table 5 Reflective wavelength at different salinity concentration

Salinity concentration (%)	Refractive index	Reflective Wavelength (nm)	Reflective intensity (dB)
0	1.3159	1556.1674	−10.0861
2	1.3303	1556.168	−10.0855
4	1.3447	1556.1692	−10.0848
6	1.3591	1556.1698	−10.084

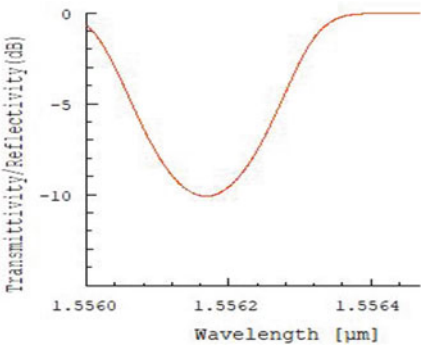

Fig. 5 Reflection spectrum at RI 1.3591

for a salinity solution of 6% concentration (RI = 1.3591). The observed sensitivity of simulated salinity sensor results is 0.6 pm/ (% change in concentration).

4 Conclusion

A Fiber Bragg grating-based sensor has been simulated. The simulation results demonstrate the feasibility of the FBG sensor for strain, temperature and salinity measurements. The observed sensitivity of Strain, temperature and salinity sensor is found to be 1.2 pm/microstrain, 13.8 pm/°C and 0.6 pm/ (% change in concentration) respectively. The sensitivity of the sensor can also be increased to some extent if different sensing materials on sensing parts such as polyaniline or microgel based structure with different compositions are used.

References

1. Mainuddin, Tyagi RK, Rajesh R, Singhal G, Dawar AL (2003) Real-time data acquisition and control system for a chemical oxygen-iodine laser. J Meas Sci Technol 14:1364–1372
2. Dohare RK, Mainuddin, Singhal G (2020) Hybrid data acquisition system for flowing medium lasers. Defence Sci J 70(3):285–291. https://doi.org/10.14429/dsj.70.14902
3. Mainuddin, Singhal G, Tyagi RK, Maini AK (2012) Diagnostics and data acquisition for Chemical Oxygen Iodine Laser. IEEE Trans Instr Meas 61(6):1747–1755
4. Jindal MK, Veerabuthiran S, Mainuddin, Razdan AK (2021) Integrated path DIAL for standoff detection of acetone vapors under topographic target condition. J Opt Laser Technol 143:107299. ISSN 0030-3992
5. Fahim F, Mainuddin M, Mittal U, Kumar J, Nimal AT (2021) Novel SAW CWA detector using temperature programmed desorption. IEEE Sens J 21(5):5914–5922
6. Fahim, Mainuddin, Rajput P, Kumar J, Nimal AT (2021) A simple and novel SAW magnetic sensor with PVA bound magnetostrictivenanopowder film. Sens Actuators A Phys 331:112926. ISSN 0924-4247

7. Seshadri DR, Li RT, Voos JE et al (2019) Wearable sensors for monitoring the physiological and biochemical profile of the athlete. npj Digit Med 2:72
8. Jindal MK, Mainuddin, Veerabuthiran S, Razdan AK (2020) Laser-based systems for standoff detection of CWA: a short review. IEEE Sens J 21(4):4085–4096
9. Mainuddin, Beg MT, Moinuddin, Tyagi RK, Rajesh R, Singhal G, Dawar AL (2005) Optical spectroscopic based In-line iodine flow measurement system-an application to COIL. J Sens Actuators B 109(2):375–380
10. Singhal G, Mainuddin, Rajesh R, Beg MT, Tyagi RK, Dawar AL (2015) Overview of optical techniques for characterization of high-power infrared gas lasers. IEEE Sens J 15(8):4165–4173
11. Mendez A (2016) Fiber Bragg grating sensors for biomedical applications. In: Photonics and fiber technology. OSA technical digest (online)
12. Majumder M, Gangopadhyay TK, Chakraborty AK, Dasgupta K, Bhattacharya DK (2008) Fibre Bragg gratings in structural health monitoring—Present status and applications. Sens Actuators A Phys 147(1):150–164. ISSN 0924-4247
13. Wang J, Zhao L, Liu T, Li Z, Sun T, Grattan KTV (2017) Novel negative pressure wave-based pipeline leak detection system using fiber bragg grating-based pressure sensors. J Lightw Technol 35:3366–3373
14. Ashik TJ, Kachare N, Kalyani Bai K, Kumar DS (2017) Analysis of simultaneous measurement of temperature and strain using different combinations of FBG. AIP Conf Proc 1849(6):1063–1070
15. Liu HB, Liu HY, Peng GD, Chu PL (2003) Strain and temperature sensor using a combination of polymer and silica fibre Bragg gratings. OptCommun 219(1–6):139–142. ISSN 0030-4018
16. Joe1 H-E, Yun H, Jo S-H, Jun MBG, Min B-K (2018) A Review on Optical Fiber Sensors for environmental monitoring. Int J Precis EngManuf-Green Technol 5(1):173–191
17. Campanella C, Cuccovillo A, Campanella C, Yurt A, Passaro V (2018) Fibre Bragg Grating based strain sensors: review of technology and applications. Sensors 18(9):3115. https://doi.org/10.3390/s18093115
18. Cervantes M, Rodriguez-Vera R (1988) Pulfrich refractometer for 1-D gradients. Appl Opt 27:4494–4496
19. Luo D, Ma J, Ibrahim Z, Ismail Z (2017) Etched FBG coated with polyimide for simultaneous detection the salinity and temperature. OptCommun 392:218–222
20. Chiang C-T, Chang C-W (2015) Design of a calibrated salinity sensor transducer for monitoring salinity of ocean environment and aquaculture. IEEE Sens J 15(9):5151–5157
21. Yadav A, Kumar J, Biswas P, Basumallick N, Bandyopadhyay S, Dasgupta K (2013) Comparison between polyimide coated fiber grating and hydrogel coated long period grating for measuring sugar and salt concentration. In: 2013 international conference on microwave and photonics, ICMAP 2013, pp 1–5. https://doi.org/10.1109/ICMAP.2013.6733536
22. Elgaud MM, Zan MSD, Abushagur AAG, Bakar AAA (2016) Analysis of independent strain-temperature fiber Bragg grating sensing technique using OptiSystem and OptiGrating. In: 2016 IEEE 6th international conference on photonics, ICP 2016, pp 1–3
23. Men L, Lu P, Chen Q (2008) A multiplexed fiber Bragg grating sensor for simultaneous salinity and temperature measurement. J Appl Phys 103:053107
24. Hang Zhou Y, XueGuang Q, Md Rajibul I, Kok-Sing L, Ahmad H (2011) Simultaneous measurement of aliphatic alcohol concentration and temperature based on etched taper FBG. Sens Actuators B Chem 202:959–963

Study of Underwater Wireless Optical Communication Link Performance for Different Water Channels

Sanjay Kumar and Shanthi Prince

Abstract A study on the performance of underwater wireless optical communication (UWOC) system has been carried out for different water channels. Here, a mathematical expression for received optical power as a function of channel attenuation coefficient and beam propagation distance between transmitter and receiver has been proposed. The proposed expression is then incorporated for estimating the performance of the proposed system with reference to acceptable quality factor (Q factor) ($\geq$6) and bit error rate (BER) ($\leq 10^{-9}$) for varying link length and data rate through Optisystem. The performance of the proposed system is also evaluated from the eye diagram of the received signal.

Keywords Underwater wireless optical communication (UWOC) · Absorption coefficient · Scattering coefficient · Turbulence · Quality factor (Q factor) · Bit-error rate (BER)

1 Introduction

High data rate underwater wireless link is inherently needed due to recent naval applications arising from the continuous rise in the marine economy. Traditional UWOC technique mainly uses acoustic signal, radio frequency signal and optical signal for underwater wireless information transfer [1]. Acoustic signal based underwater wireless data transfer technique provides long range communication (in order of several kilometers). But data rate and propagation speed is very low in case of acoustic based communication technique. Moreover, transceiver used in this technique is bulky, expensive and energy intensive. Whereas RF based communication technique provides high data rate and high propagation speed as compared to acoustic based technique. But, RF signal is highly attenuated in marine water and hence limited to very low range communication [1, 2].

S. Kumar · S. Prince (✉)
Department of Electronics and Communication Engineering, SRM Institute of Science and Technology, Kattankulathur 603203, Tamil Nadu, India
e-mail: shanthip@srmist.edu.in

M. Tiwari et al. (eds.), *Optical and Wireless Technologies*, Lecture Notes in Electrical Engineering 892, https://doi.org/10.1007/978-981-19-1645-8_4

Underwater wireless optical communication (UWOC) is a propitious technology which provides energy—efficient high data rate with low negative effects on the environment as compared to conventional underwater wireless communication techniques [3–6], whereas the reliability of UWOC system is highly affected by absorption and scattering as well as turbulence [7–10]. Attenuation due to absorption and scattering is estimated with respect to the absorption coefficient ($a(\lambda)$) as well as scattering coefficient ($b(\lambda)$) that depends on the wavelength of optical signal used. Overall attenuation due to absorption and scattering is the linear combination of $a(\lambda)$ and $b(\lambda)$, given as [1, 4]

$$C(\lambda) = a(\lambda) + b(\lambda). \tag{1}$$

Laser beam with blue and green wavelengths (450 and 550 nm) are the attenuation window for marine water [11]. Turbulence is caused due to change in salinity levels, alterations in temperature, air bubbles inside the underwater channel [12, 13]. To achieve robust, reliable and long range underwater wireless communication, a lot of analysis has been carried out but most of the analysis is theoretical. To characterize the underwater turbulent channel, an equation based on stochastic model has been presented in [14]. To study the propagation properties of optical signal in underwater environment, a weighted Gamma function based channel modeling is presented in [15]. Channel modeling based on lognormal function is used to investigate the performance of turbulent underwater channel in [9, 10]. Fluctuation in salinity is a major cause of turbulence inside water channel. Performance of UWOC at different salinity has been analyzed in [16]. In this paper performance analysis of UWOC is carried out experimentally as well as simulating the UWOC system for different channel conditions.

2 System Model of UWOC Link

A UWOC test-bed link is set in the laboratory environment for the analysis of the link performance in various channel conditions. Figure 1 shows the system model of UWOC link and Fig. 2 depicts experimental setup established. A monochromatic optical beam of 450 nm and transmission power of 3 mW is deployed in water present in a glass chamber of dimension: 180 cm (length), 45 cm (breadth), and 60 cm (height). A message signal, obtained from a waveform generator at transmitter (Tx), is used to modulate the laser beam using intensity modulation technique with the help of modulator and driving circuit. Semiconductor photodetector at the receiver (Rx) is connected with an optical power meter is used to receive the transmitted signal. Specification of components used in the experimental setup is listed in Table 1.

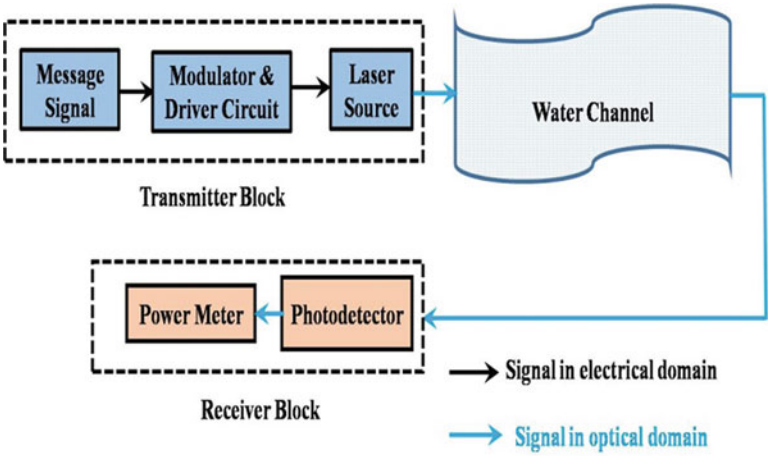

Fig. 1 System model of the proposed UWOC system

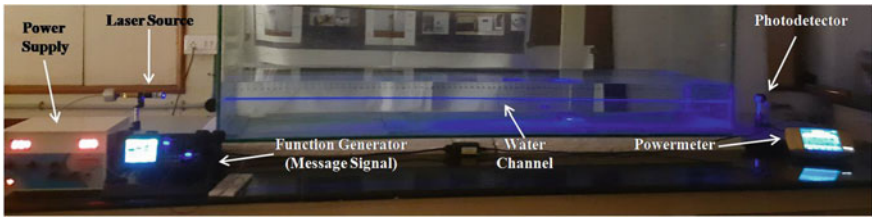

Fig. 2 Experimental setup of the proposed UWOC system

Table 1 Specifications of components used in experimental setup

Components	Parameters	Values
Laser source	Wavelength	450 nm
	Transmitted power	3 mW
Photodetector	Detection range	420 to 1080 nm
	Measurable power	6 nW to 300 mW
Powermeter	Power range	4 pW to 30 kW
UWOC channel	Glass chamber dimension	180 × 45 × 60 cm

3 Mathematical Channel Modeling

Power is received at different link length for different channels; tap water channel (TWC) as well as saline water channel (SWC) with salt concentration of 35 gm/L. The variations in received optical power with link length are illustrated in Fig. 3. Figure 3 illustrates that received power is decreased with link length for both channel

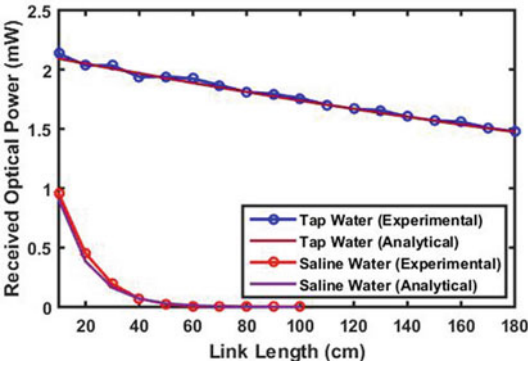

Fig. 3 Experimental and analytical fitting of optical power at receiver with link length for different channel conditions

conditions. The received power is considerably reduced in saline water based UWOC link. Optical absorption and scattering are the major reasons of decrement in received optical power. The fitting of the resultant data from the experiment with standard mathematical expression governing Beer–Lambert law [17–19], as provided in (2), is then performed.

$$P_r = P_0 * \exp(-\alpha * x), \tag{2}$$

where P_r represents the optical power obtained at Rx for a link length of x, P_0 is the emitted laser power from the waterproof encasing and α is the overall attenuation coefficient, as provided in (1).

After fitting the Beer-Lambert's law, given by (2), the attenuation coefficient 'α' has been obtained. Figure 3 clearly illustrates similar values for experimental and analytical values with reference to TWC and SWC. The resultant value of α for TWC is 0.1561 m^{-1} with root mean square error (RMSE) of 0.0109. Similarly, the resultant value of α for SWC is 8.037 m^{-1} with RMSE of 0.0471. As such, (1) is the best fit, which approximately models the distribution of the data obtained through experiment with higher goodness of fit.

Apart from the optical fading due to absorption and scattering effects in the UWOC channel, the beam divergence also results to degradation in link performance. The amount of beam divergence depends on the type of UWOC link length. For smaller link lengths, it is not significant. Equation (2) is consistent for small UWOC link length, while, the negative effects of the beam divergence on link performance are higher for longer UWOC link length. Thus, (2) needs to be modified for longer UWOC link length. The amount of the optical power obtained at the Rx due to divergent beam for a link length of x is given as [17]

$$P_r = P_0 \left(\frac{d_r}{d_t + \theta_s x} \right)^2, \tag{3}$$

where P_0 is the emitted beam power, d_t and d_r are the diameters of Tx and Rx aperture, θ_s represent beam divergence angle. By considering Eqs. (2) and (3), the analytical expression for long range UWOC communication is expressed as,

$$P_r = P_0\left(\frac{d_r}{d_t + \theta_s x}\right)^2 \exp(-\alpha * x). \tag{4}$$

4 Simulation of UWOC System

For estimating the performance of underwater wireless optical communication link with various link length, data rate and transmitted power with respect to acceptable Q factor and bit error rate, an UWOC link is simulated in optisystem. Figure 4 presents the block diagram of the simulated UWOC system.

UWOC system consists of a continuous wave laser as an optical source. The wavelength of laser source is 450 nm. According to centre for Devices and Radiological Health regulation 21 CFR and ANSI Z136.1, lasers used for underwater applications should be Class IIIa or IIIb. The range of power output of Class IIIa and IIIb are 1 mW to 5 mW and 5 mW to 500 mW respectively. At higher power levels, IIIb laser is considered as definite eye hazard. Therefore, considering safety of marine life, maximum transmitted laser power is kept at 200 mW [20]. Electrical signal is generated by electrical signal generator in accordance with pseudo random bit sequence generated by PRBS generator. Electrical signal is modulated by continuous wave laser source using amplitude modulator. A matlab component representing water channel is designed using Eq. (4). Modulated signal is fed to water channel. Transmitted signal is then received with the help of photodetector and the signal is analyzed by eye diagram analyzer. Parameters which are used in simulation are listed in Table 2.

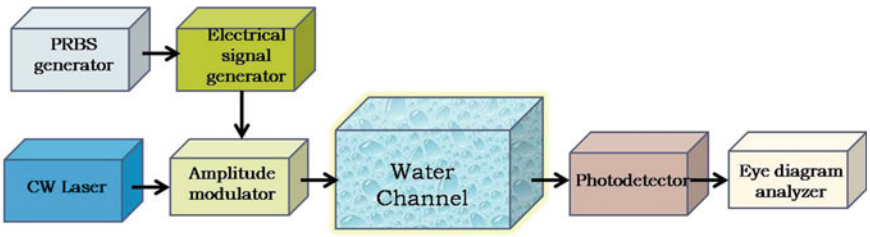

Fig. 4 Block diagram of simulated UWOC system

Table 2 Simulation parameters

Parameters	Values
Laser wavelength	450 nm
Transmitted laser power	30, 200 mW
Transmitted data rate	10, 100 Mbps, 1 Gbps
Photodetector responsivity	0.45 A/W

5 Results and Discussion

The modulation index of amplitude modulator of the proposed UWOC system is considered as unity. Similarly, the responsivity of the photo-detector is considered as 0.45 A/W. Maximum achievable link length for acceptable bit error rate ($\leq 10^{-9}$) and Q factor (≥ 6) at different data rate for 30 and 200 mW of input laser power for TWC and SWC are tabulated in Table 3 and Table 4, respectively.

Table 3 shows that the highest link length in TWC achieved for acceptable Q-Factor and bit error rate at 10 Mbps for 30 mW and 200 mW are 18 m and 21.6 m, respectively. However, the maximum achievable link lengths at 1 Gbps are reduced to 13.6 m and 17.1 m for 30 and 200 mW, respectively.

Table 4 depicts that, for SWC, maximum link length achieved for acceptable Q-Factor and bit error rate with data rate of 10 Mbps for 30 mW and 200 mW are 80 cm

Table 3 Maximum link length achieved at different data rates with various laser transition powers in TWC

Data rate	Input power (mW)	Link length (m)	Q-Factor	BER
10 Mbps	30	18	6.03	$1.55\ e^{-9}$
	200	21.6	6.25	$1.99\ e^{-10}$
100 Mbps	30	15.8	6.07	$6.19\ e^{-10}$
	200	19.4	6.01	$9.00\ e^{-10}$
1 Gbps	30	13.6	6.45	$5.30\ e^{-11}$
	200	17.1	6.01	$9.32\ e^{-10}$

Table 4 Maximum link length achieved at various data rates for different input powers in SWC

Data rate	Input power (mW)	Link length (cm)	Q-Factor	BER
10 Mbps	30	80	6.05	$7.83\ e^{-9}$
	200	91	6.43	$6.27\ e^{-11}$
100 Mbps	30	72	6.47	$4.75e^{-11}$
	200	84	6.27	$1.78e^{-10}$
1 Gbps	30	66	6.03	$4.76e^{-9}$
	200	77	6.09	$5.38e^{-10}$

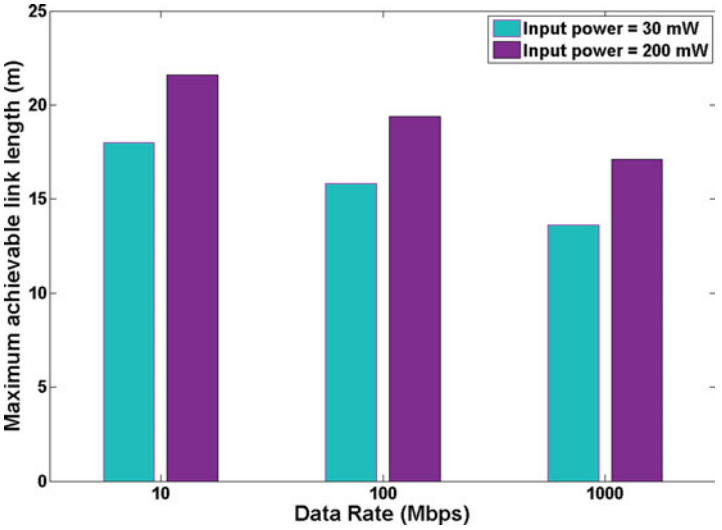

Fig. 5 Maximum achievable link lengths at different data rates for various laser transmission powers in tap-water channel

and 91 cm, respectively. However, the maximum achievable link lengths at 1 Gbps are reduced to 66 cm and 77 cm for 30 mW and 200 mW, respectively.

The variations in highest achievable link length at different data rates with input laser powers of 30 mW and 200 mW for the considered UWOC channels, i.e. TWC and SWC, are shown in Fig. 5 and Fig. 6, respectively.

It can be observed from Figs. 5 and 6 that as the input power increases, maximum achievable link length of UWOC system also increases at a fixed data rate for both TWC and SWC. However, the increments in link length are not significant when it is compared to the value by which input laser power has been increased. Also, the maximum achievable link length decreases with increased data rate at a constant laser transmission power for both water channels but again the decrement in link length is not significant. It can also be observed from Figs. 5 and 6 that maximum achievable link length of UWOC system is considerably decreased for SWC as compared to TWC. The main reason for decrement in maximum achievable link length is high attenuation of optical power in SWC as compared to TWC which reflects from the obtained very high attenuation coefficient value (8.037 m^{-1}) for SWC as compared to TWC (0.1561 m^{-1}).

Eye diagram of signal at Rx of UWOC link at 200 mW of input power for data rate of 10 Mbps at 21.6 m link length and 1 Gbps at 17.1 m link length for tap water channel are presented in Fig. 7(a) and Fig. 7(b), respectively. Figure 8(a) and (b) illustrates signal eye diagram at same laser transmission power for 10 Mbps at 91 cm link length and 1 Gbps at 77 cm link length for saline water channel, respectively.

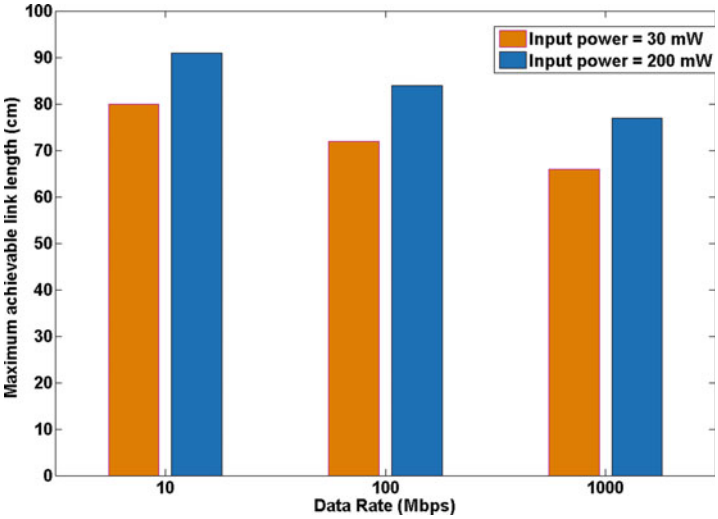

Fig. 6 Maximum achievable link lengths at various data rates for different transmission powers in saline water channel

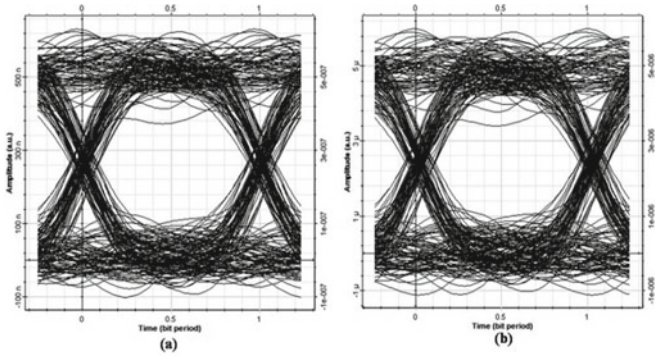

Fig. 7 Eye diagram of received signal at 200 mW input power for data rate of **a** 10 Mbps at 21.6 m link length and **b** 1 Gbps at 17.1 m link length for TWC

Quick visualization of the quality of signal is achieved by considering signal Eye diagram [21]. A clear open eye indicates minimal distortion and good signal—to—noise ratio. It is clear from Figs. 6 and 7 that eye opening is clear and hence quality of received signal is good.

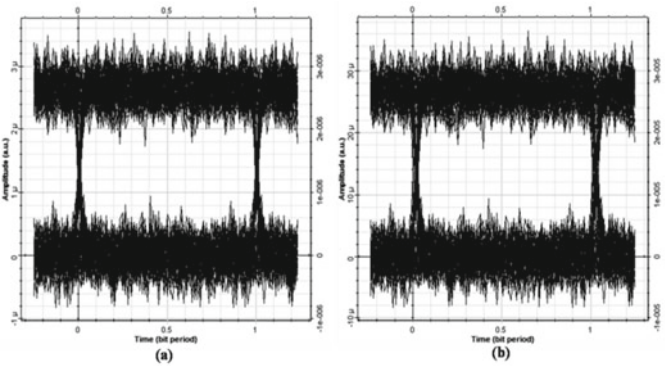

Fig. 8 Eye diagram of received signal at 200 mW input power for data rate of **a** 10 Mbps at 91 cm link length and **b** 1 Gbps at 77 cm link length for SWC

6 Conclusion

The experimental and simulation study is conducted for performance analysis of UWOC link for different channel conditions in terms of link length and data rate. On the basis of experimental outcomes, the attenuation coefficient of the UWOC channel under study is evaluated by curve fitting. The fitting is then implemented to model the water channel for further simulation. The performance of UWOC has been analyzed in terms of acceptable quality factor and bit error rate for varying link length and data rate. Maximum achievable link length of UWOC system increases with increase in input laser power at a constant data rate for both TWC and SWC but the increments in link length is not significant when it is compared to the value by which input laser power has been increased. Also, the maximum achievable link length decreases with increased data rate at a constant input laser power for both UWOC channels but again the decrement in link length is not significant. It is also observed that maximum achievable link length of UWOC system is considerably decreased for SWC as compared to TWC. Eye diagrams are used to analyze the quality of received signal.

Acknowledgements The authors acknowledge Naval Research Board (NRB), DRDO, Government of India for funding. They also acknowledge SRM Institute of Science and Technology for the infrastructural support.

References

1. Kaushal H, Kaddoum G (2016) Underwater optical wireless communication. IEEE Access (4):1518–1547. https://doi.org/10.1109/ACCESS.2016.2552538

2. Al-Halafi A, Oubei HM, Ooi BS, Shihada B (2017) Real-time video transmission over different underwater wireless optical channels using a directly modulated 520 nm laser diode. J Opt Commun Netw 9(10):826–832. https://doi.org/10.1364/JOCN.9.000826
3. Khalighi MA, Gabriel CJ, Pessoa LM, Silva B (2017) Visible light communications: theory and applications. In: Underwater visible light communications, channel modeling and system design, pp 337–372. CRC-Press. https://doi.org/10.1201/9781315367330
4. Zeng Z, Fu S, Zhang H, Dong Y, Cheng J (2016) A survey of underwater optical wireless communications. IEEE Commun Surv 19(1):204–238. https://doi.org/10.1109/COMST.2016.2618841
5. Zhu S, Chen X, Liu X, Zhang G, Tian P (2020) Recent progress in and perspectives of underwater wireless optical communication. Progr Quant Electron 100274. https://doi.org/10.1016/j.pquantelec.2020.100274
6. Sun X, Kang CH, Kong M, Alkhazragi O, Guo Y, Ouhssain M, Weng Y, Jones BH, Ng TK, Ooi BS (2020) A review on practical considerations and solutions in underwater wireless optical communication. J Lightw Technol 38(2):421–431. https://doi.org/10.1109/JLT.2019.2960131
7. Ramavath PN, Udupi SA, Krishnan P (2020) High-speed and reliable underwater wireless optical communication system using multiple-input multiple-output and channel coding techniques for IoUT applications. Opt Commun 461:125229. https://doi.org/10.1016/j.optcom.2019.125229
8. Hema R, Sudha S, Aarthi K (2021) Performance studies of MIMO based DCO-OFDM in underwater wireless optical communication systems. J Mar Sci Technol 26(1):97–107. https://doi.org/10.1007/s00773-020-00724-7
9. Yadav A, Kumar A (2020) Performance analysis of underwater 2D OCDMA system. In: Optical and wireless technologies: proceedings of OWT 2019, vol 648, p 477. https://doi.org/10.1007/978-981-15-2926-9_53
10. Yadav A, Kumar A, Deegwal JK, Singh G, Kumar A (2022) Channel capacity of underwater channel using OCDMA system. In: Optical and wireless technologies. Springer, Singapore, pp 567–572. https://doi.org/10.1007/978-981-16-2818-4_60
11. Duntley SQ (1963) Light in the sea. J Opt Soc Am A 53:214–233. https://doi.org/10.1364/JOSA.53.000214
12. Korotkova O, Farwell N, Shchepakina E (2012) Light scintillation in oceanic turbulence. Waves Random Complex Media 22(2):260–266. https://doi.org/10.1080/17455030.2012.656731
13. Nikishov VV, Nikishov VI (2000) Spectrum of turbulent fluctuations of the sea-water refraction index. Int J Fluid Mech Res 27(1):82–98. https://doi.org/10.1615/InterJFluidMechRes.v27.i1.70
14. Zhang H, Cheng J, Wang Z, Dong Y (2018) On the capacity of buoy-based MIMO systems for underwater optical wireless links with turbulence. In: IEEE international conference on communications (ICC). IEEE, pp 1–6. https://doi.org/10.1109/ICC.2018.8422435
15. Zhang H, Dong Y (2016) Impulse response modeling for general underwater wireless optical MIMO links. IEEE Commun Mag 54(2):56–61. https://doi.org/10.1109/MCOM.2016.7402261
16. Kumar S, Prince S, Aravind JV, Santosh Kumar G (2020) Analysis on the effect of salinity in underwater wireless optical communication. Marine Geores Geotechnol 38(3):291–301. https://doi.org/10.1080/1064119X.2019.1569739
17. Ghassemlooy Z, Popoola W, Rajbhandari S (2012) Optical wireless communications: system and channel modelling with Matlab®. CRC Press. https://doi.org/10.1201/b12687
18. Priyalakshmi B, Mahalakshmi K (2020) Channel estimation and error correction for UWOC system with vertical non-line-of-sight channel. Wirel Netw 26:4986–4997. https://doi.org/10.1007/s11276-020-02376-2
19. Pang W, Wang P, Guo L, Chen W, Li A, Tian H, Liu S (2019) Performance investigation of UWOC system with multiuser diversity scheduling schemes in oceanic turbulence channels. Opt Commun 441:138–148. https://doi.org/10.1016/j.optcom.2019.02.049

20. https://www.deepsea.com/knowledgebase/technical-resources/diode-lasers-in-underwater-applications/
21. Bosu R, Prince S (2018) Reflection assisted beam propagation model for obstructed line-of-sight FSO links. Opt Quant Electron 50(2):1–21. https://doi.org/10.1007/s11082-018-1381-8

Simulation of Power Transfer in Plasmonic Waveguide Coupler

Vishakha Takhar, Mohit Sharma, Brajraj Singh, and Manoj Mishra

Abstract This article investigates the power transfer dynamics in a Plasmonic waveguide coupler. The coupler is designed by cutting two parallel air grooves in a silver metallic sheet. The structure of the designed coupler is simulated using the finite difference-time-domain method, to find the impact of the wavelength of the radiation and types of the metals on power transfer characteristics in the coupler.

Keywords Plasmonics waveguide · Plasmonics coupler · FDTD method

1 Introduction

Presently, plasmonics broke the barrier of diffraction limit and provided nano-scale miniaturization of the active and passive optical devices. The plasmonics use surface plasmon polaritons [1, 2], which are the evanescent waves trapped at the interface of a medium with a positive dielectric constant (air or glass) and a negative dielectric constant (metals). The *Plasmons* are the quantized quasiparticle of the plasma oscillations of the free electron gas density of the metal, when the Plasmon is coupled with the photon, it creates another quasiparticle called a *Plasmon Polariton*. The Plasmon Polaritons of the interface of the metal and the dielectric are called *Surface Plasmons Polaritons* (SPPs). The SPPs propagate along the surface of the metal until it is absorbed in the metal or radiated out in the free-space [3]. The plasmonics offers a wide range of prospective applications in active and passive devices, for example, biological nano-sensors [4], sub-wavelength imaging [5], and merging of electronic circuits into photonic devices [6]. The multilayer metallic waveguide is an important optical structure as it fabricates couplers, modulators, and beam splitters in integrated optics [7]. The coupler is a crucial component for low-loss active and

V. Takhar
Department of Physics, IIT Gandhinagar, Gandhinagar 382 355, Gujarat, India

V. Takhar · M. Sharma · B. Singh · M. Mishra (✉)
Department of Physics, SLAS, Mody University of Science and Technology, Lakshmangarh, Sikar 332 311, Rajasthan, India
e-mail: manoj2712@gmail.com

M. Tiwari et al. (eds.), *Optical and Wireless Technologies*, Lecture Notes in Electrical Engineering 892, https://doi.org/10.1007/978-981-19-1645-8_5

passive plasmonic devices [8–14], because it produces various switching circuits and logic gates. This article presents a numerical investigation on Plasmonic coupler on power transfer dynamics between the waveguides in metal-insulator-metal (MIM) configuration.

2 Modeling and Simulation

The structure of the Plasmonics coupler has been shown in Fig. 1, which has been simulated using the *finite difference time domain* (FDTD) method under PML (*perfectly matched layer*) boundary conditions [15]. The coupler structure is made up of noble metals ('Ag', 'Au', 'Cu' or 'Al') sheets by cutting air waveguides on them. The value of refractive indices of various metals has been taken from Ref. [16]. The two waveguides of length $L = 600$ nm and width $w = 50$ nm are set 9 nm apart from each other so that only a single TM mode radiation can be excited. For the waveguide separation $d = 9$ nm, the transfer of power between the waveguides is maximum [13]. A fundamental TM mode is launched by a dipole source [17] on the first waveguide and the power is recorded in both waveguides along with length 'L' to study the power transfer from the first waveguide to the second waveguide along the propagation length for the white light radiation of wavelength range 600 to 1600 nm in various metal-air interfaces.

When a unit power is launched in the first waveguide of the coupler then the power keeps on transferring completely from the first waveguide to the second waveguide and vice versa, until the power of the radiation does not fade away due to the attenuation. The distance between two consecutive points where the power in both waveguides becomes the same is called *coupling length* 'L_c'. The effect of wavelength of radiation on the coupling length L_c can be clearly seen in Fig. 2 for the 'Ag'-air interface. It has been found that the coupling length is more for the higher wavelength

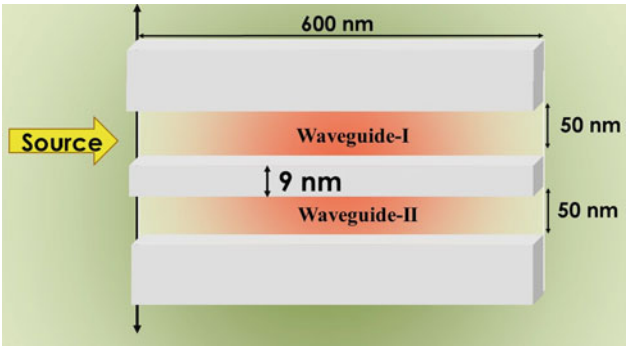

Fig. 1 Schematic diagram of the proposed plasmonic coupler.

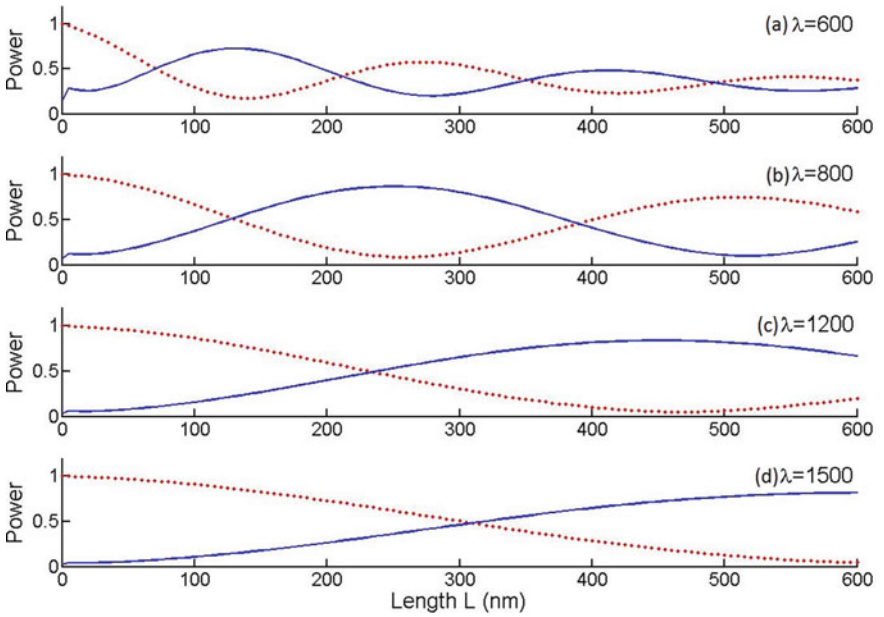

Fig. 2 Power switching dynamics in the coupler for 'Ag'-air interface along length L for $\lambda = 600$, 800, 1200 and 1500 nm.

radiation than lower wavelength radiation. Hence to get fast switching of radiation of lower wavelength is more useful.

Further, the numerical experiments have been repeated for the various metal-air interfaces by changing the metals ('Ag', 'Au', 'Cu', or 'Al') at the interface to see the effect of metals on the power switching dynamics. It is observed in Fig. 3(a)–(d) that the coupling length is moreover the same for the 'Ag', 'Au', and 'Cu' but is longer for the 'Al'. Further, for the lower wavelength side, the coupling is weak for 'Cu'. Hence, it can be concluded that only 'Ag' and 'Au' are appropriate metals for these types of applications. The performance of 'Al' and 'Cu' could not provide the desired result.

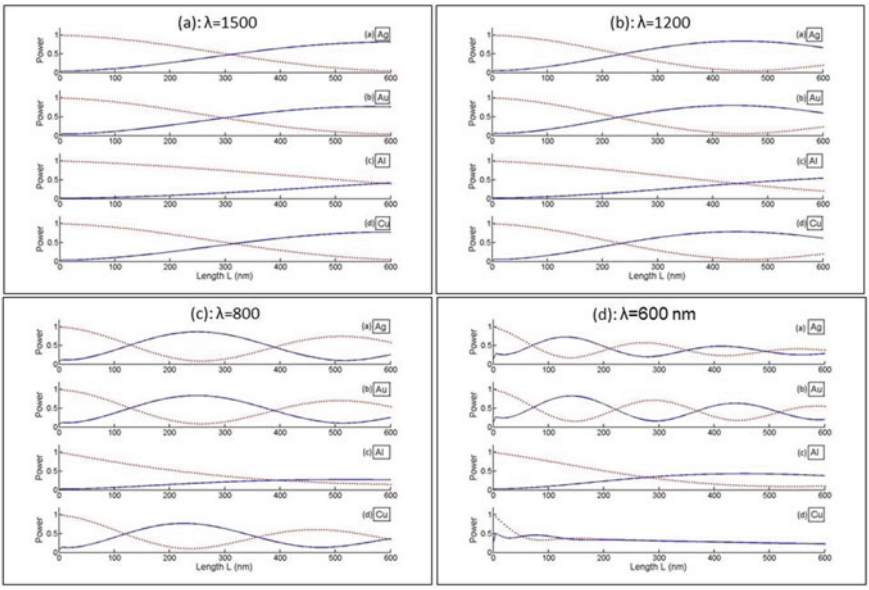

Fig. 3 Power switching dynamics in the coupler for various metal-air interfaces along length L; **a** $\lambda = 1500\,\text{nm}$, **b** $\lambda = 1200\,\text{nm}$, **c** $\lambda = 800\,\text{nm}$, and **d** $\lambda = 600\,\text{nm}$.

3 Conclusion

This article simulated a plasmonic coupler using the *finite-difference-time-domain* (FDTD) algorithm to reveal power switching properties between the rectangular waveguides. It is found in the proposed structure that the coupling length is a function of input radiation's wavelength and the *coupling length* increases on an increase in wavelength. Further, it has been noted in the present structure that *'Ag'* and *'Au'* are more suitable metals than *'Al'* and *'Cu'* for making nano-scale couplers. Such types of couplers can be utilized in various switching circuits and logic gates.

Acknowledgement The author MM is thankful to DST-SERB for the fast track project grant (***FTP/PS-211/2012***).

References

1. Maier SA (2007) Plasmonics: fundamentals and applications. Springer, New York
2. Economou EN (1969) Surface plasmons in thin films. Phys Rev 182(2):539
3. Ritchie RH (1957) Plasma losses by fast electrons in thin films. Phys Rev 106(5):874
4. Geim AK, Novoselov KS (2010) Nanoscience and technology: a collection of reviews from nature journals. Assembly Autom 20:11–19

5. Fang N, Lee H, Sun C, Zhang X (2005) Sub-diffraction-limited optical imaging with a silver superlens. Science 308(5721):534–537
6. Ozbay E (2006) Plasmonics: merging photonics and electronics at nanoscale dimensions. Science 311(5758):189–193
7. Ding F, Bozhevolnyi SI (2019) A review of unidirectional surface plasmon polariton metacouplers. IEEE J Sel Top Quantum Electron 25(3):1–11
8. Chelladurai D, Doderer M, Koch U, Fedoryshyn Y, Haffner C, Leuthold J (2019) Low-loss hybrid plasmonic coupler. Opt Express 27(8):11862–11868
9. Lim HJ, Kwon MS (2014) Efficient coupling between photonic and dielectric-loaded surface plasmon polariton waveguides with the same core material. IEEE Photonics J 6(3):1–9
10. Peng X, Hao R, Ye Z, Qin P, Chen W, Chen H, Jin X, Yang D, Li E (2017) Highly efficient graphene-on-gap modulator by employing the hybrid plasmonic effect. Opt Lett 42(9):1736–1739
11. Haffner C, Heni W, Fedoryshyn Y, Niegemann J, Melikyan A, Elder DL, Baeuerle B, Salamin Y, Josten A, Koch U, Hoessbacher C (2015) All-plasmonic Mach-Zehnder modulator enabling optical high-speed communication at the microscale. Nat Photonics 9(8):525–528
12. Xu W, Zhu ZH, Liu K, Zhang JF, Yuan XD, Lu QS, Qin SQ (2015) Toward integrated electrically controllable directional coupling based on dielectric loaded graphene plasmonic waveguide. Opt Lett 40(7):1603–1606
13. Mishra M, Jhajharia P, Jana S (2021) Power exchange dynamics for performance optimization in a miniature plasmonic waveguide coupler. Optoelectron Adv Mater-Rapid Commun 15:207–212
14. Haffner C, Chelladurai D, Fedoryshyn Y, Josten A, Baeuerle B, Heni W, Watanabe T, Cui T, Cheng B, Saha S, Elder DL (2018) Low-loss plasmon-assisted electro-optic modulator. Nature 556(7702):483–486
15. Inan US, Marshall RA (2011) Numerical electromagnetics: the FDTD method. Cambridge University Press, Cambridge
16. Palik ED (ed) (1998) Handbook of optical constants of solids, vol 3. Academic Press, Orlando
17. Tao J, Huang XG, Lin X, Zhang Q, Jin X (2009) A narrow-band subwavelength plasmonic waveguide filter with asymmetrical multiple-teeth-shaped structure. Opt Express 17(16):13989–13994

Analysis for Cost Optimized EO Design of a Reversible Boolean Function Using MZIs

Shashank Awasthi, Barnali Chowdhury, Muhammad Arif Jalil, Jalil Ali, Preecha Yupapin, Sanjeev Kumar Metya, and Alak Majumder

Abstract The concept of making any logical (Boolean) function reversible is gaining much attention in the recent past for its applications in nanotechnology, quantum dot cellular automata and quantum computing etc. The use of reversible Boolean function not only simplifies back tracing, but it also allows efficient computation because of the non erasure of stored data, which lowers heat dissipation. This paper selects a reversible Boolean expression and explores its realization using electro-optic Mach-Zehnder Interferometer. Various design combinations are explored to implement the cost optimized reversible configurations. The designs are carried out in OptiBPM platform and the truth table is verified using power equations simulated in MATLAB.

Keywords Reversible gates · Reversible Boolean function · Mach-Zehnder interferometer

1 Introduction

When a thermodynamical system is capable to return to its initial state it is called reversible system and during the process energy is conserved [1]. The conventional electronic system is not reversible and dissipates $kTln2$ amount of heat energy (HE) [2] for each bit of Boolean, logical or arithmetical operation where k is Boltzmann constant and T is absolute temperature. The concept of reversibility was coined

S. Awasthi (✉) · B. Chowdhury · S. K. Metya · A. Majumder
i-CAS Lab, National Institute of Technology Arunachal Pradesh, Jote, India
e-mail: shashank.1801@gmail.com

M. A. Jalil
Universiti Teknologi Malaysia, Johor Bahru, Malaysia

J. Ali
Asia Metropolitan University, Masai, Johor, Malaysia

P. Yupapin
Institute of Vocational Education Northeastern Region - 2, Sakonnakhon, Thailand

M. Tiwari et al. (eds.), *Optical and Wireless Technologies*, Lecture Notes in Electrical Engineering 892, https://doi.org/10.1007/978-981-19-1645-8_6

Table 1 Truth table for conventional and reversible XOR

Input		Output		
		Conventional XOR	Reversible XOR	
X1	Y1	Z1	Z2(=X1)	Z3
0	0	0	0	0
0	1	1	0	1
1	0	1	1	1
1	1	0	1	0

in [3] considering the idea of thermodynamics to reduce the HE. Additionally, the significance of a reversible system can be understood from the truth table mentioned in Table 1, where it compares a conventional and reversible XOR (RXOR) (also called as Feynman gate [4]) operation. Unlike non-reversible XOR, the RXOR has distinct input output combination that makes the back tracing of input easier. Photons being superior than electrons both in terms of speed and heat dissipation factor, a few very prominent reversible gates are realized in [4–6]. Using various optical switches (OS) that are discussed in [7] are used to implement reversible logic/Boolean functions. One of the key OS namely electro-optic (EO) Mach-Zehnder Interferometer (MZI) is discussed in [5].

MZI switch uses an optical input (laser source); however the electrode voltage (EV) decides the appearance of light at the output port. Out of many materials (e.g., barium titanate, lithium tantalate, gallium arsenide) that are used in the designing the MZI switch, Titanium diffused Lithium Niobate (Ti-LN) is mostly used due to its better EO tensor coefficient that significantly reduces the magnitude of EV [8]. Authors in [8] have proposed a reversible 3:8 decoder using a cascaded configuration of Feynman, Optimized Fredkin & Fredkin gate and can be extendable to $N : 2^N$. This work presents a case study of a cost-optimized EO-MZI design of a random Boolean function based on Modified Fredkin gate (MFG) and the above mentioned RGs in cascaded arrangement.

Thus the paper is organized as follows; Sect. 2 reviews the electro-optic MZI based reversible gates, Sect. 3 deals with the selection of random Boolean function and its implementation using reversible gates, Sect. 4 validates the truth table of the Boolean function using MZI power modelling simulated in MATLAB and lastly Sect. 5 concludes the paper.

2 Literature of Electro-optic MZI Based Reversible Gates

The EO-MZI is a 2×2 optical switch as discussed in [5]. It comprises of two 3-dB couplers interconnected with interferometric arms lying under the three electrodes as shown in Fig. 1.

The input to MZI is a light source in laser form of wavelength 1300 nm [6] which is given to port A as shown in Fig. 1 (also called as upper input port and the bottom port is called lower input port). The 3-dB couplers first split and then combine the light to make it available at the respective output port depending on the EV applied at electrode 2 (E2). It is to be noted that the other two electrodes E1 and E3 are always kept grounded. Thus, MZI behaves either as a bar switch or cross switch depending on the EV applied. Usually as discussed in [8] 6.8 V is considered as logic '1' for bar state and 0 V is considered as logic '0' for cross state. Based on MZI switching behaviour various reversible gates have been discussed in literature and are summarized below in Table 2.

The term optical cost mentioned in Table 2 determines the number of MZIs used in the RGs; whereas optical delay defines the number of MZIs working in parallel to complete the mathematical computation. All these RGs are multiple input-output gates and it is possible to make them to behave like a conventional electronic gate by

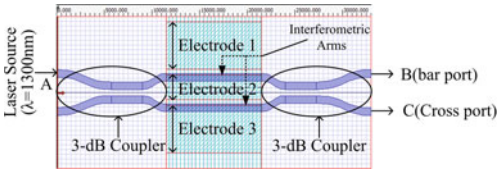

Fig. 1 EO-MZI design architecture from OptiBPM tool.

Table 2 Reversible gates; mathematical expressions, optical cost and delay

Gate	Mathematical expression	Optical cost	Optical delay
Feynman gate (FeG) [4]	P = A Q = A ⊕ B	2	2
Fredkin gate (FG) [4]	P = A Q = $\overline{A}$B ⊕ AC R = $\overline{A}$C ⊕ AB	5	2
Optimized Fredkin gate (OFG) [8]	P = A Q = $\overline{A}$B ⊕ A$\overline{C}$ R = AB ⊕ $\overline{A}$ $\overline{B}$	5	2
Modified Fredkin gate (MFG) [5]	P = A Q = B R = C(A⊕B) + D(A⊙B) S = C(A⊙B) + D(A⊕B)	8	3

Table 3 Various Ancilla combination representing conventional gates from RGs

RG	RG input(s)				RG output(s)				Conventional gate
	A	B	C	D	P	Q	R	S	
FeG	A	1	–	–	A	$\overline{A}$	–	–	NOT
	1	B	–	–	1	$\overline{B}$	–	–	NOT
FG	A	B	0	–	A	$\overline{A}$B	AB	–	AND
	A	0	C	–	A	AC	$\overline{A}$C	–	AND
	A	0	1	–	A	A	$\overline{A}$	–	NOT
	A	1	C	–	A	$\overline{A}$+AC	A+C	–	OR
OFG	A	B	0	–	A	$\overline{A}$B	AB	–	AND
MFG	A	1	0	1	A	1	A	$\overline{A}$	NOT
	A	B	0	D	A	B	A⊙B	A⊕B	XNOR, XOR
	0	B	0	1	0	B	$\overline{B}$D	BD	AND
	0	B	C	1	0	B	C+$\overline{B}$	B+C	OR
	1	B1+B2	0	1	1	B1+B2	B1+B2	$\overline{B1}.\overline{B2}$	NOR

keeping some of the inputs to a fixed value. These fixed value inputs are also termed as 'ancilla input'. For example, in Feynman gate (FeG), when the second input is kept at logic '1' (i.e., B = 1) the output expression will become Q = $\overline{A}$ and that shows FeG acts like a conventional NOT gate. Accordingly, considering various ancillas for different RGs it is likely to obtain some of the electronic gates as summarized in Table 3.

3 Selection of Boolean Function and Its EO MZI Realization Using Reversible Gates

It has been noted that not all Boolean functions are reversible, thus a specific condition is required to make the function reversible. Also, note that subset of multiple output functions can be reversible and can be defined as: a function with n inputs and m outputs such that $f : Z^n \rightarrow Z^m$ is called a reversible function only if it satisfies the bijection property. This implies that a function must have equal number of inputs and output. Mathematically it can be expressed as $f \in B_{n,n}$. It is mentioned in [9] that $\log_2(\zeta(f))$ are the number of additional outputs required where ζ defines the maximum times the output pattern (repetition of same output multiple times for different input combinations) can be generated by f. Further, to maintain the input output combination, number of inputs might need to be increased accordingly. Thus, reversible functions can be given as $f^{"} : Z^{m+\log_2(\zeta)} \rightarrow Z^{m+\log_2(\zeta)}$, here $f^{''}$ defines the complete reversible function. Lets consider an example; $f^{'}(x, y) = x.y$ (i.e., x ∧ y). Since, $f^{'}$ is a non-reversible function and it defines the 'AND' operation, thus logic '0' repeats itself three times for input combinations of 00, 01 and 10 i.e., $\zeta = 3$.

Table 4 Truth table for $f''(x, y, z)$

Input			Output		
x	y	z	p	q	r
0	0	0	0	0	0
0	0	1	0	0	1
0	1	0	0	1	0
0	1	1	0	1	1
1	0	0	1	0	0
1	0	1	1	0	1
1	1	0	1	1	1
1	1	1	1	1	0

Thus, to make this expression reversible an additional $\log_2(\zeta(f)) = \log_2(3) = 2$ outputs need to be introduced at the output section without disturbing the main functionality. Moreover, to check if an extra input is required the function is given by $1 + [\log_2(\zeta(f))] - 2 = 1$ [9]. Hence the resulting expression is given as $f''(x, y.z) = x.y \oplus z$. The truth table for the given reversible Boolean function is shown in Table 4. From Table 4 it is evident that, no output combinations are repeating for any input combinations and that satisfies the condition of reversibility. The following combinations are explored to implement this reversible Boolean function (RBF) in the presented case, where we are considering only four RGs such as FeG, FG, MFG and OFG.

3.1 Optimized Fredkin Gate and Feynman Gate

Figure 2a shows the block structure proposed to implement the RBF and Fig. 2b shows the MZI architecture for the same. Here one OFG and FeG are cascaded to obtain the desired expression. Since, final expression is a 3×3 logic, it is required to assume one ancilla input at the OFG to get the 'AND' operation of first two inputs at the last output port of OFG. Thus, the third input is taken as logic '0' i.e., a constant 0V is supplied to MZI2 and MZI4 as shown in Fig. 2b. Since, FeG describes the reversible XOR operation (refer Table 2), the third input of the expression i.e., input z is given to first input of FeG or at MZI6 as shown in Fig. 2b. Thus, to get the 'XOR' operation of output 'xy', it is fed to MZI7 as an electrode voltage resulting in the desired output. Since, OFG uses 5 MZIs and FeG comprises of 2 MZIs, the total optical cost incurred is 7 and optical delay is 4. The calculated garbage outputs are three with one ancilla input at OFG's third input port.

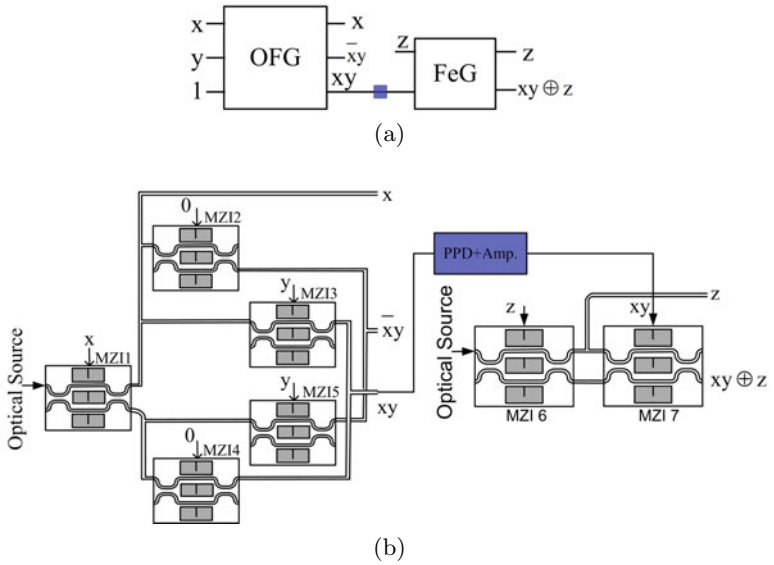

Fig. 2 Implementation of RBF using OFG and FeG **a** Block architecture **b** MZI schematic.

3.2 Modified Fredkin Gate and Feynman Gate

Figure 3a shows the block diagram in another attempt to obtain the desired result of RBF. MFG is a 4×4 gate and thus it is required to have two ancillas as logic '0' and two variable inputs viz. 'x' and 'y'. Figure 3b shows the MZI schematic architecture of the same where the circuit before PPD is MFG and later half is FeG. Thus, the logic '0' ancilla is given to MZI1, MZI3 and MZI6 as they are responsible to receive the first and third input. However, MZI2, MZI7 and MZI8 are fed with input 'x' and the remaining MZIs i.e., MZI4 and MZI5 are given with input 'y'. Referring to Table 3 (MFG column) the last port of the MFG yields the AND operation which is then similarly transferred to FeG as mentioned in earlier case. This yields the final result as $xy \oplus z$. In this architecture, the total garbage output produced is 4. Considering the optical cost since MFG uses 8 MZIs & FeG has 2 MZIs, the total optical cost is 10 with optical delay is 5.

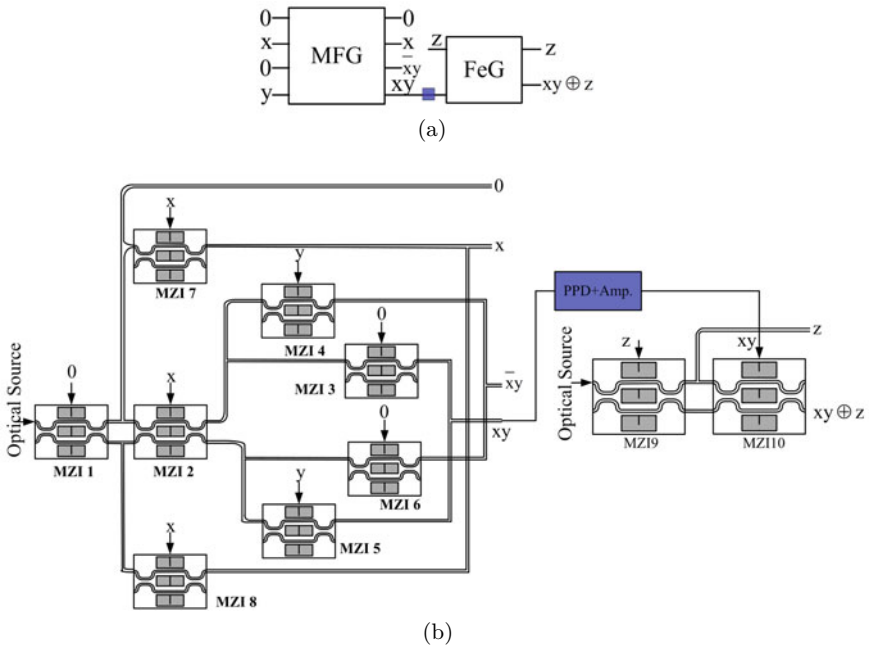

Fig. 3 Implementation of RBF using MFG and FeG **a** Block architecture **b** MZI schematic.

3.3 Fredkin Gate and Modified Fredkin Gate

The cascade combination of Fredkin gate (FG) and MFG as shown in Fig. 4 is also capable of yielding the desired RBF. To obtain the result in the following combination three ancillas are to be considered; one at FG (since it is a 3×3 gate) as logic '1' at the third input and other two are at MFG as logic '0' and '1' at the third and fourth input respectively. It is evident from Fig. 4 that there is one major benefit of this architecture i.e., in getting the desired expression the third output produces the compliment of fourth output (or desired expression). Figure 4b shows the input given to respective MZIs. The total optical cost of the design is 13 with an optical delay of 5.

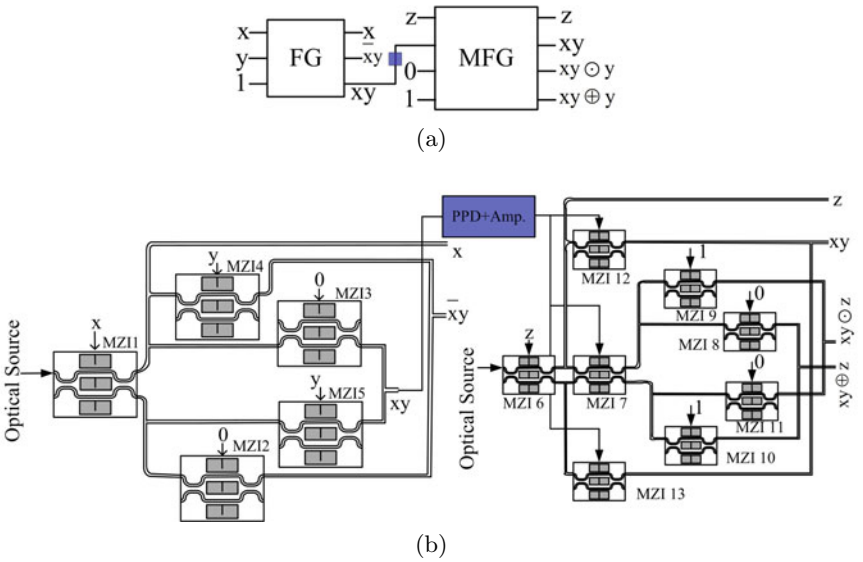

Fig. 4 Implementation of RBF using FG and MFG **a** Block architecture **b** MZI schematic.

3.4 Fredkin and Feynman Gate

The cascade combination of Fredkin and Feynman gate results in getting the desired RBF as shown in Fig. 5. The design structure is similar to the combination of OFG

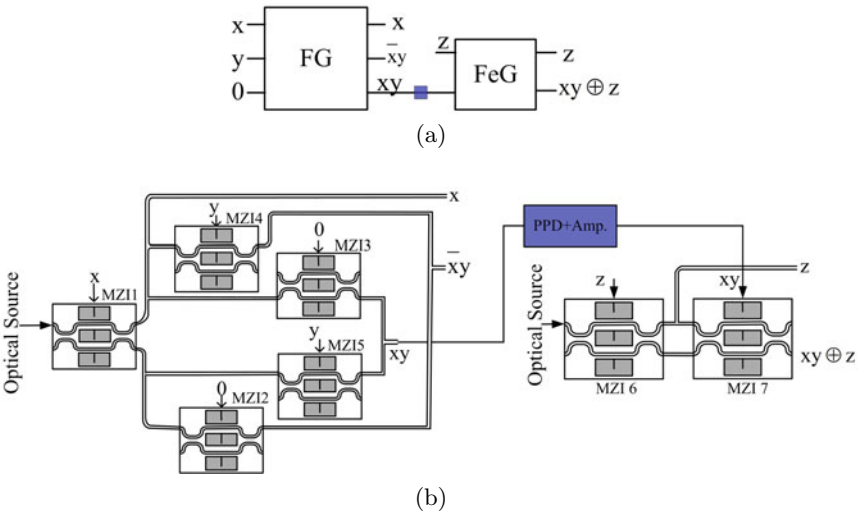

Fig. 5 Implementation of RBF using FG and MFG **a** Block architecture **b** MZI schematic.

and FG with unchanged optical cost and delay i.e., 7 and 4. Hence, considering all the combinations it has been found that first and last combination i.e. OFG+FeG and FG+FeG yields the optimized EO RBF design using the given four RGs with optical cost of 7 and optical delay of 5.

4 Power Modelling and Truth Table Validation

For every MZI the availability of light at the output port is defined by the power it has at the final port of respective MZIs after traversing through the waveguides and it is given by the following expression [5];

$$P_B = sin^2\left(\frac{\Delta\phi_1}{2}\right) \& P_C = cos^2\left(\frac{\Delta\phi_1}{2}\right) \tag{1}$$

Equation 1 defines the power at the output port of each MZI when the laser source is applied to upper input port of MZI, however if the laser source is given to lower input port, then the equation becomes;

$$P_B = cos^2\left(\frac{\Delta\phi_1}{2}\right) \& P_C = sin^2\left(\frac{\Delta\phi_1}{2}\right) \tag{2}$$

Thus, using Eqs. 1 and 2 the power equation can be written for every combination however, the following power modelling is done for the very first combination due to its minimum optical cost and delay. Hence Eq. 3 shows the power equation of OFG+FeG combination, where $\Delta\phi_n$ represents the change in phase of the respective MZIs upon the application of EV and n portrays the MZI number. For example $\Delta\phi_6$ is for MZI6, $\Delta\phi_7$ is for MZI7.

$$P_{(OFG+FeG)} = sin^2\left(\frac{\Delta\phi_6}{2}\right) cos^2\left(\frac{\Delta\phi_7}{2}\right) + cos^2\left(\frac{\Delta\phi_6}{2}\right) sin^2\left(\frac{\Delta\phi_7}{2}\right) \tag{3}$$

The above Eq. 3 is then simulated in MATLAB to validate the truth table shown in Table 1. Figure 6 shows the MATLAB simulation for Fig. 2, where the first row shows the output for input combination 000 to 011 and second row represents the output for inputs 100 to 111. From Fig. 6 results, it has to be noted that the curves where they rise from 0 to 1 V represents logic '1', where as the flat line or no line shows logic '0'. There is an exception for last input combination '111' where the curve raises to 0.5 V and again drops to 0V and this also defines logic '0'. The following MATLAB simulation validates the truth table as mentioned in Table 4.

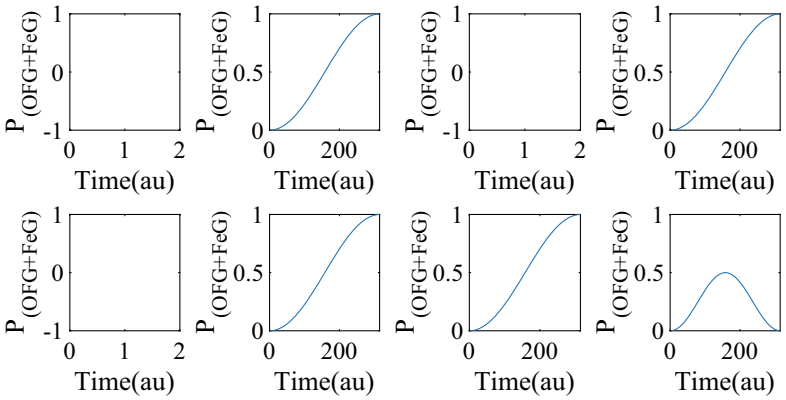

Fig. 6 MATLAB simulation results for OFG+FeG to validate Table 4.

5 Conclusion

Defining any Boolean function in reversible form needs a mathematics and, in the process, the complete equation gains some extra (garbage) outputs & extra (may or may not be ancilla) inputs. Thus, this paper aims to design a reversible Boolean function (RBF) based on electro-optic (EO) Mach-Zehnder interferometer reversible gates. Various combinations have been explored to implement the RBF and the cost optimized design is validated with the power equations simulated in MATLAB. The optical cost and delay are also calculated in each case viz. OFG+FeG, MFG+FeG, FG+MFG and FG+FeG and the least optical cost and delay are found for first and last case as 7 and 4 respectively.

Acknowledgement Authors would like to thank Visvesvaraya PhD scheme, MeitY Govt. of India for all the supports they have provided.

References

1. Norton JD (2017) Thermodynamically reversible process. Am J Phys 85:135–145
2. Landauer R (1961) Irreversibility and Heat Generation in the computing Process. IBM J Res Dev 5:183–191
3. Bennett CH (1973) Logical reversibility of computation. IBM J Res Dev 17:525–532
4. Kumar S, Chanderkanta, Raghuwanshi SK (2016) Design of optical reversible logic gates using electro-optic effect of lithium niobate based Mach-Zehnder interferometers. Appl Opt 55:5693–5701
5. Awasthi S, Metya SK, Majumder A (2020) Optical configuration of modified Fredkin gate using lithium-niobate-based Mach-Zehnder Interferometer 59(23):7083–7091

6. Awasthi S, Metya SK, Majumder A (2020) Electro-optic Reversible Toffoli Gate with optimal count of LiNbO3 Mach-Zehnder Interferometer. In: 2020 IEEE nordic circuits and systems conference (NorCAS), Oslo, Norway, pp 1–7
7. Singh P, Tripathi DK, Jaiswal S, Dixit HK (2014) All-optical logic gates: designs, classification and comparison. Adv Opt Technol 2014(275083):1–13
8. Awasthi S, Chowdhury B, Haider Z, Ali J, Yupapin P, Metya SK, Majumder A (2021) Optical configuration of an N:2^N reversible decoder using LiNbO3-based Mach-Zehnder interferometer. Appl Opt 60(16):4544–4556
9. Wille R, Lye A, Niemann P (2016) Checking reversibility of Boolean function. In: 8th international conference on reversible computation, vol 9720. Springer, Cham, pp 322–337 (2016)

TIR-ORQPM Technique for Generating Highly Efficient Second Harmonic

Moumita Saha and Sumita Deb

Abstract The generation of highly efficient second harmonic wavelength has been analyzed in this work by introducing the concept of optical rotation quasi-phase-matching technique by total-internal-reflection in yttrium oxide coated rectangular slab of magnesium oxide-doped lithium niobate crystal. At specific bounce sites inside the slab, the combined impact of optical rotation quasi-phase-matching and fractional quasi-phase-matching methods based on total-internal-reflection has resulted in highly improved conversion efficiency. The thin-film is introduced to regulate the phase-shifts caused by the propagation of *p*—and *s*-polarized light during total internal reflection at the slab-film interface. A graphical representation has been carried out using computer-aided simulation for a second harmonic wavelength of 514.5 nm while considering the effects of surface roughness, absorption and nonlinear law of reflection. Results show a peak conversion efficiency as high as 30.5%.

Keywords ORQPM · TIR · Electro-optic chiral · Second harmonic · Thin-film · Wave mixing · Underwater communication

1 Introduction

Over the last few years, quasi-phase-matching (QPM) technique has become a vital area of study. Many studies have indicated some popular methods for fabricating QPM waveguides, such as nonlinear material's periodic poling [1]. Fabrication error is the main weakness of this periodic poling approach [2], and it causes phase error between the interacting fields. This error results in a gradual decrease in the harmonic production [1, 2]. The revolution had taken place in 1962 when Armstrong et al. [3] presented the total-internal-reflection (TIR) based QPM technique which was carried forward by Boyd and Patel [4] as well as by Komine et al. [5] for second harmonic generation (SHG). The concept of fractional QPM was then introduced by Haïdar in

M. Saha (✉) · S. Deb
Department of Electrical Engineering, National Institute of Technology, Agartala, India
e-mail: er.moumitasaha@gmail.com

M. Tiwari et al. (eds.), *Optical and Wireless Technologies*, Lecture Notes in Electrical Engineering 892, https://doi.org/10.1007/978-981-19-1645-8_7

2005 [6]. Then, a surprising difference between the obtained results due to theoretical and experimental TIR-QPM technique has been addressed by Raybaut et al. in 2008 [7]. This difference is basically due to the destructive interference effect and had been explained by Bloembergen and Pershan's nonlinear law of reflection [8]. This destructive interference can be avoided by rotating the plane of polarization, according to Lewis Z. Liu et al. in 2012 and the concept is termed as optical rotation quasi-phase-matching (ORQPM) [9]. As per ref. [9], the efficiency of the circularly polarized harmonic generated by this ORQPM technique is approximately five times more efficient than the linearly polarized harmonics generated due to conventional QPM technique. Moreover, in 2012, L. Shi had demonstrated that, the polarization of an electro-optic (EO) chiral material can be controlled by the application of external electric field [10]. The conceptual accomplishment of this ORQPM approach has been compiled with the TIR phenomenon in our prior SHG study [11], third—and fourth-harmonic generation study [12], allowing polarization rotation controlled by an external electric field. In ref. [11], the ideal ORQPM condition cannot be achieved during SHG owing to the threshold limits of the crystalline slab under study. As a consequence, in this analysis, we attempted to minimize the deviation from the optimal ORQPM method as much as possible. The proposed frequency converter model requires a high level of flexibility in order to satisfy the QPM criterion while also triggering constructive interference of the produced light through polarization rotation without exceeding the allowable limits. Therefore, the concept of thin film used in ref. [11, 12] and [13] has also been incorporated here. The basic idea of this thin film inclusion had been described by Azzam in 1985 [14] and implemented in 2009 [15] for making the reflected light independent of polarization. The modified phase-shift equations during TIR for *p*-polarized (δ_{TP}) and *s*-polarized (δ_{TS}) light in presence of thin film have been considered for this numeric analytical work [11–13]

$$\delta_{TP} = \frac{4\pi}{\lambda} d_1 \left(N_1^2 - N_0^2 \sin^2 \varphi_0\right)^{1/2} - 2\tan^{-1} \frac{N_1^4 N_0 \cos\varphi_0 \sqrt{N_0^2 \sin^2 \varphi_0 - N_2^2}}{N_0^2 N_2^2 \left(N_1^2 - N_0^2 \sin^2 \varphi_0\right)} \quad (1)$$

$$\delta_{TS} = \frac{4\pi}{\lambda} d_1 \left(N_1^2 - N_0^2 \sin^2 \varphi_0\right)^{1/2} - 2\tan^{-1} \frac{N_0 \cos\varphi_0 \sqrt{N_0^2 \sin^2 \varphi_0 - N_2^2}}{\left(N_1^2 - N_0^2 \sin^2 \varphi_0\right)} \quad (2)$$

where, N_1 is the refractive index of thin film.

d_1 is the thin film thickness.

λ is the wavelength of the monochromatic incident light.

The incident angle φ_0 should be smaller than the light reflection critical angle of medium 0—medium 1 interface but greater than the light reflection critical angle of medium 0—medium 2 interface [15].

The light reflection critical angle at the medium 0—medium 1 interface is

$$\varphi_{C01} = \sin^{-1}\left(\frac{N_1}{N_0}\right) \quad (3)$$

The light reflection critical angle at the medium 0—medium 2 interface is

$$\varphi_{C02} = \sin^{-1}\left(\frac{N_2}{N_0}\right) \tag{4}$$

Therefore, the requisite for TIR at the medium 0—medium 2 interface, in the presence of medium 1(thin layer) is

$$\varphi_{C02} < \varphi_0 < \varphi_{C01} \tag{5}$$

And the provision for excluding TIR from the interface of the medium 0—medium 1, is [14]

$$N_0 \sin\varphi_0 < N_1 \tag{6}$$

As a result, the objective of this article is to give a better analysis of the ORQPM technique based on TIR by regulating the rotation period considerably closer to the ideal ORQPM scenario. The effect of surface roughness, absorption loss, and the interference effect of nonlinear law has been comprehended for SHG in this analysis.

2 Operational and Structural Analysis of Proposed Work

2.1 Geometrical Topology

Figure 1 portrays the geometrical topology of the proposed rectangular thin film coated semiconductor slab [11, 12].

Here, the crystal length is defined by L, crystal thickness by t, thin film thickness by d_1, bounce length by L_1 and the entry point of the driving radiation by X. The monocromatic light propagates through TIR and the optic axis is parallel to the horizontal plane.

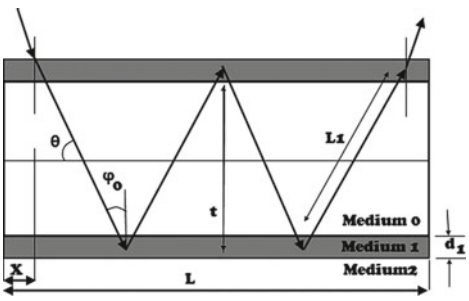

Fig. 1 Topology of semiconductor slab for the frequency conversion by ORQPM technique

2.2 Numeric-Analytical Study of the TIR-ORQPM Approach for SHG

The purpose of the proposed frequency converter is to generate highly efficient SH by the TIR-ORQPM technique in an EO chiral material under the influence of an external electric field. The ideal condition for ORQPM is $2L_c = 2L_r$, *i.e.*, the rotation period ($2L_r$) should be equal to double the coherence length. However, in our previous work of SHG [11], we were unable to fulfil this condition and settle down with a compromising state of $2\ L_c = 12L_r$ at a cost of efficiency drop. Therefore, the goal of this study is to achieve a near-optimal ORQPM condition while keeping the other variables within their allowable ranges. Here, the optical path length (L_B) and the external electric field (E) control the polarization rotation [10–12] as:

$$\beta = \frac{2}{\Lambda} \frac{\gamma_{51} E}{(1/n_e)^2 - (1/n_o)^2} L_B \tag{7}$$

where, Λ is the domain thickness, γ_{51} is EO coefficient for an applied external electric field along the y axis of MgO:LN crystal, n_e and n_o are the refractive indices of the extraordinary and ordinary wave respectively. Moreover, the bounce length (L_1) is regarded as domain thickness, Λ [11, 12]. The Eq. (7) is bounded with several conditions, such as the optical path length should be matched with the rotation period *i.e.,* $L_B = 2L_r$ and within this length, the condition of 2π polarization rotation has to be fulfilled as well. Therefore, to fulfill all the conditions while maintaining a proper slab thickness, the considered rotation period has to be eight times the coherence length *i.e.*, $2L_r = 8L_c$. Furthermore, the threshold limit of the applied electric field is maintained by considering the per bounce length as $\frac{8}{101}L_c$ *i.e.*, 101 bounces are required to rotate the polarization plane of the generated SH by 2π. Therefore, the SH field for ORQPM will be produced after every 101 bounces and that for fractional QPM at every bounce, as $L_1 = \frac{8}{101}L_c$. Consequently, the combined effect of ORQPM and fractional QPM is available after 101, 202, 303, 404, … bounces and so on. Here, the considered polarization configuration is *p*–*p*–*s* (type-I phase-matching) as it shows the lowest wave vector mismatch and thereby the generated harmonic field is *s*-polarized. This generated harmonic field is not aligned parallel to optic axis and hence the component wave (*p* and *s*) propagation has been considered for our mathematical analysis. This type of propagation generates an additional TIR phase-shift which affects the global phase-shift. Therefore, considering all the consequences, the generated harmonic field amplitude is written as [11]:

$$\text{For ORQPM}: A_{2\omega\_y(ORQPM)}(L_1) = 4\pi \left(\frac{2\omega}{n_{2\omega}c}\right) d_{pps} A_\omega^2 \left[\frac{2i\Delta k L_1 - e^{-i2\Delta k L_1} + 1}{4\Delta k}\right] \tag{8}$$

$$\text{For fractional QPM}: A_{2\omega\_y(Fractional QPM)}(L_1) = 4\pi\left(\frac{2\omega}{n_{2\omega}c}\right)d_{pps}A_{\omega}^{2}\left[\frac{1-e^{-i2\Delta kL_1}}{\Delta k}\right] \tag{9}$$

where $\Delta k = k_{2\omega} - 2k_{\omega}$, $n_{2\omega}$ is the optical index of the material for generated SH, A_{ω} represents the input beam field amplitude, $A_{2\omega}$ represents the generated beam field amplitude and the propagation direction is along the z-axis. For any intermediate length L_j, s-wave can be rewritten as [11]

For ORQPM: $A_{2\omega\_y\_s(ORQPM)}\left(L_j\right)$

$$= \left\{e^{-i(\Delta\varphi_1+\delta_{TS1})}\cos\theta + e^{-i(\Delta\varphi_2+2\delta_{TS2})}\cos^2\theta + \ldots + e^{-i(j-1)(\Delta\varphi_{(j-1)}+\delta_{TS(j-1)})}\cos^{(j-1)}\theta\right\}A_{2\omega\_y(ORQPM)}(L_1) \tag{10}$$

For fractional QPM: $A_{2\omega\_y\_s(Fractional QPM)}\left(L_j\right)$

$$= \left\{e^{-i(\Delta\varphi_1+\delta_{TS1})}\cos\theta + e^{-i(\Delta\varphi_2+2\delta_{TS2})}\cos^2\theta + \ldots + e^{-i(j-1)(\Delta\varphi_{(j-1)}+\delta_{TS(j-1)})}\cos^{(j-1)}\theta\right\}A_{2\omega\_y(Fractional QPM)}(L_1) \tag{11}$$

For any intermediate length L_j, p-wave can be rewritten as [11]

For ORQPM: $A_{2\omega\_y\_p(ORQPM)}\left(L_{j-1}\right)$

$$= \left\{e^{-i(\Delta\varphi_1+\delta_{TS1})}\sin\theta + e^{-i(\Delta\varphi_2+2\delta_{TS2})}\sin^2\theta + \ldots + e^{-i(j-1)(\Delta\varphi_{(j-1)}+\delta_{TS(j-1)})}\sin^{(j-1)}\theta\right\}A_{2\omega\_y(ORQPM)}(L_1) \tag{12}$$

For fractional QPM: $A_{2\omega\_y\_p(Fractional QPM)}\left(L_{j-1}\right)$

$$= \left\{\begin{array}{c} e^{-i(\Delta\varphi_1+\delta_{TS1})}\sin\theta + e^{-i(\Delta\varphi_2+2\delta_{TS2})}\sin^2\theta + \ldots \\ +e^{-i(j-1)(\Delta\varphi_{(j-1)}+\delta_{TS(j-1)})}\sin^{(j-1)}\theta \end{array}\right\}A_{2\omega\_y(Fractinal QPM)}(L_1) \tag{13}$$

As a result, the net SH electric field amplitude for n number of bounces as [11]: $A_{2\omega\_y}(L_1 + L_2 + L_3 + \ldots + L_n)$

$$= \sum_{j=1}^{n}\left\{\begin{array}{c} A_{2\omega_{y_{s(ORQPM)}}}\left(L_j\right) + A_{2\omega_{y_{s(Fractional QPM)}}}\left(L_j\right) \\ +A_{2\omega\_y\_p(ORQPM)}\left(L_{j-1}\right) + A_{2\omega\_y\_p(Fractional QPM)}\left(L_{j-1}\right) \end{array}\right\} \tag{14}$$

where n = 101, 202, 303, …

The net SH electric field $A_{2\omega\_y}$ is used to calculate the time-average SH intensity as:

$$I_{2\omega\_y} = \frac{n_{2\omega}c}{2\pi}\left|A_{2\omega\_y}\right|^2 \tag{15}$$

Finally, the SH peak conversion efficiency is determined by the combined field effect of ORQPM and the fractional QPM approach, as:

$$\eta_{SHG\_TIR-ORQPM\_fractional QPM} = \frac{I_{2\omega\_y}(z)}{I_p} \times 100\% \tag{16}$$

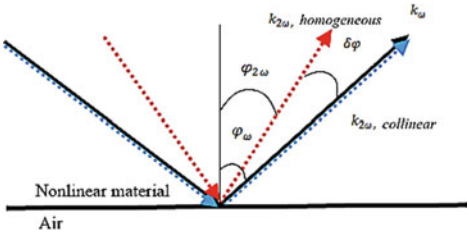

Fig. 2 Snell-Descartes law

I_p is the fundamental beam intensity assumed to be undepleted.

2.3 *Losses and the Interference Effect of the Nonlinear Law of Reflection*

A significant amount of efficiency drop is observed due to the absorption and roughness. The linear absorption coefficient α_ω is much less than 1 but its effect cannot be neglected. At each point of reflection, there is a reflection loss due to the surface roughness and is determined in terms of reflection coefficient R [16] (Fig. 2).

$$R \approx 1 - \left(\frac{4\pi n_j \sigma \cos\varphi_0}{\lambda_j}\right)^2 \tag{17}$$

where $j = \omega$ for the fundamental wave and $j = 2\omega$ for the generated SH, and σ is the standard deviation of surface roughness ($\sigma = p - v$ value/12) [16]. The p–v value is peak to valley value of the semiconductor's surface. However, the interference effect of the nonlinear law of reflection may cause destructive or even constructive outcome of interacting waves due to the non-collinearity effect of the generated homogeneous SH. According to reflection law of Bloembergen and Pershan [8], a nonlinear medium generates a collinear and a homogeneous SH field, which satisfies the Snell–Descartes law for a SHG situation:

$$N_\omega \sin\varphi_\omega = N_{2\omega} \sin\varphi_{2\omega} \tag{18}$$

The variation of angle between the generated homogeneous and generated collinear SH is:

$$\delta\varphi \approx -\frac{\delta N}{N} \tan\varphi_\omega \tag{19}$$

where $\delta N = N_{2\omega} - N_\omega$ is the optical dispersion and $N \approx N_\omega \approx N_{2\omega}$ [7].

3 Simulation Outcomes

3.1 Parameter Specification

The proposed scheme could be realized more precisely by the graphical representation of the simulation outcomes. The computer-aided simulation has been carried out by considering a crystal slab of 22 mm long (L), 125 μm (t) thick with a thin layer coating of 2.0 μm (d_1) for an incident angle of $\varphi_0 = 40°$, while the collimated optical beam entry point to the semiconductor slab is $X = 0.85$ mm (Fig. 1). The corresponding refractive indices of the chosen materials (MgO:LN and Y_2O_3) [11] have been estimated by the temperature dependent dispersion formula for the driving and generated radiations. The operating temperature (T) and the non-critical phase matching temperature (T_{ncpm}) are 300 K and 115 °C respectively. The period of rotation requires 64.79 kV/mm external electric which is less than the threshold limit of 65 kV/mm [17] for the chosen material. The input Gaussian beam having 100 μm waist, 100 mW power and *p–p–s* polarization is considered for the computer-aided simulation. The corresponding d-coefficient for the chosen polarization configuration can be expressed as [18]:

$$d_{pps} = d_{31} \sin\theta - d_{22} \cos\theta \sin 3\varphi \tag{20}$$

where θ is the angle between the wave vector and the optic axis, φ is the azimuthal angle and considered to be 90° for getting maximum effective d-coefficient value. The value of d_{31} and d_{22} for MgO:LN are considered to be 4.4 pm/V [18] and 6.6 pm/V [19] respectively. The absorption coefficient ($\alpha_\omega \approx \alpha_{2\omega}$), EO coefficient and the p–v value for MgO:LN are chosen to be 0.02 cm^{-1} [20], 0.96×10^{-5} cm/KV [19] and 6 nm [21].

3.2 Results Obtained for SHG on Y_2O_3 Coated MgO:LN Rectangular Slab

The equation for the conversion efficiency, considering the added field impact of TIR-ORQPM and fractional QPM technique, in Sect. 2.2, is for a loss less system without considering the nonlinear law of reflection. The recombinational effect of the nonlinear law of reflection shows significant impact on the conversion efficiency curve, which is also shown in Fig. 3. The recombinational effect is a combination of destructive and constructive interferences since the generated collinear SH field faces a 2 π phase-shift and the generated homogeneous SH field goes through different phase-shifts during TIR. The phase difference between the two mentioned SH field (collinear SH field and the homogeneous SH field) is nearly π after 35, 98, 162 bounces and the resultant field is fully destructive after these bounces. This destructive interference causes zero peak conversion efficiency at those particular bounce

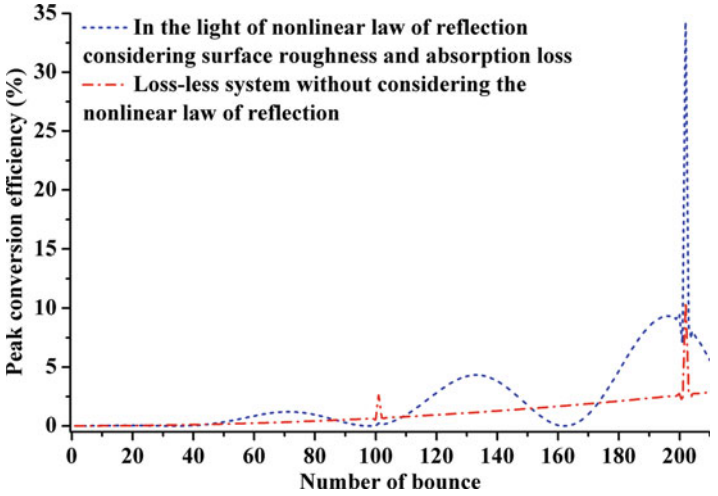

Fig. 3 Graphical representation of peak conversion efficiency vs number of bounce for SHG by TIR-ORQPM and fractional QPM technique **a** in the light of nonlinear law of reflection considering absorption and roughness **b** loss-less system without considering the nonlinear law of reflection

points, as shown in Fig. 3. After every destructive interference, there is a consistent decrement in the phase difference between the generated collinear and homogeneous SH field and a gradual increase in the peak conversion efficiency. Therefore, after the gradual decrease, the resultant SH field becomes constructive while the phase difference is zero *i.e.*, after 71, 133, 196 bounces, as shown in Fig. 3. However, the fractional QPM is occurred in every bounce and the ORQPM is taking place only at 101^{th} and 202^{th} bounces due to the polarization rotation of $2\ \pi$ as discussed in the 2.2 section. Hence, the combined field effect of the fractional QPM and ORQPM technique is appeared in 101^{th} and 202^{th} bounce and shows sudden peaks in the efficiency graph (Fig. 3). Moreover, a huge deviation has been observed between the most constructive point and the most efficient point as the interacting length plays an important role in this scenario. Now, considering all the circumstances (interacting length, added field effect and high constructive point), the simulation outcome shows the highest peak conversion efficiency point in Fig. 3.

3.3 Influence of Incident Angle

The angle of incidence is one of the most impactful controlling factors for global phase-shift, and its fluctuation causes a significant reduction in the efficiency, while the other operating and geometrical parameters are assumed to be unchanged. This decrease in efficiency is basically due to phase mismatch. Figure 4 shows the fluc-

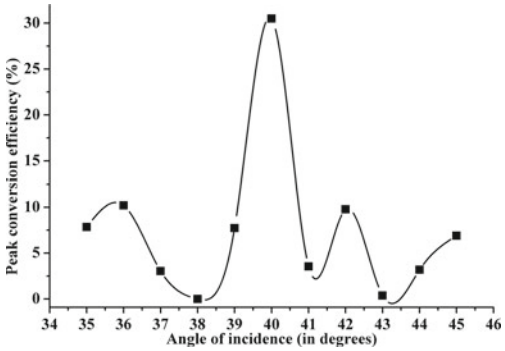

Fig. 4 Variation of peak conversion efficiency under the influence of incident angle

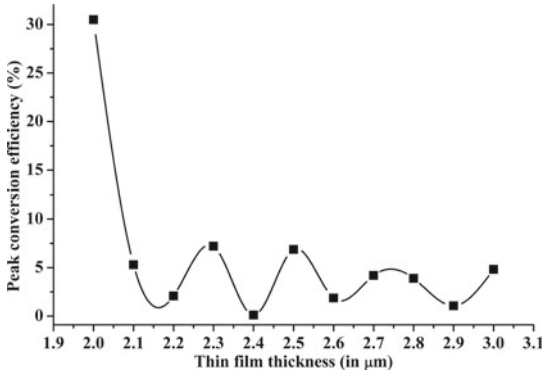

Fig. 5 Variation of peak conversion efficiency under the influence of thin film thickness

tuation of peak conversion efficiency w.r.t the incident angles and enunciate 40° as the most suitable one.

3.4 Affect of Thin Film Thickness

The thin film thickness plays an important role in the controlling of global phase-shift, and a slight variation causes a significant reduction in the peak conversion efficiency, while the other operating and geometrical parameters are constant. The reason behind this decrease is basically due to phase mismatch. Figure 5 shows the change of peak conversion efficiency w.r.t the thin film thickness and states 2.0 μm as the most suitable one.

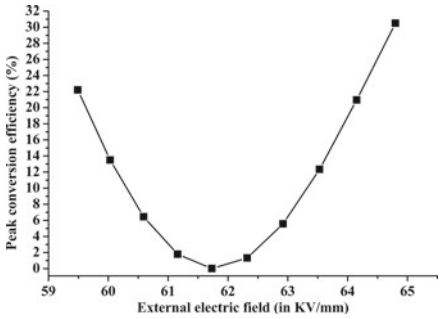

Fig. 6 Variation of peak conversion efficiency under the influence of external electric field

3.5 Influence of External Electric Field

The applied external electric field particularly controls the polarization rotation. As a result, if we alter the amplitude of the electric field, the rotation period will change accordingly, resulting in a variation in the peak conversion efficiency (Fig. 6). The period of rotation is 101, 102, 103, 104, 105, 106, 107, 108, 109, 110 for an external electric field of 64.79 kV/mm, 64.15 kV/mm¸ 63.53 kV/mm, 62.92 kV/mm, 62.32 kV/mm¸ 61.73 kV/mm, 61.16 kV/mm, 60.59 kV/mm¸ 60.03 kV/mm, 59.49 kV/mm respectively. However, Rayleigh range is maintained upto 210 bounces only. Hence, the rotation period at bounce no 106, 107, 108, 109 and 110 cannot be considered, as they violate the Rayleigh range during their second point of satisfying ORQPM condition and hence reflects low efficiency.

3.6 Influence of Input Power

A linear rise has been observed in the efficiency curve while increasing the input power as shown in Fig. 7.

3.7 Comparison Chart

Now, the reported SHG results can be compared with the proposed approach of achieving SHG. This comparison will help us to know that this process of SHG by TIR-based fractional QPM and ORQPM process has better performance in terms of peak conversion efficiency and fabrication complications (Table 1).

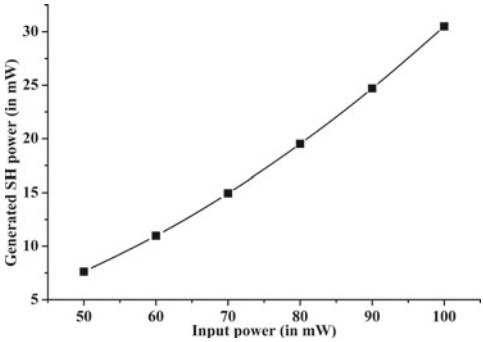

Fig. 7 Variation of peak conversion efficiency under the influence of input power

Table 1 Comparison of the proposed technique with the reported processes

Sl no	References	Efficiency	Phase-matching technique	Material used & its fabrication	Wavelength
1	[22]	0.2%	QPM	Periodically poled potassium niobate	926 nm (Fund)
2	[23]	16.5%	QPM	Periodically poled potassium niobate	488 nm (SH)
3	[24]	8%	QPM	Periodically poled lithium niobate thin-film wafer-bonded on silicon substrate and rib-loaded with silicon nitride channel	1580 nm (Fund)
4	[11]	32% (400 mW input power)	TIR based fractional & ORQPM	Rectangular slab of MgO doped LN crystal coated with a thin layer of Y_2O_3	532 nm (SH)
5	Proposed	30.50% (100 mW input power)	TIR based fractional & ORQPM	Rectangular slab of MgO doped LN crystal coated with a thin layer of Y_2O_3	514.50 nm (SH)

4 Discussions

The reported findings are specific to a given combination of structure, external electric field, operating temperature and wavelength. The proposed scheme outperforms conventional geometrical structures such as periodically polled or parallel (without thin film) slabs. The structural reconstruction of a parallel semiconductor slab generally used for the frequency conversion process has been accomplished by inserting

a thin coating on the surface, which has made it a favorable module for the TIR-ORQPM technique. This TIR-based ORQPM technique has already been realized in our previous work [11] for 532 nm SHG presenting 32% efficiency for 400 mW input power without fulfilling the ideal ORQPM condition and had to settle down with a conceding of efficiency drop for $2L_c = 12L_r$. Here, in this analysis we have tried to minimize this deviation from the ideal ORQPM condition and ended up with $2L_c = 8L_r$. There is a high chance of further improvement for more optimization of this rotation period. Furthermore, the frequency conversion process is dependent not only on the polarization rotation period but also on the phase-matching condition. This phase-matching condition is realized through the global phase-shift, which is controlled by the thin-film thickness. However, the polarization rotation is controlled by an external electric field. Variation of the material and thickness of the thin-film can build an immense effect on the global phase-shift of the interacting beams when travelling through TIR phenomenon and gives us an adequate facility to select suitable incident angle for further progression of our proposed scheme. The incident angle selection is the most crucial part of the proposed technique as it has to look after the electric field and operating temperature threshold limits. Moreover, the prime focus of this analytical approach is to improve the peak conversion efficiency without hampering the other parameters. A comparative conversion efficiency curve has been shown in Fig. 4 for a loss less system without considering the nonlinear law of reflection and a system in the light of nonlinear law of reflection considering absorption and reflection losses. The graphical representation of the outcome for 514.5 nm wavelength considering the limiting factors can signify the mathematical derivation of this paper demanding high efficiency. Thus, assuring high efficiency, this device is believed to be beneficial for underwater communications [25] and for medical applications as well [26]. Besides these applications, it can be used in laser lighting displays because of its flexibility in visible transmission window. The peak conversion efficiency obtained is 30.50% for 100 mW input power and shows much higher conversion efficiency than any other conventional QPM technique.

5 Conclusion

In conclusion, we may characterize the suggested scheme's topology as a thin-film coated (Y_2O_3) rectangular slab of MgO doped LN crystal and highlight its excellent peak conversion efficiency for the rotational phenomena of the polarization plane. This rotational phenomenon has been controlled by an external electric field. During the polarization rotation it is very difficult to satisfy the global phase-shift condition only by varying the incident angle and hence the thin-film concept has been incorporated. The proposed converter provides higher peak conversion efficiency in the visible spectrum range than the other conventional frequency converters. The nobility of this proposed scheme is the SHG by rotating the plane of polarization of the input radiation under the influence of a convenient external electric field across the semiconductor material. The chosen semiconductor material should flaunt circular

birefringence by the provocation of external electric field so that we can control the rotation of the polarization plane. This polarization rotation of the interacting beams along with the propagation distance is constant and the period of rotation should be equal to $2L_c$ for an ideal ORQPM situation. In the meantime, we have to look after the threshold limit of the other operating and the structural parameters. Therefore, we may need to compromise with the ideal ORQPM condition and settle for the $8L_c$ rotation period. This $8L_c$ period of rotation can be achieved after every 101 bounces by an external electric field of 64.79 kV/mm. It is clear from the graphical evaluation that a slight fluctuation in incident angle, thin-film thickness, and electric field can make a huge impact on peak conversion efficiency. The conversion yield-limiting elements are included in the computer-aided simulation and provide a peak conversion efficiency of 30.50% for an input power of 100 mW while generating 514.5 nm SH wavelength. Thus, by regulating the polarization rotation in a bulk EO chiral material, this extremely efficient frequency converter can effectively contribute to the phenomenon of TIR-based phase-matching phenomenon.

References

1. Magel GA, Fejer MM, Byer RL (1990) Quasi-phase-matched second-harmonic generation of blue light in periodically poled LiNbO3. Appl Phys Lett 56(2):108–110. https://doi.org/10.1063/1.103276
2. Fejer MM, Magel GA, Lim EJ (1990) Quasi-phase-matched interactions in lithium niobate. Edited by Howard R. Schlossberg and Raymond V. Wick, 213, San Diego. https://doi.org/10.1117/12.962160.
3. Boyd GD, Patel CKN (1966) Enhancement of optical second-harmonic generation (SHG) by reflection phase matching in ZnS and GaAs. Appl Phys Lett 8:313–315
4. Komine H, Long WH, Tully JW, Stappaerts EA (1998) Quasi-phase-matched second-harmonic generation by use of a total-internal-reflection phase shift in gallium arsenide and zinc selenide plates. Opt Lett 23:661–663
5. Haïdar R (2005) Fractional quasi-phase-matching by Fresnel birefringence. Appl Phys Lett 88:211102
6. Armstrong JA, Bloembergen N, Ducuing J, Pershan PS (1962) Interactions between light waves in a nonlinear dielectric. Phys Rev 127(6):1918–1939. https://doi.org/10.1103/PhysRev.127.1918
7. Raybaut M, Godard A, Toulouse A, Lubin C, Rosencher E (2008) Fresnel phase matching: exploring the frontiers between ray and guided wave quadratic nonlinear optics. Opt Express 16(22):18457. https://doi.org/10.1364/OE.16.018457
8. Bloembergen N, Pershan PS (1962) Light waves at the boundary of nonlinear media. Phys Rev 128(2):606–622. https://doi.org/10.1103/PhysRev.128.606
9. Liu Lewis Z, O'Keeffe Kevin, Hooker Simon M (2012) Optical rotation Quasi-Phase-matching for circularly polarized high harmonic generation. Opt Lett 37(12):2415. https://doi.org/10.1364/OL.37.002415
10. Shi L, Tian L, Chen X (2012) Electro-optic chirality control in MgO:PPLN. J Appl Phys 112:073103
11. Saha M, Deb S, Mandal PK, Medhi B, Saha A (2021) Highly efficient second-harmonic generation in an electro-optic chiral material using total-internal-reflection-based optical rotation quasi-phase-matching technique. Opt Eng 60(6):066104. https://doi.org/10.1117/1.OE.60.6.066104

12. Saha M, Deb S (in press) Highly efficient third and fourth harmonic generation using total-internal-reflection based optical rotation quasi-phase-matching. Phys Wave Phenom. Accessed on 13 Sept 2021
13. Saha M, Deb S, Medhi B, Barma MD (2020) Utilization of thin-film to control total phase shift during total-internal-reflection. In: 2020 IEEE international women in engineering (WIE) conference on electrical and computer engineering (WIECON-ECE). https://doi.org/10.1109/WIECON-ECE52138.2020.9398045
14. Azzam RMA (1985) Simultaneous reflection and refraction of light without change of polarization by a single-layer-coated dielectric surface. Opt Lett 10(3):107. https://doi.org/10.1364/OL.10.000107
15. Azzam RMA (2009) Total internal reflection without change of polarization using a right-angle prism with half-wavelength-thick optical interference coating. Opt Lett 34:371–373
16. Haïdar R, Forget N, Kupecek P, Rosencher E (2004) Fresnel phase matching for three-wave mixing in isotropic semiconductors. J Opt Soc Am B 21(8):1522. https://doi.org/10.1364/JOSAB.21.001522
17. Minet Y, Reis L, Szabados J, Werner CS, Zappe H, Buse K, Breunig I (2020) Pockels-effect-based adiabatic frequency conversion in ultrahigh-Q microresonators. Opt Express 28(3):2939–2947. https://doi.org/10.1364/OE.378112
18. Nikogosyan DN (2005) Nonlinear optical crystals: a complete survey. Springer, New York, p 163
19. Bonghoon K, Rhee BK, Joo G-T (2006) Variation of electro-optic coefficients in MgO-doped LiNbO3 single crystals. Mat Lett 60(17–18):2306–2308. https://doi.org/10.1016/j.matlet.2005.12.144
20. Schwesyg JR, Markosyan A, Falk M, Kajiyama MCC, Jundt DH, Buse K, Fejer MM (2011) Optical loss mechanisms in magnesium-doped lithium niobate crystals in the 300 to 2950 Nm wavelength range. In: Advances in optical materials, AIThE3. OSA, Istanbul. https://doi.org/10.1364/AIOM.2011.AIThE3
21. Zhenyu Z, Bo W, Nianmin Z, Chaoge X (2014) High-efficiency super-smooth chemical mechanical polishing method for lithium niobate crystal (China: Publication of CN103978406A) Application CN201410197096.5A (2014). Application publication date 13 Aug 2014
22. Meyn JP, Klein ME, Woll D, Wallenstein R, Rytz D (1999) Periodically poled potassium niobate for second-harmonic generation at 463 nm. Opt Lett 24(16):1154–1156
23. Uebernickel M, Fiebig C, Blume G, Paschke K, Eppich B, Güther R, Erbert G (2008) 400 mW and 16.5% wavelength conversion efficiency at 488 nm using a diode laser and a PPLN crystal in single pass configuration. Appl Phys B 93:823–827. https://doi.org/10.1007/s00340-008-3235-8
24. Rao A, Malinowski M, Honardoost A, Talukder JR, Rabiei P, Delfyett P, Fathpour S (2016) Second-harmonic generation in periodically-poled thin film lithium niobate wafer-bonded on silicon. Opt Express 24(26):29941–47. https://doi.org/10.1364/OE.24.029941
25. Kaushal H, Kaddoum G (2017) Applications of lasers for tactical military operations. IEEE Access 5:20736–20753
26. Peng Q, Juzeniene A, Chen J, Svaasand LO, Warloe T, Giercksky K-E, Moan J (2008) Lasers in medicine. Rep Progr Phys 71:056701

Multi Band Cactus Shaped Monopole MIMO Antenna for Wireless LAN and X Band Satellite Communication Applications

Jayshri Kulkarni, Shailesh Kulkarni, and Chow-Yen-Desmond Sim

Abstract In this research work, T-Shaped Monopole (TSM) Multiple input multiple output (MIMO) antenna with connected ground is designed and analyzed for wireless local area network (WLAN) and X-band satellite communication applications concurrently. Each TSM applied for MIMO configuration, consists of T-shaped as a main radiator which further is branched into two asymmetrical inverted-F shaped radiators on each side forming a cactus shaped structure and a partial ground plane to achieve impedance matching characteristics. The cactus shaped MIMO antenna is excited by 50 Ω microstrip feed line to induce two resonances at 5.20 GHz in lower frequency (F_L) band and 9.70 GHz in upper frequency (F_U) band. Further analysis confirms that fractional impedance bandwidth (FIB) of 10.60% (4.90–5.45 GHz) and 27.80% (8.72–11.55 GHz) are achieved in F_L and F_U band, respectively with minimum mutual coupling of −20 dB, gain 3 dBi and efficiency of 65% in both the desired operating bands. Moreover, the MIMO diversity parameters are also analysed for the validation of MIMO applicability.

Keywords Monopole antenna · WLAN · X-band · MIMO · And microstrip feed line

1 Introduction

In the presence of global pandemic COVID 19, MIMO technologies incorporating multiband antennas plays a very significant role to implement the concept of "Learn

J. Kulkarni · S. Kulkarni (✉) · C.-Y.-D. Sim
Department of Electronics and Telecommunication Engineering, Vishwakarma Institute of Information Technology, Pune, India
e-mail: Shailesh.kulkarni@viit.ac.in

J. Kulkarni
e-mail: Jayashri.kulkarni@viit.ac.in

C.-Y.-D. Sim
e-mail: cysim@fcu.edu.tw

Department of Electrical Engineering, Feng Chia University, Taichung, Taiwan

M. Tiwari et al. (eds.), *Optical and Wireless Technologies*, Lecture Notes in Electrical Engineering 892, https://doi.org/10.1007/978-981-19-1645-8_8

from home" and "work from home". Therefore, with the support of MIMO technology, this paper presents the design and analysis of two port cactus shaped MIMO antenna for wireless and satellite communication applications. Recently, a lot outstanding research efforts have been bestowed on the development of single/multiband/MIMO antenna [1–10].

A MIMO antenna incorporating two antenna array elements operating in X-band is revealed in [1]. An electronic band gap (EBG) structure is utilized to realize high isolation upto −22 dB in the working band of (8.00–12.00 GHz). However, the MIMO antenna possess the size of 55 × 49 mm^2 and is printed on FR-4 substrate having thickness of 1.6 mm. However, the EBG structure always require a size greater than 0.1λ, which makes the structure complicated in practical implementation. This in turn affects the radiation features of the complete wireless devices. In order to reduce the size of antenna array as well as complexity and also to operate the antenna array in X band similar to [1], a microstrip fed patch antenna with the size of 43 × 43 mm^2 is described in [2]. The described antenna is printed on expensive Rogers RT duroid 5880 substrate having thickness of 1.27 mm. However, while forming MIMO configuration, the antenna elements need to be closely packed with the conductive elements which leads in deteriorating the performance of MIMO antenna. Apart from the above, the antennas reported in [1–2] operate in single band only. An orthogonally placed, two port microstrip fed MIMO antenna operating in WLAN/INSAT/Super extended-C band is revealed in [3]. Here, in this antenna a parasitic rectangular strip and slots are inserted in the ground which helps to improve isolation upto 16 dB. Further, an orthogonal arrangement of antenna elements radiates orthogonally with each other which results in reduction of mutual coupling of antenna elements. A two element MIMO antenna working in (6.30–12.50 GHz) covering entire X-band application is reported in [4]. In this antenna an air gap in the radiator of antenna element is introduced which offer minimum isolation of −35 dB in the functioning band. However, MIMO antenna has footprint of 66 × 23 mm^2 and is engraved on expensive 3.2 mm thick RT duroid substrate. To minimize the fabrication cost of the antenna, a four port MIMO antenna with minimum isolation of −20 dB for simultaneous functioning in entire sub 6 GHz and WLAN band is reported in [5]. The size of reported antenna is 30 × 40 mm^2 and designed on cost effective FR-4 substrate of 1.6 mm.

To accommodate the advantages of coplanar waveguide (CPW) fed technique, a two port MIMO antenna covering the bandwidth of sub-6 GHz/Wi-Fi-5/V2X/DSRC/Wi-Fi-6/INSAT-C is reported in [6]. The reported MIMO antenna uses FR-4 substrate and has designed volume of 32 × 22 × 0.8 mm^3. A triple band microstrip fed arc shaped antenna with inverted L-shaped stubs is communicated in [7]. The reported antenna operates in WLAN (2.48–2.4835, 5.15–5.875 GHz) and X-band (7.25–7.75 GHz) for wireless and satellite communication applications. However, the reported antenna is effective to partial bandwidth requirement of X-band. In order to cover the entire bandwidth of X-band, a coaxial fed S-shaped patch antenna is reported in [8]. The size of antenna is 20 × 17.2 mm^2 and is built on economical 1.6 mm FR-4 substrate. However, the prob feeding technique may

result in fabrication difficulty and spurious radiation. A multiband and compact flexible ultra-wide band (UWB) antenna and CPW fed antennas are reported in [9–10]. However, the antenna [9–10] are single antenna element and does not provide high data rates and low latency.

In this manuscript, a dual band cactus shaped monopole MIMO antenna with connected ground and high isolation for wireless and satellite communication applications is proposed. This cactus shaped MIMO antenna consists of two antenna elements with a minimum footprint of 30 × 30 mm^2 for each element. To reduce a mutual coupling between the cactus shaped antennas, two symmetrical inverted U-shaped structure are introduced from ground planes. The proposed cactus shaped MIMO antenna is designed, analyzed and simulated using CST software to operate in F_L (4.90–5.45 GHz) and F_U (8.72–11.55 GHz) with minimum isolation of −20 dB.

The manuscript is arranged as follows: Sect. 2 illustrates the layout and evolution mechanism of single cactus shaped antenna, Sect. 3 explains the MIMO geometry with decoupling structure, Sect. 4 gives insights on results and discussion. To prove the novelty and contribution, a performance comparison is presented in Sect. 5 and finally, paper is concluded in Sect. 6.

2 Layout and Evolution Mechanism of Cactus Shaped Antenna

The simplified design layout of single monopole antenna is depicted in Fig. 1 for wireless and satellite communication operation. The proposed antenna consists of

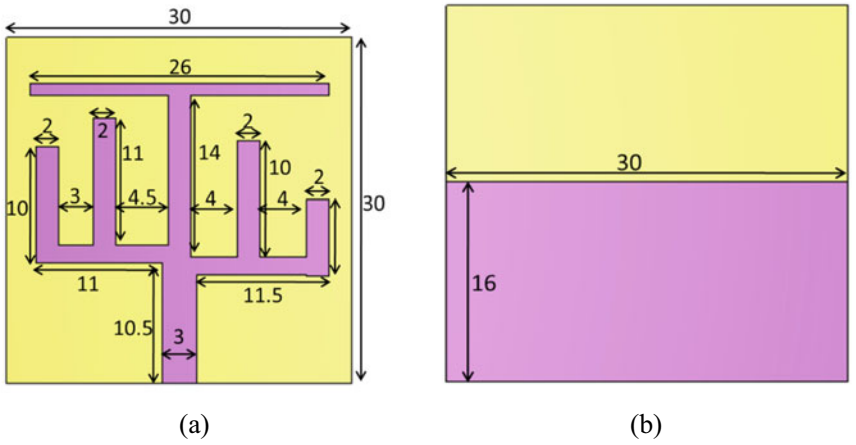

Fig. 1 Geometry and layout of proposed cactus shaped antenna (all dimensions in mm) **a** Front view **b** Back view

T-shaped main radiator which is further branched into two asymmetrical inverted-F shaped radiators on each side, forming a cactus shaped structure and a partial ground plane to achieve impedance matching characteristics. The proposed single cactus shaped antenna is designed on FR-4 substrate having a size of 30 × 30 mm^2 (thickness 0.8 mm, loss tangent 0.025 and dielectric permittivity of 4.3.

2.1 *Evolution Mechanism of Proposed Cactus Shaped Antenna*

The evolution mechanism of proposed cactus shaped antenna is illustrated in Fig. 2. For analyzing the operating mechanism of proposed cactus shaped antenna, the reflection coefficient curve (S_{11}) dB of each step is depicted in Fig. 2. Initially, to achieve bandwidth of X-band (F_U) band, a feed line with an inverted F-shape structure on right side as shown in Fig. 2 is excited by 50 Ω microstrip feeding line. Due to proper impedance matching and accurate feeding arrangement, the step-1 is able to induce a resonance at (10.70–11.30 GHz) which can be easily noted from Fig. 2. However, the induced bandwidth is very less. Therefore, in order to enhance the impedance bandwidth of setp-1, a step-2 is developed where, another inverted-F shaped structure to left of step-1 is branched out without disturbing the feeding position as shown in Fig. 2b. The corresponding S_{11} curve of step-2 is shown in Fig. 2. It is noted that the step-2 is able to enhance bandwidth in the frequency range of (8.72–11.55 GHz)

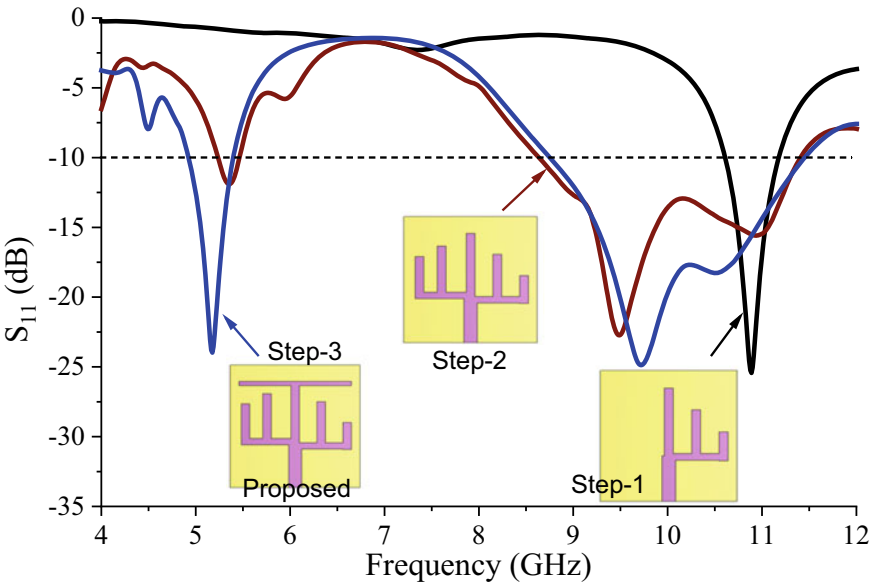

Fig. 2 Step wise design of proposed antenna

because the elongation of current path flowing through all radiator for longer time. The step-2 antenna could operate in F_U band with frequency range of (8.72–11.55 GHz), conforming the bandwidth need of X-band.

Further, to have another resonance at 5.2 GHz, a horizontal strip is added on top of the vertical strip extended from feedline forming a T-shape structure. The length of T-shaped radiator to resonate at required frequency is calculated by using below Eq. (1)

$$\lambda = \frac{C}{\sqrt{\varepsilon_{eff}} f} \tag{1}$$

where in Eq. (1), $\varepsilon_{eff} = \frac{\varepsilon_r + 1}{2}$, ε_r is dielectric permittivity of FR-4 substrate and C is speed of light in 3×10^8 m/s.

This structure termed as step-3 helps in inducing a resonance at 5.20 GHz covering a frequency range of (4.90–5.45 GHz) as shown in Fig. 2. Thus, the proposed cactus shaped antenna induces two resonances at 5.20 and 9.70 GHz operating in frequency band of F_L (4.90–5.45 GHz) and F_U (8.72–11.55 GHz), respectively as visualized in Fig. 2.

Further, to perceive more about working principal of proposed cactus shape antenna, a surface current distribution (A/m) is analyzed in Fig. 3. From Fig. 3a, it is noted that a more amount of current is flowing through T-radiator, confirming that this structure contributes to induce a resonance at 5.20 GHz with impedance bandwidth of 10.62% (4.80–5.45 GHz). Further, at resonance 9.70 GHz, analyzed from Fig. 3b, more amount of current is flowing through two asymmetrical F-shaped radiators thus inducing an impedance bandwidth of 27.8% (8.72–11.55 GHz).

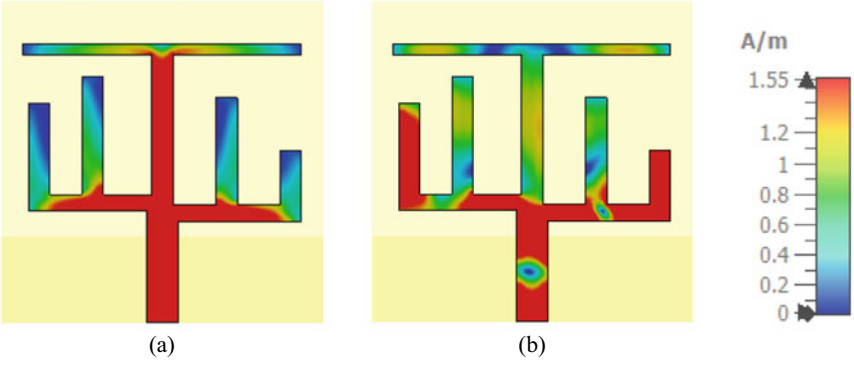

Fig. 3 Surface current distribution of proposed antenna **a** 5.2 GHz **b** 9.7 GHz

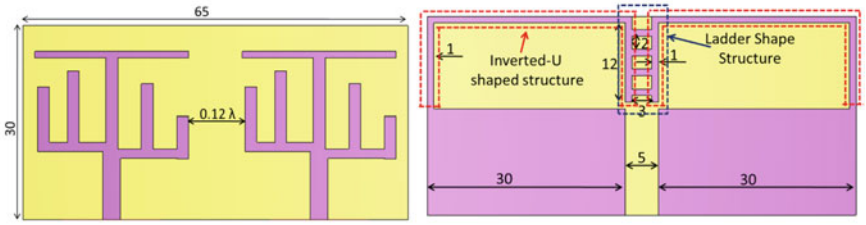

Fig. 4 Geometry and layout of proposed TSM MIMO antenna (all dimensions in mm) **a** Front view **b** Back view

3 Proposed Cactus Shaped MIMO Antenna Geometry

The proposed cactus shaped MIMO antenna has designed footprint of 65 × 30 mm^2(1.12λ × 0.52λ) and comprises of two antenna elements located at an edge-to-edge distance of 0.12λ (where λ is free space wavelength measured at 5.20 GHz) on top layer of FR-4 substrate as depicted in Fig. 4a. Figure 4b depicts that the bottom layer of FR-4 substrate which basically consists of two partial ground plane, two symmetrical inverted U-shaped structure branched out from the partial ground planes. Further, these two inverted-U shaped structures are connected using 4 horizontal strips of 1 × 3 mm^2 each forming a ladder structure at the centre. This structure serves as a decoupling structure to reduce the mutual coupling of antenna elements and also enhances the diversity performance of proposed MIMO antenna.

4 Results and Discussion

The proposed cactus shaped MIMO antenna design is validated by comparing the scattering parameters including reflection coefficient curve and transmission coefficient curve. However, due to analogy of S_{11}–S_{22} and S_{12}–S_{21}, only S_{11} and S_{12} curves are illustrated in Fig. 5. From the Fig. 5, it is visualized that antenna element operates in F_L and F_U bands with the same bandwidth as it is achieved in Fig. 2, while the S_{12} curve shows that the minimum mutual coupling between antenna elements is − 20 dB in both the operating bands of F_L and F_U.

Moreover, to realize the operating mechanism of decoupling structure, an electric filed intensity distribution (V/m) is analyzed in Fig. 6. This analysis is performed under the condition that when one antenna element (port 1) is active, other antenna element (port 2) is matched with 50 Ω load impedance. From Fig. 6, it is visualized that both the antenna elements remain protected from electric field of each other as amount of current flows through the decoupling structure.

The three-dimensional (3D) and two-dimensional (2D) radiation patterns of the proposed cactus shaped MIMO antenna at 5.20 and 9.70 GHz are depicted in Figs. 7

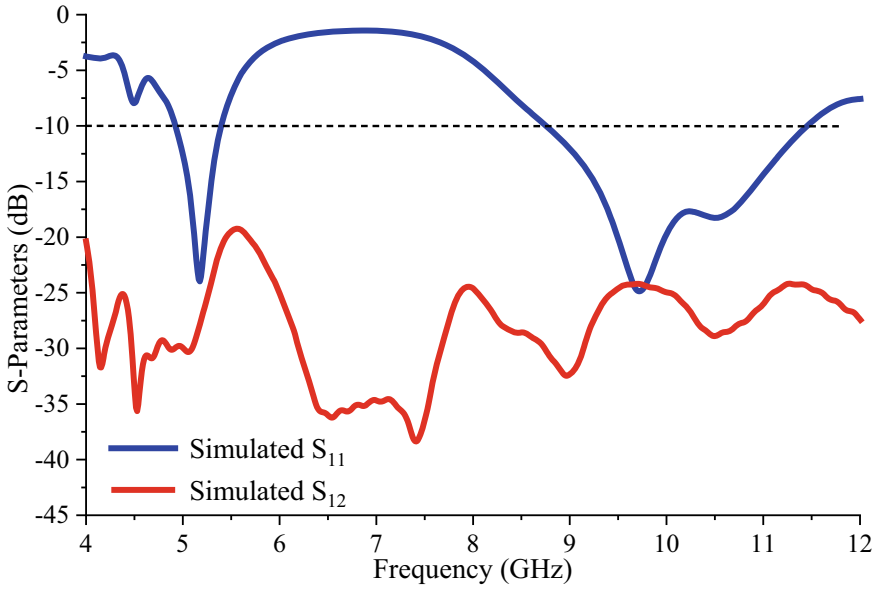

Fig. 5 S-Parameters of proposed MIMO antenna

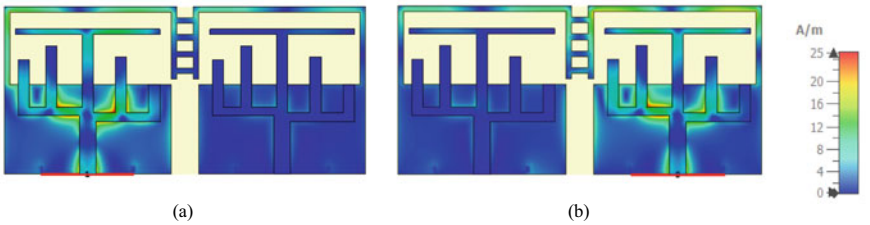

Fig. 6 Electric filed intensity distribution (V/m) **a** When port-1 is excited **b** when port 2 is excited

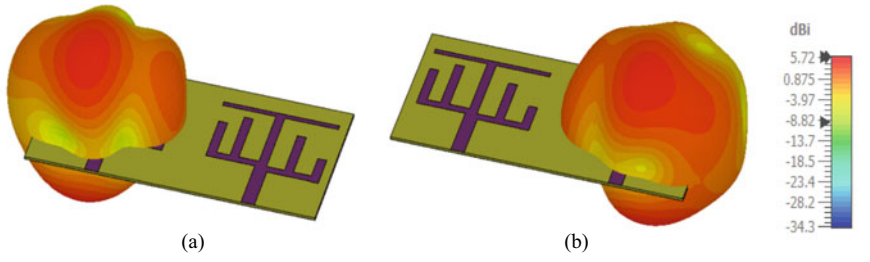

Fig. 7 3D radiation pattern of proposed MIMO antenna **a** Antenna-1 **b** Antenna-2

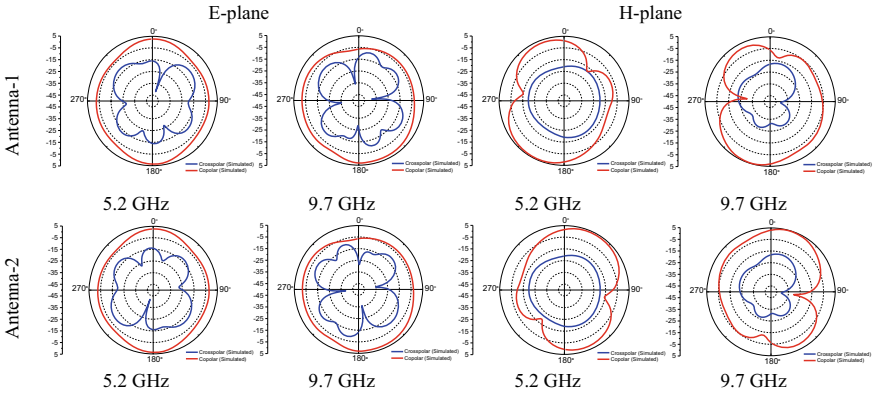

Fig. 8 2D radiation pattern of proposed MIMO antenna

and 8, respectively. Both the radiation patterns are matched with each other with negligible nulls and obtained by keeping only one antenna element active, while the other one is terminated with 50 Ω load impedance. At both the resonances, the radiation patterns are just like a monopole, whose co-polar radiation is an omnidirectional radiation with higher magnitude than cross polar radiation in the plane at the both the resonant frequencies.

The gain and efficiency of the proposed cactus shaped MIMO antenna is shown in Fig. 9(a). The minimum gain is 3.5 dBi at 5.2 GHz and 3 dBi at 9.7 GHz, whereas radiation efficiency is 65% at 5.20 GHz and 70% at 9.70 GHz. The correlation coefficient is an important metric to calculate the diversity performance of proposed cactus shaped MIMO antenna and plotted in Fig. 9(b). From this figure, it is visualized that the ECC of the proposed cactus shaped MIMO antenna is well below 0.05 whereas the DG is well above 9.95 throughout the operating band.

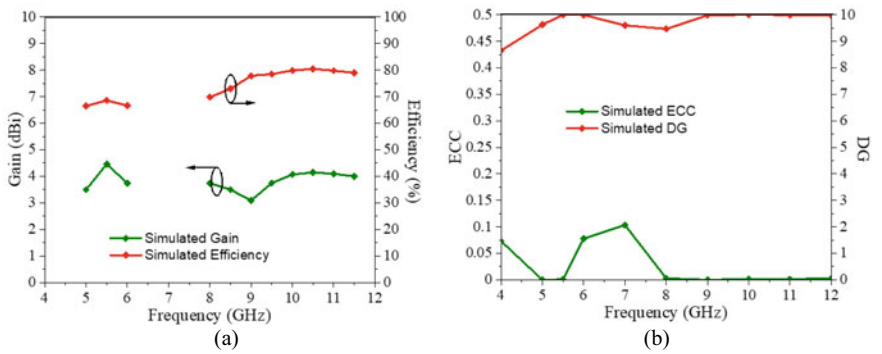

Fig. 9 **a** Gain and efficiency **b** ECC and DG

Table 1 Performance comparison of proposed cactus shaped MIMO antenna

Ref.	Antenna element	Band (GHz)	Dimension (mm^2)	Thickness (mm)	Substrate	Gain (dBi)
[1]	Single	8.00–12.00	55 × 49	1.6	FR-4	2.2
[2]	Single	8.00–12.00	43 × 43	1.27	RT-Duroid	7.4
[3]	Two	4.64–9.00	25 × 34.80	1.6	FR-4	4.21
[4]	Two	8.00–12.00	66 × 33	3.2	RT Duroid	6.0
[7]	One	2.28–2.57/ 5.00–6.27/ 7.11–7.96	18 × 34.5	0.8	FR-4	1.0
[8]	Single	8.69–9.14/ 10.47–11.48/ 11.53–11.98	20 × 17.2	1.6	FR-4	2.5
[9]	One	1.33–11.11	35 × 35	0.2	FR-4	3.3
[Proposed]	Two	4.90–5.45/ 8.72–11.55	65 × 30	0.8	FR-4	3.0

5 Performance Comparison of Proposed Cactus Shaped MIMO Antenna

For validating the performance of the proposed cactus shaped MIMO antenna, a comparative study is tabulated in Table 1. The parameters considered for performance are no. of antenna elements, operating bands, dimension, thickness, type of substrate used and gain.

The advantages of proposed cactus shaped MIMO antenna are as follows:

1. The proposed MIMO antenna has less dimensions than [4] and cost effective than [2, 4].
2. The proposed MIMO antenna has two antenna elements as compared with all except [3, 4].
3. The proposed MIMO antenna operates in dual band unlike [1, 2, 3] with relatively thin thickness unlike [4].
4. The proposed MIMO antenna exhibit high gain as compared to [1] and [7]

6 Conclusion

A cactus shaped monopole MIMO antenna with inverted-U shaped (connected with ladder) as a decoupling structure is presented for WLAN and X-band application. The proposed cactus shaped MIMO antenna with interconnected ground operates at (4.90–5.45 GHz) WLAN and (8.72–11.55 GHz) X-band with minimum isolation of −20 dB. The MIMO antenna also exhibit gain of above 3 dBi, efficiency above 65%, ECC below 0.05 and DG above 9.95 throughout the operating frequency band.

Finally, a comparison between the current state of art and the proposed cactus shaped MIMO antenna is presented. From the comparative study it can be concluded that the proposed cactus shaped MIMO antenna a good contender for WLAN and X band applications.

References

1. Saxena G, Jain P, Awasthi YK (2019) High isolation EBG based MIMO antenna for X-band applications. In: 2019 6th international conference on signal processing and integrated networks (SPIN), pp 97–100
2. Varghese NM, Vincent S, Kumar OP (2016) Design and analysis of cross-fed rectangular array antenna; an X-band microstrip array antenna, operating at 11 GHz. In: 2016 international conference on advances in computing, communications and informatics (ICACCI), pp 1261–1265
3. Banerjee J et al (2020) An orthogonally oriented multiband MIMO antenna for WLAN, C-band and X-band wireless applications. In: 2020 IEEE Calcutta conference (CALCON), pp 328–332
4. Babu KJ, Kumar BK, Boddu SR, Krishna KSR (2017) Design of a MIMO dielectric resonator antenna with air gap for X-band applications. In: 2017 progress in electromagnetics research symposium - Fall (PIERS - FALL), pp 1835–1838
5. Jayshri K, Arpan D, Sim CYD (2020) Wideband four-port MIMO antenna array with high isolation for future wireless systems. Int J Electron Commun (AEU) 128:1–14
6. Kulkarni J, Desai A, Sim C-Y (2021) Two port CPW-fed MIMO antenna with wide bandwidth and high isolation for future wireless applications. Int J RF Microw Comput Aided Eng 31:1–16
7. Zhi R, Han M, Bai J, Wu W, Liu G (2018) Miniature multiband antenna for WLAN and X-band satellite communication applications. Progr Electromagn Res Lett 75:13–18
8. Samsuzzaman M, Islam MT (2014) Inverted S-shaped compact antenna for X-band applications. Sci World J 2014:11
9. Kumar S, Khan T (2018) CPW-fed UWB flexible antenna for GSM/WLAN/X-band applications. In: 2018 5th international conference on signal processing and integrated networks (SPIN), pp 126–129
10. Kulkarni J (2020) Design and analysis of multiband CPW-fed antenna for industrial wireless applications. In: 2020 IEEE 7th Uttar Pradesh section international conference on electrical, electronics and computer engineering (UPCON), pp 1–5

Experimental Analysis of ACO with Modified Firefly and Modified Genetic Algorithm for Routing in FANETs

Amrita Yadav, Anshuman Shastri, and Seema Verma

Abstract The paper presents the performance evaluation of Nature-Inspired algorithms (NIA) namely Ant Colony Optimization (ACO) with newly implemented modified Firefly algorithm (MFA) and modified Genetic algorithm (MGA) for routing in Flying ad-hoc network (FANET). The use of NIA in FANET is required because FANET has quite different characteristics than that of other ad-hoc networks. The major area of concern in FANET is routing and no efficient routing algorithm has been developed for this issue. NIA is an optimization algorithm which process on the basis of nature of animals. NIA is divided into swarm based and evolutionary algorithm. This paper performs the evaluation and comparison of swarm-based algorithms and evolutionary algorithm on the performance parameters like successful packet delivery, end-to-end delay, overhead and throughput. As per the simulation results, MFA outperforms ACO and is the most efficient algorithm with MGA being the least efficient one.

Keywords Routing · Network · FANET · ACO · Firefly · Genetic algorithm · Performance · Algorithm

1 Introduction

Flying ad-hoc network (FANET) is a network which consist of group of many Unmanned aerial vehicles (UAV). The UAVs are connected to ground stations for

A. Yadav (✉)
Department of Computer Science, Banasthali Vidyapith, Tonk, India
e-mail: amrita.yadav26@gmail.com

A. Shastri
School of Automation, Banasthali Vidyapith, Tonk, India
e-mail: anshumanshastri@banasthali.in

S. Verma
School of Physical Sciences, Banasthali Vidyapith, Tonk, India
e-mail: vseema@banasthali.in

M. Tiwari et al. (eds.), *Optical and Wireless Technologies*, Lecture Notes in Electrical Engineering 892, https://doi.org/10.1007/978-981-19-1645-8_9

proper communication between them. FANETs are dynamic in nature because of their continuous moving nodes or UAVs.

There is also frequent change in topology because of their consistent node mobility. These special factors make FANET different from other ad-hoc networks. There are many major concerns in proper data transmission in FANETs. Routing is one of the major issues in FANETs. After the unsatisfactory results of many conventional routing algorithms in FANET, Nature Inspired Algorithm (NIA), because of their efficient results according to previous research done, can be claimed as the major rescue for the routing solution in FANETs.

Ant Colony Optimization (ACO), Firefly algorithm (FA), and Genetic algorithm (GA) are the three NIA on which the performance evaluation is performed in this paper.

ACO is selected because of its ability to adapt to changes dynamically which is required in UAVs. FA is another optimization algorithm which is used for network analysis and is dynamic in nature. These algorithms provide great results in the field of ad-hoc networks. Till now they have not been majorly used in flying ad-hoc networks.

In this paper, an experimental implementation of three NIAs i.e. ACO, FA, and GA and modified version of FA and GA has been given and further the results of these algorithms are compared to find which is the most suitable algorithm for routing in FANET.

NIA has a wide scope from the beginning. These algorithms provide sufficiently good results in all sorts of ad-hoc networks. Following is the work done till now on few of the majorly used swarm intelligence algorithms including ACO and FA:

The comparison of AntHocNet and BeeAdhoc is done with DSR, DSDV, AODV for routing in FANETs [1]. The simulation results of the modeling shows that the bio-inspired algorithms AntHocNet and BeeAdHoc outperforms the traditional routing algorithms AODV, DSDV and DSR. Another computing technique based on Bio-inspired algorithms is analyzed [2]. In this technique, the analysis is done on the basis of behavior of animals. A scheme based on clusters is proposed further [3]. This scheme is known as Bio-Inspired Clustering Scheme. It uses hybrid mechanism based on glow-worm swarm optimization and krill herd. Another protocol is proposed based on bio-inspired method [4]. The performance of the proposed protocol is showed with various other algorithms on different parameters. [5] This paper shows uses Bee colony algorithm for routing in FANETs.

There is also a wide use of Genetic algorithms in ad-hoc networks. Although major work is not been done in GA for FANETs, but it has been used broadly in various other wireless networks. Following is the literature work cited by scholars:

A GA based on multipath distance vector protocol is proposed [6]. The simulations results show that optimized goals are achieved by the proposed algorithm. MEGA (Maximum enhanced genetic algorithm), an improved GA which uses local search technique was introduced [7]. Another optimization method to find the shortest path in an ad-hoc network using genetic algorithm is given [8]. An energy efficient routing protocol is proposed by researchers [9]. According to the simulation results, delivery rate of this protocol is increased by 40% when compared to other protocols.

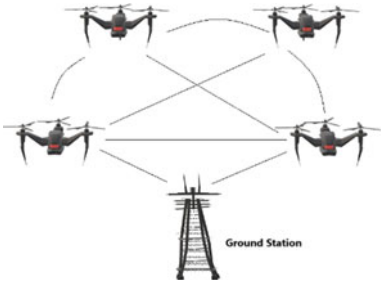

Fig. 1 Multiple UAVs connected to ground station

Another clustering-based algorithm is developed later [10]. The algorithm improves the parameters of previously developed algorithms namely Bio-inspired clustering scheme and energy aware link-based clustering.

2 Existing Algorithms

Nature-inspired algorithms are the algorithms which observes and analyzes the biological phenomena of living organisms [11]. These algorithms are used for complex optimization problems. NIA has shown tremendous results in past in the field of routing. Nature-inspired algorithms are classified into two categories. One is Genetic algorithms (GA) and the other is Swarm intelligence (SI) algorithms. Both of these algorithms are inspired by the behaviour of animals.

Genetic algorithms are a part of evolutionary computing [12]. Genetic algorithm is used to find or select optimal path. It represents chromosomes which are the set of solutions.

The other type of algorithm is Swarm Intelligence. Swarm intelligence are also used for path selection in wireless ad-hoc networks. It is a subfield of Artificial Intelligence which is related to intelligent behaviour of swarms [13]. There are many algorithms which come under the category of swarm intelligence algorithms. The algorithms like Fish swarm algorithm, Cat swarm algorithm, Chicken swarm optimization algorithm, flock based are all swarm-intelligence algorithms which are based on the behaviour of animals.

2.1 Ant Colony Optimization (ACO)

Ant Colony Optimization (ACO) is a Swarm based Intelligence algorithm. The algorithm was proposed by Dorigo [14]. It is among one of the popular algorithms used for routing. ACO is an optimization method that imitates the nature of ants when they move for the search of food. It uses ants and analyze the pattern of moving

ants. These ants travel from one point to another in search of food. ACO is used to find the shortest path during the travel of ants when they start from their source to destination.

2.2 Firefly Algorithm

Another swarm-intelligence algorithm introduced by Yang in 2008 is Firefly Algorithm [15]. It is based on the behavior of fireflies. In this algorithm, the shortest and optimal path can be computed by analyzing the behaviour of firefly. The algorithm uses the flash lights of fireflies for the analysis. Whenever a firefly is moving the other firefly gets attracted to it its flash light. Therefore, the attractiveness of firefly is directly proportional to the brightness of a firefly depending upon the objective function. The brightness of firefly reduces when the distance between them increases which means distance and brightness are inversely proportional to each other [16].

The fireflies update depends on the real time performance of fireflies and according to that the location will get updates. The parameters in this algorithm are fixed which means the search behaviour will be same in all iterations for any state.

Modified Firefly Algorithm (MFA)
A new modified algorithm is proposed in this paper which can make routing in FANETs more efficient. This new approach is based on clustering mechanism. In this approach, the nodes are divided into many clusters. All the clusters have cluster head. The cluster head is selected based on the residual energy. Node with the highest residual energy is selected as cluster head.

2.3 Genetic Algorithm

Genetic Algorithms (GA) are search based meta-heuristic algorithm belonging to the class of Evolutionary algorithms (EA). These algorithms are based on the mechanism of natural selection and genetics.

Modified Genetic Algorithm (MGA)
The proposed method is location-based routing for FANETs using mobile coverage concept. It allows the neighbor node to communicate in assigned coverage network area to find the nearby neighbor nodes and detect the malicious nodes in the coverage area. This ensures less packet loss during transmission.

Table 1 Simulation parameters

Parameter	Value
Simulation area	1000 * 1000 m
Simulator	Ns-3.26
Mobility model	Random waypoint mobility model
Channel type	Wireless channel
Protocols used	ACO, modified firefly, modified GA
Nodes	50
Packet size	1024 bytes
Simulation time	20 s

3 Parameters and Methods

Network simulator, ns-3.26 is used for simulation. The data considered for simulation of the following algorithms: ACO, Firefly algorithm and Genetic algorithm is shown in Table 1.

The parameters used to analyze the performance of routing algorithms ACO, MFA, and MGA are Packet Delivery Ratio, End-to-End delay, Throughput, Routing overhead.

4 Results and Discussion

For simulation, the test analysis of routing algorithms ACO, Modified Firefly algorithm and Modified Genetic algorithm is given. The results show that all three algorithms have fine possibility to be used as an effective solution for routing in FANET.

Table 2 shows the values at 50^{th} node for all the algorithms considered for simulation. The packet delivery ratio is highest in modified firefly algorithm. ACO is having the second-best packet delivery ratio whereas modified genetic algorithm has lowest ratio. This is because the modified firefly algorithm (MFA) is the most accurate of all the algorithms in respect to successful packet delivery. The end-to-end delay

Table 2 Comparison of algorithms

Parameters	ACO	MFA	MGA
PDR	92	98	90
E2E delay (ms)	12.4	13	15
Overhead	10.5	9	10.5
Throughput	627	640	606

is an important parameter while packet transmission. This depends upon the node availability and link stability. ACO has the lowest delay following MFA. These two algorithms are efficient in both the factors. Overhead is the next parameter considered. MFA shows the lowest overhead generated. ACO and MGA shows the same overhead. Fourth and most important parameter is throughput. MFA again has the highest throughput of all the algorithms which makes it the most optimal algorithm in terms of successful packet transmission. ACO comes second in terms of throughput with a difference of around 2% whereas MGA shows the least throughput with a difference of 7%.

5 Conclusion and Future Scope

The idea of using of swarm intelligence algorithms has created new dimensions for routing in Flying ad-hoc networks. Since routing in FANETs is not an easy task, NIA has brought it altogether as an emerging solution for routing. Many conventional algorithms have already been used and still used to find an effective solution to this problem. The paper presents performance comparison of the most extensively used ACO algorithm with the modified version of firefly and genetic algorithm. As per the analysis, modified firefly algorithm outperforms all other swarm-intelligence algorithms on all the parameters. ACO performs second best after MFA. Therefore, from the analysis it can be said that ACO and FA are the two algorithms which have potential to act as an optimal routing solution.

Thus, enhancing ACO and other swarm-based algorithms on more parameters can be considered as a future work to solve the routing issue. Another novel swarm-based algorithm can also be proposed to improve routing in FANETs.

References

1. Leonov AV (2017) Applying bio-inspired algorithms to routing problem solution in FANET. Bull South Ural State Univ Ser Comput Technol Autom Control Radioelectron 17(2):5–23. https://doi.org/10.14529/ctcr170201
2. Darwish A (2018) Bio-inspired computing: algorithms review, deep analysis, and the scope of applications. Future Comput Inform J 3(2):231–246. https://doi.org/10.1016/j.fcij.2018.06.001
3. Khan A, Aftab F, Zhang Z (2019) BICSF: bio-inspired clustering scheme For FANETs. IEEE Access 7:31446–31456. https://doi.org/10.1109/access.2019.2902940
4. Tropea M, Santamaria AF, Potrino G, Rango FD (2019) Bio-Inspired recruiting protocol For FANET in precision AGRICULTURE domains: pheromone parameters tuning. 2019 Wirel Days (WD). https://doi.org/10.1109/wd.2019.8734209
5. Zhao B, Ding Q (2019) Route discovery in flying ad-hoc network based on bee Colony Algorithm. In: 2019 IEEE international conference on artificial intelligence and computer applications (ICAICA). https://doi.org/10.1109/icaica.2019.8873436
6. Shawara M, Sarhan A, Elfishawy N (2017). Energy aware ad-hoc on demand multipath distance vector (EA-AOMDV). In: 2017 13th international computer engineering conference (ICENCO). https://doi.org/10.1109/icenco.2017.8289807

7. Hampiholi AS, Vijaya Kumar BP (2018) Efficient routing protocol in IoT using modified genetic algorithm and its comparison with existing protocols. In: 2018 3rd international conference on circuits, control, communication and computing (I4C). https://doi.org/10.1109/cimca.2018.8739759
8. Pal D, Shah D, Bhagat SK (2019) Design of a genetic algorithm based shortest path routing with different mutation techniques. In: 2019 IEEE international conference on electrical, computer and communication technologies (ICECCT). https://doi.org/10.1109/icecct.2019.8869243
9. Sang Q, Wu H, Xing L, Ma H, Xie P (2020) An energy-efficient opportunistic routing protocol based on trajectory prediction for FANETs. IEEE Access 8:192009–192020. https://doi.org/10.1109/access.2020.3032956
10. Aissa M, Abdelhafidh M, Mnaouer AB (2021) EMASS: a novel energy, safety and mobility AWARE-BASED clustering algorithm For FANETs. IEEE Access 9:105506–105520. https://doi.org/10.1109/access.2021.3097323
11. Mellouk A, Hoceini S, Zeadally S (2011) A bio-inspired quality of Service (QOS) routing algorithm. IEEE Commun Lett 15(9):1016–1018. https://doi.org/10.1109/lcomm.2011.071211.110741
12. Seetaram J, Kumar PS (2016). An energy aware genetic algorithm multipath distance vector protocol for efficient routing. In: 2016 international conference on wireless communications, signal processing and networking (WiSPNET). https://doi.org/10.1109/wispnet.2016.7566488
13. Sahingoz OK (2013) Networking models in flying ad-hoc networks (FANETs): concepts and challenges. J Intell Rob Syst 74(1–2):513–527. https://doi.org/10.1007/s10846-013-9959-7
14. Khan WA, Hamadneh NN, Tilahun SL, Ngnotchouye JMT (2016) A review and comparative study of firefly algorithm and its modified versions. Optim Algorithms Methods Appl. https://doi.org/10.5772/62472
15. Yang XS, He X (2013) Firefly algorithm: recent advances and applications. Int J Swarm Intell 1(1):36. https://doi.org/10.1504/ijsi.2013.055801
16. Fidanova S, Luque G, Roeva O, Ganzha M (2019) Ant colony optimization algorithm for workforce planning: influence of the evaporation parameter. In: Proceedings of the 2019 federated conference on computer science and information systems. https://doi.org/10.15439/2019f300

Theory of Characteristics Mode Based Design of a Planar Monopole Antenna with Polarization Diversity for FSS and SAR Application

Reshmi Dhara

Abstract Here, using Theory of characteristics Mode (TCM) a single feed planar monopole antenna is demonstrated. After TCM analysis dominant modes of the radiator are identified. Using appropriate feeding method and modified ground plane the dominants modes are excited to achieve quad impedance band (IB) with polarization diversity characteristics. The design antenna which is proposed here involves two L-shaped radiators with two asymmetric cross slots within it creates mutual coupling to attain dual circularly polarized (CP) bands. To generate quad impedance bandwidth (IBW) defective ground plane is utilized on the reverse side of the substrate. The proposed antenna covered the quad simulated IBs are from 3.631–4.167, 6.542–8.494 GHz, 8.859–10.253 GHz and 10.8494- beyond 15 GHz respectively. The simulated dual ARBWs span over 3.865–4.069 GHz within 1st IB and 8.888–9.785 GHz within 3rd IB. This antenna can be used for S- and X-band, particularly Fixed Satellite Service (FSS) and Synthetic Aperture Radar (SAR) applications.

Keywords TCM · Quad band · Polarization diversity · Axial ratio bandwidth · Impedance bandwidth · FSS · SAR

1 Introduction

Recently, multi band antennas with polarization diversity have satisfied multiple necessities of many devices in wireless communication systems. In personal mobile and global position system (GPS) devices, antennas through omni-directional radiation are particularly suitable. On the other hand, several communication devices for example global navigation satellite systems, point-to-point communication systems, and other satellite communication systems, antennas with unidirectional radiation patterns are growing by means of an integral technology. To generate vertically/horizontally omni-directional dual-polarized radiation it's needed to superimposed two radiations from a vertically polarized monopole antenna and a horizontal

R. Dhara (✉)
Department of Electronics and Communication Engineering, National Institute of Technology Sikkim, South Sikkim, Ravangla 737 139, India
e-mail: reshmidhara@nitsikkim.ac.in

M. Tiwari et al. (eds.), *Optical and Wireless Technologies*, Lecture Notes in Electrical Engineering 892, https://doi.org/10.1007/978-981-19-1645-8_10

polarized loop antenna. Now in communication system where the astronomical research is the main attention, several uses communication devices are essential as a substitute to single communication typical device. As a consequence of the striking characteristics like lower footprint, simpler geometry, and lighter in weight, planar monopole antennas help as an utmost suitable practise. This is known to all that a conventional monopole antenna in longitudinal direction creates linearly polarized (LP) wave. But the foremost drawbacks of LP wave expected at dual-band process are lower sensitivity, multipath fading to the positioning between the transmitting and receiving antennas, lower mobility, and like that [1–3]. This could be overwhelmed to a great scope consuming the circularly polarized antennas. Henceforth, dual band antennas by means of two different frequency bands instantaneously functioning dual circular polarization (left hand circular polarization (LHCP) and right-hand circular polarization (RHCP)), are significantly widespread over dual band antennas with two orthogonal (vertically/horizontally) linear polarizations. The requirement of multiple antennas decreases due to using a multiband antenna with dual polarization characteristics. The CP antenna is very attractive for many wireless systems as no strict orientation between transmitting and receiving antenna is required and encountering interference. To fulfilments these necessities of multi band antenna presentation together linear and circular polarization, various methodologies have been used by many researchers [4–8].

TCM analysis is a great tool which give the analyzation of existing dominant modes within the radiator at the desired resonant frequency. However, the TCM analysis is lacking in previously reported literature for the multiband antennas. Here, the proposed CP antenna also utilizes the analysis of TCM tools for the multi impedance bands and polarization diversity characteristics.

Inspired by the aforementioned the whole thing, a simple quad band monopole antenna with LHCP in 1st band, LP in 2nd, LHCP in 3rd and LP in 4th bands are proposed in this paper. The proposed design can support 3.631–4.167 GHz (535.6 MHz, f_{rc1} = 3.9 GHz, 13.73%), 6.542–8.494 GHz (1951.8 MHz, f_{rc2} = 7.52 GHz, 25.96%), 8.859–10.253 GHz (1134.3 MHz, f_{rc3} = 9.56 GHz, 14.59%) and 10.8494- beyond 15 GHz (4150.6 MHz, f_{rc4} = 12.92 GHz, 32.19%). The simulated dual ARBWs span over 3.865–4.069 GHz (203.7 MHz, f_{cp1} = 3.97 GHz, 5.14%) within 1st IB and 8.888–9.785 GHz (897.3 MHz, f_{cp2} = 9.34 GHz, 9.6%) within 3rd IB. To design a quad antenna, it has been appropriately improved in a method so that it can sustenance together linear and circular polarizations.

An actual good reflection coefficient, widespread ARBW and dependable radiation features are gained for the implemented antenna. It became apparent that the implemented antenna is simple and make available for wider LP, CP frequency bands.

This paper is presented like: Sect. 2: Design Procedure of Antenna; Sect. 3: Simulation Justifications and Discussions; and lastly Sect. 4: Conclusion.

2 Design Procedure of Antenna

Design of the Radiator

The progress steps of the radiator are represented in Fig. 1. The reflection coefficient and axial ratio bandwidth progress plots of the designed radiator are shown in Figs. 2(a) and (b). First in Antenna.1 is designed at a resonating frequency 3.6 GHz using a rectangular radiator and a ground plane rectangular in size on the reverse side of the substrate for FSS application. Here a centre feed microstrip line is utilized to fed the antenna. But the IBW is very poor at this frequency and also got a CP in the higher frequency region (12.8 GHz). To improve the IBW and to satisfy the multiband characteristics by using the same dimension of the antenna its need to create additional current paths. For that reason, two L-shaped radiators are used by modifying the rectangular shaped radiator. The gap between two radiators create a coupling effect [9], due to generation of capacitance between them. This gap creates additional current path that increase IBW in addition to improve ARBW performance compared to earlier stage. To improve ARBW performance more also an asymmetric feed [8] is used in this step. Better impedance matching network can be performed by using this feeding structure. But this Antenna.2 generate only a small CP (9.89 GHz) band. In next stage for improving the ARBW performance more, two slots asymmetric in size [10–12] are edged from two L-shaped radiator gives Antenna.3. These two slots generate two very small CP bands resonating at frequency 3.78 GHz and 9.4 GHz respectively. These asymmetric slots [10, 11, 13] create two orthogonal electric field

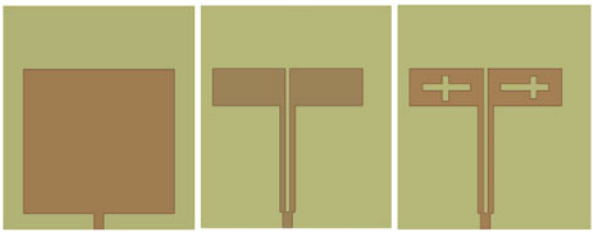

Fig. 1 Improvement of implemented antenna

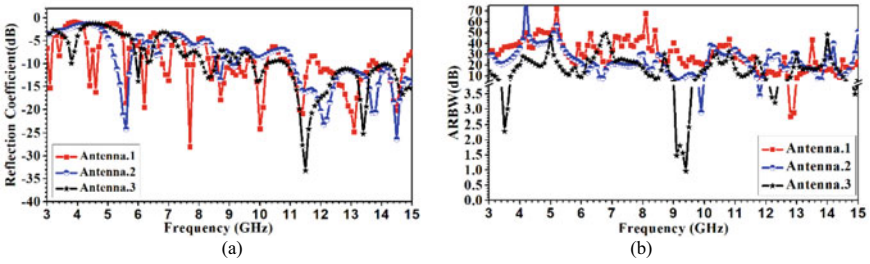

Fig. 2 Evaluation of **a** Reflection coefficient and **b** Axial ratio bandwidth for Antenna. 1–3

with equal amplitude at these two-resonating frequencies. But this Antenna.3 gives reflection coefficient is not so good in lower frequency region but moderate in higher frequency region. So, to identify the existing modes within the same radiator it is need to study TCM analysis of this radiator.

TCM Analysis and Design of Proposed Antenna

The TMA analysis is done by using the radiator without feeding structure [12, 14]. Here radiator is considered to be zero thickness with PEC and the ground plane, substrate is considered to be infinite and results are analysed in Figs. 3. Figure 3(a) described the plot of eigenvalues versus frequency plot of the fourteen fundamental characteristic modes. The eigenvalues ($\lambda_n = 0$) for modes 2, 3, 5, 6, 7, 8, 9, 11, 12, 14, 15, 17 18, 22 are dominant modes, whereas no mode are inductive mode as it has very high eigenvalues ($\lambda_n > 0$) and 1, 4, 10, 13, 16, 19, 20 and 21 modes are capacitive mode as it has low high eigenvalues ($\lambda_n < 0$).

From Fig. 1(b) the plot of characteristics angle versus frequency plot of the fourteen fundamental characteristic modes. Here mode 2, 3, 5, 6, 7, 8, 9, 11, 12, 14, 15, 17 18, 22 are crosses 180° axis line at their resonant frequencies which are dominant modes. Whereas 1, 4, 10, 13, 16, 19, 20 and 21 modes are non-resonant modes as they doesn't cross 180° axis line.

Similarly Fig. 1(c) described large model significance value around 1 are dominant at their resonant frequencies for mode 2, 3, 5, 6, 7, 8, 9, 11, 12, 14, 15, 17 18, 22 and model significance (<0.2) for 1, 4, 10, 13, 16, 19, 20 and 21 modes which are non-resonant modes.

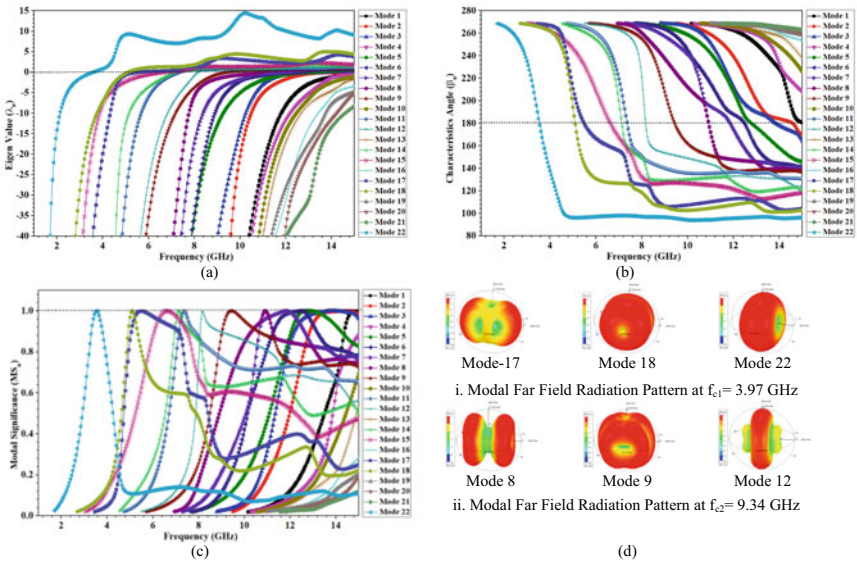

Fig. 3 TCMs analysis for different modes **a** Eigen values, **b** Characteristics angle, **c** Modal significance and **d** Radiation pattern

From Fig. 3 after TCM analysis it has been revealed that there are 14 existing dominant modes within the radiator from 3–15 GHz resonating frequency region. The dominant modes of the radiator are resonating at 3.54 GHz (Modes 22), 5.09 GHz (Modes 18), 5.48 GHz (Modes 17), 6.63 GHz (Modes 15), 7.13 GHz (Modes 14), 7.36 GHz (Modes 11), 8.17 GHz (Modes 12), 9.44 GHz (Modes 9), 10.92 GHz (Modes 8), 11.85 GHz (Modes 7), 12.48 GHz (Modes 6), 12.78 GHz (Modes 5), 13.84 GHz (Modes 3), 14.58 GHz (Modes 2). So, from this TCM analysis it can be conclude that if one researcher design the feed and ground plane properly there may be the possibility to get good IBW within 3–15 GHz band region. After parametric analysis it is identified that asymmetric microstrip line feed and a defective ground plane [9] can be able to excite above dominant modes.

Two degenerated modes generate a CP mode when the phase among them is 90° and amplitude is equal.

Here Fig. 3d(i)–(ii) shows radiation pattern for modal far field of the radiator for different modes at two CP resonating Frequencies. Figure 4d(i) depicts that mode 18 and 22 radiate in +z direction at $f_{c1} = 3.97$ GHz ad they are fundamental modes along y and x direction correspondingly. As the phase difference between them is 90° so these two orthogonal modes are able to generate a CP at $f_{c1} = 3.97$ GHz resonating frequency. Figure 3d(ii) depicts that mode 9 and 12 radiate in +z direction at $f_{c1} =$ 9.34 GHz and they are fundamental modes along y and x direction correspondingly. As the phase difference between them is 90° so these two orthogonal modes are able to generate another CP at $f_{c1} = 3.97$ GHz resonating frequency. The other Modes lead to cancelation of electric field in the far field zone at +z direction so they are undesired to generate CP mode.

The designed antenna simulated structures is shown in Fig. 3(a) and (b) and it helps to achieve quad impedance bands which are resonating at the centre frequencies of 3.9 GHz, 7.52 GHz, 9.56 GHz and >12.92 GHz respectively and it's also give dual CP bands, resonating at 3.97 and 9.34 GHz, results shown in Fig. 4(a) and (b). Since it satisfied our purpose, it definite to select finalized this design and analysed its performance. The size of the microstrip antenna is 70 × 60 mm^2. Commonly available, low cost workable FR4-epoxy substrate thickness of 1.6 mm, having εr =

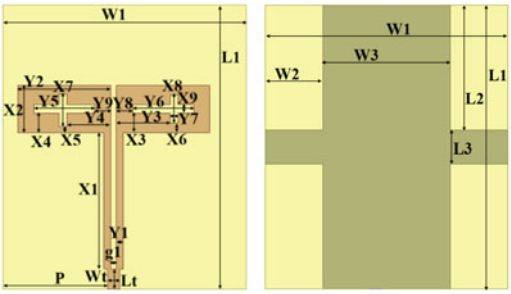

Fig. 4 Dimension of proposed antenna

Table 1 Proposed antenna optimal dimension

Parameter	Value (mm)	Parameter	Value (mm)	Parameter	Value (mm)
L1	70	L2	30.9	L3	8.2
W1	60	W2	14.3	W3	31.4
Lt	5	Wt	3	g1	1.4
X1	33.5	X2	11.7	X3	4.8
X4	4.8	X5	1.7	X6	2.0
X7	7.8	X8	7.0	X9	2.1
Y1	1.7	Y2	23	Y3	13.2
Y4	10.8	Y5 = Y6	15	Y7	2.0
Y8 = Y9	4	P	25.8	h	1.6

4.4 and loss tangent $tan\delta = 0.02$ is utilized to simulated the implemented antenna. Comprehensive optimal dimensions have been recorded in Table 1.

3 Simulation Justifications and Discussions

To design the antenna, use simulation software, Ansys Electronics Desktop 2020 R1. The designed antenna enclosed the quad simulated IBW ranged from 3.631–4.167 GHz (535.6 MHz, $f_{rc1} = 3.9$ GHz, 13.73%), 6.542–8.494 GHz (1951.8 MHz, $f_{rc2} = 7.52$ GHz, 25.96%), 8.859–10.253 GHz (1134.3 MHz, $f_{rc3} = 9.56$ GHz, 14.59%) and 10.8494- beyond 15 GHz (4150.6 MHz, $f_{rc4} = 12.92$ GHz, 32.19%) depicts in Fig. 5(a).

Figure 5(b) also depicts the simulated ARBW of the implemented antenna**.** The simulateddual ARBW span over 3.865–4.069 GHz (203.7 MHz, $f_{cp1} = 3.97$ GHz, 5.14%) within 1st IB and 8.888–9.785 GHz (897.3 MHz, $f_{cp2} = 9.34$ GHz, 9.6%) within 3rd IB.

Figure 5(b) simulated input impedance is depicting at 50 Ω microstrip feed line for the real (Resistance) and imaginary (Reactance) parts. Within the IBs impedance match is good because the real part (resistance) of the impedance closer to 50 Ω and the imaginary part (reactance) is closer to 0 Ω.

From Fig. 5(c) using smith chart one can see that on resonance frequency 3.7, 3.9, 7.5, 9.6, 12.92, and 15.0 GHz the normalized impedance ($\overline{Z}11$) values are close to 1 whereas the complex reflection coefficient magnitude (Γ) values are also very small. So above values depict that best matching can occur on resonance frequencies because real part of $\overline{Z}11$ approaches to 50Ω and imaginary part tends to 0Ω. Also, VSWR value on those frequencies is also <2. The Q-value on those lower resonating frequencies in addition to higher resonating frequencies is also very small. That signify widest IBW can occur due to small Q-factor. At centre resonating frequencies also depicts that impedance matching can occur on those frequencies as VSWR value

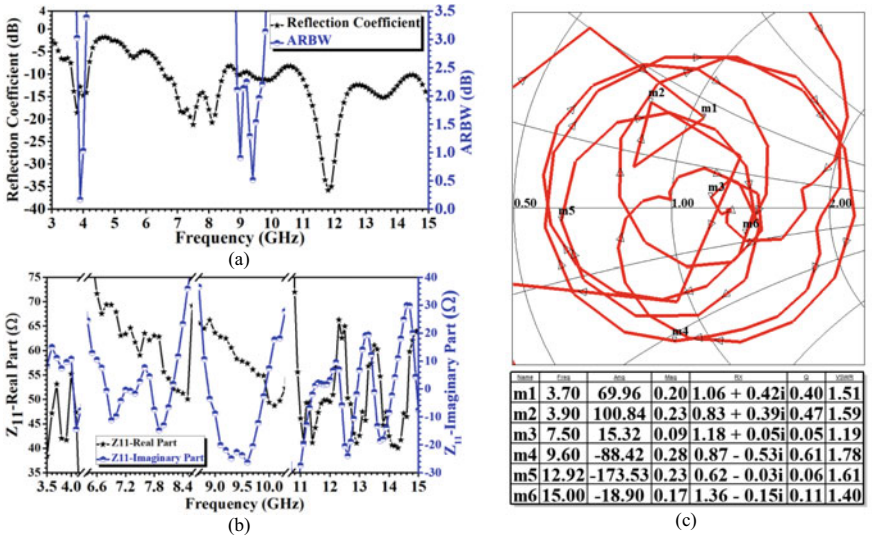

m1	3.70	69.96	0.20	1.06 + 0.42i	0.40	1.51
m2	3.90	100.84	0.23	0.83 + 0.39i	0.47	1.59
m3	7.50	15.32	0.09	1.18 + 0.05i	0.05	1.19
m4	9.60	-88.42	0.28	0.87 - 0.53i	0.61	1.78
m5	12.92	-173.53	0.23	0.62 - 0.03i	0.06	1.61
m6	15.00	-18.90	0.17	1.36 - 0.15i	0.11	1.40

Fig. 5 (a) Simulated reflection coefficient and ARBW curves comparisons, (b) Simulated impedance (Real and Imaginary) vs. Frequency curves, (c) Results of the effect of complex reflection coefficient (Γ), normalized input impedance (Z11), Q-factor and VSWR using Smith Chart for the Implemented Antenna

<2. From this Smith chart it's also clear that the graph rotates four times nearly equal to kick point (SWR = 1) which prove quad impedance bands are generate by using the same structure.

Figure 6(a) depicts the radiation efficiency (simulated) for the designed antenna respecting frequencies. The ranges of radiation efficiencies in between 74–99% for the quad IBs. The maximum efficiency is 99.17% at 7.1 GHz. Figure 6(a) also depicts the at peak gains respecting frequency. The gain is within 2.20–6.01 dBi for quad the impedance bands and the peak gain is maximum 6.01 dBi at 7.1 GHz.

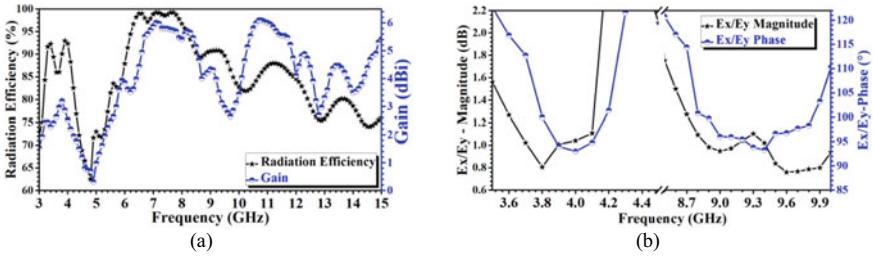

Fig. 6 Implemented Antenna **a** Gain and radiation efficiency, **b** E_X/E_Y magnitude and phase plot vs. Frequency

Figure 6(b) depicts the Ex/Ey magnitude is closely equal to 1 or 0 dB within the dual CP bands and phase difference among them is also nearly 90°. This demonstrates that the dual bands gratify CP conditions [13].

Well defined, LHCP and RHCP are detected in Fig 7(a), (c) and (b), (d) which are illustrating the radiation patterns at $\varphi = 0°$ (XZ plane) and $\varphi = 90°$ (YZ plane) at $f_{cp1} = 3.97$ GHz and $f_{cp2} = 9.34$ GHz. At broadside direction on two CP resonating frequencies the radiations observed are LHCP whereas the polarization (co and cross) difference are 32.47 dBi, and 22.57 dBi, correspondingly. Because of the asymmetric inset feeding radiator, the distribution of current is productive, due to that reason radiation is somewhat slanting from its broadside direction.

To understanding the generation of the dual CP modes at 3.97 and 9.34 GHz, a qualitative study is depicted in Fig. 8. The normalized currents distribution from the below figures it is observed that for four separate time moments (t = 0, t = T/4, t =

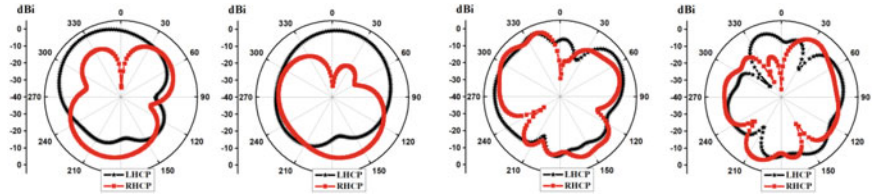

Fig. 7 Radiation patterns for (LHCP and RHCP) in the **a**, **c** XZ ($\varphi = 0°$) and **b**, **d** YZ ($\varphi = 90°$) planes

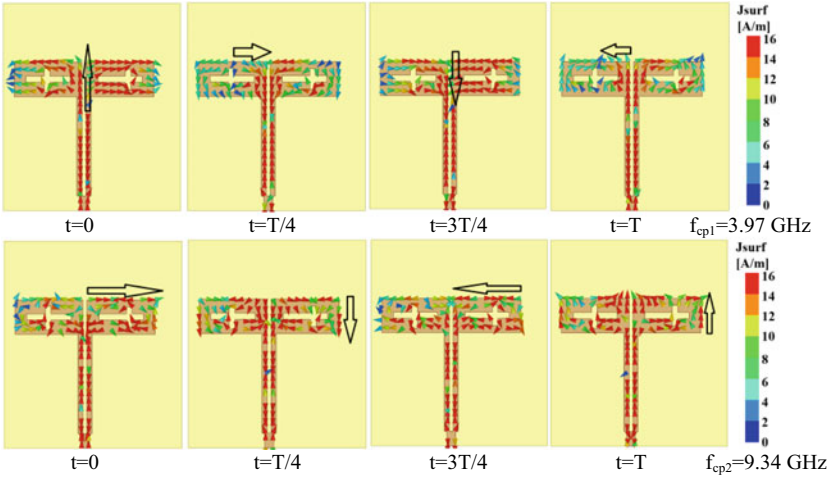

Fig. 8 Simulated current distribution at $f_{cp1} = 3.97$ GHz and at $f_{cp2} = 9.34$ GHz

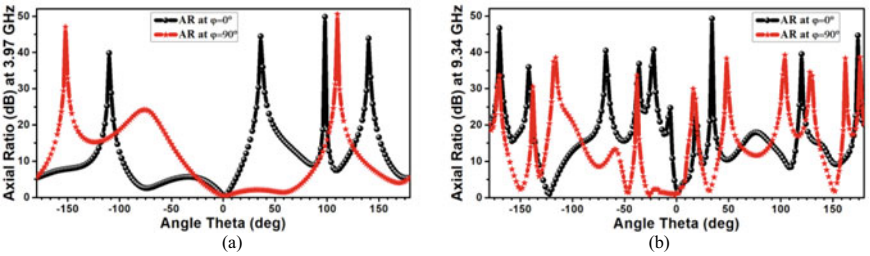

Fig. 9 Axial ratio beam width vs. θ° at XZ plane (φ = 0°) and YZ plane (φ = 90°) **c** f_{cp1} = 3.97 GHz, **b** f_{cp2} = 9.34 GHz for the proposed antenna

3 T/4, t = T where for one cycle T is the total time period), dual CP modes could be accomplished at f_{cp1} = 3.97 GHz, f_{cp2} = 9.34 GHz which are LHCP.

The simulated axial ratio beam width f_{cp1} = 3.97 GHz and f_{cp2} = 9.34 GHz are plotted vs. θ° in Fig. 9(a) and (b). As obtained the results through simulation, at fcp1 the implemented antenna has a 3 dB AR beam width over vertical θ angle of about 17° at XZ (φ = 0°) plane and 89° at YZ (φ = 90°) plane. So, at broadside direction the difference between co- and cross plane simulated 3 dB AR beam width is 72° at f_{cp1} = 3.97 GHz. Similarly, at f_{cp2} the implemented antenna has a 3 dB AR beam width over vertical θ angle of about 5° at XZ (φ = 0°) plane and 35° at YZ (φ = 90°) plane. So, at broadside direction the difference between co- and cross plane simulated 3 dB AR beam width is 30° at f_{cp2} = 9.34 GHz.

4 Conclusion

In this paper TCM analysis helps to create a great extent simpler method to design a quad IB with polarization diversified monopole antenna assessment compare to former design techniques. The implemented antenna showing LHCP in 1st IB, LP in 2nd IB, LHCP in 3rd IB and LP in 4th IB are comprehended by employing changes in ground plane and asymmetric feeding network of two L-shaped planar monopole antenna with two asymmetric cross shaped slots. The proposed antenna (size 70 × 70 mm^2 i.e. 1.378 × 1.181 $\lambda_g{}^2$, λ_g = guided wavelength at 3.6 GHz) gives quad IBW, are 13.97, 25.96, 14.59 and 32.19% resonating at 3.9, 7.52, 9.56, and 12.92 GHz respectively. The dual CP bands of this antenna (5.14% at f_{cp1} = 3.97 GHz and 9.6% at f_{cp2} = 9.34 GHz) can support S- and X band specially FSS and SAR applications in a single device.

References

1. Toh BY, Cahill R, Fusco VF (2003) Understanding and measuring circular polarization. IEEE Trans Educ 46(3):313–318. https://doi.org/10.1109/TE.2003.813519
2. Yu D, Gong SX, Xu Y, Wan YT (2015) Dual-band dual-polarized circular microstrip patch antenna with the curved slots on the ground. Progr Electromagn Res 51:27–31. https://doi.org/10.2528/PIERL14112004
3. Langston WL, Jackson DR (2004) Impedance, axial-ratio, and receive-power bandwidths of microstrip antennas. IEEE Trans Antennas Propag 52(10):2769–2774
4. Bao XL, Ammann MJ (2011) Wideband dual-frequency dual-polarized dipole-like antenna. IEEE Antennas Wirel Propag Lett 10:831–834. https://doi.org/10.1109/LAWP.2011.2164609
5. Ding K, Gao C, Wu Y, Qu D, Zhang B, Wang Y (2017) Dual-band and dual-polarized antenna with endfire radiation. IET Microwaves Antennas Propag 11(13):1823–1828. https://doi.org/10.1049/iet-map.2017.0124
6. Bag B, Biswas P, Biswas S, Sarkar PP (2019) Wide-bandwidth multifrequency circularly polarized monopole antenna for wireless communication applications. Int J RF Microwave Comput Aided Eng 29(3):e21631. https://doi.org/10.1002/mmce.21631
7. Madaka KCR, Muthusamy P Mode investigation of parasitic annular ring loaded dual band coplanar waveguide antenna with polarization diversity characteristics. Int J RF Microwave Comput Aid Eng e22119. https://doi.org/10.1002/mmce.22119.
8. Dhara R, Jana SK, Mitra M (2020) Tri-band circularly polarized monopole antenna for wireless communication application. Radioelectron Commun Syst 63(4):213–222. https://doi.org/10.3103/S0735272720040044
9. Dhara R (2021) A compact dual band dual polarized monopole antenna with enhanced bandwidth for C, X, and Ku band applications. Progr Electromagn Res Lett 96:65–72. https://doi.org/10.2528/PIERL20121903
10. Singh AK, Patil S, Kanaujia BK, Pandey VK (2020) A novel printed circularly polarized asymmetric wide slot antenna for digital cellular system. Microw Opt Technol Lett 62(3):1438–1447. https://doi.org/10.1002/mop.32177
11. Ellis MS, Effah FB, Ahmed AR, Kponyo JJ, Nourinia J, Ghobadi C, Mohammadi B (2020) Asymmetric circularly polarized open-slot antenna. Int J RF Microwave Comput Aided Eng 30(5):e22141. https://doi.org/10.1002/mmce.22141
12. Dhara R, Yadav S, Sharma MM, Jana SK, Govil MC (2021) A circularly polarized quad-band annular ring antenna with asymmetric ground plane using theory of characteristic modes. Progr Electromagn Res 100:51–68. https://doi.org/10.2528/PIERM20102006
13. Dhara R, Mitra M (2020) A triple-band circularly polarized annular ring antenna with asymmetric ground plane for wireless applications. Eng Rep 2(4):e12150. https://doi.org/10.1002/eng2.12150
14. Dhara R (2021) Design of a miniaturized CPW fed Z-shaped monopole antenna using theory of characteristics modes for bandwidth enhancement. Sādhanā 46(2):1–14. https://doi.org/10.1007/s12046-021-01610-7

A Survey Paper on Evolution of Vanet Towards IOV

R. Bindu, M. Preethi Sejal, and H. Chetan

Abstract Internet of Vehicles (IOV) is what came through after a significant metamorphosis of the conventional VANET technology, wherein it interacts with different entities such as vehicles, roads, pedestrians, parking lots, and city infrastructure and provides real-time communication between them. Vehicular Ad Hoc Networks (VANETs) is a kind of Mobile ad hoc network (MANETs)-where the topography of the wireless network is constantly changing due to the high mobility of vehicles. The numerous applications of machine learning algorithms and 5G technologies have played a key role in the versatile applications for the Internet of vehicles. In this paper, we briefly look at the various routing protocols, mobility models, problems, and possible solutions in the security features and the implementation methods of a smarter VANET. Also, we take a look at the progression between VANET from MANET to 5G-LTE. And we come to conclude, that VANET using IEEE 802.11n is the most efficient one.

Keywords VANET · MANET · 5G-LTE · Routing · Protocol · IOV · ML · Safety and Security · IEEE 802.11n

1 Introduction

Information and communication technology together is a driving force behind much automotive industry and our society's upcoming innovations. Mobile communications have changed our lives tremendously over a couple of decades, allowing us to exchange information in any circumstance. A key component of an Intelligent Transportation System (ITS) is the Vehicular Communication Network (VANET), which permits communication between vehicles. The techniques used in MANET (Mobile Ad-Hoc network) are modified to achieve this and the same was proposed

R. Bindu · M. Preethi Sejal (✉) · H. Chetan
CMR Institute of Technology, Bangalore, India
e-mail: sejal11virgo@gmail.com

H. Chetan
e-mail: chetan.h@cmrit.ac.in

M. Tiwari et al. (eds.), *Optical and Wireless Technologies*, Lecture Notes in Electrical Engineering 892, https://doi.org/10.1007/978-981-19-1645-8_11

by professors Z. D. Chen, H. Kung, and D. Vlah in their article [1] published in the year 2001. This new paradigm of vehicle and infrastructure information sharing enables a variety of applications for safety, traffic performance, driver assistance, infotainment, and urban sensing integrated into modern vehicle designs [2].

In the year 2013, the US Department of Transportation along with 8 major automotive manufacturers initiated a vehicle-to-vehicle communication for a short collaborative project with an objective to determine how drivers can make use of this system in safety application and to record their response [3]. A current trend is to form a global heterogeneous network and to integrate every other technology to form a smart city [4].

Before the 5th Generation was involved in the vehicle network, interaction types were restricted to vehicles and RSU (Roadside units) and communication has now improved where vehicles can communicate with their human drivers, pedestrians, other vehicles, roadside infrastructure units in real-time. The IOV supports network communications like Intra-Vehicle, Vehicle to Vehicle (V2V), Vehicle to Infrastructure (V2I), Vehicle to Cloud (V2C), and Vehicle to Pedestrian (V2P). In the context of 5G, these networks are referred to as Vehicle to everything (V2X) communication [2] (Fig. 1).

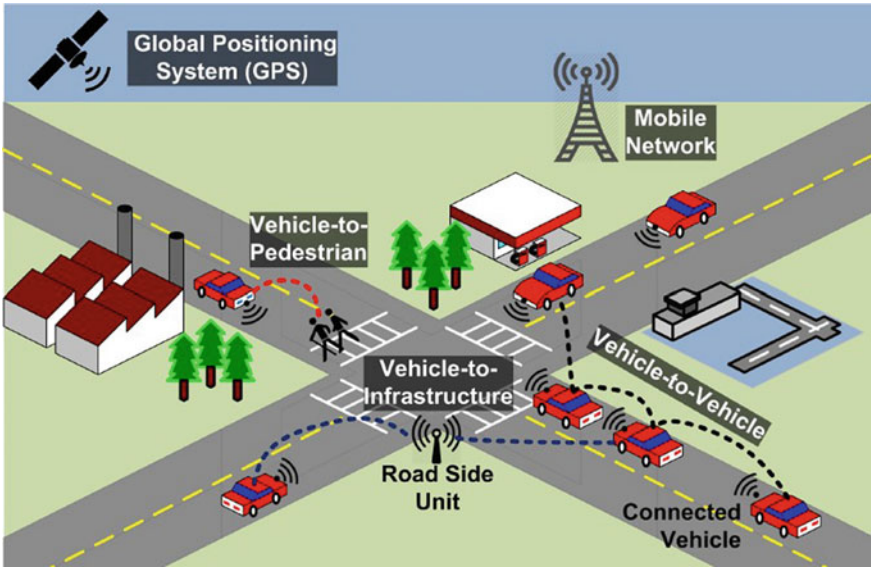

Fig. 1 V2X communication network

2 Literature Survey

2.1 VANET Routing Protocols: Proposed Challenges and Solutions

1) THE HIERARCHY
VANET routing protocols are classified taking into account the method of route updating and position accusation Surmuk Singh et al. in [5] demonstrated the hierarchy of the protocols categorizing based on the type of communication established in network and node positions details.

2) CASE STUDY OF VARIOUS ROUTING PROTOCOLS
Routing protocols in Ad-hoc networks are used to get information about the routing path and the data transmission among nodes.

Table 3 describes the various protocols used in VANET's and gives a comparative study.

2.2 Security in VANET

Security in VANET deals with several aspects such as threats posed to availability, authentication and identification, privacy and integrity, and data trust [2]. Table 2 summarizes the possible attacks under these aspects and poses solutions

2.3 Mobility Models

Mobility models are created to illustrate mobile users' patterns of movement and display the variation in location, speed, and distance. Mobility models can be broadly classified into two types:

Macroscopic Mobility Model: This mobility model takes into account movement restrictions posed by bridges, roads, crossroads, and traffic lights during vehicle movement trace generation. It describes the generation of vehicle traffic, such as traffic speed, traffic density, and initial car distribution.

Random Mobility Model: In such a model, with no restriction, mobile nodes move randomly and freely. Destination, speed, and direction are randomly selected and are independent of other nodes.

Gauss Morkev Mobility Model: The random way-point model will autonomously produce node velocity and direction on past history. It decides directly from its preset range, so an abrupt stop and sharp turn problem can be triggered. Gauss Morkev

model first calculates the speed and direction of motion for each node. After which, nodes move with the computed velocity and direction for a time.

Mobility Model Generation Tool: These tools produce traces of motion to interpret the vehicle's behavior on the road. Microscopic mobility model: Street Random Way Point or STRAW is a method that in which using urban topologies, mobility patterns from the tiger database are generated. STRAW incorporates complex intersection control by means of traffic lights and signs. With such a feature the vehicle shows a more dynamic response when it reaches the intersection. STRAW model's limitation is that it doesn't provide specifics of traffic flows. This also does not indicate a change *of lane.*

2.4 Implementation of VANET

The main objective of VANET is to establish the communication within the vehicles referred to as moving nodes. VANET supports various types' network communication such as V2V, V2I, Intra-vehicle communication, V2B. The evolution of 5G techniques led to the more versatile Interaction among Vehicular nodes such as V2C and V2P. The Various Methods used to implement VANET Communication is described in Table 4.

3 Disscussion

3.1 Features of VANET

A VANET has certain specific characteristics including some similar characteristics as MANET like Omni directional broadcasting [13]:

3.1.1 Highly Dynamic Topology

Vehicle speed and radio propagation a vehicle network is highly dynamic. Cars drive faster in urban environments at the range of 60 km/h to over 120 km/h. We too can travel in various directions. And vehicles may enter or exit the network easily in a very less time, which contributes to regular and fast changes in topology.

3.1.2 Frequently Disconnected

Highly dynamic topology leads to regular timing shifts that insure that communication between two vehicles disappears rapidly as information is transmitted.

3.1.3 Geological Communication

Automobiles usually rely on their spatial position to reach this differs from other networks where an Identity or User ID marks the primary vehicle or target population.

3.1.4 Limited Mobility and Prediction

VANETs have a highly dynamic topology, but typically cars have a certain pattern of mobility limited by bridges, roads and highways, lights, speed limits, traffic conditions and driving behavior. This differs from other networks in which the primary vehicle or target population is identified by an Identity or User ID.

3.1.5 Reduced Versatility and Prediction

VANETs have a highly dynamic topology, but Vehicles movement can be predicted on bridges, roads and highways, signals with speed limits and constant traffic conditions.

3.1.6 System of Propagation

Traditionally the VANETs run in three environments: Urban, Rural and Highways the propagation concept is assumed to be free space on a highway but the signal may be disrupted by projecting the wall panels around the roads in Urban and Rural environment. The propagation paradigm in a VANET, like any other network, has to consider the effects of the disruption in wireless communication from other vehicular nodes and the existence of rapidly scattered access points. All of these problems motivate the researchers to the form new communication protocols.

3.2 The IEEE 802.11p/WAVE System

- IEEE 802.11p/WAVE (Wireless Exposure for Vehicle Environment) is the widely used system for allowing wireless communication in vehicle setups.
- IEEE 802.11p releases specifications for the physical (PHY) and MAC layers to enable 5.9 GHz frequency communication in VANET. In the WAVE stack protocol series, IEEE 1609 interacts with the 11p working group to create additional layer

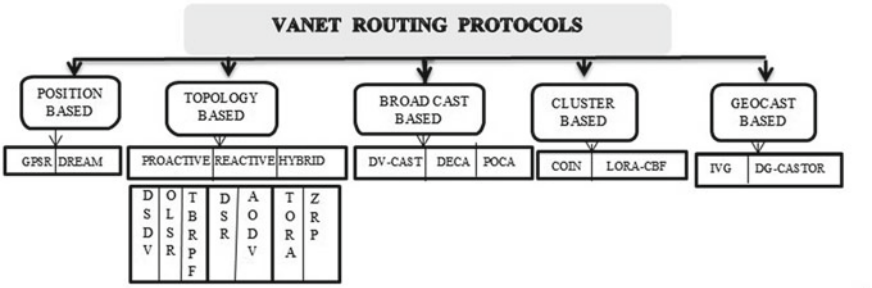

Fig. 2 Routing protocol hierarchy

parameters as shown in Fig. 2. WAVE also includes, in addition to standard Internet Protocol (IP) transfers, the exchange of proprietary short messages (WAVE short message, WSM) to enable high-priority and time-sensitive communication.

- 1609.4 is an upgrade in the IEEE 1609 protocol family of the MAC layer802.11p for multichannel service. According to the IEEE 1609.4 coordination scheme; both vehicles track the control channel during the CCH phase and (optionally) turn to one service channel during the SCH span [14].

4 Applications

Depending on the communication types that are available at VANET i.e. Vehicle-vehicle, vehicle-infrastructure, and application classes. Application classes are as follows [15]:

- **Safety Applications** – These are used to ensure road safety, avoid road accidents, and track the environment of the vehicles. Classifications can follow the intersection of collision avoidance, public safety, sign extension, vehicle inspection and repair, other vehicle details [16], real-time traffic information, the transmission of cooperative messages, post-crash warning [17].
- **Comfort Applications**: The aim of such applications is to provide drivers/passengers with weather information, road conditions, estimations, availability of parking, the nearest restaurant, any distance, automatic toll plaza, and multimedia file sharing [17].
- **Productive Applications**: Such applications target environmental benefits, time usage, and fuel Savings [17].
- With the advent of machine learning, VANET's can further be improvised with better accuracy, precision and predictability in all of the above-mentioned applications [4] (Fig. 3 and Table 1).

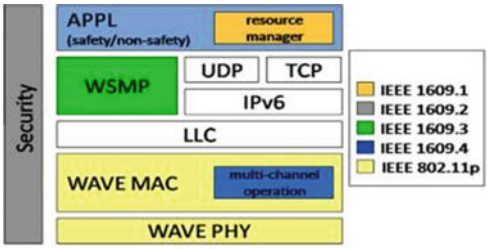

Fig. 3 WAVE stacks

Table 1 ML technologies to detect security attack [4]

Machine learning structure	Function/Task	Type of attack	Detection type
NN	Misuse detection	N/A	Misuse detection
Bayes learning; RF; ADA boost	Malicious attacks detection	N/A	Anomaly detection
Bayes learning	Mobility prediction and anomaly detection	N/A	Anomaly detection
SVM	Collaborative intrusion detection	Sybil; wormhole; black hole	Hybrid detection
Q-learning	Secure strategy selection	Eavesdropping; Jamming	N/A
SVM, K-means	Intrusion detection	Attack free	Hybrid detection
DNN	Misuse detection	Sink-hole; Packet dropper; DOS	Misuse detection
VSM	Malicious attacks detection	N/A	Anomaly detection
Bayes learning	Detecting complex and coordinated attacks	Anomaly detection	Anomaly detection
K-means	Intrusion detection	N/A	Anomaly detection
RF	Intrusion detection	Attack free	Hybrid detection
RF	Intrusion detection	Attack free	Hybrid detection
DNN	Misuse detection	N/A	Misuse detection
NN	Fault detection	Fault data injection	Anomaly detection

Table 2 Comparisions study of security attacks [1, 8–10]

Types of attacks	Possess a threat to	Solutions
DOS	Availability Authentication and Identification	Signature-based authentication mechanisms Deployment of trusted hardware
Brute force	Authentication and Identification Confidentiality	Augmented digital signatures and GPS data Encrypt data with great importance
Greedy behavior	Availability	Switch between channels. If the issue persists, VANET should be switched off
Tunneling	Authentication and Identification	Secure communication architecture
Malware spamming	Availability	Frequency hopping technique FHSS consists of a cryptographic algorithm
Message saturation	Authentication and Identification Integrity and data trust	Timed efficient stream loss-tolerant authentication Two directions reporting
Message fabrication	Availability	Time stamping mechanism
Grey hole	Authentication and Identification	Electronic license plate (ELP)
Sybil attack	Availability	Message linkable group signatures (MLGS) scheme
Key and/or certificate replication	Authentication and Identification Confidentiality Integrity and data trust	Validation check with CRL Controlling manufacturer employees to prevent tampering Digital certificates
Wormhole	Availability Authentication and Identification Integrity and data trust	Packet leashes mechanism Timed efficient stream loss-tolerant authentication Plausibility check
Replay	Authentication and Identification Integrity and data trust	Plausibility validation network VPKI
Timing attack	Availability	Cryptographic solution using timestamps
Eavesdropping	Privacy Confidentiality	Augmented digital signatures and digital GPS SAT (Situation—aware trust)

(continued)

Table 2 (continued)

Types of attacks	Possess a threat to	Solutions
Tracking	Privacy	Anonymity techniques such as key changing algorithms
GPS spoofing and position faking	Privacy	Location clocking techniques AMOEBA
MITM	Privacy Integrity and data trust	Encrypt data with great importance, application of VIPER algorithm Authorized access to hardware and software
Masquerading	Integrity and data trust	Deployment of trusted hardware
Node impersonation	Integrity and data trust	MLGS (message linkable group signature)
Broadcast tampering	Integrity and data trust	Threshold-based trust
Blackhole	Integrity and data trust	Group communication in which group key management system (GKM) is responsible for keys

5 Conclusion

In this paper, we have briefly done a comparative study on various routing protocols and implementation methods looking into numerous research papers. Also, we briefly discuss several mobility models in VANET. Although, in the security domain we still have a lot of areas to improve, with the advent of machine learning tools integrated with VANET there has been a significant development. This paper suggests that IEEE 802.11n is an efficient method for delay-sensitive and bandwidth-hungry devices. It operates relatively well in urban environments. IEEE 802.11n seems to be very significant in terms of delay and allows for improvement of the speech. 5G LTE-V integrated with machine learning tools is the future of VANET. Hence, today VANET has a wider range of applications with increased efficiency as it aids to Smarter City.

Table 3 Comparisons of various routing protocol [5–7]

Protocols	Position based	Proactive	Reactive	Broadcast based	Cluster based	Geocast based
Description	The best path is chosen using the geographical position of the node. The routing path is easily detected by knowing the position of the neighbor of the source node and destination in the packet header	These Protocols chooses a route path which is dependent on shortest path Algorithms The routing updates are performed periodically. It updates every routing path including those paths which are not in use	The routing paths are created only when the nodes need to send data packets. It is chosen when the network should contain a limited number of routing paths to be created for data transmission among nodes	These Protocols Floods the data packets with all available nodes within a broadcast domain over the entire vehicle network. Usually, these are used when the target vehicular node is not inside the range of transmission	The Clusters are formed by grouping all the vehicular nodes with similar characteristics and data is transmitted using a direct path. The communication among nodes is taken by the cluster head	Mobile Just in time Multi-casting (MOBICAST) paradigm is used to build the communication among vehicular nodes. The area of Coverage and time are the main concerns of these protocols
Forwarding methods	Heuristic Method	Wireless Multihop Forwarding	Wireless Multihop Forwarding	Wireless Multihop Forwarding	Wireless Multihop Forwarding	Wireless Multihop Forwarding
Recovery strategy	Carry and Forward	Multihop Forwarding	Carry and Forward	Carry and Forward	Carry and Forward	Flooding
Environment	Urban	Urban	Urban	Highway	Urban	Highway
Realistic traffic flow	√√	√√	XX	√√	XX	√√
Digital map requirement	XX	XX	XX	XX	XX	XX
Virtual equipment requirement	XX	XX	XX	XX	√√	XX

(continued)

Table 3 (continued)

Protocols	Position based	Proactive	Reactive	Broadcast based	Cluster based	Geocast based
Advantages	- Improved Performance in Highway Environment - Reduced Process Overhead	- Discovery of Routing path in prior is not required-low latency in real-time application	- Data Broadcasting on Demand - Beaconless-Notifies the system when link failure is encountered	- Data Assurance I.e.., risk of losing data is very less-minimized overhead	-Scalable to the changing network dimensions	- Improved Congestion Control - Reduced Network overloading - Reliability of data in high dynamic topology
Drawbacks	-Mandatory usage of GPS-Location Server may enter deadlock state any time	- Unnecessary Wastage of bandwidth-unused paths are not separated - Increased Storage complexity with expanding networks	- Excess Flooding resulting In a disruption -high latency in Real-time application	- Consumes more bandwidth - Replicated data is delivered to the node	- Delay induced in a highly dynamic network - Increased work overhead	- Delay in data transmission caused due to network disconnection
Real-time application	Road safety, Traffic Control Management	Wireless sensor Network	Network Traffic Reduction	Weather Forecast, Emergency Alerts	Database formation in ML based implementation	Road safety, Accidents Tracking
Examples	(GPSR) Greedy perimeter stateless routing, Distance routing effect algorithm for mobility (DREAM)	Destination sequenced Distance Vector (DSDV), Topology Broadcast based on reverse path forwarding (TBRPF), Optimized linked State Routing (OLSR)	Dynamic Supply Routing (DSR), Temporally ordered Routing Protocol(TORA), Ad-Hoc On-Demand Distance Vector Routing (AODV)	Distributed Vehicular Broadcast Protocol (DV-CAST), Density aware reliable broadcasting Protocol (DECA), Position aware of the reliable broadcasting protocol (POCA)	Clustering For open inter vehicular communication network (COIN), Location Routing Algorithm with Cluster-Based. Flooding (LORA_CBF)	Inter-Vehicle Geocast Protocol (IVG), Direction Based Geocast Routing protocol (DG-CASTO**R**)

√√-YES XX-NO

Table 4 Comparisons of various routing

Paper	Method used	Description	Challenges faced	Proposed solution
z	Dedicated short range communication (DSRC) (V2V Implementation)	The combination of DSRC and GPS is used as a WIFI-like low cost wireless protocol with 360 ° view of similarly equipped vehicles within a given range MAC and PHY layers are used to strengthen network security	Channel estimation and lack of time diversity in PHY layer. Package collision And Congestion in MAC layer	- DSRC upper layer decoupling to 802.11p PHY / MAC supporting multiple technologies - Upgrading to more advanced PHY technologies such as MIMO (802.11n) support and multiple stream support (802.11ac)
[11]	Cognitive Network Strategy	- Cognitive radio is a completely programmable and configurable intelligent device - Its Transmitter design ensures efficient use of the spectrum of channels. The transmission of data at the end is done using TCP protocols	The direct communication between vehicles by means of single hope may fail due to the high dynamic channel condition and continuous varying speed of vehicles. Spectrum sensing	- The cross-layer design approach is used to tackle spectrum sensing together with access decision, physical layer modulation and coding scheme - The wireless channel and primary use of the network are modeled as a Markov finite state process
[12]	Cooperative Relay and MIMO techniques	- Cooperative Relay is a multi-antenna cooperative, i.e. Multiple input and output, strategy to boost network channel capacities for any given set of bandwidths that exploit user diversity by interpreting the transmitted signal in combination with the direct signal in wireless multi-hop networks	- The highly dynamic changes in network caused multipath fading which are commonly seen in wireless communication - Conflicting trade off among various parameter and run time optimal cooperative node selection	- IEEE 802.11 carrier sense multiple access (CSMA)-based MAC techniques are used to overcome multipath fading

(continued)

Table 4 (continued)

Paper	Method used	Description	Challenges faced	Proposed solution
[3]	Orthogonal frequency division multiplexing under IEEE 802.11p	- IEEE 802.11 is a collection of physical layer (PHY) specification and use Media Access control (MAC) for implementing WLAN in certain Frequency Band .It helps to establish communication among the high speed vehicles, stationary vehicles and infrastructure	- The unstable oscillations of OFDM system are very prone to the Doppler shift and the frequency offset. It's performance can be degraded if orthogonality is ruined due to inter channel interference (ICI) and inter-symbol interference (ISI)	The IEEE 802.11 p along with Long term evaluation (LTE) standards is used in order to overcome the challenges described
[13]	5G LTE-V with Ml	- Machine learning algorithms are implemented in distributive manner by involving each connected vehicle in learning with the local parameters and making a decision for the specific situation of each vehicle - The directionality of mmWave V2X communications is enhanced by analyzing the situation properly leading towards a reasonable example of learning the particular Environment of each connected vehicle	- Fundamental trade in SIMO high mobility communication systems between Doppler diversity and channel estimation errors - Reduced coding gain because of channel estimation errors	- Optimum energy allocation between pilot and data symbols that simultaneously maximizes the order of diversity and minimizes the loss of coding gain for high mobility system and uses imperfect state information on the channel

References

1. Lin X, Lu R, Zhang C, Zhu H, Ho P, Shen X (2008) Security in vehicular ad hoc networks. IEEE Commun Mag 46(4):88–95. https://doi.org/10.1109/MCOM.2008.4481346
2. Tai H, Tran T, Nguyen T, Kazmi SM, Le L, Hong CS, Hanzo L (2019) Next-generation Wireless Solutions for the Smart Factory, Smart Vehicles, the Smart Grid and Smart Cities, 2019 Preprints
3. Kumar V et al (2013) Applications of VANETs: present and future. Commun Network 05:12–15. https://doi.org/10.4236/CN.2013.51B004

4. Tang F, Kawamoto Y, Kato N, Liu J (2020) Future intelligent and secure vehicular network toward 6G: machine-learning approaches. Proc IEEE 108(2):292–307. https://doi.org/10.1109/JPROC.2019.2954595
5. Data communication in VANETs: Protocols, applications and challenges. Ad Hoc Networks 44:90–103, ISSN 1570-8705, https://doi.org/10.1016/j.adhoc.2016.02.017
6. Mahamadu MA, Wu J, Ma Z, Zhou W, Tang Y, Fan P (2018) Fundamental tradeoff between Doppler diversity and channel estimation errors in SIMO high mobility communication systems. IEEE Access 6:21867–21878. https://doi.org/10.1109/ACCESS.2018.2826438
7. Kaur R Cognitive Radio for Vehicular ad-hoc network (CR-VANET): problems and solutions. https://doi.org/10.13140/RG.2.2.18108.08325
8. Yang F, Wang S, Li J, Liu Z, Sun Q (2014) An overview of internet of vehicles. China Commun 11(10):1–15. https://doi.org/10.1109/CC.2014.6969789
9. Azees M, Jegatha VP, Deborah L (2016) Comprehensive survey on security services in vehicular ad-hoc networks. IET Intell Transp Syst 10(6):379–388. https://doi.org/10.1049/iet-its.2015.0072
10. Hasrouny H, Samhat AE, Bassil C, Laouiti A VANet security challenges and solutions: A survey
11. Ahmed E, Gharavi H (2018) Cooperative vehicular networking: a survey. IEEE Trans Intell Transp Syst 19(3):996–1014. https://doi.org/10.1109/TITS.2018.2795381
12. Chen W, He R, Matolak DW, Tellambura C, Sheng Z (2018) IEEE access special section editorial: high mobility 5G LTE-V: challenges and solutions. IEEE Access 6:40221–40225. https://doi.org/10.1109/ACCESS.2018.2855266
13. Lim K, Manivannan D (2016) An efficient protocol for authenticated and secure message delivery in vehicular ad hoc networks. Veh Commun 4:30–37. ISSN 2214-2096. https://doi.org/10.1016/j.vehcom.2016.03.001
14. Amadeo M, Campolo C, Molinaro A (2012) Enhancing IEEE 802.11p/WAVE to provide infotainment applications in VANETs. Ad Hoc Netw 10(2):253–269
15. Arul Jothy MK, Murugesan D (2016) An enhanced self-scheduled access control in vehicular ad hoc networks (VANET). In: 2016 international conference on information communication and embedded systems (ICICES), Chennai, pp 1–5. https://doi.org/10.1109/ICICES.2016.7518908
16. Cunha F et al (2016) Data communication in VANETs: protocols, applications and challenges. Ad Hoc Netw 44:90–103
17. Sumayya PA, Shefeena PS (2015) VANET based vehicle tracking module for safe and efficient road transportation system. In: Procedia Comput Sci 46:1173–1180. ISSN 1877-0509. https://doi.org/10.1016/j.procs.2015.01.030
18. Liu L et al (2019) A secure and efficient group key agreement scheme for VANET. Sensors (Basel, Switzerland) 19(3):482. https://doi.org/10.3390/s19030482
19. Ghori R, Zamli KZ, Quosthoni N, Hisyam M, Montaser M (2018) Vehicular ad-hoc network (VANET): review. In: 2018 IEEE international conference on innovative research and development (ICIRD), Bangkok, pp 1–6. https://doi.org/10.1109/ICIRD.2018.8376311
20. Dharaskar B, Dharaskar R, Thakare VM (2018) A review on security in vehicular network. https://doi.org/10.13140/RG.2.2.16091.05923
21. Kim H, Wymeersch H, Garcia N, Seco-Granados G, Kim S (2018) 5G mmWave vehicular tracking. In: 2018 52nd Asilomar conference on signals, systems, and computers, Pacific Grove, pp 541–547. https://doi.org/10.1109/ACSSC.2018.8645553
22. Vehicular Communications (2017) 7:7–20, ISSN 2214-2096. https://doi.org/10.1016/j.vehcom.2017.01.002
23. http://www.sciencedirect.com/science/article/pii/S2214209616301231
24. Karimireddy T, Bakshi AGA (2016) A hybrid security framework for the vehicular communications in VANET. In: 2016 international conference on wireless communications, signal processing and networking (WiSPNET), Chennai, pp 1929–1934. https://doi.org/10.1109/WiSPNET.2016.7566479

25. Dixit M, Kumar R, Sagar AK (2016) VANET: Architectures, research issues, routing protocols, and its applications. In: 2016 international conference on computing, communication and automation (ICCCA), Noida, pp 555–561. https://doi.org/10.1109/CCAA.2016.7813782
26. Barskar R, Ahirwar M, Vishwakarma R (2016) Secure key management in vehicular ad-hoc network: a review. In: 2016 international conference on signal processing, communication, power and embedded system (SCOPES), Paralakhemundi, pp 1688–1694. https://doi.org/10.1109/SCOPES.2016.7955730
27. Al-Sultan S, Al-Doori MM, Al-Bayatti AH, Zedan H (2014) A comprehensive survey on vehicular AdHoc network, Elsevier, p 380392P23. https://doi.org/10.1155/2019/2423915

Beam Forming Impact on the Next Generation Wi-Fi IEEE802.11ay in mm Wave Frequency Band

Prem Chand Jain, Nallapalem Neeraj Srinivas, and Yasaswini Vellisetty

Abstract The next generation Wireless Local area network IEEE802.11ay (Wi-Fi) is an enhancement of 802.11ad in unlicensed 60 GHz mm Wave frequency band. The millimeter (mm) Wave frequency band 6–100 GHz range provides more BW to achieve higher data rate but it supports only 50 to 200 m short range. The 802.11ay leverages the latest development in MIMO (Multi-input multi-output antennas), channel bonding, and enhanced beam formation to minimize spectral efficiency and provide better quality of service for large number of user stations. This upgrade offers significant speed and range improvements. Beam forming technology has been introduced in 60 GHz mm wave frequency band to compensate high path losses, and oxygen absorbing some mm wave frequencies signal. Beam formation can be effectively utilized in mm wave frequency band. It aims to generate different beams for different user stations using an array of antennas elements at the Access Point (AP) to communicate between different user stations. The effective beams undergo minimum power loss and co-channel interferences, and are aimed to direct towards the user station. In this paper we have simulated different types of arrays and analyzed different beam contours that are generated from the arrays of antennas to transmit to the user station.

Keywords 802.11ay · Antenna · Array · Beam formation · Beam shape · Directivity · Millimeter wave

P. C. Jain (✉) · N. N. Srinivas · Y. Vellisetty
Electrical Engineering Department, School of Engineering, Shiv Nadar University, Greater Noida (UP), India
e-mail: Premchand.jain@snu.edu.in

N. N. Srinivas
e-mail: ns620@snu.edu.in

Y. Vellisetty
e-mail: yv294@snu.edu.in

M. Tiwari et al. (eds.), *Optical and Wireless Technologies*, Lecture Notes in Electrical Engineering 892, https://doi.org/10.1007/978-981-19-1645-8_12

1 Introduction

The IEEE802.11ad wireless local area network (WLAN) introduced in 2012 for high data rates of 6.75 Gbps in the unlicensed 60 GHz frequency band for short transmission range. It could not provide required very high data rates and transmission range for current applications like 4k/8k resolution display, Augmented Reality (AR)/Virtual reality (VR) used in 5G mobile communication. The next generation 802.11ay also operating at 60 GHz frequency band introduced to achieve very high data rates of the order of 100 Gbps and transmission range of 300–500 m through multiple data streams and high channel BW. In place of 2.16 GHz BW used in 802.11ad it has been enhanced to 8.64 GHz BW in 802.11ay which is obtained through four channel bonding each having 2.16 GHz BW. The 802.11ay is intended to replace Ethernet (Wired Local area network IEEE802.3), integrate AR/VR headsets and glasses, Vehicle to others (V2X) communication, and to transmit large data between cloud and mobile devices very quickly. It can also connect to base station (BS) to core network in cellular communication. In 5G, cost effective small cells are connected with Macro cell (Hetnet) to extend coverage in crowded environments. Densification of small cells produces massive backhaul traffic in the core network. Employing fiber cable in dense small cell for backhaul results in a drastically increase in cost and difficulties in implementing. Wireless backhaul using 802.11ay can offer a scalable and cost effective solution. The mm wave frequency band 28, 60 GHz (unlicensed) can provide multi-Gigbit transmission and can solve problem of the backhaul in 5G.

In a few years, Beam formation is moved out from research environment into commercial deployment, first in 4G-LTE and 5G networks, and now in IEEE802.11ay deployments. The 802.11ay vision relies on a successful roll out of mm Wave frequency technology. The 60 GHz mm wave frequency band suffers heavy path loss, do not propagate well through obstacles such as walls, and oxygen absorption (15 dB per km at 60 GHz). To compensate the path loss high gain antenna elements are required. These antenna elements with input RF signal create narrow beam signal focused in a very specialized direction. This approach strengthens the signal and reduces co-channel interference from other user's signal. The increased SNR due to the beam formation increases range for both outdoor and indoor coverage. A large number of radiating antenna elements are required to generate very narrow beam to transmit all available power in certain direction instead of wasting power in many directions. Each antenna element is fed with same RF signal but phase and magnitude of signal fed to each antenna element is precisely adjusted. It needs full control of magnitude and phase of signal received by each antenna element. The phase and magnitude of antenna element's signal is controlled digitally in nsec. time period to achieve faster beam steering of the required beam. A large number of active antenna elements in two-dimension (2-D) grid at Access Point (AP) can support 3D-beam forming algorithm which exploits the elevation and azimuth dimensions. It creates highly directional beams that can be redirected to specific location or device.

2 Related Work

Reference [1] describes design of IEEE802.11ay using MIMO, channel bonding, and enhanced beam formation. Impact of mm wave radio propagation in 802.11ay design has also been discussed. Ref. [2] discussed mm wave cost effective 5G backhauling considering hybrid beam forming, full duplexing, routing, special reuse scheduling. Ref. [3] focuses 5G era in which shift towards network efficiency with 5G systems is based on dense HetNet architecture. However, HetNet incorporate set of frequency bands including macro cells in licensed band (LTE) and small cells in unlicensed bands (Wi-Fi). New higher frequency band (mm wave) may be deployed in small cell to enable ultrahigh data rate services. Ref. [4] discussed key elements incorporated in IEEE802.11ay including scheduling, beam formation, link maintenance that supports fixed wireless access networks. Ref. [5] stated that IEEE802.11ay can achieve 176 Gbps data rate by using 8.64 GHz total BW. YouTube videos [6] and [7] is helpful to understand basics of antennas and beam forming, and Ref. [8] in understanding and implementing the beam management.

3 Methodology

High gain antennas are required to compensate the path loss in mm wave frequency band. The most efficient way to achieve larger gains is by using an array of antenna elements. An array of antenna elements with half wavelength spacing provides maximum directivity. Antenna gain is directly related with directivity. This can be expressed as an antenna gain (dB) equal to $10\log_{10} N$, where N is number of antenna elements. Doubling N doubles the gain to 3 dB with half power beam-width to 32°, quadruple the N, the gain increased to 6 dB with 15° half power beam-width [9]. Antenna arrays consists of two or more antennas where the gain of all these antennas are combined for an increased and better performance. In-phase signals strength adds constructively, while out of phase signal strengths decreases destructively. The antenna arrays also help in generating different kinds of beams, which is being analyzed for the uniform linear arrays (ULA) and uniform rectangular arrays (URA) in this paper. By controlling the phase and amplitude of RF signal fed to each antenna element, it is possible to dynamically shape the beam. It can alter the beam shape and direction as well. The aim is to increase the directivity and hence to reduce the path losses. Beams formed by the antenna arrays can be directed towards the user station.

3.1 Uniform Linear Array

In a uniform linear array (ULA), the array elements are uniformly spaced along a straight line. There should be minimum two elements to form an array. The uniform array is formed by using identical antenna elements with equal RF signal magnitudes and with a progressive phase. The elements of the antenna are arranged in linear pattern like a matrix of N × 1 (horizontal direction) or 1 × N (vertical direction) and they are uniformly spaced from each other. The minimum number of such antenna elements could be 2 × 1 or 1 × 2. The different shapes of the beams can be obtained from these arrays by varying the factors like the spacing of the elements, distance between the elements of antenna, the number of antenna elements, the geometry of the elements of the array, and the phase of the signal in each antenna element. In a uniform linear array, the antenna elements are fed with a RF signal of equal amplitude and equal phase shift between the elements. The RF signal of any antenna array can be concentrated in any arbitrary direction by changing the phase of each antenna element. This type of antenna array is called Phased array antenna. This kind of increased directivity helps in increasing the range and reducing the interference. By using the phased array techniques in this paper we observed that the power density of the beam is not uniformly distributed. The shift in beam pattern is observed by applying individual antenna phase shifts from –90 to 90°. The shape of the beam formed resulted into main lobe which helps to transmit most of the RF signal, and the side lobes which disperse the radiated power away from the main lobe.

3.2 Uniform Rectangular Array

The array elements are distributed in a y-z plane with the beam direction along the positive x-axis. The spacing between the elements are uniform for uniform rectangular array (URA). The elements of the antenna are arranged in a matrix of M × N and they are uniformly spaced from each other. We have observed different shapes of the beam of URA arrays by varying the factors like the spacing of the elements, distance between the elements of antenna, the number of antenna elements, the geometric arrangement of the elements of the array, values of M and N, and the phase of each antenna element. The number of rows (M) and columns (N) may be equal in order to form a perfect main lobe. If the M and N are not equal then depending on the value of M and N, one can observe flat beams in the x- and y-direction. All the antenna array responses are simulated and plotted using MATLAB. We have compared directivity and power level of various beams formed. Directivity is the measure of the concentration of an antenna's radiation pattern in a particular direction. Directivity is a function of the radiation pattern of the antenna where it is assumed that all the power applied to the antenna array is radiated in a particular direction. As the concentration of the signal increases, the directivity of the beam radiated is also increases. Antenna gain is the product of antenna efficiency and directivity. It is expressed in decibels (dB).

Uniform Rectangular Array is better for transmitting the beam to the user station and these arrays are used widely in the 802.11ay, which operates in mm Wave frequency band around 60 GHz. In this frequency range the signals are blocked by different obstacles which results in poor coverage and reduced data speeds for both uplink and downlink.

4 Results

The simulation of uniform linear array (ULA) with 2D-Polar and Magnitude plots, and uniform rectangular array (URA) with 3D-Power and magnitude plots have been carried out using MATLAB.

4.1 2D-Simulation of ULA

The 2D-polar plots and the 2D-magnitude plots for different array elements with different sizes of antennas are observed. The main lobe of the two-dimensional polar plot is shown in Fig. 1. It shows 2D-Polar plot for 4 linear antennas and 8 linear antennas with different steering angles [–90 to 90] degree. Beam-width is wider with 4 antenna elements and getting narrow down with 8 elements which effectively increases the range as we increase the number of antennas elements. Beam-width is getting wider at different steering angles (0 to 90 and –90°).

From the 2D-magnitude plot in Fig 2, one can observe the transmission beams with different steering angles. Here also it is observed that as the antenna elements are increasing, the beam width is decreasing and hence the range of the beam is increasing. Beam-width is getting wider here as well with different steering angles.

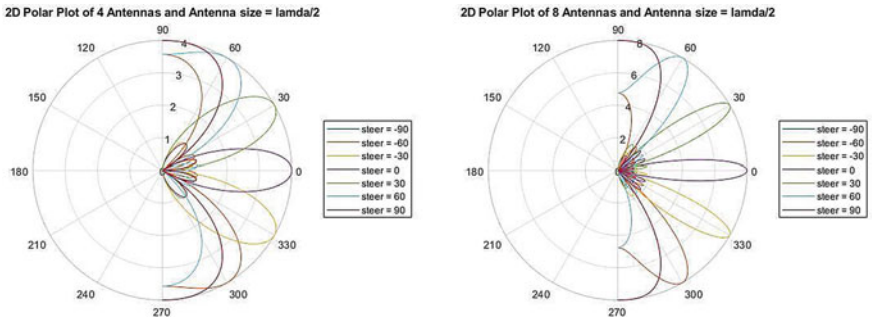

Fig. 1 2D-Polar plot for the 4 and 8 antennas when the patches are phased to direct the main beam toward (0, 30, 60, 90, –30, –60, –90°)

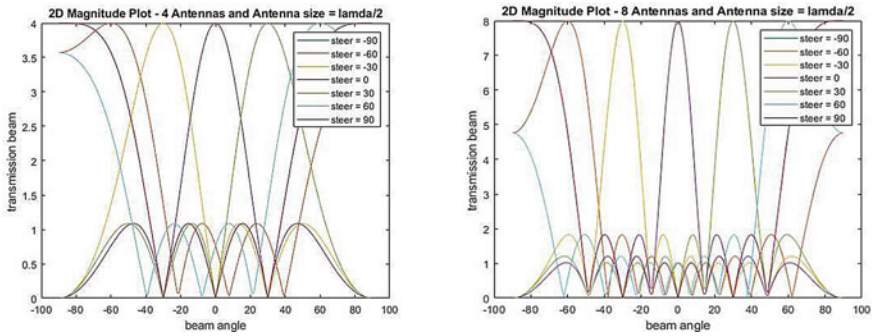

Fig. 2 2D-Magnitude plot for the 4 and 8 antennas when the patches are phased to direct the main beam toward (0, 30, 60, 90, –30, –60, –90°)

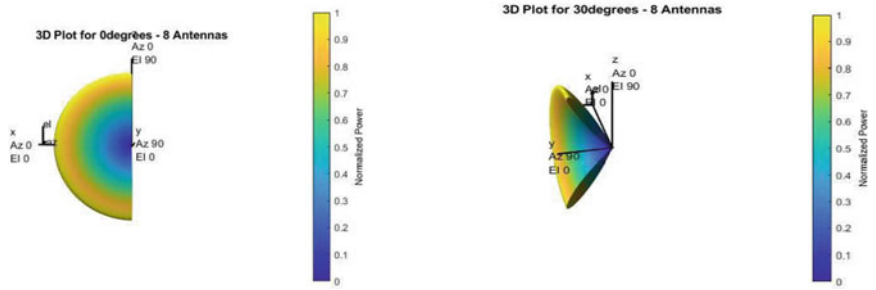

Fig. 3 3D-Power plot for the 8 antennas when the patches are phased to direct the main beam toward (0, 30°)

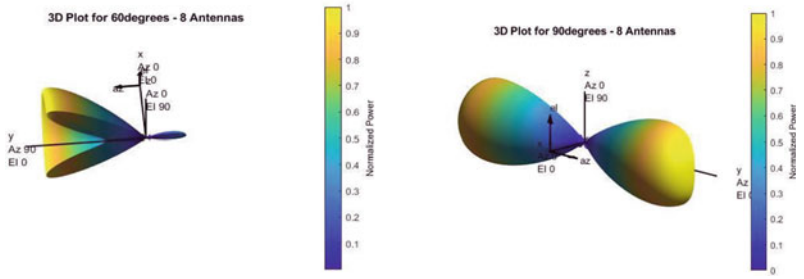

Fig. 4 3D-Power plot for the 8 antennas when the patches are phased to direct the main beam toward (60, 90°)

4.2 3D–Simulation of ULA

From Figs. 3, 4 and 5 it can be seen that the maximum amount of normalized power is represented by yellow color of the 3D-plot, and blue color represents the minimum

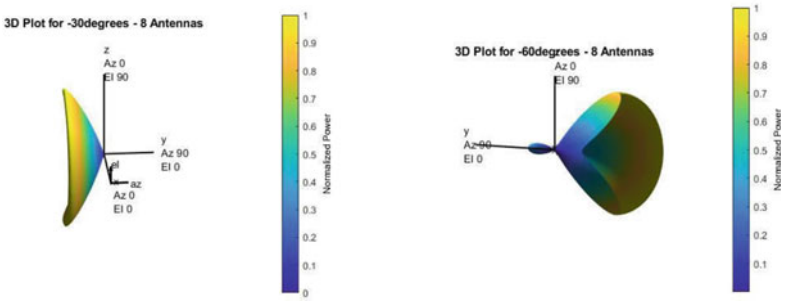

Fig. 5 3D-Power plot for the 8 antennas when the patches are phased to direct the main beam toward (30, –60°)

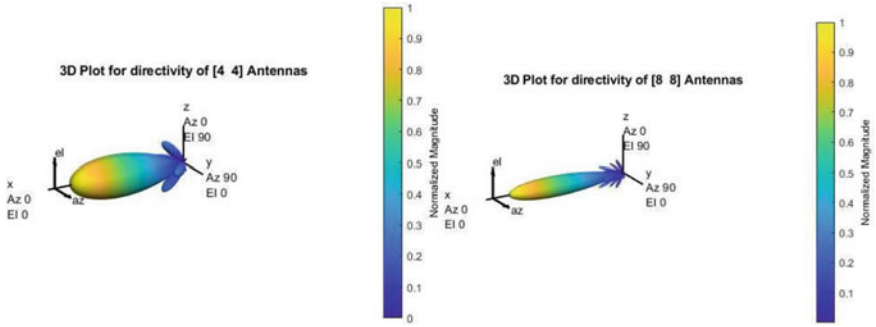

Fig. 6 3D-Magnitude plot for the 4 × 4 array and 8 × 8 array when the patches are phased to direct the main beam toward (0°)

normalized power. The shapes of the transmitted beams in 3D-plot are inappropriate for the user device. If we direct this beam to user device, it leads to a total wastage of Power in mm Wave frequency band because the beam formation is not directional as shown in Figs. 3, 4 and 5. Figures 3, 4 and 5 also show the plots for different steering angles.

4.3 3D-Simulation of URA

Beam formation using uniform rectangular array has been implemented to obtain 3D-plots considering directivity of the beam and the power of the beam. Depending on the value of M and N in the matrix M × N, one can observe different beam shapes. If the M and N are equal, one can observe a minimum number of side-lobes with a desired main lobe directed to the user station. Directivity and Power patterns shown in Figs. 6 and 7 are the normalized 3D-Plots. The range is normalized with absolute

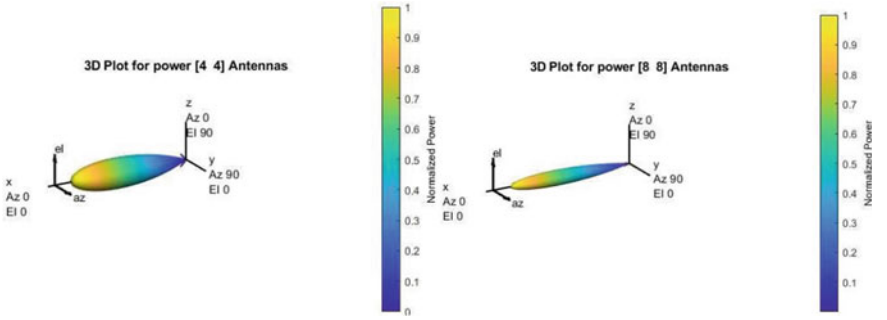

Fig. 7 3D-Power plot for the 4 × 4 array and 8 × 8 array when the patches are phased to direct the main beam toward (0°)

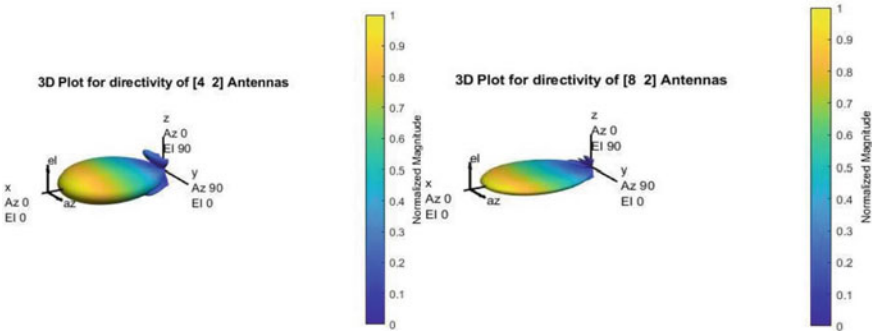

Fig. 8 3D-Magnitude plot for the 4 × 2 array and 8 × 2 array when the patches are phased to direct the main beam toward (0°)

distances. The range and the power of the different antenna arrays are simulated and represented by different colors for good visualization. Figures 6 and 7 show the 3D-Magnitude and Power plots for 4 × 4 and 8 × 8 rectangular antenna arrays. As the number of antennas elements increases, one can observe more directivity and hence more range. The Pattern function from MATLAB is used for simulation. It generates a normalized graph by giving the transmitted beam range, power, and directivity.

If the value of M and N in the M × N rectangular array are different, then we observe that the main lobe has flattened with respect to a smaller number of antennas. If we increase the number of antenna elements in M by fixing the N, we observe further flatness in the beam. Using this type of array, we can reduce the transmitted power of beam and range by changing the M and N antenna elements according to the requirement of the user station. Simulation for normalized 3D-Magnitude plots were carried out and represented by different colors (yellow with maximum magnitude and blue with minimum magnitude). Figure 8 shows the flatness of the beam for 4 × 2 and 8 × 2 rectangular array. One can see that the flatness is more with 8 × 2 array compared to 4 × 2 array.

5 Conclusions

In this paper important features of IEEE802.11ay are discussed, and studied how the beam formation at mm wave frequency band can reduce the path loss and co-channel interferences? Different phased arrays in space to implement, and different beam shapes using different kinds of antenna arrays studied, and then analyzed, and molded according to the requirements of the desired user station. The uniform linear and rectangular arrays have been simulated, and analyzed different contours of beams generated by the different array of antennas to be transmitted to the user station, and found that the effective beams undergo minimum path loss and co-channel interferences. In future the mm Wave beam forming can be extended to connect integrated access and backhaul (IAB) for large number of small cells deployment in 5G without using optical fiber cables.

Acknowledgements The authors are very much thankful to Dr. Jitendra Prajapati, EE Dept. to help in the simulation using MATLAB. The authors are also grateful to Prof. Dinkar Prasad, Head, EE Dept., and Associate Dean, School of Engineering, for providing necessary resources and infrastructure to complete this project, and to Prof. S. Sen, Dean, School of Engg., Shiv Nadar University, G. Noida (UP) for their encouragement, and permission to publish this paper.

References

1. Ghasempour Y, Claudio RCMS, Cordeiro C, Knightly EW (2017) IEEE802.11ay: next generation 60 GHz communication for 100 Gbps Wi Fi. IEEE Commun Mag 55:186–192
2. Feng W, Li Y et al (2016) Millimetre-wave backhaul for 5G networks: challenges and solutions. Sensors 16(892):1–17
3. Bangerter B, Talwar S, Arefi R, Stewart K (2014) Networks and devices for the 5G era. IEEE Commun Mag 52:90–96
4. Cheng C, Kendem O, Claudio RCMS, Cordeiro C (2019) Millimeter-wave fixed wireless access using IEEE802.11ay. IEEE Commun Mag 57:98–104
5. Wolfgong W (2019) WLAN 802.11ay: up to 176 Gbps over the air. Rodhey and Schwartz Wireless News, 221/19, pp 26–27
6. Use of mm Wavelengths and Beam Forming with 5G. https://www.youtube.com/watch?v=6li8CZmrg84
7. Basics of Antennas and Beam-forming - Massive MIMO Networks. https://www.youtube.com/watch?v=xGkyZw98Tug
8. 5G/NR beam Management. https://www.sharetechnote.com/html/5G/5G_Phy_BeamManagement.html
9. Hamady MN (2020) Beam formers explained, Commscope, WP-114491-EN(06/00)

Superstrate Microstrip Antenna for 5G Wireless Communication Applications

Amit Patel, Hiren Mewada, Alpesh Vala, Sagar Patel, Dharmendra Chauhan, and Palak Patel

Abstract In today's era, the coexistence of human-centric and machine-type applications will lead to a large diversity of communication characteristics. Some of these applications can be supported by today's mobile broadband networks and their future evolution. However, some other applications will impose additional and very diverse requirements on mobile and wireless communication systems that the fifth generation (5G) will have to support various requirements for different stakeholder like 5G new radio technology. This paper contributes the design of planar superstrate antenna for 5G NR frequency bands (b41/n41) for USA, China and South Korea as well as sub-millimeter wave application. The proposed antenna is resonated at three resonant frequencies 2.5, 5.2, and 7.08 GHz respectively and provides more than 500 MHz bandwidth. Moreover, the antenna is designed on Fr4 substrate material having a dielectric constant 4.4 and loss tangent, which is very cost effective. The achieved gain and radiation efficiency for the proposed antenna are more than 2 dB and 85% respectively. The total volume occupied by the antenna is 28 × 26 × 1.6 mm. The simulation has been carried out using Computer simulation Technology (CST) software.

1 Introduction

The wireless sector has grown at a breakneck pace over the last few years, both in terms of mobile technology and customer base. Mobile wireless technologies have gone through four or five generations of technological revolution and evolution, starting with the 0G network and progressing to the 4G network. Furthermore Communication over wireless channel is challenging [1, 2] because of several factors,

A. Patel (✉) · A. Vala · S. Patel · D. Chauhan · P. Patel
V. T. Patel Department of Electronics and Communication Engineering, Chandubhai S Patel Institute of Technology, Charotar University of Science and Technology, Changa, Anand, Gujarat, India
e-mail: amitvpatel.ec@charusat.ac.in

H. Mewada
Prince Mohammd Bin Fahad University, Al Khorba, Saudi Arabia

M. Tiwari et al. (eds.), *Optical and Wireless Technologies*, Lecture Notes in Electrical Engineering 892, https://doi.org/10.1007/978-981-19-1645-8_13

channel fading, limitation of power resources especially on the mobile terminals, spectrum availability etc. One of the available technologies to overcome the challenges and fulfil the demands is multiple input multiple output (MIMO) system i.e. the use of multiple antennas at both the transmitter and the receiver. Now a day multiuser concepts are used in MIMO systems [3] called Massive MIMO to increases the radio coverage of the system. Massive MIMO antenna system is also one of the fundamental technologies in the next 5G (fifth generation) networks [4].

Now a day's, 5G NR will play an important role in the modern era of communications, which promises ubiquitous connectivity as well as ultra-reliable and low-latency transmissions. Furthermore reliable communications are fundamental requirements for today's wireless applications like 5G NR. Different countries have already proposed their 5G NR bands like USA and China b41/n41 (2.5/2.6 GHz) and for South Korea 2.3–2.39 GHz.

Many planar antennas have been proposed for 5G wireless communication applications [6–10]. However, to achieve better performance in terms of either gain or bandwidth, they have to compromise with other parameter. Here, we have taken up the challenge to design a multilayer planar antenna, which gives a better gain and bandwidth without increasing the volume of the structure.

In the proposed design, it contains two layers of Fr4 substrate in which the first layer is consists of monopole antenna at top layer and defected ground structure. The second layer consists of circular patch antenna. The overall structure of the proposed antenna is compact and support three resonant frequencies 2.5, 5.2 and 7.08 GHz, respectively.

2 Design

Multilayer antenna concept for the wireless applications is designed and fabricated here. The top view of the structure is shown in Fig. 1a. The proposed antenna has a square geometry of 30 mm, and a 0.035 mm copper layer. It is designed and printed on 1.6 mm thickness substrate of FR4 having a dielectric constant 4.4 and

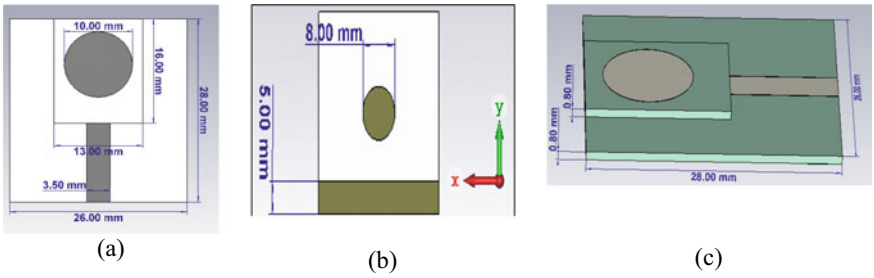

(a) (b) (c)

Fig. 1 **a** Top view of the proposed antenna, **b** Back view of the proposed antenna, **c** perspective view

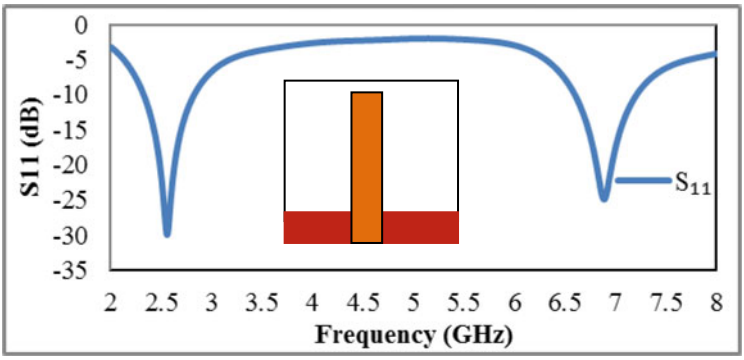

Fig. 2 Return loss of the proposed antenna contains monopole feed and coplanar ground

loss tangent. The antenna is driving by a printed monopole proximity feed and two circular patches. One circular patch is printed on the bottom layer of FR4 and second on the top layer of another FR4 (the superstrate). Coplanar ground plane has been proposed as shown in Fig. 1b, whose height and width are 5 and 30 mm, respectively. 3D perspective view (side) of the proposed antenna is shown in Fig. 1c.

The important aim of the proposed antenna is resonant at two different modes by inserting the circular patches. For the simulation of the proposed antenna, we have used Computer Simulation Technology (CST) software. Initially, a simulation has been carried out for coplanar ground plane and monopole feed and it is shown in Fig. 2. The structure has been resonates at two different frequencies: (i) 2.56 GHz and (ii) 6.89 GHz. Both frequencies having a –10 dB bandwidth are 550 MHz (2.32 to 2.82 GHz) and 610 MHz (6.59 to 7.20 GHz), respectively.

We have introduced the small circular patch having a diameter of 4 mm at the center of ground plane and superstrate (FR4 material) with a diameter of 10 mm circular patch. It creates the capacitive effects and reduces the second resonant frequency from 6.89 to 6.2 GHz while reducing the –10 dB bandwidth. It is shown in Fig. 3. It is resonates at 2.52 and 6.2 GHz frequencies. However, shifting of resonant frequencies reduces the operating bandwidth.

To improve the operating bandwidth without compromise of the first resonant frequency, the Chris-cross patch has been introduced on the ground plane as shown in Fig. 4. The Chris-cross patch has been optimized in such a manner that it resonates at 2.5 and 5.2 GHz as shown in Fig. 5. It has a –10 dB bandwidth of 300 MHz (2.38 to 2.68 GHz) and 150 MHz (5.18 to 5.33 GHz), respectively.

Another alternate to increase the –10 dB bandwidth is to use substrate having a wider thickness. The comparison of return loss with different thickness of substrate is shown in Fig. 6. It indicates that while increasing the thickness of substrate from 0.8 to 1.6 mm return loss is improved from 15 to 25 dB and –10 dB bandwidth becomes wider (approximately 1000 MHz). The current density on the proposed antenna is shown in Fig. 7. The 3D gain plots of the proposed antenna at both the resonant frequencies (2.5 and 5.2 GHz) are shown in Figs. 8 and 9, respectively. It

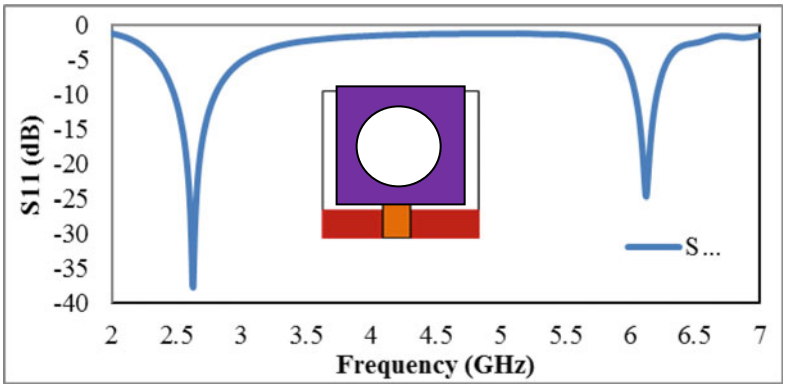

Fig. 3 Return loss of the proposed antenna contains circular path in the ground

Fig. 4 The Chris-cross patch on the ground

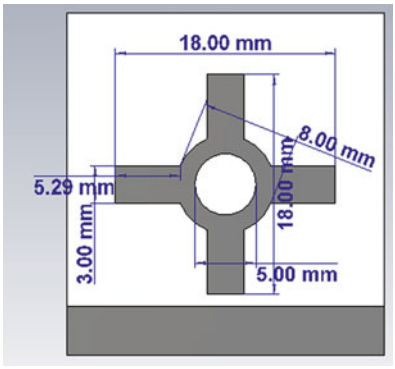

Fig. 5 Return loss with Chris-cross patch on the ground plane

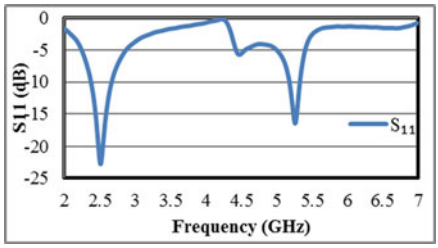

Fig. 6 Return loss with different dielectric thickness

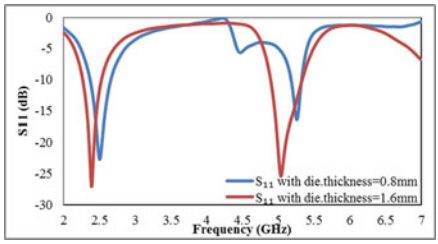

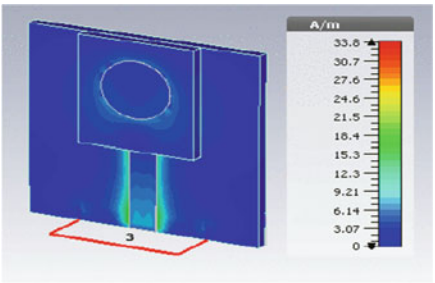

Fig. 7 The current distribution on the proposed antenna

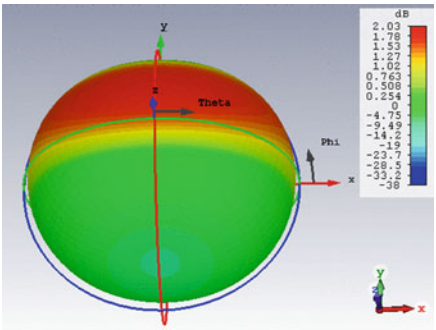

Fig. 8 Gain at 2.5 GHz

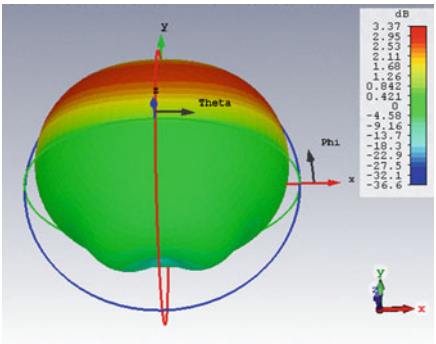

Fig. 9 Gain at 5.2 GHz

gives gain value 2.03 and 3.37 dB at 2.5 and 5.2 GHz, respectively. The gain value can be increased by increasing the physical area of the structure.

The voltage standing wave ratio (VSWR) of the proposed antenna is 1.13 and 1.15 at 2.5 and 5.2 GHz, respectively. It is shown in Fig. 10. The total efficiency is more than 85% at both the resonant frequencies, which is shown in Fig. 11. We have created another modification in the proposed antenna is introduction of an oval slot in top patch which narrow down the second resonant frequency for frequency selective operation. It is shown in Fig. 12. Figure 13 gives the return loss of the proposed antenna with an oval slot on the top of the patch which reduces the –10 dB

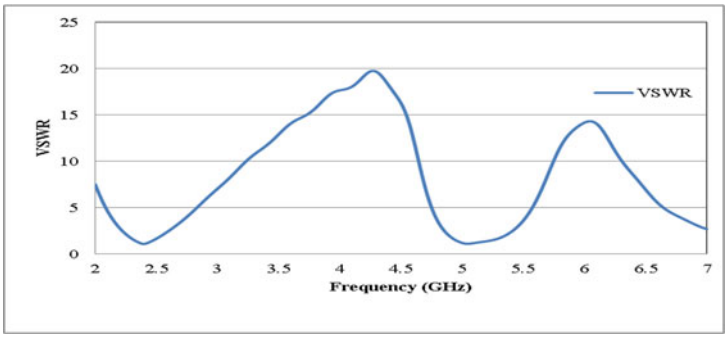

Fig. 10 VSWR of the proposed antenna

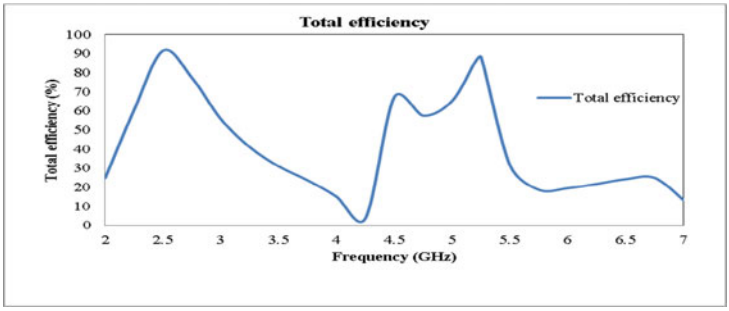

Fig. 11 Total efficiency of the proposed antenna

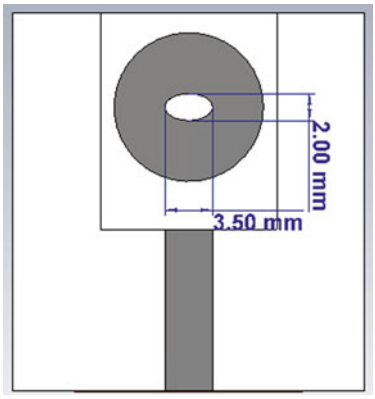

Fig. 12 Defect (oval shaped) on top patch

bandwidth at the second resonant frequency as well as resonated at 3rd resonant frequency at 7.06 GHz. Moreover, to prove the superiority of the proposed design, we have compared the design with other models interms of various parameters as shown in Table 1.

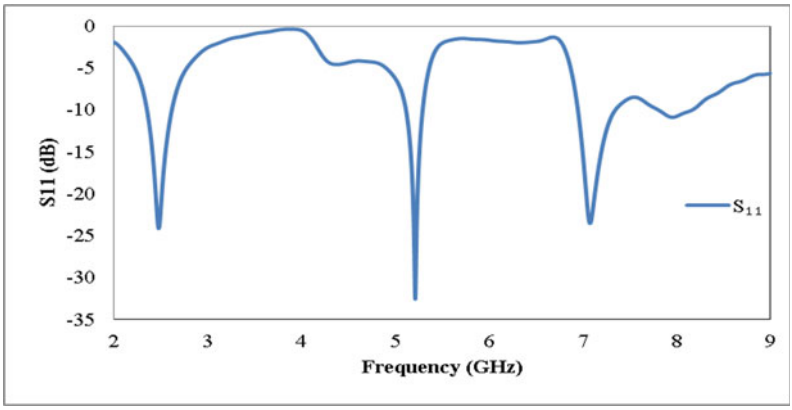

Fig. 13 Tri-band response by modifying oval slot in the proposed antenna

Table 1 Proposed antenna vs. other models

Reference	Resonant frequency (GHz)	– 10 dB Bandwidth (MHz)	Gain (dB)	Efficiency (%)	Physical dimensions (mm^3)
[7]	2.42, 5.22, 5.92	<100	1.72, 7.86, 6.97	–	55.5 × 42.75 × 1.5
[10]	1.8, 5.2, 7	>300	1.83, 0.73, 3.6	97, 90, 77	30 × 20 × 1.52
[11]	1.5, 2.43, 2.86	>200	>1	–	78.6 × 8.4 × 1.6
[12]	2.38, 1.53	>200	0.78, 2.5	–	110 × 65 × 1.6
[13]	5.775	>100	2.54	–	24.7 × 20.8 × 1.6
This work	2.5, 5.2, 7.08	>500	2.03, 3.37, 3	91, 87, 88	28 × 26 × 1.6

3 Conclusion

This paper proposed the superstrate patch antenna for wireless communication applications, which resonates at 2.5, 5.2 and 7.08 GHz frequencies. The proposed antenna is design of FR4 substrate having total volume of 28 × 26 × 1.6 mm. The performances of the proposed antenna have been compared with the other already proposed antenna in terms of resonant frequencies, bandwidth, gain, efficiency and physical dimensions, which proves the superiority of the design.

Acknowledgements This work is sponsored under the CHARUSAT Seed Research Grant scheme. Authors would like to thank CHARUSAT University for providing simulation and testing facilities to carry out this research.

References

1. Patel SB, Bhalani J, Trivedi YN (2020) Performance of full rate non orthogonal STBC in spatially correlated MIMO systems. Radioelectron Commun Syst 63(2):88–95. https://doi.org/10.20535/S0021347020020041
2. Patel S, Bhalani J (2018) Near optimal receive antenna selection scheme for MIMO system under spatially correlated channel. Int J Electr Comput Eng 8(5):3732–3739. https://doi.org/10.11591/ijece.v8i5.pp3732-3739
3. Vannithamby R, Talwar S (2017) Massive MIMO communications. In: Towards 5G: Applications, Requirements and Candidate Technologies, pp 342–364. Wiley. https://doi.org/10.1002/9781118979846.ch15
4. Chataut R, Akl R (2020) Massive MIMO systems for 5G and beyond networks—overview, recent trends, challenges, and future research direction. Sensors 20(10):2753. https://doi.org/10.3390/s20102753
5. Hamad EKI, Abdelaziz A (2019) Metamaterial superstrate microstrip patch antenna for 5G wireless communication based on the theory of characteristic modes. J Electr Eng 70(3):187–197. https://doi.org/10.2478/jee-2019-0027
6. Patel A, Vala A, Goswami R, Mahant K (2017) SIW based wideband horn antenna. IOP Conf Ser Mater Sci Eng 225(1):012263
7. Refaat SM, Abdalaziz A, Hamad EK (2021) Tri-band slot-loaded microstrip antenna for internet of things applications. Adv Electromagn 10(1):21–28. https://doi.org/10.7716/aem.v10i1.1514
8. Kachhia J, Patel A, Vala A, Patel R, Mahant K (2015) Logarithmic slots antennas using substrate integrated waveguide. Int J Microw Sci Technol. https://doi.org/10.1155/2015/629797
9. Patel A, Vala A, Goswami R, Mahant K (2016) Square loop slots loaded substrate integrated waveguide based horn antenna. Microw Opt Technol Lett 58(7):1577–1582. https://doi.org/10.1002/mop.29857
10. Kumar P, Ghivela GC, Sengupta J (2018) Design and analysis of multiple bands spider web shaped circular patch antenna for IoT application. In: 2018 8th IEEE India international conference on power electronics (IICPE), pp 1–5, 13–15 December 2018. https://doi.org/10.1109/IICPE.2018.8709444
11. Munir A, Soba J (2015) Multiband printed antenna composed of an array of split ring resonator. In: 2015 European radar conference (EuRAD), Paris, France, 9–11 September 2015. https://doi.org/10.1109/EuMC.2015.7346036
12. Satheesh A, Chandrababu R, Rao IS (2017) A compact antenna for IoT application. In: 2017 international conference on innovations in information, embedded and communication systems (ICIIECS), Coimbatore, India, 17–18 March 2017. https://doi.org/10.1109/ICIIECS.2017.8275921
13. Elijah AA, Mokayef M (2020) Miniature microstrip antenna for IoT application. Mater Today Proc 29(1):43–47. https://doi.org/10.1016/j.matpr.2020.05.678

Evolution of TDM-PON to WDM-PON Using Downstream MSK and Remodulated Upstream ASK

Debanjan Sarkar, Sanjeev Kumar Metya, Subramanyam Nagaraj, and P. K. Anand Prem

Abstract Here, a migration scheme from legacy Time Division Multiplexed Passive Optical Network to the next generation Wavelength Division Multiplexed Passive Optical Network is studied and analyzed with Minimum shift keying (MSK) modulation for WDM-PON downstream signal. Without changing the existing infrastructure of TDM-PON, WDM-PON is incorporated. The combined TDM and WDM downstream signals in central office (CO) are passed through a 30 km Single mode fiber (SMF) without dispersion compensation and detected at respective ONUs after separating wavelengths from each other. In WDM-PON, downstream signal is reused to modulate the upstream signal. Performance analysis of legacy TDM-PON and co-existing TDM-PON are compared on the basis of Bit Error Rate (BER) and eye diagrams.

Keywords Bit error rate (BER) · Minimum shift keying (MSK) · TDM-PON · WDM-PON

1 Introduction

Demands of additional services by users in the existing network infrastructure are increasing day by day. In this regard, passive optical network (PON) is the most favorable access network. The system has been widely deployed due to its high performance, low cost and fulfillment of user bandwidth on demand. Time division multiplexed Passive optical network (TDM-PON) is one of them. In TDM-PON the bandwidth and hardware located in the central office (CO) are shared by all the users. Thus, network cost is reduced by compromising the bandwidth [1]. So, to increase the bandwidth and bit rates Wavelength division multiplexing (WDM) technique

D. Sarkar (✉) · S. Nagaraj · P. K. Anand Prem
Sri Venkateswara College of Engineering and Technology (SVCET), Chittoor 517127, Andhra Pradesh, India
e-mail: debanjan.sarkar1@gmail.com

S. K. Metya
National Institute of Technology Arunachal Pradesh, Jote 791113, India

M. Tiwari et al. (eds.), *Optical and Wireless Technologies*, Lecture Notes in Electrical Engineering 892, https://doi.org/10.1007/978-981-19-1645-8_14

is used in PON [2–4]. In WDM-PON both downstream and upstream transmission rate increases due to the dedicated wavelength provided to each user. WDM-PON is actually termed as next-generation PON [5]. In many places where copper-based access networks are used, are replaced directly by WDM-PON to meet users need. This type of replacement is termed as green field deployment [6]. But, the places where TDM-PON already exists, the replacement of such network by WDM-PON network is difficult. In this case, brown field deployment i.e. migration solution for TDM-PON to WDM-PON is used. To keep the TDM-PON user unaffected and to protect the past investment on the network infrastructure, the co-existence of TDM-PON and WDM-PON is desirable [7, 8].

Thus both the network should share the same infrastructure including Optical Distribution Network. The TDM-PON signal can be separated from WDM-PON using a suitable filter. Due to non-existence of such filter in TDM-PON crosstalk arises. To reduce crosstalk between new PON and legacy PON, many researchers provided solutions. Authors in [9, 10] used a particular high-frequency line coding to shape the upgraded signal's spectrum. However, this scheme reduces bit rates. The upgrade signal can be shifted beyond the baseband of legacy ONU receivers using sub carrier multiplexing (SCM). This approach compromises the expense and complicatedness of radio frequency (RF) components [11]. Colorless ONU's schemes such as spectrum-sliced light sources [12], ASE-injected Fabry-Perot lasers [13] and upstream re-modulation [2] are used to reduce the cost and complexity of the WDM-PON system. Upstream re-modulation is widely used in WDM-PON because the upstream signal can be transmitted reusing the downstream signal. Upstream re-modulation technique is used here.

In this paper, migration of TDM-PON to WDM-PON scheme has been analyzed and investigated. Here, Minimum shift keying modulation (MSK) technique is used to modulate the downstream data in WDM-PON and the same wavelength is reused for upstream signal transmission. Here, Legacy TDM-PON infrastructure is upgraded by including new wavelength channels for downstream and upstream without changing the original network infrastructure. Thus increasing the capability, scalability and converge of the whole network.

2 TDM-PON and WDM-PON Co-existence Architecture

Figure 1 depicts the architecture of the co-existence of TDM-PON and WDM-PON. The top block represents the TDM-PON. In TDM-PON the downstream signals are amplitude modulated. The lower block represents the WDM-PON. In WDM-PON the downstream signals are MSK modulated. The wavelength generated by continuous wave (CW) lasers for TDM and WDM are different from each other. The combined MSK modulated WDM downstream signals and the combined amplitude modulated TDM downstream signals are coupled and sent through a fiber. At the receiver side, the wavelength for TDM-PON is separated from the WDM-PON wavelengths. The TDM-PON wavelength is then split by a power splitter and sent to

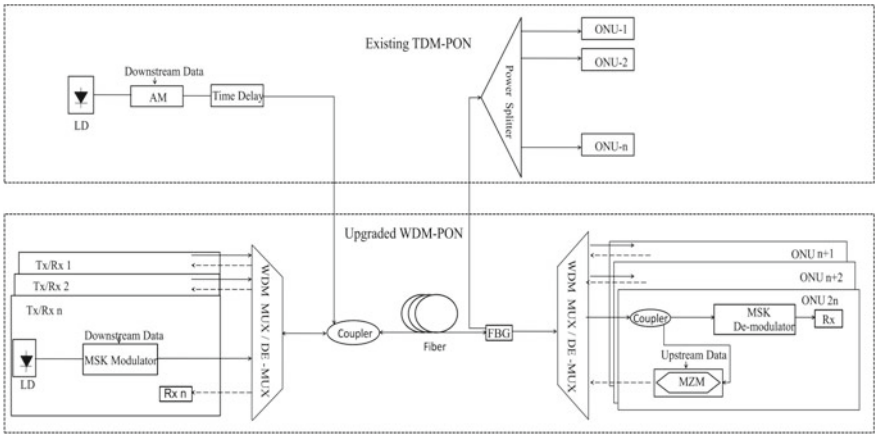

Fig. 1 Co-existing architecture of TDM-PON and WDM-PON. LD: laser diode, MZM: mach zehnder modulator, T_X = transmitter, R_X = receiver

individual ONU for data recovery. In WDM-PON, the wavelengths carrying MSK modulated downstream data are de-multiplexed and send to each ONU. In each ONU, the MSK modulated signal is split into two parts. One part is used for data recovery after passing through MSK de-modulator and the other part is used for upstream re-modulation. The upstream re-modulated signal is revert to the CO via the fiber already used and uncovered at each transmitter.

3 Simulation Setup

Figure 2 depicts the simulation setup of the migration scheme. In this simulation, a total of eight users have been considered. Four are existing users who got access to the TDM-PON network and the rest four are new users who got access to upgraded WDM-PON network. In TDM-PON block, in CO the CW laser having wavelength, $\lambda = 1549.95$ nm is fed to four amplitude modulator (AM) and each AM is driven by 2.5 Gbps PRBS with word length $2^{10} - 1$. Then each amplitude modulated wave is delayed by an interval of $(\frac{1}{bit\ rate} \times$ channel no.) seconds and combined using a power combiner. In WDM-PON block the four CW laser having wavelengths, $\lambda_1 = 1549.75$ nm, $\lambda_2 = 1549.55$ nm, $\lambda_3 = 1549.35$ nm, and $\lambda_4 = 1549.15$ nm are used in transmitter1 (T_x1), transmitter2 (T_x2), transmitter3 (T_x3) and transmitter4 (T_x4) respectively. In each transmitter, the carrier generated is fed to MSK modulator (designed as per [3]) which is driven by a 10 Gbps downstream PRBS with word length $2^{10} - 1$. As a result, four MSK modulated downstream signals are generated. Date rate of 2.5 Gbps for each user in case of TDM-PON and 10 Gbps for each user in case of WDM-PON has been considered i.e. for existing TDM-PON the total data rate is 10 Gbps and the after up-gradation to WDM-PON the data rate for WDM-

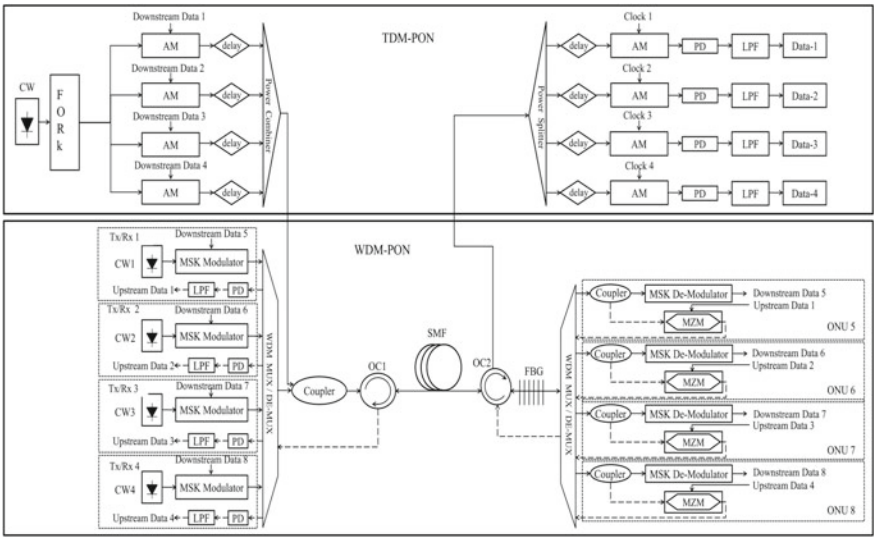

Fig. 2 Simulation setup of co-existing TDM-PON and WDM-PON. LD: laser diode, MZM: mach zehnder modulator, OC: optical circulator, FBG: fiber Bragg grating, SMF: single mode fiber, PD: photo detector

PON is 40 Gbps. Data rate higher than the above mentioned can be achieved either by decreasing the fiber length or increasing the BER and power penalty. According to recommendations of ITU-T G.989x, passive optical networks can support data rate of 40 Gbps. As the aim of the system is to send the data at reasonable distance so the data rate mentioned above has been chosen. These signals are then multiplexed by a 4:1 multiplexer. The combined TDM-PON's amplitude modulated downstream signals and WDM-PON's MSK modulated downstream signals are coupled using a 3 dB coupler. The spectrum of the combined signals is shown in Fig. 3 having resolution 0.01 nm. The coupled signal is first fed to an optical circulator (OC) before being sent through a 30 Km single mode fiber (SMF) (Dispersion 16.75 ps/nm-km, Dispersion slope 0.075 ps/nm^2-km, Affective area 80 μm^2, Attenuation 0.2 dB/km, Nonlinearity index 2.6×10^{-20} m^2/W). At the receiver, the received signal is then passed through another OC and a fiber bragg grating (FBG) having bandwidth 0.2 nm and reflectivity 99%. FBG is used to separate λ from WDM wavelengths. Then the signal carried by λ is fed to a power splitter in legacy TDM-PON network. The signal is then split into four parts and send to four different ONUs of the TDM-PON. In each ONU, the received downstream modulated signal is first delayed by the same time interval as used in CO for transmission and then fed to an AM which is driven by a clock of 2.5 Gbps. Then the output of the AM is directly fed to a photo-detector (PD) for conversion to electrical domain. Finally, the downstream data is detected by the user after passing through a low pass filter (LPF).

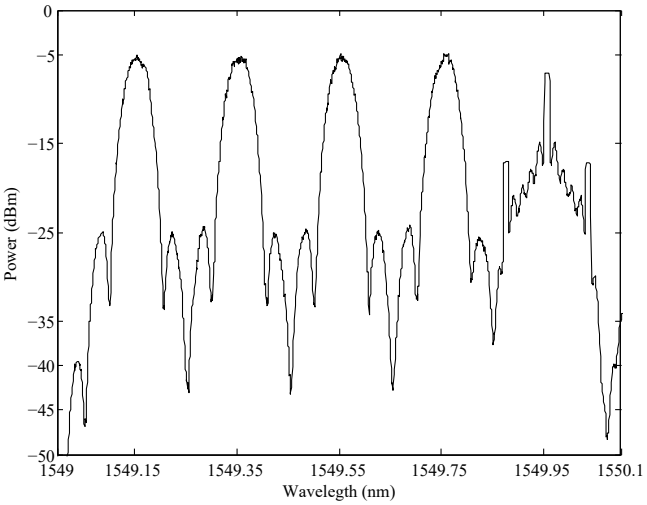

Fig. 3 Spectrum of the combined signals

In WDM-PON, the combined signal at the output of the FBG is first de-multiplexed using 1:4 WDM de-multiplexer. Then the individual signals are sent to the ONU. In each ONU, the MSK modulated signal is split into two portions. One section is used to recover the downstream data after passing through MSK demodulator. Another part is used to re-modulate the upstream data. Without considering the synchronization issue, the upstream signal can be set into MSK modulated signal, as MSK modulated signal posses constant amplitude. Therefore, the downstream signal is used to produce the upstream signal. Hence, the downstream MSK modulated signal is externally modulated by an MZM with 2.5 Gbps PRBS upstream data with word length $2^{10} - 1$. The modulated upstream data is then transmitted back to the individual transmitter via the same 30 km fiber and successfully recovered.

4 Result and Discussion

To analyze the performance of the system BER v/s received optical power curves for all the signals are considered. Also, the BER of upgraded TDM-PON and legacy TDM-PON signals are compared. The purpose of the comparison is to find the effect on the performance of TDM-PON signals due to the addition of WDM-PON signals. In this system, all the signals are transmitted simultaneously through a 30 km SMF without dispersion compensation. The performances of the signals are analyzed based on the received optical power differences between back to back (B2B) and after 30 km transmission.

Figure 4(a), 4(b), 5(a) shows the BER curves of amplitude modulated downstream TDM signals, MSK modulated downstream WDM signals and upstream signals respectively after up gradation of the system. Eye diagrams of the respective signals are shown in the inset of the respective figures. In the figures, both B2B and after transmission curves are considered to study the power penalty of each signal. Similarly, Fig. 5(b) shows the BER curve for both B2B and after transmission of the legacy TDM signals. Eye diagrams for these signals are depicted in the inset of the Figure. Table 1 shows the power penalty of all the signals.

From Fig. 4(a) and Table 1 we can see, that BER of 10^{-9} can be achieved for all the downstream TDM signals after up gradation at approximately same received optical power. The power penalty between B2B and after transmission are almost same for all the downstream TDM signals. Similarly, from Fig. 4(b) and Table 1, it is

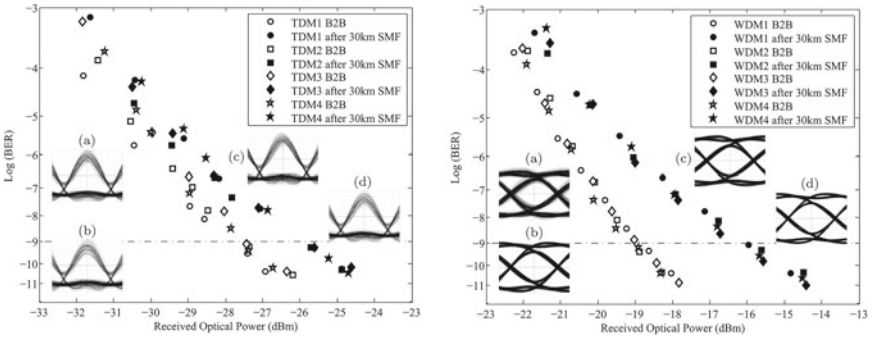

Fig. 4 BER Curve for **a** Downstream TDM signals after up gradation **b** downstream MSK modulated WDM signals after up gradation. Inset: eye diagrams a) signal 1 b) signal 2 c) signal 3 d) signal 4

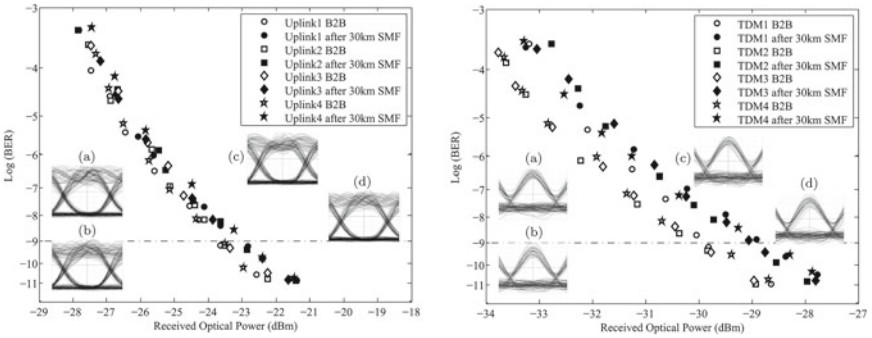

Fig. 5 BER Curve for **a** upstream signals after up gradation **b** Downstream legacy TDM signals. Inset: eye diagrams a) signal 1 b) signal 2 c) signal 3 d) signal 4

Table 1 Power penalty of all the signals

Downstream/upstream signal		Received power		
		B2B (dBm) (Approx.)	After transmission (dBm) (Approx.)	Penalty (dB)
Downstream TDM signals	TDM1	−27.65	−25.9	1.75
	TDM2	−27.6	−25.95	1.65
	TDM3	−27.45	−25.85	1.6
	TDM4	−27.55	−25.85	1.7
Downstream MSK signals	WDM1	−18.9	−16.1	2.8
	WDM2	−19.1	−16.2	2.9
	WDM3	−18.95	−16.15	2.8
	WDM4	−19.15	−16.2	2.95
Upstream signals	Uplink1	−23.85	−23.2	0.65
	Uplink2	−23.7	−23.1	0.6
	Uplink3	−23.5	−22.9	0.6
	Uplink4	−23.55	−22.9	0.65
Legacy TDM downstream signals	TDM1	−29.85	−28.95	0.9
	TDM2	−29.95	−29	0.95
	TDM3	−29.95	−28.95	1
	TDM4	−29.9	−28.9	1

observed that the power penalty for all downstream MSK modulated WDM signals are same. Also, the power penalties between B2B and after transmission of all the upstream signals are almost same as seen from Fig. 5(a) and Table 1.

Figure 5(b) shows the BER versus received optical power of the TDM signal before migration. From the Figure, it is clear that the power penalty between B2B and after transmission for downstream signal 1, signal 2, signal 3 and signal 4 are approximately 0.9, 0.95, 1, and 1 dB respectively. Thus power penalties of all are almost same. Eye diagrams can be seen in the inset of the figure.

From the above figures it is seen that power penalties among similar kind of signals are almost same i.e. we can say that irrespective of the number of users in the network, the end users will get error-free signals with same strength on demand.

Now if we compare the received optical power at 10^{-9} between TDM-PON after up gradation and legacy TDM-PON signals then crosstalk due to upgrade can be determined. From Fig. 4(a), 5(b) and Table 1, it can be observed that error-free transmission i.e. at BER of 10^{-9} after transmission is achieved for downstream TDM1, TDM2, TDM3, and TDM4 signals before up gradation is about −28.95, −29, −28.95, and −28.9 dBm respectively, whereas the same is achieved for TDM signals after up gradation is about −25.9, −25.95, −25.85, and −25.85 dBm respectively. So, a power penalty of 3.05, 3.05, 3.1, and 3.05 dB are observed for TDM1, TDM2, TDM3, and TDM4 signals respectively after upgrade. From this, we can

conclude that crosstalk on the existing system resulting from up gradation is nearly about 3 dB. A 3 dB power penalty signifies 50% of the optical power has been either lost or received. But above 3 dB power penalty means the system will lose more power i.e. the system will not be considered an ideal system. It can also be said from the above observation that in the designed system the performance of legacy TDM is not affected much after the migration of the existing TDM-PON to WDM-PON. Authors in [7, 14] showed the TDM-PON to WDM-PON migration schemes based on DPSK/ASK. WDM-PON systems have been implemented in [3, 15–18]. Also authors in [3, 17, 18] showed that in WDM-PON system MSK performs better than that of DPSK. Hence, if the same system with the same specifications is constructed using DPSK instead of MSK, the MSK-based system will perform better than the DPSK-based system, as observed from [3, 17, 18].

5 Conclusion

A migration scheme from TDM-PON to WDM-PON with MSK modulation in WDM-PON without changing the existing infrastructure is successfully analyzed. All the downstream and upstream signals are successfully detected after 30 km transmission via SMF without using dispersion compensation. Part of the downstream MSK signals is used to re-modulate the upstream signals and found that due to this approach upstream signal suffers from less power penalty and cross talk. The legacy TDM-PON signals are also compared with the upgraded TDM-PON signals and a power penalty around 3 dB for all the TDM signals are observed after upgrade. Thus it can be concluded that crosstalk due to upgraded signal is not much high. From the analysis we can infer that this migration scheme with using minimum additional cost in the existing fiber infrastructure, will provide new users high-speed data on demand. Also, it is found that the performance of the upstream signal is satisfactory with the reuse of optical wavelength.

References

1. Yeh CH, Chow CW, Wang CH, Shih FY, Wu YF, Chi S (2008) Using four wavelength-multiplexed self-seeding Fabry-Perot lasers for 10 Gbps upstream traffic in TDM-PON. Opt Express 16(23):18857
2. Zhang H, Cheng X, Xu Z, Yeo YK (2012) A novel combined WDM-PON with a single shared DI using downlink DPSK and uplink remodulated OOK signals. Opt Commun 285(6):992
3. Sarkar D, Metya SK (2018) Wavelength division multiplexed passive optical network-based optical overlay of two multicast/one unicast data using intensity modulation/minimum shift keying. Opt Eng 57(8):086113
4. Metya SK, Janyani V, Bansal D, Modani SG (2012) Miller coding-based wavelength remodulation for optical access network. IEEE Photonics Technol Lett 24(19):1715
5. Kazovsky LG, Shaw WT, Gutierrez D, Cheng N, Wong SW (2007) Next-generation optical access networks. J Lightwave Technol 25(11):3428

6. Recommendation ITU-T G.987.1 (01/2010): 10-Gigabit-Capable Passive Optical Networks (XG-PON): General Requirements, ITU-T G.987.1
7. Zhou Q, Ma J, Lu Y, Huang L, Chen B (2014) A novel evolution to remodulated WDM-PON based on DPSK/ASK orthogonal modulation. In: Optics and photonics for information processing VIII, vol 9216, p 92160U. International Society for Optics and Photonics
8. Vetter P (2012) Next generation optical access technologies. In: European conference and exhibition on optical communication, p Tu-3. Optical Society of America
9. Hsueh YL, Rogge MS, Shaw WT, Kim J, Yamamoto S, Kazovsky LG (2005) Smooth upgrade of existing passive optical networks with spectral-shaping line-coding service overlay. J Lightwave Technol 23(9):2629
10. Lu Y, Gong Y, Wei Y, Hu M, Zhou X, Li Q (2014) A smooth and gradual evolution to next generation PON based on simple line-coding. IEEE Photonics Technol Lett 26(5):512
11. Heron RW, Pfeiffer T, Veen DT, Smith J, Patel SS (2008) Technology innovations and architecture solutions for the next-generation optical access network. Bell Labs Tech J 13(1):163
12. Lee J, Chung YC, DiGiovanni D (1993) Spectrum-sliced fiber amplifier light source for multichannel WDM applications. IEEE Photonics Technol Lett 5(12):1458
13. Kim HD, Kang SG, Le CH (2000) A low-cost WDM source with an ASE injected Fabry-Perot semiconductor laser. IEEE Photonics Technol Lett 12(8):1067
14. Chow CW, Yeh CH (2013) Using downstream DPSK and upstream wavelength-shifted ASK for Rayleigh backscattering mitigation in TDM-PON to WDM-PON migration scheme. IEEE Photonics J 5(2):7900407
15. Zeng Y et al (2019) A novel CAP-WDM-PON employing multi-band DFT-spread DMT signals based on optical Hilbert-transformed SSB modulation. IEEE Access 7:29397–29404
16. Ullah R, Bo L, Ullah S, Yaya M, Tian F, Xiangjun X (2019) Proposing simulation model for multi-wavelength source offering 40 Gbps WDMPON using AWG with a single laser. Comput Appl Eng Educ 27(6):1299–1307
17. Sarkar D, Metya SK (2018) Performance investigation of 110-Gbps optical MSK system using a Quad Mach-Zehnder IQ modulator. Opt Quantum Electron 50(1):1–9
18. Sarkar D, Metya SK (2019) Minimum shift keying based protection mode capable wavelength division multiplexed passive optical network optical overlay system. Opt Quantum Electron 51(8):1–16

Broadband Light Source for Optical Communication Applications Using Silicon Nanowire Embedded Pentagonal Photonic Crystal Fiber

Lavanya Anbazhagan and Geetha Ganesan

Abstract In this paper, a Silicon nanowire embedded pentagonal Photonic Crystal Fibre (PCF) based Broadband Light Source is proposed as a potential candidate for the Optical Communication systems. The dispersion and nonlinearity characteristics of the PCF are analyzed by the Finite Element Method. The propagation of the Secant Hyperbolic pulse through the proposed PCF is studied by numerically solving the Nonlinear Schrödinger Equation using Split-Step Fourier Method. A Soliton pulse of 25 W peak power and duration of 50 fs at 1550 nm is used for the generation of a broadband light signal.

Keywords Silicon nanowire PCF · Broadband light source · Finite element method · Nonlinear Schrödinger Equation · Optical communication system

1 Introduction

The tremendous applications of Photonic Crystal Fibre (PCF) are attributable to its versatility in design parameters. The Supercontinuum Generation (SCG) using micro-structured fiber, pioneered by Ranka et al. [1], grabbed the attention of the research community. The supercontinuum finds application in Optical Coherence Tomography (OCT), Spectroscopy, and as a broadband light source. The wavelength Division Multiplexing (WDM) technology enhances the transmission capacity of the fiber. The multi-wavelength source requisite limits the viability of the WDM system. The available multi-wavelength sources are mode-locked lasers at MHz repetition rate and EDFA or SOA-based ring lasers, but each having its constraints [2]. The broad continuous spectrum obtained from PCF will be a promising alternative source. The SCG is the consequence of the synergy of multifaceted nonlinear processes

L. Anbazhagan (✉) · G. Ganesan
Department of Electronics and Communication Engineering, College of Engineering, Guindy, Anna University, Chennai, India
e-mail: lavanyaanbazhagan04@gmail.com

G. Ganesan
e-mail: geetha@annauniv.edu

M. Tiwari et al. (eds.), *Optical and Wireless Technologies*, Lecture Notes in Electrical Engineering 892, https://doi.org/10.1007/978-981-19-1645-8_15

such as self-phase modulation, cross-phase modulation, stimulated Raman scattering, and four-wave mixing [3]. The inadequate nonlinear coefficient of silica inhibits the wider broadening of the spectrum. Many research works concentrated on the implementation of hybrid structures, chalcogenide glasses, and liquid infiltration techniques to enhance the nonlinearity of the PCF.

There are a considerable number of research works that strive to broaden the supercontinuum spectrum by altering the existing Silica PCF. The hexagonal PCF with the reduced air hole diameter in the innermost cladding ring is investigated [4]. The supercontinuum of 600 nm is obtained when the 50 fs pulse with 2 kW pump power at 800 nm propagated through the proposed PCF of 50 cm length. The defective core PCF of 1 m length reported an octave-spanning of the broadband continuum when the soliton pulse of 0.1 ps pulse width and 1 kW peak power pumped at the wavelength of 1550 nm [5]. A hybrid Silica PCF with a silicon core of length 10 mm achieved 2000 nm spectral broadening when pumping 20 fs and 3 kW pulse at 1550 nm [6].

The Chalcogenide glasses exhibit an extended transparency window from visible to MIR, since they possess the advantages of large refractive index and high nonlinear coefficients [7–10]. A modified hexagonal tellurite PCF with a high nonlinear coefficient of 378.1 W^{-1} km^{-1} and ultra-flattened dispersion over 0.7 μm is designed. The Secant hyperbolic pulse with 5 kW peak power and FWHM of 176 fs after propagated through the 5 cm length fiber resulted in the supercontinuum spectrum of 2900 nm toward MIR wavelength [11]. An As_2Se_3 -based chalcogenide PCF with concentric rings consisting of air-holes is modelled. With the fiber length of 4 mm, a 100 fs Secant hyperbolic pulse with the peak power 10 kW at the pump wavelength of 4.357 μm attained the supercontinuum of 1034 nm [12]. The As_2S_3 core octagonal PCF with a very high nonlinearity of 14,387.43 W^{-1} km^{-1} is proposed. The injected pump pulse of width 20 fs having a 3 kW peak power at 1.55 μm in 10 mm long fiber attained an ultra-broad SC spectrum of 3.7 μm [13].

The photonic nanowire of subwavelength diameter can exhibit excellent optical properties such as light-matter interaction and strong light confinement when embedded into the core region of PCF. Silicon nanowires exhibit high nonlinearity due to the large surface-to-volume ratio. The core diameter of silicon nanowire is very less than single-mode fibre that results in less effective area thereby, high nonlinearity is obtained. Hence, Silicon nanowire is regarded as the potential candidate for nonlinear applications. The Si-nanowire embedded PCF with different core geometries are investigated, and it is found that circular core outperforms others in terms of obtained output spectral width. The pulse of 20 fs FWHM and peak power of 25 W propagated through PCF at 1.3 μm resulted in a 900 nm broad spectrum [14]. A comparative study on the optical characteristics is carried out between tellurite nanowire PCF and Ge-doped silica PCF. The tellurite nanowire core PCF outperforms the other in terms of its higher nonlinearity coefficient and higher numerical aperture [15]. Si-nanowire of 300 nm embedded in spiral lattice PCF exhibited flattened dispersion with high nonlinearity of 3176 W^{-1} m^{-1} at 0.45 μm. With a PCF length of 2 mm, a broad spectrum of 500 nm is obtained [16]. Si-nanowire embedded PCF possess a very high nonlinearity of 1358 W^{-1} m^{-1} at 0.8 μm. Investigation of

SCG with low pulse energy of 2.5pJ at a different pump wavelength of 0.8, 1.3, and 1.55 μm is carried out. A supercontinuum of 1250 nm is attained at 0.8 μm with 2 mm length PCF and is found to be suitable for OCT applications [17].

In this work, Silicon nanowire embedded pentagonal lattice PCF is proposed for broadband signal generation in Optical Communication systems. The reported literature on Si-nanowire embedded PCF did not focus on SCG centered around the third communication wavelength of 1550 nm, which is suitable for Optical communication applications. This work considers spectral broadening around 1550 nm that is achieved by tailoring the radius of the Si-nanowire. A comparative study on the characteristics of the PCF, such as nonlinear coefficient and dispersion of silica PCF, hybrid PCF with As_2S_3 core, and our proposed PCF with Si-nanowire core, is carried out. The dynamics of the pulse propagation through the three PCF structures are investigated by solving the Nonlinear Schrödinger equation using the Split Step Fourier Method. A very high nonlinearity and zero-dispersion wavelength near the pump wavelength are obtained for the proposed PCF. A Secant hyperbolic pulse having 50 fs FWHM with a peak power of 25 W at 1550 nm injected as the pump input into the proposed PCF of length 1 cm resulted in 685 nm broadened spectrum in the wavelength range 1235–1920 nm.

2 Material and Design

This work contemplates three different PCF designs to substantiate the significance of the proposed design. The asymmetric pentagonal lattice results in high birefringence compared to the conventional hexagonal lattice, and so pentagonal lattice is taken into consideration for our design. Figure 1a depicts a simple PCF design that has silica as the background material and air holes in the cladding region. The schema in Fig. 1b is a hybrid PCF that incorporates As_2S_3 in the core region. The proposed design has silicon nanowire embedded in the core, which is illustrated in Fig. 1c. The nonlinear refractive index coefficient of As_2S_3($n_2 = 4.8 \times 10^{-18}$ m^2 W^{-1}) is

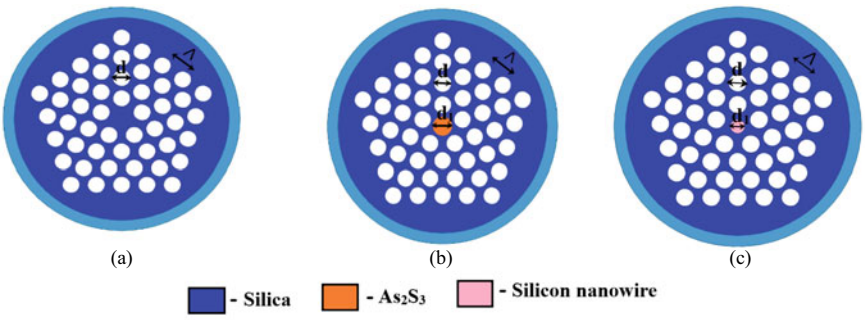

Fig. 1 Design layout of **a** Silica PCF **b** As_2S_3 core PCF **c** Silicon nanowire core PCF

two orders of magnitude larger than that of the conventional Silica ($n_2 = 3 \times 10^{-20}$ m^2 W^{-1}). However, the nonlinear refractive index coefficient of Si-nanowire ($n_2 = 9 \times 10^{-18}$ m^2 W^{-1}) is higher compared to As_2S_3. The structural parameters that are considered for the PCF design are the diameter of the air hole (d), the spacing between the two air holes termed as pitch ($\wedge$), and the diameter of the material embedded core (d_1).

A very high nonlinearity and ultra-flattened dispersion characteristics of fiber are desired to achieve effective spectral broadening, which can be obtained by appropriate tailoring of the structural parameters. In PCF, the value of air filling ratio d/$\wedge$ should be less than 0.43, for the single-mode behaviour to be sustained endlessly [18]. Hence the air filling ratio d/$\wedge$ is fixed at 0.42 with $\wedge = 2$ μm and d = 0.84 μm. The diameters of the As_2S_3 core and Si-nanowire core are optimized to achieve the desired characteristics.

3 Numerical Method

The wavelength dependent refractive index of Silica (n_{si}) [19], As_2S_3 (n_{As}) [20] and Silicon-nanowire [21] are formulated by the Sellmeier equation:

$$n_{si}(\lambda) = \sqrt{1 + \frac{0.6961663\lambda^2}{\lambda^2 - 0.0684043^2} + \frac{0.4079426\lambda^2}{\lambda^2 - 0.1162414^2} + \frac{0.8974794\lambda^2}{\lambda^2 - 9.86161^2}} \quad (1)$$

$$n_{As}(\lambda) = \sqrt{1 + \frac{1.8983678\lambda^2}{\lambda^2 - 0.0225} + \frac{1.9222979\lambda^2}{\lambda^2 - 0.0625} + \frac{0.8765134\lambda^2}{\lambda^2 - 0.1225} + \frac{0.1188704\lambda^2}{\lambda^2 - 0.2025} + \frac{0.9569903\lambda^2}{\lambda^2 - 750}} \quad (2)$$

$$n_{sinanowire}(\lambda) = \sqrt{1 + \frac{10.6684293\lambda^2}{\lambda^2 - 0.301516485^2} + \frac{0.003043478\lambda^2}{\lambda^2 - 1.13475115^2} + \frac{1.54133408\lambda^2}{\lambda^2 - 1104^2}} \quad (3)$$

Maxwell's Master Wave Equation is solved to determine the effective refractive index and the field distribution in the designed PCF [22]:

$$\nabla \times (\nabla \times E) - k_0^2 \in_r E = 0 \quad (4)$$

where k_0^2 is the eigen value and $\in_r$ is the relative permittivity.

From the solutions obtained through the Master Wave Equation, the characteristics of the PCF are analytically calculated using the following equations [23]:

$$\text{Effective Area } A_{eff} = \frac{\left[\iint |E(x,y)|^2 dxdy\right]^2}{\iint |E(x,y)|^4 dxdy} \quad (5)$$

$$\text{Nonlinear coefficient } \gamma = \frac{2\pi}{\lambda} \frac{n_2}{A_{eff}} W^{-1} m^{-1} \quad (6)$$

$$\text{Dispersion coefficient } D = -\frac{\lambda}{c}\frac{d^2 Re\left[n_{eff}\right]}{d\lambda^2} \tag{7}$$

where A_{eff} is the effective area in μm^2; E(x,y) is the electric field; λ is the operating wavelength; n_2 is nonlinear refractive index coefficient; $Re[n_{eff}]$ is the real part of effective refractive index, and c is the velocity of light in free space.

The propagation of light through the PCF is studied by numerically solving the Nonlinear Schrödinger Equation (NLSE) using Split-Step Fourier Method (SSFM) [23]:

$$\frac{\partial}{\partial z}A(z,t) + \frac{\alpha}{2}A(z,t) - \sum\nolimits_{n\geq 2}\beta_n \frac{i^{n+1}}{n!}\frac{\partial^n}{\partial t^n}A(z,t) = i\gamma\left(1 + \frac{i}{\omega_0}\frac{\partial}{\partial t}\right)A(z,t)\int_{-\infty}^{\infty} R(t')\left|A(z,t-t')\right|^2 dt' \tag{8}$$

where $A(z,t)$ is the slowly varying envelope of the propagating pulse, β_n is the n^{th} order dispersion that accounts for the dispersion effects in the fiber by expanding the propagation constant $\beta(\omega)$ using Taylor series. The response function R(t) is given by

$$R(t) = (1 - f_R)\delta(t) + f_R h_R(t) \tag{9}$$

where f_R represents the fractional contribution of the delayed Raman response and its value is 0.18 and $h_R(t)$ is the Raman response function given by

$$h_R(t) = \frac{\tau_1^2 + \tau_2^2}{\tau_1 \tau_2^2} exp(-t/\tau_2) sin(t/\tau_1) \tag{10}$$

where $\tau_1 = 12.2$ fs and $\tau_2 = 32$ fs are the parameters that provide a good fit to the actual Raman-gain spectrum.

A Secant hyperbolic optical pulse with peak power P_0 and FWHM of T_0 is considered at the input and the pulse evolution through the PCF is given by

$$A(z,T) = \sqrt{P_0}\,\text{sech}\frac{T}{T_0} \tag{11}$$

The Dispersion length L_D and Nonlinear length L_{NL} are calculated using

$$L_D = \frac{T_0^2}{|\beta_2|} \tag{12}$$

$$L_{NL} = \frac{1}{\gamma P_0} \tag{13}$$

where β_2 is the GVD parameter and, γ is the nonlinear coefficient of the fiber; T_0 is the FWHM and P_0 is the peak power of the pulse input.

4 Results and Discussion

The three different PCF structures that are considered for this study are analyzed using COMSOL Multiphysics 5.2a, a Finite Element Method (FEM) solver. The modal field distribution is obtained using the Wave Optics Module, which is used to solve the Master Wave Equation. The higher-order dispersion terms will become dominant if the PCF is pumped near its zero-dispersion wavelength. To generate broadband light around 1550 nm, the Zero-dispersion wavelength of the proposed PCF needs to be tailored around 1.55 μm. The commercially available Er-doped femtosecond fiber lasers, such as Femtolite Ultra Bx-60, CF1550-HP, and Buccaneer, can be used as pump source at 1.55 μm.

4.1 Tailoring the Characteristics of the Proposed PCF

The dispersion (D), effective area (A_{eff}), and nonlinear coefficient (γ) characteristics of the As_2S_3 core and Si-nanowire core PCFs are tailored by varying the core radius.

The dispersion characteristics for different As_2S_3 core radius and Si-nanowire core radius (r_1) as a function of wavelength are exhibited in Fig. 2.

As the radius of the core increases, the refractive index contrast between the core and cladding increases resulting in increased effective refractive index. Since the wavelength dependence of the dispersion characteristics is related to the refractive index, the increase in the radius of the core increases the effective refractive index, which in turn shifts the zero-dispersion wavelength towards the higher wavelength region, as observed in Fig. 2. The optimum value of core radius is chosen as 0.95 μm for As_2S_3 core and 0.48 μm for Si-nanowire core since for that value of the radius, the desired zero-dispersion wavelength around 1.55 μm is obtained.

The effective area and nonlinear coefficient as a function of wavelength are analytically calculated for various core radius, and the results are depicted in Fig. 3a and b for As_2S_3 PCF and for Si-nanowire embedded PCF is in Fig. 3c and d, respectively.

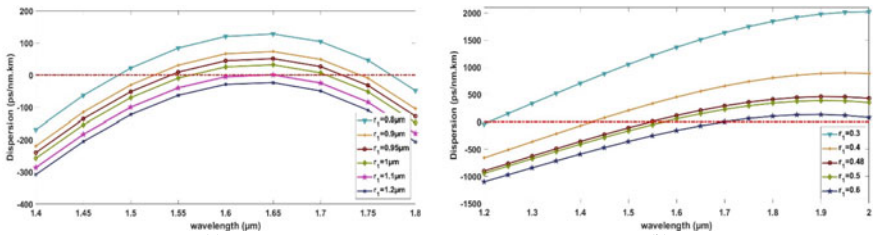

Fig. 2 The Dispersion characteristics of the PCF for different radius of **a** As_2S_3 core **b** Silicon nanowire core

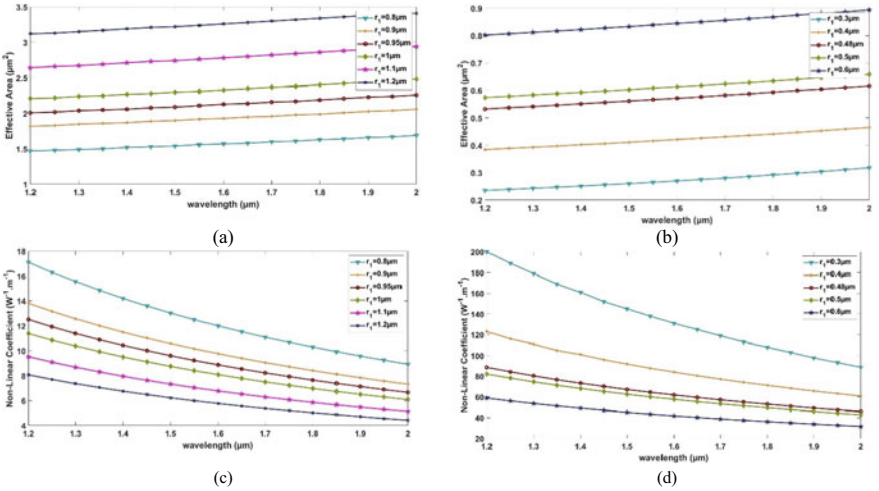

Fig. 3 Effective area of **a** As_2S_3 core **b** Si-nanowire core and Nonlinear coefficient of **c** As_2S_3 core **d** Si-nanowire core

Figure 3a and b show that the effective area increases with an increase in the radius of the core region. The nonlinear coefficient tends to decrease with an increase in the radius of the core, since it is inversely related to the effective area, as evident from Fig. 3c and d.

The combination of high nonlinear refractive index coefficient (n_2) and less effective area results in a high nonlinear coefficient (γ) that enhances spectral broadening. A less effective area and a high nonlinear coefficient are obtained for the As_2S_3 radius of 0.8 μm and Si-nanowire radius of 0.3 μm. However, to achieve spectral broadening around 1550 nm, zero-dispersion wavelength near 1.55 μm and also a moderate nonlinear coefficient at 1.55 μm are obtained for the As_2S_3 radius value of 0.95 μm and Si-nanowire radius of 0.48 μm. Hence these values are decided as the optimum radius.

4.2 Characteristics Comparison of the Three PCF Design

The effective refractive index, dispersion, effective area, and nonlinearity characteristics of the three PCFs are exhibited in Fig. 4.

From Fig. 4a it is observed that the Silica PCF has the least effective refractive index contrast. The value of the effective refractive index increases by incorporating different materials in the core region. The effective refractive index of Si-nanowire embedded PCF is higher compared to that of As_2S_3 core PCF. The comparison of the dispersion characteristics of three different PCFs is illustrated in Fig. 4b. Even though the zero-dispersion wavelength is tailored to be around 1550 nm (Sect. 4.1),

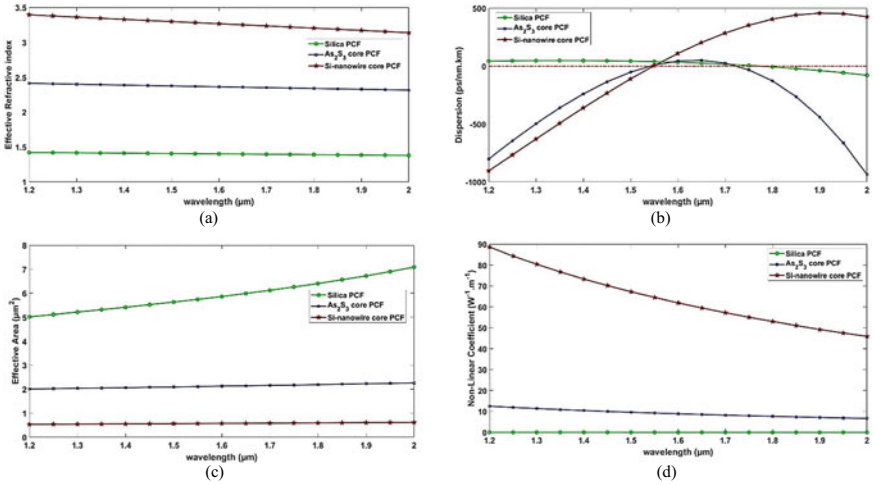

Fig. 4 Comparison of the characteristics of three PCF structure **a** Effective refractive index **b** Dispersion **c** Effective area **d** Nonlinear coefficient

the Si-nanowire embedded PCF has flattened dispersion compared to As_2S_3 PCF. It is evident from Fig. 4c and d that the Si-nanowire embedded PCF has the least effective area and higher nonlinearity coefficient. Hence the Si-nanowire embedded PCF outperforms the other two PCF structures in terms of ultra-flattened dispersion and high nonlinearity coefficient, which is the requirement for Supercontinuum generation.

4.3 Pulse Propagation Analysis

The NLSE of the proposed PCF is formed with the values of nonlinear coefficient (γ), GVD parameter (β_2), and third-order dispersion parameter (β_3), obtained from FEM analysis, and it is numerically solved using SSFM. The values of the fiber parameters for three different PCF structures are presented in Table 1.

Table 1 Parameter values for three different PCFs

Parameters of the PCF	Silica PCF	As_2S_3 PCF	Si-nanowire PCF
γ (W^{-1} m^{-1})	0.021	9.2	64.5
β_2 (s^2/m)	$-$ 3.358 $\times$ 10^{-26}	$-$ 11 $\times$ 10^{-27}	$-$ 5.1 $\times$ 10^{-27}
β_3 (s^3/m)	1 $\times$ 10^{-40}	1.64 $\times$ 10^{-39}	3.812 $\times$ 10^{-39}
L_D (m)	0.027	0.82	0.014
L_{NL} (cm)	190	0.434	0.062

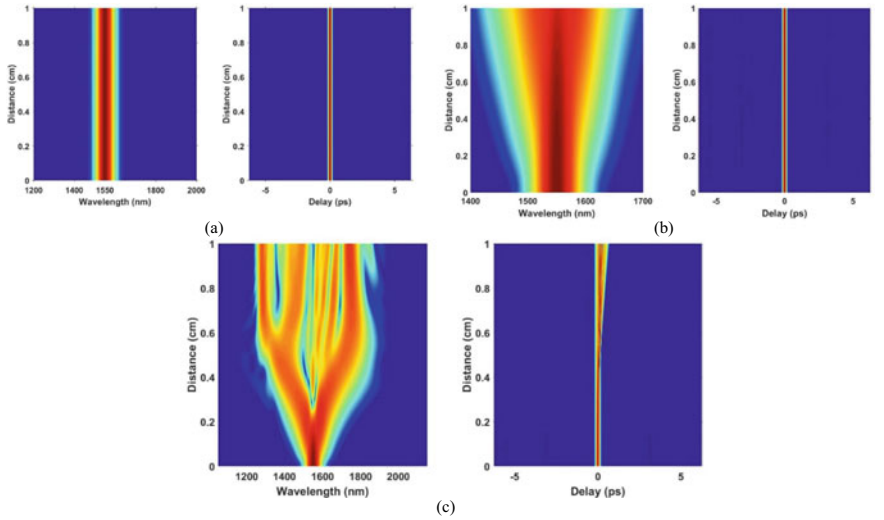

Fig. 5 Spectral and temporal evolution of the pulse through **a** Silica PCF **b** As_2S_3 core **c** Si-nanowire core

The achievement of spectral broadening is further justified by analysing the propagation of a Secant hyperbolic pulse with the peak power of 25 W and 50 fs FWHM through the PCF. The spectral and temporal dynamics of pulse evolution for three different PCFs of the same length of 1 cm at the specified distance are numerically solved and represented by the pseudo colour plot as in Fig. 5.

For Silica PCF, $L_D >> L$ and $L_{NL} >> L$, which implies that neither dispersive nor nonlinear effects come into the picture during the propagation of pulse. It functions as the bare medium for optical pulse transportation and finds application in optical communication systems. For both As_2S_3 core and Si- nanowire core PCF, $L_D >> L$ and $L_{NL} < L$, the pulse evolution is governed by the nonlinear effect, namely, Self Phase Modulation (SPM) that results in the spectral broadening. The spectral broadening of 240 nm has been attained by the As_2S_3 core PCF, whereas a broadening of 685 nm is achieved for Si- nanowire core PCF as observed from Fig. 5. The enhanced spectral broadening of the Si-nanowire core is attributed to its higher nonlinear coefficient compared to As_2S_3. The comparison of the proposed PCF with some of the similar recent research work is tabulated in Table 2.

Our proposed PCF transcends the cited works in terms of low peak power of 25 W and the broadened spectrum of width 685 nm centered around the desired optical communication wavelength. The broadening of the spectrum with very low input power is attributed to the large nonlinear coefficient of 64,500 W^{-1} km^{-1}.

Table 2 Comparison of the proposed PCF with that of the related works found in the Literature listed in the references

Ref	Length of the PCF (cm)	FWHM	Peak power (kW)	Nonlinear coefficient W^{-1} km^{-1}	Broadened spectral width (nm)
[5]	100	0.1 ps	1	38.3	2200
[6]	1	20 fs	3	14,609.84	2000
[13]	1	20 fs	3	14,387.43	3700
[4]	50	50 fs	2	116.76	600
[12]	0.4	100 fs	10	375	1034
[11]	5	176 fs	5	378.1	2900
Our work	**1**	**50 fs**	**25**	**64,500**	**685**

5 Conclusion

In this paper, a Silicon nanowire embedded pentagonal PCF-based broadband source for optical communication applications is proposed. A comprehensive study is carried out by comparing the characteristics of three different PCF designs. The optimum values obtained by tailoring the structural parameters are the air filling fraction d/$\wedge$ = 0.42 with pitch $\wedge$ = 2 μm, d = 0.84 μm, the radius of As_2S_3 core = 0.95 μm and radius of Si-nanowire core = 0.48 μm, to achieve the desired characteristics. The optimized PCF has a zero-dispersion wavelength around 1550 nm, and a very high nonlinear coefficient of 9.2 W^{-1} m^{-1} and 64.5 W^{-1} m^{-1} at 1550 nm is obtained for As_2S_3 and Si-nanowire core, respectively. A Soliton pulse of 25 W peak power and 50 fs FWHM centered at 1550 nm propagated through the proposed PCF of length 1 cm, gone through spectral broadening that resulted in the generation of broadband light of spectral width 685 nm. Thus our proposed PCF-based broadband light source will be a potential candidate for optical communication applications. Our future work is to realize a multiwavelength light source for WDM (Wavelength Division Multiplexing) systems that falls in the C band by spectrum slicing the broadened spectrum with 0.8 nm wavelength spacing, which complies with ITU-T G 694.1 DWDM standard.

Acknowledgements Lavanya. A is grateful to Anna University, Chennai, for Anna Centenary Research Fellowship (CFR/ACRF-2020/AR1), which supported her to carry out this research work.

References

1. Ranka JK, Windeler RS, Stentz AJ (2000) Visible continuum generation in air–silica microstructure optical fibers with anomalous dispersion at 800 nm. Opt Lett 25(1):25. https://doi.org/10.1364/OL.25.000025

2. Bakopoulos P et al (2007) Multi-wavelength laser source for dense wavelength division multiplexing networks. In: OFC/NFOEC 2007 - 2007 conference on optical fiber communication and the national fiber optic engineers conference, Anaheim, pp 1–3, March 2007. https://doi.org/10.1109/OFC.2007.4348886
3. Dudley JM, Genty G, Coen S (2006) Supercontinuum generation in photonic crystal fiber. Rev Mod Phys 78(4):1135–1184. https://doi.org/10.1103/RevModPhys.78.1135
4. Nair AA, Boopathi CS, Jayaraju M, Mani Rajan MS (2019) Numerical investigation and analysis of flattened dispersion for supercontinuum generation at very low power using hexagonal shaped photonic crystal fiber (H-PCF). Optik 179:718–725. https://doi.org/10.1016/j.ijleo.2018.11.021
5. Sharafali A, Nithyanandan K (2019) Ultra-broadband continuum generation in silica based defective core photonic crystal fiber. Optik 191:121–131. https://doi.org/10.1016/j.ijleo.2019.06.014
6. Sakr H, Hussein RA, Hameed MFO, Obayya SSA (2019) Analysis of photonic crystal fiber with silicon core for efficient supercontinuum generation. Optik 182:848–857. https://doi.org/10.1016/j.ijleo.2019.01.104
7. Troles J, Brilland L (2014) Chalcogenide microstructured optical fibers for infrared applications. In: Chalcogenide Glasses, pp 411–437. Elsevier
8. Yue Y et al (2012) Octave-spanning supercontinuum generation of vortices in a As2S3 ring photonic crystal fiber. In: Conference on lasers and electro-optics 2012, San Jose, California, p CTh4B.6. https://doi.org/10.1364/CLEO_SI.2012.CTh4B.6
9. Saini TS, Kumar A, Cherif R, Sinha RK, Zghal M (2015) Design and analysis of rectangular core photonic crystal fiber for supercontinuum generation. In: Presented at the SPIE Optical Engineering + Applications, San Diego, p 95860G, August 2015. https://doi.org/10.1117/12.2187884
10. Hoang VT et al (2018) All-normal dispersion supercontinuum generation in photonic crystal fibers with large hollow cores infiltrated with toluene. Opt Mater Express 8:3568–3582
11. Huang T, Huang P, Cheng Z, Liao J, Wu X, Pan J (2018) Design and analysis of a hexagonal tellurite photonic crystal fiber with broadband ultra-flattened dispersion in mid-IR. Optik 167:144–149. https://doi.org/10.1016/j.ijleo.2018.04.016
12. Li J, Zhao F, Hui Z (2019) Mid-infrared supercontinuum generation in dispersion-engineered highly nonlinear chalcogenide photonic crystal fiber. Mod Phys Lett B 33(19):1950211. https://doi.org/10.1142/S0217984919502117
13. Balani H, Singh G, Tiwari M, Janyani V, Ghunawat AK (2018) Supercontinuum generation at 155 μm in As_2S_3 core photonic crystal fiber. Appl Opt 57(13):3524. https://doi.org/10.1364/AO.57.003524
14. Abdosllam MA, Gunasundari E, Senthilnathan K, Sivabalan S, Nakkeeran K, Ramesh Babu P (2014) Supercontinuum generation in silicon nanowire embedded photonic crystal fibers with different core geometries, Suzhou, China, p 923319, August 2014. https://doi.org/10.1117/12.2069497
15. Hossain MdA, Namihira Y, Yasui T, Higa H, Hai NH (2013) Tellurite nanowire core photonic crystal fiber. In: 2013 international conference on advanced technologies for communications (ATC 2013), Ho Chi Minh, Vietnam, pp 648–651, October 2013. https://doi.org/10.1109/ATC.2013.6698194
16. Gunasundari E, Senthilnathan K, Ramesh Babu P, Sivabalan S, Nakkeeran K (2013) Supercontinuum generation in a silicon nanowire embedded spiral photonic crystal fiber. In: Workshop on recent advances in photonics (WRAP), New Delhi, pp 1–2, December 2013. https://doi.org/10.1109/WRAP.2013.6917657
17. Gunasundari E, Senthilnathan K, Ramesh Babu P, Ebenezar J, Nakkeeran K (2017) Supercontinuum generation in a silicon nanowire embedded photonic crystal fiber for optical coherence tomography applications. In: Ebenezar J (ed) Recent Trends in Materials Science and Applications. SPPHY, vol 189. Springer, Cham. https://doi.org/10.1007/978-3-319-44890-9_8
18. Saitoh K, Koshiba M (2005) Numerical modeling of photonic crystal fibers. J Light Technol 23(11):3580–3590. https://doi.org/10.1109/JLT.2005.855855

19. Malitson IH (1965) Interspecimen comparison of the refractive index of fused silica. J Opt Soc Am 55:1205–1209
20. Rodney WS, Malitson IH, King TA (1958) Refractive index of arsenic trisulfide. J Opt Soc Am 48:633–636
21. Tatian B (1984) Fitting refractive-index data with the Sellmeier dispersion formula. Appl Opt 23:4477–4485
22. Knight JC, Birks TA, Atkin DM, Russell PSJ (1996) Pure Silica single-mode fibre with hexagonal photonic crystal cladding. In: Optical fiber communication conference (1996), paper PD3, p PD3, February 1996
23. Agrawal GP (2007) Nonlinear Fiber Optics. Elsevier Science. https://books.google.co.in/books?id=b5S0JqHMoxAC

Disaster Management System Using Free Space Optical Communication

R. G. Sangeetha, C. Hemanth, V. Prasanth, and Sanjay Ram

Abstract The preservation of lives and property during natural or man-made disasters is referred to as disaster management. During times of disaster, all the existing infrastructure may be destroyed. In this paper, we propose a prototype of a free space optics-based disaster management system. Free space optics-based communication systems can be quickly established as compared to other communication systems. In this paper, we use three sensors to detect disasters such as earthquakes and floods. Using a free space optic communication system, we transmit the detected disaster using a voice-based communication system.

Keywords Free space optics · Disaster management · Hardware implementation

1 Introduction

Because of changes in climatic conditions, India is experiencing a slew of natural calamities. Floods, droughts, cyclones, earthquakes, and landslides are all relatively frequent in Indian landscapes. Disaster management is a process that deals with the strategies and methods used to safeguard or preserve people and property in the event of a disaster. Setting up the infrastructure for communication would be easier and faster using wireless communication. In this paper, we propose and implement a prototype of a disaster management system using Free Space Optical (FSO) communication.

FSO is a communication technique that wirelessly transmits data for networking by using light traveling in free space. This is in contrast to the use of optical fiber cable. FSO is a communication technique in which free space functions as a medium between transmitter and receiver, which must be in the line of sight (LOS) for optical signal transmission to be effective. The medium might be air, space, or a vacuum. This method may be utilized for communication during the day and at a lower cost.

R. G. Sangeetha · C. Hemanth (✉) · V. Prasanth · S. Ram
VIT Chennai, Chennai, Tamilnadu, India
e-mail: hemanth.c@vit.ac.in

M. Tiwari et al. (eds.), *Optical and Wireless Technologies*, Lecture Notes in Electrical Engineering 892, https://doi.org/10.1007/978-981-19-1645-8_16

FSO has several advantages, including high bandwidth and the absence of a spectrum license. The presence of foreign entities such as rain, fog, and haze, physical blockage, scattering, and air turbulence are all variables that affect FSO transmission. The operation of FSO networks is identical to that of OFC (optical fiber cable) networks, with the only difference being that optical beams are delivered through free air rather than OFC cores, which are glass fiber. FSO is a LOS (line of sight) technology that allows for data, audio, and video communication at a maximum transmission rate of 10 Gbps.

The primary goal of this paper is to alert the surrounding areas if there is a disaster in the area, to realize a transmission-reception system to transfer sound via Laser without any guiding medium, to use Intensity Modulation with negligible quality loss, and to detect the disaster using sensors such as an IR sensor, a fire sensor, and a water sensor.

Because India is a growing country, it requires some creativity in the event of a calamity. This is possible because of contemporary technologies that aid in processing, communication, and device control. We can detect earthquake, landslide, and cyclone characteristics using a sensor interface in 8051 microcontrollers. Laser communication is ideal for this application.

1.1 Literature Survey

Mitigating the effects of atmospheric turbulence on signal fading is discussed in [1]. Turbulence-induced fading can be minimized when the receiver aperture is larger than the correlation length of intensity variations. By optimizing the beam width for a fixed coding rate, a link margin gain of 5 dB over a nominal beam width is achieved in severe turbulence channels [2]. A link margin gain of 5 dB above a nominal beam width is attained in severe turbulence channels by optimizing the beam width for a fixed coding rate [3]. The authors in [4] have discussed the management of disasters like tsunami and earthquakes using IoT. The Shelter Exchange System is discussed in [5], which facilitates message communication between shelters and the outside world. A shelter communication system is proposed in [6], where the Shelter Exchange System facilitates message communication between shelters and between shelters and the outside world.

2 Proposed Work

During disasters, the entire communication network fails, and it becomes tough to set up the entire infrastructure in a short period. The FSO communication system can be quickly established without much infrastructure in a time-efficient manner. The complete equipment may be put on the roof of the building, from which a link to a remote site without internet access can be created. In areas of disaster, an outdoor

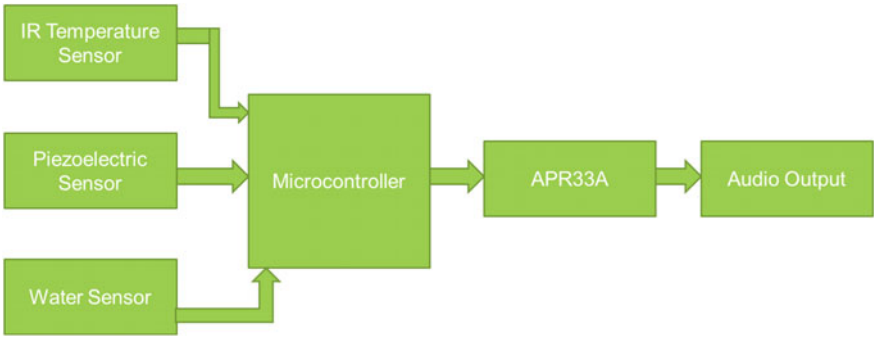

Fig. 1 Block diagram of the disaster detection system

FSO system consisting of an FSO transmitter can be easily installed on roofs and can be used to connect to remote FSO reception units.

In this paper, we propose to implement an FSO based disaster detection and management system in Hardware. The disaster detection system consists of a piezoelectric sensor, and temperature sensor to detect earthquakes, and a raindrop detection sensor to detect heavy rainfalls and cyclones. Figure 1 depicts the disaster detection system consisting of the different sensors interfaced with the microcontroller.

As a precursor for earthquakes, scientists have found that the stress stored in rocks in tectonically active locations might appear as temperature fluctuation via an energy transformation process [7]. A rise in land surface temperature was observed before an earthquake. To mimic this situation in our prototype, we have used an IR temperature sensor (MLX90614) and a piezoelectric sensor. We may transmit an infrared wave to the surface and analyze the wave that returns to the sensor to get temperature data using the IR temperature sensor.

To detect heavy rainfalls and cyclones, we have used a raindrop detection sensor. It has a circuit that collects the raindrops. As raindrops gather on the circuit board, they form parallel resistance pathways monitored by the op-amp. The lower the voltage output, the lower the resistance (or, the more water). For example, a fully dry board will cause the module to produce 5 V. Using this sensor, we mimic the rainfalls and cyclones.

These sensors are connected to the input ports of a microcontroller. Inside the microcontroller, a program is dumped, which compares the sensor readings with the threshold values. The microcontroller is then connected to the APR33A module, a high-quality audio recording and playback device. Prerecorded messages are stored inside this module corresponding to each of the events/calamities. Whenever the values from the sensor exceed the threshold, these prerecorded message is played as shown in Fig. 1. This audio output is then amplified and given to the laser driver module. The laser communication device uses a laser beam to convey sound or music signals. The laser beam's intensity varies with the loudness of the sound input. The laser driver modulates the audio signal and feeds the Laser source, transmitted over the free space. Using a solar panel, the fluctuation in the strength of the laser

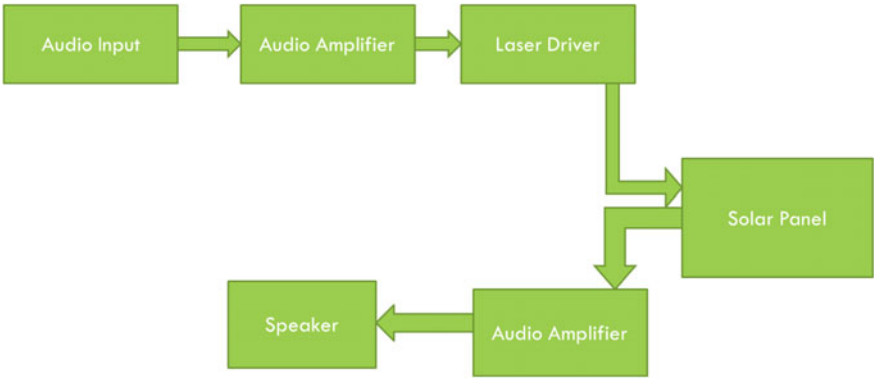

Fig. 2 Block diagram of the disaster announcement system

beam is translated into a variation in the voltage level. The voltage fluctuation on the solar panel is amplified and replayed by a speaker using a low-voltage audio power amplifier, as shown in Fig. 2. The maximum output of the audio amplifier LM386 is 1 W. This indicates the residents of the area about the calamity.

3 Methodology

The following steps indicate the methodology followed in this paper for the implementation of the FSO based disaster management system.

- Digitize sound waves; for this, we used an electric microphone.
- Configure the APR33A voice module by recording the messages.
- Interface the microcontroller with the voice module via relays.
- Interface all three (IR temperature, piezoelectric, raindrop detection) sensors with the microcontroller.
- Once the sensor voltage exceeds the threshold, the required voice message is played by the APR33A.
- Message from the APR33A is transmitted.
- The transmitter sends the audio data to the transmitting unit using an aux cable.
- An amplifier is used to amplify the message.
- The transmitting unit converts the electrical signal into light and transmits it to the receiving unit in free space.
- The receiving unit converts this light signal and converts it back into an electrical signal.
- Another amplifier is used to overcome the attenuation.
- This signal is fed to the speaker.

4 Results and Discussion

In this section, we present the results and circuits implemented. Figure 3 depicts the circuit for voice recording and playback. This is accomplished through the usage of APR33A. Pins 21 and 22 are used to attach the microphone. To record the message, Pin 12 of the APR33A is grounded. Pins 13, 14, and 15 are only utilized here since only three output messages are required. The message must be recorded at a particular pin, which must be grounded.

Figure 4 depicts the interface of the APR33A and sensors to the AT89S51 microcontroller. Three sensors are utilized, and the output is played as audio. Relays are used to turn on and off the message to be played. Figure 5 depicts the transmitter circuit. Figure 6 depicts the receiver circuit, in which a solar panel receives the modulated light signal from the transmitter, amplifies it, and sends it to the speaker.

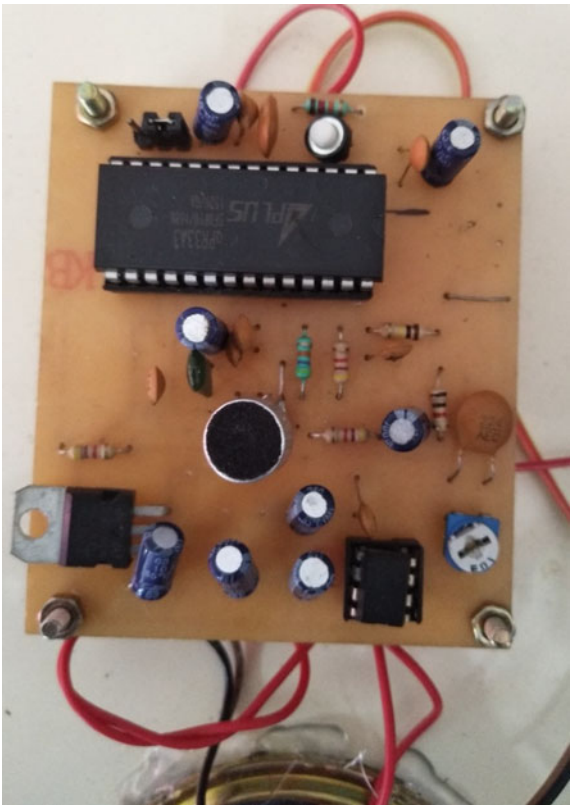

Fig. 3 APR33A circuit

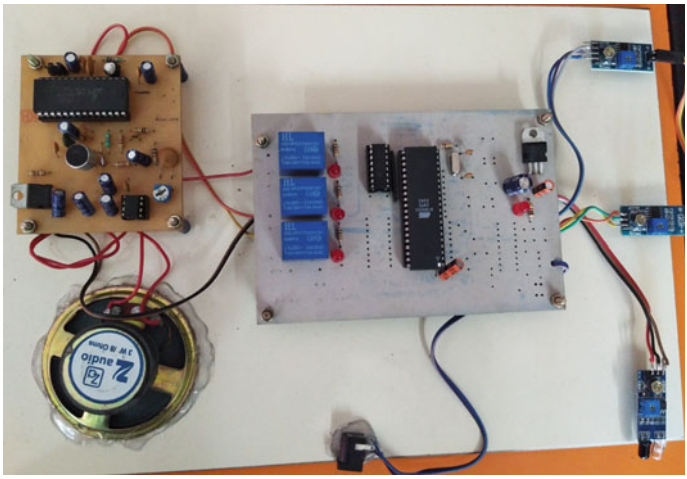

Fig. 4 APR33A, the sensor interface part

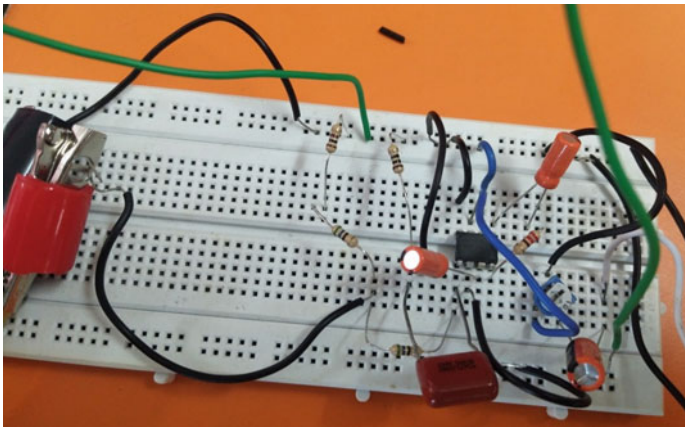

Fig. 5 Transmitter circuit

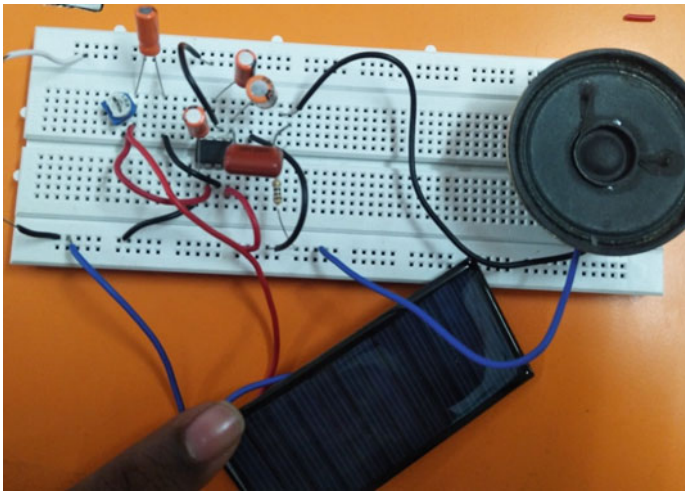

Fig. 6 Receiver circuit

5 Conclusion and Future Scope

We created a prototype of an FSO-based disaster management system in this article. Three sensors were used to identify natural disasters like earthquakes and floods: An infrared temperature sensor, a piezoelectric sensor, and raindrop sensors. Using a LASER source, the detected information is transmitted as voice messages over free space. This transmitted data is processed and amplified by a solar panel before being sent to a speaker as part of a public announcement system. Furthermore, due to the vast capacity of a free space optical communication system, medical emergency reports may be transmitted to doctors and hospitals for immediate care.

References

1. Zhu X, Kahn JM (2002) Free-space optical communication through atmospheric turbulence channels. IEEE Trans Commun 50(8):1293–1300
2. Farid AA, Hranilovic S (2007) Outage capacity optimization for free-space optical links with pointing errors. J Lightwave Technol 25(7):1702–1710
3. Sharma M, Chadha D, Chandra V (2016) High-altitude platform for free-space-optical communication: performance evaluation and reliability analysis. IEEE/OSA J Opt Commun Networking 8(8):600–609
4. Sakhardande P, Hanagal S, Kulkarni S (2016) Design of disaster management system using IoT based interconnected network with smart city monitoring. In: 2016 international conference on Internet of Things and applications (IOTA). IEEE

5. Mase K (2012) Communication service continuity under a large-scale disaster: providing a wireless multihop network and shelter communication service for a disaster area under the Great East Japan Earthquake. In: 2012 IEEE international conference on communications (ICC). IEEE
6. Wang X, Cheng G (2018) Design and implementation of universal city disaster recovery platform. In: 2018 2nd IEEE advanced information management, communicates, electronic and automation control conference (IMCEC). IEEE
7. Mase K (2011) How to deliver your message from/to a disaster area. IEEE Commun Mag 49(1):52–57
8. Vigneshwaran S, Muthumani I, Sivanananthа Raja A (2013) Investigations on free-space optics communication system. In: 2013 international conference on information communication and embedded systems (ICICES). IEEE
9. Jasmine S, Robinson S, Malaisamy K (2015) Investigation on free-space optical communication for various atmospheric conditions. In: 2015 2nd international conference on electronics and communication systems (ICECS). IEEE
10. Saraf AK et al Detecting Earthquake Precursor: A Thermal Remote Sensing Approach, geospatial world. https://www.geospatialworld.net/article/detecting-earthquake-precursor-a-thermal-remote-sensing-approach/
11. Jeyaseelan J, SriramKumar D, Caroline BE (2020) Disaster management using free space optical communication system. Photonics Network Commun 39(1):1–14

Vision-Based Assistive Systems for Visually Impaired People: A Review

Sandeep Mandia, Ashok Kumar, Karan Verma, and Jitendra Kumar Deegwal

Abstract This research reviews the current state of vision-based assistive solutions for the visually impaired (VI). The paper focuses primarily on camera-based assistive system solutions. We focused the review on vision-based assistive solutions proposed for VI people. The sensors, image processing algorithms, and wireless communication protocols employed in the survey have been summarised. Acoustic output devices were used in addition to cameras, Radio Frequency Identification (RFID), and Global Positioning System (GPS). Vision-based assistive solutions have evolved from traditional image processing techniques to machine learning to deep learning for assistance for VI users. Wi-Fi and Bluetooth devices are the most common wireless technologies used by vision-based assistive systems. The literature does not adequately leverage the optimization of deep learning models for edge devices.

Keywords Visually impaired people · Vision-based assistive systems · Wireless technologies

1 Introduction

A significant population in the world is visually impaired. As per World Health Organization (WHO) world report on vision published in 2019, at least 2.2 billion people are visually impaired [1]. It becomes challenging for the person with a vision disability to do their chores. The vision-impaired condition makes the person's life

S. Mandia (✉) · A. Kumar
Department of Electronics and Communication Engineering, Government Mahila Engineering College, Ajmer 305002, India
e-mail: smandia20@gmail.com

K. Verma
Department of Computer Science and Engineering, National Institute of Technology, Delhi 110040, India

J. K. Deegwal
Department of Electronics Instrumentation and Control Engineering, Government Engineering College, Ajmer 305025, India

M. Tiwari et al. (eds.), *Optical and Wireless Technologies*, Lecture Notes in Electrical Engineering 892, https://doi.org/10.1007/978-981-19-1645-8_17

dependent on a caregiver. That is very expensive and difficult in this fast-moving world.

According to a study, visually impaired people face falls, traffic-related injuries, and occupational injuries [2]. People with reduced visual acuity are 1.7 times more prone to fall and 1.9 times more prone to multiple falls than those with full sight. A hip fracture is between 1.3 to 1.9 times more likely for persons with visual impairment than an average person. As per another study [3], 15% of people with vision disability collide obstacles every month on average, and 40% of people with vision disability fall every year because they hit obstacles. In particular, aerial obstacles, such as awnings, tree branches, and similar objects typically have no projection on the ground or floor [4]. Visually impaired people are generally facing two types of dangers. One is a collision with aerial obstacles in the front and the second fall. Addressing these problems can prevent mishappening.

Traditionally white stick and guide dogs are used to provide guidance when visually impaired people go out independently. The aerial obstacle cannot be localized using the white stick or guide dog. The solution to these problems is to have an assistance system that gives information regarding aerial or ground obstacle well in advance to the visually impaired person so that s/he can protect self from the obstacle. There is much scope in the improvement of the assistance system for visually impaired people. There have been various smart assistant systems proposed by researchers from different parts of the globe that address ground obstacle avoidance. There are solutions in which addresses both aerial and ground obstacle avoidances have.

A general approach towards vision-based assistive systems includes processing of camera input using image processing-based algorithms. The processed output and other outputs from other sensors are used for decision-making; based on this, the VI user receives feedback. Figure 1 shows a generalized approach to the vision-based assistive system for VI users. The processing includes feature extraction from the frames capture by the camera. The decision making utilizes a basic thresholding technique to a sophisticated machine learning or deep learning-based approach. The VI user receives feedback based on the decision made through various means.

As the camera mimics the task performed by the human eye, vision-based assistive systems are most suitable for assistance to VI people. The advancement in the

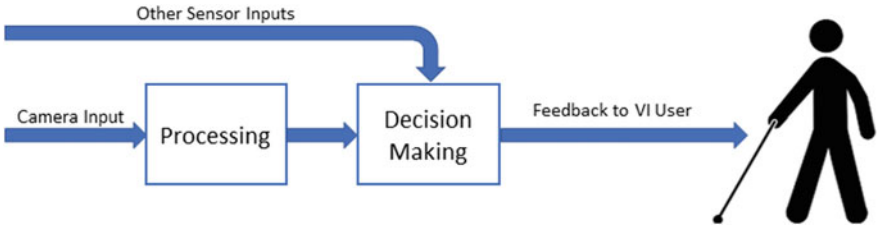

Fig. 1 A general approach to the vision-based assistive system

development of algorithms and extensive use of deep learning in computer vision further makes it a promising candidate for the solution.

The remainder of the paper is organized as follows: Sect. 2 discusses the literature review of the existing vision-based solutions for visually impaired people based on sensors, processing techniques, and wireless communication techniques. Section 3 concludes this paper with future directions for the said problem.

2 Investigation of AI-Based Vision Assistive System for VI People

A mobile camera-based solution for visually impaired people is reported [5] for indoor Fig. 2(a). The pre-defined paths were marked with colour tapes, and the mobile camera was used to track the path. Extended Kalman Filter (EKF) and Weighted Moving Average Filter (WMA) are used to overcome optical flow errors. Arianna is a framework for determining a safe walking path in interior environments. The solution is based on a video camera incorporated inside a smartphone device at the hardware level. The user feedback is positive. Vibration patterns are used to transfer information. A series of interest locations, denoted by arrows, are used to design the walking path. QR codes can be scanned, or a path on the floor can be followed.

It [6] introduced a new marker-based technique called mobile vision (MV). The technology is incorporated on a smartphone device in an indoor context and uses special colour markers Fig. 2(b). The user is directed via red, green, and blue colour markers to locate interesting sites, such as restrooms, elevators, or exits. Feedback messages are delivered via text-to-speech transcripts.

The Smart Vision navigation framework is presented in [7], which combines GPS, Wi-Fi localization with GIS (Geographic Information System) [8], passive RFID tags, and computer vision algorithms for outdoor scenarios. The system is not intended to replace the white cane but rather to supplement it by alerting the visually impaired (VI) user to impending dangers. Here, a database with prospective objects of interest (e.g., elevator, welcome desk, plants, cash machine, and telephone booth) is being created Fig. 2(c). The reference images stored a priori are sought among video frames captured by the camera during the test. The approach, however, is extremely sensitive to camera movement and is strongly reliant on the amount of the training sample. Furthermore, it experiences adaptability issues, since for a bigger dataset with various objects of interest, the computational time increments fundamentally.

A deterrent location and order strategy totally coordinated on a standard cell phone is presented in [9] that is more, reached out in [10] Fig. 2(e). The framework is intended to work with the VI client route in both indoor and open-air conditions. In [9], creators propose distinguishing the block's area by extricating interest focuses that are followed between progressive casings utilizing the standard Lucas-Kanade

Fig. 2 Vision-based assistive systems reported for VI users [5–21]

algorithm Fig. 2(d). The object's movement is recognized from the camera development with the assistance of many homographic changes grouped by applying the Random sample consensus (RANSAC) calculation [11]. The identified objects are additionally arranged by joining the Histogram of Oriented Gradients (HOG) descriptor into a Bag of Visual Words (BOW) portrayal. Even though the framework generally returns great outcomes, it can't identify huge, level designs or effectively gauge the distance between the VI client and a check. In [10], the creators proposed addressing the previously mentioned constraints by coordinating ultrasonic sensors inside the framework. The methodology shows promising outcomes; however, it demonstrates to be delicate when various moving obstructions are available in the scene.

In [12], a computer vision-based way-finding technology is suggested that helps independent access to indoor but unfamiliar locations Fig. 2(f). The system consists of a camera, microphone, computer, and Bluetooth earpieces on the hardware level. The framework uses a geometric design mixed with a corner and edge recognition method to detect doors, elevators, and cabinets. The system may then discriminate between foreground and background objects using an optical character recognition approach. A Canny edge detector is utilized for the detection of doors and Optical Character Recognition for text classification.

A system proposed in [13] includes a module for identifying textiles Fig. 2(g). Four clothing textures can be distinguished using a new Radon Signature descriptor: Plaid, striped, patternless, and irregular and eleven clothing colours. Although both modules were created with individuals with disabilities in mind, no studies or tests with actual VI users have been conducted too far. Furthermore, the framework is incapable of handling object occlusion or operating in real-time.

Developments in the Crosswatch system for providing guidance to visually impaired travellers at traffic intersection is discussed, and also new functionalities are described [14] Fig. 2(h). The panoramic image processing was used for the analysis of the crossroad view. The VI user captured the panoramic image of the viewpoint by rotating the camera for 360°. Another traffic light recognizer is proposed to detect traffic light signals for VI users [15] Fig. 2(i). The Active Optical Unit (AOU) is extracted from the image captured, and based on the AOU, the distance between VI users and the traffic light is calculated.

ShopMobile II has been proposed for supermarket grocery shopping for VI users [16]. The navigation is based on the barcode scanner on the products in the supermarket. The barcode localization and decoding are done by using computer vision algorithms. The localization of the barcode is based on the number of zero to one and one to zero transitions on two horizontal lines on the image.

Molina et al. proposed the use of visual nouns for VI user navigation in both indoor and outdoor situations in [17]. The system generates mosaic images, which are then used to help the VI navigate around streets and corridors. Signage, visual text, and visual icons are considered visual nouns. However, a number of open conditions must be met for the system to be beneficial to VI people: (1) development of an appropriate human-machine interface; (2) integration into a wearable assistive device; and (3) development of an acoustic or haptic interface.

Another system for VI people is proposed utilizing a smartphone camera to capture panoramic images and a Graphic Processing Unit (GPU) server to extract features from an image or a short video [18] Fig. 2(j). The modelling of images was done by converting the image into the HSI colour model and then taking the projection of H, S, I and gradients to calculate the Omni-projection. The Fast Fourier Transform (FFT) of the normalized projection curves was taken. In the query stage, the frame is processed the same and compared with all the modelled images. The closest matching frame is obtained using phase curves of the Omni-directional images. The use of multi-core CPUs or GPUs is proposed for enhancing computational speed.

A robust banknote recognition system is proposed based on computer vision for blind people [19] Fig. 2(k). The banknote dataset was collected in various circumstances and labelled with note values. The Speeded Up Robust Features (SURF) have been utilized for matching for banknotes. The authors claim to have achieved 100% true recognition and 0% false recognition rate. Similarly, another smartphone-based USA currency note recognition system was proposed [20] Fig. 2(l). The system utilizes the Principal Component Analysis (PCA) based image recognition method, Eigenfaces, to recognize currency notes. The authors have achieved a 99.8% of accuracy rate and 7 frames per second processing speed. The processing was done on a Grayscale image that was converted from an RGB image [20]. Another mobile application based Indian currency note recognition system is proposed [21] Fig. 2(m). A median filter and histogram equalization are utilized for noise removal and image enhancement. Morphological operations are performed for feature extraction, and these features are used for currency note matching and recognition.

A vision-based system is proposed for VI users during walking, jogging, and running [22] Fig. 2(n). The system utilizes image processing for lines and lane detection on the road in the outside environment. The system uses a camera and haptic gloves for feedback. The haptic gloves were fitted with vibration motors, and the commands to the VI user were encoded in the form of sequences of vibration in the haptic gloves. The extraction is done by using probabilistic Hough Line Transform.

The Charge Coupled Device (CCD) camera-based assistance gadgets have been more convenient and comfortable to manage than sensory systems. However, when estimating the real distance between the VI user and a detected obstacle, these solutions have low accuracy. Any monocular system has the drawback of being unable to determine the global object scale only on a frame. The concern is exacerbated when dealing with outdoor environments since scale drifts between map sections and their projected motion vectors are more common [23].

The E-vision system is proposed for VI users for three distinct daily activities: Supermarket visit, public administration Building visit, and outdoor walk [24] Fig. 2(o). The system exploits the classification and Optical Character Recognition (OCR) for supermarket visits, OCR and object detection & face and emotion recognition for administrative building visits, and face recognition & text-to-speech conversion techniques for outdoor environments.

A Convolutional Neural Network (CNN) based wearable travel system for VI users for indoor and outdoor environments has been proposed [25]. The system is capable of providing environment perception and navigation for VI users. The system utilizes an Inertial Measurement Unit (IMU) for the acquisition of the altitude angle of the camera. A smartphone is utilized for position acquisition, navigation, object detection, and acoustic feedback to the VI user. A lightweight CNN based PeleeNet [26] object detection model trained on the MS COCO dataset has been used in the system. Another similar deep earning based wearable assistive system for VI users to enhance the environment perception has been proposed [27]. The CNN-based segmentation and obstacle avoidance system is proposed that utilizes CPU and GPU computation power for real-time performance. The smartphone is utilized for touch

Table 1 Summary of vision-based assistive systems for VI users

Ref. No.	Sensors	Image processing techniques	Wireless communication	Remarks
[5]	Mobile camera	Optical Flow with EKF and WMA	–	Pre-defined area for movement
[6]	Mobile Camera, Acoustic signal	Distance-based one-class-classifier	–	Manual installation of markers
[7]	Camera, RFID, GPS	SURF (Speeded Up Robust Features)	Wi-Fi	It covers both indoor and outdoor
[9]	Camera	Lucas-Kanade Algo, Bag of Visual Words (BoVW)	–	It covers both indoor and outdoor
[10]	Camera, Ultrasonic sensors, Microphones	Support Vector Machine with Aggregated Descriptors	Bluetooth	Use of two sensors for detection
[12]	Camera, Microphone	Canny Edge Detector, OCR	Bluetooth	It covers only indoor environments with few detections
[13]	Camera, Microphone	Wavelet sub-band, Random Signature Descriptor	Bluetooth	For clothing pattern detection, not for movement assistance
[14]	Camera, Microphone, GPS, GIS	Panoramic image processing	–	Covers only outdoor environment
[15]	Camera, Accelerometer, Gyroscope	AOU detection	–	Specific to traffic light application in the outdoor environment
[16]	Mobile camera	Computer vision algorithm	–	Shopping assistance
[17]	Camera	Computer vision algorithm	–	It covers both indoor and outdoor
[18]	Smartphone camera, omnidirectional lens (GoPano)	HSI model, Omni-projection curves, FFT	–	Addresses only indoor environment
[19]	Camera	SURF	–	Confined to banknote detection
[20]	Smartphone camera, Acoustic output	PCA based eigenfaces algo	–	Confined to banknote detection

(continued)

Table 1 (continued)

Ref. No.	Sensors	Image processing techniques	Wireless communication	Remarks
[21]	Smartphone camera, Acoustic output	Median Filter, Morphological operation, Histogram equalization	–	Confined to banknote detection
[22]	Camera, Haptic Glove	Thresholding, Probabilistic Hough Line Transform	Bluetooth Low Energy	Addresses outdoor environment specific to a track
[24]	Camera, Acoustic output	OCR, Object detection, Face & emotion recognition	Wi-Fi	Addresses only indoor environment
[25]	Camera, IMU, Smartphone	PeleeNet, text to Speech, Speech Recogniser	–	Covers both indoor and outdoor with deep learning-based object detection model
[27]	Camera, Acoustic output, smartphone	FuseNet	Bluetooth	Covers both indoor and outdoor with deep learning-based segmentation model

interface to provide environmental information to the VI user. A CNN based FuseNet [28] has been utilized for the segmentation of captures image frames.

Table 1 summarises the literature based on sensors used, image processing techniques used for decision making, and wireless communication techniques used for feedback to the VI user.

3 Conclusion

In this research, a literature review of computer vision-based solutions for visually challenged people is presented. Table 1 shows the survey summary, categorizing the studies based on the sensors used, image processing algorithms used, and communication techniques used by the individual study. This study suggests that standard digital image processing techniques were used in the early days of computer vision-based assistive solutions for VI users, and machine learning and deep learning techniques recently. Wi-Fi and Bluetooth have been used in the majority of studies where wireless communication techniques have been used. Many assistive systems have used a simple camera, and others have used RFID, GPS, GSM, Ultrasonic sensor, sound output, and other technologies along with the camera. Researchers have begun to apply deep learning approaches for assistive solutions for VI users as machine learning, and deep learning techniques have grown with the arrival of good computation powers to machines. However, carrying computational power devices

for vision-based assistive solutions is inconvenient for VI users. The deep learning models may be optimized for edge inference using current optimization techniques. Quantization and layer pruning are part of the deep learning model optimization process. With the optimization of deep learning models for inference on edge devices, vision-based assistive solutions can be upgraded.

References

1. WHO W (2019) World report on vision. Geneva: World Health Organization; 2019. Licence: CC BY-NC-SA 3.0 IGO. World Health Organization
2. Legood R (2002) Are we blind to injuries in the visually impaired? A review of the literature. Inj Prev 8:155–160. https://doi.org/10.1136/ip.8.2.155
3. Manduchi R, Kurniawan S Watch Your Head, Mind Your Step: Mobility-Related Accidents Experienced by People with Visual Impairment, vol 11
4. Chang W-J, Chen L-B, Chen M-C et al (2020) Design and implementation of an intelligent assistive system for visually impaired people for aerial obstacle avoidance and fall detection. IEEE Sens J 20:10199–10210. https://doi.org/10.1109/JSEN.2020.2990609
5. Croce D, Giarre L, La Rosa FG, et al (2016) Enhancing tracking performance in a smartphone-based navigation system for visually impaired people. In: 2016 24th mediterranean conference on control and automation (MED), pp 1355–1360. IEEE, Athens
6. Manduchi R (2012) Mobile vision as assistive technology for the blind: an experimental study. In: Miesenberger K, Karshmer A, Penaz P, Zagler W (eds) Computers Helping People with Special Needs. ICCHP 2012. LNCS, vol 7383, pp 9–16. Springer, Heidelberg. https://doi.org/10.1007/978-3-642-31534-3_2
7. Du B, Barroso J (2011) The SmartVision navigation prototype for blind users
8. Kammoun S, Macé MJM, Oriola B, Jouffrais C (2012) Towards a geographic information system facilitating navigation of visually impaired users. In: Miesenberger K, Karshmer A, Penaz P, Zagler W (eds) Computers Helping People with Special Needs. ICCHP 2012. LNCS, vol 7383, pp 521–528. Springer, Heidelberg. https://doi.org/10.1007/978-3-642-31534-3_77
9. Tapu R, Mocanu B, Bursuc A, Zaharia T (2013) A smartphone-based obstacle detection and classification system for assisting visually impaired people. In: 2013 IEEE international conference on computer vision workshops, pp 444–451. IEEE, Sydney, Australia
10. Mocanu B, Tapu R, Zaharia T (2016) When ultrasonic sensors and computer vision join forces for efficient obstacle detection and recognition. Sensors 16:1807. https://doi.org/10.3390/s16111807
11. Lee J, Kim G (2007) Robust estimation of camera homography using fuzzy RANSAC. In: Gervasi O, Gavrilova ML (eds) Computational Science and Its Applications – ICCSA 2007. ICCSA 2007. LNCS, vol 4705, pp 992–1002. Springer, Heidelberg. https://doi.org/10.1007/978-3-540-74472-6_81
12. Tian Y, Yang X, Yi C, Arditi A (2013) Toward a computer vision-based way-finding aid for blind persons to access unfamiliar indoor environments. Mach Vis Appl 24:521–535. https://doi.org/10.1007/s00138-012-0431-7
13. Yang X, Yuan S, Tian Y (2014) Assistive clothing pattern recognition for visually impaired people. IEEE Trans Hum Mach Syst 44:234–243. https://doi.org/10.1109/THMS.2014.2302814
14. Coughlan JM, Shen H (2013) CrossWatch: a system for providing guidance to visually impaired travelers at traffic intersection. J Assist Technol 7:131–142. https://doi.org/10.1108/17549451311328808

15. Mascetti S, Ahmetovic D, Gerino A, Bernareggi C, Busso M, Rizzi A (2016) Supporting pedestrians with visual impairment during road crossing: a mobile application for traffic lights detection. In: Miesenberger K, Bühler C, Penaz P (eds) Computers Helping People with Special Needs. ICCHP 2016. LNCS, vol 9759, pp 198–201. Springer, Cham. https://doi.org/10.1007/978-3-319-41267-2_27
16. Kulyukin VA, Kutiyanawala A (2010) Demo: shopMobile II: eyes-free supermarket grocery shopping for visually impaired mobile phone users. In: 2010 IEEE computer society conference on computer vision and pattern recognition - workshops, pp 31–32. IEEE, San Francisco
17. Molina E, Zhu Z, Tian Y (2012) Visual nouns for indoor/outdoor navigation. In: Miesenberger K, Karshmer A, Penaz P, Zagler W (eds) Computers Helping People with Special Needs. ICCHP 2012. LNCS, vol 7383, pp 33–40. Springer, Heidelberg. https://doi.org/10.1007/978-3-642-31534-3_6
18. Hu F, Zhu Z, Zhang J (2015) Mobile panoramic vision for assisting the blind via indexing and localization. In: Agapito L, Bronstein M, Rother C (eds) Computer Vision - ECCV 2014 Workshops. ECCV 2014. LNCS, vol 8927, pp 600–614. Springer, Cham. https://doi.org/10.1007/978-3-319-16199-0_42
19. Hasanuzzaman FM, Yang X, Tian Y (2012) Robust and effective component-based banknote recognition for the blind. IEEE Trans Syst Man Cybern C 42:1021–1030. https://doi.org/10.1109/TSMCC.2011.2178120
20. Grijalva F, Rodriguez JC, Larco J, Orozco L (2010) Smartphone recognition of the US banknotes' denomination, for visually impaired people. In: 2010 IEEE ANDESCON, pp 1–6. IEEE, Bogota, Colombia
21. Manikandan K, Sumithra T (2015) Currency recognition in mobile application for visually challenged
22. Mancini A, Frontoni E, Zingaretti P (2018) Mechatronic system to help visually impaired users during walking and running. IEEE Trans Intell Transport Syst 19:649–660. https://doi.org/10.1109/TITS.2017.2780621
23. Tapu R, Mocanu B, Zaharia T (2020) Wearable assistive devices for visually impaired: a state of the art survey. Pattern Recogn Lett 137:37–52. https://doi.org/10.1016/j.patrec.2018.10.031
24. Kalaganis FP, Migkotzidis P, Georgiadis K et al (2021) Lending an artificial eye: beyond evaluation of CV-based assistive systems for visually impaired people. In: Antona M, Stephanidis C (eds) Universal Access in Human-Computer Interaction. Access to Media, Learning and Assistive Environments. HCII 2021. LNCS, vol 12769, pp 385–399. Springer, Cham. https://doi.org/10.1007/978-3-030-78095-1_28
25. Bai J, Liu Z, Lin Y et al (2019) Wearable travel aid for environment perception and navigation of visually impaired people. Electronics 8:697. https://doi.org/10.3390/electronics8060697
26. Wang RJ, Li X, Ling CX (2019) Pelee: a real-time object detection system on mobile devices. arXiv:180406882 [cs]
27. Lin Y, Wang K, Yi W, Lian S (2019) Deep learning based wearable assistive system for visually impaired people. In: 2019 IEEE/CVF international conference on computer vision workshop (ICCVW), pp 2549–2557. IEEE, Seoul, Korea (South)
28. Hazirbas C, Ma L, Domokos C, Cremers D (2017) FuseNet: incorporating depth into semantic segmentation via fusion-based CNN architecture. In: Lai SH, Lepetit V, Nishino K, Sato Y (eds) Computer Vision – ACCV 2016. ACCV 2016. LNCS, vol 10111, pp 213–228. Springer, Cham. https://doi.org/10.1007/978-3-319-54181-5_14

Secure Visible Light Communication Using ZCC Codes for the Underwater Communication

Ajay Yadav, Ashok Kumar, Rahul Mukherjee, Arjun Kumar, Jitendra Kumar Deegwal, and Ghanshyam Singh

Abstract In this research work, performance of spectral amplitude coding-optical code division multiple access (SAC-OCDMA) system is evaluated in presence of strong turbulence and different water types. The performance of the SAC-OCDMA system is good in presence of pure sea and clean ocean. Error probability of 10^{-3} is feasible with pure sea and clear ocean when the number of users is more than four with transmitted power of 30 dBm. For a four user SAC-OCDMA system, error probability of 10^{-3} is not feasible when the transmitted power is below 27 dBm (transmitted power eye safety limit is 27 dBm (500 mW)) in coastal water.

Keywords UWOC · 2D · ZCC · Gamma-Gamma · SAC-OCDMA

1 Introduction

With the advent of 5G communication, researchers are targeting high data rate, and low latency multiple access network in the underwater environment. Due to low data rate (10–100 kbps) and low speed (≈1500 m/s), acoustic communication systems will not be able to meet the requirements of 5G and 6G communication. The lower speed of acoustic signals causes high latency in the underwater long-distance communication. As a result, synchronization and decoding of multiple access techniques like optical code division multiple access (OCDMA) is affected. For 6G communication, wireless optical communication (WOC) is a promising solution in the underwater channel as compared to acoustic communication. The advantages of

A. Yadav (✉) · R. Mukherjee · A. Kumar
Department of Electronics and Communication Engineering, Bennett University, Greater Noida, Uttar Pradesh 201310, India
e-mail: ajayyadavbsz@gmail.com

A. Kumar · J. K. Deegwal
Department of Electronics and Communication Engineering, Government Mahila Engineering College, Ajmer, Rajasthan 305002, India

G. Singh
Department of Electronics and Communication Engineering, MNIT, Jaipur, Rajasthan 302017, India

M. Tiwari et al. (eds.), *Optical and Wireless Technologies*, Lecture Notes in Electrical Engineering 892, https://doi.org/10.1007/978-981-19-1645-8_18

WOC over acoustic communication are high data rate, better security, and very low latency. Although WOC is superior to acoustic communication in few performance parameters, it suffers from attenuation and turbulence in the underwater channel. Attenuation and turbulence affect the performance in the underwater environment by limiting the distance of communication up to few meters [1].

For the multi-user communication system, OCDMA is very useful due to asynchronous access, security, and good performance during heavy data traffic. Spectral amplitude coding-OCDMA (SAC-OCDMA) is considered for this evaluation for the underwater channel due to zero multiple access interference (MAI). Various codes like modified quadratic congruence (MQC) codes, double weight (DW) code family, Khazani-Syed (KS) code, random diagonal (RD) code, etc. have been reported in literature [2]. The performance of the code improves with increase in code-weight. Depending up on the code weight, the various codes can be used for multimedia services like voice, video, and data transmission. In this work, double weight multi-diagonal (DW-MD) code is used in SAC-OCDMA system. The performance of the SAC-OCDMA system is evaluated in the moderate and strong turbulence regimes along with the attenuation due to different water types. Pure sea, clear ocean, and coastal water have attenuation coefficients of 0.056, 0.15 and 0.305 m^{-1}, respectively [3]. The research is organized into various Sections as: Sect. 2 describes the UWOC SAC-OCDMA system. The mathematical analysis of SAC-OCDMA system and effect of various parameters on error probability is studied in Sect. 3. The results are discussed in Sects. 4.

2 SAC-OCDMA System

The block diagram of SAC-OCDMA system is shown in Fig. 1. The incoherent source like LED or broadband laser emits broad spectrum which is fed to the encoder. In the encoder, chip sequence of the DW-MD code is assigned, and different wavelengths

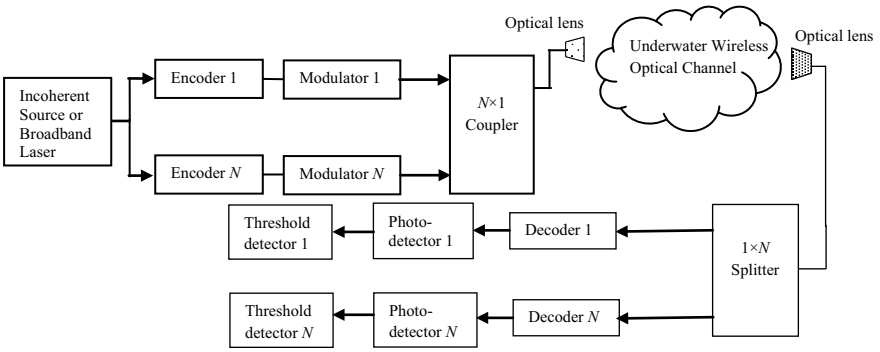

Fig. 1 Underwater wireless optical communication SAC-OCDMA system

are allocated to the chip sequence. External modulator like Mach-Zehnder modulator is used after the encoder to modulate the encoded signal [2]. Further, the modulated data bits are combined using $N \times 1$ coupler and transmitted via optical lens. The optical lens collimates the optical signal to avoid beam divergence. The transmitted signal undergoes attenuation and fading in the underwater channel. At the receiver, the data bits are recovered using splitter, decoder, photodetector and threshold detector.

3 Channel Modeling

When the optical signal is transmitted from the optical lens then the beam diverges. The spreading of the optical signal around the transmitter optical lens is called beam divergence. The optical signal absorption and scattering along with the beam divergence is well explained by Beer-Lambert's law which is given by [4].

$$\beta = \frac{A}{\pi\left(\frac{\varphi_s L}{2}\right)^2} e^{-\gamma l} \tag{1}$$

where A is the receiver aperture area, ϕ_s the beam divergence angle (in radian), l the link length (meters), and γ represents the attenuation factor (m^{-1}), respectively.

In the underwater channel, the impact of turbulence is also present along with the beam divergence, absorption and scattering. At few places, the effect of turbulence is very prominent. To study the effect of strong turbulence in the underwater channel, gamma-gamma probability density function (pdf) model is used in this research work. Gamma-gamma pdf is described as

$$f_X(x) = \frac{2(\alpha\beta)^{\frac{\alpha+\beta}{2}}}{\Gamma(\alpha)\Gamma(\beta)} x^{\frac{\alpha+\beta}{2}-1} \mathrm{K}_{\alpha-\beta}\left(2\sqrt{\alpha\beta x}\right) \tag{2}$$

Here α and β are small- and large-scale eddies, respectively. $\Gamma(.)$ is the gamma function, and $K_n(.)$ is the modified Bessel function of second kind. For DW-MD code, when w is the code weight, and N is the number of users supported then code length (L) is wN. The received power P_R is given by [4].

$$P_R = \beta \frac{P_T w}{NL} \tag{3}$$

where P_T is the transmitted power. The number of photons absorbed per chip time is [5].

$$\lambda_s(x) = \frac{\eta x P_R}{hf} \tag{4}$$

The various parameters in Eq. (4) are quantum efficiency η, Planck's constant h and average optical frequency f. The output of APD for data bit "1" can be represented with Gaussian conditional pdf as given by

$$f_{Y1}(y|x, b = 1) = \frac{1}{\sqrt{2\pi\sigma_1^2(x)}} \exp\left(-\frac{(y - \mu_1(x))^2}{2\sigma_1^2(x)}\right) \tag{5}$$

The mean and variance for data bit "1" is defined as

$$\mu_1(x) = GT\left[w\lambda_s(x) + L\left(\lambda_b + \frac{I_b}{e}\right) + (wN - w)\lambda_s(x)/M_e\right] + LTI_s/e \tag{6}$$

and

$$\sigma_1^2(x) = G^2FT\left[w\lambda_s(x) + L\left(\lambda_b + \frac{I_b}{e}\right) + (wN - w)\lambda_s(x)/M_e\right] + \frac{LTI_s}{e} + L\sigma_{Th}^2 \tag{7}$$

Similarly, the conditional output pdf for data bit "0" is illustrated as

$$f_{Y0}(y|x, b = 0) = \frac{1}{\sqrt{2\pi\sigma_0^2(x)}} \exp\left(-\frac{(y - \mu_0(x))^2}{2\sigma_0^2(x)}\right) \tag{8}$$

The mean and variance for data bit "0" is given by

$$\mu_0 = GT\left[L\left(\lambda_b + \frac{I_b}{e}\right)\right] + LTI_s/e \tag{9}$$

and

$$\sigma_0^2 = G^2FT\left[L\left(\lambda_b + \frac{I_b}{e}\right)\right] + \frac{LTI_s}{e} + L\sigma_{Th}^2 \tag{10}$$

The various parameters used in the Eqs. (6, 7, 9 and 10) are APD gain G, photons due to background noise λ_b, bulk leakage current I_b, surface leakage current I_s, extinction ratio M_e, excess noise factor F_e, and thermal noise per chip ${\sigma_{Th}}^2$, respectively. The intensity modulation and direct detection (IM/DD) error probability is given as

$$P_e(x) = \frac{1}{2}\left[Q\left(\frac{\mu_1(x) - Th}{\sigma_1(x)}\right)\right] + \frac{1}{2}\left[Q\left(\frac{Th - \mu_0}{\sigma_0}\right)\right] \tag{11}$$

The average probability of error P_E is

$$P_E = \underset{Th}{Min} \int_0^{\infty} P_e(x) f_X(x) dx \tag{12}$$

Gamma-Gamma pdf $f_x(x)$ and brute search algorithm is used to minimize the probability of error with respect to receiver threshold *Th*.

4 Results and Discussion

The performance of the SAC-OCDMA system is evaluated in the presence of strong turbulence and various water types. The receiver aperture diameter is 5 cm, link length is 20 m, and beam divergence angle is 12 mrad in the analysis. For mathematical simplicity, the average wavelength of 532 nm is used from the visible light spectrum. Also, the attenuation is less in the water at this wavelength. Figure 2 shows the variation of error probability with transmitted power in the underwater channel. The performance of four user SAC-OCDMA system is best in the pure sea and deteriorates in the clear ocean and coastal water. For $P_E = 10^{-3}$, the transmitted power P_T is 19, 27 and 40 dBm for pure sea, clear ocean, and coastal water, respectively. The increase in transmitted power decreases the error probability.

For $P_T = 30$ dBm, the error probability is varied with the number of users (N) as shown in Fig. 3. For $P_E = 10^{-3}$, 5 and 11 users are required in clear ocean and coastal water when $P_T = 30$ dBm. In presence of coastal water, it is not feasible to obtain $P_E = 10^{-3}$ irrespective of transmitted power for $N \geq 4$. The increment in

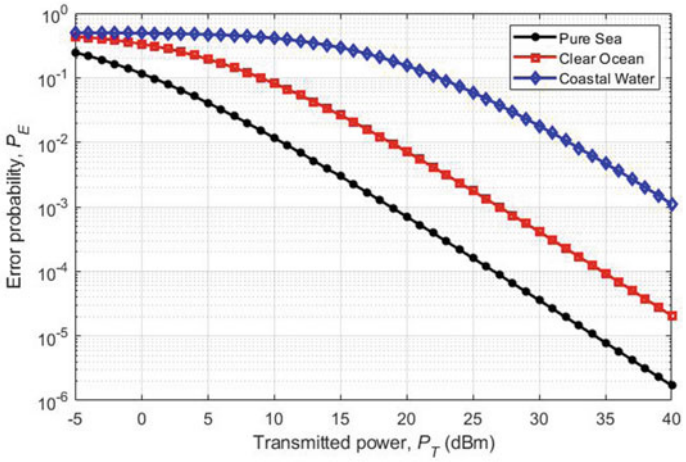

Fig. 2 Error probability versus transmitted power of SAC-CDMA system in the underwater channel

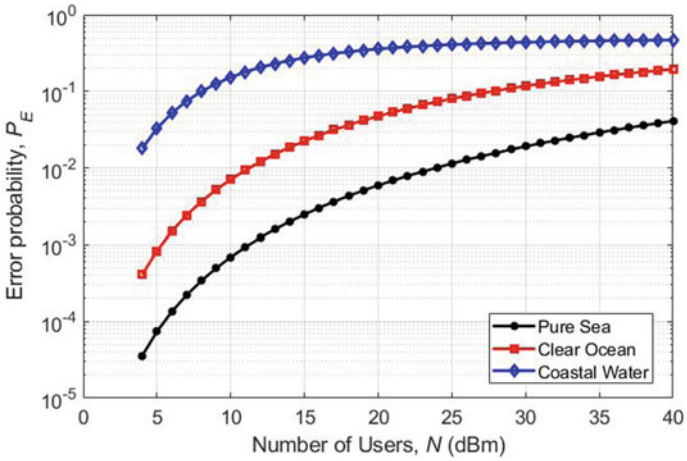

Fig. 3 Error probability versus number of users of SAC-CDMA system in the underwater channel

the number of users increases P_E. For $P_E = 10^{-3}$, the number of users should be less than 5 and 11 at $P_T = 30$ dBm. The transmitted power above 27 dBm is also not eye safe. To obtain error probability less than 10^{-6}, performance enhancement techniques like aperture averaging, diversity techniques like multiple input multiple output (MIMO), forward error correction (FEC) can be used in the SAC-OCDMA system [6, 7]. Secure visible light communication can play very important role in 5G and 6G communication. It can be used as a secure mode of communication in boats, ships, and aircraft carriers.

5 Conclusion

In the underwater environment, SAC-OCDMA system is a secure communication with low latency, and large bandwidth. The performance of the SAC-OCDMA system in presence of strong turbulence and attenuation by different water types is studied. It has been analyzed that performance is good in presence of pure sea and clear ocean. With strong turbulence and coastal water, performance of the SAC-OCDMA system is very poor. Performance enhancement techniques like space diversity, time diversity and error correcting codes can improve the performance of SAC-OCDMA system.

Acknowledgements This work is the part of the TEQIP Collaborative Research Scheme under project grant ID 1-5727948610 funded by National Project Implementation Unit (NPIU), New Delhi, India.

References

1. Akhoundi F, Jamali MV, Hassan NB, Beyranvand H, Minoofar A, Salehi JA (2016) Cellular underwater wireless optical CDMA network: potentials and challenges. IEEE Access. 4:4254–4268. https://doi.org/10.1109/ACCESS.2016.2593398
2. Li H (2020) Development and performance improvement of a novel zero cross-correlation code for SAC-OCDMA systems. J Opt Commun 1–13. https://doi.org/10.1515/joc-2020-0086
3. Yadav A, Kumar A (2020) Performance analysis of underwater 2D OCDMA system. In: Janyani V, Singh G, Tiwari M, Ismail T (eds) Optical and Wireless Technologies. LNEE, vol 648, pp 477–484. Springer, Singapore. https://doi.org/10.1007/978-981-15-2926-9_53
4. Yadav A, Kumar A, Deegwal JK, Singh G, Kumar A (2022) Channel capacity of underwater channel using OCDMA system. In: Tiwari M, Maddila RK, Garg AK, Kumar A, Yupapin P (eds) Optical and Wireless Technologies. LNEE, vol 771, pp 567–572. Springer, Singapore. https://doi.org/10.1007/978-981-16-2818-4_60
5. Yadav A, Kar S, Jain VK (2017) Performance analysis of wireless OCDMA multi-user system based on new 2-D code in presence of atmospheric turbulence and various weather conditions. In: 9th international conference on communication systems and networks (COMSNETS), Bengaluru, pp 109–115. https://doi.org/10.1109/COMSNETS.2017.7945365
6. Yadav A, Kar S, Jain VK (2018) Performance enhancement of double hard-limited 2D OCDMA system using aperture averaging and spatial diversity. IET Commun 13(5):583–593. https://doi.org/10.1049/iet-com.2018.5787
7. Chandhu SR, Jaiswal A (2021) Quantized feedback-based space shift keying in visible light communication. 2021 National Conference on Communications (NCC), pp 1–6. https://doi.org/10.1109/NCC52529.2021.9530033

Wireless Technology Contribution for Aviation Safety

Monika, Seema Verma, and Pardeep Kumar

Abstract Advanced wireless technologies are in more demand for the efficient and safe air travel. Increased air traffic congestion along with unpredicted weather conditions, poses lot of challenges for the safe air travels. Today's advanced wireless technologies could help us to achieve that required level of accuracy by providing better connectivity and communication among different airplanes and air-traffic control stations. In this paper, we have discussed various wireless technologies like 5G, Augmented Reality (AR), Aeronautical Mobile Airport Communication System (AeroMACS), Wireless Avionics Intra-Communications (WAIC), Internet of Things (IoT), System Wide Information Management (SWIM). After this study, we analyzed that each technology has its own capability and is able to transmit the data among different on board systems in the plane and air traffic control systems on the ground. These technologies are going to play a key role to improve the communication among ground controllers and other aircraft.

Keywords Wireless technologies · Aviation safety · 5G · IoT · Augmented reality · Aeronautical Mobile Airport Communication System · Wireless Avionics Intra-Communications

1 Introduction

For safe and effective airline operations, new wireless communication techniques and technologies are required. Wireless technologies are becoming increasingly signifi-

Monika (✉)
Department of Computer Science, Banasthali Vidyapith, Jaipur, India
e-mail: mor.monika@gmail.com

S. Verma
Department of Electronics, Banasthali Vidyapith, Jaipur, Rajasthan, India

P. Kumar
Department of Electronics and Communication Engineering, SGT University, Gurugram, Haryana, India

M. Tiwari et al. (eds.), *Optical and Wireless Technologies*, Lecture Notes in Electrical Engineering 892, https://doi.org/10.1007/978-981-19-1645-8_19

cant in aviation. For safe flights, the National Aeronautics and Space Administration (NASA) is trying to improve hyper spectral communications, air traffic controlling and networking schemes. On-board aviation control and communications data are critical for aircraft monitoring and safety. The airplanes should be connected to ground airport tracking and monitoring systems, where several measurements of these aircraft subsystems should be sent for analysis during flight to reduce flight accidents or the likelihood of any on-board subsystem failures [3]. Wireless communication is being investigated for use in the aerospace sector to replace various cable connections since it offers a number of benefits, including low weight, resilience, system maintenance, ability to expand, modularity and lesser cost [6, 7, 22]. Wireless on-board communications systems are gaining traction in the aerospace industry, with the goal of improving flight safety, lowering aircraft costs, and reducing environmental impact. However, there are other concerns, including security, coexistence, navigation, surveillance, engine performance, air-to-ground communication and aircraft-to-aircraft communication as shown in Fig. 1. In complex missions and risky locations, this development in wireless technology is extremely valuable and mission-enhancing for army aircraft [14].

In aerospace, wireless applications range from in-flight entertainment (IFE), which requires a lot of multiuser, multimedia-grade bandwidth, to wireless sensing, command, control, and Prognostics Health Monitoring (PHM) systems, which demand a lot of reliability but not a lot of capacity. In addition, non interference with aircraft electronics, anti-jamming property, high level of security and a dedicated reserved frequency band are among critical requirements needed for emerging wireless applications in aerospace [23].

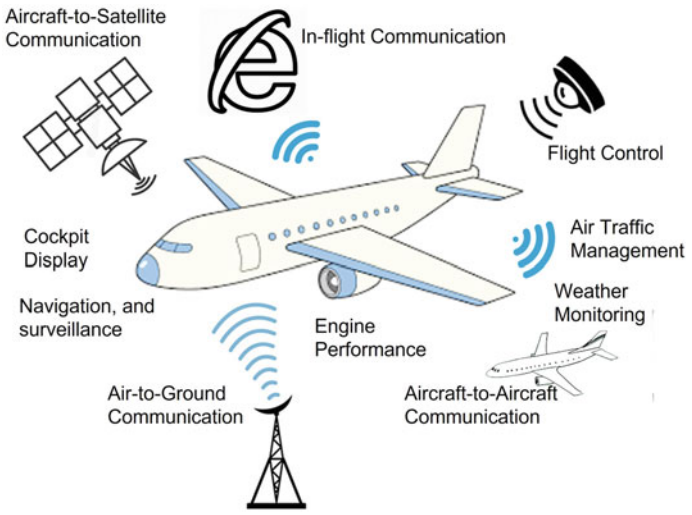

Fig. 1 Wireless technology in aviation

This research aims to provide an overview of associated wireless technologies which can be implemented for aircraft-safety essential applications.

Rest of the paper is organized as follows: Sect. 2 describes the wireless technologies suitable for aviation safety enhancement, Sect. 3 gives an overview of research challenges to be faced during implementation of these technologies and concluding remarks with future scope are given in Sect. 4.

2 Wireless Technologies for Aviation Safety

For its use, the wireless technological solutions should be cost-efficient and able to provide real time data transmission with more accuracy and security. There could be many challenges to the implementation of these solutions like design constraints, operational constraints and overall system cost. Those must be able to ensure safety of higher priority with the ability to detect the real time behavior of the aircraft of the aircraft and send the information to the control room ensuring minimum congestion in the wireless spectrum [16, 20].

2.1 5G

5G is an intangible but increasingly important technology in our life. The radio frequency spectrum underpins our dependency on wireless communications, and radio frequencies are critical for business, mobile phones, autonomous technologies, and aircraft. A prospective communication system based on 5G stratospheric platforms can provide efficient and increased communication performance, as well as be a cost-effective solution for constructing aviation communication networks [3, 9]. The Federal Aviation Administration (FAA) and NASA are carrying out some program like Integration Pilot Program to gain a better understanding of the safety argument for employing wireless networks for data exchange in low-altitude airspace [11]. COVID-19 is a watershed moment in aviation history, posing new challenges for airport stakeholders. Early adopters can use the rise of 4G private networks and 5G in aviation to limit pandemic risks and optimization hygiene practices at airports while lowering congestion and streamlining ground operations. 5G-enabled devices can help to promote preventative actions and best practices. Passenger tracking systems and flow management solutions (such as XOVIS), which are now used to measure queue times and handle capacity restrictions, can detect congested regions where social distancing has to be improved.

2.2 Wireless Augmented Reality (AR)

In the aviation industry, wireless augmented reality is seen as one of the necessary advances to ensure that processes are safe. In terms of safety, the aviation sector has come a long way. There is, however, still potential for development. The most critical areas that require improvement are pilot errors which accounts for 85% of all aircraft accidents [18]. These devices provide more advanced visualization, allowing the pilot to take the best decisions and ensure a safe and secure journey. By making use of AR, the pilots can have 360-degree view with virtual images to have clear visibility of the air traffic and other environmental changes. In terms of aircraft maintenance, AR offers real time information using 3D scanning and sensors. This proper maintenance of the aircrafts will result into setting the higher safety standards in aviation industry [2].

2.3 AeroMACS

AeroMACS, or Aeronautical Mobile Airport Communication System, is a wireless broadband system designed to assist airport communication. AeroMACS is a wireless technology that offers security, flexibility, scalability, and compatibility. It's utilized for ground-to-aircraft communications in Air Traffic Control (ATC) and Air Traffic Management (ATM) systems, as well as airline operations applications like Airline Operational Control (AOC) and other airport infrastructure applications. This technology is projected to improve safety and provide for the need for an effective broadband communication system to ensure secure and safe flight management, as well as give connectivity to A/C, operational support vehicles, and workers on the airport surface [5, 21].

2.4 Wireless Avionics Intra-Communications (WAIC)

For decades, wired technology has been used in the aerospace industry as a means of intra-unit communication. WAIC is a type of radio communication that allows two or more points on a single aircraft to communicate with each other. It uses low transmission power. WAIC has the potential to reduce aircraft wiring by 30% by using wireless devices to communicate data between aircraft systems that function for safety and regularity of flight over radio frequencies rather than wires. By eliminating electrical wire between aircraft systems, WAIC technology increases aircraft safety and efficiency. The implementation of WAIC system would result into reliable monitoring of the moving and rotating parts along with weight reduction and improving fuel efficiency due to reduction in complexity of the electrical wiring on the aircraft. The observation of behavior of moving parts includes keeping an eye

on brake conditions, tyre pressure, etc. The real time status of these functions is provided to the pilot for any required action in case of any failure. Other potential safety applications of the WAIC system include smoke detection, cabin pressure, emergency lighting, door sensors, engine sensors, humidity detection, flight control position feedback, etc. WAIC devices may be used to replace or supplement future applications that cannot be served by wires alone [10, 17].

2.5 IoT in Aviation Safety

This technology has changed the aviation industry in many ways. Specifically, this technology can provide support for regular monitoring of the aircrafts. This would result into more reliable and efficient operation of the aircraft with higher predictive and preventive maintenance. For a long time, the Internet of Things (IoT) has held immense potential, but the convergence of 5G, mature AI programmes, and the ubiquity of sensors embedded in lower-cost hardware is bringing this vision to reality. Today's aircraft are designed with large numbers of IoT sensors. These sensors can monitor pressure, temperature, vibration and other environmental measurements. After this, the whole computations can be streamlined to different supporting facilities on the ground for further analysis. This inspection would help in early detection of any deviation from the normal, unexpected variation and failure of any hardware. So, this predictive maintenance using IoT sensors can boost aviation safety standards. The Internet of Things (IoT) provides a network of data-producing devices and assets that communicate and boost airport efficiency. IoT could also be the connection that connects developing technologies in the aviation industry, allowing the digital era of aviation to completely thrive. Dysfunctional parts might be recognized in mid-flight and a signal sent to the ground, where a repair part could be quickly made and delivered to the repair station via an autonomous vehicle or drone [15, 19].

2.6 System Wide Information Management (SWIM)

In civil aviation, a new technology called System Wide Information Management (SWIM) allows for efficient and secure information sharing. This system is created to support NextGen Air Transportation System. This will revolutionize the data exchange to enable National Airspace System (NAS) innovations and operational excellence. SWIM was established by the FAA in 2007 to create an information-sharing platform and to offer a single access point for aviation data. It allows for the efficient integration of current air traffic monitoring systems, resulting in global services that are seamless. The concept's purpose is to create a platform for open data sharing among operators, airports, ANSPs, and meteorology services. The SWIM protocol provides a platform for any actor to design solutions based on a defined database of parameters that all subscribers can comprehend [13, 22].

3 Challenges with Wireless Technology for Aviation

Wireless technology has the ability to transform how our world connects and how quickly we interact online. The aerospace and defense sector is enthused about wireless potential to alter so many aspects of our life, but it must be implemented safely. Alarm bells have been sounding from reliable sources in recent years about how the deployment of wireless technology could significantly influence the safety of low-level aviation operations.

3.1 Radar Altimeters

This instrument is used to give an idea about height of the airplane above the ground to the pilot. The altimeter uses radio frequencies just above the 4 GHz band to measure the height of the aircraft and the ground. An altimeter is an essential instrument for takeoffs, landings, and low-altitude flying, as well as providing essential input to other systems like collision avoidance systems. There is a significant possibility that 5G communication systems operating in the 3.7–3.98 GHz range may interfere with radar altimeters on all types of aircraft planes and pilots were unaware of their distance from the ground due to a full altimeter malfunction [4].

3.2 Managing the RF Emissions of Consumer Electronics

When it comes to RF emission rules for consumer devices, the FCC currently does not consult with the FAA. This kind of collaboration would be ideal. If the predicted rise of wireless technology results in sufficiently serious interference concerns, then severe control measures may be required. The FCC, for example, might mandate wireless device manufacturers to incorporate override capability so that they can be switched off by a centrally broadcast control signal during key fight phases like takeoff and final approach.

3.3 Radio Interference

The term “radio interference” refers to a variety of situations in which transmissions from sources, other than authorized users of an RTF frequency, interfere with radio reception. Commercial radio stations on the ground frequently cause radio interference. Interference can make communication difficult, if not impossible, leading to communication breakdown. The workload on pilots and Air Traffic Control offices (ATCO) has also increased as a result of radio interference.

3.4 Security

Wireless networks are naturally vulnerable to security risks due to their broadcast nature. Data integrity and authentication are crucial parts of ensuring the aircraft's safety-critical functions. In the context of wireless-enabled avionics, security attacks were investigated using an adversarial model. Jamming attack, Man-in-the-Middle assault, and False alarm are the most common attacks for WAIC [16].

3.5 Reliability and Latency

To estimate and control the state of the aircraft, fight control systems rely on the network's high reliability and restricted latency. Noise generated by the avionics, multi-path from the walls, and interference from other aircraft, on the other hand, have a significant impact on the signal strength of avionics environments. The criteria for wireless aviation are more demanding than those for typical monitoring and open-loop control applications using industrial wireless networks in terms of reliability and timeliness [16].

3.6 Energy Efficiency

Another major challenge for wireless technology implementation is energy constraint. For flawless operation of any wireless technology, all the nodes must be able to operate for longer duration. However, the wireless nodes or devices are generally battery operated. Hence, there is a need to properly choose the energy resources to improve the overall efficiency of the system installed on the airplane. Furthermore, there will be a need to replace used batteries by the aircraft operators. This might be resulting in an increased overall cost of maintaining wireless nodes in comparison to nodes which are able to communicate by only using wireless mediums [8].

3.7 Natural Disturbing Factors

The aircraft might be operational in poor weather conditions and harsh environments. This could result in various temperature, humidity, air pressure conditions and solar activities. Wireless communications systems are generally highly vulnerable to natural disturbance factors in comparison to shielded wired communication systems. These natural disasters can be variations in atmospheric gases, various solar activities, lightning or thunderstorms and hydrometer activities. All these natural activities possibly deteriorate the transmitted signal quality [12].

4 Conclusion and Future Scopes

Safety is going to be the key factor behind the future success and growth of the aviation industry. In this paper, various existing wireless technologies for aviation safety have been discussed along with benefits and challenges. Advancements and developments in sensors and communication technologies are playing a big role in improving the overall implementation strategies of the aviation sector in the world. Now, it's time to develop more advanced wireless technologies to take the existing infrastructures to the next level by keeping in focus the safety of the passengers and staff. Lots of promising wireless technologies are available today but still further research is required to develop a specific wireless technology which can promise to be successful in terms of security, safety predictions, ability to deal with different environmental condition and communication range.

References

1. Home. https://waic.avsi.aero/about/benefits/
2. Benefits of augmented reality in commercial aviation, March 2018. https://www.goodworklabs.com/how-ar-can-help-in-improving-aviation-safety/
3. Albagory Y (2020) Modelling, investigation, and feasibility of stratospheric broadband mm-wave 5g and beyond networks for aviation. Electronics 9(11):1872
4. Ayre K (2021) Losing connections: 5g wireless technology and the potential risk for aviation. https://www.lexology.com/library/detail.aspx?g=7af7174e-f5c4-4cbf-82f5-5ba011cefed7
5. Bartoli G, Fantacci R, Marabissi D (2013) Aeromacs: A new perspective for mobile airport communications and services. IEEE Wirel Commun 20(6):44–50
6. Dalğıran Y (2018) Wireless communication for aircraft. https://www.linkedin.com/pulse/wireless-communication-aircraft-yasemin-dalgiran-mba
7. Dang DK, Mifdaoui A, Gayraud T (2012) Fly-by-wireless for next generation aircraft: challenges and potential solutions. In: 2012 IFIP wireless days. IEEE, pp 1–8
8. Dilhac JM, Bafleur M (2014) Energy harvesting in aeronautics for battery-free wireless sensor networks. IEEE Aerosp Electron Syst Mag 29(8):18–22
9. Dureja R, Rozier EW, Rozier KY (2017) A case study in safety, security, and availability of wireless-enabled aircraft communication networks. In: 17th AIAA aviation technology, integration, and operations conference, p 3112
10. Elliott K (2017) Development of wireless avionics intra-communications. https://interactive.aviationtoday.com/development-of-wireless-avionics-intra-communications/
11. Garrett-Glaser B (2020) What will 5g bring to the aviation industry? http://interactive.aviationtoday.com/what-will-5g-bring-to-the-aviation-industry/
12. Lin L, Chen X, Hu R, Zhao Z (2020) The refraction correction of elevation angle for the mean annual global reference atmosphere. Int J Antennas Propag 2020
13. Lootens KJB, Efthymiou M (2021) The adoption of network-centric data sharing in air traffic management. In: Research anthology on reliability and safety in aviation systems, spacecraft, and air transport. IGI Global, pp 127–151
14. Matti E, Johns O, Khan S, Gurtov A, Josefsson B (2020) Aviation scenarios for 5g and beyond. In: 2020 AIAA/IEEE 39th digital avionics systems conference (DASC). IEEE, pp 1–10
15. Muskan: 8 applications of IoT in aviation industry. https://www.analyticssteps.com/blogs/8-applications-iot-aviation-industry

16. Park P, Di Marco P, Nah J, Fischione C (2020) Wireless avionics intracommunications: a survey of benefits, challenges, and solutions. IEEE Internet Things J 8(10):7745–7767
17. Reji P, Shobha K, Kumar A, Karthik S et al (2020) Wireless intra-aircraft communication system. In: 2020 international conference on computer communication and informatics (ICCCI). IEEE, pp 1–5
18. Ruishan S, Lei W, Ling Z (2007) Analysis of human factors integration aspects for aviation accidents and incidents. In: International conference on engineering psychology and cognitive ergonomics. Springer, pp 834–841
19. Satair. https://blog.satair.com/iot-implementation-aviation-industry
20. Schmidt JF, Neuhold D, Bettstetter C, Klaue J, Schupke D (2021) Wireless connectivity in airplanes: challenges and the case for UWB. IEEE Access 9:52913–52925
21. Team EFY (2021). https://www.everythingrf.com/community/what-is-aeromacs
22. Team EFY (2018) New wireless technologies to help meet aviation demands. https://www.electronicsforu.com/technology-trends/tech-focus/wireless-technologies-help-aviation-demands
23. Zahmati AS, Fernando X, Kojori H (2011) Emerging wireless applications in aerospace: benefits, challenges, and existing methods. In: 2011 4th annual Caneus fly by wireless workshop. IEEE, pp 1–4

Comparing the Performance of ANFIS, LOG10-ANFIS and LOG10-PSO-ANFIS for Universal Theoretical Wireless Signal Propagation Prediction Modelling

Oteri Malack, Kibet Philip, and Kihato Peter

Abstract In the process of undertaking wireless signal propagation modelling, different methods have been used including deterministic and empirical models. This study is aimed at comparing the performance of predicting wireless signal propagation using Adaptive Neural Fuzzy Inference System (ANFIS), log10 distance (LOG10D)-ANFIS and LOG10D Particle Swarm Optimization (PSO) trained ANFIS for universal theoretical wireless signal prediction modelling. The last two being a modification of the original ANFIS. The predicted and target signal strength mean error (ME), root mean square error (RMSE) and standard deviation (SD) parameters were determined and compared. The study was undertaken using the one slope and two ray ground reflection models in the process of obtaining the data to be predicted. The obtained values were then used in the modeling process where it was found that the LOG10D-PSO-ANFIS model gave the closest prediction as compared to those of LOG10DANFIS and ANFIS models.

Keywords QoS · LOG10D · LOG10D-ANFIS · PSO · Wireless

1 Introduction

Wireless networks are becoming widely used. The line of sight (LOS) communication between the transmitter and the receiver are usually affected by a number of obstacles in both indoor and outdoor environments. The microwave and radiowave

O. Malack (✉) · K. Philip
Department of Telecommunication & Information Engineering, School of Electrical Electronics and Information Engineering, College of Engineering and Technology, JKUAT, Nairobi, Kenya
e-mail: omaeoteri@jkuat.ac.ke

K. Philip
e-mail: kibetlp@jkuat.ac.ke

K. Peter
Department of EEE, School of Electrical Electronics and Information Engineering, College of Engineering and Technology, Jomo Kenyatta University of Agriculture and Technology, Nairobi, Kenya
e-mail: pkihato@jkuat.ac.ke

M. Tiwari et al. (eds.), *Optical and Wireless Technologies*, Lecture Notes in Electrical Engineering 892, https://doi.org/10.1007/978-981-19-1645-8_20

spectra are the most commonly used based on electromagnetic spectrum. These two types of waves are affected by these obstacles since they don't penetrate through. Different ranges of power levels have to be used to enable the signals to cover longer distances depending on the type of technology used. Also, to try and increase the quality of service (QOS), various methods have been applied in modelling signal propagation. These methods include the traditional empirical one slope, dual slope, multiwall, Hata-Okumura among others. The current methods that include Artificial Neural Networks (ANN) and ANFIS, the most current technique, that combines neural networks and fuzzy logic that is used in function approximation besides other very many applications like classification [3]. In the process of training the ANFIS structure, a number of methods are used that include genetic algorithm and PSO which was originally done by Doctor Kennedy and Eberhart in 1995, and other AI processes. The PSO concept deals with the imitation of the intelligence of swarms or flocks as they move to a target as they search for food [9]. In this study, the prediction of received signal strength indication (RSSI) of wireless networks was done using ANFIS, LOG10-ANFIS and LOG10-PSO-ANFIS where the last two are based on modified ANFIS.

1.1 Statement of the Problem

Currently, the use of wireless communication networks is becoming ubiquitous in our lives both at home, work or even on the move. Various researchers have continued to look at the different methods that can be used to improve the quality of service (QoS) to take care of the growing demand. After going through most of these research findings, we thought it important to add to the contributions by undertaking this study. We used PSO trained ANFIS because it is many advantages that include high accuracy in function approximation and good computational efficiency in terms of resources. The ANFIS was modified to make it even more accurate in relation to RSSI prediction.

1.2 Research Objectives

Main objective;
To Compare the performance of PSO trained LOG10D-ANFIS, LOG10D-ANFIS and ANFIS in wireless signal prediction modelling.

Specific objectives

1. Obtain the RSSI with variation of distance using one slope and two-ray ground reflection models.
2. Obtain RMSE and graphical comparisons for the performance of PSO trained LOG10D-ANFIS, LOG10D-ANFIS and ANFIS.

2 Literature Review

2.1 Introduction

Wireless networking is a concept that uses radio and microwaves to transmit data from the source to a given destination. The source and destination are fitted with different types of wireless technologies that include Wi-Fi, Bluetooth, ZigBee for wireless local area networks (WLANS), antennas for cellular and radars for satellite communication systems. The antennas are very important components in relation all wireless communication related technologies since they are responsible for picking up incoming signals or radiating outgoing wireless signals [4, 5]. Depending on the device type these antennas can be mounted externally or embedded inside the device's hardware enclosure [2, 6]. In the process of designing for the optimum location of these communicating devices to ensure high QoS, the radio engineers need to use different models in predicting the wireless signal propagation. A number of methods have been used before and currently the artificial intelligence (AI) based methods seem quite promising. ANFIS is a very good example that blends the neural networks and fuzzy logic concepts into a powerful function approximation tool [3]. The training section is implemented using PSO which also very efficient and powerful in obtaining the optimal solution from the ANFIS. PSO, as indicated earlier, simulates the social behavior of swarms as they search for food like vultures moving to a carcass. This is achieved by using an algorithm that is based on common information of every particle (global) and the information owned by the particle itself (personal) [9]. This works in a way that all the particle positions are compared to pick the best according to the objective function.

2.2 Methods used in Signal Prediction

COST231 One-Slope Model

Empirical models are characterized by the use of empirical parameters obtained through thorough measurements done in a number of environments with similar or different features. The COST231 One-Slope model (OSM) is considered to be the simplest since it is based on the distance between the transmitter and the receiver without any obstacles along LOS. The only influence with respect to this is the decay factor usually obtained from the inverse square law [5]. Depending on the environment type, there are different types of obstacles. These obstacles affect the signal propagation based on the factor n which increases with increase in obstacle density resulting to higher levels of losses L(d) as represented in Eq. (1). For free space the factor n is given by 2.

$$L_{OSM} = (d_0) + n10\left(\frac{d}{d_0}\right) \tag{1}$$

where: L_{OSM}……..Predicted signal loss (dB)
$L_0(d_0)$……Signal loss at distance d from transmitter (dB)
n……..Power decay factor (–)
d……..Distance between antennas (m)
d_0…….Reference distance between antennas (usually 1 m) (m)

Two-Ray Ground Reflection Model
The two-ray ground reflection model (TRGRM) uses the 4^{th} power law together with antenna and base station heights. Its expression is given by;

$$L = L_o(d_0) + 10 \propto \log \frac{d}{d_0} - 20\log h_m - 20\log h_b \quad (2)$$

where,
$L_o(d_0)$ = Loss at a distance of 1 m
$\alpha = 4$ path loss exponent
d = distance between Tx and Rx
h_m = mobile station antenna height
h_b = base station antenna height

2.3 Artificial Neural Networks

According to [2] indoor radio propagation has a number of obstacles that include furniture, walls, floors and appliances while for outdoor environments foliage, hills, precipitation and dust are the main obstacles. All these obstacles will affect the way signals propagate. In modeling propagation, a number of parameters must be considered which include construction materials and permittivity of the other obstacles' materials, types of interiors, locations within a building and the location of transmitter and receiver antennas. Apart from traditional methods, artificial neural networks can be used in the process of wireless signal prediction. The system transforms the input in terms of various parameters that affect the signal level like distance, frequency and obstacles to a target output RSSI. The inputs will include the different obstacle parameters resulting one single output of received signal strength indication. These neural network-based models are evaluated using a number of parameters that include root mean square error (RMSE), mean error (ME) and standard deviation (σ) generated from the difference between the predicted and target values [12, 13].

2.4 Adaptive Neuro-Fuzzy Inference System (ANFIS)

Adaptive Neuro-Fuzzy Inference System (ANFIS), being a blend of Artificial Neural Network (ANN) and Fuzzy Logic (FL), was proposed in [7]. This combination results

to a very powerful system which takes advantage of the strengths of both and offsets their limitations. The ANN is made up of simple processing elements connected in series, parallel or combined form to manipulate data. The elements are used to mimic the biological nervous system of living organisms. The system functions are determined by elements' connectivity. A straight-line equation is used to model one neuron where the its output is compared with the target output to obtain the difference. This difference often referred to as the error is then used to vary the gradient (weight) and the y-intercept (bias) to reduce the difference to as minimum as possible. This is the basis on which the ANN works which is referred as computing with number. The Fuzzy Logic (FL) on the other hand deals with the concept of computing with words that refer to different levels not necessarily 0 and 1 [8]. For instance, when dealing with temperature one can use low, medium and high. This relates to the concept of fuzzy sets where inputs are transformed into a degree to which they belong to the fuzzy sets referred to membership functions [4]. The level of belonging ranges from 0 to 1. This also includes the use of a knowledge base where inferences are developed from based on the if then statements. Combining these two concepts brings with it the learning power of ANN and the knowledge base of fuzzy logic where observations are used to come up with inferences.

Basic ANFIS Architecture

Besides the other popular type 1 and 2, the ANFIS architecture described in this research is based on type 3 fuzzy inference system. This is characterized by the Takagi and Sugeno's (TKS) if-then rules [3]. In this case a constant term is added to the linear combination of the input variable to obtain the output with the final output being computed by taking the weighted average of each rule's output. The representation in Fig. 1 is a type 3 ANFIS architecture with two inputs x and y as well as one output, z. x can be distance and z is RSSI in the case of signal propagation modelling.

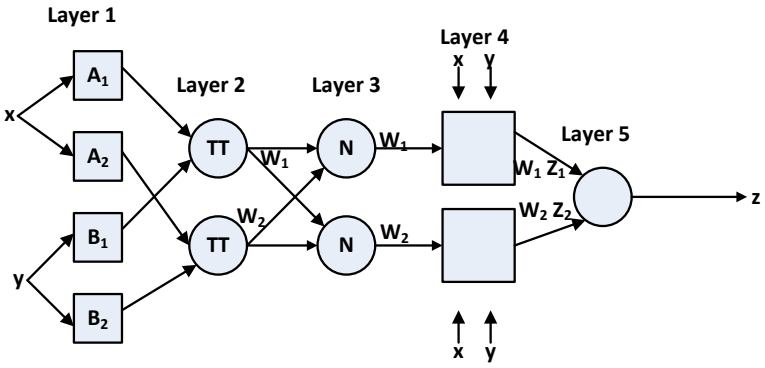

Fig. 1 Type 3 ANFIS architecture

Ordinary ANFIS

The ordinary ANFIS consists of the following rules.

Rule 1: *If x is* A_1 *and y is* B_1, *then* $z_1 = p_1x + q_1y + r_1$

Rule 2: *If x is* A_2 *and y is* B_2, *then* $z_2 = p_2x + q_2y + r_2$

The ANFIS structure is equivalent to the a supervised, feed-forward neural network consisting of five layers where one layer is input, three layers are hidden and one layer is the output layer. The functions of each layer are described below.

Layer 1 (Fuzzy Layer): In this layer all the nodes are adaptive whose function is to generate the membership grades of the input vectors. This process is referred to fuzzification. There are a number of membership functions that can be used but for this case the bell-shaped (Gaussian) function with maximum equal to 1 and minimum equal to 0 is used to implement the node function. Equation 3 describes the relation to transform the inputs generating the level of belonging between 0 and 1.

$$O_i^1 = f(x, a, b, c) = \mu_{Ai}(x) = \frac{1}{1 + |(x - c_i)/a_i|^{2b_i}} \qquad \mu_{Ai}(x) = \exp\left\{-\left[\left(\frac{x - c_i}{a_i}\right)^2\right]^{b_i}\right\} \quad (3)$$

where O_i^1 is the output of the i^{th} node in the first layer, $\mu_{Ai}(x)$ is the level of belonging of input x in relation to variable A_i. The parameter set $\{a_i, b_i, c_i\}$ are responsible for determining the shapes of the membership functions. These parameters are called premise parameters.

Layer 2 (Product Layer): The nodes, which are fixed in nature, in this layer determine the firing strength of a rule. This is usually obtained by multiplying the membership functions associated with the rules. They receive their input from layer one in terms of a range from 0 to 1. Equation (4) gives the relation for obtaining the product that depends on the number of inputs. The output is basically the firing strength of a particular rule;

$$w_i = O_i^2 = \mu_{Ai}(x).\mu_{Bi}(y), i = 1, 2 \quad (4)$$

In this layer, any other type of T-norm operator that performs fuzzy AND operation can be applied.

Layer 3 (Normalized Layer): The nodes in this layer are used to determine the ratio of the i[th] rule's firing strength to the total of all firing strengths. They are not adaptive and represented as in Eq. (5);

$$\overline{w} = O_i^3 = \frac{w_i}{w_1 + w_2}, i = 1, 2, \quad (5)$$

The manipulations in this layer result to a normalized output and hence the name normalized layer.

Layer 4 (Defuzzify Layer): As the name suggests, the output values resulting from the inference of rules are generated. This is done by determining the contribution of each rule to the overall output. This process in called defuzzification. The parameters $\{p_i, q_i, r_i\}$, referred to as consequent parameters, in this layer are modifiable during the training process. This layer is adaptive with node function given in Eq. (6);

$$\overline{w_i} z_i = O_i^4 = \overline{w_i}(p_i x + q_i y + r_i) \tag{6}$$

The manipulation is such that the output from layer 4 is used on the consequent parameters together with the inputs as represented in the equation.

Layer 5 (Total Output Layer): This layer is responsible for computing the overall output. This is done by performing a summation of the individual rules' contribution. As shown in Fig. 1, this layer consists of one fixed node to implement the computation. The summation process is as represented in Eq. (7).

$$\sum_i \overline{w_i} z_i = O_i^5 = \frac{w_i z_i}{\sum_i w_i} \tag{7}$$

Section 2.5 discusses the PSO algorithm in relation to how it is applied to modify the two sets of modifiable parameters.

2.5 Particle Swarm Optimization (PSO)

This technique, developed by Eberhart and Kennedy in 1995, is a global optimization technique [10]. Global optimization is a concept used in mathematics and numerical analysis to obtain a maxima or minima of a function. Its algorithm is motivated by the social behavior of living organisms like flocks of birds and schools of fish. The behavior is such that the swarms of particles (the organisms) are guided towards the most promising section of the search space [11].

The approach of PSO is iterative and can be described by the following steps:

Step 1: The first step involves the initialization of a number of parameters associated with the population that include the population size, positions and velocities of agents, and the number of weights and biases.
Step 2: The second step is to set the current best fitness achieved by particle p as *pbest* representing the personal best. Comparing all the *pbest* values the one with best value is set as *gbest* and stored in the variable *gbest* representing the global best in relation to all the particles.
Step 3: The next step is to evaluate the desired optimization fitness function f_p for each particle based on the Mean Square Error (MSE) over a given data set.
Step 4: Step four is to compare the evaluated fitness value f_p as obtained in step three for each particle with its *pbest* value. In the case where f_p is less than

pbest, the *pbest* variable contents are replaced by f_p since it is better than the value already stored. Also, the $best_{xp}$ variable contents are replaced by x_p where x_p represents the current coordinates of particle p, while $best_{xp}$ represents the corresponding coordinates to particle *p's* best fitness reached so far.

Step 5: In step five, the objective function value is determined for new positions of each particle for all particles. The *pbest* value is replaced by the current value in the case where a better position is achieved by an agent. Based on the information in step 1, the *pbest* values help in generating the *gbest* value which is the best as compared with the others according to the objective function. In this case where the new *gbest* value is better than previous *gbest* value, the *gbest* value is replaced by the current *gbest* value which is then stored. If f_p is less than gbest then *gbest* stores the value *p*, where *gbest* represents the particle having the overall best fitness calculated over all particles in the swarm.

Step 6: In this step the velocity and location of the particle are modified according to Equations 8 and 9, respectively.

Step 7: Step seven involves each particle *p* being flown according to Equation 8.

Step 8: In step eight if stopping criteria for instance the maximum number of predetermined iterations (epochs) is exceeded, then stop otherwise go back to step 3 until convergence is reached.

$$V_i = wV_{i-1} + acc * rand() * \left(best_{xp} - x_p\right) + acc * rand() * \left(best_{xgbest} - x_p\right) \tag{8}$$

where *acc* performs the function of controlling how far the particles fly from each other and is referred to as the acceleration constant while *rand* is function that generates a uniform random number between 0 and 1.

$$x_p = x_{pp} + V_i \tag{9}$$

V_i represents the current velocity of the particle while V_{i-1} represents the previous velocity with x_p being the current location of the particle. x_{pp} in this case represents the previous location of the particle while *i* is the particle index. The coordinates, best_{xp} and $\text{best}_{\text{xgbest}}$ in step 5, are used to pull the particles towards the global minimum [11].

Learning by PSO

The learning process also known as training and the validation are part of the important concepts that make a model, taking an example of ANFIS, accurate. Training involves repeating a set of input-output patterns to a model in this case ANFIS. In this process the adaptive parameters of the ANFIS are modified to give an output that is as close to the target output as possible. When the training process is done, the ANFIS adaptive parameters are able to give an output that has minimal error [11]. Many methods are available to perform the function of training ANFIS but in our study PSO is used. Our modified ANFIS consists of two sets of parameters which require training by the PSO algorithm. They are referred to as the antecedent

part or premise parameters and the conclusion part or consequent parameters. The premise parameters consist of are $\{a_i, b_i, c_i\}$ that give rise to the membership functions assumed Gaussian as in Eq. (3). As indicated earlier a_i represents the standard deviation of membership functions and controls the width of the "bell" while c_i is center of the peak and b_i controls the height of the membership functions (MFs). The consequent parameters, also modified during the training process, are represented by $\{p_i, q_i, r_i\}$ to affect the inputs accordingly [11].

Applying PSO for Training ANFIS Parameters

In relation to this research, both the premise and consequent parameters are modified using PSO. In both of them there are 3 sets of trainable parameters, for the premise part $\{a_i, b_i, c_i\}$ and for the consequent $(\{p_i, q_i, r_i\})$ each of which have N genes. In this case, N represents the number of MFs. The fitness to be used is defined as root mean square error (RMSE) obtained from the target and actual model outputs [11]. This starts from initializing the parameters randomly which are then updated using PSO algorithm as described in section D. For every iteration, the parameter sets are being updated a process that continues until the set criteria is reached.

Evaluation Criteria

The evaluation criteria involve the process of using both the actual output of the system and the target output. An error is obtained by comparing the two and determining the difference. From the difference, the MSE which is fitting function is as defined in Eq. 10;

$$MSE = \frac{1}{N}\sum_{i=1}^{N}\left(y_i - \widehat{y_i}\right)^2 \tag{10}$$

where N is the total number of data points, y is the target output value while $\hat{y}$ is the ANFIS predicted output value.

A number of iterations are done to ensure that MSE converges to a minimum value. The other parameters that can be used to determine the model accuracy are the mean absolute error (ME) as represented in Eq. 11, the standard deviation (SD) as represented in Eq. 12 and root mean squared error (RMSE) as shown in Eq. 13. The mean absolute error is given by;

$$e_i = \left|P_{target} - P_{simulated}\right|, \quad \overline{e} = \frac{1}{N}\sum_{i=1}^{N} e_i, \tag{11}$$

where terms *target* and *simulated* denote received signal strength that are obtained by the theoretical models and the others simulated by the ANFIS model, while N is total number of samples. The standard deviation is given by;

$$\sigma = \sqrt{\frac{1}{N}\sum_{i=1}^{N}(e_i - \overline{e})^2} \tag{12}$$

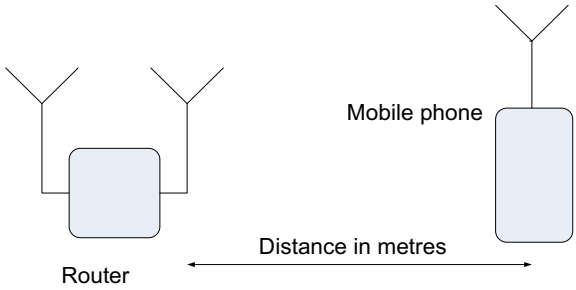

Fig. 2 Diagram of the set up to obtain RSSI

The root mean squared error (RMSE) can be obtained through the expression;

$$RMSE = \sqrt{\frac{1}{N}\sum_{i=1}^{N}\left(y_i - \widehat{y_i}\right)^2} \tag{13}$$

3 Research Methodology

3.1 Setup for Obtaining RSSI

The steps for obtaining the RSSI values are as follows;

i. Based on the selected models, obtain the expected RSSI with distance variation using MATLAB.
ii. Using the ANFIS MATLAB toolbox obtain the predicted RSSI values for ANFIS, LOG10D-ANFIS and LOG10D-PSO-ANFIS based on modified ANFIS.
iii. Compare the performance of the three models based on their ME, SD and RMSE values (Fig. 2).

3.2 Modified ANFIS with log10d

The modified ANFIS, as represented in Fig. 3, has an additional layer outside the ordinary ANFIS five layers. This layer is responsible for modifying the input data by applying the log to base 10 operator which, then feeds the ordinary ANFIS to process the modified data resulting to accurate output values. All the other five layers retain their functions as indicated in Eqs. 3 to 7. The rules incorporating the log to base 10 operator are given as follows for single input;

Rule 1: *If* $log10x$ *is* A_1 *then* $z_1 = p_1 log10x + r_1$
Rule 2: *If* $log10x$ *is* A_2 *then* $z_2 = p_2 log10x + r_2$
x = distance and z = RSSI

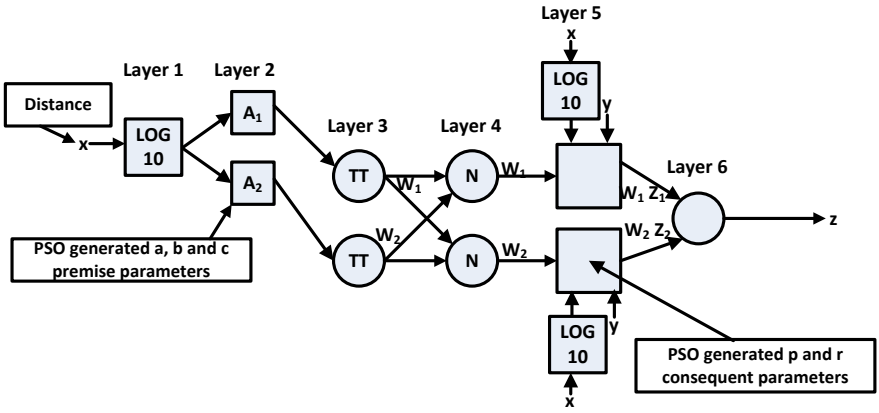

Fig. 3 Modified type 3 ANFIS Architecture

Figure 3 is a representation of our modified type 3 ANFIS architecture with one input distance (x) and one output, RSSI (z). In this case the input is passed through a logarithmic function, that is log to base 10, before it is passed to the second layer where the premise parameters (a, b and c) that determine the level of belonging are modified using PSO training algorithm. The output is then taken through the different other layers accordingly. In layer 5 the consequent parameters p and r are also modified using the same PSO algorithm with the distance input x passed through the same logarithmic function. The final layer 6 gives the predicted RSSI.

3.3 Data Analysis

This study used the MATLAB in the generation of the graphs based on the content analysis technique. The findings and related discussions are presented in Sect. 4.

4 Findings and Discussions

4.1 Results

Based on the MATLAB analysis, the following parameters were generated after training and testing.

One Slope Model (OSM)

Two-Ray Ground Reflection (TRGR)

4.2 Discussions

The graphs generated using the values obtained from one slope model and the two-ray ground reflection model and predicted are as shown Figs. 4, 5 and 7. Figure 4 shows

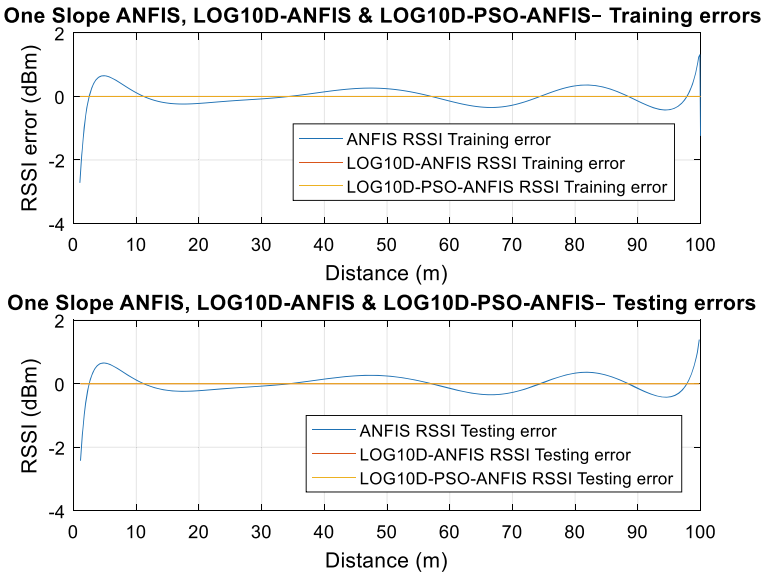

Fig. 4 OSM ANFIS, LOG10D-ANFIS and LOG10D-PSO-ANFIS training and testing errors

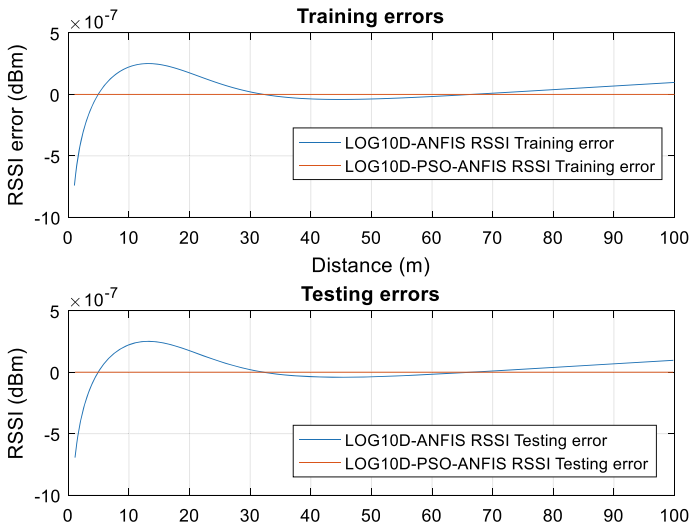

Fig. 5 OSM LOG10D-ANFIS and LOG10D-PSO-ANFIS training and testing errors

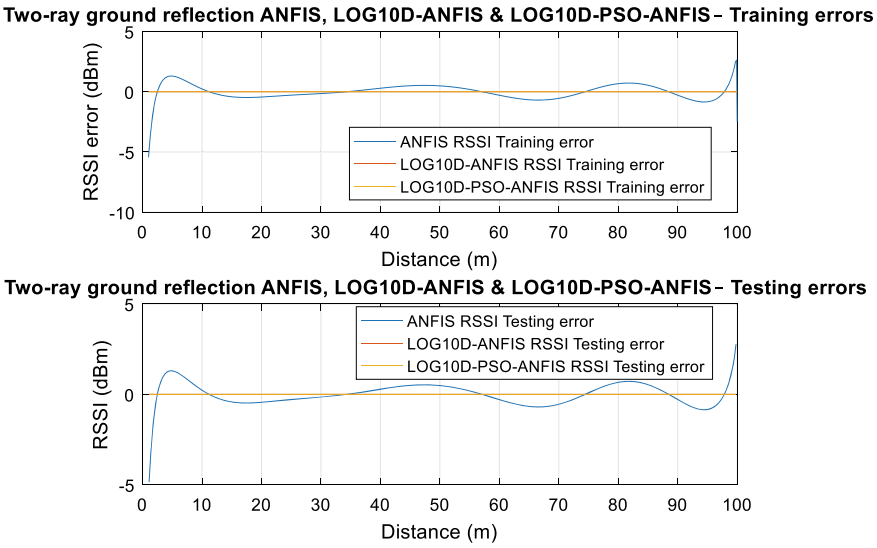

Fig. 6 ANFIS, LOG10D-ANFIS and LOG10D-PSO-ANFIS training and testing errors

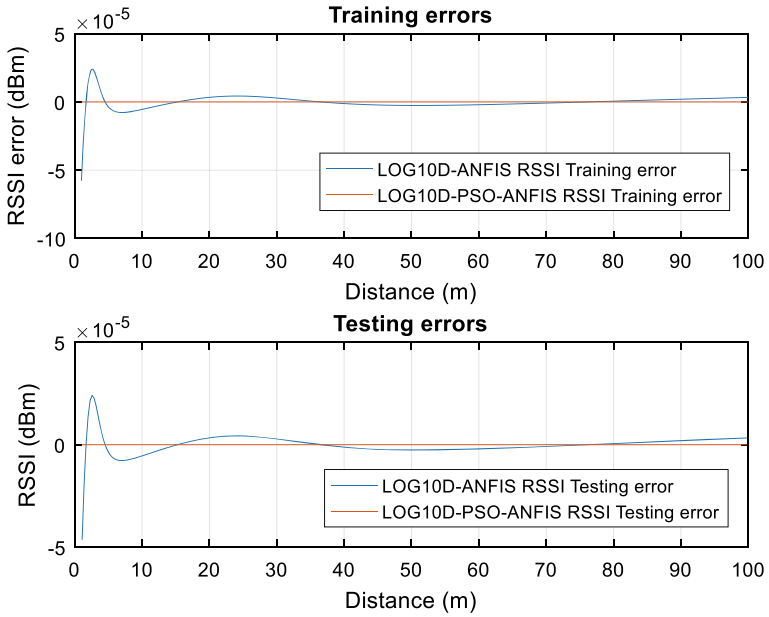

Fig. 7 TRGRM LOG10D-ANFIS and LOG10D-PSO-ANFIS training and testing errors

Table 1 Training parameters

	RMSE	ME	Standard deviation
ANFIS	0.3180	0.2315	0.2183
LOG10-ANFIS	1.1652e–07	7.6010e–08	8.8374e–08
LOG10-PSO-ANFIS	4.7379e–15	2.9535e–15	3.7074e–15

the OSM ANFIS, LOG10D-ANFIS and LOG10D-PSO-ANFIS training and testing errors while Fig. 5 is an indication of the OSM LOG10D-ANFIS and LOG10D-PSO-ANFIS training and testing errors. Figures 6 and 7 show similar graphs for the TRGR model. Tables 1, 2, 3 and 4 give the training and testing parameters for both the one slope and the two-ray ground reflection models. It is noted that the training root mean squared error (RMSE), mean error (ME) and standard deviation (SD) were in the 10^{-15} range in both OSM and TRGR models, for PSO trained LOG10D-ANFIS. These parameters are in the range of 10^{-07} to 10^{-08} for LOG10D-ANFIS and 10^{-01} for ANFIS respectively, while the testing mean error (ME), root mean squared error (RMSE) and standard deviation (SD) were in the same ranges as well.

Table 2 Testing parameters

	RMSE	ME	Standard deviation
ANFIS	0.3146	0.2302	0.2148
LOG10-ANFIS	1.1637e–07	7.5947e–08	8.8309e–08
LOG10-PSO-ANFIS	4.7169e–15	2.9126e–15	3.7158e–15

Table 3 Training parameters

	RMSE	ME	SD
ANFIS	0.6360	0.4629	0.4365
LOG10D-ANFIS	4.7600e–06	2.7336e–06	3.8997e–06
LOG10D-PSO-ANFIS	2.2234e–15	7.3238e–16	2.1009e–15

Table 4 Testing parameters

	RMSE	ME	SD
ANFIS	0.6292	0.4604	0.4295
LOG10D-ANFIS	4.6777e–06	2.7183e–06	3.8125e–06
LOG10D-PSO-ANFIS	2.0471e–15	6.1079e–16	1.9568e–15

5 Conclusions and Recommendations

5.1 Conclusion

Considering the one slope and two-ray ground reflection models predicted RSSI values, it is noted that they are closest to the target values for the LOG10D-ANFIS than the LOG10D-ANFIS and the plain ANFIS models. Since all the other models have similar results, the obtained membership functions can be used to generate a universal model which increases the accuracy in signal prediction modelling for placement of transmitters and receivers.

5.2 Areas of Further Study

Areas of future research can include extending the same analysis to the other models and the use of other training methods whose resulting parameters can be compared.

References

1. Sohail A, Ahmad Z, Ali I (2013) Analysis and measurement of Wi-Fi signals in indoor environment, vol 1
2. Scholz DIP, Kathrein-Werke KG (2000) Basic antenna principles for mobile communications. Polarization 45(45):12
3. Jang JS (1993) ANFIS: adaptive-network-based fuzzy inference system. IEEE Trans Syst Man Cybern 23:665–685
4. Gharghan SK, Nordin R, Jawad AM, Jawad HM, Ismail M (2018) Adaptive neural fuzzy inference system for accurate localization of wireless sensor network in outdoor and indoor cycling applications. IEEE Access 6:38475–38489
5. Erunkulu OO, Zungeru AM, Lebekwe CK, Chuma JM (2020) Cellular communications coverage prediction techniques: a survey and comparison. IEEE Access 8:113052–113077
6. Turner D, Savage S, Snoeren AC (2011) On the empirical performance of self-calibrating wifi location systems. In: 2011 IEEE 36th conference on local computer networks (LCN). IEEE
7. Mongia PK, Singh BJ (2013) Planning and optimization of wireless LANs through field measurements. arXiv preprint arXiv:1309.1184
8. Sumathi S, Paneerselvam S (2010) Computational intelligence paradigms: theory & applications using MATLAB, CRC Press Taylor & Francis Group
9. Kennedy J, Eberhart R (1995). Particle swarm optimization. In: Proceedings of IEEE international conference on neural network, Perth, Australia, pp 1942–1948. IEEE Service Center Piscataway
10. Kennedy J, Eberhart RC (1995) Particle swarm optimization. In: Proceedings IEEE international conference neural networks, pp 1942–1948

11. Hassan R, Cohanim B, de Weck O (2005) A comparison of particle swarm optimization and the genetic algorithm. In: Presented at the AIAA/ASME/ASCE/AHS/ASC 46th structures, structural dynamic materials conference, Austin, April 2005
12. Wu L et al (2020) Artificial neural network based path loss prediction for wireless communication network. IEEE Access 8:199523–199538
13. Ahmadien O, Ates HF, Baykas T, Gunturk BK (2020) Predicting path loss distribution of an area from satellite images using deep learning. IEEE Access 8:64982–64991

Different Approaches of Diagnosing Depressed and Non-depressed Patients

Prajakta R. Naregalkar and A. A. Shinde

Abstract Depression has become a very common problem nowadays. Depression affects the mental state, so the patient suffering from it faces a problem of communicating his/her condition to the doctor. The depression is diagnosed on the basis of questionnaire set by the psychiatrist. This questionnaires are the different scales related to the symptoms for assessment of depression. Apart, from the questionnaire there are also laboratory test available for diagnosing depression. In the recent years, there are many techniques used for diagnosis like machine learning. Deep learning and Data mining methods. As depression is dependent on multiple disorders, so diagnosing it by using multiple modalities will be effective as compared to that of single modality. The single factor approaches are EEG, FMRI, Speech Signals; Twitter data etc. The multimodal approach will combine the different depression techniques to give a efficient or effective diagnosis. This paper reviews a different depression detection system that uses single modality and multiple modalities to diagnose depression. The survey shows the depression detection using multiple modalities has higher performance as compared to single modality approach.

Keywords KNN · SVM · EEG · CNN · MDD

1 Introduction

As per the findings of WHO depression is the severe cause of disability. Clinical depression is a serious matter of concern should not be ignored at all. The method used for diagnosis currently is based on interview questionnaires scales like DSM-IV, PHQ-8, and BDI-2 etc. through that a psychiatrist analyzes severe, moderate or mild type of depression. The patient or the individual may suffer from more than one

P. R. Naregalkar (✉) · A. A. Shinde
Department of Electronics and Communication, Bharati Vidyapeeth (Deemed To Be University) College of Engineering, Pune, India
e-mail: pdkulkarni@bvucoep.edu.in

A. A. Shinde
e-mail: aashinde@bvucoep.edu.in

M. Tiwari et al. (eds.), *Optical and Wireless Technologies*, Lecture Notes in Electrical Engineering 892, https://doi.org/10.1007/978-981-19-1645-8_21

disorder or else one or more individuals may show different symptoms, according to the scale used. Hence there is a requirement of building an automatic system for detecting depression. There are no such standard laboratory tests to diagnose depression. But, recently machine learning, deep learning data mining methods that developed are useful for detection of depression in the field of psychiatry.

Depression means loss of interest, loss of appetite, sleep disorders, losing self confidence, less energy efficiency and low concentration. Different studies shows that a constant depression phase may even leads to suicide of an individual. Early diagnosis are the only solution to prevent the life of an individual. Also, many of the patients have not been identified as depressed, the individual remains in the same state of depression for longer time and is not diagnosed even after the several visits to physician, Therefore automatic screening and early diagnosis for detection to avoid further problems.

Over the past few year EEG data sets using machine learning approach has given promising results. The accuracy or the performance output using EEG is far better compared to other modalities. Electroencephalogram (EEG) is the brain activity and is more appropriate modality due to its neuroimaging feature, noninvasive technique as well cost effective and accessible to the patient. As human brain is non-linear in nature and the frequencies associated with it can be correlated with the depression analysis. Thus the paper aims to survey the various machine learning algorithm used on the EEG dataset on the basis of comparison factors like accuracy, specificity, sensitivity for depressed patients.

Typical steps followed on EEG dataset for detecting healthy and depressed subjects are mentioned here. The very step is the recording of EEG, then preprocessing the data to remove all the muscle and eye movements i.e. artifacts with proper filtering process. Next is the feature extraction wherein we have to consider, the linear and nonlinear features related to EEG. Third step is the feature selection to form the feature vector of similar characteristics and more relevant for analyzing depressed and non-depressed patients. the last step is to find a suitable classifier, machine learning algorithm with effective performance to predict depression. We have chosen to focus on the combination of physiology (i.e. non-linear analysis of EEG with the machine learning approach) with the clinical approach of psychiatry, use of standard scales. As we believe that combining physiology and psychiatry will definitely improve the current scenario of clinical methods and helpful for evaluation of depression.

2 Problems and Challenges

The diagnosis of depression is having following problems:

- Depression does not have specific symptoms that person suffering from it cannot show any specific changes so it is very difficult to detect it. In some of the patient's mood swings, loss of appetite, digestion problem, sleep disorders symptoms are

observed. This leads to imbalance in the overall body functioning. In the early stage again it is very difficult to detect depression as in the early state there are very les changes in the physical state of the patient. Depression closely affects the emotional state of the patient People suffering from depression avoid to communicate with physician and hide the truth because of this depression state remains for longer period of time destroying the patients healthy condition.

- There is no standard laboratory test available for analysis of depression. The clinical approach used by the psychiatrist is assessment through the interview questionnaire which is a time consuming and it will also dependent on the psychiatrist interpretation. This all depends on how the patient responds to the psychiatrist questions and in turn psychiatrist evaluation. There are different standard scales used in the clinical depression like Personal Health Questionnaire Depression Scale(PHQ-8), Hamilton Depression Rating scale; Diagnostic & statistical Manual of Mental Disorders (DSM-IV) etc. So, this is all based on what types of question are asked in the scale, and the patient's response to the questions, as well as the psychiatrist assessment.

The diagnosis of depression faces the following challenge:

- Depression is a multimodel mental illness and dependent on information from the multiple sources leading to find the complexity of depression. Depression affects the mental, physical and emotional state of health so there are different modalities used like speech, video, twitter data etc. Analysis for diagnosing depression. The different modalities stated are all based on using a single approach. Depression detection using a single modality will not be sufficient for diagnosing accurately.
    - Depression using multimodal approach will be more effective as far as performance considered with single modality. Multimodal approach means combining for e.g. speech features and EEG analysis. Thus fusing one or more approach together will ultimate give good prediction analysis. Depression prediction on EEG dataset with the machine learning approach involves feature extraction, feature selection, classifier etc.

3 Depression Diagnosis on the Basis of Machine Learning Approach with EEG Dataset (A Single Modality Approach)

Depression can be analyzed by using a single modality or combining one or more features i.e. multimodal approach. The single modal approach consists of brain activity EEG, video analysis, speech features, twitter data or MRI etc. The single modality is effective as there is a detailed study of each and every aspects of the single feature. In this paper, depression detection using EEG on the basis of various machine learning algorithms are discussed based on accuracy achieved by a specific technique.

Milena Cukic et al. [12] reviewed all the papers from 2008 till May 2019 for classification of depression using machine learning approach based on EEG dataset. In this paper, author reviewed the commonly used parameters versus the recommended parameters. After reviewing the paper it is concluded that EEG electrodes used for recording EEG must be 19 + electrodes. The feature extraction method to be used is a Principal component analysis (PCA) or Genetic algorithm (GA).Feature selection must be non-linear analysis as a human brain is non-linear in nature. The features recommended are fractal and non-linear. The classifier machine learning algorithm used may be Support Vector machine (SVM) or the Laso embedded regularization accuracy obtained will be more realistic result.

Chamandeep Kaur et al. [8] focused on compare effectiveness of the physical denoising approaches based on (DWT) Discrete Wavelet Transform & (WPT) Wavelet Packet Transform combined with (VMD) Variational Mode Decomposition VMD-DWT & VMD-WPT. Features extracted were Mean Hjorth parameter and Shannon entropy. Feature selection method is detrended fluctuation analysis (DFA) with defined mode selection criteria. Dataset consists of 34 MDD patients & 30 Healthy Controls. The classifiers used are the Random Forest (RF) & Support Vector Machine (SVM). The best accuracy of 98.51% is achieved for random forest.

Jing Zhu et al. [5] proposes a content based ensemble method (CBEM) to promote the depression accuracy, generating data subsets by the content of the experiment free- viewing eye-tracking & task-state EEG. For this, 17 Parietal electrodes are used with 15 linear features. GSW method is used for feature selection. The CBEM gains accuracies of 82.5% and 92.73%.

For implementation of depression detection Betul Ay et al. [3] uses a single channel EEG data with database of 15 normal & 15 depressed subjects. For evaluation K-fold cross validation is used. The main motivation for this paper is this is a fully automatic detection of depression using raw EEG signals. The feature extraction selection classification operations are executed automatically using single channel EEG signals as input. Here, Deep Hybrid model is developed using Convolutional Neural Network (CNN) & long-short term memory (LSTM) to detect depression using EEG signals. CNN-LSTM model has provided 99.12% & 97.66% classification accuracies for the right & left hemisphere EEG signal respectively.

This paper Yousef Mohammadi et al. [4] presents a machine learning approach to discriminate the depressed subjects to four different levels of depression using a Katz fractal classifier. Nonlinear features including fuzzy entropy (FuzzyEn), Katz fractal dimensions (KFD) & fuzzy fractal dimension (FFD) is used. The 19-channel EEG data is recorded with a accuracy of 90.00%.

In [2] Devalunchari Ramalingam et al. included a algorithm filtered wall able to filter unwanted messages to identify only the filter messages posted on platform for improving predictability for neural networked to get accurate results. Different feature analysis techniques used are spectral category (S^*) & Spectral category (S). The classifier algorithm used are Logistic Regression (SLR), Multilayered Perceptron Neural Network (MLPNN), Support Vector Machine (SVM) & Random forest (RF) with a highest accuracy of 82.2%.

Wajid Mumtaz et al. [9] proposed a machine learning framework involving EEG-derived synchronization on likelihood (SL) features as input data for automatic diagnosis of MDD. The feature selection is based on rank based with tenfold cross validation is used for validation process. Classifiers used Support Vector Machine (SVM), logistic Regression (LR) & Naïve Bayesian (NB). The SVM has achieved a highest accuracy of 98% sensitivity 99.9% & specificity as 95%.

In [11] U Rajendra Acharya et al. proposed a novel computer model approach for EEG-based screening of depression by a deep neural network using machine learning algorithm of convolution. The proposed technique automatically feeds the input EEG signals to differentiate depressive & normal subjects excluding a semi-manually selected set of features to be fed into a classifier for classification. The dataset comprises of 15 normal & 15 depressed patients with bipolar EEG signal. The proposed algorithm achieved accuracy of 93.54% & 95.96% from left & right hemisphere respectively.

Chein-Te Wu et al. [1] demonstrated the use of CK-SVM classifier with three types of relative EEG power features from different frequency bands. Conformal Kernel Support Vector Machine (CK-SVM), linear discrimination analysis (LDA) conventional SVM & quadratic discriminant analysis was used. Among all the classifiers CK-SVM outperformed with yielding an accuracy of 83.64% developed.

This paper Jing Yang et al. [6] a database of 17 depressed and 17 normal subject with the help of 16- electrode EEG. Feature extracted are 10 linear & 8 non- linear using Greedy step wise for feature selection. Classifiers used Bayes net SVMC (Linear as kernel), KNN, J48 & Random Forest. Highest accuracy is achieved by KNN with is 83.24%

Hanshu cai et al. [7] presented a case based reasoning identifying depression. EEG data were collected using a portable 3-electrode EEG data device applying multiple classifiers like SVM, KNN, Naive Baye's & Decision tree. The paper selected four linear & four non linear features. The database consists of 86 depressed & 92 normal controls. The highest accuracy is obtained with KNN is 81.44% (Table 1).

4 Depression Diagnosis on the Basis of Multimodal Approach

Depression diagnosis using multimodel approach means combining more than one feature to diagnose depression. As depression is a multifactor disorder by using more than one feature prediction of depression can be done in the early stages as well as with a very accurate performance.

Dingxinfang et al. [10] presented a multimodal machine learning approach involving EEG, eye tracking & galvanic skin response data as input to classify depression patients & healthy controls. Galvanic skin response was recorded during the

Table 1 Single modality approaches in depression detection

Author	Elect rodes	Features	Classifier/ML models	Accurac y (%)
Milena Čukić et al.	19+	Fractal & Non-linear	Commonly used is SVM Recommended LASO embedded regularization	Typically >95% or 99%
Chamandeep Kaur et al.	19-channel EEG	Mean, Hjorth parameter and Shannon entropy	Random Forest (RF) and Support vector machine (SVM)	98.51 98.07
Jing Zhu et al.	17 parietal electrodes	15 linear features	1. BayesNet 2. Logistic Random Forest 3. NaiveBayes 4.SVM (Linear) 5. SVM (RBF) 6. KNN 7. J48	82.5 92.73
Betul Ay et al.	Single channel EEG		CNN-LSTM Random Splitting	99.12 97.66
Yousef Mohammadi et al. 2019	19-Channel	Nonlinear features fuzzy entropy Katz fractal dimension fuzzy fractal dimension (FFD)	Fuzzy function based on neural network (FFNN)	90.00
Devakunchari Ramalingam et al			1. Logistic Regression 2. Multilayer Perceptron Neural Networks 3. Support Vector Machine 4. Random Forest	82.2
Wajid Mumtaz et al.	19-channel	Synchro nization likelihoo d (SL) features	1. Support vector machine (SVM), 2. Logistic regression (LR) and 3. Naïve Bayesian (NB)	98
U Rajendra Acharya et al.	bipol ar EEG signal		13 layer Convolutional Neural Network (CNN)	93.5 96.0

(continued)

Table 1 (continued)

Author	Elect rodes	Features	Classifier/ML models	Accurac y (%)
Chien-Te Wu et al.	29 Electrodes	EEG power features from different frequency bands (delta, theta, alpha, beta, and gamma	Conformal kernel support vector machine machine learning classifiers: Linear discriminant analysis, conventional SVM, quadratic discriminant analysis	83.64
Jing Yang et al.	16 electrodes	10 linear and 8 nonlinear	1. Baye's Net 2. SVM (linear kernel) 3. KNN 4. J48 5. Random Forest	83.24
Hanshu Cai et al.	3 Electrodes	Four linear & 4 Nonlinea r features	1. SVM 2. KNN 3. Naive Bayes 4. Decision Tree	81.44

whole experimental by a biofeedback unit. Classifiers used were logistic regression & random forest. The best accuracy was obtained is 79.63%.

Yashika et al. [14] describes a novel method of combining both EEG signal analysis & facial emotion recognition through video analysis. Here 64- channel EEG is used. Preprocessing is done by independent component analysis (ICA), then the feature extraction by wavelet decomposition. Feature selection is based on standard deviation mean & entropy along with along with three frequency band of EEG. For emotion recognition through video analysis is done with the help of Japanese Female Facial expression (JAFFE) database. Classifiers used as decision tree and ANN. Using both EEG & Facial recognition gives a higher accurate results.

This paper zhijang wan et al. [16] developed the machine learning method for discriminating MDD & normal control based on multichannel EEG data & signal channel EEG data collected from forehead scalp to differentiate MDD. Discrete wavelet Transform is used to decompose the signals into S Subband components. Genetic Algorithm is used to select the effective feature select. Classifiers used are Random Forest (RF), Linear discriminant analysis (LDA), KNN classification & regression tree (CART). CART-GA algorithm achieves the highest accuracy of 86%.

Lukasz Tyszczuk smith et al. [13] study aims to compare the different combinations of physiological signals in detecting depression, heart rate variability & skin conductance response data on 27 participants were analyzed with the different features extracted & different classifiers were used LDA, SVM, KNN & binary decision tree. Different HRV & SCR features are extracted & fed to the classifier, Heart rate variability achieved 81% accuracy while SCR showed 78%.

Table 2 Multimodal approaches in depression detection

Sr.no	Author	Multiple modalities used	Accuracy/Performance
1	Dingxinfang et al.	EEG, EYE tracking & Galvanic skin response	79.63%
2	Yashika et al.	EEG Signals & video analysis	–
3	Zhijang Wan et al.	Single channel EEG data & Multiple EEG Channel	86%
4	Lukaz Tyszczuk smith et al.	Heart rate variability & skin conductance response	81% & 78%
5	Xiaoweizhang et al	EEG & Vocal signals	%

Xiaowei zhang [15] this study combined the physiological behavior % the EEG and vocal signals together fused to make the detection of depression more effective and accurate. The EEG and vocal features are fed to the classifiers such as SVM, GNB, RF, GP, KNN, & MLP. Grid search & K fold cross validation is used for feature selection & validation respectively. Compared with the single modality, fusion method gained a better performance for depression detection. The accuracy obtained from this fusion is 76.40% (Table 2).

5 Comparative Analysis of Signal Modality and Multimodalities Approach Depression Detection

- Single modality approach takes its consideration only one technique in which detailed study is possible for improving overall performance of depression diagnosis. But, depression will affect the entire body of healthy individual. The individual suffering from depression will affects not only physical state but also mental and emotional state. Single modality approaches are video analysis, EEG the brain activity, speech behavioral features, eye tracking etc. This type of analysis will concentrate on the only one single feature for e.g. EEG means it will give observations from the brain only. As depression is a multi disorder problem there has to be findings from different more modalities to improve the diagnosis.
- Multiple modalities take into consideration more than one modality. The fusion of more than one modality is the multiple modality approach. In multiple modalities different factors will be considered. The multiple modalities means for e.g. combining EEG with video analysis or EEG with speech features. So thus multiple modalities will enhance the performance leading to perfect diagnosis.

6 Conclusion

The paper surveyed the different single modality and multiple modalities approaches for detection of depression. The paper reviewed shows that more preferable approach is by using machine learning algorithms on recorded EEG signals. It is also observed that multiple modalities shows higher performance as compared with single modality approach. In the future work depression levels have to be diagnosed for evaluating a depressed individual. Also more emphasis is to be given on the Data Mining, Artificial Neural Networks techniques to improve the efficiency as compared to machine learning algorithms used. In the future a best depression system has to be built which will be also helpful for clinicians for the early diagnosis of depression.

References

1. Wu C-T, Dillon DG, Hsu H-C, Huang S, Barrick E, Liu Y-H (2018) Depression detection using relative EEG power induced by emotionally positive images and a conformal kernel support vector machine. Appl Sci 8(8):1244
2. Ramalingam D, Sharma V, Zar P (2019) Study of depression analysis using machine learning techniques. Int J Innov Technol Explor Eng (IJITEE) 8(7C2)
3. Ay B, Yildirim O, Talo M et al (2019) Automated depression detection using deep representation and sequence learning with EEG signals. J Med Syst 43:205
4. Mohammadi Y, Hajian M, Moradi MH (2019) Discrimination of depression levels using machine learning methods on EEG signals. In: 2019 27th Iranian conference on electrical engineering (ICEE), pp 1765–1769
5. Zhu J, et al (2019) Toward depression recognition using EEG and eye tracking: an ensemble classification model CBEM. In: 2019 IEEE international conference on bioinformatics and biomedicine (BIBM), pp 782–786
6. Yang J, et al (2018) Resting state EEG based depression recognition research using voting strategy method. In: 2018 IEEE international conference on bioinformatics and biomedicine (BIBM), pp 2666–2673
7. Cai H, Zhang X, Zhang Y, Wang Z, Bin H (2020) A case-based reasoning model for depression based on three-electrode EEG data. IEEE Trans Affect Comput 11(3):383–392. https://doi.org/10.1109/TAFFC.2018.2801289
8. Kaur C, Bisht A, Singh P*, Joshi G (2021) EEG signal denoising using hybrid approach of variational mode decomposition and wavelets for depression. Sciencedirect Biomed Signal Process Control 65:102337
9. Mumtaz W, Ali SSA, Yasin MAM, Malik AS (2018) A machine learning framework involving EEG-based functional connectivity to diagnose major depressive disorder (MDD). Med Biol Eng Comput 56(2):233–246. PMID: 28702811
10. Ding X, Yue X, Zheng R, Bi C, Li D, Yao G (2019) Classifying major depression patients and healthy controls using EEG, eye tracking and galvanic skin response data. J Affect Disord 15(251):156–161. PMID: 30925266
11. Acharya UR, Oh SL, Hagiwara Y, Tan JH, Adeli H, Subha DP (2018) Automated EEG-based screening of depression using deep convolutional neural network. Comput Methods Progr Biomed
12. Čukić M, López V, Pavón J (2020) Classification of depression through resting-state electroencephalogram as a novel practice in psychiatry: review. J Med Internet Res 22(11):e19548. PMID: 33141088 PMCID: 7671839

13. Smith LT, et al (2020) Using resting state heart rate variability and skin conductance response to detect depression in adults. In: 2020 42nd annual international conference of the IEEE engineering in medicine & biology society (EMBC), pp. 5004–5007
14. Katyal Y, Alur SV, Dwivedi S, Menaka R (2014) EEG signal and video analysis based depression indication. In: 2014 IEEE international conference on advanced communications, control and computing technologies, pp 1353–1360
15. Zhang X, Shen Z, Din Z, Liu J, Wang G, Hu B (2019) Multimodal depression detection: fusion of electroencephalography and paralinguistic behaviors using a novel strategy for classifier ensemble. IEEE J Biomed Health Inf 23(6):2265–2275
16. Wan Z et al (2019) Single-Channel EEG-based machine learning method for prescreening major depressive disorder. Int J Inf Technol Decis Mak 18(5):1579–1603

Enabling Real-Time Vehicle-to-Vehicle (V2V) Communication for Intelligent Transportation System (ITS)

Karan Verma, Ashok Kumar, Leandro Melo de Sales, Sudesh Kumar, Ajay K. Sharma, and Nehul Singh

Abstract The rapid advancement in the automobile industry and the ease with which vehicles can be acquired has resulted in a significant rise in the number of vehicles on the road. Vehicles have been upgraded from time to time to provide all kind of facilities to the commuters. Security features of the vehicle have also been enhanced, with the addition of airbags, seatbelts and so on. Still, however, there are many situations in which security has not been provided in complete sense, like prevention of accidents from occurring. There are also many other areas, where vehicles of present age cause problems to the commuters like traffic jams, human proximity detection, and so on. All these have led to the need of emergence of an Intelligent Transportation System, which embodies intelligence and provides innovative solutions such as traffic monitoring, blind crossing, preventing two or more vehicles from colliding, real-time route computation to the destination, and many more. This very idea of Intelligent Transportation System can be realized with the help of a communication paradigm, VANET (Vehicular Ad-Hoc Network), which ensures vehicle-to-vehicle communication.

K. Verma (✉)
National Institute of Technology, New Delhi, India
e-mail: karan.verma.phd@gmail.com

A. Kumar
GWEC, Ajmer, India
e-mail: kumarashoksaini@gmail.com

L. M. de Sales
Universidade Federal De Alagoas-UFAL, Maceió, Brazil
e-mail: leandro@ic.ufal.br

S. Kumar
SMVD University, Jammu, India
e-mail: sudesh.bhadu@smvdu.ac.in

A. K. Sharma
Dr. B R Ambedkar National Institute of Technology, Jalandhar, India
e-mail: sharmaajayk@nitj.ac.in

N. Singh
Department of Computer Science and Engineering, IIIT Sricity, Chittoor, India
e-mail: nehul.s20@iiits.in

M. Tiwari et al. (eds.), *Optical and Wireless Technologies*, Lecture Notes in Electrical Engineering 892, https://doi.org/10.1007/978-981-19-1645-8_22

Keywords VANET · Intelligent Transportation System (ITS) · Edge learning · Wireless Local Area Network (WLAN) · Internet of Things (IoT) · Mobile Ad-Hoc Networks

1 Introduction

As per a latest prediction, more than 20 billion things will be connected to each other via the Internet by 2020, in which vehicles will form the majority. VANET is based upon this very idea of a large web of vehicles and a Wireless Local Area Network (WLAN), which can connect all the vehicles and will enable communication between them. The main goal of VANET is development of an Intelligent Transportation System (ITS), which can help in providing the much needed safety services to the vehicles. Vehicular Ad Hoc Network (VANET) is a special category of Mobile Ad-Hoc Networks (MANET). However, they can be separated from other ad hoc networks because of their architectures, characteristics of vehicle movement, and the fact that vehicles move only on roads which are generally fixed and static, provides it an edge over other mobile networks, where there is no fixed pattern of movement of nodes. As a result, VANETs pose many unique networking research problems and challenges, which include routing, security issues, scalability and so on. Inter-vehicular communication will provide safety-related services to the vehicles. In case of an accident, all the vehicles nearby to the accident area can be informed about the critical situation, by continuously broadcasting information about this critical situation to other vehicles. Also, if a particular vehicle breaks down, it can provide information about other nearby vehicles to the driver. Such kind of inter-vehicular communication between different vehicles will help in the development of autonomous vehicles, as well as smooth traffic flow (Fig. 1).

VANETs can also provide many other services to the commuters, such as the facility to send emails, download and play music, surf internet. All in all, Inter-vehicular communication will be a crucial step towards making vehicles smart nodes, which can provide quite a number of services and facilities to the users. Internet of Things (IoT) can play a significant role in handling the increased no. of vehicles on the road. As, if we consider traditional problems like speed checking, pollution surveillance and so on, traditional solutions like timely checking of pollution, CCTV checking of vehicular speeds, or speed trackers, tend to fail, with increasing no. of vehicles under supervision, as the efficiency by which a traffic management authority can handle these problematic situation decreases sharply. One of the proposed methodologies to tackle such situation is the Internet of Vehicles (IoV). The Internet of Vehicles (IoV) [1] is an association of an inter-vehicular network, an intra-vehicular network, and the vehicular mobile Internet. Based on this, Internet of Vehicles helps in wireless communication and information sharing between V2X (where V stands for vehicle and X for vehicle, road, human or internet) according to standard communication protocols.

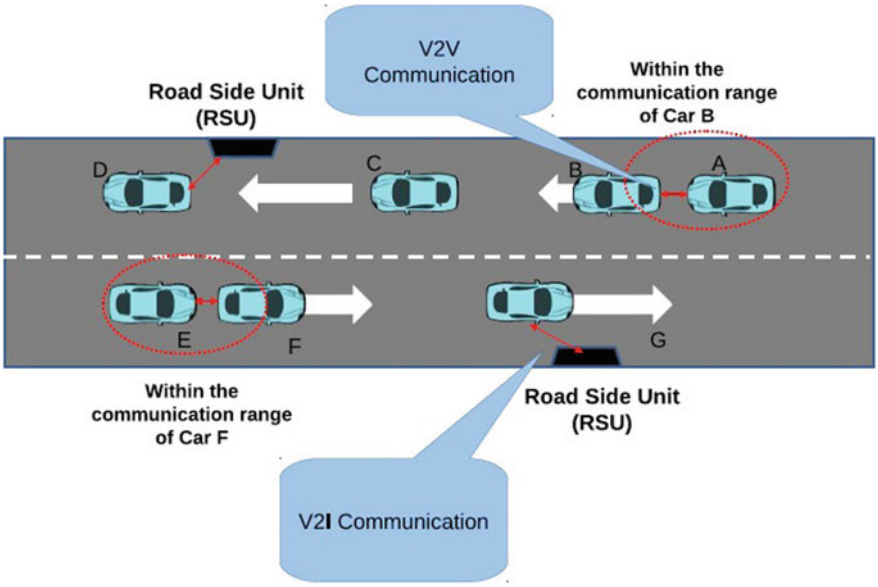

Fig. 1 An image describing communication in VANET

2 Literature Review

Routing protocols for VANET has been an area of research since many years. There has been quite a no. of algorithms proposed as well as implemented till now. Most of the algorithms proposed earlier suffered from the limitation that they made use of static data, which did not provide reliable information.

Over the years, protocols such as AODV [2] and other similar protocols were proposed, which used flooding to obtain the path between source and destination. There have been other algorithms like VADD [5], which required the vehicles to store the information, until they find a next hop to transmit. Then, Santos R A, Edwards R.M, et al. [7] proposed a scheme in which vehicles will be divided into groups and each group will have a cluster head. All the communication between nodes belonging to two different groups will be occurring via the cluster heads. The following table discusses some of the routing protocol studied, along with their strengths and weaknesses (Table 1).

Table 1 Summary of related work and required modification of VANET routing protocols

Research paper	Proposed scheme	Strengths	Limitations
Perkins C. E, Belding-Royer E and Das S [2]	In this protocol, route discovery is on-demand. The route is made only when the source node has to transmit packets to the target node	The advantage of this protocol is that the routes are established on demand basis, as well as the easy identification of the destination by its sequence numbers	The disadvantage of AODV protocol is the control overhead generated due to number of Route Reply to a single Route Request message
Lochert C, Mauve M, Fler H, Hartenstein H [3]	This protocol works best in city scenario, which are similar to real-world streets, and it does not require any extraneous data such as a map	The algorithm is highly suitable for VANET and has a moderate performance in sparse density cases	This algorithm displays poor scalability
B.C. Seet, G. Liu, B.S. Lee, C.H. Foh, K.J. Wong, K.K. Lee [4]	A-STAR uses fixed information regarding the traffic and assumes that buses commute on roads or streets that are more probable of having large number of vehicles. A-STAR therefore select these roads for transmitting of data packet	The algorithm is scalable and has internet suitability	The major drawback of this scheme was the fact that it used static data and not real-time data
Zhao J and Cao G [5]	The algorithm is based on store and transmit approach, in which a moving node has the packet till it has a new vehicle in its transmission range to forward the packet	This protocol exhibits high throughput and Packet Delivery Ratio	The protocol does not have internet suitability
J. Bernsen and D. Manivannan [6]	This routing protocol for VANETs makes use of an undirected graph in order to represent the roads and their intersections, where the vertex in the graph is the point at which the roads meet, and the roads are represented by the edges	It performs monitoring of traffic actively and in real-time	Packet overhead and unnecessary usage of known edge list with routing packets are some of the weaknesses the algorithm suffers from

(continued)

Table 1 (continued)

Research paper	Proposed scheme	Strengths	Limitations
Santos R A, Edwards R.M, Seed L N, and Edwards A [7]	This algorithm uses cluster head for forwarding of message packets	This routing protocol is well suited for networks having large no. of nodes because it provides good scalability	The algorithm is not suitable for sparse density of nodes

3 Research Gap

While most of the known routing algorithms for VANET have made an attempt in ensuring an efficient delivery of message from one vehicular node to another, however due to fast vehicles movement, dynamic exchange of information and relatively higher speed of moving nodes, finding and keeping routes is a very important task in VANETs. The following are the key points which the current VANET routing algorithm lack from.

1. A major requirement in protocol design in VANETs is how to improve reliability of minimum-delay routing algorithms to simultaneously lower the delay in delivery time and the number of message retransmissions.
2. To design a routing protocol for a city, the interference by large buildings along roads should be taken into account. A robust routing algorithm efficient against interference should be developed for a city environment.
3. Temporary gaps or loss of connectivity in networks are quite common on most roads.

   So, real-time data is required for routing, and not static data.
4. Reduction in congestion in the network due to excessive number of packets required for discovering the real-time traffic information.
5. Packet Overhead should also be kept under check, by minimizing or avoiding unnecessary information in message packets as much as possible.

4 Methodology Proposed

The VANET routing scheme, which has been formulated for V2V communication, is an optimization of the greedy approach to routing. The protocol sends messages using those routes, which it considers as reliable, after monitoring the traffic, through its components for monitoring of traffic. This monitoring of traffic is done in runtime, by voluntarily sending a probe message along the roads or streets, as well as passively by monitoring messages, that traverses a particular node. The reliability information of a street is also propagated along with the traffic monitoring step, so no broadcasting, flooding or any other means, which can cause network congestion needs to be used. The street reliability data is distributed among all the nodes in a

better way by piggybacking all the data on the probe packets. In order to take benefit of the piggybacked data, in complete lifetime of the probe packet, the routes can be calculated as and when required at any street intersection junction, during the transmission of the message. This process of recalculating the route is a portion of the route recovery, in case no next node can be obtained in the present route. Like any other greedy routing algorithm for VANET, this protocol finds its neighbouring nodes, with the help of the probe message, utilizes location-based routes, and uses a greedy approach to transmit the packet to the target. A node also identifies the location of its neighbouring nodes using the probe message. After knowing the coordinates of the destination, it can choose the appropriate forwarding node, and continue this process, until the destination obtains the message.

The protocol has a basic information of the geographical position of all the streets and their meeting point, which has been supplied to it through static pre-loaded data. So, the protocol uses this street-awareness to route messages along the streets through vehicles. Also, the protocol generates a route from source to target, such that these routes are anchored at certain geographic locations, mainly the street intersections. The protocol does not follow a completely greedy approach from start to end, but, in fact, it sends packet greedily between two anchor points, which it finds as reliable.

4.1 Traffic Monitoring

Monitoring of the traffic in the algorithm is done in two ways—active monitoring and passive monitoring, which are performed in run-time. In active monitoring, the main aspect is the probe packet, which is simply a message that is sent time-to-time by nodes, which are present closer to the street vertex in the network. The probe message after being sent by a vehicle, which is present near a street intersection point, is greedily forwarded to the desired next-hop nodes along the road that is meeting on that vertex. Since, the end node for a probe message is unknown to the sending node, thereby the probe message keeps on traversing the current edge, until it is received by a node which is near to the opposite street vertex. In case of no next node being available for transferring the probe packet, it is dropped. However, if the packet has been successfully delivered to the node at the opposite end, then all the nodes along that road will be aware of the connectedness of the edge at that moment. The probe sent to the neighboring street edges also function the same way except the fact that they are sent with a time limit or distance limit, so that they cover only one of the vehicle in its path and obtain as well as distribute information regarding the street edges among themselves. The probes perform dual functions of traffic detection as well as distribution of traffic information. While transmitting the probe packet, the sender node also has to add edge list with the probe packet, in which it will add information about all the edges, which are known to it, along with their weights, as well as the last time it received any update regarding that particular edges' weight. When that packet goes through intermediate nodes, they will analyze all the information present in the known-edge list. They will find out whether they

have the information regarding a particular edge present in the list or not. If they have a more recent information, then they will make necessary changes in the probe packet, otherwise they will take the most recent update about that edge from the probe. Also, if they have information about an edge, which probe packet does not contain, then they will also add that information in the packet. A node on generating the probe packet does not simply add information about all the edges, in fact, it makes a selection from all the available nodes. The nodes do not include information about those edges, whose weight is marked as default value, or the one whose weight it does not know. From the remaining ones, it excludes all those edges, whose weight has not been updated since the last time they were shared. All this exclusion of edges is done to reduce the network congestion as well as the packet overhead.

4.2 Determination of Reliable Path

In any routing algorithm attempting to find the shortest path between two nodes, the edge weight is generally a reflection of the distance between those two nodes. However, in this algorithm, edges are assigned weight, but they are not based on the distance between two nodes, but on the reliability of the path between two nodes. This means that, if any road segment is found to be connected or traversable by a probe packet, then that edge will be assigned the minimum weight. Similarly, on finding an edge to be disconnected will result in that edge being assigned the maximum weight possible. After assigning weights to all the edges, Dijkstra algorithm can be run to find the path with the least weight and highest reliability. After this path is obtained, it is written down in the packet along with the reliability value of each edge.

4.3 Calculation of Reliability Value of a Path

In order prefer information about edges which have are more recent, the protocol assigns the reliability weight of a road as the number of milliseconds elapsed since that road was last covered by any probe message. As per this algorithm, a road which has been traversed recently in the past will have a lower weight as compared to the one which was traversed some time ago. And as the recent information is more likely to be correct, so road segments with lower weight will be preferred over those with larger weights, while finding the path from source to destination. A node relies upon the probe message to assign weight to a particular edge. If a node finds that a probe packet has traversed an edge, that means that particular edge is connected or reliable, and will be assigned the minimum weight. The weight assigned will keep on increasing linearly with time, so as to indicate that the information about the route is not recent. And in cases, when a node finds out that an edge is not traversable by a probe packet and is disconnected, it will assign it the maximum possible weight, until it gets new information regarding the connectedness of the road. Apart from

calculating the values of the edges on the go, all the nodes may also assign some pre- defined static values to the edges/roads. In case, it has been a long time since a probe packet has conveyed the message to the node regarding the connectedness of a road, the node can assign a default value to that edge, to indicate that the information regarding this edge is quite old, and the edge should be avoided, if we have a better path not traversing that edge.

4.4 Routing of Data Packets

For sending the message from source to the destination, firstly, the location of the destination node is obtained. After obtaining the information about the position of the target node, the distance between the source and the destination is calculated. If the calculated distance is found out to be small, such that both the nodes are within the radio range of each other, then the source node greedily sends the packet towards the target node. In case the two nodes—source and the destination are not within the range of each other, then the source node will consult its street graph, and then will run the Dijkstra algorithm to find out the most reliable path. The path from the source to the destination is generally obtained in the form of street intersection points, known as anchor points, and the whole path is known as the anchor path. The anchor path is written around the message packet in the header. Each node finds the next node to transfer the packet to, such that the packet reaches successfully to the destination. All the intermediate nodes look up the anchor path in the header of the message packet and determine the next node, which is within its range and closer to the next anchor point in the path to the destination, and send the packet to it.

5 Implementation

The algorithm proposed in the previous section was implemented using MATLAB. An user- interface was developed to ensure generalization of the proposed routing algorithm for VANET. The user-interface requires the users to provide the following details to begin simulation.

1—No. of nodes/vehicles, 2—Source Node, 3—Destination Node (Fig. 2).

The simulation results obtained from the implementation can be divided into two sections—1. Varying the number of nodes and 2. Varying the time period of routing update probe packet.

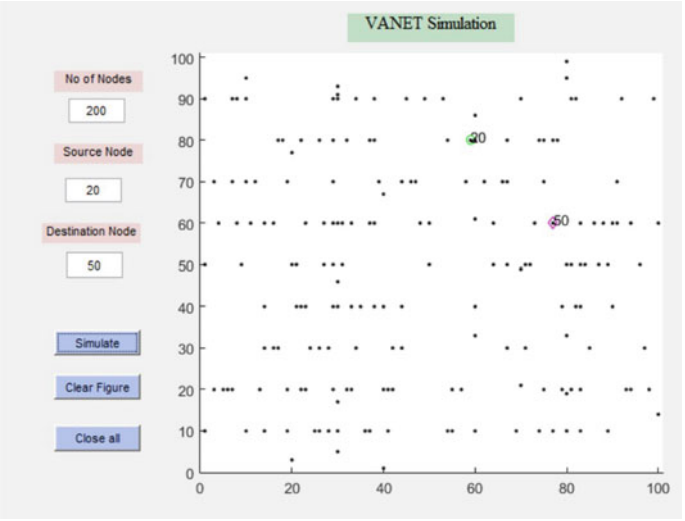

Fig. 2 User-interface for VANET simulation

5.1 Based on Number of Nodes

The number of nodes affects the node density, which is the no. of nodes or vehicles per unit distance. The result of the routing algorithm under various cases are as follows.

CASE 1—Number of Nodes = 200
INITIAL—THROUGHPUT

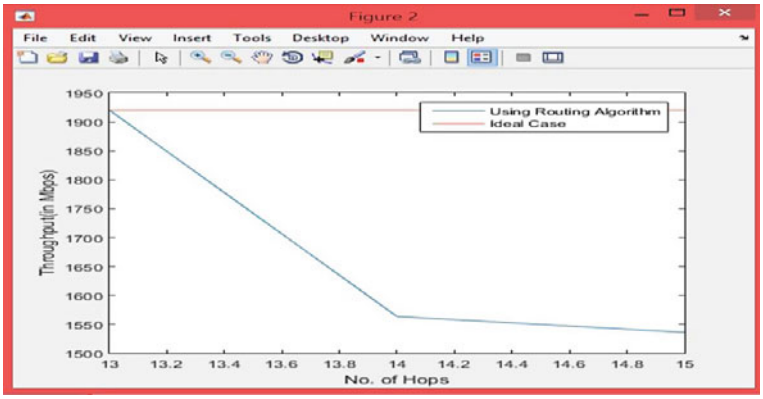

In the above graph, the throughput was similar to the ideal case, when the no. of hops between source and destination was lesser, and, thereafter, it has decreased.

CASE 2 Number of Nodes = 1000
INITIAL—THROUGHPUT

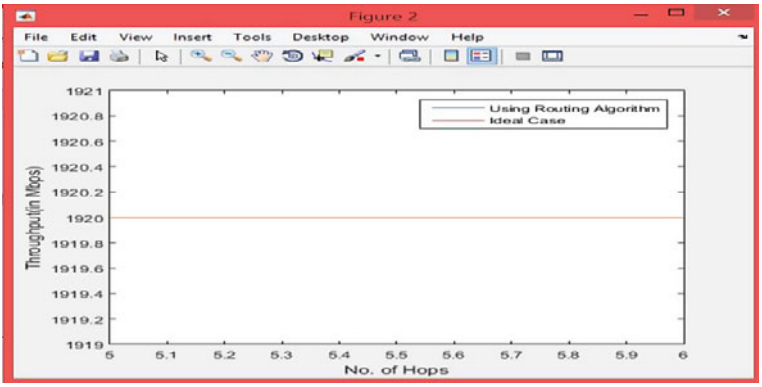

5.2 Based on Routing Updation Time Period

As in the proposed algorithm, a node present near to a street vertex sends a probe packet periodically. The periods may vary, and the following cases represent the working of the algorithm for different routing updation time period, given that each node took approximately 1.2 s to change their current position to a new one.

CASE 1—Routing updation time period = 20 ms
THROUGHPUT

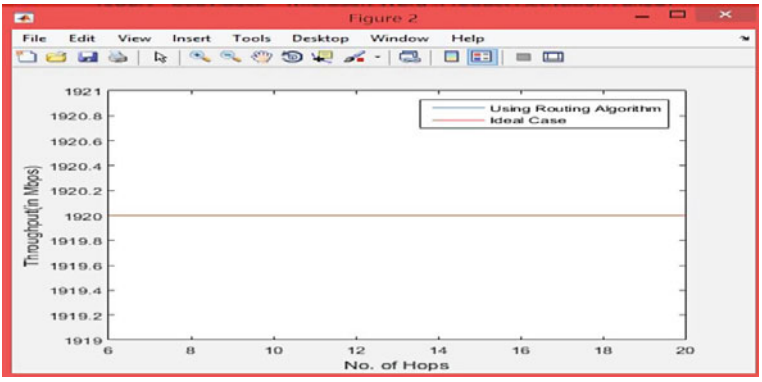

As the routing updating period is quite low, so most of the nodes quickly got information regarding any changes in the network topology, and thereby, the throughput is same as the ideal case, and there is no packet loss.

CASE 2 Routing updation period = 500 ms
THROUGHPUT

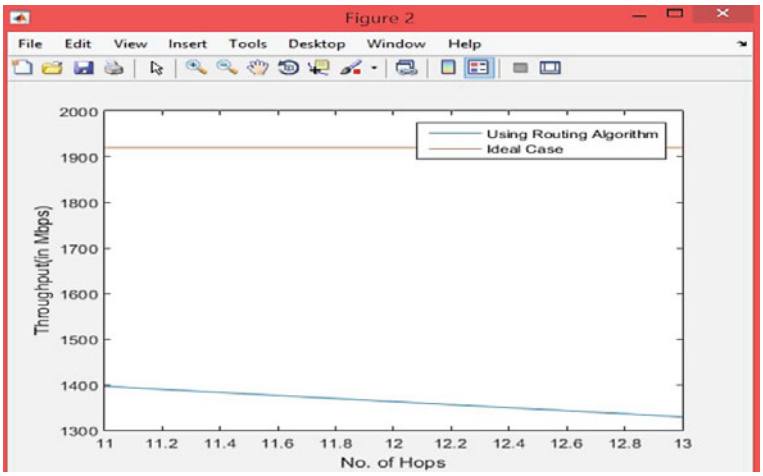

The above graph shows that the throughput has been highly reduced, because of the very large routing updating time period.

6 Comparison with Existing Work

In order to find out the performance of the proposed algorithm for ensuring real-time vehicle-to-vehicle communication, a comparison with one of the existing protocol in the field was done, under similar conditions. RIVER [6] protocol was used for comparison with our work, and the results are depicted as follows -

1—Routing packet header size
In RIVER protocol, each routing packet needed to store information in the form of edge-list, but in our proposed work, routing packet do not need to store any such information (except in case of link failure), resulting in a significant amount of reduction in packet overhead.

2—Reduced Convergence Time
Another area, where the proposed scheme outperforms the RIVER is the time required for all the nodes to converge to any kind of changes in the network topology. Since, RIVER depends upon the routing packets to carry such information, our

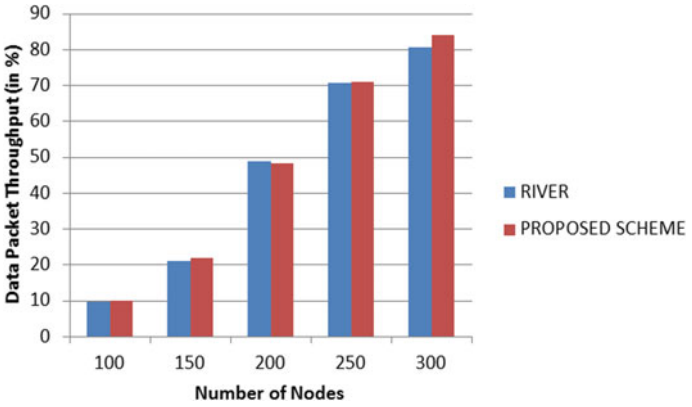

Fig. 3 Data Packet throughput comparison

scheme uses probe packet for this. There can be large no. of scenarios, such as when there is no routing packet moving through nodes having the updated information, other nodes in RIVER will not be updated about a particular change, but in the proposed scheme, since the probe packet travels to adjoining road as well with a distance limit and obtains the updates, all the nodes converge to the network changes quickly, without the need of any routing packet carrying the information.

3—Data Packet throughput

The Data Packet throughput of both the scheme under similar condition was obtained, as shown in the figure below.

As can be seen from the figure above, the proposed scheme has almost similar or better packet throughput in most of the cases. Add to the fact that the throughput of the proposed scheme has been obtained with reduced packet overhead as well as reduced convergence time signifies the scheme proposed (Fig. 3).

7 Conclusion

The proposed algorithm is expected to overcome most of the limitations summarized in the research gap. The algorithm was simulated using MATLAB, and simulation results under various situation were also presented. The algorithm works by ensuring that it finds the most reliable path from source to target, and at the same time, keeps in check the traffic congestion in the network as well as the packet overhead. The algorithm simulated worked well when the node density, or the no. of vehicles in the network were medium to high. However, its efficiency in cases when the no. of nodes are quite less, such that when most of the vehicles are not able to find another one in its range, is something that can be worked upon more. Overall, the algorithm selected the most suitable path in terms of reliability to send data, with a reduced

packet overhead as well as reduction in the number of probe packets that need to be sent as well, which is the real strength of the algorithm proposed.

There are still areas where further work can be carried upon in this algorithm. This includes the fact that efficiency of this algorithm can be improved for cases when the no. of nodes or vehicles are less in number. Also, in cases, when there is no next node within the range of a vehicle for transferring the packet, the packet is simply dropped. Mechanism similar to store and forward in such kind of situations can be studied and implemented. The algorithm tries to store information regarding all the routes in the network, even about those routes that are never going to be accessed by that node, so more research can be carried out regarding how to avoid storing information about all the routes, and still get better results.

References

1. Yang F, Wang S, Li J, Liu Z, Sun Q (2014) An overview of internet of vehicles' China communications, vol. 11. IEEE
2. Perkins CE, Belding-Royer E, Das S (2003) Ad hoc on-demand distance vector (AODV) routing. http://www.ietf.org/rfc/rfc3561.txt
3. Kumar N, Verma K, Annu (2020) Security for mobile system: 5G. In: Proceedings of international conference on optical & wireless technologies (OWT). LNEE, vol 648. Springer, pp 189–198
4. Lochert C, Mauve M, Fler H, Hartenstein H (2005) Geographic routing in city scenarios (poster). In: MobiCom 2004. ACM SIGMOBILE Mob Comput Commun Rev (MC2R) 9(1):69–72
5. Verma K, Hasbullah H (2013) Prevention of DoS attacks in VANET. J Wirel Pers Commun 73(1):95–126
6. Seet BC, Liu G, Lee BS, Foh CH, Wong KJ, Lee KK (2004) A-STAR: a mobile ad hoc routing strategy for metropolis vehicular communications. In: Proceedings of the third international IFIP-TC6 networking conference, networking technologies, services, and protocols; performance of computer and communication networks; mobile and wireless communications (NETWORKING 2004), vol 3042/2004 of Lecture notes in computer science. Springer, Heidelberg, pp 989–999
7. Verma K, Hasbullah H (2015) Bloom-filter based detection scheme (BFICK) for Denial of Service attack in VANET. J Secur Commun Netw 8(5):864–878
8. Zhao J, Cao G (2008) VADD: vehicle-assisted data delivery in vehicular ad hoc networks. IEEE Trans Veh Technol 57(3):1910–1922
9. Annu, Verma K, Kumar N (2020) Security in wireless sensor network using IPSEC. In: Proceedings of international conference on optical & wireless technologies (OWT). LNEE, vol 648. Springer, pp 177–188
10. Bernsen J, Manivannan D (2012) RIVER: a reliable inter-vehicular routing protocol for vehicular adhoc networks. Comput Netw 17, 56:3795–3807
11. Verma K, Kumar H, Sharma AK (2020) Preventing DoS attack in VANET by novel RBS-IP-CHOCK model. In: Proceedings of international conference on optical & wireless technologies (OWT 2020). Springer (Accepted)
12. Santos RA, Edwards RM, Seed LN, Edwards A (2004) A location based routing algorithm for vehicle to vehicle communication. In: Proceedings of 13th international conference on computer communications and networks, pp 221–226

Dual Band – Notch Elliptic Shaped Monopole UWB Filtering Antenna

Abhishek Patel and Manoj Singh Parihar

Abstract In this paper a compact elliptical monopole UWB Antenna is analyzed. Proposed structure covers the frequency band of UWB spectrum defines from 3.1 to 10.6 GHz. Symmetrical and Monopole structure of this proposed UWB Antenna is helping to achieve the good matching of impedance. Although multiple interfering frequency bands are existing in the define UWB spectrum. Filtering characteristics have been incorporated to eliminate the effect of existing interfering bands. Two $\lambda_g/2$ rectangular split ring resonators (R-SRR) are used within the monopole radiator. These R-SRR are producing notch in WiMAX and X-Band of UWB spectrum. Commercially available software CST Microwave Studio has been used for design and simulation of proposed prototype. Results achieved from the simulation are showing the desired performance characteristics of proposed prototype. Return loss of the proposed UWB Antenna is better than −10 dB and gain and efficiencies are in good agreement as desired.

Keywords UWB · Antenna · Resonator · Monopole · Planner · Band – Notch · R-SRR · SWB

1 Introduction

In the year of 2002, due to increasing demand of UWB applications, FCC (Federal Communication Commission) has permitted to use of the frequency band from 3.1 to 10.6 GHz, known as Ultra-Wide Band, for the commercial purpose [1]. UWB have wide applications in field of modern wireless communication system, military communication, imaging system, satellite communication system and radar technology [2, 3]. Qualities like higher data resolution, less interference, low cost of

A. Patel (✉) · M. S. Parihar
Department of Electronics and Communication Engineering, PDPM Indian Institute of Information Technology Design and Manufacturing, Jabalpur, India
e-mail: 20pece01@iiitdmj.ac.in

M. S. Parihar
e-mail: mparihar@iiitdmj.ac.in

M. Tiwari et al. (eds.), *Optical and Wireless Technologies*, Lecture Notes in Electrical Engineering 892, https://doi.org/10.1007/978-981-19-1645-8_23

design, higher data transmission rate, low complexity, less spectral power density etc. thrust this UWB frequency band to emerge as a new technology which would be easily available and user friendly [4].

Various types of structures of proposed microstrip UWB antenna are available in the literature resources. Rectangular, Circular, Elliptical, Triangular, semi-circular, rectangular-cum-circular structures are commonly used. To achieve the better results from the antenna, designer should prefer the symmetrical structure. Monopole structures are used because of twice the directivity of dipole structured antenna and also helps to achieve good matching [5–8].

However, there are existing interfering bands in the UWB frequency band. These bands are WiMAX, WLAN, C-Band and X-Band which produces interference to the UWB frequency band. Several methods like ring resonator method, filtering method etc. are available to eliminate the effects of interfering bands. In this paper the addition of rectangular split ring resonator (R-SRR) is used to suppress the effect of WiMAX and X-Band from the UWB Spectrum [9–17].

In this paper elliptical shaped structure has been designed and simulated. The design specifications are elaborated in the Sect. 2. Section 3 covers the analysis of parameters used to design the proposed structure. Simulated results and other required results and performance analysis is arranged in the Sect. 4. Finally, the concluded remarks are drawn in the Sect. 5.

2 Design Specifications of UWB Antenna

The proposed structure of UWB Filtering Antenna is made of FR-4 (Lossy) material with a dielectric constant of 4.3 and loss tangent of 0.025. Thickness of the substrate is 1 mm. Dimensions of the substrate is 36×38 mm^2 and the elliptic shaped radiating patch on the top layer is excited with 50Ω microstrip feedline. FIT based CST Microwave Studio is used to obtained the simulation results of proposed UWB Filtering Antenna [18]. Complete structure with dimension parameters is shown in Fig. 1 and optimized value of parameters are mentioned in Table 1.

2.1 UWB Antenna Design

The proposed structure of UWB antenna is shown in Fig. 1 optimized dimension of the elliptic shaped radiating patch is achieved by analyzing the parameters of proposed structure, which is discussed in Sect. 3. Ground of this monopole UWB antenna is etched with rectangular cum circular slot to achieve better impedance matching and the reflection coefficient has been depicted in Fig. 2.

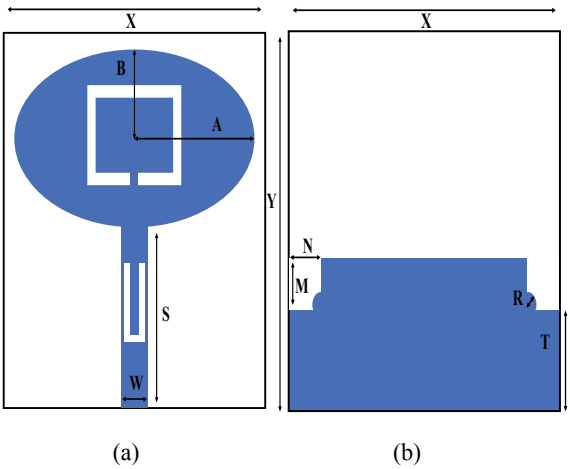

Fig. 1 Geometry of proposed UWB antenna **a** Top view and **b** Bottom vview

Table 1. Optimized dimensions of the proposed ffiltering antenna

Parameter	A	B	C	D	E	F	G	J	K
Value (mm)	16	9	5	1.5	0.35	0.35	0.4	0.4	8.5
Parameter	L	M	N	R	S	T	W	X	Y
Value (mm)	5.2	6	6	2.5	19	13	2	36	38

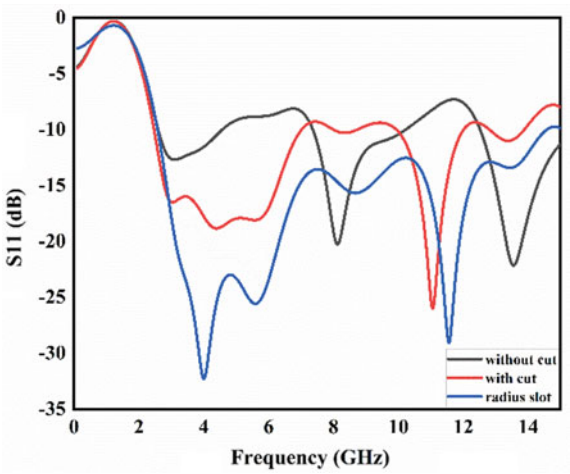

Fig. 2 Reflection coefficient of proposed UWB antenna

2.2 Resonators Design

To design the filtering antenna, the necessary steps comprise with the design of filter which will create notch in the WiMAX and X-Band of the UWB spectrum. Two

$\lambda_g/2$ resonators are used to create the notch in above mentioned frequency bands. Narrowband response in the WiMAX band is achieved due to C type resonator, with center frequency at 3.5 GHz. Simulated result of C-Type resonator is shown in Fig. 3. Another resonator has designed with U-Type structure and producing narrowband response in the X-Band of UWB spectrum. This resonator is designed with center frequency of 8.4 GHz. S-parameter of this resonator achieved after the simulation is shown in Fig. 4.

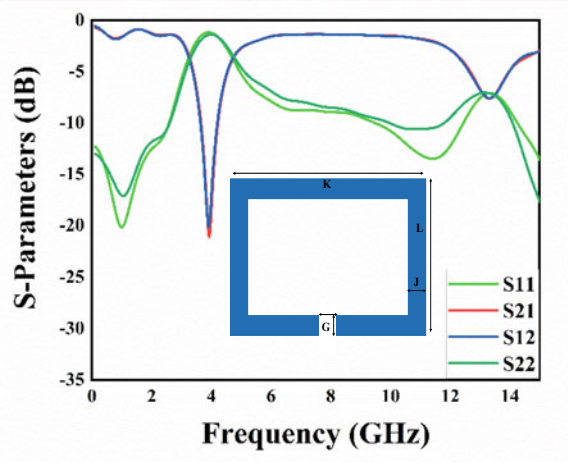

Fig. 3 S – parameters of C-type resonator

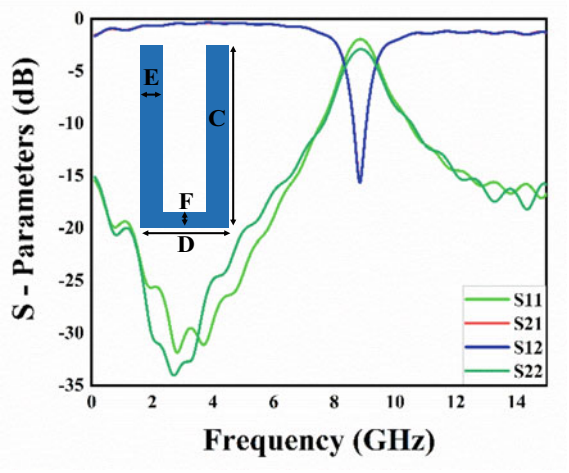

Fig. 4 S – parameters of U-type resonator

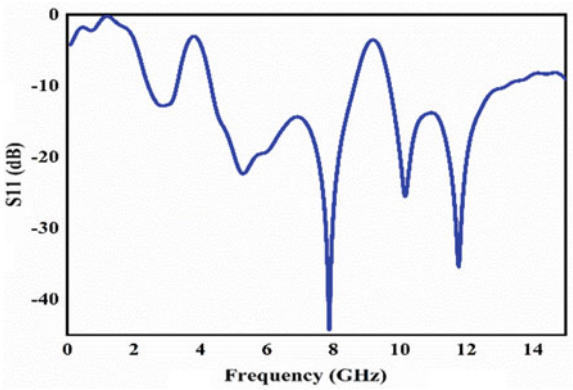

Fig. 5 S11 of proposed UWB filtering antenna

2.3 UWB Filtering Antenna Design

Antenna and filter have been designed and simulated separately in the previous step of this section. Now the next step is to design the filtering antenna by merging the design in the single patch shown in Fig. 1. The return loss of the proposed filtering antenna obtained from the simulation is shown in Fig. 5. Other simulated results have been discussed in the Sect. 4.

3 Parametric Analysis

To optimize the dimension of the proposed structure, analysis of parameters has been performed in this section.

3.1 Major Axis of Elliptic Patch

As the ellipse have two dimensions, in which major axis is one of them. Fig. 6 shows the effect of major axis of the radiating elliptic patch. At A = 16 mm, the spectrum covers the spectrum which defines for the UWB. Hence the optimized value of major axis is taken as A = 16 mm.

3.2 Minor Axis of Elliptic Patch

Reflection coefficient of different values of minor axis of elliptic patch is shown in Fig. 7. As B increases from lower to higher value, the return loss going more deeper

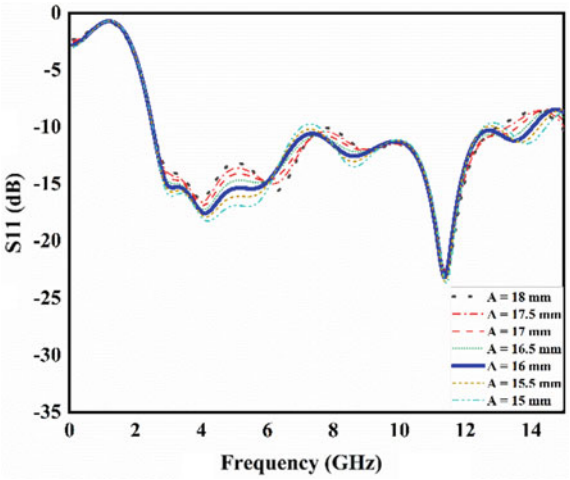

Fig. 6 S11 of parametric analysis on major axis of elliptic patch

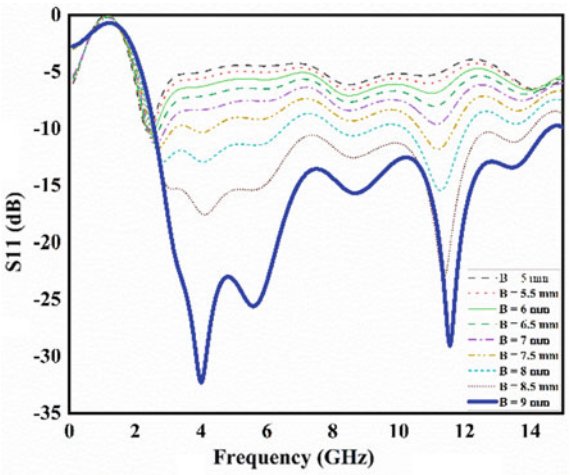

Fig. 7 S11 of parametric analysis on minor axis of elliptic patch

than previous one. The optimized value of minor axis is taken as B = 9 mm because at this value spectrum covers the UWB frequency range significantly with less return loss.

3.3 Length of U-Shaped Resonator

Optimization of length of U-shaped resonator has been explained in this section. As length changes from lower to higher value the S21 also changes from higher

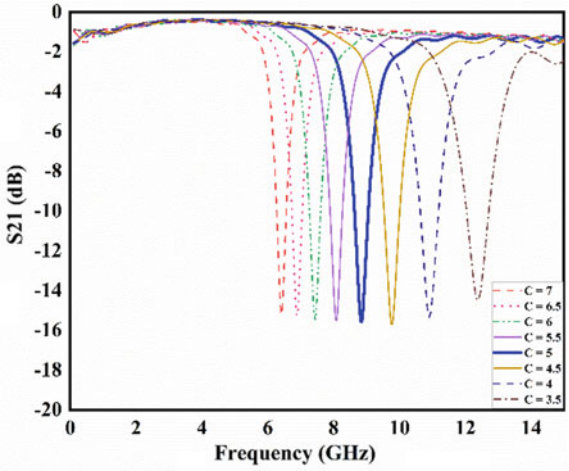

Fig. 8 S21 of Parametric analysis on length of U-shaped resonator

frequency to lower frequency shown in Fig. 8. At half wavelength of central frequency S21 shows expected result.

3.4 Width of U-Shaped Resonator

For creating notch in X-Band, U-shaped resonator has been used. In Fig. 9 variation of width of this resonator has been explained. As width increases from D = 0.9 to D = 1.8 mm, the notch goes deeper and at the value of D = 1.5 mm, S21 shows significant result. Hence value of length has been taken as D = 1.5 mm.

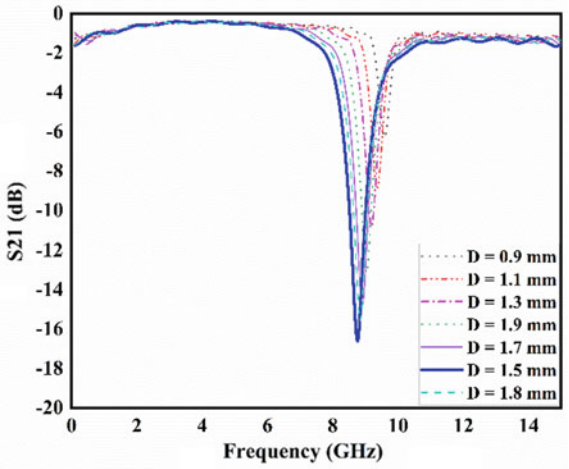

Fig. 9 S21 of parametric analysis on width of U-shaped resonator

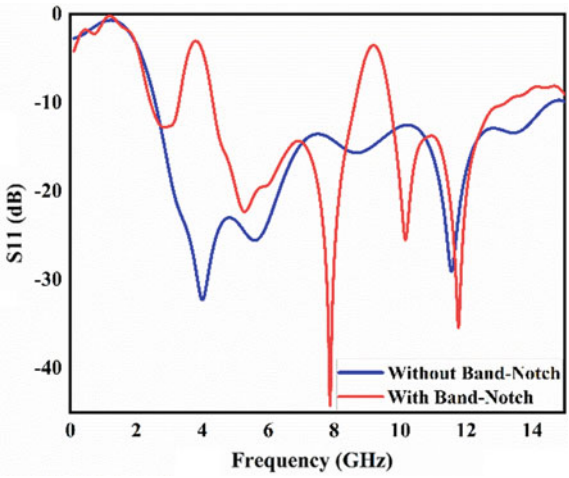

Fig. 10 Reflection ccoefficient of proposed filtering aantenna with and without Band-Notch

4 Results and Discussion

4.1 Reflection coefficients of proposed Filtering Antenna

Results obtain from the simulation of reflection coefficients of structure shown in Fig. 10 explains that good matching is achieved and reflection coefficient is below −15 dB in the pass band and above −4 dB in stop band also covering the spectrum of UWB band.

4.2 Gain and Efficiency of proposed Filtering Antenna

In the Fig. 11 explaining the simulated results that realized gain is negative for stop band and below −5 dBi in WiMAX Band and below −2 dBi in X-Band and above 3 dBi in the pass band and total efficiency with and without notch band is above 60% in pass band and below 20% in stop band.

4.3 Far-field pattern of proposed Filtering Antenna

The simulated normalized far-field pattern in x-z plane and in y-z plane in various frequencies are shown in Fig. 12. In x-z plane E-filed showing omnidirectional pattern at 4 GHz and at 6 GHz and at 7.5 GHz E-field observes directional pattern and at 12.5 GHz which is beyond the UWB band, E-field converse as more directive and showing the butterfly shape. Unit of the E-field pattern showing plot is Theta/Degree

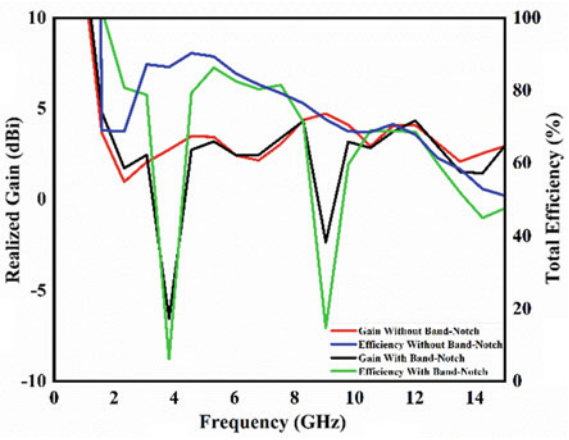

Fig. 11 Gain and efficiency of proposed filtering antenna

vs dBV/m. H-field pattern observes in the y-z plane and omnidirectional pattern showing at 4 GHz and at 6 GHz. Direction pattern observed at 7.5 GHz and at 12.5 GHz. Unit of the plot showing H-filed pattern is Theta/Degree vs dBA/m.

4.4 Surface current distributions of proposed Filtering Antenna

The simulated surface current distributions without notch bands and at notch bands are shown in Fig. 13. The surface current distribution without notch bands at frequencies 5 and at 7.5 GHz are shown in Fig. 13(a) and (b), explains that current is completely concentrated at radiating elliptic patch. In the WiMAX band at 3.5 GHz the surface current distributed mainly at C-shaped resonator shown in Fig. 13(c). In the X-Band the surface current concentrated at U-shaped resonator shown in Fig. 13(d).

5 Conclusion and Future Scope

The design of a compact monopole elliptic UWB filtering antenna is proposed in this paper. Reflection coefficient of proposed antenna shows return loss below −14 dB and covers the entire UWB spectrum also covers frequency beyond the UWB spectrum hence this antenna can also be used in super wideband (SWB) application. C-shaped and U-shaped resonators are producing Band-Notch in WiMAX band and in X-band respectively. Simulated Realized gain is above 3 dBi in pass band and below −2 dBi in stop band also efficiency is less than 20% in stop band and above 60% in pass band which is in good condition and normalized far-field pattern shows good results.

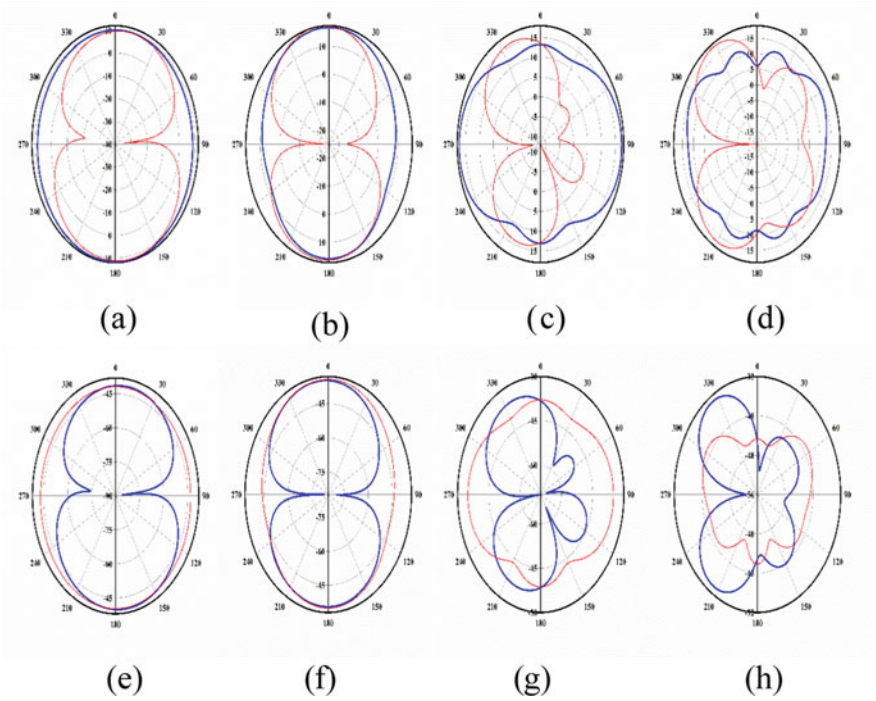

Fig. 12 Simulated normalized far-field pattern of proposed filtering antenna - in x-z plane: **a** 4 **b** 6 **c** 7.5 **d** 12.5 GHz and in y-z plane: **e** 4 **f** 6 **g** 7.5 and **h** 12.5 GHz Co Pol. Cross Pol. (pol. = Polarization)

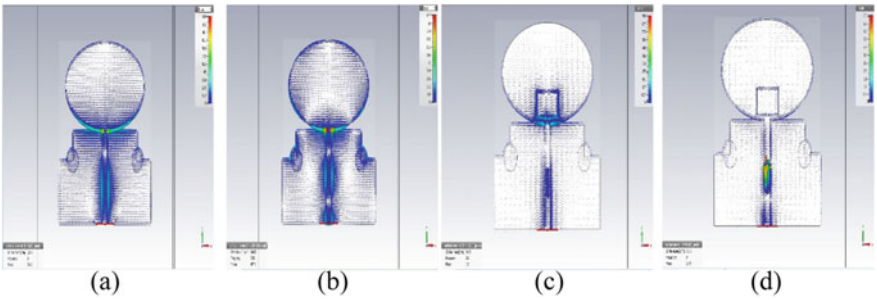

Fig. 13 Simulated surface current distribution of proposed Antenna without band notch **a** at 5 GHz **b** at 7.5 GHz and with band notch **c** at 3.5 GHz and **d** at 9 GHz

The proposed UWB antenna can be utilized for modern wireless communication applications.

References

1. Federal Communications Commission, Washington, DC (2002) FCC report and order on ultrawideband technology
2. Balanis CA (2016) Antenna theory: analysis and design. John Wiley and Sons, Hoboken
3. Pozar DM (2012) Microwave engineering, 4th edn. Wiley, New York
4. Lim EG, Wang Z, Lei C-U, Wang Y, Man K (2010) Ultrawideband antennas—past and present. IAENG Int J Comput Sci 37:304–314
5. Jung J, Choi W, Choi J (2005) A small wideband microstrip-fed monopole antenna. IEEE Microw Wirel Compon Lett 15:703–705
6. Ray KP, Ranga Y (2007) Ultrawideband printed elliptical monopole antennas. IEEE Trans Ant Propagat 55(4)
7. Chung K, Park H, Choi J (2005) Wideband Microstrip-fed monopole antenna with a narrow slit. IEEE Microw Opt Technol Lett 47:400–402
8. Thomas KG, Lenin N, Sivaramakrishnan R (2006) Ultrawideband planar disc monopole. IEEE Trans Ant Propag 54:1339–1341
9. Ryu KS, Kishk AA (2009) UWB antenna with single or dual bandnotches for lower WLAN band and upper WLAN band. IEEE Trans Ant Propag 57(12):3942–3950
10. Zhu L, Sun S, Menzel W (2005) Ultra-wideband (UWB) bandpass filters using multiple-mode resonator. IEEE Microw Wirel Compon Lett 15(11):796–798
11. Hong J-S, Lancaster MJ (2001) Microstrip filters for RF/microwave applications. Wiley, Hoboken
12. Roberto G, Guyette AC (2015) Reconfigurable multi-band microwave filters. IEEE Trans Microw Theory Tech 63(4):1294–1307
13. Tang M-C, Wang H, Deng T, Ziolkowski RW (2016) Compact planar ultrawideband antennas with continuously tunable, independent band-notched filters. IEEE Trans Ant Propag 64(8):3292–3301
14. Dikmen CM, Çimen S, Çakır G (2013) A novel ultrawideband antenna with switchable notch band. Microw Opt Technol Lett 55(7):1461–1466
15. Ojaroudi N, Ojaroudi M (2013) A novel design of reconfigurable small monopole antenna with switchable band notch and multi-resonance functions for UWB applications. Microw Opt Technol Lett 55(3):652–656
16. Kundu S (2020) A compact printed ultra-wideband filtenna with low dispersion for WiMAX and WLAN interference cancellation. Indian Academy of Sciences, Sadhana
17. Saha C, Siddiqui JY, Antar YMM (2019) Multifunctional ultrawideband antennas: trends, techniques and applications, 1st edn. CRC Press, Boca Raton
18. CST Microwave Studio 2019. www.cst.com

A Low-Profile Dual-Band Meander-Line Antenna for Sub-6 GHz 5G Applications

Swati Sharma and Rekha Mehra

Abstract This article presents the design of a dual-band, low profile, wideband antenna for sub-6 GHz 5G applications. The antenna structure consists of a square slot patch antenna fed with microstrip line, a meander line (ML) structure inside square slot and partial ground plane (PGS). The process of miniaturization of a microstrip patch antenna by the use of ML and PGS is presented in this paper. The size optimization of proposed antenna is performed by parametric analysis. Proposed antenna presents 62% miniaturization than a square patch antenna. The overall dimension of the antenna is $0.3 \times 0.3 \times 0.02\lambda_0$. The antenna has a dual band performance and resonates from 3.34–4.25 GHz and 4.65–7.07 GHz covering all the three bands n77/n78/n79 of new radio (NR) allocated for 5G communication in sub-6 GHz range by ITU-R and WRC-19. Result shows that the presented antenna has a maximum radiation efficiency of 86%, realized peak gain of 2.59 dBi, impedance bandwidth (IBW) of 910 MHz and 2.42 GHz while radiates in linear polarization (LP) manner.

Keywords Meander line · Sub-6 GHz · 5G communication · Partial ground structure

1 Introduction

Data traffic is growing rapidly due to the increase in number of smartphone users, connections of internet of things (IoT), cellular videos and smart cities. 5G wireless technology is designed to provide consumers with multi-gigabit data rates (Gbps), ultra-low latency, enhanced security, large network capacity, and a consistent user experience [1]. To accommodate 5G, the key spectrum is allocated into three bands: low-band (up to 1 GHz), sub-6 GHz band (1 to 6 GHz), and mmWave band (above 24 GHz) [2]. Several nations are focusing on the sub-6 GHz band for 5G deployment. The major reason for choosing the mid-band frequency over the mmWave frequency

S. Sharma (✉) · R. Mehra
Government Engineering College, Ajmer, India
e-mail: swati.sharma777@gmail.com

M. Tiwari et al. (eds.), *Optical and Wireless Technologies*, Lecture Notes in Electrical Engineering 892, https://doi.org/10.1007/978-981-19-1645-8_24

appears to be that propagation losses are more at higher frequencies, propagation loss includes atmospheric losses and path losses [3].

Antennas are indeed a integral component of all mobile communication systems. Because the globe has already adopted the 5G communication technology, antenna design for 5G smart phones and base stations is in demand. Furthermore, the sub-6 GHz antenna must coexist with other services band antennas such as Wi-MAX, WLAN, and LTE. The 5G antenna should be small enough to be integrated in mobile devices. Microstrip patch antennas have become the preferred choice among many types of antennas because to their desirable characteristics of low-profile, lightweight, low-cost, and easy integration with MIC and MMIC circuits [4]. So far a few number of antennas have been presented for midband of 5G, an ellipse-shaped patch antenna[5], a dual-polarized magneto-electric antenna [6] and a rectangular patch [7]. However these antennas are having very large dimensions and are unable to achieve the n79 band. The other reported articles for sub-6 GHz are comprised of two substrate layers [8]and 4-pin diodes applied on the two substrates [9]. These antenna are having larger volume which restricts their application in portable devices. To overcome the issue of large size and volume, the concept of meander line based antenna is utilized in the proposed antenna. Meander line has a advantage of simple structure, electrically small dimension, and low profile [10]. ML technique also introduces dual/multiband resonance [11] and wideband response by considering the unequal size of MLs in antenna system [12].

In this paper, a compact, dual band antenna is proposed for 5G sub-6 GHz applications. It comprises of a square slot patch antenna, MLs and partial ground plane. This antenna resonates from 3.34–4.25 GHz and 4.65–7.07 GHz and covers all the three bands of new radio (NR) allocated by ITU-R and WRC-19 for 5G-sub-6 GHz, i.e., n77(3.3–4.2 GHz), n78 (3.3–3.8 GHz) and n79 (4.4–5.0 GHz) [13]. In Sect. 2 antenna geometry and its step-wise evolution is explained, Sect. 3 presents the results and their analysis followed by a conclusion in Sect. 4.

2 Antenna Design

In this section, the stepwise design of the proposed antenna is explained in detail. The antenna is fabricated on FR-4 substrate ($\varepsilon_r = 4.3$, $h = 1.6$ mm), with the dimension of 24×24 mm. The simulation is performed using CST microwave studio suite. The proposed antenna is designed in four steps (Ant_1 to Ant_4) as shown in Fig. 1 and their corresponding simulated $|S_{11}|$ (dB) plot is shown in Fig. 2.

Ant_1 is a simple square patch antenna fed with 50 Ω microstrip line, which shows a single band performance and resonate at 10 GHz. In Ant_2 the length of ground plane is reduced to create partial ground plane (PGS) along with this a slot is created in square patch. This step is majorly responsible for size reduction as it shifts the resonance at 3.76 GHz. In Ant_3 an asymmetric ML is created inside the square slot of patch. The different width of ML creates different resonance and adjacent resonances increases the bandwidth hence creates 3.7 GHz wideband (3.4–7.13) GHz. Now to

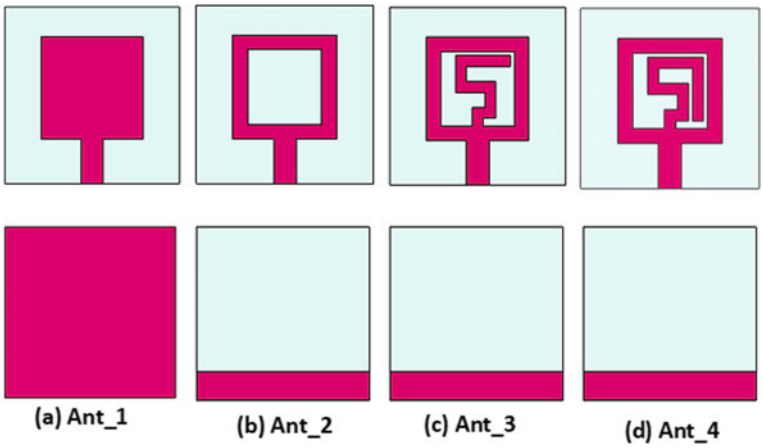

Fig. 1 Design steps of the proposed antenna **a** Microstrip fed square antenna **b** square slot antenna with PGS **c** ML based antenna **d** Bar along with ML antenna

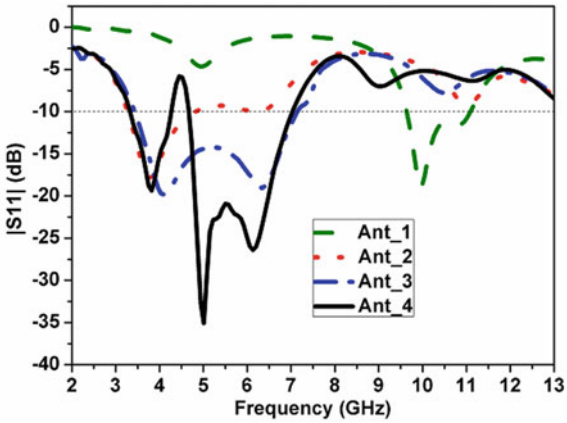

Fig. 2 Simulated $|S_{11}|$ (dB) Parameter graph at different stages of antenna design

introduce a notch within this band a bar is created along y-direction. This notch effectively removes the portion of the spectrum that does not fall inside the 5G sub-6 GHz range. Ant_4 gives a dual band performance and covers the n77/n78/n79 bands of new radio. The comparison of design steps, resonating frequency and their respective impedance bandwidths (IBW), are summarized in Table 1. The schematic diagram of the ML loaded patch antenna is displayed in Fig. 3 and the optimized values of parameters are shown in Table 2. The width (Wp) of patch is calculated as:

$$W_P = \frac{c}{2f_0\sqrt{\frac{\varepsilon_r+1}{2}}}$$

Table 1 Comparison of impedance bandwidths and resonation frequencies of the Ants. 1–4

Antenna steps	Antenna structure	No. of bands	Center frequency (GHz)	IBW (GHz)
Ant_1	Square patch antenna, full ground	1	10	9.64–11.09
Ant_2	Square slot antenna, PGS	1	3.76	3.26–4.83
Ant_3	ML loaded antenna, PGS	1	4.08	3.40–7.13
Ant_4	Bar along with ML antenna, PGS	2	3.8, 5	3.34–4.25, 4.65–7.07

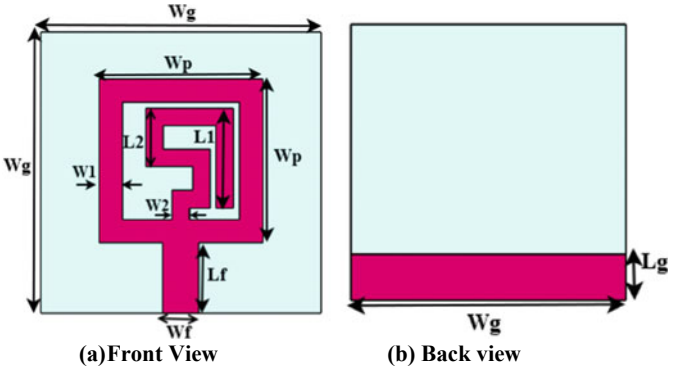

Fig. 3 The schematic diagram of the ML loaded patch antenna

Table 2 Parameters of the proposed antenna with its dimensions

Parameter	Value (mm)	Parameter	Value (mm)	Parameter	Value (mm)
Wg	24	Wp	14	L1	8.5
L2	1.5	W1	2	W2	1.5
Wf	3.1	Lf	6	Lg	4

Here $f_0 = 3.8\ GHz$, $\varepsilon_r = 4.3$ and $c = 3 \times 10^8\ m/\text{s}$.

The parametric analysis is performed in Fig. 4(a) to (d), to see the effect of different dimensional parameters on resonating frequencies and IBW, by varying one parameter at a time and keeping other parameters constant. The length of the bar (L1) varies in Fig. 4(a), and it has been observed that for values other than the optimal value i.e. L1 = 8.5 mm, the $|S_{11}|$ plot does not cover the n79 (4.4–5 GHz) band of mid 5G. In Fig. 4(b) the length of partial ground plane (Lg) varies from 2 to 6 mm. This can be observed that for lower values than optimized value of Lg, the $|S_{11}|$ plot does not cover the entire n77 (3.3–4.2 GHz) band and for higher value the $|S_{11}|$ versus frequency plot does not cover the bands of 5G sub-6 GHz. Similarly the

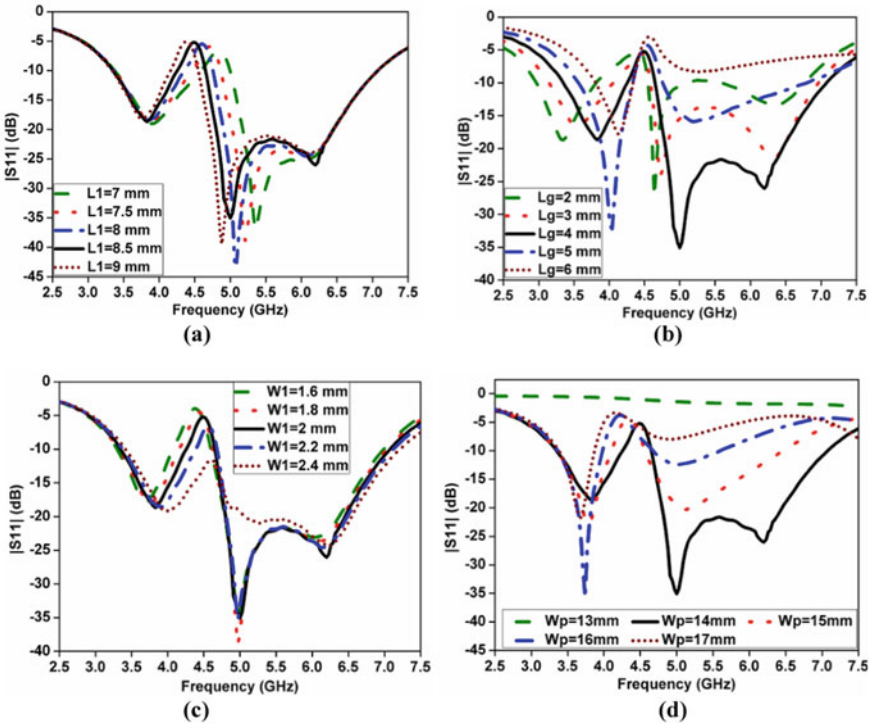

Fig. 4 Parametric analysis of ML loaded patch antenna for resonating frequencies by varying **a** length of Bar **b** Hight of PGS **c** Thickness of slot **d** Width of the patch

variation in the width of the slot (W1) effects the bandwidth coverage of 5G bands as shown in Fig. 4(c). The width of the patch (Wp) is the key factor for the resonance of the proposed antenna and effect of varying Wp from 13 to 17 mm is shown its effect in Fig. 4(d).

3 Results and Analysis

The simulated $|S_{11}|$ (dB) parameter is shown in Fig. 5, which shows that the proposed structure has a dual band characteristics and resonates from 3.34–4.25 GHz and 4.65–7.07 GHz. The surface current distribution analysis has been done at peak resonating frequencies i.e. 3.8 and 5 GHz and presented in Fig. 6. At 3.8 GHz the intensity of current is high at the edges of patch and in between the square slot and bar connected to ML, due to the coupling capacitance occurred between them. Which implies that the fundamental resonance at 3.8 GHz, occurs due to square patch antenna. At 5 GHz, as shown in Fig. 6(b) the intensity of current is high at the entire part of ML and around ML, hence this resonance is due to the ML.

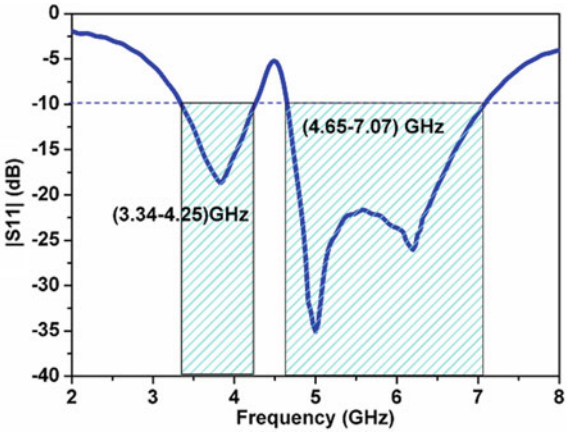

Fig. 5 Simulated $|S_{11}|$ graph of the ML loaded patch antenna

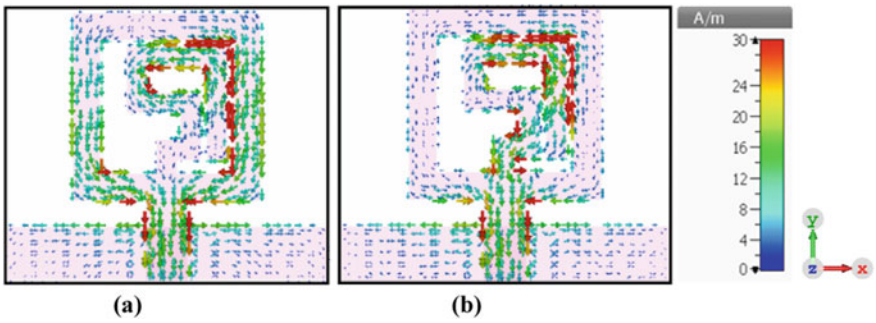

Fig. 6 Simulated distribution of current vectors of proposed antenna at **a** 3.8 GHz **b** 5 GHz

The co-polar and cross-polar radiation pattern of the proposed antenna has been simulated in the XZ plane and YZ plane which is shown in Fig. 7. Which shows that the level of cross polarization is very less than the level of co-polarization.

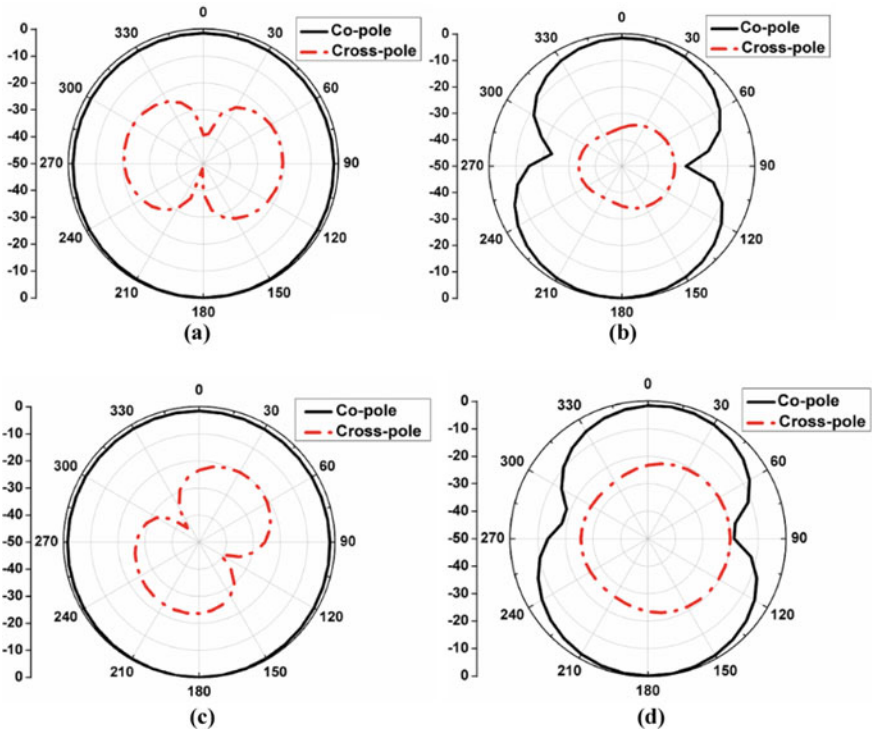

Fig. 7 Simulated radiation patterns of proposed antenna at **a** 3.8 GHz in XZ plane **b** 3.8 GHz in YZ plane **c** 5 GHz in XZ plane **d** 5 GHz in YZ plane

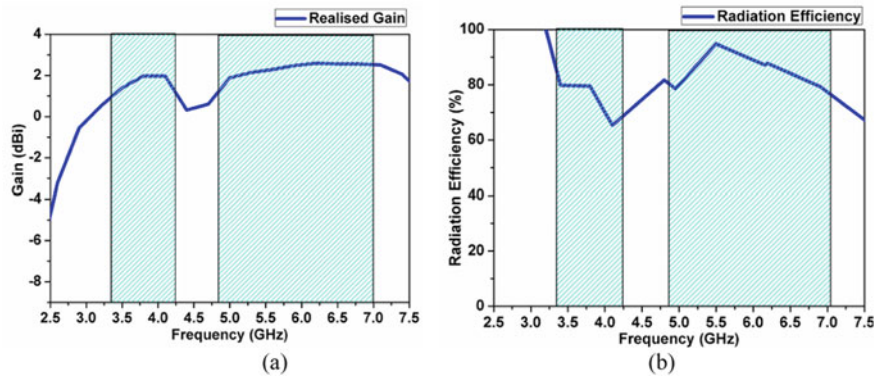

Fig. 8 **a** The simulated gain plot **b** The radiation efficiency plot of ML loaded microstip antenna

The simulated gain over the frequency plot is shown in Fig. 8(a), which depicts that the gain is stable in entire range between 2 to 3 dBi. The radiation efficiency

Table 3 Comparison of the proposed antenna with other published 5G sub-6 GHz antenna

Ref. no	Size of antenna (mm^3)	No. of bands	Band (GHz)	Profile	Efficiency (%)	Substrate	5G bands covered
[5]	180 × 60 × 1.6	1	3.28–3.78	Planar	NC	FR-4	N78
[6]	150 × 150 × 21	1	3.05–4.42	3D	NC	Not specified	N77/n78
[7]	114× 77 × 1.6	1	2.35–2.45	Planar	NC	RT Duriod	–
[8]	63 × 51.2 × 4.5	1	2.84–5.17	3D	64	FR-4	N77/78/79
[9]	100 × 100 × 5.7	1	3.39–3.62	3D	96.5	FR-4	N78
Proposed work	2 4 × 24 × 1.6	2	3.34–4.25, 4.65–7.07	Planar	95	FR-4	N77/78/79

* NC = Not calculated

over the frequency plot of this antenna is illustrated in Fig. 8(b), which shows that the efficiency of the antenna is always greater than 80% in the entire range. It depicts that the proposed LP antenna works efficiently in compete band. Table 3 shows the comparison of the proposed antenna with previously published work on the 5G sub-6 GHz antenna. This can be deduced from the table that the proposed antenna is quite compact than other cited references [5–9] while it covers all the three bands (n77/n78/n79) assigned for 5G, sub-6 GHz.

4 Conclusion

A compact, dual band, low profile, wideband antenna is designed and analyzed in this paper. The compact size antenna is achieved by using partial ground structure and square slot patch antenna. By placing bar along with asymmetric ML inside square slot patch, dual band compact antenna has been achieved. This antenna exhibit 910 MHz and 2.42 GHz wide IBW ranging from 3.34–4.25 GHz and 4.65–7.07 GHz respectively. The radiation pattern was studied at two different frequencies 3.8 GHz and 5 GHz in XZ and YZ plane. The antenna exhibits a stable gain of 5.7 dBi and peak radiation efficiency of 95%. The proposed antenna covers n77/78/79 bands allocated for 5G sub-6 GHz communication by ITU-R and WRC-19, hence it can be a good candidate for 5G sub-6 GHz communication.

References

1. IEEE: IEEE 5G and beyond technology roadmap white paper. https://5g.ieee.org/images/files/pdf/ieee-5 g-roadmap-white-paper.pdf
2. Qualcomm Technologies: Spectrum for 4G and 5G (2017). https://www.qualcomm.com/media/documents/files/spectrum-for-4gand-5 g.pdf
3. Reddy TS, Mohammad A, Chaudhary RK (2019) Four-port MIMO cognitive radio system for midband 5G applications. IEEE Trans Antennas Propag 19:5634–5645
4. Azim R, Meaze AA et al (2021) A multi slotted antenna for LTE/5G Sub-6 GHz wireless communication applications. Int J Microw Wirel Technol 13(5):486–496
5. Arya AK, Kim SJ, Kim S (2020) A dual-band antenna for LTE-R and 5G lower frequency operations. Prog. Electromagn. Res. Lett. 88:113–119
6. Sun J-N, Li J-L, Xia L (2019) A dual-polarized magneto-electric dipole antenna for application to N77/N78 band. IEEE Access 7:161708–161715
7. Sarade, S.S., Ruikar, S.D., Bhaldar, H.K.: Design of microstrip patch antenna for 5G application. In: Pawar, P., Ronge, B., Balasubramaniam, R., Vibhute, A., Apte, S. (eds) Techno-Societal 2018. Springer, Cham (2020). https://doi.org/10.1007/978-3-030-16848-3_24
8. An W, Li Y, Fu H, Ma J, Chen W, Feng B (2018) Low-profile and wideband microstrip antenna with stable gain for 5G wireless applications. IEEE Antennas Wirel Propag Lett 17:621–624
9. Jin G, Deng C, Yang J, Xu Y, Liao S (2019) A new differentially-fed frequency reconfigurable antenna for WLAN and Sub-6 GHz 5G applications. IEEE Access 7:56539–56546
10. Khaleghi A (2007) Dual band meander line antenna for wireless LAN communication. IEEE Trans Antennas Propag 55:1004
11. Bhattacharjee S, Mitra M et al (2017) An effective SAR reduction technique of a compact meander line antenna for wearable applications. Prog. Electromagn. Res. M 55:143
12. Sharma, S., Mehra, R.: A dual-band, dual-polarized, CPW-fed wideband antenna loaded with via less CRLH-MTM TL for 5G mm-Wave communication. AEUE - Int. J. Electron. Commun. **141**, 153950 (2021)
13. Electronics Packaging Society: Heterogenous integration roadmap (HIR). https://eps.ieee.org/images/files/HIR_2019/HIR1_ch12_5G.pdf/. 2019 Edition. Accessed Oct 2019

Design of Closed Loop Mach-Zehnder Interferometer for Path Length Stability

Jyoti Gondane and M. S. Panse

Abstract Optical coherent detection techniques are important techniques for accurate detection of optical signals. Optical coherent detection consists of Mach-Zehnder interferometer which provides beating between two optical beams. Inside an interferometer an optical signal is divided into two parts with a beam splitter. These two beams travel in test and reference arms of optical interferometer and gets combined at another beam splitter. If the path lengths traveled by test beam and reference beam is equal inside an interferometer, then test beam and reference beam shows constant phase relationship with each other. The constant phase relationship between two beams is the most important characteristics of an interferometer as it enables extraction of modulated frequency components in the test arm. If one of the mirrors in Mach-Zehnder interferometer is mounted on piezo actuator, then it is possible to precisely control the path difference between two beams. In this research paper, a PID controlled closed loop operation of Mach-Zehnder interferometer is demonstrated.

Keywords Mach-Zehnder interferometer · PID controller · Piezo Actuator · Fringes

1 Introduction

Mach-Zehnder interferometer is an important tool for many sensing applications. It is widely used for indirect measurement of frequency of any device under test which is placed in test arm of interferometer. The two interfering optical signals shows constant phase relationship with each other. To achieve a constant phase between the two optical signals, the length of interferometer's arms needs to be continuously changed [1]. The path stability is important factor to achieve the phase stability.

J. Gondane (✉) · M. S. Panse
Department of Electrical Engineering, Veermata Jeejabai Technological Institute (VJTI), Mumbai, India
e-mail: jagondane@el.vjti.ac.in

M. S. Panse
e-mail: mspanse@el.vjti.ac.in

M. Tiwari et al. (eds.), *Optical and Wireless Technologies*, Lecture Notes in Electrical Engineering 892, https://doi.org/10.1007/978-981-19-1645-8_25

The interferometers which are constructed with the free space optical devices are highly configurable devices but show less stability [2]. Various techniques are used to stabilize the path difference in test and reference arm of interferometer. There are many factors like environmental noise, temperature fluctuations stability of optical holders, which contribute to phase uncertainty. Various feedback techniques are used to phase lock to a particular setpoint with a feedback loop [3]. Many literatures have suggested that stability of a Mach-Zehnder interferometer can be increased by using a Fabry-Perot interferometer in one of the arms. Fabry-Perot interferometer uses the multiple reflections between boundaries of two partial reflecting mirrors [4]. As it is placed in the same reference arm of interferometer, both interfering fields and therefore, the interferometer phase is automatically stabilized. In this paper, we explain the implementation of Mach-Zehnder interferometer with a piezo driven mirror and verify its basic properties like interference visibility and phase stability [5]. The Fig. 1 shows experimental setup of basic Mach-Zehnder interferometer. It consists of a laser source, two beam splitters and two mirrors. The optical signal from laser diode gets divided into two parts by beam splitter 1. The reflected signal from first beam splitter travels the path of length L_1 in the test arm of interferometer, while the transmitted signal from the first beam splitter travels the path of length L_2 in the reference arm of the interferometer [6].

Both the optical signals interfere at another beam splitter and forms an interference pattern. If the path length L_1 in the test arm and path length L_2 in the reference arm of the interferometer are equal, then path difference between two arms Both the optical signals interfere at another beam splitter and forms an interference pattern. If the path length L_1 in the test arm and path length L_2 in the reference arm of the interferometer are equal, then path difference between two arms (ΔL) becomes zero. becomes zero [7]. The phase difference ($\Delta\varphi$) associated with these two signals show constant phase relationship with each other. The phase difference between the two optical signals is given by equation

$$\Delta\varphi = \frac{2\pi}{\lambda}\Delta L \tag{1}$$

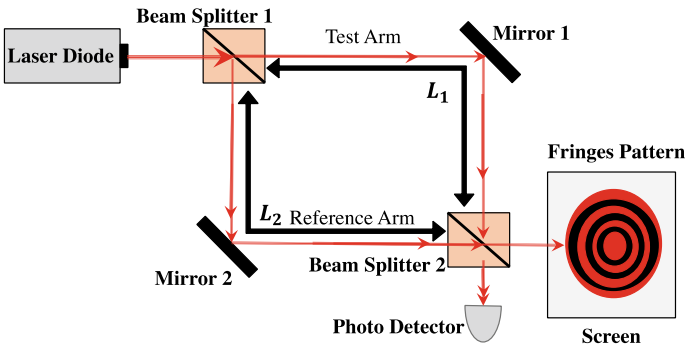

Fig. 1 A basic Mach-Zehnder interferometer

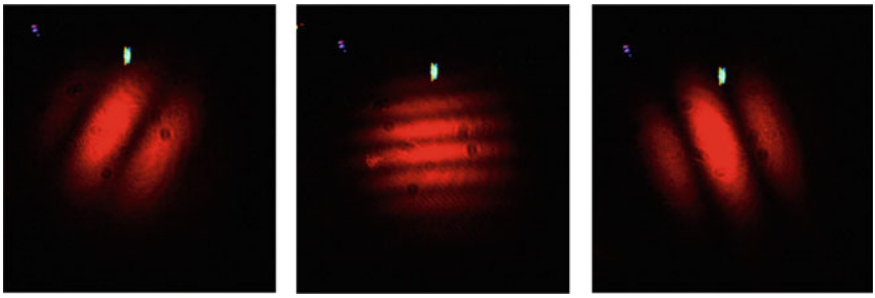

Fig. 2 Fringe patterns shows constructive and destructive interferences in M-Z interferometers

The interference pattern formed at detector shows constructive and destructive interference which is dependent of path difference (ΔL) between the two signals [8]. The condition for constructive interference is given by

$$\Delta L = \lambda, \quad \text{for } m = \pm 1, \pm 2, \pm 3 \ldots \tag{2}$$

The condition for destructive interference is given by

$$\Delta L = \left(m + \frac{1}{2}\right)\lambda, \quad \text{for } m = \pm 1, \pm 2, \pm 3 \ldots \tag{3}$$

The constructive and destructive interference pattern obtained at detector are in the form of fringes which are periodic bands of maximum and minimum light intensity which are termed as maxima and minima respectively. The Fig. 2 shows fringe pattern of a basic Mach-Zehnder interferometer.

2 PID Controlled Closed Loop Optical Interferometer

Proportional-Integral-Derivative (PID) controllers are widely used feedback controllers. The PID controller requires input of process variable (PV) and a setpoint (SP). The process variable is the parameter of system which needs to be controlled and the setpoint defines the desired value for that system parameter [9]. A PID controller analyze the system output value, and it inputs the controller output value to the system to move the process variable toward the setpoint value. A PID controller calculates the difference between SP and PV and generates the error value $e(t)$ as shown in Fig. 3. It applies the correction based on proportional (P), integral (I) and derivative (D) terms. However, in this research only PI controller is used for phase sensitivity as use of differentiator (D) delays the response time of the process. A PID control variable $u(t)$ is given by [10]

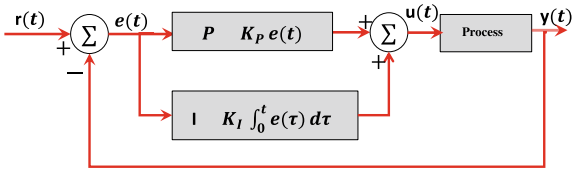

Fig. 3 Structure of PI controller for phase stability

$$u(t) = K_P e(t) + K_I \int_0^t e(\tau) d\tau \tag{4}$$

where K_P is proportional gain and K_I is proportional gain. There is a relative phase drift between the test signal and the reference signal that varies randomly. To nullify this phase drift, a feedback mechanism is proposed in which one of the mirrors is mounted on a piezo driven actuator. This piezo actuator is driven by PID controller. A PID controller is chosen because of its relative simplicity and possibility to control the rate of fringe drift. In the setup one of the mirrors is manually controlled to produce a fringe drift. A 25 μm pin hole is used to keep track of the fringes. After that signal is obtained on photodiode. The voltage signal from the photodiode is read by the data acquisition device (DAQ). Figure 4(a) shows the PID controller used in this setup. The piezo used is Thor Labs PAS009 piezo which has range of 40 μm. The piezo actuator works on the principle of the converse of the piezoelectric effect [11] The piezoelectric effect is observed when electric field is applied on a piezoelectric material, a strain is produced in the material that leads to expansion and contraction of the material depending upon the polarity of the applied signal. A piezo actuator which is capable of moving at a maximum frequency of 1 kHz is used in this setup. To fulfil the voltage requirements of the piezo-actuator, a piezo inertia actuator controller driver (Thorlabs K-cube series driver) is used which is capable of supplying voltage in the range of 0–75 V, that corresponds to a movement in the range of 0–40 μm. The piezo driver is driven by a voltage signal which has amplification factor of 7.5 [12]. The piezo controller and mirror mounted piezo is shown in Fig. 4(b) and Fig. 4(c) respectively. By setting up a Mach-Zehnder interferometer, the hysteresis of the piezo-actuator and the amplification factor of the piezo driver is measured. The hysteresis and amplification plot is shown in Fig. 5(a) and (b). A camera module is used to exactly identify and lock the fringes. Figure 6 shows complete system setup for closed loop operation of Mach-Zehnder interferometer.

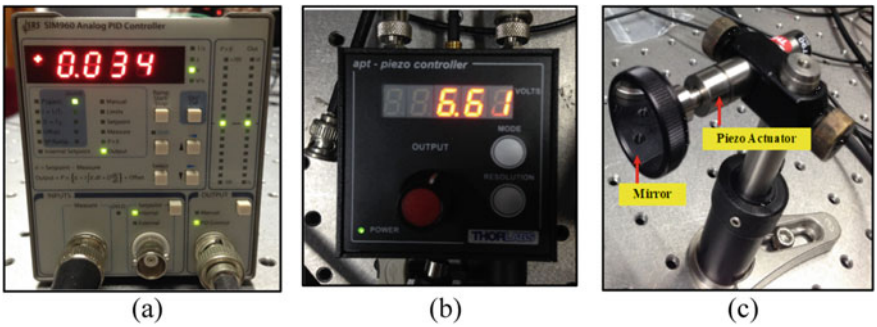

Fig. 4 **a** PID controller, **b** High voltage amplifier for piezo actuator, **c** Mirror mounted on piezo actuator

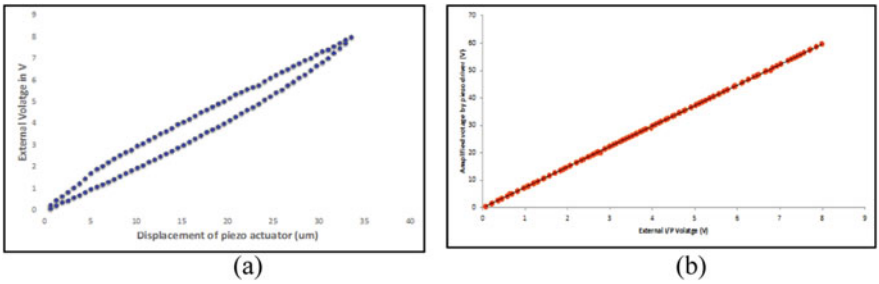

Fig. 5 **a** Piezo movement with applied external voltage, **b** Voltage amplification by high voltage amplifier

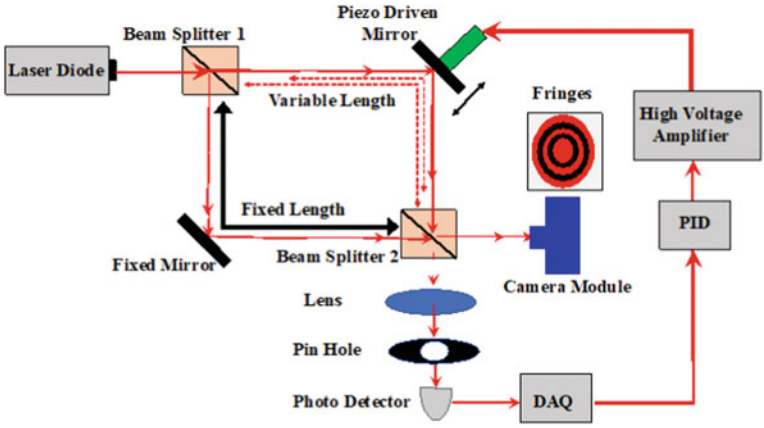

Fig. 6 A closed loop Mach Zehnder interferometer with piezo driven mirror

3 Experimental Results and Observations for Closed Loop M-Z Interferometer

The laser source used in this experiment is semiconductor laser with wavelength (λ) of 660 nm, laser line width ($\Delta\lambda$) of 12 nm and power of 20 mW. Setpoint is chosen within the maximum and minimum voltage levels which are given as input to PID. PID generates an error signal by calculating the difference between Process Variable (PV) and Set Point (SP). By tuning the PID parameters (P and I), this error signal is minimized by creating an output voltage [13]. This output drives the piezo-actuated mirror after amplification through the piezo driver. So, the piezo-actuated mirror is driven in such a way that the error signal gets minimized which is an indicator of a constant phase between the reference and the test signal [14]. A camera module is used to identify the fringes which are required to be locked. Figure 7 shows the fringe pattern image obtained with camera module. In this case, all the fringes are marked ($m = \pm 1, \pm 2$) around the central fringe ($m = 0$). The locking of a particular fringe number becomes important in order to measure the dynamic range of interferometer for multiple sensing applications [16–20]. The fringe number is identified and its corresponding voltage is measured at photo detector. The measured voltage of fringe acts as SP for PID controller. The PID operation for different SP and PV is shown in Fig. 8. Figure 9 represents the drift of fringes with time without the PID correction and with PID correction. When both piezo and PID are off, the fringes continuously changes position at photo detector and camera. When only Proportional output (P) is turned on, the process variable (PV) oscillates between actual position and SP position. After turning on Integrator output (I), the PV and SP are matched with minimum difference. Figure 10 shows the behaviour of detector when Integrator (I) output is turned off and turned on. Figure 11 shows the photodetector out when

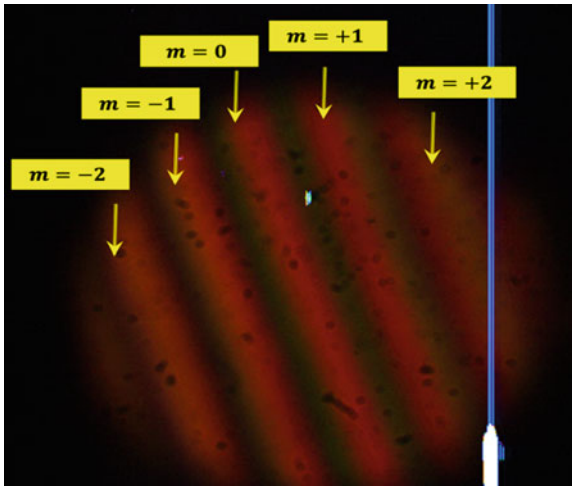

Fig. 7 Locked maxima fringes identified camera module

both P and I controller are turned on. The similar condition for multiple fringes are obtained.

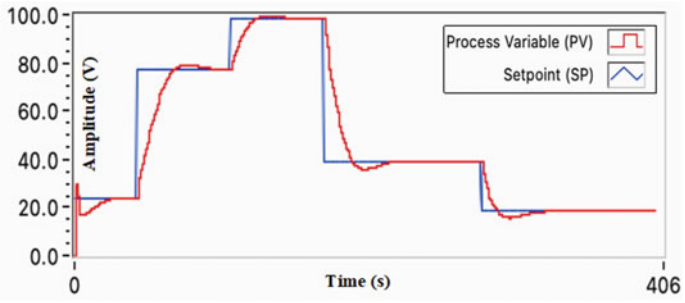

Fig. 8 Length adjustment in M-Z interferometer with PID controller

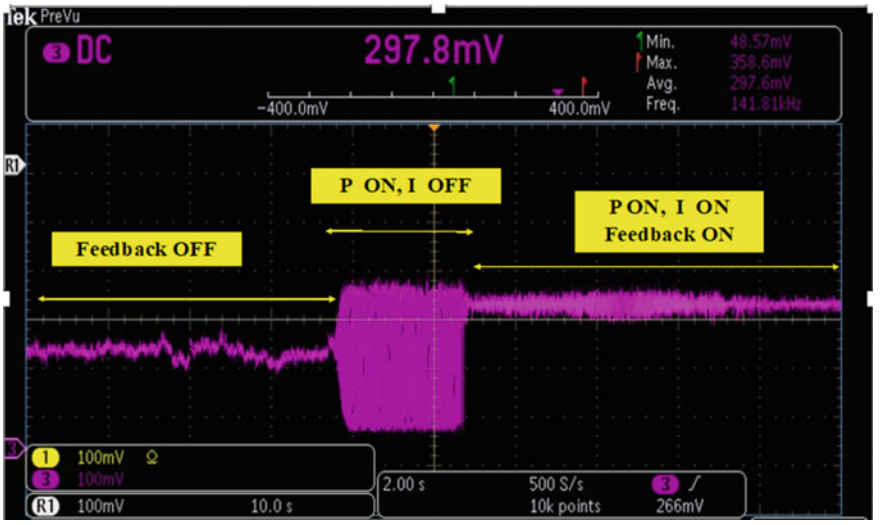

Fig. 9 Detector output with PID controller OFF and ON

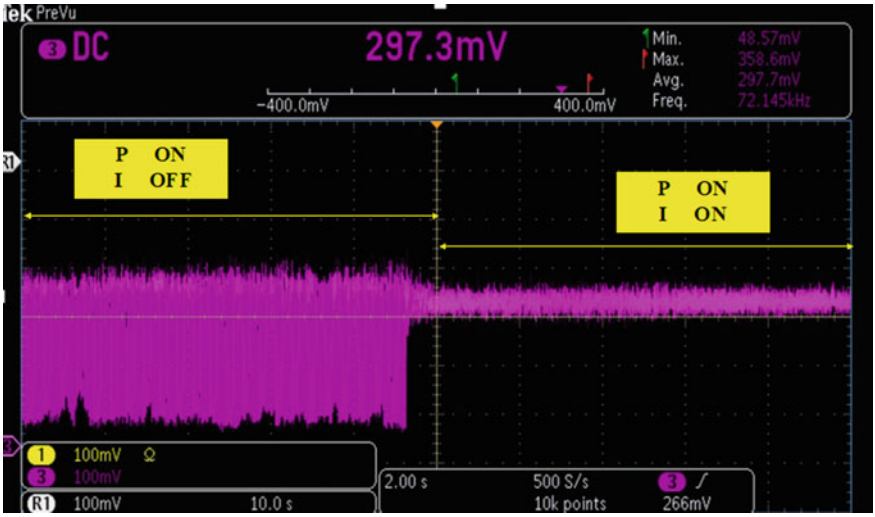

Fig. 10 Detector output with I controller OFF and ON

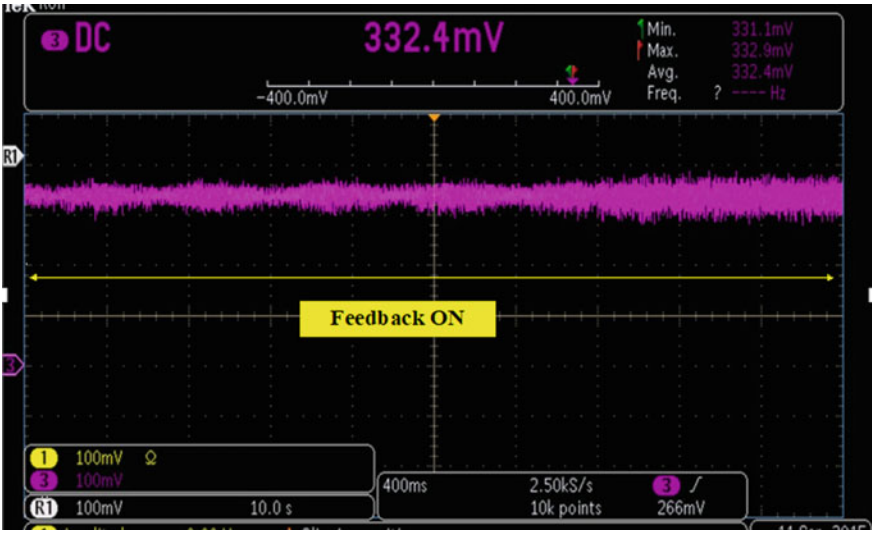

Fig. 11 Detector output with PI controller ON

4 Conclusion

The experimental setup is extremely delicate and the phase drift is not associated with some particular measurement technique, but depends upon the temperature, humidity fluctuations, air currents, vibrations etc. Therefore, it is very difficult to perform the

any experiment which requires good phase stability in open loop interferometer. The locking of particular fringes showed that it is important to minimize this drift to accurately extract the phase information of any subject under test in the test arm of interferometer. The PID feedback locks the fringes which are result of interference between two arms. With piezo driven mirror, the path length inside an interferometer can be changed in the range of $\pm 1\,\mu$m. The two consecutive fringe maxima are separated by $\frac{\lambda}{2}$, thus overall path length of interferometer can be controlled with more precision. This research paper explains the concept of closed loop interferometry by locking of fringes. Fringes are locked by measuring their corresponding voltage at photo detector and by using that voltage as SP for PID controller input. The camera module works in synchronization with photodetector and preforms the operation of marking and identifying a particular fringe. After locking, the interferometer can be used for multiple sensing applications like measurement of vibration, temperature, pressure, flow etc. The device under test has to be placed at testing arm of Mach–Zehnder interferometer. The fluctuations arising due to mechanical instability of setup and environment factors (like temperature, noise and humidity) will be nullified by piezo driven mirror which is placed in test arm of interferometer.

References

1. Mičuda M et al (2014) Highly stable polarization independent Mach-Zehnder interferometer. Rev Sci Instrum 85(8):083103
2. Rawankar A et al (2013) Design studies on compact four mirror laser resonator with mode-locked pulsed laser for 5 μm laser wire. Nucl Instrum Methods Phys Res Sec A 700:145–152
3. You Y et al (2012) Measurement of beam waist for an optical cavity based on Gouy phase. Nucl Instrum Methods Phys Res Sec A 694:6–10
4. Aarathy ER, Rawankar A, Kumar NS (2018) Measurement of parameters of frequency-locked two-mirror laser resonator. In: Janyani V, Tiwari M, Singh G, Minzioni P (eds) Optical and Wireless Technologies. LNEE, vol 472. Springer, Singapore. https://doi.org/10.1007/978-981-10-7395-3_31
5. Rawankar AA et al (2014) Pulsed green laser wire system for effective inverse Compton scattering. In: IBIC 2014 - 3rd international beam instrumentation conference, Monterey, United States, September 2014
6. Donati S, Norgia M (2018) Overview of self-mixing interferometer applications to mechanical engineering. Opt Eng 57(5):051506
7. Gondane J, Panse MS (2021) Development of an optical system for non-contact type measurement of heart rate and heart rate variability. Appl Syst Innov 4(3):48
8. Mule S, Rawankar A, Singh B, Gujar M (2020) Measurement of angular velocity and tilt angle of two-dimensional fiber-optic gyroscope with Sagnac effect. In: Janyani V, Singh G, Tiwari M, Ismail T (eds) Optical and Wireless Technologies. LNEE, vol 648. Springer, Singapore. https://doi.org/10.1007/978-981-15-2926-9_14
9. Suda M, Pacher C, Peev M, Dušek M, Hipp F (2013) Quantum Inf Process 12:1915
10. Niwa Y et al (2009) Appl Opt 48:6105
11. Thorlabs. https://www.thorlabs.com/newgrouppage9.cfm?objectgroup_id=1280
12. Thorlabs. https://www.thorlabs.com/newgrouppage9.cfm?objectgroup_id=2421
13. Rawankar A, Gondane J, Ravankar A (2017) Angular piezo actuator controlled laser resonator for precise sensing of respiratory diseases. In: Proceedings of the 3rd international electronic conference on sensors and applications, vol 1, p 38

14. Donati S, Falzoni L, Merlo S (1996) A PC-interfaced, compact laser-diode feedback interferometer for displacement measurements. IEEE Trans Instrum Meas 45(6):942–947
15. Roos PA, Stephens M, Wieman CE (1996) Laser vibrometer based on optical-feedback-induced frequency modulation of a single-mode laser diode. Appl Opt 35:6754–6761
16. Merlo S, Donati S (1997) Reconstruction of displacement waveforms with a single-channel laser-diode feedback interferometer. IEEE J Quantum Electron 33(4):527–531
17. Beheim G, Fritsch K (1986) Range finding using frequency-modulated laser diode. Appl Opt 25:1439–1442
18. Shinohara S, Yoshida H, Ikeda H, Nishide K, Sumi M (1992) Compact and high-precision range finder with wide dynamic range and its application. IEEE Trans Instrum Meas 41(1):40–44
19. de Groot PJ, Gallatin GM, Macomber SH (1988) Ranging and velocimetry signal generation in a backscatter-modulated laser diode. Appl Opt 27:4475–4480
20. Özdemir ŞK, Ito S, Shinohara S, Yoshida H, Sumi M (1999) Correlation-based speckle velocimeter with self-mixing interference in a semiconductor laser diode. Appl Opt 38:6859–6865

Distributed Raman Amplifier in O, E, S, C & L Band DWDM Network

Anand Prakash and Sharbani Roy

Abstract Optical Fiber communication can smoothly operate in the wavelength region lie within 1260–1650 nm where transmission loss is minimum. In the present article, performance of Distributed Raman Amplifier (DRA), within above band through simulation technique on MATLAB platform has been observed. Present observations have realized by defining new embedded block sets for multichannel amplification. Observed results have been found by studying the variation in output power and its respective gain of DRA with respect to spectral variations in Co-pumping configuration and for the same input power value in all channels. From above observations, it has been realized that flatness in output power of DRA is comparatively better in C & L-band. Observed gain flatness in E-band is comparatively better than O & S band but inferior to C & L. It is well known that optical communication lying within O to L band is always usable for long haul communication with such a high speed data transmission rate of 100 Gbps and from our present observations, it can be justify that communication link set up in C, L and in next E-band is preferable.

Keywords DRA · Multiplexed channel · Low-loss wavelength region

1 Introduction

Optical fibre communication system conducts well in low loss wavelength transmission region. From 850 nm-band, O-, E-, S-, C-, L-Band and also in the combination of SC-band, CL-band and SCL-band as per requirement optical amplifier can smoothly operate. The invention of Distributed Raman Amplifier (DRA) has contributed in the

A. Prakash (✉) · S. Roy
Department of Electronics Engineering, Indian Institute of Technology (Indian School of Mines), Dhanbad 826104, Jharkhand, India
e-mail: anand.16dp000056@ece.iitism.ac.in

Department of Electronics and Communication Engineering, Ramgarh Engineering College, Ramgarh 825101, Jharkhand, India

M. Tiwari et al. (eds.), *Optical and Wireless Technologies*, Lecture Notes in Electrical Engineering 892, https://doi.org/10.1007/978-981-19-1645-8_26

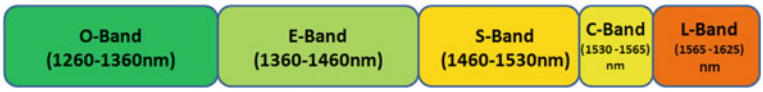

Fig. 1 Optical communication wavelength region

tremendous growth of communication capacity using Wavelength Division Multiplexing (WDM) and Dense wavelength division multiplexing (DWDM) [1]. Some salient features of DRAs [2–4] are:

- Higher Bit rate.
- Longer Amplification span.
- Reduced Non-linear penalty.
- Closed Channel spacing.

The above features make DRA as the most important enabling technology of WDM systems and networks.

The main motivation of the article is to realize the performance of DRA in various wavelength region in Co-pumping configuration [2]. Above motivation led to DRA designed based on two coupled equations [2] for the mathematical modelling of DRA, representing the electromagnetic field propagation down to fibre, formed by the incident signal and pump energy. Optical communication low loss wavelength region ranges from 1260 to 1625 nm [5–7], and is divided into five wavelength bands referred to as the O-, E-, S-, C- and L-bands, as shown in Fig. 1. In addition to O- to L-band, two more bands 850 nm and U-band. Ub-band is used in network monitoring purpose while the 850-nm-band is the primary wavelength for multimode fibre optical communication systems.

1.1 Raman Scattering and DRA Model

Spontaneous Raman Scattering occurs in optical fibres when a pump wave is scattered by the fibre fabricating silica molecules, that is shown in the energy level diagram [2] of Fig. 2.

Some pump photons give up their energy to create other photons of reduced energy of a lower frequency; the remaining energy is absorbed by silica molecules,

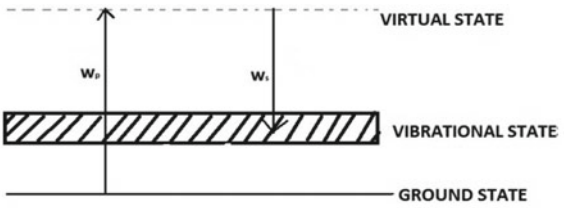

Fig. 2 Energy level in SRS process

which end up in an excited vibration state. As shown in energy level diagram the vibration energy dictates the value of the Raman shift as: $\Omega_R = \omega_p - \omega_s$. Spontaneous Raman scattering is an isotropic process and occurs in all directions. The Raman scattering process becomes stimulated if the pump power exceeds the threshold value. Variations in the pump and signals power along the distributed Raman amplifier length can be studied by solving two coupled equations [1, 2] and which in the case of Co-pumping takes the form as:-

$$\frac{dP_s}{dz} = -\alpha_s P_s + \left(\frac{g_R}{a_p}\right) P_p P_s \tag{1}$$

$$\frac{dP_p}{dz} = -\alpha_p P_p - \frac{\omega_p}{\omega_s}\left(\frac{g_R}{a_p}\right) P_p P_s \tag{2}$$

where α_s and α_p represents fibre losses at the signal and pump frequencies ω_s and ω_p. The term ω_p/ω_s results from different energies of pump and signal photons and also disappear if these equations are written in terms of photon numbers.

Considering small-signal amplification case, where pump depletion can be neglected i.e. last term of (2). By putting the value of $P_p(z) = P_p(0)\exp(-\alpha_p z)$ in (1), where z is distance in km, and may vary for different pump positions from z = 0 to z = L [1], the signal power at the output of an amplifier of length 'L' is given by

$$P_s(L) = P_s(0)\exp\left(\frac{g_R P_p(z) L_{eff}}{a_p} - \alpha_s L\right) \tag{3}$$

where P_s(L) = Signal power at the output of an amplifier of Length L.

g_R = Raman-gain coefficient
a_p = Cross sectional area of the pump inside the fibre
α_s = Signal attenuation constant
α_p = Pump attenuation constant
L = Fibre–length
$L_{eff} = [1 - exp(-\alpha_p L)/\alpha_p]$ is the effective interaction length, α_p represents fibre losses for optical fibre, L_{eff} is approximated to $1/-\alpha_p$ as $-\alpha_s L >> 1$ practically.

Schematic view of multiplexing/demultiplexing based optical Distributed Raman Amplifier is shown in Fig. 3. having Forward & Backward Pumping configuration along with multiplexed optical signals having wavelength $\lambda_1, \lambda_2 \ldots\ldots \lambda_n$ are various and $\alpha_{s(1,2,3\ldots.n)}$ are corresponding signal attenuation constant for wavelength $\lambda_1, \lambda_2 \ldots\ldots \lambda_n$.

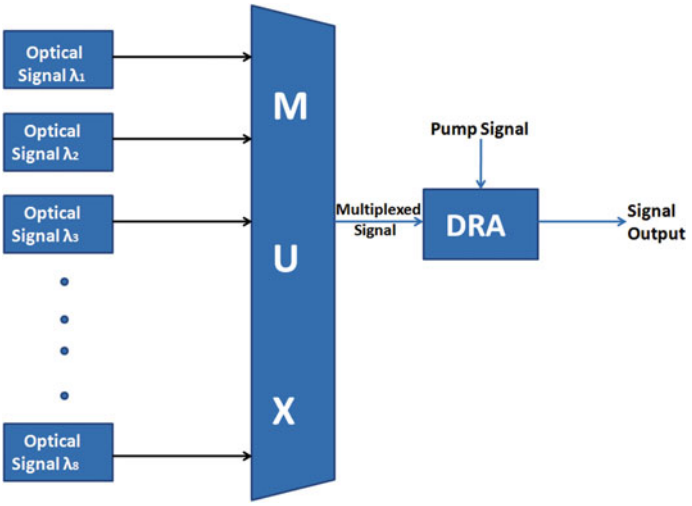

Fig. 3 Schematic view multichannel amplification of DRA

1.2 Realization of DRA

DRA transmitter portion is realized using various embedded block sets mentioned in Fig. 4. It is based on the two coupled equations and represented specific block sets such as:

(a) Multiple Optical Source/Signal/Channel (b) Multiplexed Optical communication link (c) Pump Power [6, 8] (d) DRA Amplification blocks etc.

Each segment having different subsections as described as Block Segment:

a) Signal stream: It can be average power of O-, E-, S-, C- and L-band signals.
b) Multiplexer: It can multiplex all the average signal powers for multi-channel amplification at particular wavelength of DRA.of multiplexed signal at their individual wavelengths.
c) DRA with fibre cable: It provides amplification based on two coupled equations (1)(2). Here all parameters of of All Wave™ Fibre cable is used at various band (Tables 1 and 2).

1.3 Results and Discussions

The variation in Signal gain (dB) and in the output power (dBm) at 100 GHz span with respect to the transmission distance at various pump positions for a multiplexed channel at 1260–1625 nm [9, 10] in O-E-S-C-& L Band has been observed. From present observation, it is found that C & L-band has comparatively better gain flattening.

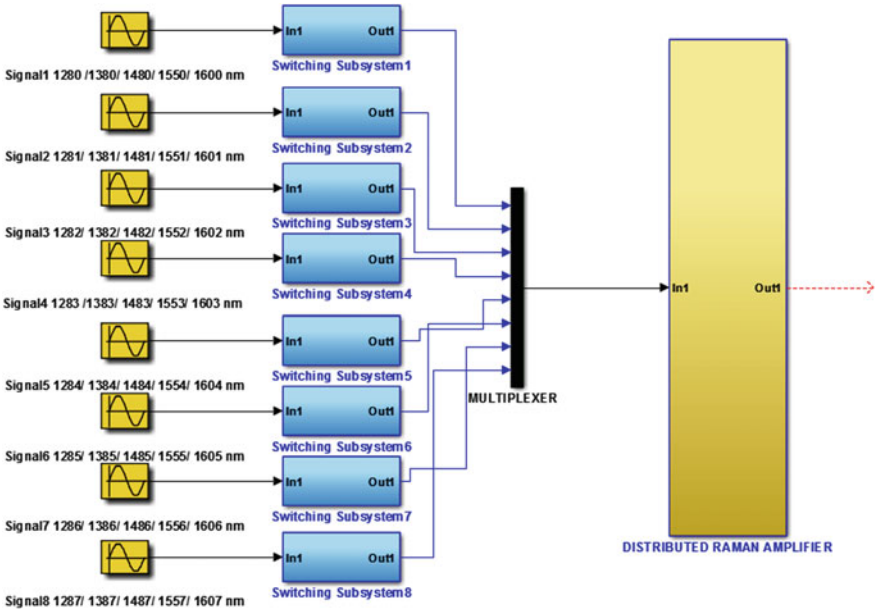

Fig. 4 Realization of multichannel DRA in O-, E-, S-, C- and L-Band

Table 1 DRA parameters of all waveTM zero water peak fibre cable

Physical meaning	Symbols	Numerical value
Cross sectional area of the pump inside the fibre	a_p	84.90 μm^2
DRA Fibre-length	L	0–20 km
Efficient Raman-gain coefficient	C_R	0.54/0.56/0.44/0.0.42 w^{-1} km^{-1} (Band dependent)
Signal attenuation constant	α_s	0.20–0.30 dB/Km (Band dependent)
Pump attenuation coefficient	α_P	0.24–0.47 dB/Km (Band dependent)

Table 2 Multichannel DRA input parameters

Physical meaning	Symbols	Numerical value
Signal power	$P_s(0)$	10 mW
Pump power	$P_p(0)$	320 mw
Pump wavelength	λ_p	1400 nm
Signal wavelength	λ_s	1260–1650 nm

From the observed gain values shown in Fig. 5 for 'O'-band, it can be realized that a number of gain peaks at different wavelengths as well as continuous gain fluctuation have been found which may be due to fluctuation in the difference of ($\omega_p - \omega_s$), where ω_p is photon frequency and ω_s is signal frequency. This effect may arise due to variation in the amorphous characteristics of silica molecules fabricating the fibre glass.

Additionally, it has also been realized that at 1284 nm the Gain is 0.70 dB, which satisfies the higher attenuation nature of 'O' band and it may be due to the value of ω_s is ver close to ω_p.

From the observed gain values shown in Fig. 6 for 'E'-band, that a peak is realized at 1384 nm whereas Gain is almost flattened in all other signal wavelengths, which may be due to good alignment between the stoke signal and pump power.

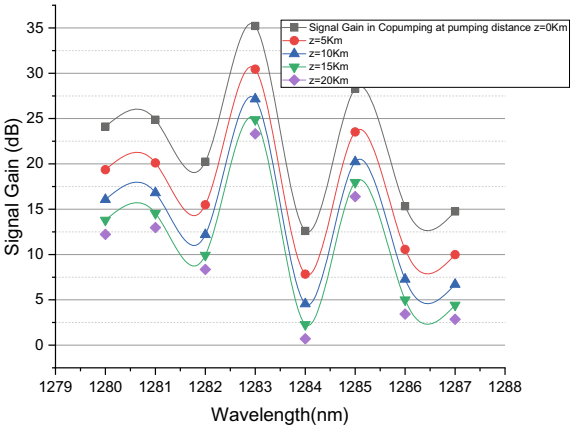

Fig. 5 O-Band: Variations of signal gain (dB) in Co-pumping configuration versus Signal wavelength = 1262–1278 nm, Input signal power = 10(mw), Pump power = 320 mw, Effective Raman-gain coefficient = 0.54 w^{-1} km^{-1}, pump attenuation constant = 0.33 dB/km, signal attenuation constant = 0.25 dB/km, Effective cross-section area = 84.90 mm^2. All Wave™ Zero Water Peak Fibre

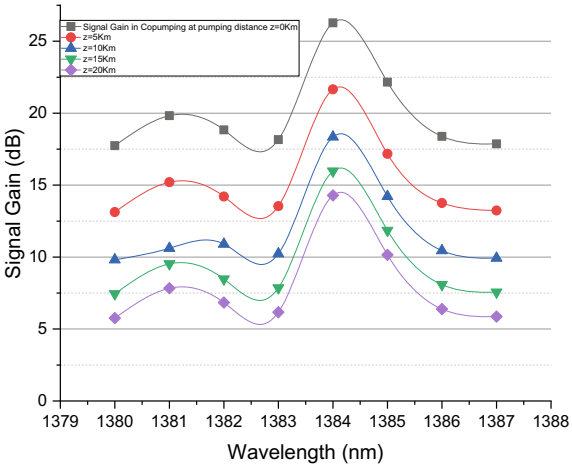

Fig. 6 E-Band: Variations of signal gain (dB) in Co-pumping configuration versus Signal wavelength = 1362–1378 nm, Input signal power = 10 mw, Pump power = 320 mw, Effective Raman-gain coefficient = 0.38 w^{-1} km^{-1}, pump attenuation constant = 0.3 dB/km, signal attenuation constant = 0.24 dB/km, Effective cross-section area = 84.90 mm^2 (All Wave™ Zero Water Peak Fibre)

From the observed gain values shown in Fig. 7 for 'S'-band, it can be realized that a number of gain peaks at different wavelengths as well as continuous gain fluctuation have been found which may be due to fluctuation in the difference of ($\omega_p - \omega_{s)}$, where ω_p is photon frequency and ω_s is signal frequency. This effect may arise due to variation in the amorphous characteristics of silica molecules fabricating the fibre glass.

From the observed gain values shown in Fig. 8 for 'C'-Band, it can be explained that satisfying the condition of lowest attenuation at 1550 nm and its nearby wavelength values in Fibre optics signal propagation, we are getting less differences among gain peaks, hence overall better Gain flattening in 'C'-Band'. This band exhibits flattened gain in 1550 nm region [2, 11].

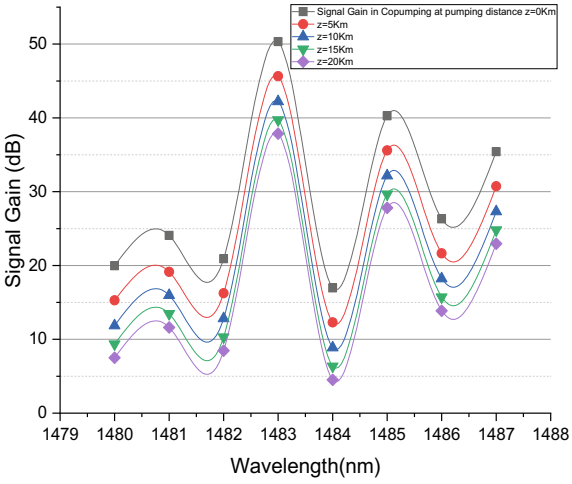

Fig. 7 S-Band: Variations of signal gain (dB) in Co-pumping configuration versus Signal wavelength = 1480–1487 nm, Input signal power = 10 mw, Pump power = 320 mw, Effective Raman-gain coefficient = 0.56w^{-1} km^{-1}, pump attenuation constant = 0.27 dB/km, Signal attenuation constant = 0.21 dB/km, Effective cross-section area = 84.90 mm^2

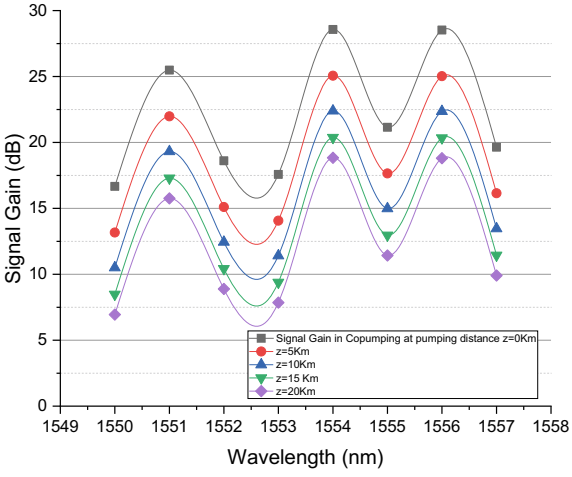

Fig. 8 C-Band: Variations of signal gain (db) in Co-pumping configuration versus Signal wavelength = 1550–1557 nm, Input signal power = 10 mw, Effective Raman-gain coefficient = 0.59 w^{-1} km^{-1}, pump attenuation constant = 0.24 dB/km, signal attenuation constant = 0.18 dB/km, Effective cross-section area = 84.90 mm^2

From the observed Gain values in 'L'-band shown in Fig. 9, it can be realized in all signal wavelengths except in 1606 nm, the Gain is almost flat which has satisfied the natural trend of 'L'-band, whereas at 1606 nm we find abrupt peak rise which may be due to good alignment between the stoke wavelength and pump wavelength which arises due to the amorphous nature of glass used in the fabrication of the fibre (Fig. 10).

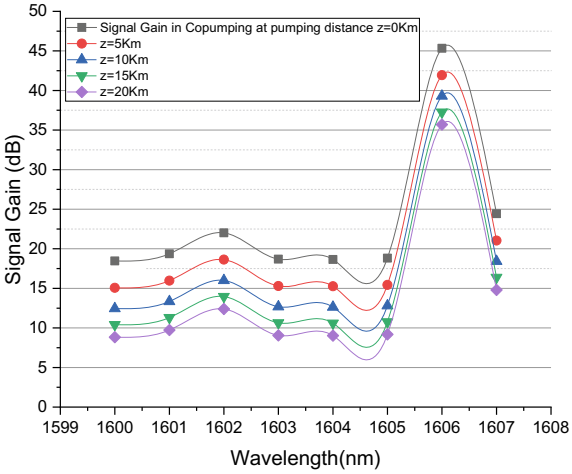

Fig. 9 L-Band: Variations of signal gain (dB) in Co-pumping configuration versus Signal wavelength = 1600–1607 nm, Input signal power = 10 mw, Pump power = 320 mw Effective Raman-gain coefficient = $0.42w^{-1}\ km^{-1}$, pump attenuation constant = 0.22 dB/km, signal attenuation constant = 0.20 dB/km, Effective cross-section area = 84.90 mm^2

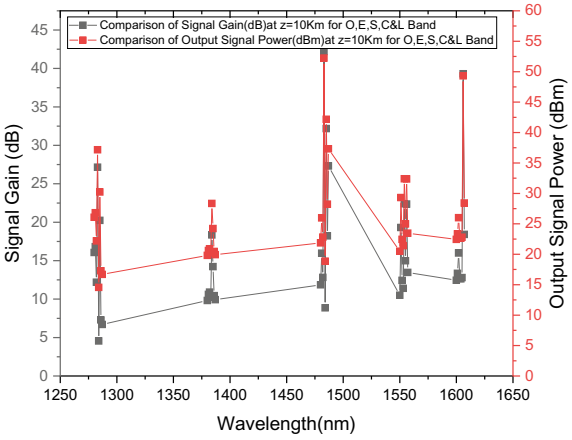

Fig. 10 Comparison of Signal gain (dB) and output signal power (dBm) Variations of O to L-Band at pumping position z = 10 km versus low loss wavelength region of O-E-S-C-L band

2 Conclusions and Future Aspects

DRA in optical network for multichannel amplification in O-E-S-C-L band has been proposed using latest Single mode fibre cable "All Wave™ zero water peak". From various graphical representation, it is observed that the output power and signal gain is flattened with minimum peak difference in C & L-band. E-band performance can be seen better than S-band. This work can be extended with mathematical modelling of a multichannel Raman amplifier with non-linearity, such as non-linear cross-talk, depletion and Four wave mixing under various types of fibre cable consideration for all bands including U-Band. We have used single co-pumping configuration which can be turned into multi-pump configuration and the signal gain & output signal power can also be realized by employing other types of pumping scheme like backward and bidirectional.

References

1. El-Naser A, Mohamed A, NabihZakiRashed A, Eid MMA (2012) Recent advances of distributed optical fibre raman amplifiers ultra wide wavelength division multiplexing telecommunication networks. IJ Comput Netw Inf Secur 4:63–74
2. Agrawal GP (2002) Fibre-optics communication system, Copyright 2002 by John Wiley & Sons, Inc., New York
3. Ho KP (2001) J Lightwave Technol 19:159
4. Norimatsu S, Yamamoto T (2000) J Lightwave Technol 18:915
5. Pradhan DD, Mandloi A (2018) Performance analysis of flat gain wideband Raman amplifier for S+C and C+L band DWDM system. Adv OptoElectron 2018:7 pages. Article ID 5703805
6. Saito LAM, Taveira PD (2008) Multipump disctrete Raman amplifier in for CWDM system in the O-Band. IEEE xplore
7. Sing SP, Singh RS (2012) Distributed Raman amplifier for the S-Band. Optoelectron Adv Mater Rapid Commun 6(11–12):1157–1159
8. Jaff PM (2009) Characteristics of discrete Raman amplifier at different pump configurations. Int J Math Comput Phys Electr Comput Eng 3(6)
9. Khalaf AAM (2015) Raman amplifier performance under new wavelength ranges. J Opt Commun 37(1)
10. Practical Aspects of Raman Amplifier, CISCO, Document Id:212834, March 2018
11. Bala Subbanna B, Divya Meenakshi LP (2013) The role of optical amplifiers in optical fiber communication. Int J Eng Adv Technol (IJEAT) 2(4). ISSN 2249-8958

Recent Research in Optical Characteristics of Nitride Based Nanoscale Heterostructures for UV Applications

Priya Chaudhary, Amit Kumar Singh, and Amit Rathi

Abstract Nanoscale heterostructures have a great potential for UV applications in the recent scenario. UV region, particularly ranging from 10 to 400 nm is significant in the field of biomedical research, water and air sterilization, semiconductor processes etc. Here some research articles are reviewed and discussed about the structural and optical characteristics of these heterostructures. Optical characteristics of nitride-based heterostructures are studied on the basis of different parameters like optical gain at room temperature, the delta layer insertion effect on ultraviolet light emission, optical gain at different well widths, varying the Al concentrations etc. To calculate optical gain k·p Hamiltonian theory and multi-band effective mass theory have been employed in several studies. Nitride-based UV heterostructures such as high power density AlGaN based ultraviolet lasers have also been discussed. AlGaN based UV lasers have application in general sterilization, sensing systems and water purification. Optical gain of deep UV laser diodes is also reviewed that have uses in the field of free-space communication, disinfection, medical diagnostic, biochemical agent detection and various other fields.

Keywords Heterostructure · AlGaN · δ-layer · Deep UV laser · Optical gain

1 Introduction

III-nitride based heterostructures have great importance due to various applications in the ultraviolet range like material processing and biochemical analysis. UV photonic devices, such as laser diodes, have recently gained prominence due to a variety of applications, including currency screening, medical diagnostics, and sterilisation of medical tools, bioagent detection, dermatology, critical communications, water purification, UV curing and photolithography and as a replacement to toxic gas lasers and large mercury lamps [1]. The UV wavelength required in these applications lie in three bands, namely, UVA band (400–320 nm), UVB band (320–280 nm), and band

P. Chaudhary · A. K. Singh · A. Rathi (✉)
Department of Electronics and Communication Engineering, Manipal University Jaipur, Jaipur, Rajasthan, India
e-mail: amitrathi1978@gmail.com

M. Tiwari et al. (eds.), *Optical and Wireless Technologies*, Lecture Notes in Electrical Engineering 892, https://doi.org/10.1007/978-981-19-1645-8_27

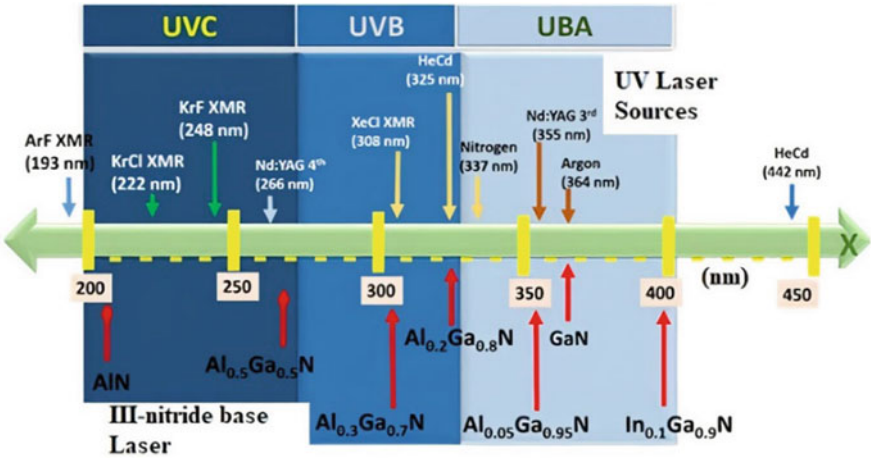

Fig. 1 Conventional laser sources with their wavelengths [6]

UVC (<280 nm), respectively [2]. Numerous applications have been recognized in the UVA region. Commercialization of laser diode with reasonable performance is already achieved, at wavelength greater than 365 nm. This type of device is utilised as both a phosphor pumping source for the broad spectrum release to emit white light and the light- source for generating fluorescence in the finding of fake currency. As we can see in Fig. 1, many applications use conventional UV laser sources.

Ultraviolet curing for ultraviolet coating process is a further application, and where the ultraviolet devices work as UV light sources and keep the benefits of longer lifespan and lesser heat production. Below the wavelength region 365 nm, the applications are in a huge variability of biomedical systems. In the region of UVB, laser diodes have the potential to be developed for skin treatment. Research indicates that in the psoriasis treatment, broadband UVB is not so operational and the risk is higher of erythema and sunburn of the non-affected skin. Without any damage from the short-wavelength exposure and to deliver effective treatment, UV LDs would be the perfect choice in the application due to being inherently narrow band light sources [3, 4, 20–22].

2 Categorical Review of Different UV Laser Heterostructures

Recently, the III-Nitride group-based laser diodes with AlGaN, InGaN and multiple quantum wells InAlGaN have been explored [5]. Group III nitride-based LDs were developed to emit the ultraviolet spectrum for many applications. To discuss the current scenario, here some papers are reviewed that are related to nitride-based laser heterostructures. Comparative study of optical and structural characteristics of

these heterostructures is done on the basis of different parameters like optical gain measured at room temperature, investigated effect of insertion of delta layer etc.

2.1 Ultraviolet Multiple-Quantum-Well Laser at Room-Temperature

Takano et al. demonstrated deep ultraviolet lasing of AlGaN multiple QW lasers at 241.5 nm at ambient temperature in 2004 [7]. At 300 K, the pumping threshold power is around 1200 $kWcm^{-2}$. At 20 K, the lasing wavelength is 231.8 nm. From 20 to 150 K and from 160 to 300 K, the temperature-dependent lasing wavelength is calculated to be 0.01 and 0.03 nmK^{-1}, respectively [7]. It's similar to the AlGaN epitaxial layer's temperature-dependent photoluminescence. The laser's cavity is made up of cleaved AlGaN facets and a SiC substrate. To determine this, it is compulsory to make the thickness of the wafer less than 100 mm. For cleaving, the thickness of the optimum wafer is 60–70 mm.

In 2012, Pecora et al. demonstrated optical gain from AlGaN/AlN MQ wells at 250 nm with strong band-structure potential fluctuations [8]. Optical gain of deep UV is achieved under optical pumping in MQWs $Al_{0.7}Ga_{0.3}N$/AlN. The modal gain of 118 $\pm$ 9 cm^{-1} achieved at 15 μJcm^{-2} excitation energy and 5 $\pm$ 1 μJcm^{-2} transparency threshold is calculated experimentally, with excited carriers of $1.4 \times 10^{17}/cm^3$. These results were calculated for the solid-state lasers at sub-250 nm emission at 300 K.

Optical gain of QW AlGaN/AlN heterostructure is obtained by Takao Oto et al., 2014 [9]. The optical gain characteristics are measured at 300 K room temperature. The QW $Al_{0.79}Ga_{0.21}N$/AlN heterostructure with 5 nm wavelength has the optical gain of 140 cm^{-1} [9].

In 2019, deep-ultraviolet LD for room temperature at 271.8 nm was demonstrated by Zhang et al. This laser diode operated at current injection for a very short wavelength at 300 K room temperature. The structure was developed on the substrate of AlN. A 271.8 nm lasing wavelength was measured with a 50 ns pulse duration and 2 kHz repetition frequency. Without impurity doping, a low operational voltage of 13.8 V was achieved at 0.4 A lasing threshold current, which is related to the current density of 25 kA/cm^2. To obtain high hole conductivity, low internal loss and high hole injection, undoped DPD is used as the p-side [10]. Table 1 shows the comparative study of ultraviolet QW lasers at room temperature.

Table 1 Ultraviolet multiple-quantum-well laser at Room-temperature

Ref.	QW structures	QW thickness (nm)	Al composition	Pulse duration (ns)	Repetition frequency (Hz)	Wavelength (nm)	Optical gain (/cm)
[7]	AlGaN MQW laser	5	0.66	–	–	241.5 (pumping power 1200 kW/cm^2)	–
[8]	AlGaN/AlN	1.5	0.7	–	–	254 (Excitation energy density-15 μJ/cm^2)	118 ± 9
[9]	AlGaN	9	0.7	50	2000	271.8	–
[10]	AlGaN/AlN	5	0.8	4	25	193 (Excitation power density-270 kW/cm^2)	240

2.2 *Effect of QW δ-layer Insertion on UV Emission and Optical Gain*

Optical gain in InGaN/GaN heterostructure has been demonstrated by Park et al. (2007) with embedded AlGaN delta layer. The optical gain of QW structure InGaN/GaN with the AlGaN δ layer is calculated using the theory of multi-band effective mass [11]. The δ layer effect is brought into being leading to low carrier density. At high carrier density (10×10^{12} /cm^2), the double quantum well structure has a large optical gain (~5600 cm^{-1}) than a single quantum well structure (3200 cm^{-1}).

The gain media of AlGaN-δ-GaN QW in mid and deep UV LDs is investigated by Zhang et al. (2013). The optical gain of AlGaN-δ-GaN QWs with fluctuating δ-GaN layer and composition of AlGaN QW are calculated. The result of this structure has enhanced ~7 times higher gain than the conventional AlGaN gain emitting at ~240 nm. By using asymmetric AlGaN-δ-GaN QW, gain is optimised with a truthful design valid for mid and deep ultraviolet lasers [12]. Gain for TE polarization with 3 nm thickness for $Al_{0.8}Ga_{0.2}N$/ GaN QW and with $N_{2D} = 1.65 \times 10^{13}$ /cm^2 at T = 300 K room temperature is obtained. For 10 to 20 Å thickness, the gain differs from ~3078 to ~3703 cm^{-1}. At 245 nm, high gain is obtained for this asymmetric structure with a dissimilar δ GaN layer. For the enhanced δ QW with Al composition of $x_1 = 0.75$ and $x_2 = 0.85$, a high gain ~3967/cm is found at λ_{peak} ~244 nm. High optical gains are achieved with λ~244-252 nm, that is ~6 to 7 times greater than conventional structure at same wavelengths.

In 2016, AlInN-δ-GaN QW structure ultraviolet lasers were proposed and investigated by Cheng Liu et al. Gain of this structure was compared with the conventional structure from ~250 to ~300 nm wavelength range. The addition of the ultra-thin GaN

layer outcomes in C-HH transition and boosted wavefunction of hole and electron, that is 3-times higher in TE polarised optical gain. Considerably low threshold carrier density is observed at 250 nm. Hence, it is estimated that the offered AlInN-δ-GaN heterostructure, can aid as a favorable different active region for high efficiency UV lasers [13].

Delta-layer insertion effect on UV emission characteristics of wurtzite oriented AlGaN/AlN QW structure is theoretically calculated [14]. The position of δ layer decides peak emission intensity. The light emission characteristics are improved in this structure that is grown on Al facet AlN substrate, this is away from AlGaN δ layer. If Al composition is increased in delta layer, the peak emission intensity also increases continuously. The spontaneous emission spectrum peak intensity is increased by ~20–30% with a blue-shift of ~10 nm of the transition wavelength (with delta layer), in comparison to conventional heterostructure without the delta-layer.

In nanoscale heterostructure, InAlN/delta-GaN/InAlN, enhanced gain for Deep-UV applications is presented by, P. A. Alvi (2020). For TE polarization mode, gain of InAlN/delta GaN/InAlN structure is determined, successfully. Achieved gain is 3 times higher than the gain of III nitride based conventional structure. At 302 nm wavelength, the obtained optical gain is around 36000/cm for 4.101ev photon energy. Calculated gains are 30618, 36204, 29286, and 26386 cm^{-1} for 2, 3, 4 and 5Å, respectively. At 283 nm wavelength, optical gain in conventional heterostructure is of ~10500 cm^{-1} with ~ 4.379 eV energy without δ GaN layer. The 2-D carrier injection density is reserved the same for both structures i.e. around 3.5×10^{12} cm^{-2}. The electric field is applied with δ-GaN layer for 100, 300 and 500 kV/cm, to achieve higher optical gain. In this range of electric field, the significant rise in optical gain is obtained as ~36750, 37600 and 38400/cm respectively [15]. Table 2 and Fig. 2 show the effect of δ-layer insertion on UV emission and optical gain in different heterostructures.

Table 2 Effect of δ-layer insertion on UV emission and optical gain

Ref.	QW Structures	δ layer	Al content	Carrier density	Wavelength (nm)	Optical gain (/cm)
[11]	InGaN/ GaN	AlGaN	0.05	$10 \times 10^{12}/cm^2$	490	5600
[12]	AlGaN-Delta-GaN	GaN	0.75	5×10^{19} $/cm^3$	244	3967
[13]	AlInN- δ - GaN	GaN	0.91	5×10^{19} $/cm^3$	293	3726
[14]	AlGaN/ AlN	AlGaN	0.8	$20 \times 10^{12}/cm^2$	255	4400
[15]	InAlN/ δGaN/ InAlN	GaN	0.82	$3.5 \times 10^{12}/cm^2$	302	36,000

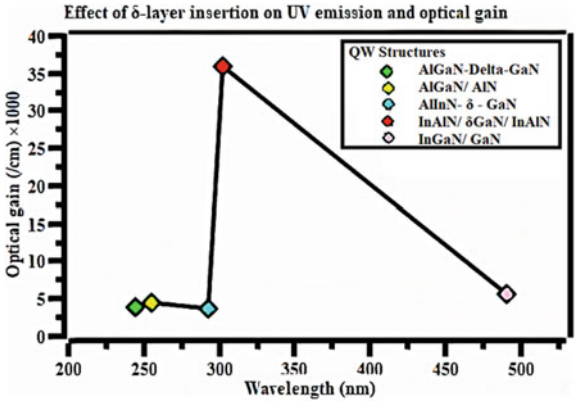

Fig. 2 Effect of δ-layer insertion on optical gain

2.3 Optical Gain for Different Nitride-Based Heterostructures

In 2015, Emanuele Francesco Pecora et al. investigated deep-UV optical gain in AlGaN based heterostructure. The heterostructure is proposed as an applicant for a deep-UV semiconductor laser with electrical pumping. Optical gain threshold of 14 $\mu J/cm^2$ is also measured. The graded region AlGaN with polarization doping, that forms p-i-n junction automatically, results in lasing under electrical injection [16].

For UV applications, the optimization of AlGaN QW heterostructure is designed by Dolia et al. (2018). This structure shows the existence of UV optical gain with AlGaN composition of 50 nm (quantum well material). This type-I heterostructure is supposed to be grown on GaN substrate. Optical gain of AlN/AlGaN/AlN nanoscale heterostructure is calculated with the help of the 6 × 6 Kohn Luttinger Hamiltonian [17]. According to the calculated result, peak optical gain is ~700 cm for energy ~5.165 eV at wavelength ~240 nm. Thus, the designed AlN/AlGaN/AlN structure is suitable as a UV source.

Richa Dolia et al. examined the effect of well width on optical gain in GaN/AlGaN structures in 2020, measuring optical gain at various well widths using the 6 × 6 k·p Hamiltonian with effective mass approximation at 100 K. The density of the injected 2D carrier is kept at $1 \times 10^{12}/cm^2$. Optical gains of 8800, 7800, 7200, and 6600 cm^{-1} are attained for different well widths of 40, 50, 60, and 70 nm, respectively. At wavelengths of 327, 340, 355, and 365 nm, respectively, these gains were obtained. According to these findings, decreasing the well width boosts gain significantly [18]. The findings will be useful in the development of tunable light sources with high intensity and shorter (UV) wavelengths.

In 2020, Bernd Witzigmann et al. presented optical gain calculation in AlGaN QW for ultraviolet emission. The Poisson formula is used to solve the Maxwell–Bloch equations in the second Born approximation. The estimated FWHM (10 meV) for homogeneous broadening and excitonic redshift (100 meV) are determined. The 39 meV inhomogeneous broadening energy is calculated using stimulated emission

Table 3 Comparative study of optical gain of nitride-based heterostructures

Ref.	Heterostructures	QW thickness (nm)	Al content	Carrier density	Wavelength (nm)	Optical gain (/cm)
[16]	AlGaN-based graded index separate confinement heterostructure	50	0.72	$1.55 \times 10^{18}/cm^3$	257	80
[17]	AlN/AlGaN/AlN	50	–	–	240	760
[18]	GaN/AlGaN	40, 50, 60, 70	–	$1 \times 10^{12}/cm^2$	327,340, 355,365	8800, 7800, 7200, 6600
[19]	AlGaN QW for UV emission	2	0.9	$5.1 \times 10^{19}/cm^3$	270	1700

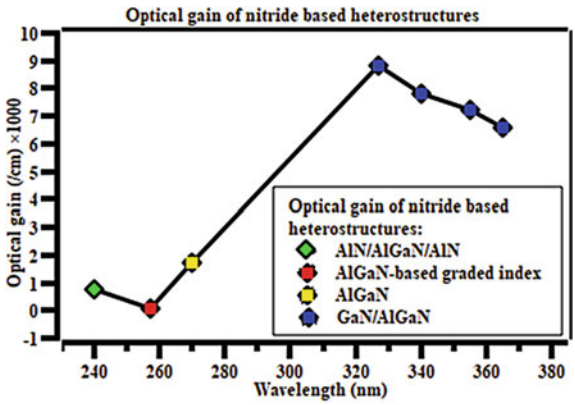

Fig. 3 Variation in optical gain of heterostructures

experimental data [19]. High TE optical gain is obtained at 2 nm thickness of wells in multiple QW structures, for single QWs thicker than 6 nm. For a QW emitting at around 270 nm with 2.2 nm thickness, optical gain ~1700/cm is calculated. Table 3 and Fig. 3 show a comparison of optical gain of different heterostructures.

3 Conclusion

A detailed overview of nitride based nanoscale heterostructures for UV applications has been presented. Nitride based heterostructures are being fabricated using advanced MOCVD and MBE techniques for various applications. Nitride-based UV

emitters have emerging applications in water purification, free-space communication, medical field, bioagent detection etc. Optical gain of these heterostructures has been reviewed under room temperature, variation in well width and insertion of delta layer. With the insertion of delta layer with increasing Al content, enhanced peak intensity of quantum well heterostructure can be achieved. These results for various recent works have been tabulated and will aid future research activities in the UV emitter design.

References

1. Khan A, Balakrishnan K, Katona T (2008) Ultraviolet light-emitting diodes based on group three nitrides. Nat Photonics 2(2):77–84. https://doi.org/10.1038/nphoton.2007.293
2. Kneissl M, Rass J (2016) III-Nitride Ultraviolet Emitters Technology and Applications. Springer, Heidelberg. https://doi.org/10.1007/978-3-319-24100-5
3. Liao C-H, Sun H, Li X (2019) Ultraviolet quantum well lasers Nanoscale Semiconductor. Lasers 139–163.https://doi.org/10.1016/b978-0-12-814162-5.00006-6
4. Parbrook PJ, Wang T (2011) Light emitting and laser diodes in the ultraviolet. IEEE J Sel Top Quantum Electron 17(5):1402–1411. https://doi.org/10.1109/jstqe.2011.2126563
5. Martens MGR (2018) Optical gain and modal loss in AlGaN based deep UV lasers. Technische Universitaet Berlin (Germany)
6. Kneissl M, Knorr A, Reitzenstein S, Hoffmann A (Eds.) (2020) Semiconductor Nanophotonics. Springer Series in Solid-State Sciences, Heidelberg. https://doi.org/10.1007/978-3-030-35656-9
7. Takano T, Narita Y, Horiuchi A, Kawanishi H (2004) Room-temperature deep-ultraviolet lasing at 241.5 nm of AlGaN multiple-quantum-well laser. Appl Phys Lett 84(18):3567–3569. https://doi.org/10.1063/1.1737061
8. Francesco Pecora E et al (2012) Sub-250 nm room-temperature optical gain from AlGaN/AlN multiple quantum wells with strong band-structure potential fluctuations. Appl Phys Lett 100(6):061111. https://doi.org/10.1063/1.3681944
9. Oto T, Banal RG, Funato M, Kawakami Y (2014) Optical gain characteristics in Al-rich AlGaN/AlN quantum wells. Appl Phys Lett 104(18):181102. https://doi.org/10.1063/1.4875592
10. Zhang Z et al (2019) A 271.8 nm deep-ultraviolet laser diode for room temperature operation. Appl Phys Express. https://doi.org/10.7567/1882-0786/ab50e0
11. Park S-H, Park J, Yoon E (2007) Optical gain in InGaN/GaN quantum well structures with embedded AlGaN δ layer. Appl Phys Lett 90(2):023508. https://doi.org/10.1063/1.2431477
12. Zhang J, Tansu N (2013) Engineering of AlGaN-Delta-GaN quantum-well gain media for mid- and deep-ultraviolet lasers. IEEE Photonics J 5(2):2600209–2600209. https://doi.org/10.1109/jphot.2013.2248705
13. Liu C, Ooi YK, Zhang J (2016) Proposal and physics of AlInN-delta-GaN quantum well ultraviolet lasers. J Appl Phys 119(8):083102. https://doi.org/10.1063/1.4942524
14. Park S-H, Ahn D (2017) Effects of a delta-layer insertion on the ultraviolet light emission characteristics of III-nitride quantum well structures. Superlattices Microstruct 112:665–670. https://doi.org/10.1016/j.spmi.2017.10.025
15. Alvi PA (2020) Enhanced optical gain characteristics of InAlN/δ-GaN/InAlN nanoscale-heterostructure for D-UV applications. Superlattices Microstruct 140:106436. https://doi.org/10.1016/j.spmi.2020.106436
16. Pecora EF, Sun H, Dal Negro L, Moustakas TD (2015) Deep-UV optical gain in AlGaN-based graded-index separate confinement heterostructure. Opt Mater Express 5(4):809. https://doi.org/10.1364/ome.5.000809

17. Dolia R, Abu-Samak M, Alvi PA (2019) Optimization of AlGaN QW heterostructure for UV applications. In: Ray K, Sharan S, Rawat S, Jain S, Srivastava S, Bandyopadhyay A (eds.) Engineering Vibration, Communication and Information Processing. LNEE, vol 478. Springer, Singapore. https://doi.org/10.1007/978-981-13-1642-5_2
18. Dolia R, Chander S, Vats VS, Alvi PA (2020) Well width effect on optical gain in GaN/AlGaN QW heterostructure. Materials Today: Proceedings. https://doi.org/10.1016/j.matpr.2020.07.143
19. Witzigmann B, Römer F, Martens M, Kuhn C, Wernicke T, Kneissl M (2020) Calculation of optical gain in AlGaN quantum wells for ultraviolet emission. AIP Adv 10(9):095307. https://doi.org/10.1063/5.0021890
20. Singh AK, Singh R, Singh K, Rathi A (2021) Optical gain enhancement and wavefunction confinement tuning in AlSb/InGaAsP/GaAsSb heterostructures. Eur Phys J B 94(6):1–5
21. Vijay J, Singh AK, Jain PK, Alvi PA, Singh K, Rathi A (2021) Optical gain characteristics of GaAs based type-II AlAsSb/InGaAs/GaAsSb nanoscale heterostructure for near infrared applications. Optoelectron Adv Mater Rapid Commun 15(March-April 2021):114–119
22. Riyaj M, et al (2019) High pressure affects on optical characteristics of AlGaAs/GaAsP/AlGaAs nano-heterostructure. Optik 181: 389–397

Designing of GaN Based Photonic Crystal Biosensor for Blood Disease Analysis

Ankit Agarwal, Nitesh Mudgal, Ankur Saharia, Dinesh Bhatia, Saurabh Sahu, Ghanshyam Singh, and S. K. Bhatnagar

Abstract In this paper a design structure is proposed to analysis the blood disease by analysing the blood component based on their refractive index. Blood is the composition of several component like plasma, haemoglobin, water, red blood cells, biotin, biotin streptavidin, glucose, and ethanol. These components play a vital role for causing the human disease. The composition of these components causes several complicated diseases like cancer, lungs disease, kidney disease. This design structure used to measure the concentration of these component in a remarkable region. If the concentration changes, the refractive index is also changes. The sensitivity of this design structure is 570 nm/RIU. The structure is designed with Gallium Nitride.

Keywords Biosensors · Finite difference time domain (FDTD) · Blood diseases · Photonic crystal · Sensitivity

1 Introduction

Now-a day's several diseases are reported in human body. These diseases are varied from person to person [1, 2]. The reason of most of the -diseases are unbalancing of blood component in human blood. As we know that Blood is the keen part in human body. Blood analysis plays a vital role in analysis the diseases related to haematological disorder [3–5]. These haematological disorders cause the several serious diseases

A. Agarwal (✉) · N. Mudgal · D. Bhatia · G. Singh
Malviya National Institute of Technology, Jaipur, Rajasthan, India
e-mail: ankitsagarwal@gmail.com

A. Agarwal · S. K. Bhatnagar
Swami Keshvanand Institute of Technology, Management & Gramothan, Jaipur, Rajasthan, India

A. Saharia
Manipal University Jaipur, Jaipur, Rajasthan, India

S. Sahu
Gyan Ganga Institute of Technology and Sciences, Jabalpur, M.P, India

M. Tiwari et al. (eds.), *Optical and Wireless Technologies*, Lecture Notes in Electrical Engineering 892, https://doi.org/10.1007/978-981-19-1645-8_28

Table 1 Normal range, refractive index, and effect of disorder for different blood component for 1550 nm wavelength [7, 9]

Blood component	Range	Refractive index	Effect of disorder
Water	30–40 mL/Kg	1.33	
Blood plasma	72 g/L	1.35	Protects the body from infection and other blood disorders
Ethanol	150 gms/L	1.36	Prevents blood cells from sticking together and forming clots
Hemo-globin	100 gms/L	1.38	Prevent blood clots, heart attacks, and strokes
Glucose	1.1–1.4 gms/L	1.4	Prevent hardening of the blood vessels
Biotin-Streptavidin	30 μg/day	1.45	Responsible for processing of protein

like heart attack, cancer, Lungs related disease, kidney related disease, Anaemia, lung cancer etc. [6].

Blood is the composition of blood plasma and red blood cells. The blood plasma consists of 55% and red blood cells consists of 45% of total blood volume [7]. This blood is also contained protein, haemoglobin, bilirubin, blood cells, ammonia, albumin, glucose, magnesium etc. [8]. Blood characteristics are diverse based on disease. These diseases change the concentration of blood composition and according to this refractive index is changes [9]. The blood composition, normal range of these human blood composition, refractive index and effect of disorder is shown in Table 1. This table represents that most of heart, lungs and kidney diseases are due to blood.

For blood composition detection, blood is taken from a normal person a process to decompose in several components.

Photonic crystal structure is a periodic arrangement of different dielectric medium [1, 10, 11]. The photonic biosensors are centred on the communication of light with the sensing analyte [12, 13]. These components are used as an analyte in phonic biosensors. When the light is passes through the sensing nodes, the propagation of optical signal is affected. This affected signal is detected at the output port to analyse the changes with respect to input signal [14].

The photonic biosensors are commonly used for detection of haematological disorder. Photonic biosensors are exercised for analysing the blood. These haematological disorders change the refractive index of whole blood [9]. The change in refractive index is detected when optical signal is passes through design structure.

For analysing the design structure quality factor, sensitivity and normalized transmission spectra is observed [15]. Quality factor (Q) is the parameter to check that how much optical signal is confine in the waveguide structure. This is the ratio of resonating wavelength and the difference between 3 dB Full Width Half Maximum (FWHM) wavelength point. Quality factor is very important parameter [16] because it shows that the r/a ratio is appropriate or not. If r/a ratio is not appropriate than signal is not confine properly.

Sensitivity defines that how minimum change in refractive index can be detected by the sensor. This parameter is very important for biosensing application, gas, and chemical sensing [17] because a slight change in concentration of analyte, refractive index is also changes. So, this parameter defines that how much change in concentration is detected by the sensor. Sensitivity of sensor is the ratio change in wavelength to change in refractive index and unit is nm/RIU [6].

2 Design Structure

The photonic crystal (PC) Structure design for blood sensing is shown in Fig. 1. This design structure is consisting of three parts input port, output port and sensing nodes as shown in Fig. 2. The Gallium Nitride is used as a substrate material. In this substrate material air holes (r) are created having the radius of 0.12 μm. the dimension of lattice in x direction is 17 and dimension of lattice in y direction is 21. The line defect is induced in the design structure. Distance between centre of two air holes is define as lattice constant (a) and value of lattice constant is 0.48 μm. The ratio of air hole radius and lattice constant should be greater than or equal to 0.25. the design parameter and refractive index of substrate is mentioned in Table 2. The dimension of nodes in sensing structure is 50 nm. This sensing structure is elliptical structure with 21 nodes in it.

Photonic band gap (PBG) is the significant property of PC structures [18, 19]. This band gap defines the range of wavelength at which the photons can travel through the design structure without any interference. Every photon has different energy level and different transmission wavelength. This wavelength distribution is shown by photonic band gap. The PBG is like semiconductor band gap structure for periodic structure and photonic band region is like the forbidden energy gap of semiconductor

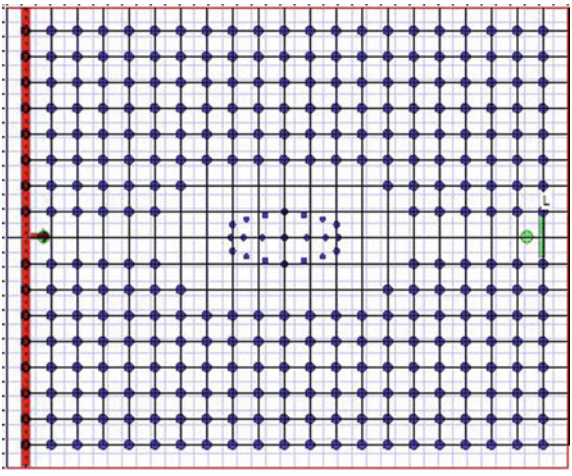

Fig. 1 Design structure of blood component detection

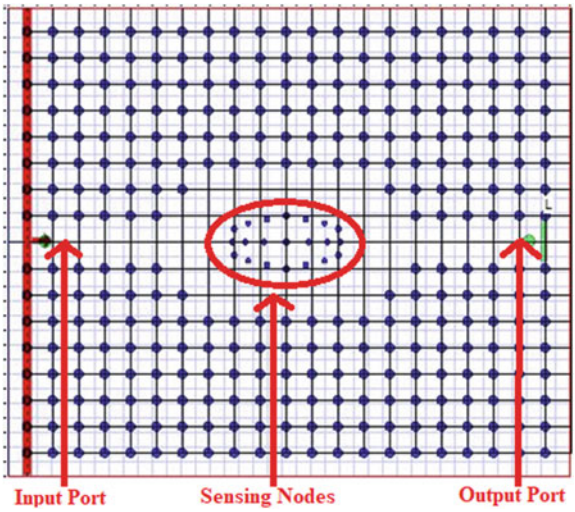

Fig. 2 Design structure with input- output port and sensing nodes

Table 2 Design parameter and dimension of design structure

Parameter	Design dimension
Lattice constant	0.48 μm
Air holes radius	0.12 μm
Nanocavity radius	0.05 μm
Lattice dimension	17*21
Refractive index of substrate	2.32 (GaN)
Refractive index of holes	1 (air)
Refractive index of sensing nodes	Refractive index of analyte

where no absorption is possible. In this PBG, photons with the similar wavelength does not travel. So, when no defect is created in the design structure the signal transmission of this wavelength is not travel through the structure. If line or point defect is introduced in the design structure the signal with this wavelength range will start travel through design structure. The normalized wavelength range is calculated by a/λ where a is lattice constant and λ is 1/f. Figure 3 shows the photonic band gap for design structure in TE mode. For the TM mode no band gap exist means no photon with magnetic field will travel through this structure. This photonic band gap lies from 0.306–0.358 μm^{-1}. So the signal wavelength travel through the waveguide should lies from 1340–1570 nm wavelength.

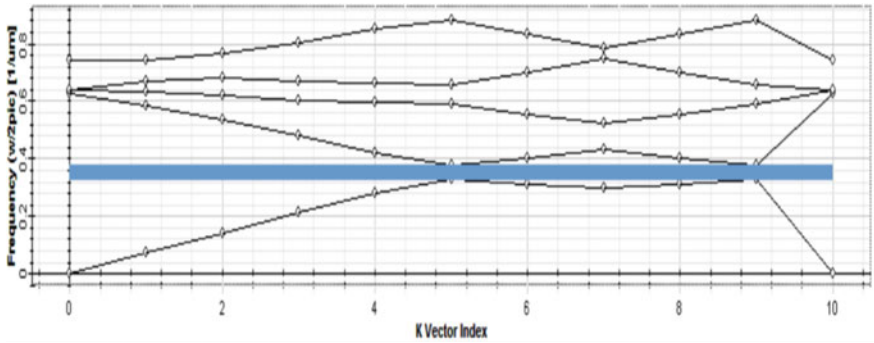

Fig. 3 Photonic band gap of design structure

3 Simulation Results

The design structure is simulate using finite difference time domain (FDTD) method. The refractive index of sensing structure nodes is changes from 1.33 to 1.45 as per the component used for analysing. Gaussian pulse having the wavelength of 1550 nm is applied as an input. The applied input signal is shown in Fig. 4. This input signal is normalized input signal. The applied signal is pass through waveguide and at receiving node output signal is received (when no analyte is used). The received signal is shown in Fig. 5. The normalized output signal power is approximate 68%. The remaining power is either absorbs by the material or transmitted in the structure (not confined in the waveguide properly). When the optical signal is pass through sensing structure, the photons will interact with the analyte refractive index. Due to the interaction the resonating peak of input signal is shifted. When the analyte having the refractive index from 1.33 to 1.45 is changes, resonant peak is shifted towards lower region due to higher refractive index. The shifting in resonating peak with respect to blood component is shown in Table 3. The wavelength of resonating peak shifted in the range of 1528–1556 nm. For different refractive indexes, the quality factor and sensitivity are calculated. The quality factor of this design is approximate 210 and the sensitivity is approximate 230 nm/RIU. The normalized transmission spectra, quality factor and sensitivity are shown in Table 3.

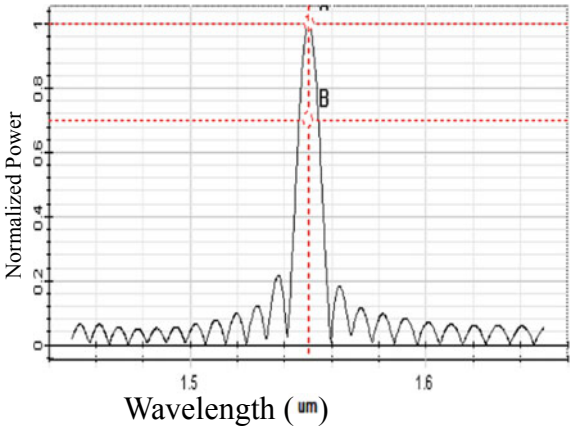

Fig. 4 Normalized signal power at input port

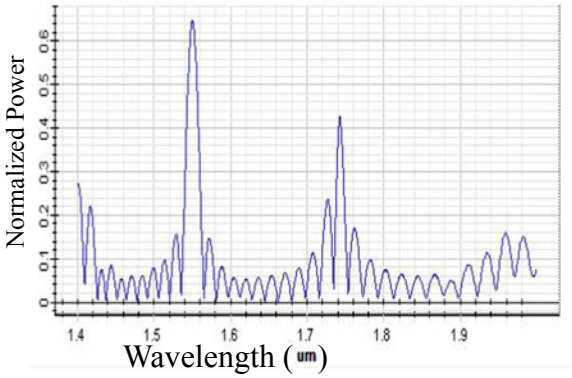

Fig. 5 Normalized signal power at output port

Table 3 Quality factor, transmission spectra and sensitivity

n	λ_o (nm)	Quality factor	Normalized transmission spectra (%)	Sensitivity (nm/RIU)
1.33	1556.1	**212**	**68.4**	–
1.35	1551.7	**217**	**67.7**	**220**
1.36	1549.3	**209**	**67.3**	**240**
1.38	1544.6	**204**	**68.5**	**235**
1.4	1539.8	**207**	**68.7**	**240**
1.45	1528.4	**203**	**67.9**	**228**

4 Conclusion

In this paper, a GaN based photonic biosensor is designed for detection of different blood components in a desired range and analysed its sensitivity, resonant peak,

and quality factor. Basically, this two-dimensional photonic crystal design structure is a having GaN as a substrate material and holes having the refractive index of air. In this Photonic crystal line defect is created and in this defect sensing nodes in ellipse geometric dimensions are created. This sensing nodes are having the refractive index of analyte. The resonating wavelength of this design structure is from 1535 to 1568 nm, for the analysing of design structure. The structural design is very compact in size (μm). So, this structure can be identified by analysing the blood components and cure at initial stage. Hence, this design structure will have vast application in biomedical.

References

1. Joannopoulos JD et al (2008) Photonic Crystals: Molding the Flow of Light, 2nd ed. Princeton
2. Hsiao FL, Lee C (2009) Novel biosensor based on photonic crystal nano-ring resonator. Procedia Chem 1(1):417–420
3. Sharma P, Sharan P (2015) Design of photonic crystal-based ring resonator for detection of different blood constituents. Opt Commun 348:19–23
4. Sharma P, Sharan P (2014) Photonic crystal-based ring resonator sensor for detection of glucose concentration for biomedical application. Int J Emerg Technol Adv Eng 4(30):702–706
5. Roggan A, Friebel M, Dörschel K, Hahn A, Mueller GJ (1994) Optical properties of circulating human blood in the wavelength range 400–2500 nm. J Biomed Opt 4(1):36–46
6. Arunkumar R, Suaganya T, Robinson S (2019) Design and Analysis of 2D photonic crystal based biosensor to detect different blood components. Photonic Sens 9(1):69–77
7. Elblbesy MA (2020) The refractive index of human blood measured at the visible spectral region by single-fiber reflectance spectroscopy. AIMS Biophys 8(1):57–65
8. Roggan A, Friebel M, Dörschel K, Hahn A, Müller G (1999) Optical properties of circulating human blood in the wavelength range 400–2500 nm. J Biomed Opt 1(1):36–46
9. Liu S et al (2019) Measurement of the refractive index of whole blood and its components for a continuous spectral region. J Biomed Opt 24(3):035003. (1–5)
10. Joannopoulos JD, Villeneuve PR, Fan S (1997) Photonic crystals: putting a new twist on light. Nature 386(6621):143–149
11. Agarwal A, Sahu S, Mudgal N, Singh G, Bhatnagar SK (2020) Photonic crystal cavities based biosensors: a review. In: IEEE Conference ICONC3, Laxmangarh, 21–22 Feb 2020
12. Fenzl C, Hirsch T, Wolfbeis OS (2014) Photonic crystals for chemical sensing and biosensing. Angewandte Chemie Int Edition 53(13):3318–3335
13. Nair RV, Vijaya R (2010) Photonic crystal sensors: an overview. Prog Quantum Electron 34(3):89–134
14. Agarwal A, Mudgal N, Sahu S, Singh G, Bhatnagar SK (2022) Design of a nanocavity photonic crystal structure for biosensing application. In: Tiwari M, Maddila RK, Garg AK, Kumar A, Yupapin P (eds.) Optical and Wireless Technologies. LNEE, vol 771, pp 321–330. Springer, Singapore. https://doi.org/10.1007/978-981-16-2818-4_35
15. Zlatanovic S, Mirkarimi LW, Sigalas MM et al (2009) Photonic crystal microcavity sensor for ultracompact monitoring of reaction kinetics and protein concentration. Sens Actuators B-Chem 141(1):13–19
16. Lee MR, Fauchet PM (2007) Two-dimensional silicon photonic crystal based biosensing platform for protein detection. Opt Express 15(8):4530–4535
17. Lee C, Thillaigovindan J, Radhakrishnan R (2008) Design and modeling of nano mechanical sensors using silicon 2-D photonic crystals. J Light Wave Technol 26(7):839–846

18. Yablonovitch E (1987) Inhibited spontaneous emission in solid-state physics and electronics. Phys Rev Lett 58:2059–2062
19. John S (1987) Strong localization of photons in certain disordered dielectric superlattices. Phys Rev Lett 58(23):2486–2489

60-GHz Millimeter Wave Antenna for 5G Wireless Communication

Akash Rawat, Gaurav Kumar Soni, Dinesh Yadav, and Manish Tiwari

Abstract In the modern wireless communication system high data rates and more bandwidth efficiencies is required. Apertures for different inventive applications will be made in automotive, medical accommodations, industry etc. which is because of the incipient 5G requisites, which recollect 1000× increment for limit and 10× higher data rates, among others. In this paper a microstrip patch antenna is proposed for 60 GHz milimeter wave next generation of wireless connectivity in 5G communication. This propsed antenna is designed with dimanisation of 4 × 4 × 0.035 mm using rogers RO3003 substrate with dielectric constant (ε_r) = 3, loss tangent (tan δ) = 0.001.

Keywords mmWave · Wireless communication · Antenna · Cellular communication · 5G technology · Higher data rates

1 Introduction

In recent scenarios wireless communications have grown expeditiously. It requires more minute contrivances to install multiband communications. As an indispensable component of the wireless correspondence organization the antenna has the main part of the design effect. The most congruous antenna for the wireless contrivances is planar inverted-F antenna (PIFAs) [1]. 5G represents the fifth generation in mobile technology. The ultra high bandwidth will provide us in 5G technology. The 5G technology is a lot better than all other generations of wireless communication like 1G, 2G, 3G & 4G technology. The celerity of the 5G is identically tantamount

A. Rawat (✉) · G. K. Soni · D. Yadav · M. Tiwari
Department of Electronics and Communication Engineering, Manipal University Jaipur, Jaipur, Rajasthan, India
e-mail: akrt1192@gmail.com

D. Yadav
e-mail: dinesh.yadav@jaipur.manipal.edu

M. Tiwari
e-mail: manish.tiwari@jaipur.manipal.edu

M. Tiwari et al. (eds.), *Optical and Wireless Technologies*, Lecture Notes in Electrical Engineering 892, https://doi.org/10.1007/978-981-19-1645-8_29

to the mm waveband [2]. In the near future, 5G will become the most puissant technology in the wireless communication. The haste of 5G is 100 MBPS to 20 GBPS, with higher data rate and better quality of accommodation than precedent versions. On the contrary since the mmWave frequency band has 30 to 300 GHz bandwidth, It is prescribed to make mmWave communication a consequential piece of 5G cellular network to provide multi gigabit communication like HDTV and UHDV [3]. The most astronomically immense numbers of recent studies are predicated on the 28 GHz band, 38 GHz band, 60 GHz band and E band (71–76 and 81–86 GHz). Due to the development of millimeter wave networks, the mobility of millimeter wave communications has brought various challenges, such as high propagation loss, congestion sensitivity, directivity etc. It is compulsory to reconsider and understand the infrastructure and protocols to resolve these issues. By cumulating its advantages and disadvantages, it can efficaciously achieve efficient network performance and potent network. Potential applications of the mmWave 5G network involve minute cellular access, cellular access, and wireless broadband. Among some open research challenges, suggestions were made for millimeter wave communication architecture and design guidelines in the protocol. Millimeter wave frequencies involving MIMO and full-duplex technology commenced and discussed in the form of the benefits and drawback of incipient physical layer technology. In additament in millimeter wave communications, it must synchronize with other networks, such as LTE and WiFi networks. Connection and coordination within sundry types of framework are essential to be able to analyze the heterogeneous networks [4–8].

In this paper a rectangular patch shape microstrip patch antenna is propsoed with rogers RO3003 substrate. The propsoed antenna is design for 60 Ghz mmwave 5G application. the geometry of the antenna is $4 \times 4 \times 0.13$ mm^3.

2 Antenna Design and Designing Parameters

The Width of the microstrip patch antenna is calculated [9]

$$W = \frac{C}{2f_r}\sqrt{\frac{2}{\epsilon_r + 1}} \tag{1}$$

where, C is speed of light and ε_r is the value of dielectric substrate.

The Length of the microstrip antenna is calculatd:

Due to fringing fields, actual size of the antenna is increased by an amount of ΔL.

$$\frac{\Delta L}{h} = 0.412\frac{(\varepsilon r_{eff} + 0.3)(\frac{w}{h} + 0.264)}{(\varepsilon r_{eff} - 0.258)(\frac{w}{h} + 0.8)} \tag{2}$$

εr_{eff} is effective refractive index and h is the hight of the substract.

$$L_{eff} = \frac{C}{2f_0\sqrt{\varepsilon r_{eff}}} \tag{3}$$

$$L = L_{eff} - 2\Delta L \tag{4}$$

This propsed antenna is designed using Rogers RO3003 substrate with dielectric constant ($\varepsilon_{r)} = 3$, loss tangent ($\tan \delta$) = 0.001. In this propsoed antenna structure ground is designed using copper metarial with specification of thickness 0.035 mm, legth is 4 mm and width is 4 mm. The specification of substrate thickness 0.13 mm, legth is 4 mm and width is 4 mm. The antenna patch is reactangular shape with dimanisation of 1.767 × 1.321 × 0.035 mm. Inset feed depth is 0.426 mm and gap is 0.4 mm. Feed line length is 1.08 mm feed line width 0.1 mm. The structure of the proposed microstrip patch antenna is illustrated in Fig. 1 and Table 1 display the geometry of the proposed microstrip patch antenna design.

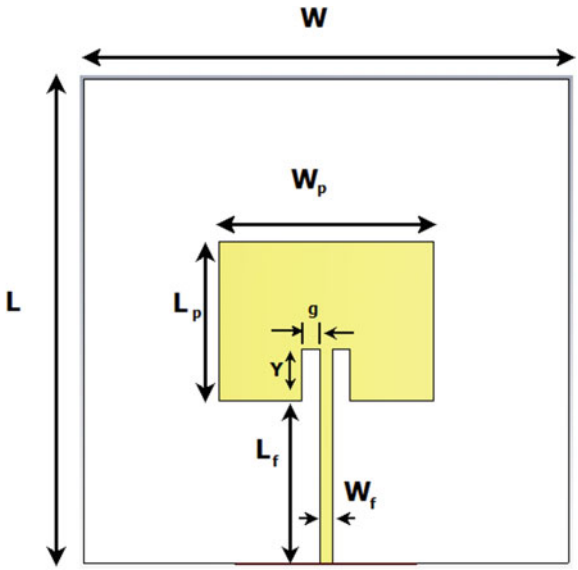

Fig. 1 Antenna design structure for 60 GHz mmWave communication

Table 1 Geometry of the proposed rectangular microstrip patch antenna

Parameters	Value (mm)
Length (L)	4
Width (W)	4
Patch Length (L_p)	1.767
Patch Width (W_p)	1.321
Antenna size	$4 \times 4 \times 0.035$
Feed line width (L_f)	1.3
Inset feed depth (Y)	0.465
Feed line length (L_f)	0.1

3 Results and Discussions

In this propsoed antenna design obtained the high gain at 60 GHz operating frequency range for mmwave wireless communcation. The magnitude of simulated return loss (|S11|) results of propsoed antenna is display in Fig. 2. In this proposed design obtained the magnitude of $|S_{11}|$ is −65 dB. The propsoed antenna design at 60 GHz operating frequency polar plot of the farfield gain is obtained 6.85 dBi, the farfield dielectivity is obtained 7.95 dBi and 3D radiation patterns through the simulation that showns in Figs. 3, 4 and 5 respectively. Figure 6 depicts efficiency of proposed antenna. The comparative analysis of proposed 60 GHz millimetre wave antenna with previously reported antennas is shown in Table 2.

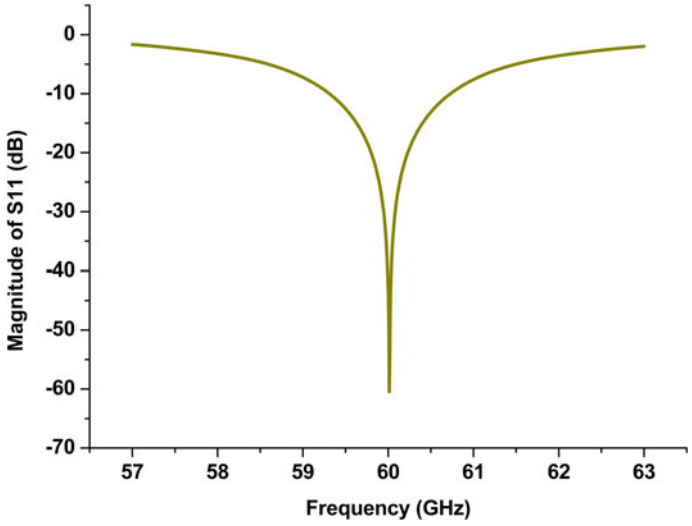

Fig. 2 Magnitude of S_{11} of the proposed antenna

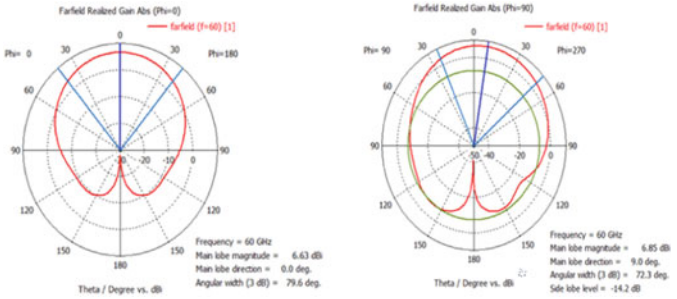

(a) phi=0 (b) phi=90

Fig. 3 Polar plot of the farfield gain of the proposed antenna at operating frequency 60 GHz

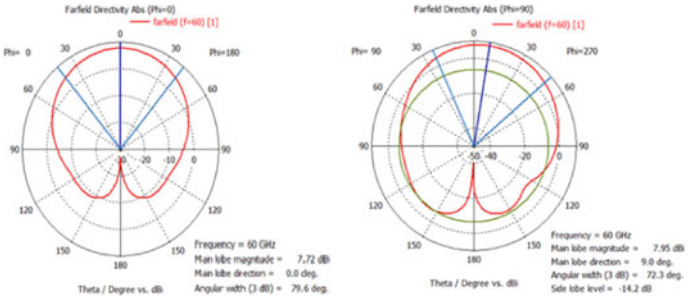

(a) phi=0 (b) phi=90

Fig. 4 Polar plot of the farfield directivity of the proposed antenna at operating frequency 60 GHz

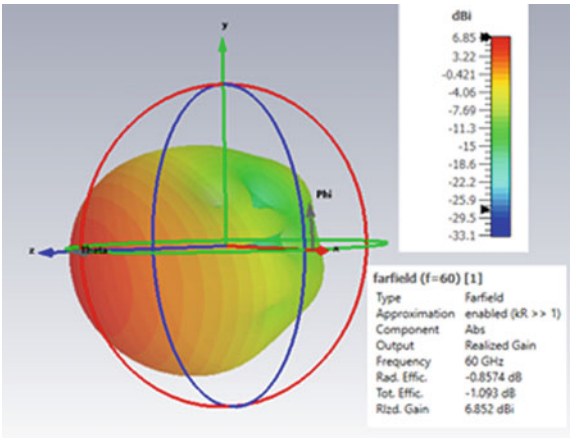

Fig. 5 3D radiation patterns at 60 GHz for proposed antenna

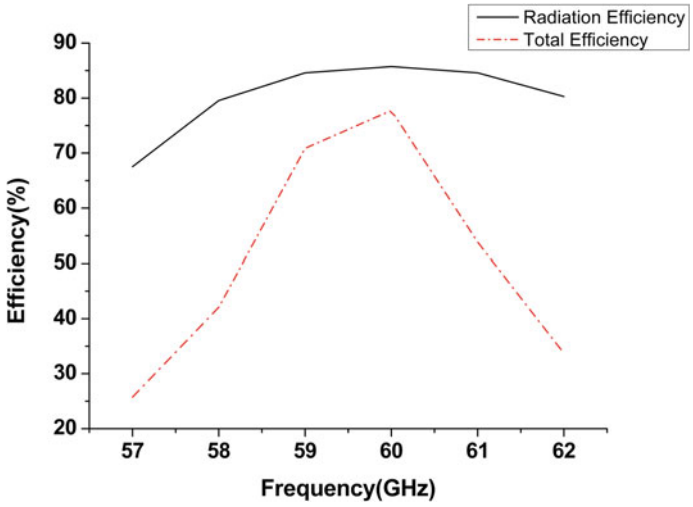

Fig. 6 Efficiency of proposed antenna

Table 2 Comparative analysis of proposed 60 GHz millimetre wave antenna with previous 60 GHz antennas

Ref	Substrate	Size (mm^3)	Gain (dBi)	S_{11} (dB)	Efficiency (%)
[10]	RT/duroid 5880	___	5.45	−17	78.5
[11]	Duroid 5870	49.7 × 31 × 3.1	4.7	−20	65
[12]	FPCB	14 × 10.5 × 1.15	10.6	−43	74
Proposed	Rogers RO3003	4 × 4 × 0.035	6.85	−65	85.8

4 Conclusion

In this paper, a compact size reactangular microstrip patch antenna design is proposed using rogers RO3003 substrate with size of antenna is 4 × 4 × 0.035 mm^3 and the dimanisation of antenna patch is 1.767 × 1.321 × 0.035 mm^3. The efficency of the propsoed antenna is 85.8%. The proposed antenna is used for the 60 GHz milimeter wave 5G wireless communication.

References

1. Yadav D, Tiwari V (2021) Frequency reconfigurable planner antennas for wireless applications: a review. In: Smart trends in computing and communications: proceedings of SmartCom 2020. Smart ınnovation, systems and technologies, p 182

2. Shukurillaevich UB, Sattorivich RO, Amrillojonovich RU (2019) 5g technology evolution. In: IEEE ınternational conference on ınformation science and communications technologies (ICISCT), pp 1–5
3. Rawat A, Soni GK, Yadav D, Tiwari M (2021) Millimeter-wave antennas for wireless cellular communication 5G and beyond mobile networks: an overview. In: Design engineering, pp 12131–12153
4. Vignesh SJ, Wadhwa P, Agarwal I, Yadav D (2020) Electromagnetically coupled high gain dual band microstrip planar antenna for mm-wave applications. In: 2020 IEEE 4th ınternational conference on electronics, materials engineering & nano-technology (IEMENTech), pp 1–5
5. Soni GK, Gour S, Sharma A (2021) Design and analysis of multi-band fractal antennas for wireless communications. In: Emerging trends in data driven computing and communications. Studies in autonomic, data-driven and ındustrial computing. Springer, Singapore
6. Bharadwaj SS, Sipal D, Yadav D, Koul SK (2020) A compact tri-band frequency reconfigurable antenna for LTE/Wi-Fi/its applications. Prog Electromagn Res M 91:59–67
7. Jangir D, Shankar G, Jain BB, Soni GK (2020) Performance analysis of LTE system for 2x2 Rayleigh and Rician fading channel. In: 2020 IEEE ınternational conference on smart electronics and communication (ICOSEC), pp 961–966
8. Singh H, Soni GK, Suryawanshi P, Shankar G (2020) Performance analysis and BER comparison of OFDM system for 4×4 MIMO fading channel in different modulation scheme. In: 2020 IEEE third ınternational conference on smart systems and ınventive technology (ICSSIT), pp 255–259
9. Bara P, Yadav D (2018) A comparative ınvestigation of microstrip patch antenna using FR-4/RT-Duroid/RO3003 materials for bluetooth and WLAN applications. In: Optical and wireless technologies. Lecture notes in electrical engineering, vol 472. Springer, Singapore
10. Haider MF, Alam S, Sagor MH (2018) V-shaped patch antenna for 60 GHz mmWave communications. In: 2018 3rd ınternational conference for convergence in technology (I2CT), pp 1–4
11. Puskely J, Pokorny M, Lacik J, Raida Z (2015) Wearable disc-like antenna for body-centric communications at 61 GHz. IEEE Antenn Wirel Propag Lett 14:1490–1493
12. Ur-Rehman M, Malik NA, Yang X, Abbasi QH, Zhang Z, Zhao N (2017) A low profile antenna for millimeter-wave body-centric applications. IEEE Trans Antenn Propag 65(12):6329–6337

High Gain Multiband Microstrip Patch Antenna for mmWave 5G Communication

Akash Rawat, Gaurav Kumar Soni, Dinesh Yadav, and Manish Tiwari

Abstract Recently, millimeter wave radio has drawn in an abundance of revenue from the scholarly community, industry, and ecumenical normalization bodies because of sundry appealing highlights of millimeter wave to give multi-gigabit transmission rate. Apertures for different inventive applications will be made in automotive, medical accommodations, industry etc. which is because of the incipient 5G requisites, which recollect 1000× increment for limit and 10× higher data rates, among others. In this paper present a multiband microstrip patch antenna design for mmWave 5G communication operating at 26, 28 and 30 Ghz frequecny range. the propsoed antenna is designed Rogers RO4003C substrate with dielectric constant ($\varepsilon_{r)} = 3.55$, loss tangent ($\tan \delta$) = 0.0021.

Keywords mmWave · Wireless communication · Antenna · Cellular communication · 5G technology · Higher data rates

1 Introduction

A Wireless communications innovation has gotten probably the best commitment to humanity. Wireless communications make it simple to send data from a disseverment without links or wires. This disseverment can go from a couple of meters to an astronomically immense number of kilometers [1]. Wireless innovation sanctions data to be moved distantly without the utilization of links. The disseverment can be short or be a few thousand kilometers [2]. Mobile communication has become a

A. Rawat (✉) · G. K. Soni · D. Yadav · M. Tiwari
Department of Electronics and Communication Engineering, Manipal University Jaipur, Jaipur, Rajasthan, India
e-mail: akrt1192@gmail.com

D. Yadav
e-mail: dinesh.yadav@jaipur.manipal.edu

M. Tiwari
e-mail: manish.tiwari@jaipur.manipal.edu

M. Tiwari et al. (eds.), *Optical and Wireless Technologies*, Lecture Notes in Electrical Engineering 892, https://doi.org/10.1007/978-981-19-1645-8_30

consequential wellspring of data trade far and wide. [3]. 5G represents Fifth Generation Wireless Systems. It depends on the IEEE 802.11ac norm. 5G builds network multifariousness to a sizably voluminous number of sodalities. Wireless World Wide Web, Dynamic Ad hoc Wireless Network (DAWN) and Authentic Wireless World will be authenticated with 5G. 5G innovation has exceptional information capacities and can assemble illimitable call volumes and perpetual information transmission in the most recent multifarious working framework [1, 4]. On the contrary since the mmWave frequency band has 30 to 300 GHz bandwidth, It is prescribed to make mmWave communication a consequential piece of 5G cellular [5, 6]. The most astronomically immense numbers of recent studies are predicated on the 28 GHz band, 38 GHz band, 60 GHz band and E band (71–76 and 81–86 GHz). Due to the development of millimeter wave networks, the mobility of millimeter wave communications has brought many challenges, such as high propagation loss, directivity, congestion sensitivity, and dynamics. It is compulsory to reconsider and understand the infrastructure and protocols to resolve these issues [7, 8]. By cumulating its advantages and disadvantages, it can efficaciously achieve efficient network performance and potent network. Potential applications of the mmWave 5G network involve minute cellular access, cellular access, and wireless broadband [9, 10]. Among some open research challenges, suggestions were made for millimeter wave communication architecture and design guidelines in the protocol. Millimeter wave frequencies involving MIMO and full-duplex technology commenced and discussed in the form of the benefits and drawback of incipient physical layer technology [11–13]. In additament in millimeter wave communications, it must coexist with other networks, such as LTE and WiFi networks. Connection and coordination within sundry types of framework are essential to be able to analyze the heterogeneous networks [14].

In this a microstrip patch antenna (MSA) design is presented with dimension of $35 \times 12 \times 0.508\ mm^3$ that work on 26, 28 and 30 GHz frequency range for mmWave 5G communication. In this propsoed antenna structure obtained the high gain and low return loss for multiband.

2 Antenna Design and Designing Parameters

This propsed antenna is designed using Rogers RO4003C substrate with dielectric constant ($\varepsilon_{r)} = 3.55$, loss tangent ($\tan \delta$) = 0.0021. In this propsoed antenna structure ground is designed using copper metarial with specification of thickness 0.035 mm, legnth is 35 mm and width is 12 mm. The specification of substrate thickness 0.058 mm. The antenna patch is with dimanisation of 3.12×4.3 mm. The proposed antennadesign illuminarate in the Fig. 1 in which used the 4 similar patch design and geometry configuration of proposed antenna design is display in Table 1.

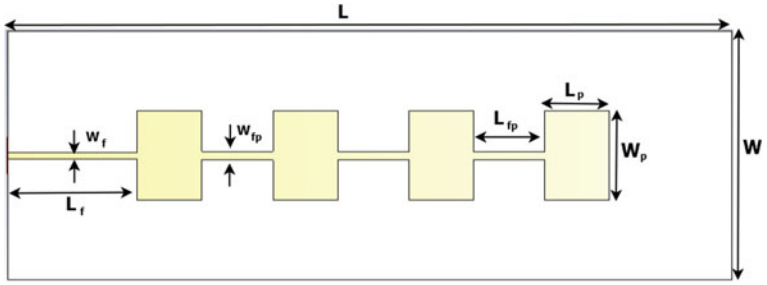

Fig. 1 Proposed multiband antenna design structure

Table 1 Multiband microstrip patch antenna dimensions

Parameters	Value (mm)
Antenna Length (L)	35
Antenna Width (W)	12
Patch Length (L_p)	3.12
Patch Width (W_p)	4.18
Length of feed line (L_f)	6.29
Width of feed line (W_f)	0.29
Patch feed line length (Lp_f)	3.44
Patch feed line width (Wp_f)	0.4

3 Results and Discussions

In the proposed design the return loss is optimize by varying the patch length and patch width. The effect on the return loss (S_{11}) by varying the patch length is display Fig. 2 and the effect on return loss (S_{11}) by varying the patch width is demonstrate in Fig. 3.

By optimizing achieve the better responce of the multiband (26, 28 and 30 GHz) at 3.12 mm patch length (L_p) and 4.18 mm of patch width (W_p). The reurn loss of the propsoed antenna design is achieved at patch size 3.12 × 4.18 mm is −21 dB at frequency responce 26 GHz, −26 dB at frequency responce 28 GHz and −19.5 dB at frequency responce 30 GHz. Figure 4 illuminated the magnitude of return loss (S_{11}) using the proposed antenna configuration for 26, 28 and 30 GHz multiband application.

In Figs. 5, 6 and 7 displayed the polar plot of the proposed antenna at frequency of 26 GHz, 28 GHz and 30 GHz respectively. The obtained gain of the proposed antenna is 10.4 dBi, 10 dBi and 5.78 dBi for 26 GHz, 28 GHz and 30 GHz frequency respectively.

In Table 2 illustrate the comparative analysis of the proposed work with the related previous work done. In proposed work lower cut-off wavelength (λ_o) is 11.538 mm and the size of proposed antenna is 3.033 λ_o × 1.04 λ_o × 0.044 λ_o. In [15] the lower

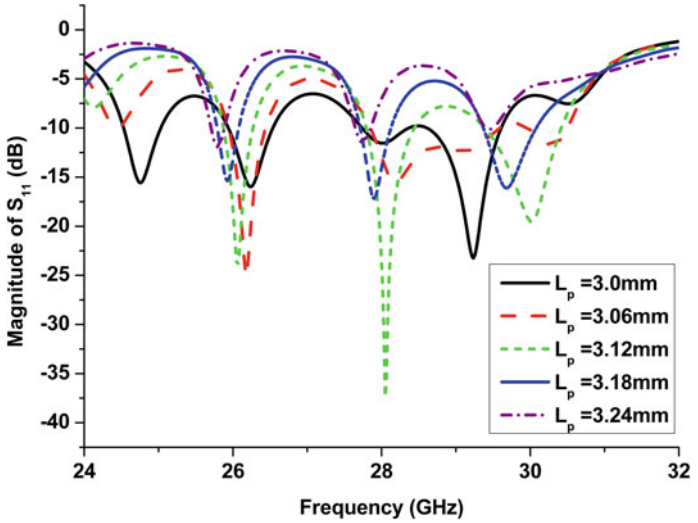

Fig. 2 Return loss (S_{11}) by varying the length of the patch

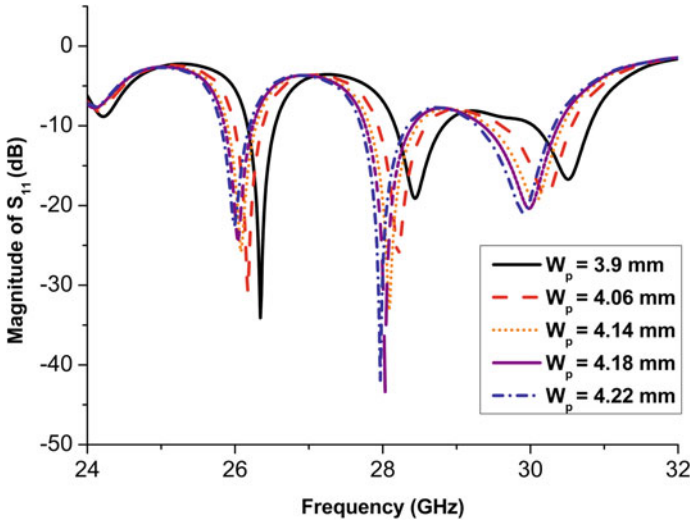

Fig. 3 Return loss (S_{11}) by varying the width of the patch

cutoff wavelength (λ_o) is 11.11 mm and the size of antenna is 1.52 λ_o × 0.67 λ_o × 0.216 λ_o. In [16] the lower cutoff wavelength (λ_o) is 10.71 mm and the size of antenna is 0.513 λ_o × 1.86 λ_o × 0.073 λ_o. In [17] the lower cutoff wavelength (λ_o) is 12 mm and the size of antenna is 0.413 λ_o × 0.571 λ_o × 0.064 λ_o. In [18] the

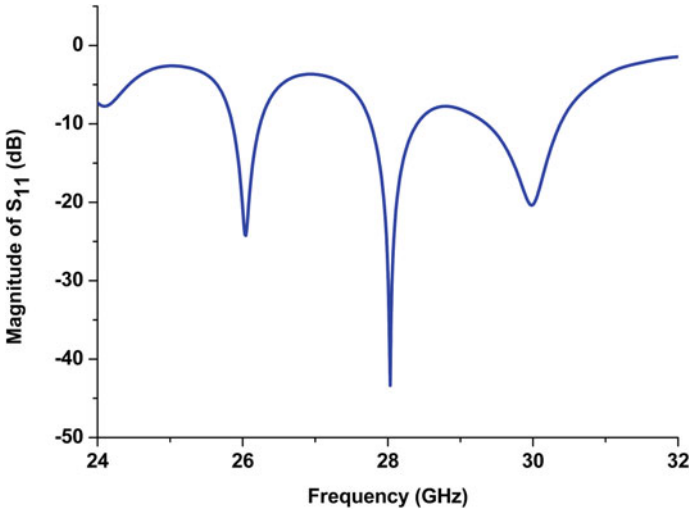

Fig. 4 Return loss (S_{11}) of the proposed antenna configuration at 26, 28 and 30 GHz for multiband application

Fig. 5 Polar plot of the proposed antenna at 26 GHz frequency

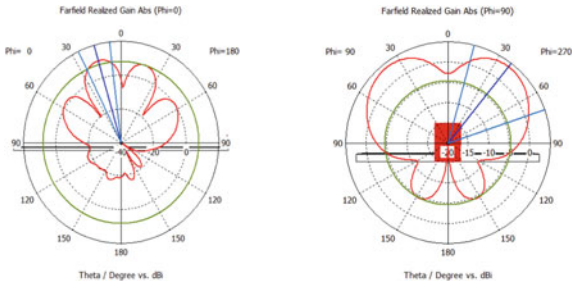

(a) phi=0 (b) phi=90

Fig. 6 Polar plot of the proposed antenna at 28 GHz frequency

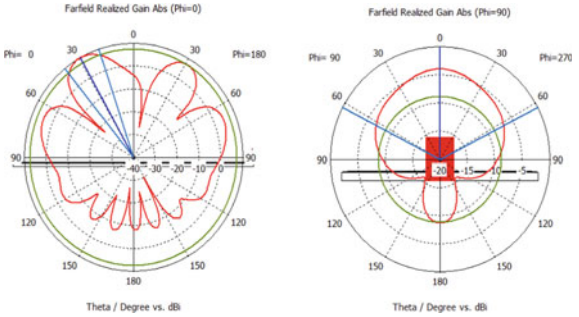

(a) phi=0 (b) phi=90

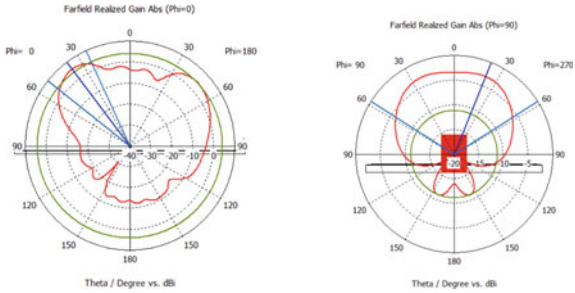

(a) phi=0 (b) phi=90

Fig. 7 Polar plot of the proposed antenna at 30 GHz frequency

Table 2 Comparative analysis of proposed mmWave 5G communication antenna with previous 5G antennas

Ref.	Freq. (GHz)	Size (mm^3) λ_o = lower cutoff wavelength	Gain (dBi)	S_{11} (dB)
[15]	27/30/33	1.52 λ_o × 0.67 λ_o × 0.216 λ_o	5.49/5.23/5.83	−12/−11/−15
[16]	28/38	0.513 λ_o × 1.86 λ_o × 0.073 λ_o	5.2/5.9	−25/−31
[17]	25/37	0.413 λ_o × 0.571 λ_o × 0.064 λ_o	6.71/1.72	−25.7/−25.73
[18]	28	1.858 λ_o × 2.8 λ_o × 0.088 λ_o	7.2	−15
Proposed	26/28/30	3.033 λ_o × 1.04 λ_o × 0.044 λ_o	10.4/10/5.78	−24.24/−43.35/−20.37

lower cutoff wavelength (λ_o) is 10.71 mm and the size of antenna is 1.858 λ_o × 2.8 λ_o × 0.088 λ_o.

4 Conclusion

In this paper, a MSA is designed for mmWave 5G communication with multiband operating frequency of 26, 28 and 30 GHz. The size of propsoed antenna is 3.033 λ_o × 1.04 λ_o × 0.044 λ_o mm^3. The obtained gain from the simulation results of the proposed multiband antenna is 10.4 dBi, 10 dBi and 5.78 dBi for 26 GHz, 28 GHz and 30 GHz frequency respectively. From the displayed in Table 2 comparative analysis of the proposed antenna work with previous other antenna work done, obtained the high gain of the proposed antenna in multiband frequency range for mmWave 5G communication applications.

References

1. Agarwal I, Wadhwa P, Vignesh SJ, Yadav D (2020) Orthogonal bird shaped multiband MIMO antenna for 5G technology with high ısolation and efficiency. In: IEEE 4th ınternational conference on electronics, materials engineering & nano-technology (IEMENTech), pp 1–5
2. Park JS, Lee HJ, Kim M (2006) Technical standardization status and the advanced strategies of the next generation mobile communications. In: IEEE 8th ınternational conference advanced communication technology, pp 884–887
3. Chen S, Sun S, Wang Y, Xiao G, Tamrakar R (2015) A comprehensive survey of TDD-based mobile communication systems from TD-SCDMA 3G to TD-LTE(A) 4G and 5G directions. China Commun 12(2):40–60
4. Lien SY, Shieh SL, Huang Y, Su B, Hsu YL, We HY (2017) 5G new radio: waveform, frame structure, multiple access, and initial access. IEEE Commun Mag 55:64–71
5. Wadhwa P, Agarwal I, Vignesh SJ, Yadav D (2020) Dual band high efficiency orthogonal double sided puzzle shaped MIMO antenna MM-wave applications. In: 4th ınternational conference on electronics, materials engineering & nano-technology (IEMENTech), pp 1–5
6. Vignesh SJ, Wadhwa P, Agarwal I, Yadav D (2020) Electromagnetically coupled high gain dual band microstrip planar antenna for mm-wave applications. In: IEEE 4th ınternational conference on electronics, materials engineering & nano-technology (IEMENTech), pp 1–5
7. Roy P, Vishwakarma RK, Jain A, Singh R (2016) Multiband millimeter wave antenna array for 5G communication. In: IEEE ınternational conference on emerging trends in electrical electronics & sustainable energy systems (ICETEESES), pp 102–105
8. Çıl A, Kahvecı S (2018) Some challenges foreseen in 5G technology. In: IEEE 26th signal processing and communications applications conference, pp 1–4
9. Huo Y, Dong X, Xu W, Yuen M (2018) Cellular and WiFi co-design for 5G user equipment. In: 2018 IEEE 5G world forum (5GWF), pp 256–261
10. Rawat A, Soni GK, Yadav D, Tiwari M (2021) Millimeter-wave antennas for wireless cellular communication 5G and beyond mobile networks: an overview. In: Design engineering, pp 12131–12153
11. Saleem S, Kumari S, Yadav D, Bhatnagar D (2020) A high ısolation UWB-MIMO antenna with dual band rejection property. In: IEEE ınternational conference on computing, power and communication technologies (GUCON), pp 212–216
12. Singh H, Soni GK, Suryawanshi P, Shankar G (2020) Performance analysis and BER comparison of OFDM system for 4×4 MIMO fading channel in different modulation scheme. In: IEEE third ınternational conference on smart systems and ınventive technology (ICSSIT), pp 255–259
13. Yadav D, Abegaonkar MP, Koul SK, Tiwari VN, Bhatnagar D (2018) Two element band-notched UWB MIMO antenna with high and uniform isolation. Prog Electromagn Res M 63:119–129
14. Bharadwaj SS, Sipal D, Yadav D, Koul SK (2020) A Compact tri-band frequency reconfigurable antenna for LTE/Wi-Fi/its applications. Prog Electromagn Res M 91:59–67
15. Jilani SF, Abbasi QH, Alomainy A (2018) Inkjet-printed millimetre-wave PET-based flexible antenna for 5G wireless applications. In: 2018 IEEE MTT-S ınternational microwave workshop series on 5G hardware and system technologies (IMWS-5G), pp 1–3
16. Ashraf N, Haraz O, Ashraf MA, Alshebeili S (2015) 28/38-ghz dual-band millimeter wave siw array antenna with ebg structures for 5g applications. In: Information and communication technology research (ICTRC), pp 5–8
17. Goudos S, Tsiflikiotis A, Babas D, Siakavara K, Kalialakis C, Karagiannidis G (2016) Evolutionary design of a dual band e-shaped patch antenna for 5g mobile communications. In: IEEE ınternational conference on modern circuits and systems technologies (MOCAST), pp 1–4
18. Park J, Ko J, Kwon H, Kang B, Park B, Kim D (2016) A tilted combined beam antenna for 5G communications using a 28-GHz band. IEEE Antennas Wirel Propag Lett 1685–1688

Analysis of Child Abduction Cases and Design of Internet of Things Based Child Safety System

Vaibhav Bhatnagar, Devershi Pallavi Bhatt, and Devanshi Ledwani

Abstract The illegal removal of a minor from the custody of the child's natural parents or legally appointed guardians is known as child abduction or child stealing. Child kidnapping is a serious offence, and it is increasing with rapid rate. Safety of a child is always a matter of concern of parents as well as school authorities. In this paper, statistical analysis of dataset of child kidnapping with different parameters such as age, gender, race, height and weight are discussed. Supervised machine learning algorithms is used to identify the pattern of abduction done by family member or outside the family. The classifier received the accuracy of 93%. Furthermore, Internet of Things based system is also proposed that will monitor the location of the child whenever child enters or exits in the school vehicle. The proposed system is designed with Arduino microcontroller, RFID reader, GSM module, GPS module, PIR sensor, and Piezo Buzzer. The system gets triggered when child enters or exits in the school vehicle and RFID tags are read that are fixed on the shoe of child. The proposed system is tested with 10 students at different time with different geographical locations.

Keywords Child · IoT · Decision tree · RFID

1 Introduction

India is the country where more than 400 million children are below of the age 18 [1]. Crimes are increasing day per day. As per the report of National Crime Bureau, a child got missing in every 10 min in India. The statistics given by NCB is shown in Fig. 1 [2].

V. Bhatnagar · D. P. Bhatt (✉)
Department of Computer Applications, Manipal University Jaipur, Jaipur, India
e-mail: pallavi25.bv@gmail.com

D. Ledwani
Department of Computer Communication Engineering, Manipal University Jaipur, Jaipur, India

M. Tiwari et al. (eds.), *Optical and Wireless Technologies*, Lecture Notes in Electrical Engineering 892, https://doi.org/10.1007/978-981-19-1645-8_31

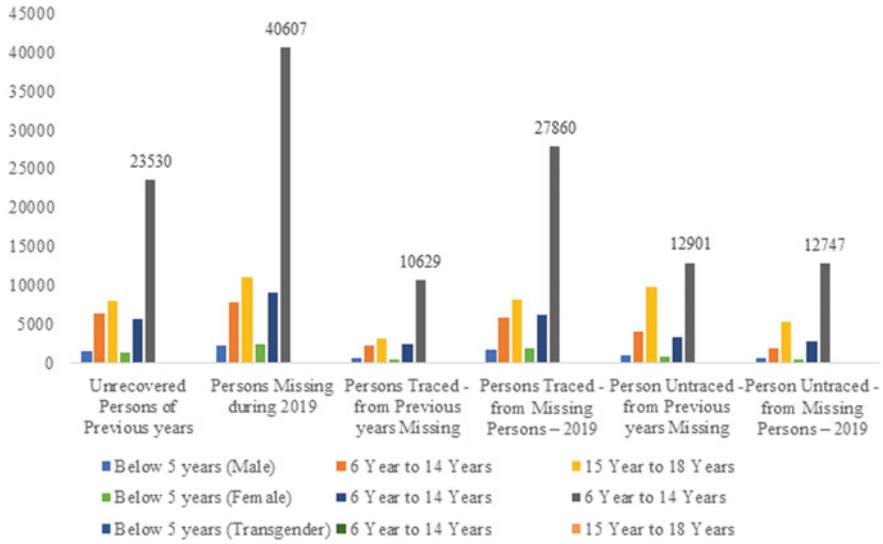

Fig. 1 Number of missing children in India

The numbers shown in the Fig. 1 are creating a necessity to have some mechanism to mitigate the problem of child missing. Internet of Things (IoT) is a good solution for this problem.

This paper has two objectives. The first objective of this paper is to identify the pattern of kidnapping among the children using Decision Tree machine learning technique. The second objective of the paper is to design an IoT based system that can trace the location of the system when student enter and exit in the school vehicle.

The paper is organized in eight sections. After the Introduction, section part discusses about related work, third part discusses about research motivation, IV part discusses about descriptive analysis, V part discussed about schematic diagram, VI part discusses about proposed work, VII part discusses about results & discussion and last VIII part is the conclusion of the paper.

In the year 2020, Madhur et al. [3], proposed an IoT-enabled digital system design combines Cloud, Mobile, and GPS technologies to pinpoint a child's exact location on a map of an event. The suggested architecture model for the sophisticated IoT-enabled smart kid safety tracking digital system defines the people, information, process, and technology architecture aspects, as well as their interactions. In the same year, Mohammad Jabirullah et al., [4], They developed child safety system using RFID. Students have RFID-based cards that are used to authenticate them. When a pupil boarded the school bus, the Raspberry sends a message to parents and the principal. This methodology is enhanced with Machine Learning. Aparajith Srinivasan et al. [5], designed a system to keep track of children's whereabouts and vital signs in real time using different everyday wearable device such as wrist band, glove, arm band and belt. This electronic system includes an Arduino controller, a Raspberry Pi,

and sensors that monitor changes in temperature, BVP (Blood Volume Pulse), and GSR (Galvanic Skin Response). A GSM and GPS module are also included in the system. With sensor data as inputs, the Decision Tree Classifier Algorithm is utilized to recognize any distress condition. The victim's location is tracked using the GPS module, and a text message is sent to the registered contact numbers using the GSM module.

In the year 2019, Dipali Badgujar et al. [6], proposed radar devices and obstacle sensors to detect the warning when the kid enters the danger zone or is approaching a dangerous object. The alert will be sent to the caregiver through mobile phone via an alarm or notice. They used ultrasonic obstacle sensor in the form of locket. This locket sends a mobile alert to the careatker, and for battery backup, a solar panel is utilized, with the energy being stored in the caretaker's shoes and being reliant on the steps taken by the caretaker.

In the year 2017, Leonardo D'Errico et al. [7], designed GPS and RFID based system for ensuring child presence in the bus and data is delivered to a server that maintains in touch with kid parents using a native Android application that interacts with a mobile RFID reader. They also designed the server application to interact with mobile vendors notifications services.

From the above literature it is found that most of the research are done on the wearable devices which can harm the body of children and most of the work is done without applying proper authentication. More than one RFID tag can be used by a single person that can mislead information. Moreover, since RFID tags are placed on the shoes of child, these RFID tags can be placed by other systems without presence of any person. Taking these points into consideration, a novel system is proposed that not only monitor the location of child but also maintains the authenticity of the system without wearing any additional gadget or sensor.

2 Analysis of Child Abduction Data

The first objective of this paper is to identify the pattern of kidnapping among the children. To identify the pattern, secondary data is used from [8] belonging to United States. The data description is shown in below Table 1. Total 273 number of cases are considered to identify.

The subsequent objectives are to identify that age, height, weight and sex affect the abduction of a child by a family member or not. Family abduction is a serious crime when a child is concealed by the family member of the child himself. Here CaseTpye is target value that contain two values of weather a child is kidnapped by family member or outsider from the family. To achieve the subsequent objectives, T-test [9] and Chi-Square [10] is applied. The P value is shown in below Table 2.

Since p value obtained is 0.004, it can be inferred that there is significance difference between Age of child abducted by family member and outside the family. Since p value obtained is 0.3, it can be inferred that there is no significance difference between height of child abducted by family member and outside the family. Since

Table 1 Description of the dataset

S. N.	Name of variable	Data types	Description
1	Age	Numeric	Age of the Child
2	Sex	Category	Gender of the Child
3	Race	Category	Skin color of the Child
4	Height	Numeric	Height of the Child
5	Weight	Numeric	Weight of the Child
6	CaseType	Category (Target variable)	Family Abduction or non-Family Abduction

Table 2 Independent t-test and chi square test

S. N.	Name of variable 1	Name of variable 2	Null Hypothesis (H_0)	P value
1	Age	CaseType	No significance difference between Age and CaseType	0.004
2	Height	CaseType	No significance difference between Height and CaseType	0.3
3	Weight	CaseType	No significance difference between weight and CaseType	0.08
4	Sex	CaseType	No association between sex and CaseType	<0.001

p value obtained is 0.08. it can be inferred that there is no significance difference between weight of child abducted by family member and outside the family. Since p value obtained is <0.001, it can be inferred that there is an association between gender of child abducted by family member and outside the family.

The next subsequent objective is to identify the pattern among the variables such as age, height, weight, sex and race of the child. Decision Tree algorithm [11] is used to identify the patter. The decision tree is shown in Fig. 2.

From the Fig. 2, that there are maximum chances of non-family Abduction when height is less than 29, age is between 10 and 16, and race is Black or Pacific islander. There are there are maximum chances of non-family Abduction when age is greater than 16 and race is race is Black or Pacific islander. There are more than 80% chances of non-family abduction when age is greater than 10 and race is or Pacific islander. There are maximum chances of family abduction when age is less than 5, height is less than 32 and race is Black or Pacific islander. However, there are also maximum chances of family abduction when age is less than 10, age is greater than 32 but race is Black or Pacific islander. There are 96% chances of a child being abducted when race is other Black or Pacific islander. The accuracy of the classifier is shown in the Fig. 3. In the Fig. 2, Family Abduction (FA) is shown in blue color and Non Family Abduction (NF) is shown in red color.

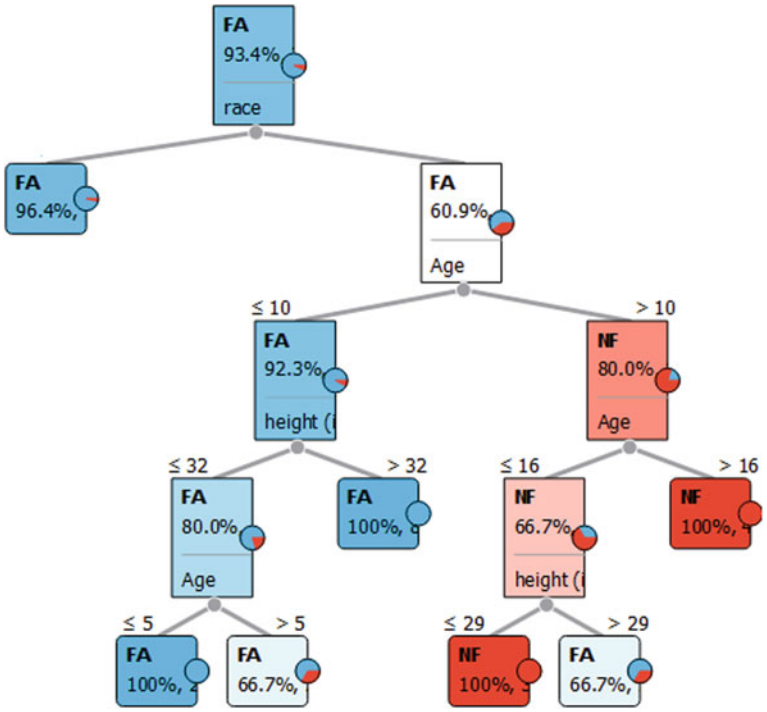

Fig. 2 Decision tree of child abduction dataset

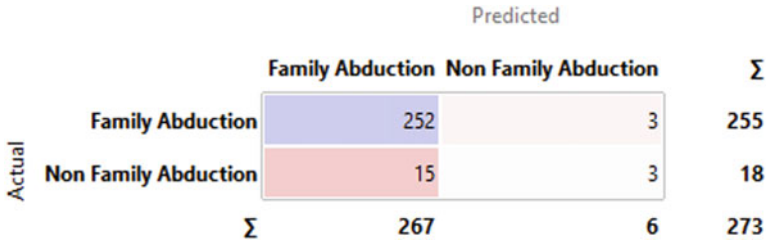

Fig. 3 Confusion matrix of decision tree

Confusion Matrix [12] shows that correct classifiers are 255 in numbers and 15 are mis-classifiers. Therefore 93% accuracy is obtained. Taking these crimes in serious considerations, Internet of Things based solution is provided for child tracking system.

After analyzing the child abduction data, it is found that a child should be traced whenever he or she go to school, because a child can even be kidnapped by the family members and outsiders. So, children tracking system is proposed using Internet of

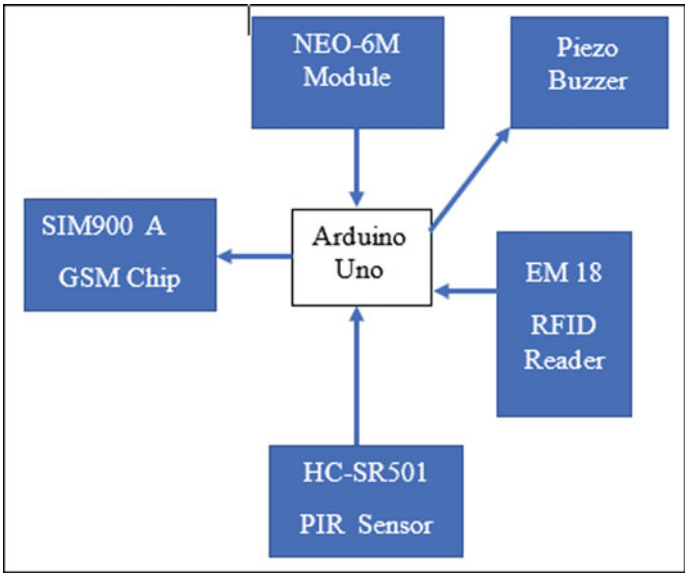

Fig. 4 Schematic diagram of prototype

Things. The proposed system will update the location of children to school and parents.

3 Schematic Diagram and Prototype

The second objective of this paper is to design an IoT based system for monitoring child safety. In this paper, the prototype system has been made for the school student who enter in the school vehicle and leave the school vehicle. The main factor to monitor is the location of child. The schematic diagram is show in Fig. 4.

The prototype is based on the fundamentals of Internet of Things. Arduino Uno is most common micro controller used to design for IoT based systems. It is very inexpensive and easily available. The prototype is designed with RFID reader [13], GPS module [14], GSM module [15], PIR sensor [16] and Piezo Buzzer [17].

4 Prototype

It has been seen in the literature that most of the work is done is to track the position of the child through GPS. In proposed system every child is carrying a RFID tag which is pasted on his shoes. When a child will enter in the school vehicle, first PIR

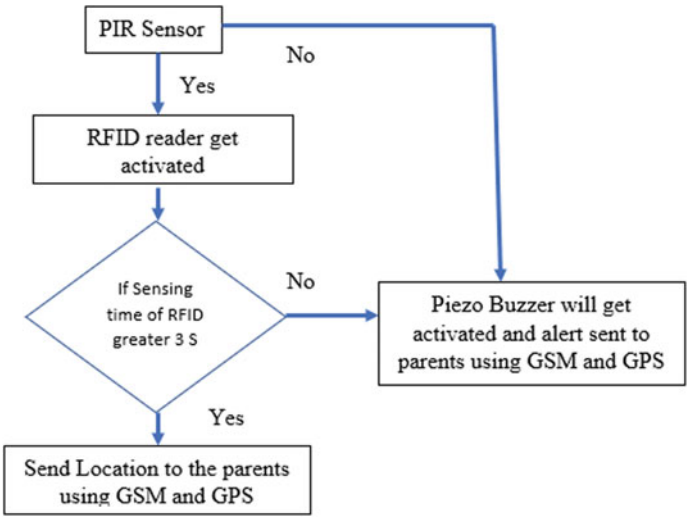

Fig. 5 Flow chart of proposed system

sensor which is fixed at the door of school vehicle will sense that there is a person is going to enter in the school vehicle. When a person is sensed by the PIR sensor, the RFID reader will get activated, by the RFID tag pasted on the shoes of child. When the child enters in the school vehicle, RFID will get activated and the location of the child will be sent to his parent using GPS and GSM Module. Here, the novelty is that if the sensing time between two RFID tags are below 3 s, the system will start giving alarm through Buzzer associated with Arduino and an alert message will be sent to both the parents of which tags are associated. Flow chart is shown in Fig. 5.

5 Testing

The prototype model is tested in a private school bus in Jaipur location (26.9124° N, 75.7873° E). Total number of 10 students have been used for trail with total number of 10 times in different locations. The location and timings are shown in Table 3.

In the below table, the sample data of testing is shown. After the 100 times of trial (10 students with each 10 trials), it is found that every time PIR sensor worked properly, GPS and GSM worked properly. Even when to RFIDs are sensed at the same time, buzzer got alert and the message is successfully sent to both the parents whose RFID tags are associated. However, slight time duration is noticed when the message is sent by the GSM and received by the smart phone.

Table 3 Testing of proposed system

S. N.	Location	Time (AM)	PIR sensor worked	GPS activated	GSM send message of location	Difference between actual location and Location sent location	Time of message received to the parent
Student 1	Malviya Nagar	7.00	Yes	Yes	Yes	No Difference found	7.03 AM
Student 2	Gopalpura Bypass	7.00	Yes	Yes	Yes	Minute Difference Found	6.58 AM
Student 3	Jagatpura	8.00	No	Yes	Yes	Alarm Message Sent	8.02 AM
Student 4	Tonk Road	7.00	Yes	Yes	Yes	No Difference found	7.03 AM
Student 5	Bani Park	8.00	Yes	Yes	Yes	No Difference Found	8.05 AM
Student 6	Murlipura	8.00	Yes	Yes	Yes	No Difference Found	8.01 AM
Student 7	Muhana Mandi	8.00	No	Yes	Yes	Alarm Message Sent	8.10 AM
Student 8	Varun Path Mansarovar	8.00	Yes	Yes	Yes	No Difference Found	8.05 AM
Student 9	Hathoj	8.00	Yes	Yes	Yes	No Difference Found	8.05 AM
Student 10	Vatika	8.00	Yes	Yes	Yes	No Difference Found	Message not Received

6 Conclusion

Children kidnapping cases are increasingly day-to-day. These crimes are taken into serious consideration. In this paper, a descriptive analysis is done on the dataset of child abduction by family member and non-family member. It is inferred that age and gender of children affect the abduction by family member and non-family member.

A decision tree is obtained for the dataset to identify the pattern of abduction. It is found that age and race play important role in abduction and weight does not play significant role in abduction of children. The objective of paper is not only the descriptive analysis of dataset of child abduction, but an Internet of Things based system is proposed to track the location. The proposed system is designed with the help of RFID reader, which is installed in the school bus, whenever a child enters or exit in the school vehicle, the current location of vehicle is sent to the school and parents with the help of GSM and GPS module. The proposed system is also validated by PIR sensor and Piezo Buzzer. The proposed system is tested 100 times with 10 students at different geographical locations. The performance of the proposed system found satisfactory in the nature. In future, this work can be enhanced by adding machine learning techniques in proposed IoT based System.

Acknowledgements This is acknowledged that, this work is sponsored by Manipal University Jaipur under the Endowment Seed Grant fund with INR 175000.

References

1. Child Popoulation. https://www.smilefoundationindia.org/ourchildren.html. Accessed 19 Aug 2021
2. National Crime Bureau. https://ncrb.gov.in/. Accessed 16 Aug 2021
3. Madhuri M, Gill AQ, Khan HU (2020) IoT-enabled smart child safety digital system architecture. In: 2020 IEEE 14th International Conference on Semantic Computing (ICSC). IEEE
4. Jabirullah M, Amru M, Raviteja D (2020) IoT based child safety management using raspberry Pi and RFID technology. In: IOP Conference Series: Materials Science and Engineering, vol. 981, no. 4. IOP Publishing
5. Srinivasan A et al (2020) Intelligent child safety system using machine learning in IoT devices. In: 2020 5th International Conference on Computing, Communication and Security (ICCCS). IEEE
6. Badgujar D, Sawant N, Kundande D (2019) Smart and secure IoT based child monitoring system. Int Res J Eng Technol (IRJET) 6(11)
7. D'Errico L et al (2017) Design and implementation of a children safety system based on IoT technologies. In: 2017 2nd International Multidisciplinary Conference on Computer and Energy Science (SpliTech). IEEE
8. Source of Data. https://www.dataworld.com/ch/home/. Accessed 1 July 2021
9. Kim TK (2015) T test as a parametric statistic. Korean J Anesthesiol 68(6):540
10. McHugh ML (2013) The chi-square test of independence. Biochemia Medica 23(2):143–149
11. Safavian SR, Landgrebe D (1991) A survey of decision tree classifier methodology. IEEE Trans Syst Man Cybern 21(3):660–674
12. Visa S et al (2011) Confusion matrix-based feature selection. MAICS 710:120–127
13. Yadav R, Nainan S (2014) Design of RFID based student attendance system with notification to parents using GSM. Int J Eng 3(2)
14. Kharisma OB et al (2019) Development of location tracking system via short message service (SMS) based on GPS unblox neo-6m and sim 800l module. J Phys Conf Ser 1363(1). IOP Publishing
15. Nasution TH et al (2017) Electrical appliances control prototype by using GSM module and Arduino. In: 2017 4th International Conference on Industrial Engineering and Applications (ICIEA). IEEE

16. Wahyuni R et al (2021) Home security alarm using Wemos D1 and HC-SR501 sensor based telegram notification. J Robot Control (JRC) 2(3):200–204
17. Ogawa T et al (2013) Energy harvesting devices utilizing resonance vibration of piezoelectric buzzer. Jpn J Appl Phys 52(9S1):09KD14

Dual Band Substrate Integrated Waveguide (SIW) Filter with Curved Comb Shape Slots on Top for High Selectivity

Tusshar Manish Sinha, Job Mathew George, Prakhar Srivastava, Diya Deenu Shetty, Amrita Dixit, Ashok Kumar, and Arjun Kumar

Abstract This article presents a dual-band Substrate Integrated Waveguide (SIW) filter using a variable comb shape slot on the top metal surface of the SIW cavity. These comb shape slots create a slow wave effect and the dual cavity produces a dual-band with high selectivity. The proposed filter used Rogers 5880 as a dielectric material with a permittivity(ε_r) of 2.2 and thickness of 0.508 mm. The simulated results obtained by HFSS 19.1 has two narrow bands at 3.6 and 7.8 GHz with the fractional bandwidth of 10.8% and 8.8% for satellite communication. The insertion loss is less than 0.6 dB and the return loss is better than 15 dB. The size of the filter is $0.88 \times 0.44\ \lambda_g{}^2\ mm^2$.

Keywords Substrate Integrated Waveguide (SIW) filter · Curved comb shape · Dual-band

T. M. Sinha (✉) · J. M. George · P. Srivastava · D. D. Shetty · A. Dixit · A. Kumar
School of Engineering and Applied Sciences, Bennett University, Greater Noida, India
e-mail: tusshar.abhishek@gmail.com

J. M. George
e-mail: job26022000@gmail.com

P. Srivastava
e-mail: prakharsrivas55@gmail.com

D. D. Shetty
e-mail: shetty.d054@gmail.com

A. Dixit
e-mail: dixitamrita01@gmail.com

A. Kumar
e-mail: arjun.kumar@bennett.edu.in

A. Kumar
Department of Electronics and Communication Engineering, Goverment Women Engineering College, Ajmer, India
e-mail: kumarashoksaini@gmail.com

M. Tiwari et al. (eds.), *Optical and Wireless Technologies*, Lecture Notes in Electrical Engineering 892, https://doi.org/10.1007/978-981-19-1645-8_32

1 Introduction

The growing interest in the wireless technology domain from researchers and industry calls for demand in the study and research into precision miniature devices which give us accuracy in practical operation at optimum bandwidth and ease of manufacturing. A bandpass filter is an integral component of any wireless device operating in the megahertz to gigahertz range, especially in this day and age there is observable crowding of devices on the wireless spectrum, filter design requires faster and better upgradations even in minuscule ranges at the fastest pace. As such great care has been taken in proposing a novel dual-band filter design in this paper that offers high selectivity to optimise the signal to noise ratio and low insertion and return loss in the order of 0.5 to 12 dB respectively. Even though Substrate Integrated Waveguides were introduced in 2003, to integrate the benefit of the good quality factor of non-planar technologies and compact size and economic feasibility of planar circuits [1], they still remain relevant today mainly for high-frequency millimeter and submillimeter applications, especially as filters because these metallic vias have been optimised in size and spacing to ensure certain modes of operation do not resonate. Existing dual-band filters based on SIW cavity resonators have been investigated. In [2] very compact size is achieved, but insertion loss is high and Q factor is decreased and in [3] capacitively-loaded SIW vias is proposed for miniaturized circuits, however excited higher-order modes are located too close to passband for accuracy in practical applications. Slots in folded SIW was a bandwidth enhancement technique introduced in [4], however, selectivity was unsatisfactory just as in the case of [5] wide bandpass filter realised using U-shaped slots on the upper plane of the substrate and H-shaped fractal defect on the ground plane of SIW cavities. Even amongst miniature bandpass filters of comparable size such as [6] and [7] which use E-shaped slots and resonators, bandwidth achieved poses room for improvement to meet present demand. In SIW with electromagnetic bandgap (EBG) structure etched with S-shaped slots [8], heavy insertion losses are observable. A substrate that creates a multi-mode resonator [9] and accomplishes narrow passband of operation with the added functionality of high selectivity and compact size is ideal for miniaturized integrated and nano-circuits.

Keeping these lofty design challenges in mind and intricately balancing the inverse relationship between bandwidth and quality factor, our paper has proposed the novel design of a filter with dual-band mode at 3.6 GHz and 7.8 GHz which has a radially cut curved comb shape slot on the top of Rogers RT Duroid 5880.

2 Dual-Band Filter Design

A new method is devised for the miniature filter design which is proposed in this paper. It is composed of a rectangular SIW cavity. It is a three-layer structure where the top and bottom are metal and between the metal layers, there is a substrate layer.

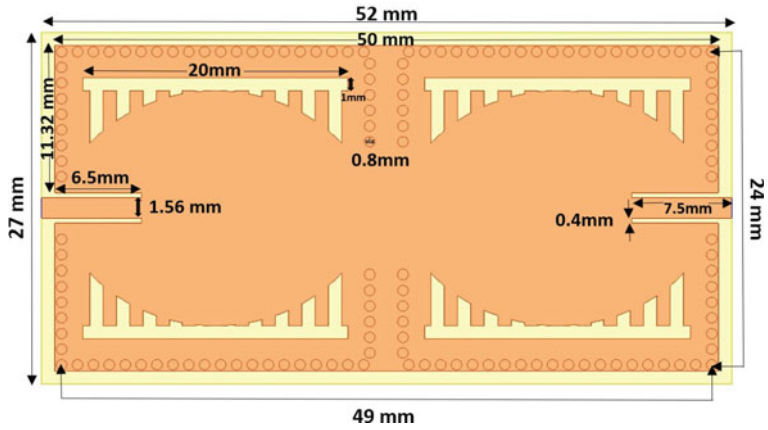

Fig. 1 Top View of proposed Dual-Band SIW BPF with its Dimensions

The proposed structure has two cavities as the design is for dual-mode. A curved comb shape structure is etched on the top metallic layer of substrate in two parts. It is composed of two rectangular SIW cavities with two feeding lines that use coplanar waveguides (CPW), and two curved comb shape slots are positioned facing each other on the edges of the cavity.

By optimizing all the dimensions, we get the proposed dual-band filter. The top view is represented in Fig. 1 with the filter's optimized dimensions.

3 Simulation Results and Discussion

The dual-band SIW bandpass filter has been realized on a 0.508-mm-thick RT/Duroid 5880 substrate with a dielectric constant of 2.2. The dimensions of the design have been mentioned in Fig. 1. The via's diameter is 0.8 mm and the pitch (spacing between the two via-centers) is 1.2 mm.

The simulation results of the designed dual-band SIW BPF are done using HFSS 19.1 software. The proposed filter has two narrow passbands at 3.6 GHz and 7.8 GHz with high selectivity. The bandwidth of the two passbands is 390 MHz and 690 MHz simultaneously. The fractional bandwidth is 10.8% for the first band and 8.8% for the second band. Within the two passbands, the return losses are both greater than 12 dB. This result is achieved through making inward curved comb shape slots utilizing different lengths of each slot which leads to the respective operation frequencies. The insertion loss is less than 0.5 dB in both bands. Also, the designed BPF exhibits exceptional selectivity when compared to its previous predecessors. Figure 2 represents the simulated S-parameter of the proposed design.

The surface current density of the proposed dual-band SIW filter is shown in Fig. 3. From the current density response, it is observed at the center frequency

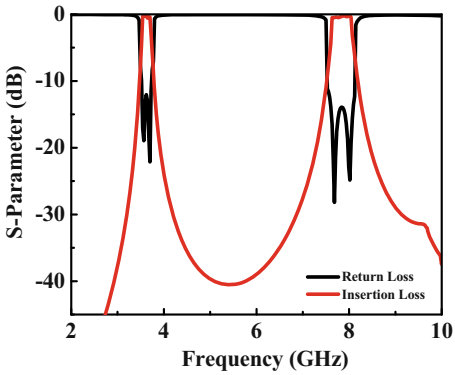

Fig. 2 S-Parameter of proposed Dual Band SIW BPF Design

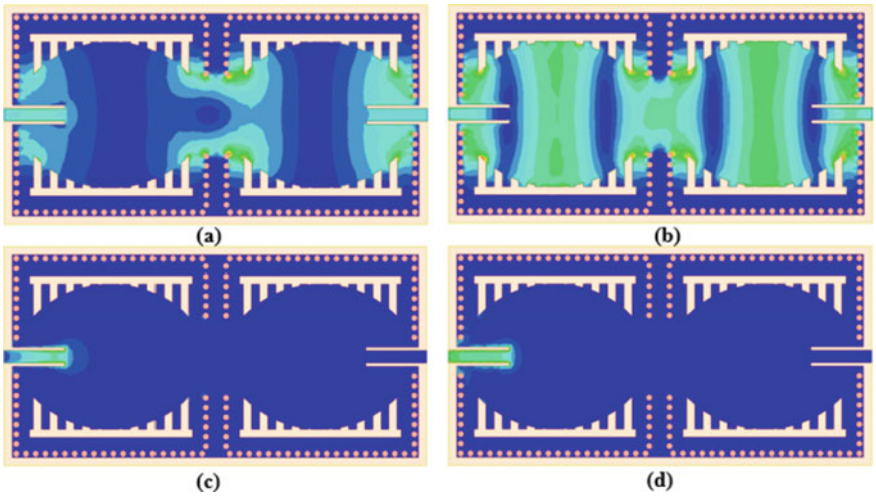

Fig. 3 Surface Current Density of proposed Dual Band SIW BPF filter at different frequencies (**a**) 3.6 GHz (**b**) 7.8 GHz (**c**) 2 GHz and (**d**) 6 GHz

of both dual bands highest current density distribution is shown at (a) and (b). By observing the (c) and (d) current distribution it concludes that after the passband no frequency is transmitted from port 1 to port 2 which means the selectivity of the proposed dual-band SIW filter is very good.

For the validation of our proposed design, these results are compared with the previously published papers. Table 1 represents the result validation. It is observed that the proposed design has less insertion loss and high selectivity.

Table 1 Comparison of proposed Dual-Band SIW BPF with other reported works

Ref	Topology	f_O (GHz)	FBW (%)	IL (dB)	Size ($\lambda g \times \lambda g$)
[7]	SIW CSRR	4.05/5.8	4.6/3.6	2/1.9	0.199 × 0.187
[9]	SIW	6.9/7.95	2.6/2.3	1.47/1.65	2.2 × 0.61
[6]	SIW E-Shape Slot	3.6/6.4	3.3/2.4	1.3/1.8	0.29 × 0.58
[8]	SIW E-Shape Slot	2.4/5.2	5.8/6.5	3/3.1	0.152 × 0.156
This Work	**SIW Curved Comb Shape Slot**	**3.6/7.8**	**10.8/8.8**	**0.5/0.6**	**0.88 × 0.44**

* f_O: Center Frequency, FBW: Fractional Bandwidth, IL: Insertion Loss, λg: Guided Wavelength

4 Conclusion

A dual narrow band substrate integrated waveguide (SIW) filter using a curved comb shape structure has been designed and simulated in this paper. The proposed design has two narrow bands at 3.6 and 7.8 GHz with the fractional bandwidth of 10.8% and 8.8%. The selectivity of the filter is very good.

References

1. Deslandes D, Wu K (2003) Single-substrate integration technique of planar circuits and waveguide filters. IEEE Trans Microw Theory Tech 51(2):593–596
2. Szydlowski L, Leszczynska N, Lamecki A, Mrozowski M (2012) A substrate integrated waveguide (SIW) bandpass filter in a box configuration with frequency-dependent coupling. IEEE Microw Wirel Compon Lett 22(11):556–558
3. Li M, Chen C, Chen W (2017) Miniaturized dual-band filter using dual-capacitively loaded SIW cavities. IEEE Microw Wirel Compon Lett 27(4):344–346
4. Muchhal N, Chakraborty A, Vishwakarma M, Srivastava S (2018) Slotted folded substrate integrated waveguide band pass filter with enhanced bandwidth for Ku/K band applications. Progr Electromagn Res 70:51–60
5. Liu J-P, Lv Z-Q, An X (2016) Compact substrate integrated waveguide filter using dual-plane resonant cells. Microw Opt Technol Lett 58(1):111–114
6. Zhang H, Kang W, Wu W (2018) Miniaturized dual-band SIW filters using E-shaped slotlines with controllable center frequencies. IEEE Microw Wirel Compon Lett 28(4):311–313
7. Dong Y, Itoh T (2011) Miniaturized dual-band substrate integrated waveguide filters using complementary split-ring resonators. In: IEEE MTT-s international microwave symposium, pp 1–4
8. Xu S, Ma K, Meng F, Yeo KS (2015) Novel defected ground structure and two-side loading scheme for miniaturized dual-band SIW bandpass filter designs. IEEE Microw Wirel Compon Lett 25(4):217–219
9. Muchhal N, Srivastava S (2019) Design of wideband comb shape substrate integrated waveguide multimode resonator bandpass filter with high selectivity and improved upper stopband performance. Int J RF Microw Comput-Aided Eng 29(9):2180

A Compact CPW Fed 2 Element MIMO Antenna for C - Band and X- Band Applications

Manan Gupta, Ashok Kumar, Arjun Kumar, Ashok Kumar, and Ajay Yadav

Abstract This article presents a two-element MIMO antenna design for C and X - band applications. The proposed design radiates at 7.1 GHz and has an overall size of (0.58 × 0.29 × 0.04) λo. Each radiating element consists of two circular arcs connected by a simple microstrip element and is fed using a CPW feed. The proposed antenna provides a fractional bandwidth of 66.1% ranging from 5.55–11.03 GHz (|S11| <− 10 dB), thus giving wideband characteristics achieved by using a CPW feed. The proposed design is simulated by using Ansys HFSS 19.1 EM simulator. To evaluate the proposed MIMO antenna performance the isolation and envelope correlation coefficient (ECC) parameters are investigated.

Keywords CPW feed · Microstrip patch antenna · Wide - Band · MIMO · ECC

1 Introduction

The past few decades have seen exceptional growth in wireless communications, thus increasing the demand for efficient communication systems, high data rate and good channel capacity. To fulfill these requirements, antennas have become inevitable, causing a need for antennas that cover wideband, compact size, and provide large gain. Microstrip antennas fulfill these required characteristics as they are also easily integrable with passive and active microwave components. Multiple input multiple output (MIMO) technique is the remedial solution to provide high data rate and more reliable communication [1]. The C - Band is widely used for modern satellites and weather radars. As defined by IEEE standards, X- Band ranges from 8–12 GHz and is used in modern radars, weather prediction, and several military devices. Both the C - Band and the X – Band provide good resistance to attenuation in the rain and other atmospheric obstructions. A 2 × 2 microstrip array having an overall

M. Gupta (✉) · A. Kumar · A. Kumar · A. Yadav
ECE Department, Bennett University, Greater Noida, India
e-mail: gmanan707@gmail.com

A. Kumar
Government Women Engineering College, Ajmer, India

M. Tiwari et al. (eds.), *Optical and Wireless Technologies*, Lecture Notes in Electrical Engineering 892, https://doi.org/10.1007/978-981-19-1645-8_33

size of (1.04 × 1.04 × 0.02) λ_o and bandwidth ranging from 3.45–3.57 GHz is depicted in [2]. A single element antenna with a ceramic DRA is proposed in [3], that provides multiband functions ranging from 3.8–4.5 GHz and 5.9–6.39 GHz. In [4], the authors proposed a two element MIMO antenna on tablets sized ground of frequency range from 1.71–2.69 GHz. Another configuration of the microstrip array for satellite communications is shown in [5], the article shows a 4 × 4 array provides a bandwidth ranging from 3.8–4.5 GHz. [6] shows a microstrip antenna with a T - shaped DGS radiating in the X - Band and having an overall size of (1.04 × 1.04 × 0.02) λ_o. A microstrip antenna having multiband characteristics in X – Band, provides a bandwidth of 270 and 440 MHz at 9.17 and 10.45 GHz, respectively [7]. A stacked configuration of microstrip antenna is proposed in [8] for multiband radiation covering both C and X bands. The proposed design has an overall size of (1.74 × 2.11 × 0.55) λ_o and gives a bandwidth of 0.596 GHz resonating at 8.56 GHz. All the above-cited articles show good radiation characteristics in the C and X – Band but at the cost of antenna size.

In this article the authors proposed a compact 2-element MIMO antenna for 5.55–11.03 GHz frequency band. This article has attempted to reduce the size of the antenna while showing a negligible effect on the radiation characteristics. Section 2 contain the design concept of proposed single and 2 element MIMO antenna with design parameters. In Sect. 3, the authors explain the results of the proposed MIMO antenna. Finally Sect. 4 conclude the paper.

2 Proposed Antenna Design

The geometry of the proposed design is shown in Fig. 1. The overall size of the antenna is (25 × 12 × 0.535) mm^3 and is printed on Rogers RT Duroid 5880, which has a relative permittivity of 2.2, 0.001 as the loss tangent and thickness of H_{sub}. Table 1 lists all the parametric values of the antenna. Each element in the double element MIMO consists of two circular arcs with an outer radius of R_1 and an inner

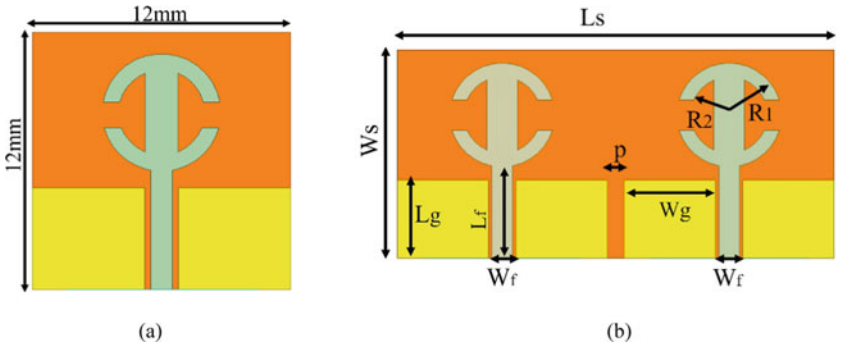

Fig. 1 Proposed design **a** single element **b** Proposed design

Table 1 Parametric values

Parameter	Parameter value (mm)	Parameter	Parameter value (mm)
L_S	25	W_S	12
Lg	5.2	Wg	4.5
Lf	5.25	Wf	1.2
R_1	3	R_2	2.2
H_{Sub}	0.5	p	1.0

radius of R_2. In each component, the circular arcs are connected by a rectangular microstrip. These radiating elements are separately excited by a simple CPW feed that acts as the ground for the proposed antenna.

3 Result and Discussion

Figure 2 depicts the simulated results of S_{11}, peak gain, peak directivity, and smith chart. These results were simulated on Ansys HFSS 19.1 EM simulator. Figure 2(a) depicts the S_{11} plot, which shows the proposed antenna radiates at 7.1 GHz and has a −10 dB bandwidth of 5.52 GHz ranging from 5.55–11.03 GHz with isolation more than 15 dB. Figure 2(a) depicts the impedance variation in the form of a smith chart, and it can be noticed we get perfect impedance matching at a single point, i.e., resonant frequency. The smith chart also shows that the loop lies within the VSWR = 2 circle, thus proving the obtained bandwidth (i.e., 5.55–11.03 GHz).

The envelope correlation coefficient (ECC) is the important parameter for MIMO diversity performance. ECC between two elements is calculated using scattering parameters using Eq. 1 [9]. Figure 3(a) shows the ECC of proposed MIMO antenna which is less than 0.02 over the operating frequency band. The peak gain of proposed

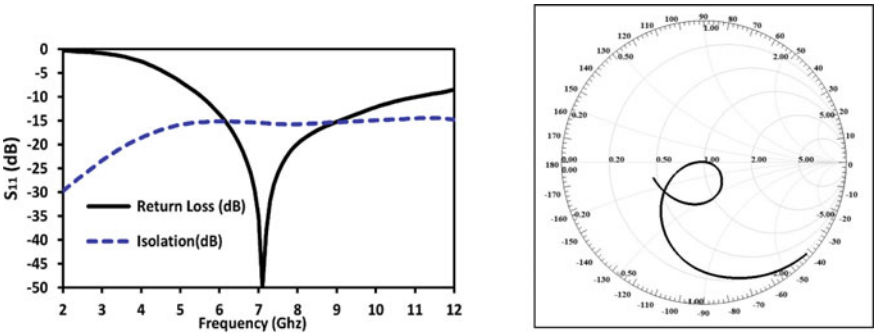

Fig. 2 Simulate **a** S – Parameter **b** Impedance variation plot (smith chart)

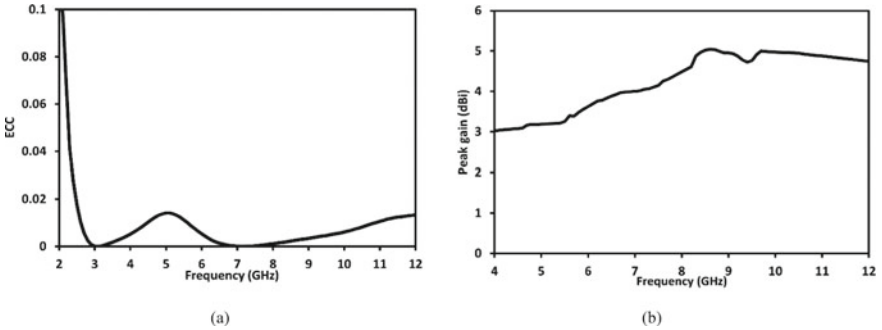

Fig. 3 **a** Envelope correlation coefficient (ECC) vs frequency **b** Peak gain (dBi)

Table 2 Comparison of proposed MIMO antenna with published work

Ref. no.	Size (mm^2)	Frequency (GHz)	Peak gain (dBi)	No. of elements	Isolation (dB)
[4]	75 × 75	4.96–5.50,	4	2	– -
[10]	20 × 30	2.60–11.20	4	4	> 20
[11]	22 × 36	3.0–11.0	5	2	> 15
[12]	25 × 40	3.39- 9.10	2.5	2	– -
This work	**25 × 12**	**5.55–11.03**	**5.1**	**2**	**> 15**

MIMO antenna is 5.1 as shown in Fig. 3(b).

$$\rho_e = \frac{|s_{11} * s_{12} + s_{21} * s_{22}|^2}{\left(1 - |s_{11}|^2 - |s_{21}|^2\right)\left(1 - |s_{22}|^2 - |s_{12}|^2\right)} \tag{1}$$

The comparison of the proposed antenna with the reported work is listed in Table 2. The comparison is made based on the overall size, gain, and bandwidth. The proposed MIMO antenna has compact size and better gain as compared to previously published paper.

4 Conclusion

The design of a two-element MIMO antenna for C and X - Band applications is proposed in this article. The design consists of circular arcs connected by simple microstrip elements that have been excited using a simple CPW feeding. This feeding technique and the unique design helped us achieve wideband characteristics and suitable impedance matching at the resonant frequency of 7.1 GHz with frequency

band from 5.55–11.03 GHz. The antenna is compact and provide an isolation of more than 15 dB overall the operating frequency band.

References

1. Luo S, Li Y, Xia Y, Zhang L (2019) A low mutual coupling antenna array with gain enhancement using metamaterial loading and neutralization line structure. Appl Comput Electromagn Soc J 34(3):411–418
2. Chen WS, Lin YC (2018) Design of 2 × 2 microstrip patch array antenna for 5G C-band access point applications. In: 2018 IEEE international workshop on electromagnetics: applications and student innovation competition (iWEM). IEEE, pp 1–2
3. Ram SK, Sourav R, Ujjal C (2018) A dual band microstrip antenna integrated with rectangular DRA for uplink and downlink C band communication. In: 2018 4th international conference on recent advances in information technology (RAIT), pp 1–4
4. Sharma SK, Wang A (2018) Two elements MIMO antenna for tablet size ground plane with reconfigurable lower bands and consistent high band radiating elements. In: 2018 IEEE international symposium on antennas and propagation & USNC/URSI national radio science meeting, pp 25–26
5. Mahatmanto, B., Pratiknyo A., and Catur A. (2020) High Gain 4× 4 Microstrip Rectangular Patch Array Antenna for C-Band Satellite Applications. In: 2020 FORTEI-International Conference on Electrical Engineering (FORTEI-ICEE),125–129.
6. Dwivedi AD, Manoj KG, Preeti SK, Deepika G, Saudan S (2017) C band, X band and Ku band corner arc microstrip patch antenna with T-slot on partial ground plane. In: 2017 international conference on innovations in control, communication and information systems (ICICCI), pp 1–4
7. Kiruthika R, Shanmuganantham T (2018) A canadian leaf shaped triple band patch antenna with DGS for X and C-Band applications. Int J Electron Commun Eng 114:502–508
8. Nejdi IH, Rhazi Y, Lafkih MA, Bri S (2018) Designing multiband multilayered microstrip antenna for UMTS, ISM, communication satellite, HiperLAN and C-Band. In: International symposium on advanced electrical and communication technologies (ISAECT), pp 1–8
9. Blanch S, Romeu J, Corbella I (2003) Exact representation of antenna system diversity performance from input parameter description. Electron Lett 39(9):705–707
10. Hatami N, Nourinia J, Ghobadi C, Majidzadeh M, Azarm B (2019) High inter-element isolation and WLAN filtering mechanism: a compact MIMO antenna scheme. AEU-Int J Electron Commun 109:43–54
11. Liu L, Cheung SW, Yuk TI (2015) Compact MIMO antenna for portable UWB applications with band-notched characteristic. IEEE Trans Antennas Propag 63(5):1917–1924
12. Zehra SW, Zahid M, Amin Y (2021) A compact 2 element MIMO antenna for UWB applications. In: 2021 IEEE Asia Pacific conference on wireless and mobile (APWiMob), pp 247–252

Multi Band Inter Connected C-Shaped Flexible Antenna for Mobile and Fixed Wireless Communication Systems

Jayshri Kulkarni, Chow-Yen-Desmond Sim, and Ajay Poddar

Abstract The Point to Point (PTP) and Point to Multi-point (PTM) radio services are offered to users in the form of fixed wireless services. These services are used in core and access networks including all equipment aspects as well as antenna parameters. The antenna is very essential part of any transmitter and receiver integrated in core and access systems. Therefore, this research article presents design and analysis of multi band inter connected C-shaped flexible antenna for 5 GHz Wireless Fidelity (Wi-Fi) mobile communication system and 8 GHz Fixed wireless communication system, functioning simultaneously. The proposed interconnected compact C-shaped flexible antenna is loaded with group of three small circles on the common branch of interconnected C-shape and another big circle at the center to obtain maximum transfer of signals from transmitter to receiver and vice versa. This complete structure is printed on Kapton Polyamide substrate having size of $15 \times 20 \times 0.2$ mm^3 and is excited using coplanar waveguide (CPW) feeding technique to achieve desired resonances at 5.4 and 8.6 GHz covering impedance bandwidth of 15.38% (5.10–5.95) GHz Wi-Fi mobile communication band and 23.11% (7.73–9.75) GHz fixed wireless communication band, respectively. Further investigation confirms flat gain of around 3 dBi, efficiency greater than 90% and omnidirectional radiation envelopes in both the desired operating bands. Moreover, in order to prove the flexibility of antenna and its effect on impedance bandwidth, gain and efficiency, a simulated experimentation of bending analysis along both X and Y axis is also carried out using CST MWS studio suit software.

J. Kulkarni (✉)
Department of Electronics and Telecommunication Engineering, Vishwakarma Institute of Information Technology, Pune, India
e-mail: jayashri.kulkarni@viit.ac.in

C.-Y.-D. Sim
Department of Electrical Engineering, Feng Chia University, Taichung, Taiwan
e-mail: cysim@fcu.edu.tw

A. Poddar
Synergy Microwave Corp, Paterson, NJ, USA
e-mail: akpoddar@synergymwave.com

M. Tiwari et al. (eds.), *Optical and Wireless Technologies*, Lecture Notes in Electrical Engineering 892, https://doi.org/10.1007/978-981-19-1645-8_34

Keywords Interconnected C-shaped antenna · 8 GHz fixed wireless system · Wi-Fi and CPW

1 Introduction

License free Wireless Access Systems (WACs) containing Radio Local Area Networks (RLANs) represent the main Broadband Wireless Access (BWA) technologies used for wireless internet access. However, the billions of communicating devices already in operation and the rapid growth is predicted to be continued for the foreseeable future. Antennas play a significant and supporting role in achieving Gigabit internet access and advanced wireless applications withing the limited frequency spectrum as users are adapted to. Apart from this, an antenna is an essential element in this communication system, and for confirming the device suitability, it should be flexible, compact and stretchable. Therefore, several non-flexible and flexible antennas functioning in various wireless bands are reported recently [1–7]. The antennas reported in [1–3] for various wireless applications like smartphone, laptop and wireless devices are application specific and based on use of type of substrate and offer the performance based on surrounding environment. However, these antennas are not flexible in nature. Recently, many flexible antennas are reported in the literature [4–7]. The antenna reported in [4] describes the design and performance analysis of conformal multiband antenna printed on Kapton Polyimide substrate using Inkjet printer technique for flexible wireless devices. The antenna reported in [5] mentions the design and fabrication of an ultra-thin flexible antenna using three flexible substrates for Internet of Things (IoT) applications. The reported antenna design operates in 2.7 and 5.8 GHz frequency bands for IoT applications. An UWB MIMO antennas are designed using Kapton polyamide substrate using inkjet printing technique. Three-dimensional (3D) paper-based 3 × 3 MIMO antenna operating in WLAN bands of 2.4 and 5 GHz is reported in [6].

Liquid Crystal Polymer (LCP) is another preferable flexible substrate reported by [7]. The reported compact triple band antenna designed using flexible LCP substrate to operate in WLAN 2.4/5.2/5.8 GHz Wireless Local Area Network (WLAN), 3.5/5.5 GHz Worldwide Interoperability for Microwave Access (WiMAX) and 5G bands. The antenna reported in [7] is the paper based flexible antenna and designed for wearable telemedicine applications. This reported antenna covers Industrial, Scientific and Medical (ISM) frequency band in the range of (2.33–2.35 GHz).

This research article presents multi band interconnected C-shaped CPW fed flexible antenna for 5 GHz Wi-Fi mobile communication system and 8 GHz Fixed wireless communication system, functioning simultaneously. The proposed antenna consists of two interconnected C-shaped radiators facing towards each other in order to minimize the capacitive coupling of two radiators. The radiators are printed on Kapton Polyimide flexible substrate of size 15 × 20 × 0.2 mm^3 and generates two resonances at 5.5 and 8.7 GHz conforming an impedance bandwidth of 13.11%

(5.13–5.85) GHz Wi-Fi band and 20.57% (7.85–9.65) GHz for fixed wireless communication band, respectively. Further, a bending analysis is also carried out in X and Y direction to validate the bending effect on impedance bandwidth.

The research article is structured as follows: Sect. 2 explains the design schematic layout and operating mechanism of proposed interconnected C-shaped flexible antenna, Sect. 3 gives insight on results and discussion followed by bending analysis in Sect. 4. Finally paper is concluded in Sect. 5.

2 Layout and Evolution Mechanism Interconnected C-Shaped Antenna

The compact designed footprint of interconnected C-shaped antenna is shown in Fig. 1 for mobile and fixed wireless communication system. The proposed interconnected C-shaped antenna consists of one C-shaped radiator, one inverted-C shaped radiator, and a CPW-fed ground plane. In this design, the top edge of the inverted C-shape is connected to the center of C-shaped radiator along with group of three small circles and one big circle. The small group of circles having radius of 0.85 mm is sandwiched in between the top strip of inverted-C and lower strip of C-shape radiator whereas the big circle of radius 1.5 mm is embedded between the lower strip of both the C and inverted C-shaped radiator. The proposed interconnected C-shaped antenna is engraved on Kapton polyamide substrate having a compact dimension of

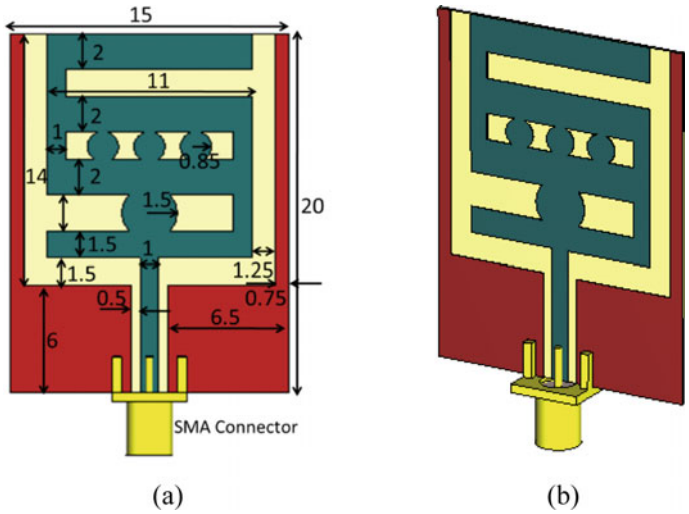

Fig. 1 Geometry and layout of proposed cactus shaped antenna (Dimensions in mm) **a** Front view **b** Perspective view

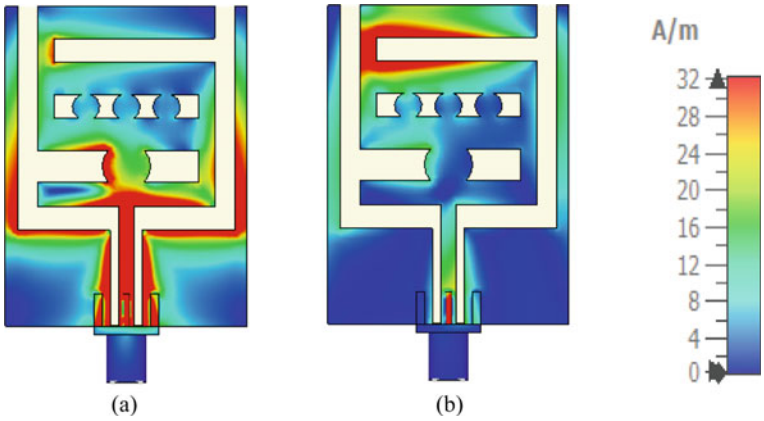

Fig. 2 Surface current distribution of proposed antenna **a** 5.4 GHz **b** 8.6 GHz

15 × 20 mm^2, thickness 0.2 mm, loss tangent 0.002 and dielectric permittivity of 3.45 and is fed using CPW-fed technique.

Further, to investigate more about working mechanism of proposed interconnected C-shaped flexible antenna, a surface current distribution (A/m) is discussed in Fig. 2. From Fig. 2a, it is visualized that maximum current is flowing in the lower part of interconnected C-shaped radiator which generates a resonance at 5.4 GHz with impedance bandwidth of 15.38% (5.10–5.95) GHz for Wi-Fi mobile communication band. Further, as visualized from Fig. 2b, maximum current is flowing through the top part of interconnected C-shaped structure which induces a resonance at 8.6 GHz with an impedance bandwidth of 23.11% (7.73–9.75) GHz for fixed wireless communication band.

3 Simulated Results and Analysis

The proposed interconnected C-shaped flexible antenna design is designed and analyzed using CST software. Figure 3 discussed the S-parameter of the proposed interconnected C-shaped flexible antenna. It is seen that antenna element induces multiple resonances at 5.4 and 8.6 GHz with simulated impedance bandwidth of 15.38% (5.10–5.95) GHz and 23.11% (7.73–9.75).

The two-dimensional (2D) field patterns of the proposed interconnected C-shaped flexible antenna at both the resonances of 5.4 and 8.6 GHz are illustrated in Fig. 4. Figure 4 depicts the co-polar and cross-polar radiation patterns in both E-plane and H-plane. It can be observed from the Fig. 4 that the co-polar radiation pattern in E-plane show omnidirectional characteristics with circular pattern passing maximum gain in all the direction whereas the cross-polar radiation pattern in H-plane is doughnut

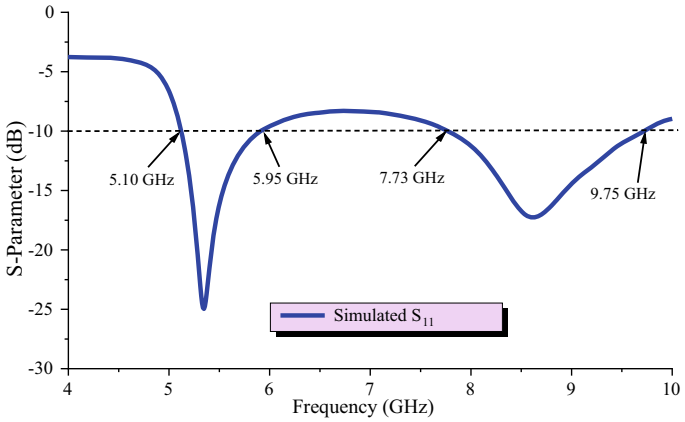

Fig. 3 S-Parameters of proposed interconnected C-shaped flexible antenna

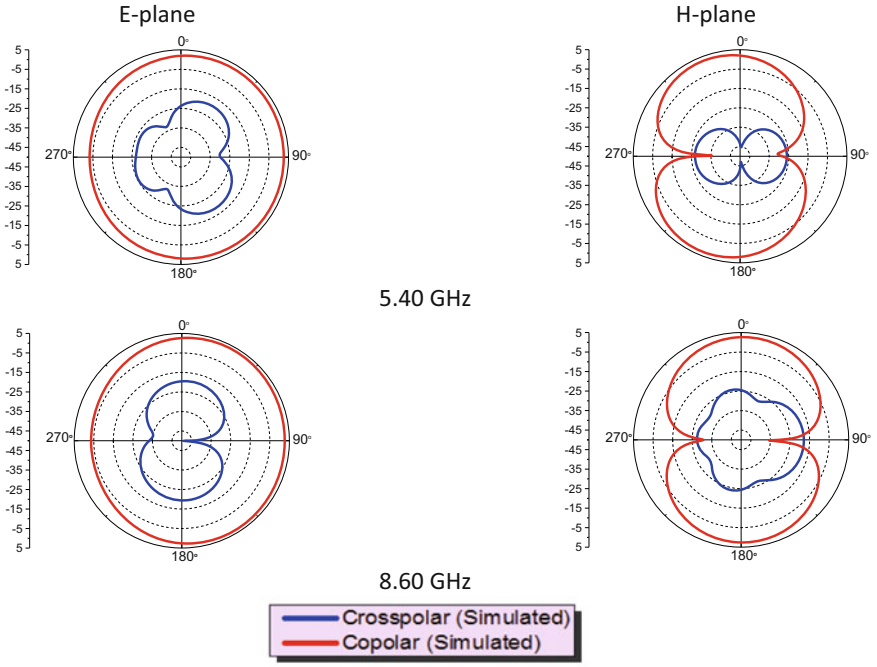

Fig. 4 2D Radiation pattern of proposed interconnected C-shaped flexible antenna

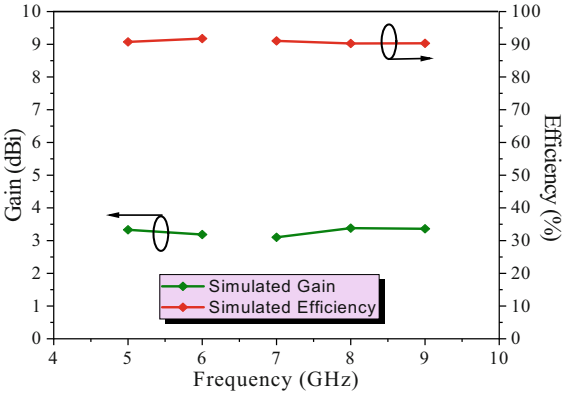

Fig. 5 Gain and Efficiency of proposed interconnected C-Shaped flexible antenna

shape, which are beneficial to be used in mobile and fixed wireless devices which are on same plane or at either side of each other.

The gain and efficiency of the proposed interconnected C-shaped antenna is illustrated in Fig. 5. The antenna shows stable gain of around 3 dB and radiation efficiency greater than 90% at both the operating bands.

4 Bending Analysis of Proposed Interconnected C-Shaped Flexible Antenna

A simulated experimentation of bending analysis is carried out in order to validate the bending performance of proposed interconnected C-shaped flexible antenna on 10 dB impedance bandwidth, gain and efficiency as shown in Fig. 6. In order to integrate the antenna in restricted space where there is restriction on height of wireless device, the proposed antenna is bended in X-direction as shown in Fig. 6a. The associated S_{11}(dB) curves are compared as shown in Fig. 6b. It is apparent that the S_{11} (dB) curves (with bending and without bending) are matching with each other with minimal deviation. However, the S_{11} (dB) curve with bending still conform the bandwidth requirement of desired operating bands. Also, it is observed that bending the antenna along X-axis have minimum effect on gain and efficiency of the proposed interconnected C-shape flexible antenna as shown from Fig. 6c.

Further, in order to check the flexibility in Y-direction, the proposed interconnected C-shaped flexible antenna is bended as shown in Fig. 7a and associated S_{11}(dB), gain and efficiency curve is shown in Fig. 7(b–c). It is validated that the S_{11} (dB) curve with bending conforms that there is negligible effect on impedance bandwidth. This validates that the proposed flexible antenna can be integrated in fixed and mobile wireless devices where space is limited in order to integrate a greater number of electronic components. From Fig. 7c, it is evident that the gain and efficiency of

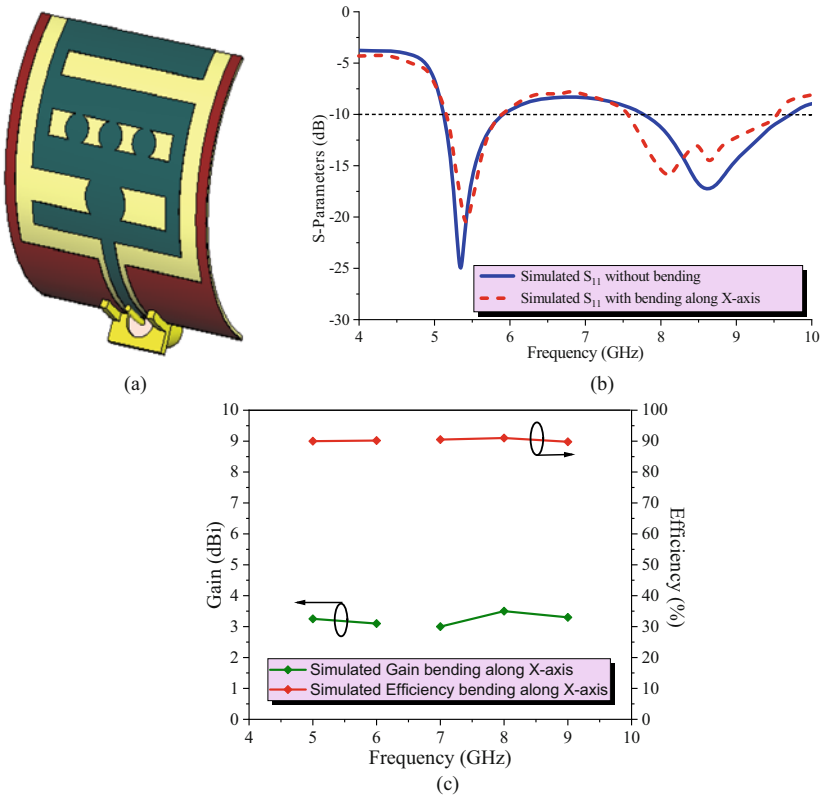

Fig. 6 Bending Analysis along X-axis antenna **a** Geometry **b** S_{11} **c** Gain and Efficiency

the proposed interconnected C-shaped flexible antenna remains unaffected when the antenna is bent along Y-axis.

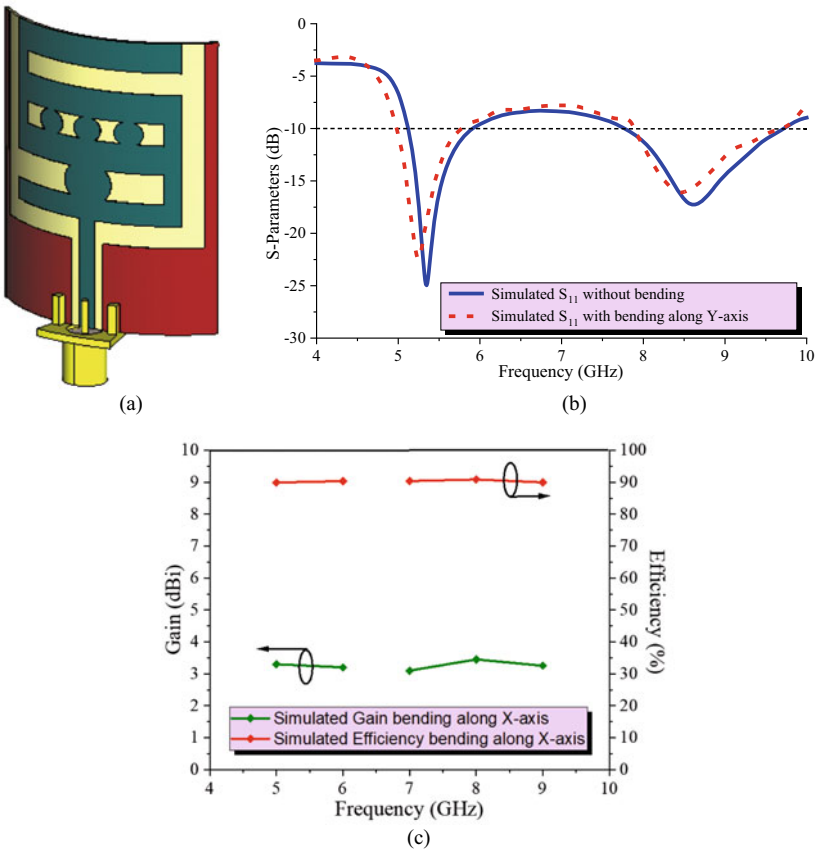

Fig. 7 Bending Analysis along Y-axis antenna **a** Geometry **b** S_{11} **c** Gain and Efficiency

5 Conclusion

An interconnected C- shaped flexible antenna for mobile and fixed wireless services is designed and analysed successfully. The proposed flexible antenna operates with impedance bandwidth of 15.38% (5.10–5.95) GHz and 23.11% (7.73–9.75) for Wi-Fi mobile wireless and fixed wireless communication systems. Furthermore, the radiation performance including flat gain 3 dBi and efficiency >90% is also achieved. The bending performance shows that the proposed antenna is flexible in nature and can be a good applicant of wireless and fixed devices where there is restricted space for antenna.

References

1. KulkarniJS (2019) A novel, compact and ultra-thin monopole antenna for wireless applications in the next-generation laptop computer. In: 2019 IEEE Indian conference on antennas and propogation (InCAP), pp 1-4. https://doi.org/10.1109/InCAP47789.2019.9134586
2. Kulkarni J, Dhabre S, Kulkarni S, Sim CYD, Gangwar RK, Cengiz K (2021) Six-port symmetrical CPW-fed MIMO antenna for futuristic smartphone devices,. In: 2021 6th international conference for convergence in technology (I2CT), pp 1–5. https://doi.org/10.1109/I2CT51068.2021.9418180
3. Kulkarni JS, Sim CYD (2020) Low-profile, multiband & wideband 'c-shaped' monopole antenna for 5G and WLAN applications. In: 2020 international conference on radar, antenna, microwave, electronics, and telecommunications (ICRAMET), pp 366–371. https://doi.org/10.1109/ICRAMET51080.2020.9298569
4. Ahmed S, Tahir FA, Shamim A, Cheema HM (2015) A compact kapton-based inkjet-printed multiband antenna for flexible wireless devices. IEEE Antennas Wirel Propag Lett 14:1802–1805. https://doi.org/10.1109/LAWP.2015.2424681
5. de Cos Gómez ME, Álvarez HF, González CG, Valcarce BP, Olenick J, Las-Heras F (2019) Ultra-thin compact flexible antenna for IoT applications. In: 2019 13th European conference on antennas and propagation (EuCAP), pp 1–4
6. Du C, Wang X, Jin G, Zhong S (2021) A compact tri-band flexible mimo antenna based on liquid crystal polymer for wearable applications. Prog Electromagn Res 102:217–232
7. Ullah MA, Islam MT, Alam T, Ashraf FB (2018) Paper-based flexible antenna for wearable telemedicine applications at 2.4 GHz ISM band. Sensors (Basel) 18(12):4214. https://doi.org/10.3390/s18124214

A Broadband Microstrip MIMO Antenna for 5G mm-Wave Applications

Shreyas Choudhary, Gaurav Jha, Ashok Kumar, and Arjun Kumar

Abstract In this paper, the authors present a 28 GHz broadband microstrip patch MIMO antenna for a 5G wireless communication system. The proposed antenna array has a central operating frequency of 28.01 GHz. The proposed antenna array is simulated on Rogers RT/Duroid5880 substrate with dielectric permittivity of 2.2. The design of the antenna array, the dimension, parameters, are simulated and optimized by using CST Studio Suite. The antenna array has a compact and robust structure with dimensions of 0.62×5.40 λo. From the simulation result, we observed that the studied antenna array has a return loss of −22.10 dB and an impedance bandwidth of 3.94 GHz. The proposed rectangular broadband microstrip patch MIMO antenna has achieved significantly improve radiation performance in terms of bandwidth and return loss.

Keywords 5G · Microstrip antenna · Mm-Wave · 5G wireless system · Array · MIMO

1 Introduction

The growing demand for more advanced wireless telecommunication systems leads to a need for advancement in the development of new technologies. The 4G system which is currently in use leads to many developments in the field of telecommunication, mobile system, IoT application, and development of many advanced systems, and it is believed that the fifth generation (5G) network system will be able to incredibly advance and enhance the capacity of current and upcoming wireless technologies by taking advantage of using a millimeter-wave (mm-wave) frequency band. In today's time, wireless technology is currently one of the most used areas in the communication system, as the whole mobile network, IoT systems, wireless internet,

S. Choudhary (✉) · G. Jha
ECE Department, Shri Mata Vaishno Devi University, Jammu and Kashmir, India
e-mail: shreyas1308@gmail.com

A. Kumar · A. Kumar
ECE Department, Bennett University, Greater Noida, India

M. Tiwari et al. (eds.), *Optical and Wireless Technologies*, Lecture Notes in Electrical Engineering 892, https://doi.org/10.1007/978-981-19-1645-8_35

and other embedded systems are dependent on it. To manage and handle this huge traffic rate, scarcity of bandwidth and the need for a good quality of millimeter of wave frequency leads to the development of the 5G technology system. The primary goal of 5G technology is to implement a high-frequency band and wide signal bandwidth to increase the transmission bit rates, providing better coverage with low power consumption at low cost. According to the 2015 radio world radiocommunication conference, it is decided to allow a frequency range of 24 to 86 GHz for future communication systems with millimeter waves [1, 2]. The antenna required for the 5G technology is needed to be broadband to support high data rates, so it can be used for a variety of applications, and also, they should have high gain. Microstrip patch antennas are mostly used in communication due to their low profile, low cost, lightweight and easy integration with devices. The main drawbacks of microstrip antenna are losses due to dielectric and surface waves due to which the bandwidth of microstrip antenna is narrow and gain is low. In modern communication, the antenna array plays an important role to improve the radiation characteristics of the antenna [3]. In [4], the authors proposed an array antenna to improve the radiation characteristics of the device with unequal arms. A sector disk radiating patch with a circular shaped slot is designed to achieve better antenna performance [5]. The authors proposed four elements patch array antennas with series feed and corporate series feed to operate from 25.15–30.87 GHz [6]. Using T-shaped monopole antenna with inverted L-grounded stub and asymmetric co-planar waveguide fed, a wide band 25.60–33.90 GHz and 7.15 dBi peak gain are achieved over the operating frequency band [7].

In this paper, the authors proposed eight-element patch MIMO antenna for 5G mm-Wave communication. Section 2 contains the design concept of the proposed antenna. In Sect. 3, the authors explain the result analysis of the MIMO antenna. Finally, Sect. 4, concludes the paper.

2 Proposed Antenna Design

Take into consideration the design of any antenna, the dimension plays an important role in the development and performance of the same. There are various shapes and structures available in the market but taking into account the best impedance matching and broader shape. This also adds into account the fact that it can be fitted very easily inside any structure and system and can radiate at its best., Rogers RT/Duroid5880 was the best-suited material for the same. It has a dielectric constant of 2.2 and tangent loss of 0.0009. The thickness of the substrate is 1.56 mm. A 50Ω inset feedline is used to excite the antenna and better impedance matching. Fig.1 illustrates the schematic design of a single microstrip patch antenna. The CST Microwave Studio is used for the simulation and optimization of the proposed antenna. The repetitive simulation and analysis or direct comparison can tell us a lot of things like gain, return loss, VSWR, and a lot more. The design dimensions of the proposed are depicted in Table 1.

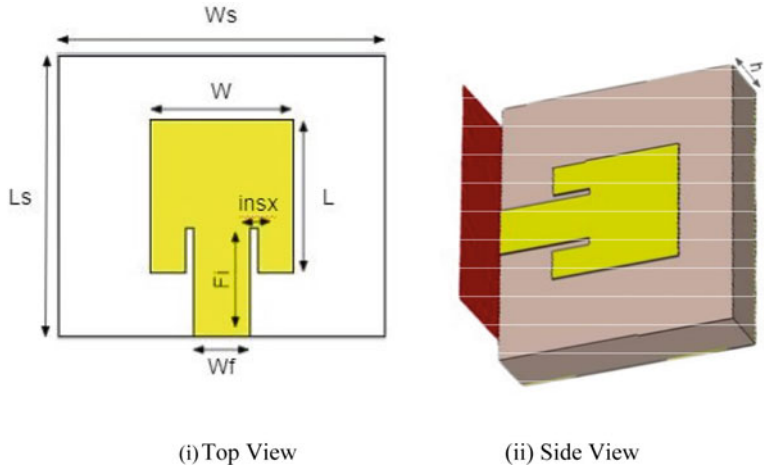

Fig. 1 The geometry of single rectangular MSPA

Table 1 Dimension of single MSPA

Parameters	Dimensions (mm)	Parameters	Dimensions (mm)
Ls	6.3	H	1.56
Ws	7.2	Wf	1.25
L	3.4	Fi	1.35
W	3.2	Insx	1.50

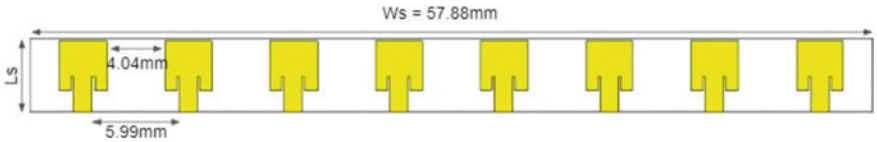

Fig. 2 The geometry of the proposed MIMO antenna (8 × 1)

To improve the radiation characteristics of a microstrip patch antenna, an eight-element array is designed and simulated. Figure 2 shows the schematic of an eight-element patch MIMO antenna with a dimension of 6.3 × 57.88 mm.

3 Results and Discussion

The simulated return loss plot and voltage standing ratio (VSWR) of a single patch antenna are shown in Fig. 3. The single microstrip patch antenna radiates at 28 GHz with an impedance bandwidth of 3GHz from 26.72–29.72 GHz. The

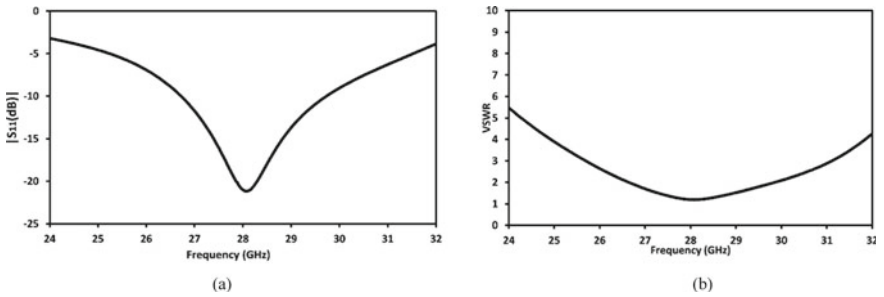

Fig. 3 Single patch antenna **a** S11 (dB) **b** VSWR

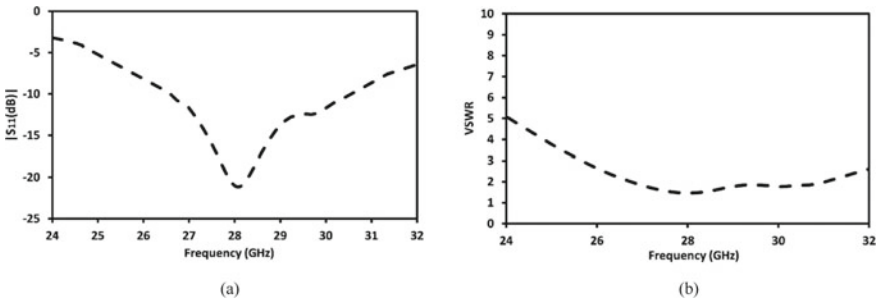

Fig. 4 Patch antenna array **a** S11 (dB) **b** VSWR

radiation characteristics of MSPA are improved by using the array concept. By using eight-element antenna array impedance bandwidths of 3.94 GHz from 26.60–30.54 GHz is achieved. Figure 4 illustrates the return loss graph and VRWR plot of the eight-element MIMO antenna.

Another important factor or the result is the far field result or the 3D antenna radiation pattern. It is the far-field plot of an antenna described in terms of spatial coordinates. It is specified using azimuth and elevation angles. Particularly, the plot shows the amount of radiated power from an antenna per unit solid angle. The gain plot is shown below in Fig. 5 and there is a comparison of gain of single element and array.

The comparison of the proposed antenna array with the reported work is listed in Table 2.

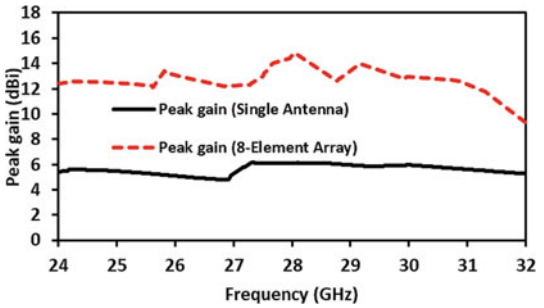

Fig. 5 Simulated peak gain (single and eight element antenna)

Table 2 Comparison of the proposed antenna with published work

Ref	Technique used/antenna type	Impedance B.W. (GHz)	Peak gain (dBi)
[6]	Four element series feed	25.15–30.87, 5.72	9.50
[8]	Phase antenna array	27.0–28.40, 1.40	8.64
[9]	Series feed phase 3 × 3 array	27.30–29.0, 1.70	14.9
[10]	Series feed array	27.20–29.00,1.70	18.0
This work	**Eight element antenna array**	**26.60–30.54, 3.94**	**14.81**

4 Conclusion

In this paper, we proposed a design of 28 GHz broadband rectangular broadband microstrip patch antenna MIMO for 5G wireless applications. From our simulation and optimization, it is highlighted that the proposed antenna array resonates at 28.01 GHz having an impedance bandwidth of 3.94 GHz from 26.60–30.54 GHz. As compared to similar works, our proposed design has achieved approximately higher performance in 3 out of 4 parameters. It will result in high gain and it is fairly simple to design and it also has a gain of 14.81 dB, which is very good for practical application and can be easily tested for implementation of its 5G technology.

References

1. Liu Y et al (2017) Non-orthogonal multiple access for 5G and beyond. Proc IEEE 105(12):2347–2381
2. Rappaport TS, Sun S, Mayzus R, Zhao H, Azar Y, Wang K, Wong GN, Schulz JK, Samimi M, Gutierrez F (2013) Millimeter wave mobile communications for 5G cellular: it will work! IEEE access 1:335–349
3. Garg R, Bhartia P, Bahl IJ, Ittipiboon A (2001) Microstrip antenna design handbook. Artech house, Norwood
4. Jam S, Malekpoor H (2016) Analysis on wideband patch arrays using unequal arms with equivalent circuit model in X-band. IEEE Antennas Wirel Propag Lett 15:1861–1864

5. Haraz OM, Ali MMM, Alshebeili S, Sebak AR (2015) Design of a 28/38 GHz dual-band printed slot antenna for the future 5G mobile communication Networks. In: 2015 IEEE international symposium on antennas and propagation & USNC/ursi national radio science meeting, pp 1532–1533
6. Maharjan J, Choi DY (2020) Four-element microstrip patch array antenna with corporate-series feed network for 5G communication. Int J Antennas Propagat
7. Kumar A, Kumar A, Kumar A (2021) A broadband circularly polarized monopole antenna for millimeter-wave short range 5G wireless communication. Int J RF Microwave Comput Aided Eng 31(2):e22518
8. Yu LC, Kamarudin MR (2016) Investigation of patch phased array antenna orientation at 28 GHz for 5G applications. Procedia Comput Sci 86:47–50
9. Khalily M, Tafazolli R, Rahman TA, Kamarudin MR (2015) Design of phased arrays of series-fed patch antennas with a reduced number of the controllers for 28-GHz mm-wave applications. IEEE Antennas Wirel Propag Lett 15:1305–1308
10. Varum T, Ramos A, Matos JN (2018) Planar microstrip series-fed array for 5G applications with beamforming capabilities. In: 2018 IEEE MTT-S international microwave workshop series on 5G hardware and system technologies (IMWS-5G), pp 1–3

CBCPW-Fed ADFD Shape On-Body Antenna for ISM Band and Sub-6 GHz 5G Applications

T. J. Sweety, Rithika, T. R. Arun, K. Sajith, Jobin Jose, and K. R. Reeha

Abstract A novel conductor backed coplanar waveguide (CBCPW) fed arrow-directed folded dipole (ADFD) on-body antenna designed for healthcare applications. The antenna can be designed by Teflon (PTFE) substrate. This material has excellent dielectric characteristics like ($\varepsilon r = 2.1$, $\tan\delta = 0.0015$) and low cost. The antenna resonates at industrial, medical, service band 2.4–2.5 GHz and fifth-generation medical service band 3.3–3.6 GHz. The minimum value reflection coefficients are −43 dB at 2.45 GHz, −21 dB at 3.4 GHz are obtained. The simulated parameter results of the designed antenna are well suitable for ISM and 5G band-based healthcare applications.

Keywords Coplanar Wave Guide (CPW) · ADFD shape · Gain · Radiation pattern · ISM · 5G medical applications

1 Introduction

In recent research, the bio-medical antenna design and developments are essential for high-speed wireless data transfer. Now the conditions of wireless communications are emerging from 4 to 5G. 5G has many advantages, high speed, less latency, etc. [1]. Recently the people are suffered as a covid 19, heart attack, cardiovascular diseases, and other various diseases. Due to the covid-19 virus, the heart attack rate increased day by day in all over the world [2, 3]. The advanced microwave and MEMS-based medical equipment are capable of observing the nano-size virus. The CPW-fed medical antennas have an essential element for continuously patient healthcare (example ECG signal) monitor by 24 h [4].

Medical communication is categorized the implantable or in-body, on-body, and off-body communication [5]. The CPW fed ADFD antenna pertinent for ISM band and 5G medical band application because its geometry, resonated frequencies, and other performance parameters are well suitable concerned with existing literature

T. J. Sweety (✉) · Rithika · T. R. Arun · K. Sajith · J. Jose · K. R. Reeha
Department of ECE, Goverment Engineering College Wayanad, Kerala 670644, India
e-mail: sweetytjothish@gmail.com

M. Tiwari et al. (eds.), *Optical and Wireless Technologies*, Lecture Notes in Electrical Engineering 892, https://doi.org/10.1007/978-981-19-1645-8_36

[5, 6]. The volume of the designed CPW-fed on body ADFD antenna is 20 × 20 × 1.6 mm^3. Jilani et al. [7] introduced the CPW fed antenna for mm-wave frequency band wearable application. The antenna resonated in the frequency range of 24 GHz to 32 GHz and was constructed by LCP polymer substrate. H Sun et al. [8] introduced a pattern reconfigurable antenna for on-body and off-body applications. The antenna was fabricated on Teflon substrate and resonated at 2.45 GHz.

This paper organizes into four parts, the part 1 given the introduction about ISM, 5GMSB band and existing literature for the CPW fed on-body antennas. Part 2 discussed design methodology and internal aspects of the ADFD antenna. In part 3 shown simulation results and discussions of the ADFD antenna. Part 4 the conclusion of the designed antenna for ISM bands and 5G bands based medical applications.

2 ADFD Antenna Design

A CPW-fed antenna is a collective structure of radiating patch, two grounds, and one central strip be positioned the same plane on the same substrate. The layers of skin, fat, muscles layers are added on the second step. The 3D view of CPW fed ADFD on body antenna is shown in Fig. 1. The top view of the ADFD antenna is shown in Fig. 2. The conductor-backed or grounded coplanar arrangement was used as a feed.

The dimensions of CPW fed on body antenna and its parametric information is shown in Table 1. The length 'L' and width 'W' of the antenna is 20 × 20 mm. The width of the CPW ground is 9.2 mm and height is 7 mm, and strip dimension is 10 mm. The CPW-fed on body antenna design through a time-domain solver; the entire dimensions are in mm-scale. The thickness of the antenna is 1.6 mm. The

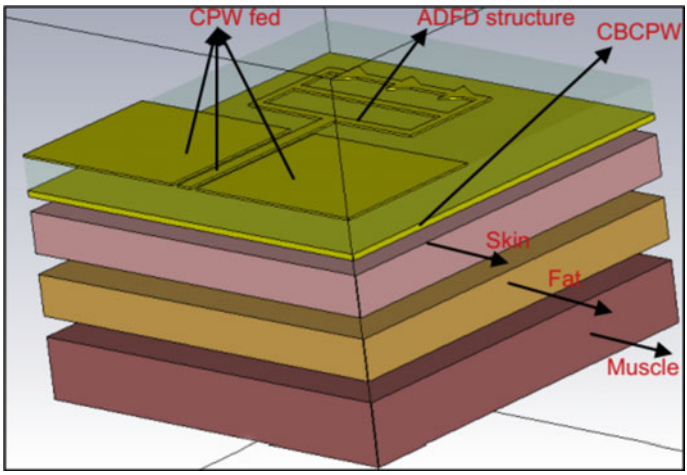

Fig. 1 3D view of CPW fed ADFD on-body antenna

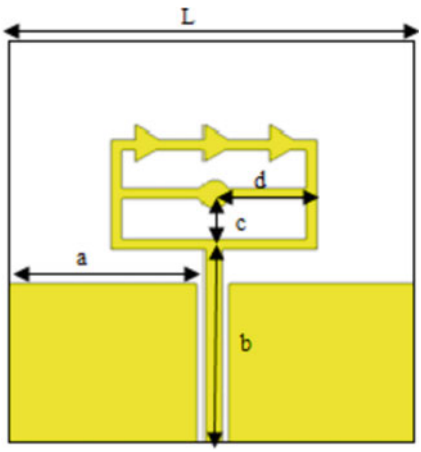

Fig. 2 Front view and dimensions of ADFD antenna

Table 1 Dimension of ADFD antenna

Dimension	Value (mm)	Dimension	Value (mm)
a	9.2	d	5.5
b	10	L	20
c	4.1	W	20

antenna used Teflon-substrate. Teflon has high mechanical strength, biocompatible, has a low dielectric constant, and low-cost. The dielectric constant values of each bio-layer are mentioned in reference [10].

3 Results and Discussion

In this section, simulated results such as VSWR plot, return loss plot, 3D radiation plots, and polar (2D) plots of both magnetic and electric fields are discussed at each resonating frequency of the ADFD CPW fed on the body antenna is given below. The Table 2 mentioned the performance comparisons of referred antenna and proposed ADFD antenna.

3.1 Reflection Coefficients and VSWR

The return loss values for CPW fed on body ADFD antenna have 43 dB at 2.45 GHz for skin layer, 37 dB at 2.49 GHz for skin and fat layer, 30 dB at 2.48 GHz for skin, fat, and muscle layer, 18 dB at 3.4 GHz for skin, 17 dB at 3.4 GHz for skin and fat,

Table 2 Performance comparisons of reference and proposed antenna

Reference	Volume (mm^3)	Gain (dB)	Bandwidth (MHz)
[9] S Fernandez, et al.	1524	−16	12
[10] T Karacolak, et al.	1265	−25	142
[11] C M Lee, et al.	790	−27	120
ADFD ant., f = 2.45 GHz	640	2.4	102
ADFD ant., f = 3.4 GHz	640	4.2	133

21 dB at 3.4 GHz for skin, fat, and muscle layer, without tissue layer the value of RC of 44 dB at 2.45 GHz and −23 dB at 3.5 GHz as shown in Fig. 3.

The bandwidth of the ADFD antenna is calculated from the return loss plot or VSWR plot [6]. Figure 4 indicated the VSWR values of ADFD antenna:1.03 at 2.45 GHz for skin, 1.2 at 2.48 GHz skin and fat, 1.2 at 2.48 GHz for muscle, 1.3 at 3.4 GHz for skin, 1.4 at 3.4 GHz for fat, and 1.12 at 3.4 GHz for muscle layer, for free space the VSWR values at 1.001 at 2.45 GHz and 1.32 at 3.5 GHz, as shown in Fig. 4..

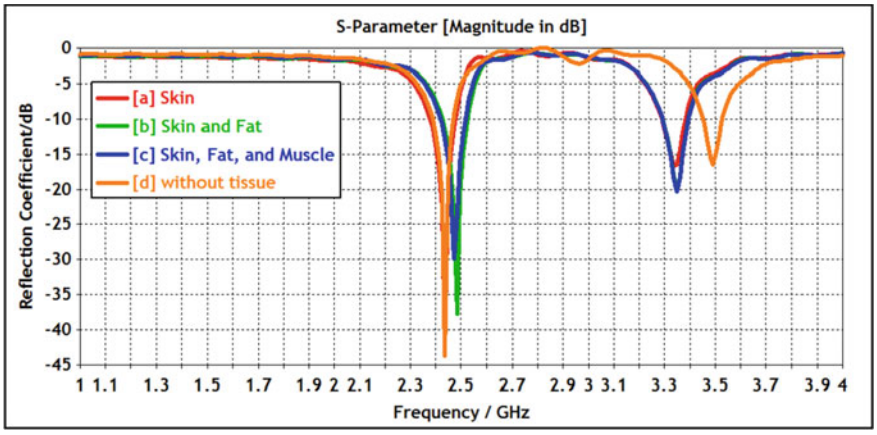

Fig. 3 Reflection coefficient plot of ADFD antenna

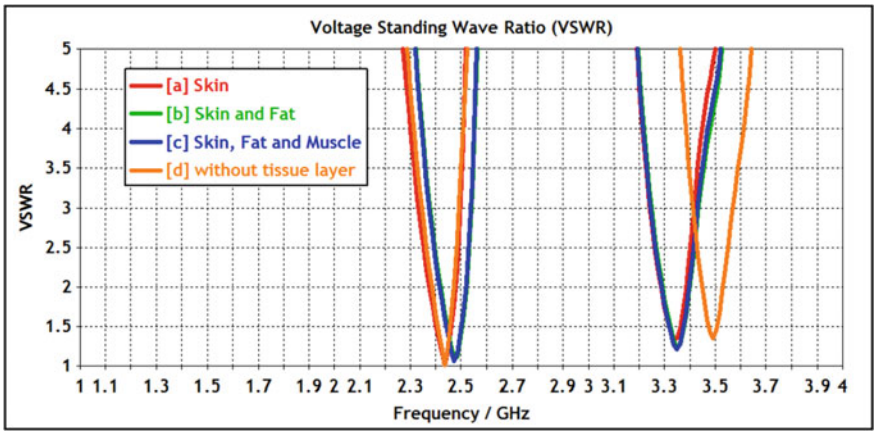

Fig. 4 VSWR plot of CPW fed ADFD antenna

3.2 Gain and E–H Field Pattern of ADFD Antenna

A radiation pattern is a 3D plot of the field strength of electromagnetic waves at a far-field distance from an antenna. Figure 5 show the gain plot of CPW fed on body antenna at various resonating frequencies. The simulated antenna gain value of 2.4 dBi at 2.45 GHz, and 4.2 dBi at 3.4 GHz, are observed.

Figure 6 shows the combined plot of both E and H field patterns at respective resonating frequencies of 2.45 and 3.4 GHz. E field pattern looks a figure of eight, and H field looks a circular shape. E-field (red color) pattern indicated the directional characteristics of CPW fed on body antenna and H-field (blue-color) the non-directional characteristics of CPW-fed on body antenna [5]. The radiation efficiency of proposed antenna is 63 percentage.

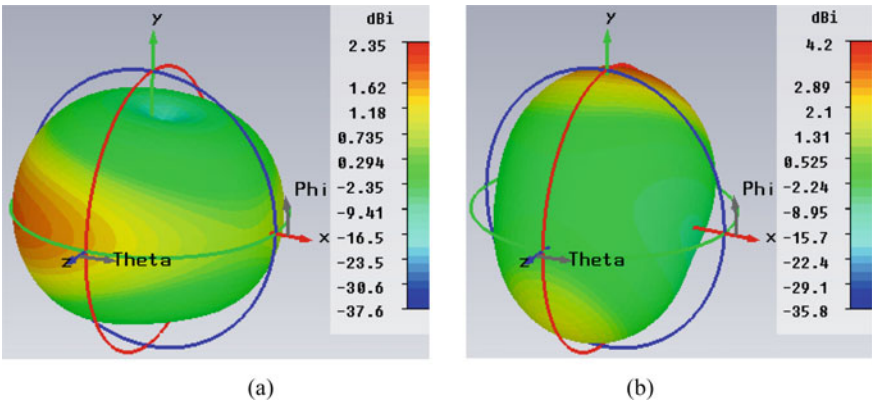

Fig. 5 Gain plot of ADFD antenna **a** at 2.45 GHz **b** at 3.4 GHz

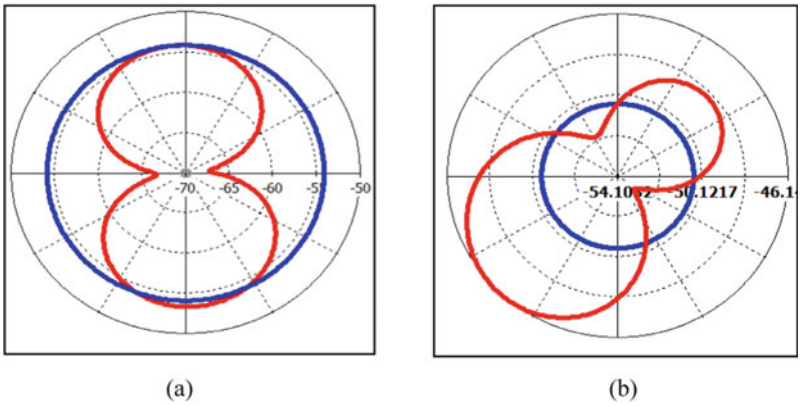

Fig. 6 E & H field plot of ADFD antenna **a** at 2.45 GHz **b** at 3.4 GHz

4 Conclusion

The CPW fed ADFD shaped antenna was designed and resonated at 2.45 and 3.4 GHz. The antenna size is 20 × 20 × 1.6 mm. The antenna resonates at 2.45 and 3.4 GHz frequency bands. The minimum value of reflection coefficient is −44 dB and VSWR value is 1.001 at 2.45 GHz is observed. The designed ADFD shape antenna is well suitable for an ISM and 5G-based healthcare applications.

References

1. Sajith K, Shanmuganantham T (2020) Design and analysis of metamaterial loaded microstrip slotted patch antenna for wireless applications. In: Lecture notes in electrical engineering (LNEE) series, vol 656. Springer Nature, pp 295-307
2. Sajith K, Shanmuganantham T (2020) CB-CPW fed SRR loaded miniaturized U-slot planar antenna for ECG monitoring. In: Lecture notes in electrical engineering (LNEE) series, vol. 656. Springer Nature, pp 11–20
3. Sajith K, Shanmuganantham T (2020) CB-ACPW fed SRR loaded electrically small antenna for ECG monitoring. In: Lecture notes in electrical engineering (LNEE) series, vol 672. Springer Nature, pp 767–772
4. Sajith K, Jobin J, Reeha KR, Kumar KB (2021) Design of compact CBCPW fed monopole antenna ECG monitoring applications. J Emerg Technol Innov Res 6:13–18
5. Sajith K, Shanmuganantham T (2019) CB-CPW fed SRR Loaded loop antenna for on-body ECG monitoring applications. J Comput Theor Nanosci 672:767–772
6. Sajith K, Shanmuganantham T (2018) Dual-band CB-CPW fed on body antenna for wearable WBAN application. Int J Eng Technol 7:1014–1017
7. Jilani SF, Greinke B (2016) Flexible millimeter-wave frequency reconfigurable antenna for wearable applications in 5G networks. In: 2016 URSI international symposium on electromagnetic theory (EMTS)
8. Sun H, Hu Y (2020) Design of pattern reconfigurable wearable antennas for body centric communications. IEEE Antennas Wirel Propagat 19:1385–1389

9. Fernandez S, Quvendo T (2010) Dual band microstrip patch antenna based on short circuital ring and spiral resonator for implantable medical device. IEEE Trans Microw Antenna 4:1048–1055
10. Karacolak T, Hood C (2008) Design of dual band implantable antenna and development of skin mimicking gels for continuous glucose monitoring. IEEE Trans Microwave Theory Techn 6:1001–1008
11. Lee CM, Luo CH (2009) Band width enhancement of planar inverted F antenna for implantable biotelemetry. Microw Opt Technol Lett 3:749

Energy Optimization in Wireless Sensor Networks Based on Firefly Optimization Technique and Hybrid Eagle with Firefly Optimization Technique

Rupa Sinha and Rekha Mehra

Abstract Wireless sensor networks (WSNs) consist of a number of sensor nodes working together for gathering and retransmitting data or information. WSNs have become increasingly popular due to their wide range of applications. They are typically used for remote environment monitoring in areas where supplying electrical power is difficult. The devices are powered by batteries and by alternative energy sources. Localization is used in WSNs to find the current location of the sensor nodes. Installation of GPS on each sensor node is expensive, further, manually configuring location details on each sensor node is not possible in dense WSNs. To make the deployment of WSNs economical, localization techniques are used. With the help of localization techniques, sensor nodes identify their location based on the information provided by an anchor node or beacon node. As the battery energy is limited for the sensor nodes, the different optimization techniques are required for energy optimization and localization. In this proposed work, the firefly optimization technique and the Hybrid Eagle with firefly Optimization technique for energy optimization with RSSI (Received Signal Strength Indication) positioning method is applied to complete the cluster and cluster head selection to optimize energy and power consumption and to increase network life cycle in WSN power consumption. The performance of both algorithms and parameters is executed in the MAT-LAB simulation platform.

Keywords WSN · Localization · Optimization · Firefly and Eagle · RSSI · Sensor node

1 Introduction

The wireless sensor network is one of the categories of self-organizing networks. The sensor network is composed of nodes. Here, the nodes have a specific name, namely "sensors" because these nodes are equipped with smart sensors [1]. The sensor node

R. Sinha (✉) · R. Mehra
Department of ECE, Government Engineering College Ajmer, Ajmer, Rajasthan, India
e-mail: rupasinha28jun@gmail.com

M. Tiwari et al. (eds.), *Optical and Wireless Technologies*, Lecture Notes in Electrical Engineering 892, https://doi.org/10.1007/978-981-19-1645-8_37

consists of a sensor, an integrated processor, a small storage device, and a wireless transceiver, all of which depend on a connected battery to function [2].

Sensors convert the recorded characteristics (such as temperature, vibration, and pressure) into a data format that the user can recognize.

Localization refers to the estimated position of each sensor node within the network [3]. The performance of WSNs is highly dependent on localization. In order to optimize localization various optimization techniques are used. Many biologically-inspired algorithms have been used for optimization of localization. These algorithms work on the principle of 'survival of the fittest'. Most popular bio-inspired algorithms are genetic algorithm, particle swarm optimization (PSO), and ant colony optimization [4]. One of the most promising recent algorithms is Firefly Algorithm (FA) proposed by Yang [5]. The Firefly algorithm help to solve multi-objective optimization problems. Data transfer and delayed route discovery are the main disadvantages of this technique. Due to this, the original FA needs to be modified or hybridized to solve diverse problems [6].

In the proposed work, the results of Firefly optimization are compared with results of Hybrid Eagle with firefly algorithm for energy optimization with Received Signal Strength Indication (RSSI) positioning method.

2 Related Work

Firefly algorithm (FA) was proposed by Yang in 2008 [5]. This algorithm mimics the way a firefly is attracted to a beacon. Fireflies have two distinctive characteristics, namely the method of mating and the hunt. Firefly use bioluminescence for producing light. The brightness of light is affected by distance between the source and observer. Firefly are attracted to brighter light. In [6] the author has reviewed various firefly algorithms. In [7] routing in the WSN, the routing algorithm uses residual energy, node distance, and energy as its statistical function to determine the path from Cluster Head (CH) to Base Station (BS). Compared to existing algorithms, this algorithm has better performance and is very useful in the Cluster Head (CH) range. In [8] compared with PSO, the firefly algorithm is applied, and as the number of hops amplifies, physical activity also decreases. It is very useful for moving in the WSN. It can save node power and add the remaining energy at a reasonable cost. In [9], and energy-efficient storage algorithm using Ant Colony optimization (ACO) and Firefly algorithms is proposed. The performance of the two algorithms is compared, and the results show that FA's efficiency is better than that of ACO in the short run. However, with increase in distance, it is observed that ACO is faster and more efficient.

Range based optimization algorithms have a drawback that they require distance (or angle) between the nodes for estimating the positions of the nodes. To overcome this limitation, in [10], another algorithm is proposed that introduces a particular mobile sink node called a mobile data transmitter (MDT), which collects data from all sensor nodes by visiting each sensor node and then forwards them to the BS, then implement the Firefly algorithm to simulate the technique. Compared to

ACO [11], this method can minimize the course length. The RSSI [12] method provides lower positioning accuracy at a lower cost. With additional hardware, the row-based approach can provide greater positioning accuracy. Although the distance-based method provides fine-grained accuracy, the use of the distance-based method will not be desirable for cost reasons.

3 Proposed System

The main aim of this proposed network model is to maximize the lifespan of wireless sensor networks. The presented techniques are based on the energy optimization approach. Energy optimization is an essential factor of the WSN to improve the performance of the system. A wireless sensor node arrangement is a complex process. These sensor nodes can transmit data packets with other sensor node at their radio frequency range. This work presents a simple energy-efficient network model based on the Firefly optimization and Hybrid (Eagle optimization and the Firefly optimization techniques) to minimize energy consumption. Received Signal Strength Indication (RSSI) positioning method is used for the localization process. The algorithm also finds the final point of the best solution. It can find the detailed analysis of energy consumed during the different tasks performed by the sensor within a network while in active mode.

Optimization is performed by Hybrid Eagle and Firefly optimization techniques. Eagles have a unique yet straightforward way of exploiting their land. It flies in the sky, searches around a few points, and climbs to the highest point, and when it comes back, it looks back and repeats the same process. Attraction is directly related to the light, and both are reduced with distance. Therefore, for two flashing fires, a fire with a lower light will move to a fire with a higher light. If no fire is brighter than each other, it will move in pairs. The brightness of the fire depends on the field of work of the target. To determine the appropriate function, the attraction depends on the intensity of the light between the two fires. Hybridized optimization provided the new predicted location of each sensor based on the beacon node positions (Fig. 1).

3.1 Network Procedure

- Initially both sensor nodes and beacon nodes are deployed in the network in a static manner.
- Localization process is performed using Hybridized Eagle-based Firefly Algorithm. This localization considered the distance, coverage area, and Received Signal Strength
- Indication (RSSI).
- The EPO algorithm mimics the eagle's habitat behavior, just like the eagle, the algorithm also finds the highest point in the optimal solution.

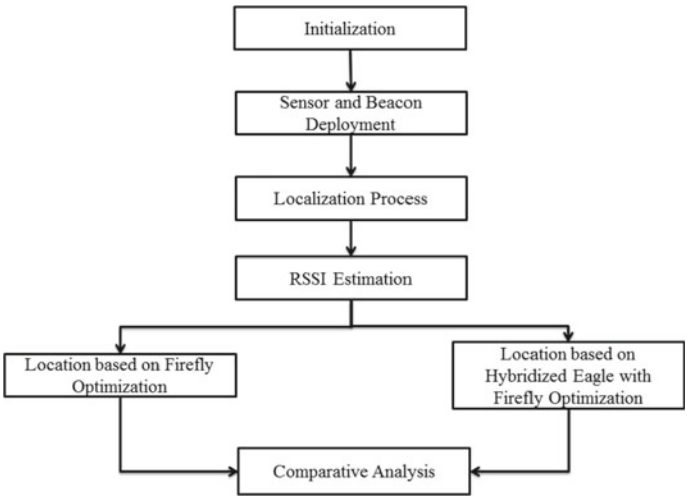

Fig. 1 Proposed flow chart

- Eagle has a straightforward but unique way to explore its terrain.
- When flying high in the sky, look around by trying a few points and moving to the highest point, then look again and repeat the same process. This repetition allows the eagle to reach the highest point.
- Fireflies are unisexual, so that firefly will be attracted to other fireflies, regardless of gender.
- Attraction is directly proportional to brightness, and both decrease as the distance increases.
- For any two flashing fireflies, the firefly with lower brightness will move to the firefly with higher brightness.
- If no firefly is lighter than the other, it will move randomly.
- The brightness of the firefly depends on the range of the objective function.
- To optimize the adaptation function, individuals are forced to move systematically or randomly in the population.
- The attraction parameter is based on the light intensity between two fireflies and is defined using an exponential function.
- Hybridized optimization provides the new predicted location of each sensor based on the beacon node positions.

3.2 Modules

- Parameter Initialization
- RSSI Estimation
- Firefly Optimization

- Hybridized Eagle with Firefly Optimization
- Comparative Analysis (Mean Square Localization Error by varying Number of Nodes)

1) **Parameter Initialization:** The parameter variables are stored in the function code. Initialization is performed by calling built-in functions that take vector or curve objects as parameters. After defining the initialization function, check that the syntax is correct.
2) **RSSI Estimation:** The received signal strength indicator (RSSI) indicates energy loss during signal transmission; The RSSI value is related to the magnitude of the signal attenuation. During signal transmission, the smaller the RSSI value, the minor will be the reduction. In general, RSSI intervals are based on empirical or theoretical models. The scope of RSSI based on model experience shows that an offline database has been created between a small number of RSSI values of nodes with known location information and their signal propagation distance. In the node positioning process, the data stored in the database is constantly compared to obtain node positioning. The theory based on the RSSI model realizes node positioning by determining the environmental parameters in the signal propagation loss model and inserting the RSSI value received from the receiving node in the model to estimate detachment among the nodes. The former method has a key; it requires many offline measurements works in the area; in addition, position accuracy is imperfect by the number of nodes and the measurement workload. The core of the latter method is to study the critical parameters in model information by accurately measuring the RSSI value. It can better reflect the hardware conditions and the actual environment. In addition, the position accuracy and improved position performance can be improved.
3) **Firefly Optimization:** Fireflies are feathered beetles or creatures that glow and flicker at night. The chemically generated light from the abdomen does not have infrared or ultraviolet frequency and is called. They use flashlights specifically to appeal to partners or swap. The flashing light is also used as a defensive warning mechanism to warn fireflies of probable natural enemies. The firefly algorithm proposed by Yang is a meta-heuristic algorithm inspired by the irregular of fireflies or the phenomenon of communication. The Firefly algorithm was formulated with the following expectations:

    - As fireflies are, they attract each other regardless of their gender.
    - Attraction is directly proportional to brightness, and fireflies with lower brightness are attracted to fireflies with higher brightness. As the distance between two fireflies increases, the attractiveness decreases.
    - If two fireflies have the same brightness, the fireflies move randomly.
    - Generations of new solutions are achieved by walking around and attracting fireflies. The brightness of the fire surface must be related to the impartial occupation of the related problem. Their appeal allows them to divide themselves into smaller groups, or each subsection is gathered around the local mode.

4) **Hybridized Eagle with Firefly Optimization:** A two-step strategy for eagle feeding. First, we assume that the eagle performs Levy walks throughout the range. Once the prey is found, it becomes a hunting strategy. Second, the hunting strategy can be measured by a close local search using any optimization method (such as the steepest descent method, downhill simplex method, or the Nelder-Mead method). Clearly, we can also use any effectual meta-heuristic algorithm (such as particle heat optimization (PSO) and fire algorithm (FA)) for centralized local search.
5) **Performance Analysis:** The mobile sensor nodes are localized using a localization approach with Firefly and Hybrid Eagle with firefly optimization algorithms. In Eagle Firefly estimation the parameter considered are: Energy Arrival (Nb), Number of active nodes (Na) = 10, Number of anchor nodes (M) = 10, Distance Measurement, RMSPE Ratio = 0.1, Network Size = 100, and a 100 by 100 area that the nodes can wander function.

After estimating all target node (NL) positions that can be located, the total positioning error is calculated. It is calculated as the average of the squared distance between the estimated node coordinates (Xi, Yi) and the actual node coordinates (xi, yi), which is expressed as:

$$f(x, y) = \frac{1}{N}\left(\sum_{i=1}^{N} \sqrt{(x_i - X_i)^2 - (y_i - Y_i)^2} - d_i\right)^2 \tag{1}$$

Meta-heuristic algorithm helps to find coordinates (x, y) of the target node that minimizes the placement error. The detached purpose of the positioning problem is average square space among the target node or anchor node, which is curtailed by an algorithm and mathematically described as:

$$E_i = \frac{1}{N_1} \sum_{i=1}^{N} \sqrt{(x_i - X_i)^2 - (y_i - Y_i)^2} \tag{2}$$

For each node, the meta-heuristic algorithm is run autonomously to find the location of the target node. The point of the transmission area is called. The for prime butterfly or anchor node in transmission area, is calculated as:

$$f(x_c, y_c) = \frac{1}{N}\left(\sum_{i=1}^{N} x_{i,} \sum_{i=1}^{N} y_{i,}\right) \tag{3}$$

a) Mean Square Error: In statistics, the Mean Squared Error (MSE) is an estimator that enables the average error squares that is, the mean squared difference between the estimated and true values. MSE is a risk function that equals the squared error less expected value.
b) Mean Localization Error: Localization error is a widely used measure of uncertainty and bias in the identification of the nodes. The average difference between the actual position of sensor nodes and the estimated position of sensor nodes is called Mean Localization Error. For calculation of Mean Localization Error,

simulation is run at a difference of 10 for a range of 50 to 150 deployed mobile sensor nodes.

c) Number of Localized Nodes: The sensor nodes are localized on several randomly deployed mobile sensor nodes. The number of mobile sensor nodes is varied from 50 to 150 nodes with interval of 10 to plot the localization error curve. The mobile sensor nodes are localized using a localizatiosn approach with Firefly and Hybrid Eagle with firefly optimization algorithms.

4 Simulation Results

Localization is performed using the Hybridized Eagle-based Firefly Algorithm. This localization algorithm considered the distance, coverage area, and Received Signal Strength Indication (RSSI). The algorithm also finds the final point of the best solution. The simulation has been performed on MATLAB software.

4.1 Parameter Initilasation

The parameter variables are stored in the function code. Initialization is performed by calling built-in functions that take vector or curve objects as parameters. After defining the initialization function, check that the syntax is correct (Table 1).

In the simulation configuration, the transmission range of beacons and mobile sensor nodes is fixed at 50 m. randomly deploy mobile sensor nodes in the target area of 100 × 100 m^2. The beacon node is deployed in the centre of the target area. RSSI measurement technology is used to estimate the distance between mobile sensor nodes and beacon nodes in a range-based localization approach.

Figure 2 shows the initial location of the mobile nodes and anchor nodes. The error in distance is minimum.

Figure 3 shows mean estimation error for the fixing of the location of mobile passive nodes. Final location of the node should have the minimum error.

Table 1 Parameter setting for simulation

Simulation environment	Value
Network dimension	100 * 100
Number of anchor nodes	10
Number of passive nodes	10
Transmission distance	1000 m
Localized area distance	50 m

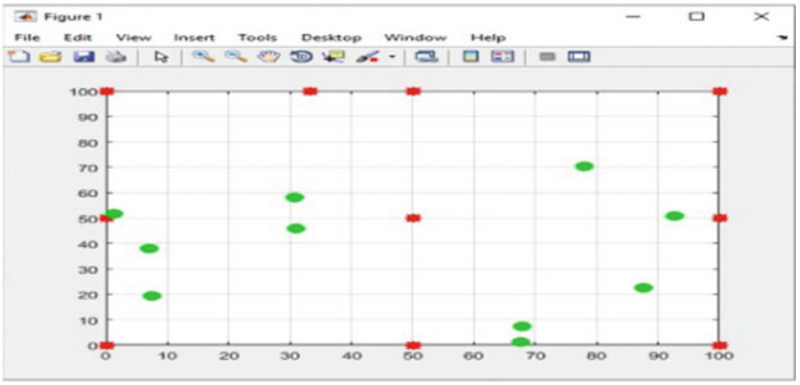

Fig. 2 Node deployment

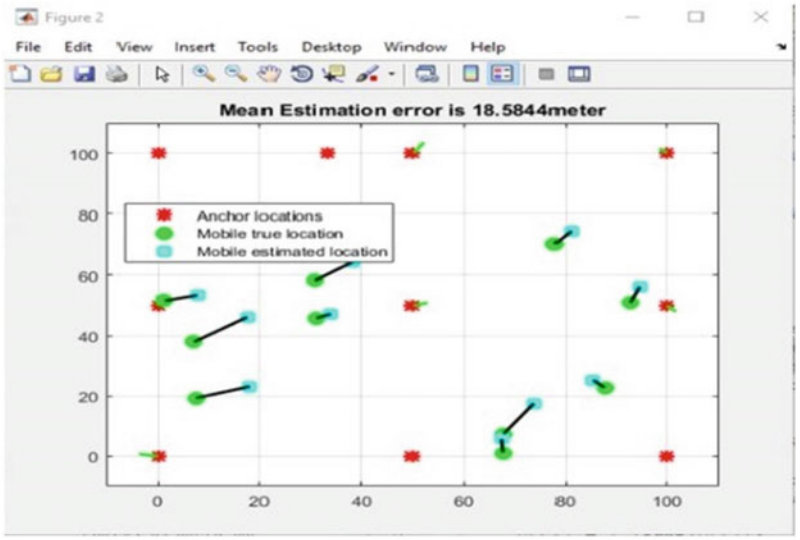

Fig. 3 Mean Estimation Error

Figure 4 shows the Mean square error for energy arrival rate at 50 nodes.

Figure 5 shows the MSE error for energy arrival rate at 100 nodes.

Figure 6 shows the Mean square error for energy arrival rate at 150 nodes. Higher the arrival rate, lower the error.

Figure 7 shows the Localization error with no. of nodes ranging from 50 to 150 nodes at the interval of 10 nodes. As the number of nodes increases, the localization error also increases.

Figure 8 shows the Localization error with the transmission distance considered for the network. Higher the transmission distance higher the localization error.

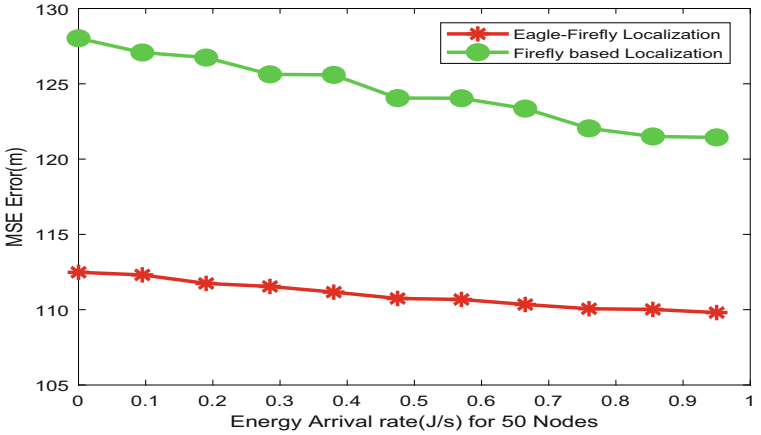

Fig. 4 MSE vs. energy arrival rate at 50 nodes

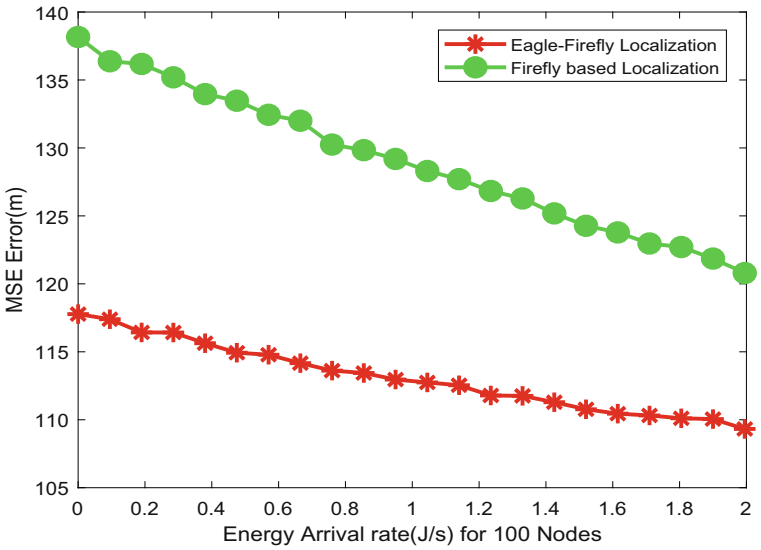

Fig. 5 MSE vs. energy arrival rate at 100 nodes

Figure 9 shows the localization error in percentage with the distance with the between the anchor node and mobile nodes. The localisation error is almost constant with the small localization area.

In the Fig. 10 the energy arrived at the nodes is shown with different number of nodes.

Figure 11 shows the comparison of the Firefly and Hybrid (Eagle with Firefly) algorithm in terms of MSE and Localization error as per Table 2.

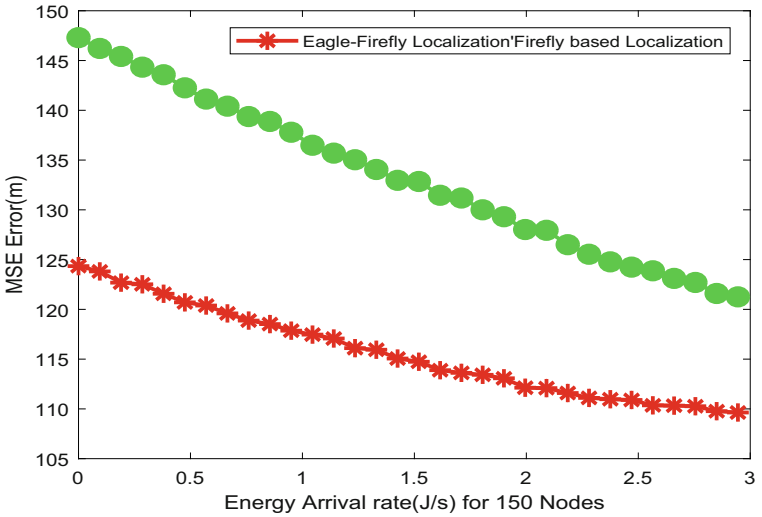

Fig. 6 MSE vs. energy arrival rate at 150 nodes

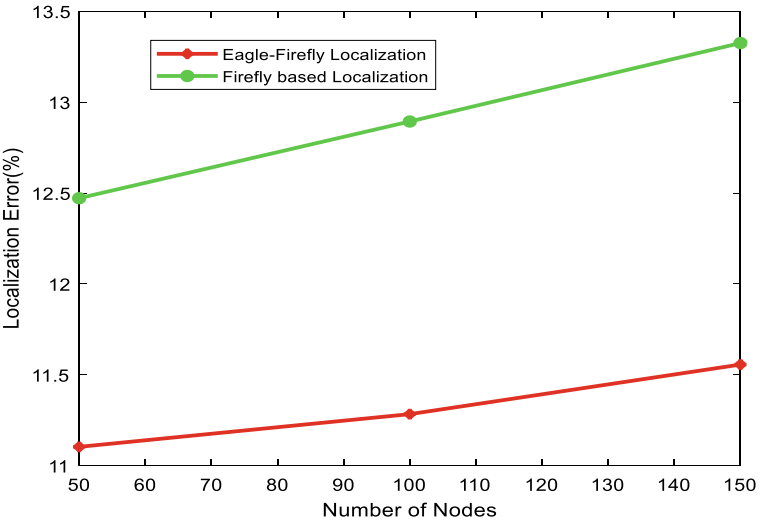

Fig. 7 Localisation error

Figure 11 and Table 2 shows the summary of results. The mean square error and localisation error for the hybrid-firefly and firefly algorithm is shown with the number of nodes.

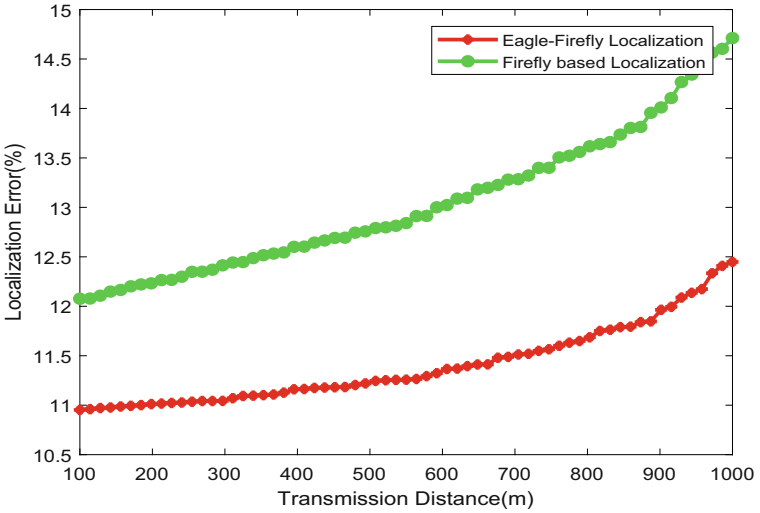

Fig. 8 Transmission error

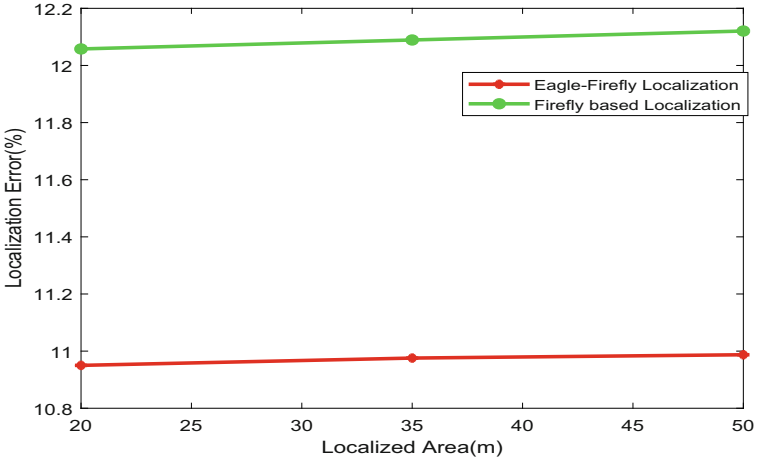

Fig. 9 Localization error

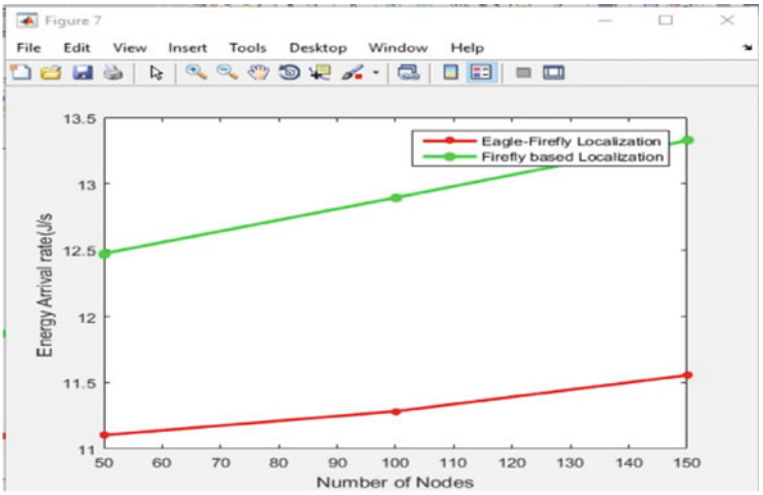

Fig. 10 Energy vs no of nodes

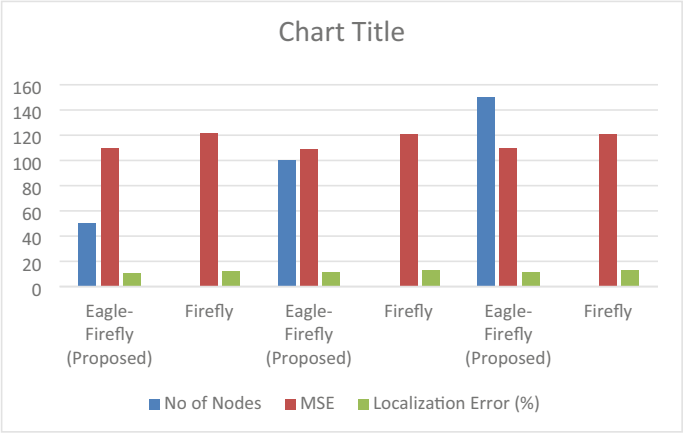

Fig. 11 Result summary

Table 2 Summary of results

Algorithm	No of nodes	MSE (m)	Localization error (%) eagle-firefly (proposed)
Eagle-firefly (proposed) firefly	50	109.8	11.00
		121.4	12.50
Eagle-firefly (proposed) firefly	100	109.3	11.25
		120.8	12.75
Eagle-firefly (proposed) firefly	150	109.6	11.60
		121.3	13.40

5 Conclusions

Wireless sensor networks are used in many applications, including environmental, military, hazardous, and overseas processing industries. Various optimization algorithms are used to reduce the localization error and improve power consumption of Wireless Sensor Networks. Firefly optimization is a popular optimization algorithm used in Wireless Sensor Networks. The Firefly optimization technique and hybrid eagle with firefly optimization technique were used to optimize the localization error and optimize energy in Wireless Sensor networks. The performance of optimization methods was executed in MATLAB simulation platform.

Based on the results, it is observed that Hybrid Eagle and Firefly with RSSI optimization method gives less localization error and more optimized power consumption than the Firefly optimization. The energy optimization is approximately 15%. The MSE at 50 nodes is comparative for Hybrid Eagle with Firefly algorithm as the respective values are 109.8 m and 121.4 m. However, with increase in the number of nodes, the difference between the algorithms is observed. MSE at 100 nodes for Hybrid Eagle with Firefly algorithm is 109.3 m, whereas for Firefly algorithm the value is 120.8 m. The gap is further increased for 150 nodes and the value for MSE for algorithms stand at 109.6 m and 121.3 m respectively. The values are available for comparative study in Table 3 of previous section. The present study also focuses on WSN design, optimization problem, and energy consumption issues in a wireless environment. Optimization problem is a significant factor in ensuring a secure.

References

1. Raj A, Prakash S (2019) Mobile data gathering approaches in wireless sensor networks: a survey. In: 2019 6th international conference on computing for sustainable global development (INDIA Com). IEEE, pp 758-762
2. Vikram N, Harish KS, Nihaal MS, Umesh R, Shetty A, Kumar A (2017) A low cost home automation system using Wi-Fi-based wireless sensor network incorporating Internet of Things (IoT). In: 2017 IEEE 7th international advance computing conference (IACC). IEEE, pp 174–178
3. Sunitha M, Karunavathi RK (2019) Localization of nodes in underwater wireless sensor networks. In: 2019 4th international conference on recent trends on electronics, information, communication & technology (RTEICT). ISBN: 978-1-7281-0630-4, https://doi.org/10.1109/RTEICT46194.2019.9016743
4. Yang XS, Gandomi AH, Yang XS, Alavi AH (2011) Mixed variable structural optimization using Firefly Algorithm. Comput Struct 89(23–24):2325–2336
5. Yang XS (2008) Firefly algorithm, nature-inspired metaheuristic algorithms, pp 79–90. https://doi.org/10.1007/978-3-642-04944-6_14.
6. Fister I, Yang XS, Brest J (2013) A comprehensive review of firefly algorithms. Swarm Evol Comput 13:34–46
7. Del Valle Y, Venayagamoorthy G, Mohagheghi S, Hernandez J, Harley R (2008) Particle swarm optimization: basic concepts, variants and applications in power systems. IEEE Trans Evol Comput 12:171–195

8. Angeline P (1998) Evolutionary optimization versus particle swarm optimization: philosophy and performance differences. In: Evolutionary programming VII. Springer, Heidelberg, pp 601–610
9. Clerc M, Kennedy J (2002) The particle swarm-explosion, stability, and convergence in a multidimensional complex space. IEEE Trans Evol Comput 6:58–73
10. Stoleru R, He T, Stankovic JA (2007) Range-free localization. In: Secure localization and time synchronization for wireless sensor and ad hoc networks. Springer, Boston, pp 3–31
11. Ye Z, Mohamadian H (2014) Adaptive clustering based dynamic routing of wireless sensor networks via generalized ant colony optimization. IERI Procedia 10:2–10
12. Zhang L, Yang H, Yu Y, Peng F (2018) A three-dimensional node security localization method for WSN based on improved RSSI-LSSVR algorithm. In: 10th international conference on measuring technology and mechatronics automation (ICMTMA). ISBN: 978-1-5386-5114-8, https://doi.org/10.1109/ICMTMA.2018.00051
13. Lin Y, Tao H, Tu Y, Liu T (2018) A node self-localization algorithm with a mobile anchor node in underwater acoustic sensor networks. IEEE Access. https://doi.org/10.1109/ACCESS.2019.2904725
14. Wan X, Shen L, Chen Z, Xu H (2018) An efficient virtual nodes-based APIT localization algorithm with low computational cost. In: IEEE 23rd international conference on digital signal processing (DSP). ISBN: 978-1-5386-6811-5, https://doi.org/10.1109/ICDSP.2018.8631829
15. Kalyani V (2018) Enhancing localization accuracy in wireless sensor networks using range-free methods and RSS measurements. In: 2018 international conference on recent trends in advanced computing (ICRTAC). ISBN: 978-1-5386-5853-6, https://doi.org/10.1109/ICRTAC.2018.8679291
16. Wan X, Shen L, Chen Z, Xu H (2018) An efficient virtual nodes-based APIT localization algorithm with low computational cost. In: IEEE 23rd international conference on digital signal processing (DSP). ISBN: 978-1-5386-6811-5, https://doi.org/10.1109/ICDSP.2018.8631829
17. Kaur A, Gupta GP, Mittal S (2020) Impact of nature-inspired algorithms on localization algorithms in wireless sensor networks. In: Nature-inspired computing applications in advanced communication networks. IGI Global, pp 1–18
18. Bhatt JG, Jani OK, Bhatt CB (2020) Automation based smart environment resource management in smart building of smart city. In: Smart environment for smart cities. Springer, Singapore, pp 93–107
19. Sharma R, Prakash S (2020) Enhancement of relay nodes communication approach in WSN-IoT for underground coal mine. J Inf Optim Sci 41(2):521–531
20. Bajaj K, Sharma B, Singh R (2020) Integration of WSN with IoT applications: a vision, architecture, and future challenges. In: Integration of WSN and IoT for smart cities. Springer, Cham, pp 79–102
21. Sharma, R., & Prakash, S. (2019, March). Latest Trends and Future Directions of Localization Algorithms in Wireless Sensor Networks. In 2019 6th International Conference on Computing for Sustainable Global Development (INDIA Com) (pp. 626-631). IEEE.
22. Kuriakose J, Joshi S, Raju RV, Kilaru A (2014) A review on localization in wireless sensor networks. In: Advances in signal processing and intelligent recognition systems, pp 599–610. https://doi.org/10.1007/978-3-319-04960-1_52
23. Singh SP, Sharma SC (2015) Range free localization techniques in wireless sensor networks: a review. In: 3rd international conference on recent trends in computing 2015 (ICRTC-2015), pp 7–16. https://doi.org/10.1016/j.procs.2015007.357

A High Bit Rate Half Adder Based on Square Lattice Photonic Crystal

Rahul Pandey, Rukhsar Zafar, Ankur Saharia, Kamal Kishore Choure, Nitesh Mudgal, Ghanshyam Singh, and Rajendra Mitharwal

Abstract In this paper an all-optical half adder is proposed that uses the concept of photonic band gap phenomenon of photonic crystal. The point and line defects are introduced in the perfect photonic crystal and the resonant characteristics are measured from output port for Gaussian modulated input signal. The parameter of photonic crystal is so selected that the bandgap of crystal lies near telecommunication wavelength centered at $\lambda = 1550$ nm. The structure is investigated using 2D FDTD method. In the absence of any one input, the output is obtained above the threshold while in the presence or absence of both the input, the signal level at output is far below the threshold. The half adder performance of is measured using response time and contrast ratio. The contrast ratio for sum and carry port is 7.58 and 9.52 dB respectively and response time is as low as 1.8 ps. This half adder supports small footprint. The high Bit rate and small footprint of proposed structure makes the device useful for optical ICs.

Keywords Photonic crystal · FDTD · Half adder · Bit rate · Contrast ratio

R. Pandey (✉) · R. Zafar
Department of Electronics and Communication Engineering, Management and Gramothan, Swami Keshvan and Institute of Technology, Jaipur, India
e-mail: rahul.pandey@skit.ac.in

R. Zafar
e-mail: rzafar@skit.ac.in

R. Pandey · K. K. Choure · N. Mudgal · G. Singh · R. Mitharwal
Department of Electronics and Communication Engineering, Malviya National Institute of Technology, Jaipur, India

A. Saharia
Department of Electronics and Communication Engineering, Manipal University Jaipur, Jaipur, India

M. Tiwari et al. (eds.), *Optical and Wireless Technologies*, Lecture Notes in Electrical Engineering 892, https://doi.org/10.1007/978-981-19-1645-8_38

1 Introduction

Nowadays the major challenge for the researchers in data communication is to attain high speed, superior channel capacity as well as at the same time maintaining low cost also. So, whenever it is required to communicate for long distances, optical communication emerges as a realization of the above requirements [1, 2]. It provides much improved way to process the data along with high data rate, also it has several other advantages like less distortion, high bandwidth and less RF interferences in data transmission [3, 4]. But these things can be possible if all optical circuits are available to work, otherwise optical to electronic conversion and vice versa make the whole process very tiresome [5, 6]. An optical signal after transmission at transmitter and before reception at receiver has to go through this process. So, this process is a stumbling step while achieving high speed in optical communication system. In this regard the use of integrated photonics seems to be a promising solution for the researchers. On-chip Nano photonics permits to use a common substrate for designing, fabrication, and integration of several nano photonic components [7–9].

Photonic crystal based optical integrated Circuit (IC) are drawing the attention of researchers because of the opportunity of fabricating them with low loss and compact size [10]. Photonic crystals (Ph.C.) are structures whose refractive indexes varies periodically in one, two or three dimensions. Analogous to the band gap in the semiconductor crystals a photonic band gap exists (PBG) in Ph.C., for which propagation of light is forbidden. PBG is defined as the frequency range for which propagation of light in Ph.C. is not allowed and is reflected back [11]. However, if point defect and line defects are introduced in Ph.C. materials, it permits those frequencies to pass. This is the unique feature of Ph.C. materials. The biggest advantage of Ph.C. over optical fiber is that it uses both total internal reflection (TIR) and PBG phenomena for signal propagation and so it offers minimum losses at tight corners [12]. The basic unit of optical Integrated circuit is optical logic gates, because logic gates can be useful in designing of other combinational and sequential logic. Ph.C. have already shown their potential in designing of all optical gates [13, 14]. In recent years many researchers have designed optical logic devices and circuits using photonic crystal (IC). Among these logic devices full adder is an important part of the data computing as it is used in ALU of CPU [13–17]. Whereas a full adder can be made using two half adders. In this paper we have designed a half adder which is based on W1 photonic crystal waveguide and series of point defects, the port C (reference port) is added along with two input ports A and B in order to obtain the desired signal level at sum and carry port. The performance of the structured adder is analyzed through performance measuring factors like contrast ratio and bit rate. The proposed adder is having high response time of 1.8 ps. The device also offers small footprint and thus is quite useful in designing an on-chip all optical half adder.

2 Design Procedure

Figure 1 shows the detailed 2D view of proposed Ph.C. Line defects and point defects are incorporated in the perfect square lattice photonic crystal which is arranged with periodic dielectric rods. The periodicity is so introduced in order to support photonic band gap phenomenon.

The PBG effect allows the certain range of frequencies to be blocked for propagation. This range of PBG is quite useful in designing optical circuits and devices. The structural parameters are as listed in Table 1.

The parameter of the design is so selected in order to have PBG near desired telecommunication wavelength. The PBG of the structure/geometry lies in the range of 0.59 (1/λ)−0.81(1/λ).as shown in Fig. 2 i.e., the corresponding wavelength range is λ = 1250 to 1700 nm. The band gap can be efficiently utilized in the case when some defects like point and line defects are deliberately added in the perfect crystal. The point defect is introduced by changing the size of rods at specific locations while line defects are added by removing rows of dielectric rods and creating a clean path for the propagation of signal that lies in the band gap. Point defects are also known

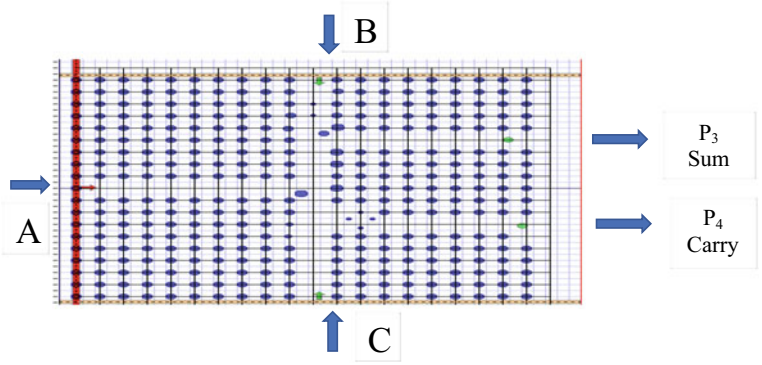

Fig. 1 Schematic design of an all optical half adder using photonic crystal with input port as A, B and P_3, P_4 as Output

Table 1 Structural Parameters and corresponding values used in structure

Sr no.	Parameters	Value
1	Refractive index of silicon rods	3.46
2	Dielectric constant of medium	1
3	Radius of rods (r)	0.12 a
4	Pitch of cell (a)	0.56 μm
5	Radius of point defect (r'), (r")	0.15 a, 0.22 a
6	input wave	Gaussian modulated continuous wave at λ = 1550 nm

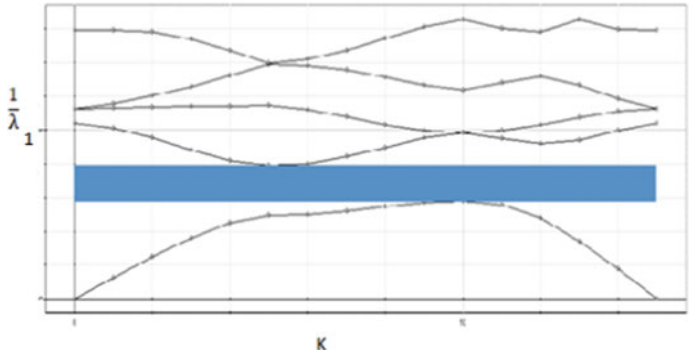

Fig. 2 Relation between Frequency Vs wave number (k). Photonic band gap is 0.59 (1/λ)–0.81(1/λ)

as cavity and line defects work as waveguide. If only one row of rods is removed, then waveguide is termed as W1 waveguide. The structure in Fig. 1 acts as a half adder and detailed working is analyzed in the next section.

3 Working Methodology and Results

In this paper two-dimension Finite difference time domain (FDTD) method is used to analyze the transmission characteristics of the discussed geometry. The inputs are given from P_1 and P_2 port and at P_3 and P_4, output is gathered. Port P_3 corresponds to sum port and P_4 is carry port. The presence of reference signal at port C helps, to attain the desired signal at sum and carry port. The working of this half adder is based on selection of threshold level and if the output signal is obtained above that level the signal is interpreted as 'High' logic otherwise it is interpreted as 'Low' logic. Based on this criteria, 3 different cases for the operation of half added is discussed.

Case 1: In the presence of any input, either from port P_1 or P_2, desired signal is coupled to the output port P_3. While the cavity R_2 resonance condition is not matched with incoming signal. So, the signal received at port P_4 is not significant.
Case 2: When both the inputs are available, the resonant condition of cavity is matched but the signal with different phase shifts adds up to a low value leads to approximately zero output at output port P_3 while considerable output is obtained at port P_4 as signal is above threshold level.
Case 3: In the absence of all the input the output is zero at both the output ports P_3 and P_4.

Figure 3(a)(b)(c) shows the transmission spectrum obtained at the output port P_3 and P_4 for all the possible condition of input port P_1 and P_2., and received transmission efficiency at sum and carry ports is summarized in Table 2.

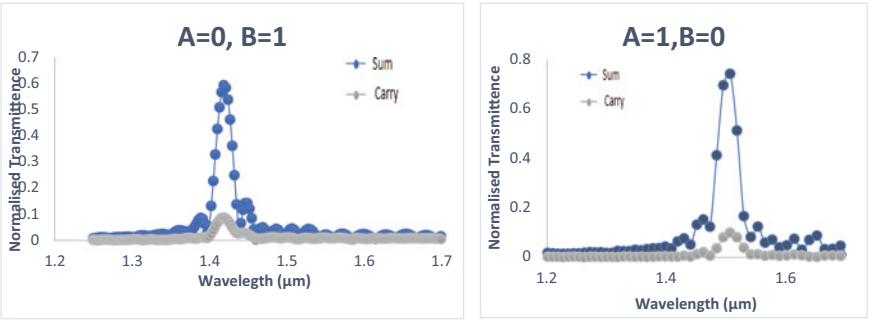

(a) **(b)**

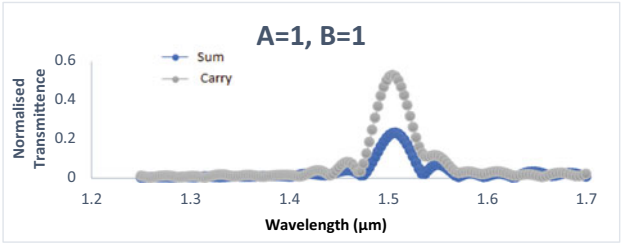

(c)

Fig. 3 **a** Transmission spectrum for input condition A = 0, B = 1 **b** Transmission spectrum for input condition = 1, B = 0 **c** Transmission spectrum for input condition A = 0, B = 1

Table 2 Transmission efficiency obtained at sum and carry port at different input condition

Input		Output	
P1	P2	P3	P4
Low	Low	0 (low)	0 (low)
Low	High	0.58 (high)	0.084 (low)
High	Low	0.74 (high)	0.09 (low)
High	High	0.23 (low)	0.52 (high)

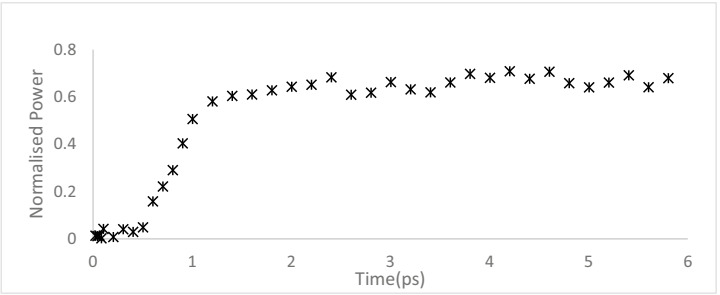

Fig. 4 Time response curve of proposed structure with response time as (1.8 ps)

The input low is corresponding to 0 and input high is corresponding to 1 signal level so that the threshold boundary for output (Both sum and carry) is considered to be 0.5. By comparing the efficiency of signal obtained at corresponding output port and threshold signal the operation of structure can be concluded as half adder. To measure the performance of proposed design three characteristics parameter are used.

1. Noise Margin: Noise margin (NM) is defined as the difference between P_{on}, P_{off} [18].
   $P_{on} = \frac{(0.74+0.58)}{2}$ and Poff. $= \frac{(0.23+0)}{2}$. So calculated the highest value of noise margin is 0.545.
2. Contrast Ratio = It is defined as, $CR = 10log(\frac{P_{on}}{P_{off}})$
   From the above formula CR for sum is calculated as 7.58 dB and for carry it is 9.52 dB.
3. Response Time = It is defined as sum of delay time and rise time and so it is calculated as 1.8 ps.

The time response of optical circuit is also an important factor that is used to measure the latency incurred during the transmission. Figure 4 shows the time evolution of proposed structure. The proposed half adder offers a response time of 1.8 ps i.e., Corresponding to bit rate of 0.55 Tbps.

The obtained bit rate is quite high and the footprint of structure is also quite small (125.44 μm^2) the condition are favorable for designing of On-chip optical ICs.

4 Conclusion

Defects in Photonic crystal can be efficiently utilized to mold the flow of photons for variety of application. W1 line defects-based waveguide with series of point defects are employed for the designing of an optical half adder, the parameters of adder are so selected that the photonic band gap covers a wide telecommunication range. The presence of reference signal helps to obtain the desired signal level at sum port and

carry port. The proposed device reports high value of contrast ratio for sum and carry port. The bit rate offered is 0.55 Tbps and response time is 1.8 ps. The high bit rate obtained through this half adder make the device viable for future optical IC. The device is also ultra-compact and the footprint is maintained to 125.44 μm^2.The small footprint and the high CR makes the proposed structure viable for future all optical ICs.

References

1. Senior JM (2009) Optical fiber communications principles and practice, 3rd edn. Pearson, London
2. Joannopoulos JD, Meade RD, Winn JN (2002) Photonic crystals: molding the flow of light. Princeton Univ. Press, Princeton
3. Bostan CG, de Ridder RM (2002) Design of photonic crystal slab structures with absolute gaps in guided modes. J opt Adv Mat 4:921–928
4. Ibhaze AE, Orukpe PE, Edeko FO (2020) High capacity data rate system: a review of visible light communication technology. J Electron Sci Technol 18:100055
5. Jamois C, Wehrspohn RB, Andreani LC, Hermannd C, Hess O, Gosele U (2003) Silicon-based two-dimensional photonic crystal waveguides. ScienceDirect Photonics Nanostruct Fundam Appl. 1:1–13
6. Singh P, Tripathi DK, Jaiswal S, Dixit HK (2014) Review article all-optical logic gates: designs, classification, and comparison. Hindawi Publ Corpor Adv Opt Technol 2014:275
7. Neisy M, Soroosh M, Ansari-Asl K (2018) All optical half adder based on photonic crystal resonant cavities. Photonic Network Commun 35:245–250
8. Rani P, Kalra Y, Sinha RK (2013) Realization of and gate in y shaped photonic crystal waveguide. Opt Commun 298:227–231
9. Noori M, Soroosh M, Baghban H (2016) Highly efficient self collimation based waveguide for mid-IR applications. Photon Nanostruct 19:1–11
10. Dutta, H.S., Goyal, A.K., Srivastava, V., Pal, S (2016) Coupling light in photonic crystal waveguides: a review. Photon Nanostruct-Fund Appl 20:41–58
11. Alipour-Banaei H, Mehdizadeh F (2013) Bandgap calculation of 2D hexagonal photonic crystal structures based on regression analysis. J Opt Commun 34:1–9
12. Kanungo V, Metya SK, Janyani V, Salim M (2013) Segmented cladding index guiding photonic crystal fiber. Opt Commun 297:147–153
13. Cui X, Ma X, Lin Q, Li X, Zhou H, Cui X (2020) Design of High-speed logic circuits with four-step RRAM-based logic gates. Circ Syst Signal Process 39(6):2822–2840
14. Ghadrdan M, Mansouri-Birjandi MA (2013) Concurrent implementation of all-optical half-adder and AND & XOR logic gates based on nonlinear photonic crystal. Opt Quantum Electron 45:1027–1036
15. Liu Q, Ouyang Z, Wu CJ, Liu CP, Wang JC (2008) All-optical half adder based on cross structures in two dimensional photonic crystals. Opt Express 16:18992–19000
16. Priyanka P, Zafar R, Kanungo V, Vyas S (2020) Photonic crystal-based all-optical half adder with high contrast ratio. J Opt Commun (2020)
17. Kumar H, Kumar L, Janyani V, Oleh B, Serhij U, Singh G (2017) Gray to binary code converter using ti-in-diffused lithium niobate based mach-zehnder interferometer. In: Advances in optical science and engineering. Springer proceedings in physics, vol 194, pp 257–262
18. Datta T, Sen M (2020) All-optical logic inverter for large-scale integration in silicon photonic circuits. IET Optoelectron 14(5):285–291

Modelling of SWAP Gate Using Compact Ring Resonator

Kamal Kishor Choure, Gaurav Kumar Bharti, Ankur Saharia, Nitesh Mudgal, and Ghanshyam Singh

Abstract In this paper model of the all-optical reversible swap gate using a single silicon ring resonator is presented. The function of the present design is based on the mutual relationship between nature of the pump signal and the source which helps in mode conversion. The FDTD simulation results given in the paper validates the proposed design. The device parameters, the source power and pump power are optimized and adjusted to achieve the optical switching. The design is all optical, simple and compact in size.

Keywords All optical reversible gate · Swap gate · Mode-Conversion · FDTD simulation

1 Introduction

Silicon photonics proved to be a most vital platform for the next generation computing, signal processing and communication applications [1]. Silicon on insulator (SOI) provides the compact size, fast switching, high bandwidth and compatibility with present CMOS technology, which are the basic needs for the next generation communication and computing [2, 3]. To get the high switching speed silicon ring resonators proved to be a best option for the optical computing [4]. The optical light signal is strongly confined in the ring structure of the RR. Recently various researchers have shown immense interest in the designing of all optical switch by utilizing the concept of electro-optic, thermo-optic and optical pump effect on the ring resonator [5–7].

K. K. Choure (✉) · N. Mudgal · G. Singh
Malaviya National Institute of Technology Jaipur, Jaipur, India
e-mail: kamalkishorchoure.09@gmail.com

G. K. Bharti
Indian Institute of Technology Guwahati, Guwahati, India

A. Saharia
Manipal University Jaipur, Jaipur, India

M. Tiwari et al. (eds.), *Optical and Wireless Technologies*, Lecture Notes in Electrical Engineering 892, https://doi.org/10.1007/978-981-19-1645-8_39

Several classical (irreversible) logics gates and digital circuits are designed by implementing the optical switching phenomenon of the ring resonators [8–10]. The reversible gates are energy conservative, thus find wide range of applications in optical and quantum computing [11]. Many researches shown their interest in the development of reversible gates through the application photonic components [12–14]. The integrated photonic based reversible gate and network are the next generation computing revolution. In this report, we have designed a reversible swap gate using a compact silicon ring resonator. The output satisfies the truth table of swap gate.

2 Model of SWAP Gate Using Compact Ring Resonator

The design of the optical ring resonator is consisting of two bus waveguide and one race track ring resonator as shown in the Fig. 1(a). The substrate material is silicon dioxide (SiO_2) and waveguide material is silicon for the design as shown in the Fig. 1(b). The input source is provided at the input port while output is taken at the through and drop port both. The nature of both, the source input and the pump input play an important role for the mode conversion in the optical ring resonator. At resonance, the input signal in the straight waveguide got coupled with the ring waveguide at resonant wavelength and output is notice at the drop port. There also some portion of the input signal is observed at the through port. In the proposed design, the output of both through port and drop are considered. The introduction of the pump pulse makes changes in the refractive index and causes mode conversion in the design. The selection of source nature and pump nature is responsible for mode conversion respectively. The phenomenon of the mode conversion is explained in [15, 16]. Based on the couple's mode theory the equation governing for mode conversion in ring resonator is below [15, 16].

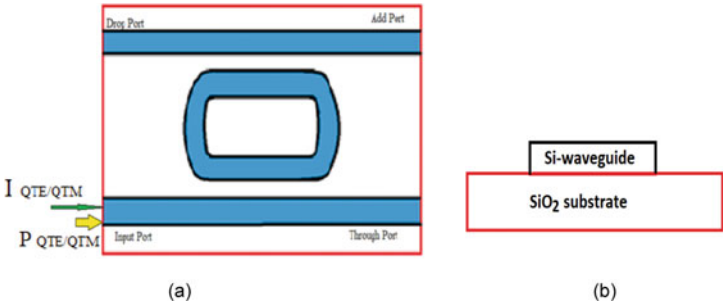

Fig. 1 **a** Design of the compact ring resonator for swap gate **b** Material for waveguide and substrate

Table 1 Swap gate truth table

Input		Output	
X_1	X_2	Z_1	Z_2
0	0	0	0
0	1	1	0
1	0	0	1
1	1	1	1

$$H_{TEEorTMM} = \frac{r_1 + \gamma\left[-r_2 cos(\varnothing)\left(1 + r_1^2\right) \pm jt_1^2 r_2 R sin(\varnothing)\right] z^{-1} + \gamma r_1 r_2^2 z^{-2}}{1 + \gamma^2 r_1^2 r_2^2 z^{-2} - 2\gamma r_1 r_2 z^{-1} cos(\varnothing)} \tag{1}$$

$$H_{TEMorTME} = \frac{j\gamma t_1^2 r_2 S z^{-1} sin(\varnothing)}{1 + \gamma^2 r_1^2 r_2^2 z^{-2} - 2\gamma r_1 r_2 z^{-1} cos(\varnothing)} \tag{2}$$

$$H_{DEEorDMM} = \frac{\gamma^{\frac{-1}{2}} t_1 t_2 z^{\frac{-1}{2}} \{r_1 r_2 [cos\left(\frac{\varnothing}{2}\right) \pm jRsin\left(\frac{\varnothing}{2}\right)] + \gamma [cos\left(\frac{\varnothing}{2}\right) \pm jRsin\left(\frac{\varnothing}{2}\right)]\} z^{-1}}{1 + \gamma^2 r_1^2 r_2^2 z^{-2} - 2\gamma r_1 r_2 z^{-1} cos(\varnothing)} \tag{3}$$

$$H_{TEMorTME} = \frac{jt_1 t_2 S sin\left(\frac{\varnothing}{2}\right) z^{\frac{-1}{2}} r_1 r_2 + z^{-1}}{1 + \gamma^2 r_1^2 r_2^2 z^{-2} - 2\gamma r_1 r_2 z^{-1} cos(\varnothing)} \tag{4}$$

where γ is total losses in the ring resonator, r_1, r_2 and t_1, t_2 are self, cross coupling coefficient of the structure and $\varnothing$ is the measure of the induced polarization.

The standard reversible swap gate consists of two input and two output. The truth table of the swap is presented in the Table 1. From the truth table of swap gate, it is observed that when both inputs are high then both outputs are high and when both inputs are low then both outputs are also low. In other condition when either of the input is low the output gets swapped.

3 Simulation Results and its Analysis

The results obtained from the FDTD simulation validated the design of the compact ring resonator-based swap gate. The derived design parameters are: coupling length = 2.1 μm, radius of the racetrack ring = 3.1 μm, resonant wavelength = 1.52 μm. coupling gap = 0.1 μm. The waveguide and substrate material are Si and SiO_2 respectively. By proper combination of the mode of source and the pump, the output has been obtained at same resonant wavelength The Figs. 2, 3, 4 and 5 justifies the Table 2.

The FDTD simulation results for different combination of input source nature and input pump nature are shown below. For our assumption quasi-TE mode (QTE) is consider to be logic "1" and quasi-TM (QTM) mode is considered to be logic "0" at

Table 2 Logical operation of swap gate

Case	Input		Output	
	Source input (I)	Pump input (p)	Through port	Drop port
Case I	0	0	0	0
Case II	0	1	1	0
Case III	1	0	0	1
Case IV	1	1	1	1

the input port. At the output the intensity below 1.5 is consider as logic "0" and the intensity above 1.5 is consider as logic "1" respectively.

Case I- When I = (QTM) and P = (QTM)
Case II- When I = (QTM) and P = (QTE)
Case III- When I = (QTE) and P = (QTM)
Case IV- When I = (QTE) and P = (QTE)

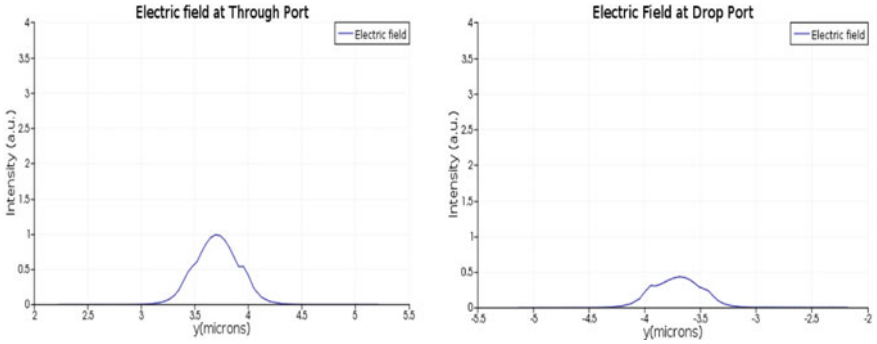

Fig. 2 Output resemble Logic "0" at through and drop port

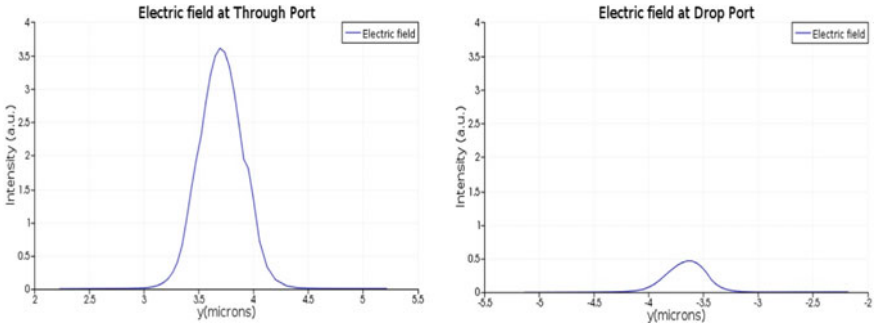

Fig. 3 Output resemble Logic "1" at through port while Logic "0" at drop port

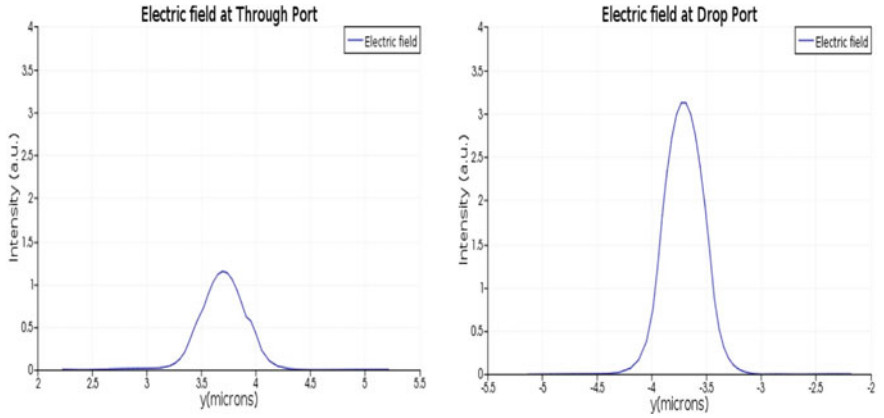

Fig. 4 Output resemble Logic "0" at through port while Logic "1" at drop port

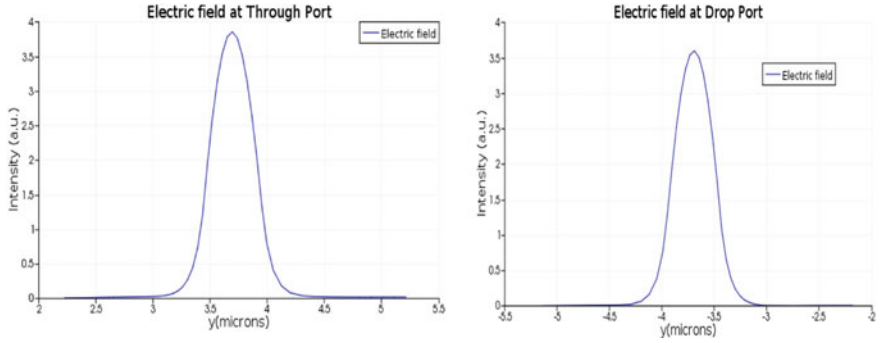

Fig. 5 Output resemble Logic "1" at through and drop port

4 Conclusion

The paper describes the swap gate based on the single compact ring resonator. The simulation results validate the design. The model shows the outstanding performance in terms of SW time. The optimum value of switching time is noted as 0.2 ps. Further study and analysis can be done for the other reversible gates. The presented model is simple in design as only one RR has been used. The presented model may found application in designing optical networks and other computing techniques.

References

1. Zhou Z, Chen R, Li X, Li T (2018) Development trends in silicon photonics for data centers. Opt Fiber Technol 44:13–23. ISSN 1068–5200, https://doi.org/10.1016/j.yofte.2018.03.009.
2. Bahadori M, et al (2017) Energy-performance optimized design of silicon photonic interconnection networks for high-performance computing. In: Design, Automation & Test in Europe Conference & Exhibition (DATE), pp 326–331. https://doi.org/10.23919/DATE.2017.7927010
3. Bogdanov S, Shalaginov MY, Boltasseva A, Shalaev VM (2017) Material platforms for integrated quantum photonics. Opt Mater Express 7:111–132
4. Rakshit JK, Chattopadhyay T, Roy JN (2013) Design of ring resonator based all optical switch for logic and arithmetic operations – a theoretical study. Optik 124(23): 6048–6057. ISSN 0030–4026, https://doi.org/10.1016/j.ijleo.2013.04.075.
5. Fayza KA, Ravindran S, Park K, Alameh K, Bengi A, Hajara AV, Lee YT (2020) Advanced realization and characterization of directed optical logic gates using electroabsorptive quantum-well-based micro ring resonator. Optik 221:164426. ISSN 0030-4026, https://doi.org/10.1016/j.ijleo.2020.164426
6. Azhigulov D, Park H-H, Ukaegbu IA (2020) Design of Si-photonics based logic gates using micro-ring resonator structures. In: Proceedings of SPIE 11274, Physics and Simulation of Optoelectronic Devices, vol XXVIII, p 112741Q. https://doi.org/10.1117/12.2541826
7. Rakshit JK, Zoiros KE, Bharti GK (2021) Proposal for ultrafast all-optical pseudo random binary sequence generator using microring resonator-based switches. J Comput Electron 20:353–367. https://doi.org/10.1007/s10825-020-01586-3
8. Saharia A, Mudgal N, Maddila RK, Singh G (2021) Elementary reflected code converter using a silicon nitride-based microring resonator. J Comput Electron 20(2):934–942. https://doi.org/10.1007/s10825-020-01644-w
9. Kumar A, Raghuwanshi SK (2016) Implementation of some high speed combinational and sequential logic gates using micro-ring resonator. Optik 127(20):8751–8759. ISSN 0030–4026, https://doi.org/10.1016/j.ijleo.2016.06.061
10. Sethi P, Roy S (2014) All-optical ultrafast XOR/XNOR logic gates, binary counter, and double-bit comparator with silicon microring resonators. Appl Opt 53:6527–6536
11. Bennett CH (1973) IBM J Res Dev 17:525
12. Bharti GK, Rakshit JK (2019) Micro-ring resonator based all optical reversible logic gates and its applications. Optoelectron Adv Mater-Rapid Commun 13:10–19
13. Rao DGS, Swarnakar S, Kumar S (2020) Design of all-optical reversible logic gates using photonic crystal waveguides for optical computing and photonic integrated circuits. Appl Opt 59:11003–11012
14. Awasthi A, Chowdhury B, Haider Z, Ali J, Yupapin P, Metya SK, Majumder A (2021) Optical configuration of an N: 2N reversible decoder using a LiNbO3-based Mach-Zehnder interferometer. Appl Opt 60:4544–4556
15. Singh MP, Bharti GK, Rakshit JK, Biswas U (2019) Design of polarization switch in a single micro-ring resonator and its application to design all-optical logic OR/NOR gates using FDTD. In: 2019 international conference on electrical, electronics and computer engineering (UPCON), pp 1–5. https://doi.org/10.1109/UPCON47278.2019.8980009
16. Morichetti F, Melloni A, Martinelli M (2006) Effects of polarization rotation in optical ring-resonator-based devices. J Light wave Technol 24(1):573–585

Study of Underwater Fruit Object Detection Using Deep Learning Model

Jinka Venkata Aravind and Shanthi Prince

Abstract Underwater autonomous vehicle operations are becoming progressively important in order to avoid the hazardous high-pressure deep-sea environment, and the relevance of underwater study and utilisation of marine resource is also rising. Computer vision is noteworthy technology for underwater autonomous vehicles study. In this research work, underwater raw data set is used for training, validating, and testing using YOLO v5 deep learning model to detect the one class (fruit) object. As the underwater images are blurry and hazy, detecting underwater objects without pre-processing is very challenging. In this study, we utilised raw data as underwater dataset to train the yolo model. The raw underwater dataset is difficult to acquire, so in the laboratory Raspberry-pi camera is used to capture the object at different angles, thereafter, data is augmented, yolo model is trained and performance parameters such as accuracy, precision, sensitivity and F1 score are analysed.

Keywords Underwater object detection · Computer vision · Autonomous vehicle · Camera sensor · Deep-sea

1 Introduction

In recent years, there has been a massive interest rise in underwater wireless sensor networks. Underwater actions and wireless communication have attracted both academia and industries attention [1]. Underwater sensor networks can be used for a variety of applications. Each implementation is vital in its own way, but some of them can help with a variety of underwater applications, including natural disaster warning system (such as high tidal waves and seismic tracking), aided navigation, oceanic data gathering, and underwater observations, environmental applications (such as pollution monitoring and biological water quality), and industrial applications [2]. The continual extension of human activities in the deep-sea, such as marine research, pipeline monitoring, military surveillance, offshore oil examination and so on, has

J. V. Aravind · S. Prince (✉)
Department of Electronics and Communication Engineering, SRM Institute of Science and Technology, Kattankulathur, Chennai, India
e-mail: shanthip@srmist.edu.in

M. Tiwari et al. (eds.), *Optical and Wireless Technologies*, Lecture Notes in Electrical Engineering 892, https://doi.org/10.1007/978-981-19-1645-8_40

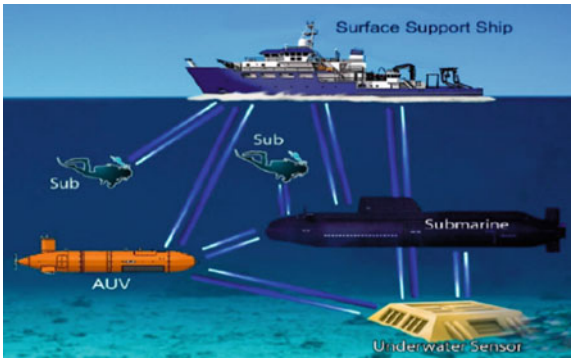

Fig. 1 Underwater applications scenarios [5]

driven demand for high data rate underwater communications. The potential technology may be use for gathering more data from sea bed, for tether free AUVs and ROVs to provides live surveillance from deep water sensors also AUV can function as a data mule, collect data through UOWC subsea sensor networks and Optical links enable submarines to interact more securely with buoys on the sea surface [3] (Fig. 1).

Underwater sensor networks (UWSNs) are utilised as primary technology in several applications viz beacons and ships, which includes numerous sensors and mobile vehicles. Underwater localization is substantial since it is the bedrock for all other capabilities, such as tracking sensor nodes, labelling data, coordinating the motion of cluster nodes, recognizing the underwater objects position [4]. Furthermore, the data collected from AUVs and ROVs such as underwater videos and images is extremely difficult to analyse. However, the regular photos and underwater images are not same due to the poor visibility and attenuation of transmitted light [7]. The absorption and scattering effects decays light exponentially with depth and distance, whereas dispersion shifts light direction [6]. This results in low contrast and blurred images.

Underwater videos and images are used for environmental monitoring to observe animal prosperity and behaviour in the context of in marine habitats [8]. Since humans naturally evaluate their environment visually, optical videos and images provides high quality, high resolution and high extensive information in an easy-to-understand format [8, 9]. Human video analysis takes more time; therefore, some automation is required to handle huge video and image data in a fast and effective way to offer information for taking quick decisions. Recently, two decades computer vision plays a major role for underwater objects detection and tracking using images and videos data from autonomous underwater vehicles and remoted operated vehicles. Due to its vast range of applications and recent technological developments, underwater object detection has gotten a lot of attention in recent years. This topic is being researched extensively in both academic and real-world applications, including security monitoring, robotic vision, autonomous driving, surveillance [10]. Among the multiple

factors and initiatives that have contributed to the rapid evolution of object detection systems, the development of deep convolutional neural networks and GPU computing capability should be noted. Deep learning models are now widely used across the whole area of computer vision, including both basic and domain-specific object detection. With this motivation in this work, we tried with small set of underwater images with one object as class and trained using YOLOv5 object detection deep learning model and studied various parameters in the coming sections.

2 Deep Learning Model

Object detection is the one of the main applications of image processing, it is a method for detecting any stationary or moving object in a real-time instance, such as an image or a video [11]. In recent two decades, Deep neural networks have emerged as the most common approach for high-quality computer vision such as object recognition, classification, and identification, in recent years. For detection purposes, earlier deep learning object identification achievements adopted classifications, in which the algorithm examines each proposed region of the image and conducts a separate classification.

In YOLO model the object detection is considered as a regression issue and directly outputs bounding box coordinates and class confidence score. In comparison to the regional proposal approach, YOLO's design is a simpler approach for object identification, and it also takes significantly less time to compute and the YOLO architecture is shown in Fig. 2. In this study, 35 images are captured using raspberry-pi camera at different angles and augmented data to increase the data set to 80 images in that 86% are allocated to training set, 9% for validating set and 5% for testing set. The Image size is 416 × 416 and in augmentation rotation −15 and +15° are applied and vertical flip, horizontal flip is also done.

The above Fig. 3 shows the Raspberry-Pi with camera module and Fig. 4 depicts camera model for capturing aquarium fish tank data at different angles. The Fig. 5

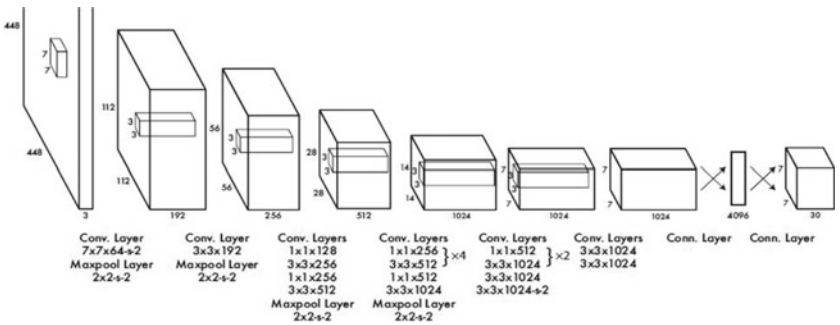

Fig. 2 Yolo architecture [12]

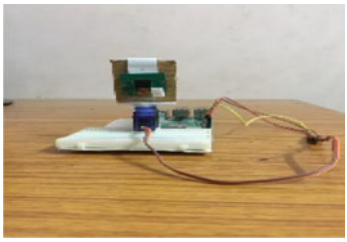

Fig. 3 Raspberry-pi with camera module

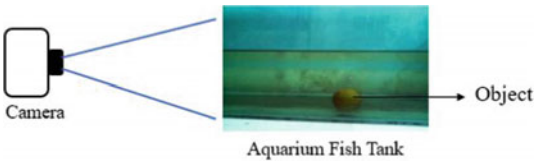

Fig. 4 Capturing image data using camera

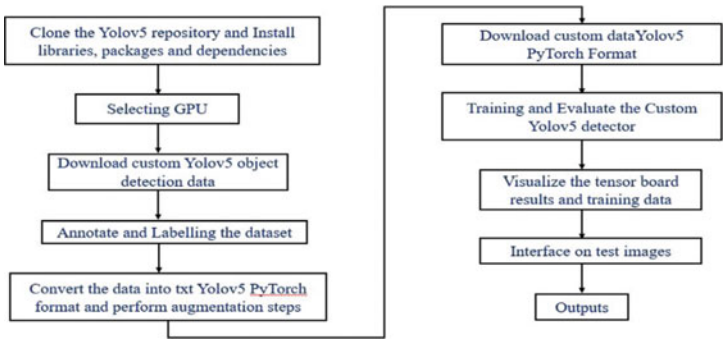

Fig. 5 Flow chart for Yolov5 deep learning model

shows the process of Yolov5 deep learning model. To get started with YOLOv5, cloning the repository and installation of packages and necessities are required. This creates programming environment for object detection training.

To accelerate training time Tesla P100 GPU is selected from colab, custom data is downloaded and then, annotated and labelled data set are converted into txt YOLOv5 PyTorch format. Thereafter, augmentation steps are executed in which -15 and $+15^{\circ}$ rotation, vertical and horizontal flip are used to increase the data set. The customized object data set in YOLOv5 PyTorch format is downloaded. YOLOv5s model is chosen for custom object detection because of less data set. In this work,

416 × 416 image size and batch size of 16 and 100 epochs are selected. After these steps, the training data is evaluated and the ground truth data, augmented data results are visualized. Finally, testing data is fed to YOLOv5 to obtain the predicted results.

3 Experimental Results

The following Fig. 6 shows the sample underwater data set for training and Figs. 7 and 8 displays the underwater data set for validation and testing.

From Figs. 9 and 10 it is clear that both the curves are almost close to 1 but the precision graph fluctuates more due to the limited data.

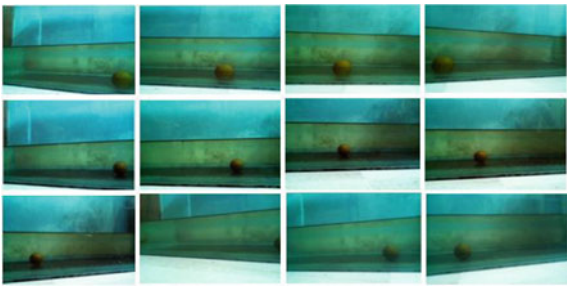

Fig. 6 Sample underwater data set for training

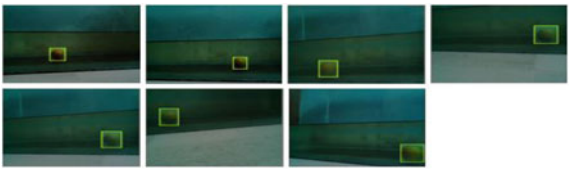

Fig. 7 Underwater data set for validation

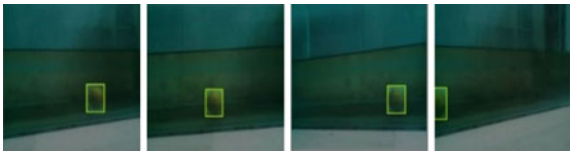

Fig. 8 Underwater data set for testing

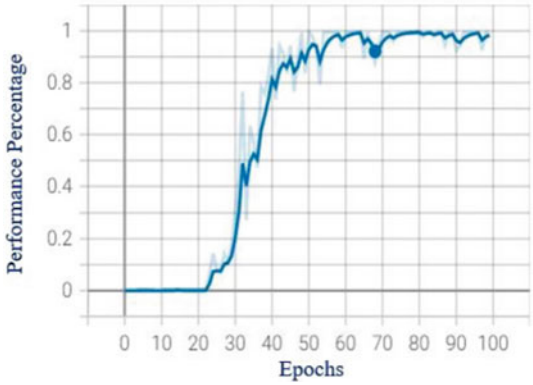

Fig. 9 Mean average precision

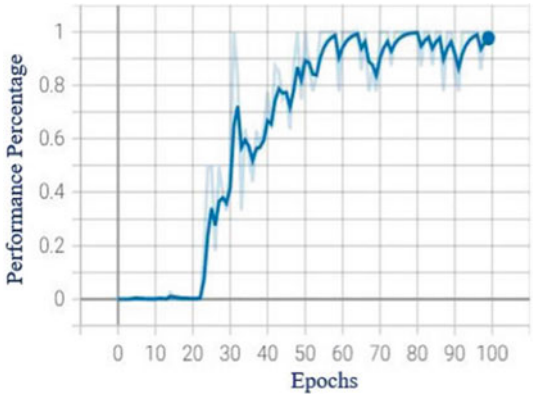

Fig. 10 Precision

From Figs. 11 and 12 shows recall and class loss graphs. It can be observed that as the epochs increase, recall approaches 1, indicating that object is recognised correctly. The class loss graph remains constant because only one class is used.

Figures 13 and 14 shows the bounding box loss and object loss. It is evident from the graphs, bounding box and object loss decreases with increasing epochs. Figures 15 and 16 shows the ground truth data and augmented training data. Figures 17 and 18 shows the predicted and actual results of testing data.

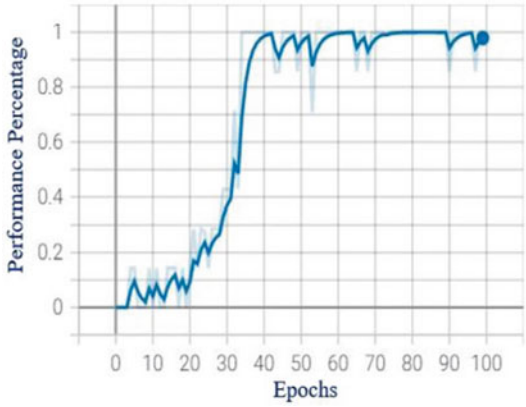

Fig. 11 Recall/sensitivity

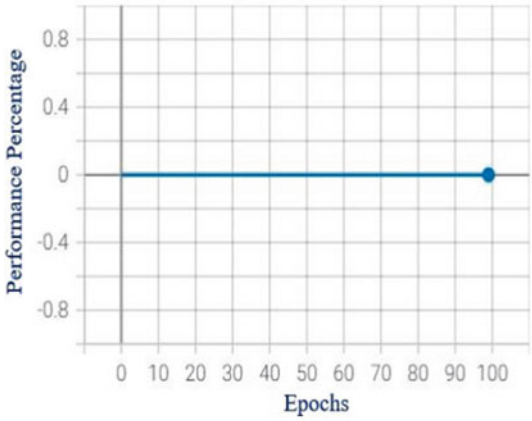

Fig. 12 Class loss

3.1 Parametric Analysis

- Accuracy is a parameter for evaluating classification models. Informally, accuracy is defined as the fraction of correct predictions to the total number of predictions.
  - The following equation can be used to calculate accuracy in terms of positives and negatives for binary classification:

$$Accuracy = \frac{TP + TN}{TP + TN + FP + FN} \tag{1}$$

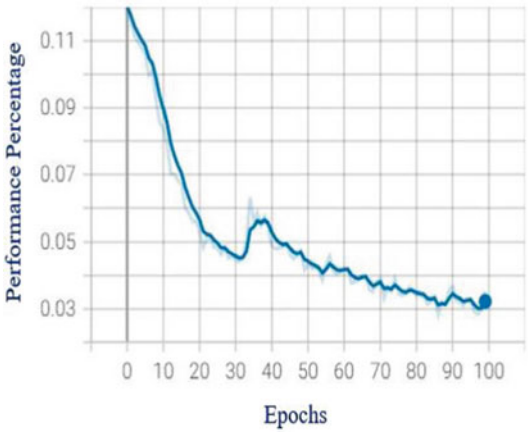

Fig. 13 Bounding box loss

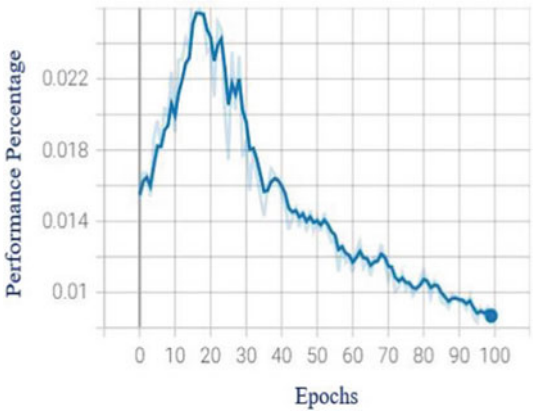

Fig. 14 Object loss

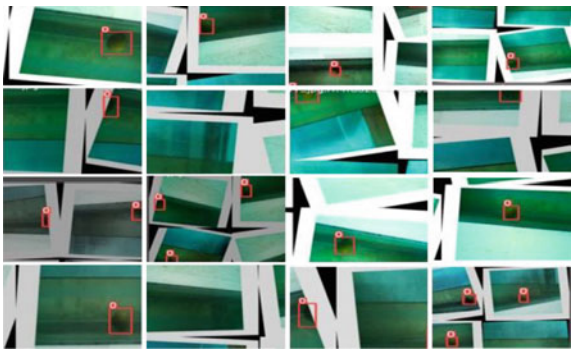

Fig. 15 Ground truth training data

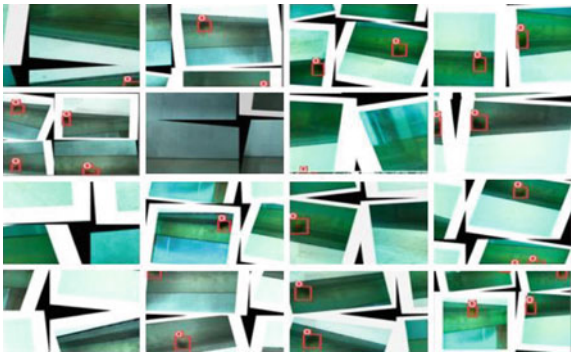

Fig. 16 Augmented training data

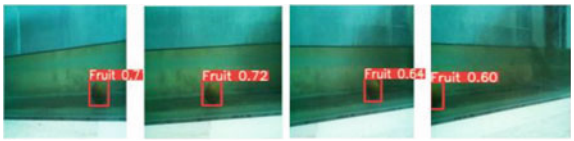

Fig. 17 Predicted results

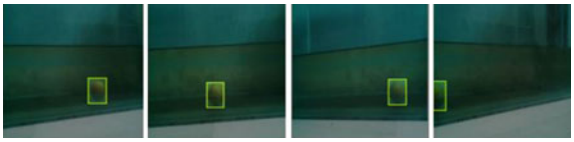

Fig. 18 Actual results

where TP = True Positives, TN = True Negatives, FP = False Positives, and FN = False Negatives.

– Precision measures how accurate a prediction is i.e., the percentage of correct predictions. Mathematically,

$$Precision = \frac{TP}{TP + FP} \tag{2}$$

Note: The precision of a model that produces no false positives is 1.0.

– Recall/sensitivity measures how good we can find all the positives
Mathematically,

$$Recall = \frac{TP}{TP + FN} \tag{3}$$

Note: The recall of a model that produces no false negatives is 1.0.

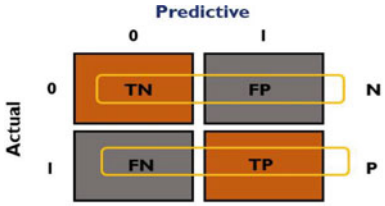

Fig. 19 Confusion matrix

– F1 Score combines precision and recall relative to a specific positive class – The F1 score is a weighted average of the precision and recall values.

$$F1Score = 2 * \frac{Precision * Recall}{Precision + Recall} \tag{4}$$

Note: The best and worst values of the F1 score are 1 and 0 respectively.

Confusion Matrix is a table that is frequently used to define the performance of a classification model on a set of test data with known true values. From Fig. 19 the actual and prediction results the confusion matrix calculations as shown in below to calculate the parameters like accuracy, precision, recall/sensitivity and F1 score.

$$Y_{actual} = [1, 1, 1, 1],\ Y_{predicted} = [1, 1, 1, 0]$$

Array ([0,01,3])

$$\text{TP} = 3;\ \text{FP} = 0;\ \text{TN} = 0;\ \text{FN} = 1$$

$$Accuracy = 0.75,\ Precsion = 1,\ Sensitivity = 0.75,\ F1\ Score = 0.85$$

4 Conclusion

In this research, Yolov5 deep learning model is trained with raw underwater image dataset captured using camera at different angles to detect the single class object. We attained decent results with accuracy of 75%, recall of 75% and F1 score of 85%. We also presented the actual and predicted outcomes of the model. In future, we will attempt to identify multiple classes with more dataset in different underwater conditions to improve the training and accuracy of the model.

Acknowledgements The authors express gratitude to Naval Research Board and the Defence Research and Development Organization (DRDO) of India for funding this study and SRM IST provided infrastructural support to the authors and also we would like to thank B.tech students for acquiring the data.

References:

1. Lin T, Huang N, Gong C, Luo J, Xu Z (2021) Preliminary characterization of coverage for water-to-air visible light communication through wavy water surface. IEEE Photon J 13(1):1–13
2. Su X, Ullah I, Liu X, Choi D (2020) A review of underwater localization techniques, algorithms, and challenges. J Sensors **2020**
3. Du J, Hong X, Wang Y, Xu Z, Zhao W, Lv N, Fei C, He S (2020) A comprehensive performance comparison of DFT-S DMT and QAM-DMT in UOWC system in different water environments. IEEE Photon J 13(1):1–11
4. Ullah I, Chen J, Su X, Esposito C, Choi C (2019) Localization and detection of targets in underwater wireless sensor using distance and angle based algorithms. IEEE Access 7:45693–45704
5. Spagnolo GS, Cozzella L, Leccese F (2020) Underwater optical wireless communications: overview. Sensors 20(8):2261
6. Yao J, Han F, Zhu H (2019) Underwater image processing and object detection based on modified YOLO method. In: The 29th international ocean and polar engineering conference. OnePetro
7. Sung M, Yu SC, Girdhar Y (2017) Vision based real-time fish detection using convolutional neural network. In: OCEANS 2017-Aberdeen. IEEE, pp 1–6
8. Xu W, Matzner S (2018) Underwater fish detection using deep learning for water power applications. In: 2018 International conference on computational science and computational intelligence (CSCI). IEEE, pp 313–318
9. Murphy HM, Jenkins GP (2010) Observational methods used in marine spatial monitoring of fishes and associated habitats: a review. Mar Freshw Res 61(2):236–252
10. Jiao L, Zhang F, Liu F, Yang S, Li L, Feng Z, Qu R (2019) A survey of deep learning-based object detection. IEEE Access 7:128837–128868
11. Mahavarkar A, Kadwadkar R, Maurya S, Raveendran S (202) Underwater object detection using tensorflow. In: ITM web of conferences, vol 32. EDP Sciences, p 03037
12. Redmon J, Divvala S, Girshick R, Farhadi A (2016) You only look once: unified, real-time object detection. In: Proceedings of the IEEE conference on computer vision and pattern recognition, pp 779–788

Internet of Lighting for Smart Cities

Lingala Thirupathi, A. Rajesh, and R. Sandeep

Abstract The term smart is an acronym for the five components, which are unique, observable, practicable, appropriate and time-based. The Internet of Things (IoT) identifies the widespread and increasing number of wireless devices as the trillions of networks of a potentially global scale running today. When the planet expands quicker, people are drawn to this clever term. India is one of the world's fastest-growing economies. The IoT offers innovative services and stimulates market shifts. The lighting industry often welcomes this transition by developing an Internet of Lighting (IoL). The term smart lighting describes three important design attributes: advanced control, solid state, and broad network connectivity in accordance with international standards. It provides an optical networking gateway as an additional function that enables coexistence with traditional Wi-Fi. In this context, various IoT-compatible wireless communication interfaces are being used to meet the lighting's needs. Related IoT systems are forecasted to expand dramatically in the entire smart housing and industrial sectors in the coming years. This paper presents the numerous options for creating and implementing IoT-based smart lighting solutions, issues related to interoperability and on-line services are addressed.

Keywords IoT · IoL · Sensor · Smart cities

1 Introduction

With regard to the illumination, a lot of focus lately, the shift has moved from bright, manufactured lights to dynamic and portable ones that can emit light in various ways to those that are both dynamic and photonic designs and come in organic. To start, this campaign, we will be implementing highly automated sensing, control algorithms and communication mechanisms on massive fleets of smart and connected vehicles to harness the power of the IoT [1]. A lighting system that improves visual comfort while also has the goal of reducing energy consumption or is designed to be adaptable

L. Thirupathi (✉) · A. Rajesh · R. Sandeep
CSE Departemnt, Methodist College of Engineering and Technology, Hyderabad, India
e-mail: thiru127@gmail.com

M. Tiwari et al. (eds.), *Optical and Wireless Technologies*, Lecture Notes in Electrical Engineering 892, https://doi.org/10.1007/978-981-19-1645-8_41

to your needs is in this manner Diverse smart lighting systems incorporate advanced illumination sensors and real-time spectral measurement as well as well as diverse applications that communicate using various protocols and options including light communications devices that support color sensors and micro spectrometers [2]. This is true for the most sophisticated lighting systems; they have lighting features beyond what's needed for the usual illumination. This ability relates to spectrally tunable functionality, as well as expanded control capability that enables the system to be remotely monitored and controlled from the Internet, opening up a whole new and fresh view of possible configurations to test system devices. Solid state lighting (or compact fluorescents) is a more effective option for most residential and commercial spaces. Declining year over year, but that is changing in small ways only.

In part due to advancements in technology, this statement is becoming increasingly likely due to our ability to predict how much light is emitted by an Light Emitting Diode (LED) will produce. Non-polluting LED-based systems also have been shown to be very advantageous in recent/current and future applications; additionally, Life Cycle Analysis (LCA) studies demonstrate that LEDs provide a net positive period of light expansion [3]. Smart lighting solutions remain relatively dynamic due to the importance of the industry in advancing features. It relates to the independent sensing capability, scalability, as well as [4] connecting the broader IoT market segments and various nodes, are expansion, extensibility, and interoperability with different application specific segments. Multi-level security mechanisms are developed in graph databases and encapsulated data frames [5][6], The technology evolving to detect early leaf diseases using neural networks and machine learning techniques [7, 8] and the survey on security issues, solutions in IoT are discussed [9]. Protection of cloud [10], framework to detect and mitigate attacks and in wireless sensor networks, ransomware avoidance techniques [11–18]. The internet revolution, impact, technology road map and features and advances in mathematics are discussed [19].The authors argues for a paradigm shift in the QoE area to cover the relationship between humans and intelligent machines [20], The authors computes an empirical model of the Immunity Region, where the level of interference does not affect LoRa communication [21]. The potential benefits as well as the challenges associated with IoT for cities are discussed [22], this paper browses the semantic annotation of the sensors in the cloud, and innovative services can be implemented and considered by bridging Cloud and IoT [23–26], In the [27], various concepts of the smart healthcare system are explored in details while bringing into the perspective of the current trends in smart healthcare systems, The authors reviewed the state-of-the-art RFID technologies in IoT Smart Homes applications [28], The authors proposed a low cost future STS to provide better service by deploying traffic update instantly in the smart cities by using the different technologies [29–31].

2 Existing Lighting Standards

Decades via constant voltage, various lighting standards like Digital Addressable Lighting Interface (DALI) and the IoT allows for many more automation technologies to be interconnected to become easily accessible and for the home. Additionally, the use of these systems has been expanded to include a larger areas and applied to entire buildings (e.g. industrial control, building automation), as in Building Automation and Network Control (BACnet) and European network standard (KNX) as opposed to systems (such as DALI), that are focused on small, specific areas (like lighting controls). Using DALI could monitor the rest of the building automation, expanding on lighting could use a higher-Net protocol. When this type of combination is possible, it is done by the use of gateways that convert communication protocols, data formats, and semantics. Additionally, these networks are incompatible with BACnet: Due to their inherent incompatibility, inter-ability problems are not so easy. Additionally, the existing standards all have a light effect on the market in a very insignificant way, measurable way, which allows for highly fragmented markets. Network for automation and control purposes that has a few predefined messages. Ancillary Research/data link/physical layer (layers) is defined by the BACnet protocol, including Attached Resource Computer NETwork(ARCNET), point-to-to- point, Ethernet as well as others. Since the demand for these applications has increased in recent years, it is currently used more frequently in the heating, cooling, and ventilation markets, but because of the difficulty and the expense per light-related issues, it is not in lighting controls. We believe that no other commercial vendor has adopted this technology even though it is defined in the industry standard, although it's highly safe. The KNX is in Europe is more common in the home and building control sector than it is in North America. Twisted Pair (TP) is the major means of long-distance interconnectivity within a wired Ethernet. In addition to these three other media, such as radio frequency (RF), infrared and Ethernet (which is known as RF Expand) are also access to the network had never been established was a major issue.

The communications and interoperability features were adopted by ITU ISO/IEC 14908 became standardized under this name. A communications protocol useful for high, especially for building automation systems on low bandwidth, which are usually, relies on twisted-pair technology, for networking devices over optic fibers, power lines, and for electronic devices over RF. Due to the proprietary design and lack of extensibility, the product's marketability was greatly reduced. All devices of a DALI system must be contained inside the control gear or connected to it in some way. As ideally, however, there is no definition for what is meant by protection that is offered by DALI. Given the strong point and extensive benefits of being extended to the IoT, expanding these lighting principles to include these features is a choice even in cases like most business process and industry software applications, a diverse range of specifics are needed, such as interoperability. This unusual complexity, the use of restrictions, along with a less-complex underlying programming model, an infeasible for integrating with existing libraries, and no protection system, result in an enormous interoperability issues. With regard to this, a new lighting standard which

is more suitable for network and power-constrained devices, as well as supporting self-expanding devices, is needed.

3 Objectives of the IoT Lightening Standard

3.1. Preservation approach: It's through IP that a service-oriented methodology can be developed. One application may be communicating with different networks at the same time, as a network is made to support multiple purposes. Bidirectional, heterogeneous devices and protocols are supported in IP. Interoperability in the end points and the points is offered via IP offers the ability for each end device to communicate without translation and for the transfer of data. Several types of applications and tools, including diagnostics and management tools are now available and the IP framework is better served by incorporating the inventions and innovations of the worldwide community. Additionally, Internet Protocol provides the most effective encryption.

3.2. Community-friendly: All applications (programs and practices) of lighting and building control open to multiple users. There is no other way to do, so expand other than having open standards, as it would provoke doubt by potential adopters the availability and license terms such as monopolistic or patent-based security. Diligence would stop investments and third-party growth, giving rise to an ecosystem of components and services, along with the presence of third-party vendors. Additionally, one can only build blocks that are made from other blocks which have already been constructed in place, rather than constructing all the individual blocks from scratch. Thus, this will aid the productivity and lower the production costs by reducing the time and effort required for standardization. For standardization to work, it must be developed in a way that can accommodate new technologies and patterns of behavior while still retaining its value.

3.3. The ability to detect security violations and their deleterious consequences as well as the use of basic and useful recovery methods are required for stable information systems. In addition, privacy requirements must be supported by the system, which include the right to remove and modify personal data or the ability to erase all of it. In order to ensure both privacy and data sharing, various safeguards must be put in place. Additional power in a modern lighting system, which is referred to as control, delivery, and interface logic puts additional strain on the electronic components that run the system. There is no danger that the overall energy performance of the IP network would be exposed by the use of Internet users.

4 Proposed Method

Variety of lighting solutions include various devices, networks, forms of networks, and numerous components, sensors are the most common, algorithms the next, and everything else is in between. Lighting control systems are sophisticated enough to analyze the day, light spectrum, which is provided by different lighting systems, or occupancy to determine the ultimate response. In certain instances, algorithms can run within devices or systems to take on the workload or handle tasks that have already been assigned to them. They may also be run outside the computer or in the cloud, which relieve device system constraints from having to send command messages. The word algorithms can refer to several cutting-edge technological solutions that are constantly shift colors, such as tunable lights, techniques that control the color response, real-time color adjustments, and techniques that help to reduce energy consumption This is becoming more important in the market due to the growing popularity of smart lighting systems that allow individuals to adjust their circadian rhythms and improve human performance and attention levels of concentration. Often, people use visually complicated lighting patterns in response to circadian rhythms. There are the key components of the design seen in the first lighting design schematic in Fig. 1.

Biases of the mind are an important aspect of autonomous algorithms attempt to adjust lighting are trained to respond to user preference and gender rather than strict input design specifications. Historically speaking, in the past decade, it has been demonstrated how lightweight influences both the biological clock that governs our circadian cycles and many other processes, such as the secretion of hormones, the body's temperature, and how it can control the production of circadian awareness.

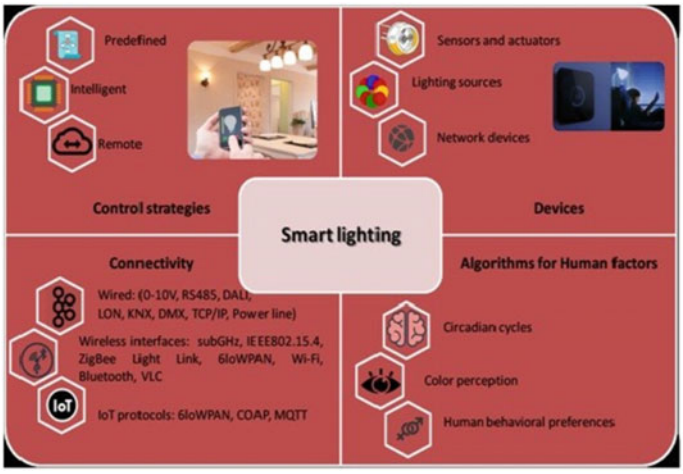

Fig. 1 Key elements for smart lighting systems

Since luminescence is the essential for circadian rhythms, and not the color correction, the range of light frequencies, from the red to the blue end of the spectrum is more prominently features this. Since it is possible to influence and manipulate a number of physiological properties through the system. Besides having total power over the human color light, the museum is also benefitting in various other fields including horticulture, fine arts, and places of assembly, which are having total spectrum control. The physical and logical levels can be seen to interact in a network at the system device level, as well as at the device hierarchy. Reliability can be increased; the practice of using various physical topologies, such as a loop, stars, or using a mixture of both star and bus is creative, resulting in various expansion possibilities. In physical installations, various types of communication networks can be laid over traditional ones by either using cables or wireless connection.

We may access the network using a local or remote network management system, such as a wired or wireless interface. The numbers of various lighting items on the market have been connected with an option to provide different networking solutions in the IoT ecosystem so as to perform better serve a wider range of purposes. These are typically found on home lighting, audio and control, 0-10V, DALI, Digital Multiplexer (DMX), Local Area Network (LAN), and power line communication are the main wired interfaces used for networking. Not only that, they use various networking interfaces including Wireless Fidelity (Wi-Fi) and infrared, but they implement wireless technology as well, such as Bluetooth, and infrared.

4.1 Sensors for Smart Lighting Platforms

In current IoT applications, the focus is shifting from standard control methods to use of digital sensors to adjust lighting mechanisms to assist in adaptive operation. If you know of light sensors and photodiodes which are sensitive to lower intensities, warn you when it's getting dim. Red, green and blue sensors are utilized for LED lighting and compact fluorescent lamp (CFL) that seek to detect their primary color, producing color mixing Red Green Blue (RGB) material as in indoor environments as well as in optical connections, but for wireless purposes the most important photo diode works technologies are visible light communication (VLC) and frequency modulation (FM) (Fig. 2).

4.2 Security View

All Open systems are networked and connected to the internet, so they are highly available to the user and can be used wherever they are at risk of being hacked, unauthorized access to the data. It has been included into the design as an intrinsic part of the device, and is entirely independent of firewalls. It has three security frameworks which can help expand the scope of the original internet security (IS), application:

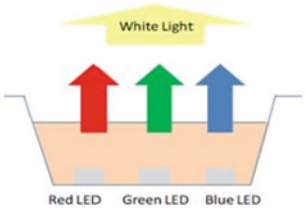

Fig. 2 Creating white light by mixing individual red, green and blue LEDs

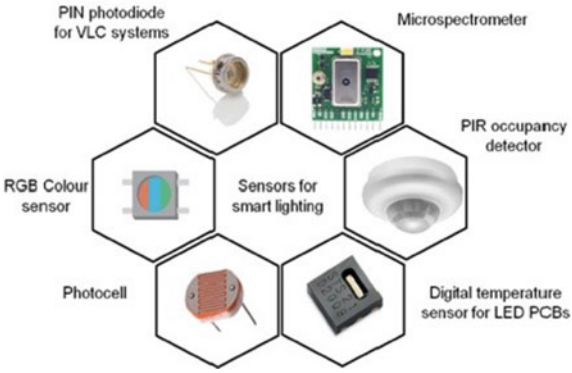

Fig. 3 Sensor technologies embedded in smart lighting

authorization, authentication, and confidentiality are offered by the internet; while additional security for the device, privacy and from attacks is offered. In order to ensure wireless security, always use a connection layer; if we use a wired links, then we can or may add an encryption layer on demand. Device to cloud Datagram Transport Layer Security (DTLS) communications take place in the framework (Fig. 3).

4.3 Communication Interfaces for Smart Lighting in the Cities

The most important aspect of a professional lighting system is a universal connectivity link, usually a wired or wireless interface. For essential infrastructures and street lighting, DALI, Power Line Connectivity, and Ethernet are necessary. Non-critical infrastructure lighting applications and systems can use several protocols, such as Wi-Fi, ZigBee or the system used in commercial traffic management. Since different technologies have advantages in different settings, these indoor LED light smart

lighting platforms prefer to use the IEEE 802.15.4, Bluetooth low energy, or sub-GHz protocols. ZigBee Light Link and 6WAN both use the same Media Access Point (AP) and super AP Layer of the IEEE 802.15.4.

The solution to the interoperability issue involves standardization of protocols to link different device types of lighting, which are useful in cases where an open ecosystem with incompatible protocols are acceptable and the devices with closed ecosystems are impractical. In this case, an extension of the interoperability is possible by using protocols such as the use of the Application Programming Interface (API) and media path quoting using both IPv4 and IPv6. In addition, if energy restrictions were applied to LED lighting devices, lightweight protocols such as Bluetooth low energy (BLE) or ZigBee light connection could be used to solve the problem. In the case of outdoor lights that are typically operated using conventional wired networking options such as Power Line Communication (PLC) or DALI connectivity options for protocols are found for beyond the scope. The Li-Fi (which means light and free of burden, but which is also known as modern wireless) focuses on transmission that is as well as the ability to provide illumination from artificial light sources. This technology takes advantage of the fact that there are only three light frequencies (380–780 nm) that make it possible to make visible by adding digital modulation to the light wavelengths that exist. There are many benefits of using LEDs, such as their inexpensive manufacture and the ability to operate in a wide frequency spectrum. Their uses include optical communications like Li-Fi, and their usability as a result further supports general lighting use, but they also further promotes other applications, like signaling. Low interferences are the key for visible light-based equipment, and high security is needed because of radio frequency radiation.

To further protect the VLC transmission even when the transmitter is located in an indoor space, time synchronization is provided. When white light is needed, RGB LEDs, phosphor coated LEDs are the most common LEDs used, and when used as backlights, with the recent advancement of OLEDs. For short range links, test beds are built between the source and receiver to monitor changes that occur between the link range, testability limits and across the link range.

5 Open Issues and Future Research

Most of the suggested application schemes and invention proposals are built on ZigBee, 6WAN. Recently, there has been an increase in interest in Low Rate Distant Area Network (LoRa) in many IoT application domains because of which, it allows devices to communicate with each other at a lower power usage but various different methods and protocols used in the construction of an street lighting system (SLS) network are needed to speak to one central lighting device.

It is essential to look at future-oriented thus creating a common communication protocol for IoT devices that can combine different Super Luminescent Emitting Diodes (SLED) schemes is one of the next big areas of IoT development smart street lighting system (SSLSs) would often takes charge of the system into their own

hands, reducing the level of system administration required, but administration and monitoring would be distributed as part of the majority of the projects.

The idea of the intelligent city focuses on connecting the various applications in order to increase the overall efficiency of urban infrastructure. Autonomous traffic solutions can turn out to be more expensive, but if it incorporates a well-managed smart technique, such as expanded intelligent capacity, it can be a cost-effective way to deal with them. The implementation of various environmental sensors (e.g., rain sensor, temperature sensor, moisture sensor, etc.) in SLS will provide the opportunity to make intelligent weather systems. Furthermore, attackers may have access to confidential information, which can lead to malicious attacks. An intruder can also conduct a sensor-based attack that will compromise the operational capacity of an SLS. It is a difficult problem because new protection measures would have to be studied for lighting control equipment. As of yet, the protocols are not fully developed, the encryption scheme is too immature or poorly specified to solve security concerns including key management and key-revocation issues need to be addressed. Not only to safeguard user privacy, but also to keep it confidential, it may be possible to use confidentiality to protect the data. Protection would be sacrificed if the systems are less powerful and cheaper than more powerful and more efficient technologies. Although strong security measures in communication protocols might affect system efficiency, making them weaker will decrease the overall security. On the other hand, if the implementation of the security mechanism is not executed correctly, disastrous results could occur. It is important to consider these problems when implementing an SLS.

6 Conclusion

All smart lighting is expected to have a huge impact in the next few years due to the utilization of LED drivers, sensors and platforms that are linked to the LED and numerous applications. An organization strives to get their lights connected to the IoT, there are various vendors behind this push to scale network functionality, expanding existing and adding new data layers and connections. Integrating LED lighting and other than those pertaining to health and wellness with systems that include circadian sensing is essential, and should be prioritized as well, since in addition to anything else they can contain information about time and place, they also provide data on environment. Wired and wireless networking also implies that lighting controls must be online, so it is not possible to take full advantage of wireless lighting systems since they can't take advantage of free lighting controls. As the complex world of wireless communications is in general is changing, organizations need to keep pace with the IoT and sophisticated lighting systems, product offerings must be altered as well when present in locations where a diverse network of devices calls for an expanding base of the proprietary protocols exists.

References

1. Alzain MA, Soh B, Pardede E (2011)MCDB: using multi-clouds to ensure security in cloud computing. In: 2011 IEEE ninth international conference on dependable, autonomic and secure computing, pp 784–791. https://doi.org/10.1109/DASC.2011.133
2. Agrawal D, Abbadi AE, Emekci F, Metwally A (2009) Database management as a service: challenges and opportunities. In: 2009 IEEE 25th international conference on data engineering, pp 1709–1716. https://doi.org/10.1109/ICDE.2009.151
3. ALzain MA, Pardede E (2011) Using multi shares for ensuring privacy in database-as-a-service. In: 2011 44th hawaii international conference on system sciences, pp 1–9. https://doi.org/10.1109/HICSS.2011.478
4. Buyya R, Yeo CS, Venugopal S, Broberg J, Brandic I (2009) Cloud computing and emerging IT platforms: vision, hype, and reality for delivering computing as the 5th utility. Fut Gener Comput Syst 25(6):599–616. ISSN 0167–739X, https://doi.org/10.1016/j.future.2008.12.001
5. Thirupathi L, Rao VNp (2021) Multi-level protection (Mlp) policy implementation using graph database. Int J Adv Comput Sci Appl (IJACSA) 12(3). https://doi.org/10.14569/IJACSA.2021.0120350
6. Thirupathi L., Rao PVN (2020) Developing a multilevel protection framework using EDF. Int J Adv Res Eng Technol 11(10):893–902. http://iaeme.com/Home/issue/IJARET?Volume=11&Issue=10
7. Pratapagiri S, Gangula R, Ravi G, Srinivasulu B, Sowjanya B, Thirupathi L (2021) Early detection of plant leaf disease using convolutional neural networks. In: 2021 3rd international conference on electronics representation and algorithm (ICERA), pp 77–82. https://doi.org/10.1109/ICERA53111.2021.9538659
8. Gangula R, Thirupathi L, Parupati R, Sreeveda K, Gattoju S (2021) Ensemble machine learning based prediction of dengue disease with performance and accuracy elevation patterns. Mater Today Proc. ISSN 2214–7853, https://doi.org/10.1016/j.matpr.2021.07.270
9. Rekha S, Thirupathi L, Renikunta S, Gangula R (2021) Study of security issues and solutions in Internet of Things (IoT). Mater Today Proc. ISSN 2214–7853, https://doi.org/10.1016/j.matpr.2021.07.295
10. Nalajala S, Thirupathi L, Pratap NL (2020) Improved access protection of cloud using feedback and de-duplication schemes. J Xi'an Univ Arch Technol XII(IV):1585–1594. https://doi.org/10.37896/JXAT12.04/897
11. Thirupathi L, Rao PVN (2020) Protected framework to detect and mitigate attacks. Int J Anal Exp Modal Anal XII(VI):2335–2337
12. Thirupathi L, Rekha G (2016) Future drifts and modern investigation tests in wireless sensor networks. Int J Adv Res Comput Sci Manag Stud 4(8)
13. Thirupati L, Pasha R, Prathima Y (2014) Malwise system for packed and polymorphic malware. Int J Adv Trends Comput Sci Eng 3(1):167–172
14. Thirupathi L, Ashok G, Mahesh T (2014) Traffic congestion control through vehicle-to-vehicle and vehicle to infrastructure communication. (IJCSIT) Int J Comput Sci Inf Technol 5(4), 5081–5084
15. Reddemma Y, Thirupathi L, Gunti S (2009) A secure model for cloud computing based storage and retrieval. SIGCOMM Comput Commun Rev 39(1):50–55
16. Thirupathi L, Nageswara RPV (2018) Understanding the influence of ransomware: an investigation on its development mitigation and avoidance techniques. Grenze Int J Eng Technol (GIJET) 4(3):123–126
17. Lingala T, Ravikanti S (2017) Social media: to deal crisis circumstances. Int J Innov Adv Comput Sci (IJIACS) 6(9)
18. Srividya V, Swarnalatha P, Thirupathi L (2018) Practical authentication mechanism using passtext and OTP. Grenze Int J Eng Technol Grenze ID: 01.GIJET.4.3.27
19. Gowda D, Sridhara B, Naveen KB, Ramesha M, Pai G (2020) Internet of things: internet revolution, impact, technology road map and features. Adv Math Sci J 9:4405–4414. https://doi.org/10.37418/amsj.9.7.11

20. Minovski D, Åhlund C, Mitra K (2020) Modeling quality of IoT experience in autonomous vehicles. IEEE Internet Things J. https://doi.org/10.1109/JIOT.2020.2975418.
21. Márquez L, Osorio JA, Calle M, Vélez J, Serrano A, Candelo-Becerra J (2019) On the use of LoRaWAN in smart cities: a study with blocking interference. IEEE Internet Things J. https://doi.org/10.1109/JIOT.2019.2962976
22. Kamel Boulos M, Al-Shorbaji N (2014) On the Internet of Things, smart cities and the WHO Healthy Cities. Int J Health Geograph 13(10). https://doi.org/10.1186/1476-072X-13-10
23. Petrolo R, Loscri V, Mitton N (2014) Towards a cloud of things smart city
24. Bhatt D, Kumar S (2018) Internet of Things: smart device for smart city. Int J Comput Appl 181:1–4. https://doi.org/10.5120/ijca2018917593
25. Solami E (2021) Replication-aware secure resource administration scheme for Internet of Things-smart city applications. Trans Emerg Telecommun Technol 32. https://doi.org/10.1002/ett.4200
26. Hirz M (2015) Internet of Things - smart mobility in smart cities
27. Njoki K (2020) Internet of things-Smart Healthcare system. Health and Technology
28. Alsinglawi B, Elkhodr M, Nguyen Q, Gunawardana U, Maeder A, Simoff S (2017) RFID localisation for internet of things smart homes : a survey. Int J Comput Netw Commun 9:81–99. https://doi.org/10.5121/ijcnc.2017.9107
29. Sharif A, Li J, Khalil M, Kumar R, Sharif M, Sharif A (2018) Internet of things — smart traffic management system for smart cities using big data analytics. https://doi.org/10.1109/ICCWAMTIP.2017.8301496
30. Medavaka A, Kiran S (2019) A comprehensive survey in internet of things smart applications 8:450–458
31. Sun H, Wang C, Ahmad BI (2017) From internet of things to smart cities: enabling technologies. https://doi.org/10.1201/b20595

The IoT in Security Architecture, Challenges, and Solutions

Anita Punia, Manish Tiwari, and Sourabh Singh Verma

Abstract The Internet of Things (IoT) is a forerunner to the smart world, as it uses ubiquitous computers and networking to simplify and supply other services, such as easy monitoring of many phenomena in our environment. Environmental and everyday goods referred to as things, objects, or machines, are improving with computing and communication technologies in the Internet of Things. An IoT architecture may provide a variety of solutions for various industries, but its primary goal is to establish a functioning, scalable, flexible, maintainable, and cost-effective IoT ecosystem. This paper analyses the challenges of security and their solutions and presents well-defined security architecture as confidentiality of the privacy and security of the user, which could result in its wider mass acceptance.

Keywords Internet of things · Privacy · Confidentiality · Security · Challenges

1 Introduction

The Internet of Things is a rather straight forward concept: it entails linking all physical places and things on the planet to the internet. IoT is one of the impending ideas of mechanical advancement in the field of organizations, which is help not just in the modern turn of events yet additionally in the everyday existence of an individual. The internet of Things (IoT), is an arranged interconnection of ordinary items of sensors fully intent on interfacing with everything [1]. The methods of protection employed to secure internet-connected or network-based devices are referred to as

M. Tiwari · S. S. Verma
Department of Electronics and communication Engineering, Manipal University Jaipur, Jaipur, India
e-mail: manish.tiwari@jaipur.manipal.edu

S. S. Verma
e-mail: ssverma80@gmail.com

A. Punia (✉)
Department of Computer and communication Engineering, Manipal University Jaipur, Jaipur, India
e-mail: annubhariya@gmail.com

M. Tiwari et al. (eds.), *Optical and Wireless Technologies*, Lecture Notes in Electrical Engineering 892, https://doi.org/10.1007/978-981-19-1645-8_42

Table 1 A comparison of previous papers

Reference	Architecture	Technology	Security	Applications	Protocols for information
[1]	√	√	√	×	×
[5]	√	√	√	×	×
[7]	√	√	√	×	×
[9]	√	√	√	√	×
[10]	√	×	√	√	×
[11]	√	√	√	√	×
[12]	√	√	√	√	×
[13]	√	×	√	×	√
[14]	√	×	√	√	×
[15]	√	×	√	√	×
[16]	√	√	√	√	×
[17]		√	√	√	√
[18]	√	√	√	√	√

IoT security. The internet of things (IoT) refers to a situation in which all objects are connected to the internet via information sensing devices for intelligent identification and management [2]. The essential objective of this article is to give a comprehension of IoT security concerns. A human with a heart monitor implant, a farm animal with a biochip transponder, or some other man-made object with a specific IP address and the ability to link to the network for data transmission can all considered things in the internet of things [3]. This paper discusses a high-level overview of the Internet of Things, including its architecture, threats, and security issues. Concerns about security issues theoretically, these problems are investigated using criteria such as authenticity, integrity, availability, and confidentiality. To show the on-going study, we use to filter the number of publications from 2013 to 2018. The various publications in emerging IoT applications are shown in Fig. 1. Many engineering opportunities have arisen because of the rapid growth of IoT technology. The rapid development of IoT technology has generated numerous engineering and scientific opportunities as well as challenges. It calls for increased research efforts from a variety of industries, including academia, business, and government. The combined efforts of these sectors should inevitably result in the creation of new protocols, architectures, and services that are desperately needed to meet the IoT's challenges. The paper is organized as; the architecture of IoT has been presented in Sect. 2. The security risks are discussed in Sect. 3. Section 4 focuses on the security issues, parameters, and solutions that IoT faces. Finally, Sect. 5 summarizes the paper with a conclusion (Table 1).

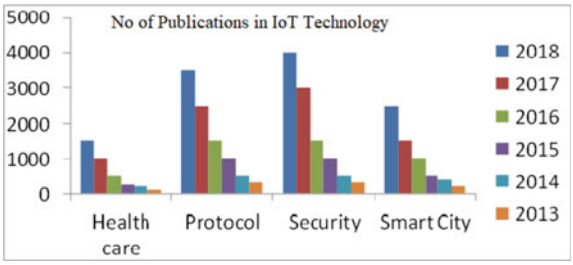

Fig. 1 The number of publications in the areas of IoT protocols, security, and emerging applications is increasing

2 IoT Architecture

The principal concepts of the Internet of Things are characterized by the four-layer architecture. The phrase "internet of things" is made up of two words: "interconnected networks" and "things," which demonstrate certain artifacts. However, at the point when these two terms are combined, they form a “global network of networks. Interconnected objects, each with its unique address, are based on a protocol for regular communication [4]. The layered architecture of IoT is described in this paper, which gives an idea of the fundamental architecture of IoT. The perception layer, Network layer, procession layer and Application layer are the layers that make up IoT [5, 6]. As seen in Fig. 1, all four layers have a large amount of data and different enabling technologies and functionality.

(i) **The perception layer:** The principal layer of IoT engineering is this. An assortment of sensors and actuators are utilized in the insight layer to gather helpful data like temperature, dampness content, interloper location, vibrations, etc.

(ii) **The network layer:** The layer ties the vision and middleware layers, as the name infers. It utilizes organizing advances like 3G, 4G, UTMS, Wi-Fi, and others to get information from the discernment layer and move it to the middleware layer.

(iii) **The procession layer:** The Middleware Layer contains progressed highlights like stockpiling, calculation, handling, and activity taking. It saves all information and sends it to the suitable PC dependent on the gadget’s location and name.

(iv) **The application layer:** Given data assembled from the middleware layer, the application layer handles all application measures. Sending messages, setting off cautions, security frameworks, turning on or off gadgets, brilliant watches, shrewd horticulture, and different assignments are all important for this application.

The list of several IoT technologies used to complete our analysis of the IoT architecture models. Similar layers of architecture (Table 2).

Table 2 IoT technologies

Communication technologies	
Short-range	RFID, Zig Bee, ANT, Z-Wave, NFC, Bluetooth, ANT
Medium range	QR Code, WiMAX, DASH7, Ethernet, EnOcean
Long range	3G/4G, GPRS, Satellite GPS, LTE, G Lora WAN GSM.
Prototype hardware	
Arduino Yun, Raspberry Pi, Arduino Uno, Hackberry, PCDuino, Cubie Board, The Rascal, Pinoccio , Beagle Bone Black, Pinoccio, Pinoccio	
Operating system	
Nano-RK, Tiny OS, Contiki, Mantis, Free RTOS, SNAP OS, Abacus OS	
Protocol	
6LoWPAN, REST, MQTT, LoRa, DTLS, Lora WAN, XMPP-IoT, SSI	

3 IoT Challenges

3.1 Security Threats and Challenges in the Internet of Things

There are three types of IoT risks:

1. Risks that is characteristic of any device on the internet.
2. Risks associated with IoT device.
3. Protection to ensure that no damage is caused, for example, by misuse of actuators.

Standard security rehearses, for instance, getting open ports on contraptions to have a spot with the essential arrangement (for example, a fridge related to the Internet to send alerts about the thing stock and temperature may use an unsteady SMTP labourer and can be sabotaged by a botnet). We will shortly audit some principle challenges.

Scalability: Scalable security solutions are needed to handle a great number of IoT nodes.

Connectivity: Another difficulty in IoT communications is to connect various ML / Devices with different capabilities in a safe manner.

End-to-End Security: OSCORE involves the use of a key exchange protocol to create a security context. However, this protocol should take into account the needs of restricted scenarios (e.g., LPWAN), as well as end-device computation and storage limitations [13].

Authentication and Trust: This forestalls a certainty connection between IoT elements from being formed, which is essential for IoT applications requiring specially appointed contact, such as the Smart City scene, between IoT components.

Identity Protection: Management of identity is a challenge because bad security practices are often enforced. For instance, a common mistake is the use of clear text/Base64 encoded device/machine-to-machine (M2M) IDs/passwords.

Attack-Resistant Security Solutions: IoT system diversity results in a need for security solutions that are attack-resistant and lightweight. They are defenceless against asset enervation assaults because IoT gadgets have restricted processing assets.

3.2 Threats and Attacks on IoT Security

To underline security risks in IoT, its shortened form has been presented as Interconnection of Dangers (IoT). Undoubtedly, IoT gadgets are especially powerless against actual attacks, programming attacks, side-channel attacks, etc. as introduced in Table 3.

Present IoT platforms are made up of a range of technology solutions from different vendors. Any of these frameworks are a diverse blend of segments repurposed from existing answers for use in uniquely fabricated stages in the expectation that the parts can cooperate securely.

Table 3 Security threats to IoT devices

Threats	Procedure for an attack	Security requirement	Examples
Physical attack	Play with the equipment and different pieces of the framework	Resistance to tampering	Micro-probing of layout reconstruction
Environment attacks	By recovering the encryption information, the attacker will discover the system encryption key.	Encryption system that is secure	Attacks on pacing, side channels, and analysis fault attack
Cryptanalysis attacks	To decrypt the data, look for cypher text.	Encryption system that is secure	Plaintext attack (known plaintext) and plaintext attack (chosen plaintext)
Software attacks	Exploit device vulnerabilities and inject malicious code into the system's own communication interface	Update antivirus software	Viruses , worms or Trojan horse are all examples of malicious software

Table 4 Taxonomy of attacks based on IoT process phases

Phase	Attack/Threat	Description
Data Collection: There are several different types of data gathering that can be used. A static (body sensors) might be utilized as the unit (sensors and chips)	Breach or Data Leakage information Authentication information Sovereignty, and information Loss, are all issues that need to be addressed	Internal or external data leakage may occur, and it can be deliberate or unintentional. Is it software or hardware
Storage: Data are often saved if the pc has its native memory. The information from homeless devices are often protected to the cloud	Accessibility, Access Control, Genuineness, Forswearing of Administration, and Detainment are for the most part instances of assaults on accessibility, access	The over-burden condition initiated by an enormous number of conveyed aggressors is known as distributed denial of service
Intelligent processing	Authentication attack	In real-time, an IoT solution offers information processing
Transmission of data	Session hijacking, flooding of the channel security, steering conventions	Interruptions, blocking, data manipulation, forgery
End-to-end term	Man or computer that is the question. Maker or thief	On-time delivery of stored data with no mistakes or alterations

3.2.1 Attack Classification for IoT Interaction Stage

An IoT approach can be thought of as a five-phase series, starting with data collecting and ending with data transmission to end users. Table 4 indicates the spectrum of assaults categorized for the five IoT phases: interpretation of data, storage, smart processing, transmission of data and end-to-end delivery [7].

3.2.2 Categorization of Attacks Based on IoT Architecture

There are different IoT models of architecture, as mentioned in Sect. 2. In general, four layers are believed to have the IoT architecture, presented in Fig. 2. At the awareness, network, and service levels, we will take a quick look at the biggest security threats. Table 5 summarizes the most significant security issues in the IoT provided as four-layer architecture (Fig. 2).

3.2.2.1 Threats to Security at the Sensing and Perception Layer

It should be customized and introduced into the actual gadgets to authorize IoT security. This implies IoT gadgets should have the option to demonstrate their character, hold their realness, sign, and encode their information to keep up with believability, and to ensure protection by confining information that is saved locally. The situation security model should be adequately unbending to forestall unapproved use while as yet being sufficiently adaptable to work with secure specially appointed interchanges with people and different gadgets on an impermanent premise [8].

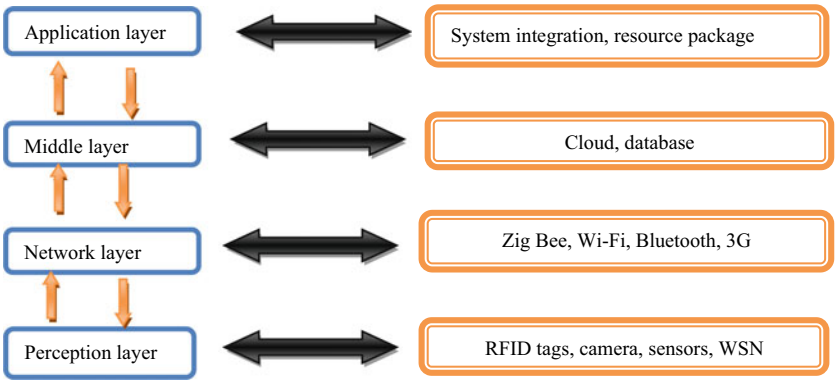

Fig. 2 Architecture of IoT

Table 5 Top Ten Vulnerabilities in IoT

Corners of security	Interface & application layer	Service support layer	Middleware/network layer	Unit/device layer
Online interface that is not stable	√	√	√	
Inadequate authentication and authorization	√	√	√	√
Network facilities that aren't stable		√	√	
Transport encryption isn't available		√	√	
Privacy nooks		√	√	√
Cloud interface that is unreliable	√			
The mobile app is insecure	√		√	√
Configuration of security is insecure	√	√	√	
Software/firmware that isn't stable	√		√	
Inadequate physical defence			√	√

Harm to Physicality: Some attackers can lack technological expertise and the destruction of devices limits their attacks. As device enclosures are often not tamper-proof, it is possible to open the devices, access their hardware through probes, and pin headers.

Capturing Node: Instead of destroying them, the information stored on the devices will be stolen by an active attacker.

Attack of the Sinkhole: They become defenceless against sinkhole assault if sensors are left unattended for significant stretches in the organization.

Attack Selective Routing: Malicious nodes can pick, drop packets, thus selectively filtering thus, some packets are selectively filtered, and the rest enabled.

Witch Strike: On the off chance that a noxious IoT hub exploits a genuine hub's disappointment, If rouge IoT hub exploits a genuine hub's disappointment, this attack occurs.

3.2.2.2 Security Threats

Layers of Network and Service Support
The IoT management framework is defined by the administration support layer (Fig. 2) and is liable for installing gadgets and clients, executing approaches and guidelines, and coordinating computerization across gadgets. At this stage, role-based access control to monitor the identity of users and devices and the actions they are allowed to take is important.

Attack by Man-in-the-Middle (MITM): Assault by Man-in-the-Middle (MITM). The Man-in-the-middle assault is a representation of the IoT's latent capacity snooping. Since device authentication requires device identity sharing, identity theft involves identity theft. All dangers of assaults on IoT frameworks should go through the mist layer in the center, which can detect and mitigate suspicious activities before they reach the device [12].

Attack Replay: This data might be ridiculed, adjusted, or replayed during the exchanging of character-related information or various certificates inside the IoT.

Denial of Service Attack: An interloper could dodge the firewall and dispatch a refusal of administration (DoS) assault, delivering the route administration difficult to reach, or convey a bogus message, driving the driver as plate [11]. In addition, most IoT developers have an embedded programming history, which makes them unaware of IoT programming and risks. Attackers could gain access to the keen home arrange and send mass messages to shrewd gadgets, like Solicitation To Send (RTS)/ Clear To Send (CTS) [15].

4 IoT Security parameters

Protection must be handled from the initial design to the services operating in the IoT lifecycle. For example, during device manufacturing, the execution of safety highlights should start.

Code marking and code confusion are a few stages that makers should take to guarantee that their device is not compromised or that a malicious user does not insert unauthorized code. Data confidentiality, safety, and trust are the key security criteria in IoT scenarios, as shown in Fig. 3. Protection is required for IoT systems as a result of IoT security issues. As a result, based on conventional security criteria, it is vital to fabricate a protected web arrangement of things, which are as per the following [19]:

4.1 IoT Solutions

The engineering of the IoT is a major method of planning the various components of the IoT so it can give network benefits and fulfil future requirements. Sensors, actuators, entryways, conventions, cloud administrations, organizations, and application workers are all essential for the IoT design, which are coordinated in different geographies to speak with each other [16]. The term "Internet of Things" refers to a large and diverse ecosystem that encompasses a wide range of connectivity kinds and application cases. As a result, discussing the IoT ecosystem as a whole is ineffective, and understanding IoT requires breaking it down into layers [20]. The fourth industrial revolution will be built on sensors and actuators. They have already altered how people view their surroundings. From urban planning to social consciousness, sensor-enabled smart cities are paving the way for a more sustainable future [21].

The following are the primary IoT phases (layers) that include the IoT architecture solution (Fig. 4).

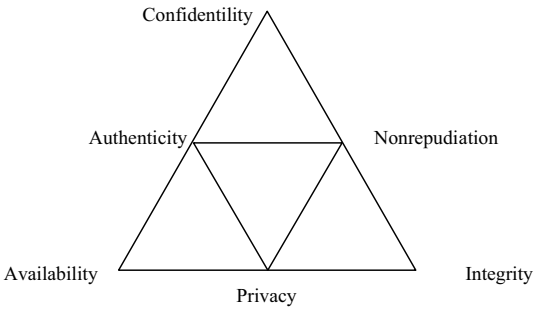

Fig. 3 Security requirements in the internet of things

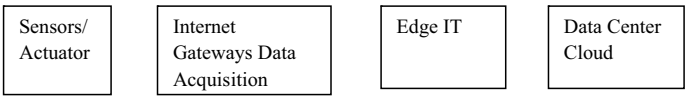

Fig. 4 Solutions of IoT

i. **Sensors/Actuators**
The instruments that can emit, receive and process data over the network are sensors or actuators. This includes GPS, electrochemistry, gyros copy, RFID, etc. Most of the sensors need connectivity through gateways to the sensors. A Local Area Network (LAN) or Personal Area Network may be used for connecting sensors or actuators. The sensor is in charge of detecting and collecting the analogy signals that represent environmental data. Analog signals are converted to digital data by the analog-to-digital converter, which then passes the data to the processing unit [22].

ii. **Gateways and Data Acquisition**
Because these sensors and actuators generate vast volumes of data, high-speed gateways and networks need to transfer data. The type of this network may be Local Area Network (LAN, such as Ethernet, Wi-Fi and so forth), Wide Area Network (WAN like 5G, GSM and so on). This framework was created to allow for the capture of multimodal data from a variety of sources and data providers, as well as to address current connectivity and communication challenges [23].

iii. **Edge IT**
Edge is the equipment and programming entryway in IoT Engineering that investigates and pre-measures information before moving it to the cloud. Edge figuring is a moderately late idea in the registering scene. It brings distributed computing administrations and utilities nearer to the end client, and quick handling and application reaction times portray it [24].

iv. **Data Center/Cloud**
Management Systems that process information through analytics, system management, and security controls are part of the Data Center or Cloud. A server farm is an area where establishments' PCs and related hardware, like peripherals, are kept up. Universities, businesses, national laboratories, hospitals, research institutes, government agencies, and other institutions could be among them [25].

5 Conclusion

The design of IoT security allows for a free, widespread infrastructure with interoperability. We conclude this paper by stating that, following the identification of the key IoT-enabling technologies, challenges, parameters, and solutions, The creation of the network architecture and framework to efficiently handle future IoT applications is the next step. Furthermore, IoT systems are implementing a variety of important technological advancements in a variety of industries. To safeguard their connected devices from malicious assaults, several suppliers and enterprises implement a variety of restrictions. More privacy and security issues have been raised as more of these gadgets are connected to our private networks and the Internet. When it comes to protecting IoT-based systems and devices, security should be a primary focus. To secure their systems from potential threats, businesses should

consider implementing numerous levels of protection. IoT data may be processed using modern analytical tools like Artificial Intelligence and Machine Learning to improve security. Blockchain is a promising solution for data security in IoT-enabled ecosystems, as it eliminates the need for central permission in the IoT network.

Reference

1. Conner M (2010). Sensors empower the "Internet of Things", pp 32–38. ISSN 0012-7515
2. Shao X (2012) Study on security issue of internet of things based on RFID. In: Fourth international conference on computational and information sciences
3. http://whatis.techtarget.com/definition/Internet-of-Things
4. INFSO D.4 (2008) Networked Enterprise & RFID INFSO G.2 Micro & Nano systems, in: co-operation with the working group RFID of the ETP EPOSS. Internet of Things in 2020, roadmap for the future, version 1.1
5. Xu X (2013) Study on security problems and key technologies of the internet of things. In: International conference on computational and information sciences
6. Yan L, Zhang Y, Yang LT (2008) The Internet of Things: from RFID to the next-generation pervasive networked systems. Auer Bach Publications
7. https://education.dellemc.com/content/dam/dell-emc/documents/en-us/2018KS_Gloukhov
8. https://it.b-ok2.org/book/3307183/d60844
9. Hany AF, Gary WB (2019) IoT security, privacy, safety and ethics, digital twin technologies and smart cities. Springer Cham, pp 123–149
10. Anca JD, Pasika R, Xu L (2019) Introduction to IoT security. John Wiley Sons Ltd., Hoboken, pp 1–37
11. Shapla K, Ismail AB, Mohd IIY, Mohamed JH, Bin SM, Aznul G (2020) A survey of security challenges, attacks taxonomy and advanced countermeasures in the internet of things. IEEE Access 8:219709–219743
12. Vikas H, Vinay C, Vikas S, Divyansh J, Pranav G, Biplab S (2019) A survey on IoT security: application areas, security threats, and solution architectures. IEEE Access 7:82721–82743
13. Pérez Salvador L, José R-H, Shahid R, Antonio S (2020) Application layer key establishment for end-to-end security in IoT. IEEE Internet Things J 7(3):2117–2128
14. Hui S, Wan J, Zou C, Liu J (2012) Security in the internet of things: a review. In: International conference on computer science and electronics engineering. IEEE, pp 648–651
15. Gil HS, Razzaq AM, Qureshi AM, Ullah S (2017) Security issues in the Internet of Things (IoT): a comprehensive study. (IJACSA) Int J Adv Comput Sci Appl 8(6)
16. Iqbal W, Abbas H, Daneshmand M, Rauf B, Bangash YA (2020) An in-depth analysis of IoT security requirements, challenges, and their countermeasures via software-defined security. IEEE Internet Things J 7(10):10250–10276
17. Meneghello Francesca, Calore Matteo, Zucchetto Daniel, Polese Michele, Zanella Andrea (2019) IoT: Internet of Threats? a survey of practical security vulnerabilities in real IoT devices. IEEE Internet Things J 6(5):8182–8201
18. Pallavi S, Smruti RS (2017) Internet of Things: architectures, protocols, and applications. J Electr Comput Eng, 1–25
19. Bhabad MA, Bagade ST (2015) Internet of Things: architecture, security issues and countermeasures. Int J Comput Appl (0975– 887) 125(14), 1–4
20. El Ahmed H (2018) Internet of Things (IoT) system architecture and technologies. Research, pp 1–3. https://doi.org/10.13140/RG.2.2.17046.19521
21. Mohammad H, Mounir A (2018) Sensors and actuators in smart cities. J Sensor Actu Netw MDPI 7:1–4
22. Wen ST (2010) Multi-sensors data fusion system for wireless sensors networks of factory monitoring via BPN technology. Expert Syst Appl 7:2124–2131

23. Perakis K, Miltiadou D, Nigro A, Torelli F, Mantas L, Magdalinou A, Mavrogiorgou A, Kyriazis D (2019) Data sources and gateways: design and open specification. Acta Informatica Medica 27(5):341. https://doi.org/10.5455/aim.2019.27.341-347
24. Wazir KZ, Ejaz A, Saqib H, Ibrar Y, Arif A (2019) Edge computing: a survey. Future Gener Comput Syst 97:1–40
25. Michael PJ, Aparna VS, Stefan RA (2015) The greening of data centers with cloud technology. Int J Cloud Appl Comput 5(4):1–23

Bio-inspired Lotus (Nelumbo Nucifera) Shaped Ultra-wide Band Planar Antenna for Wireless Applications

Ushaben Keshwala, Sanyog Rawat, and Kanad Ray

Abstract The paper presents novel lotus (Nelumbo nucifera) shaped ultra-wide band antenna for wireless applications. The antenna is designed on FR-4 substrate of size 17 × 14 mm^2. The initial antenna of semicircular path is modified to proposed prototype of lotus shaped patch by inserting sinusoidal tapered petals in the semicircular patch. The impedance bandwidth is enhanced from 4.2–9.1 GHz to 3.5–15.0 GHz by making partial ground to stair case shaped DGS. The antenna achieves ultra-wide band width in the range of 3.5–15.0 GHz (11.5 GHz) with maximum gain of 1.8 dBi at 11.4 GHz.

Keywords Ultra-wide band · Lotus shaped antenna · Bio-inspired antenna · Defected Ground Structure (DGS)

.

1 Introduction

With the rapid advancement of wireless communication systems, the use of antennas in base stations and portable terminals must meet increasingly strict criteria, such as miniaturization, integration with other systems, and multiband or broadband operation. The evolution of advances in communication technologies and the ever-increasing demand by users for compact communication devices have required a

U. Keshwala
Department of Computer Science and Engineering, Amity School of Engineering and Technology, Amity University, Noida, Uttar-Pradesh, India

S. Rawat (✉)
Department of Electronics and Communication Engineering, Manipal University Jaipur, Jaipur, India
e-mail: sanyog.rawat@jaipur.manipal.edu

K. Ray
ASAS, Amity University, Jaipur, Rajasthan, India

M. Tiwari et al. (eds.), *Optical and Wireless Technologies*, Lecture Notes in Electrical Engineering 892, https://doi.org/10.1007/978-981-19-1645-8_43

shift in the design approach in order to achieve compact and robust antenna structures. Over the time Biomimicry or Biomimetics has evolved through integration with engineering. So, nature can be used as solution base in some problems found in engineering and modern science [1, 2].

The standard IEEE802.15 which uses the 3–10 GHz frequency spectrum for high data rate ultra-wide band applications has recently attracted considerable attention in the wireless communication industry [3]. Ultra-Wideband is defined as any communication system that has a bandwidth of more than 500 MHz or more than 25% of the operating center frequency. The Federal Communications Commission (FCC) allocated a bandwidth of 7.5 GHz, i.e. from 3.1 to 10.6 GHz, to unlicensed use for UWB applications [4, 5]. Various UWB antennas have been proposed for UWB applications [6, 7].

Due to the ability of the Bio-inspired structure to reduce the size while improving the perimeter, it has been used in the development of antennas structures for wideband applications. The bio- inspired geometries used for antennas design can be divided in to two categories: bio-inspired geometries in animals and bio-inspired geometries in plants. For instance, various bio-inspired antenna structures have been proposed for a wideband antenna applications [8–13]. A bio-inspired Carica Papaya leaf shaped antenna is proposed with impedance bandwidth of 1.9–6.2 GHz for GSM1900, UMTS, WLAN, LTE, WiMAX, C-band, X-band, and sub6 GHz fifth-generation bands applications [8]. A rectangular patch antenna with hybrid fractal slot (Koch-Minkowski and Koch-Koch) along with partial ground plane has been presented for wideband applications [9]. A leaf-shaped bowtie slot antenna with frequency of operation in the range of 3.1–10.6 GHz has been proposed for UWB applications [10]. In [11] a tulip loop antenna with impedance bandwidth of 6–14.5 GHz has been proposed for wide band applications. A 50×43 mm^2 lotus shaped antenna with impedance bandwidth of 1.4–10 GHz has been introduced [12]. A lotus shaped dual band antenna is presented in [13] for bluetooth and UWB applications.

In this paper we propose novel lotus (Nelumbo nucifera) shaped antenna, designed with sinusoidal tapered eight petals for ultra-wide bandwidth for wireless applications. The fundamental structure is lotus shape patch with defected ground structure of stair case shape for the bandwidth enhancement.

2 Antenna design

The proposed UWB antenna of Fig. 1 has been obtained through the step-by-step evolution of the semicircular shape radiating structure of Fig. 2(a), by cutting sinusoidal petal shapes in semicircular patch as shown in Figs. 2(b) and (c). The final proposed prototype is lotus (Nelumbo nucifera) shaped antenna with defected ground structure (DGS) as shown in Fig. 1(b).The proposed compact antenna is designed on low cost FR-4 substrate as patch and conducting lotus shaped patch and DGS staircase shaped ground. Figure 1 illustrates the final prototype structure with detailed configuration of the antenna. The radiating patch is printed on the one side of substrate and

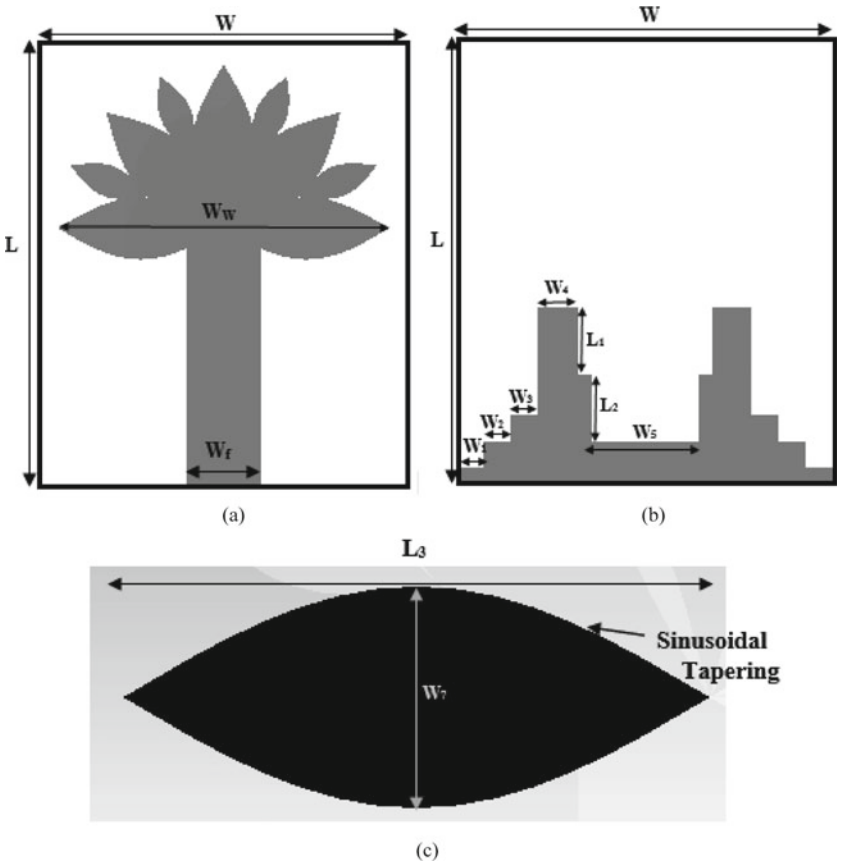

Fig. 1 Proposed lotus shaped antenna **a** Front view **b** Back view **c** Expanded view of petal

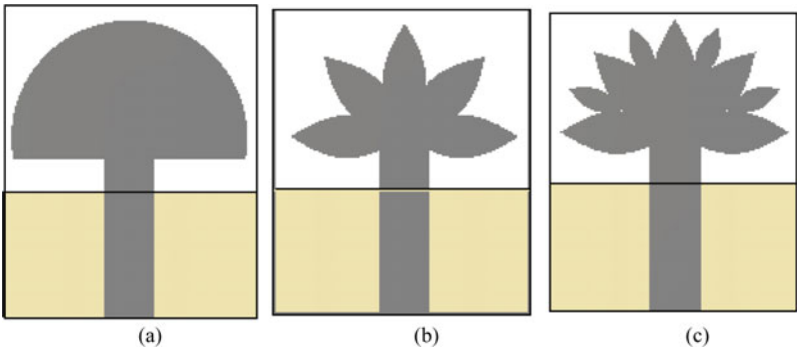

Fig. 2 Evolution steps of an antenna deign **a** Antenna 1 **b** Antenna 2 **c** Antenna 3

Table 1 Optimized parameters of an antenna

Parameters	Value (mm)	Parameters	Value (mm)	Parameters	Value (mm)
L	17	L_g	7	W_2	1
W	14	W_f	2.8	W_3	1
W_w	12.56	W_1	1	W_4	1.5
L_1	2.5	L_2	2.5	L_3	6.28
W_5	4	W_7	2.4		

fed by microstrip line of width W_f =2.8 mm. The optimized geometrical parameters of the final prototype is presented in Table 1.

The antenna 1 is the semicircular patch with radius of 6.28 mm. The antenna 1 is then modified by cutting five petals with sinusoidal tapering. The expanded view of single petal is presented in Fig. 1(C). The length of the petal is 6.28 mm and width of the petal is 2.4 mm. In third iteration the antenna 3 is obtained by adding a small petals in between the five petals of bigger size. The size of the smaller petals is half of the bigger petals. The return loss characteristic for the three antenna design steps is presented in Fig. 3. From the presented curve it can be observed that the lower cut cut-off frequency is reduced for antenna 3 i.e. after adding the smaller size petals.

To improve the obtained impedance bandwidth the partial ground is modified to DGS (Defected Ground Structure).The partial ground is modified to staircase shaped and two rectangular slots are etched in the upper part of the partial ground.

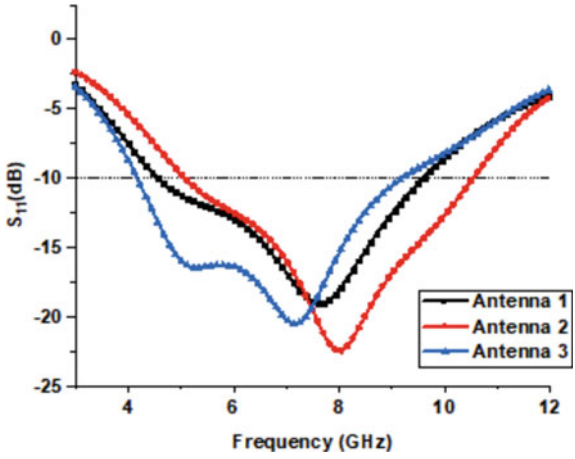

Fig. 3 Variation of return loss for three antenna design

3 Results and discussion

The final prototype is presented in Fig. 1, consisting of lotus shaped radiating patch with eight petals and DGS. The performance of antenna considerably enhanced in terms of impedance bandwidth by introducing defects in the ground plane. The designed antenna is capable of operating in the ultra-wide bandwidth from 3.5–15.0 GHz (11.5 GHz). The simulated return loss characteristic and VSWR for the proposed design is shown in Fig. 4. As it can be noted from the curve that the antenna resonates at 4.7 and 13.31 GHz. To understand the detail of antenna mechanism the surface current and radiation patterns are plotted at resonating frequencies.

The gain of the antenna is varying between 0.21–1.8 dBi. As it can be observed from Fig. 6 the radiation efficiency and total efficiency is above 60% with maximum total efficiency of 72.2% at 10.3 GHz. The surface current is distributed in the full patch, mostly at the edges of the sinusoidal petals at lower as well as at the high resonating frequencies. The current is mainly flowing at the outer edges of the stair case ground at lower frequency, on the other hand the current is mainly flowing in the middle of the ground plane at higher frequency.

As presented in Fig. 8 the main lobe direction of E-filed is at 180° at 4.7 GHz and E-filed is bidirectional at 13.31 GHz with main lobe at 40°. The H-field main lobe is 210° with 3 dB angular width of 115.3° at lower resonating frequency and at higher frequency of resonance the H-field of 73.3° angular width is at 200°. The comparison of the state of art with proposed antenna is presented in Table 2 (Figs. 5 and 7).

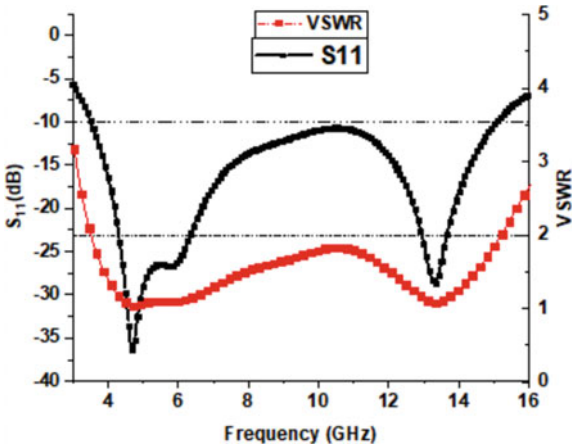

Fig. 4 Variation of S11 and VSWR with frequency

Table 2 Comparisons of proposed work with reported antenna

Reference	Size of antenna(mm^2)	BW (GHz)	Gain (dBi)	Efficiency of antenna
[7]	43 × 28	3.03–9.15	2.8	–
[8]	59.25 × 35.7	1.9–6.2	10.22	–
[9]	45 × 38.92	7.74–10	5.6	–
[12]	50 × 43 mm	1.42–10	–	–
[13]	44 × 42	2.3–2.6 3.3–12	6.2	25–97%
Proposed antenna	17 × 14	3.5–15.0	1.8	72.2%

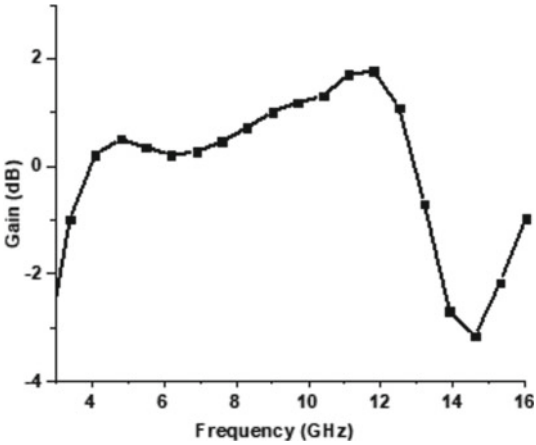

Fig. 5 Variation of gain with frequency

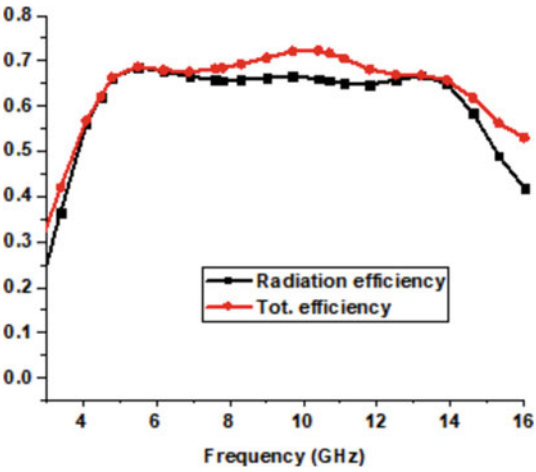

Fig. 6 Total efficiency and radiation efficiency

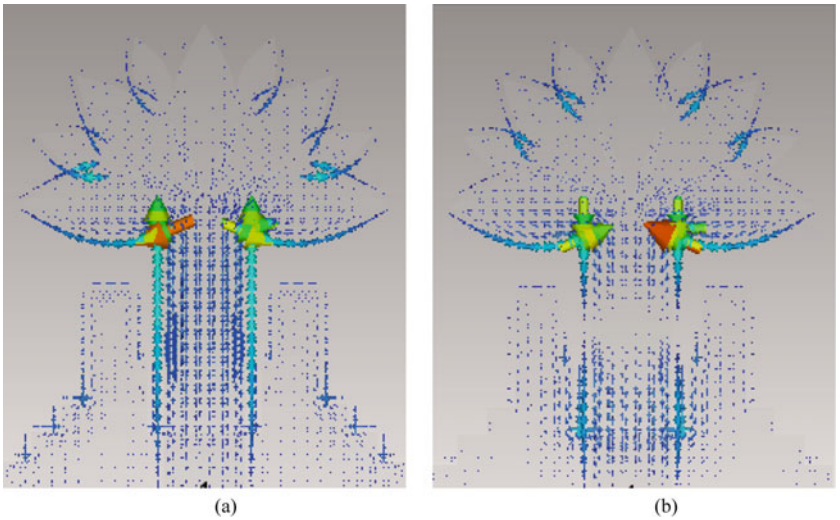

Fig. 7 Surface current distributions at resonating frequencies **a** 4.7 and 13.31 GHz

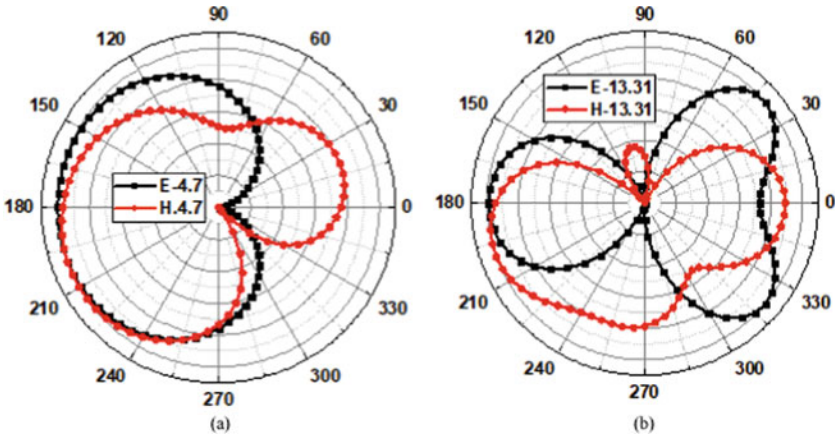

Fig. 8 Radiation pattern at resonating frequencies **a** 4.7 and 13.31 GHz

4 Conclusion

A novel lotus shaped compact antenna of size 17 × 14 mm^2 is presented for wireless applications. The antenna is designed by modifying the semicircular patch to lotus shape by inserting sinusoidal tapered petals in the patch. The impedance bandwidth acquired by proposed prototype ranges from 3.5 –15.0 GHz (11.5 GHz). The positive gain is obtained in the range of 4.0–12.9 GHz with maximum gain of 1.8 dBi at 11.4

GHz. The compact size, novel shape, and ultra-wide bandwidth makes an antenna suitable for wireless applications.

References

1. Bar-Cohen Y (2006) Biomimetics-biologically inspired technologies. CRC Press, Boca Raton
2. Benyus JM (1997) Biomimicry: innovation inspired by nature. William Morrow, New York
3. Khan MI, Khattak MI, Witjaksono G, Barki ZU, Ullah S, Khan I, Lee BM (2019) Experimental investigation of a planar antenna with band rejection features for ultra-wide band (uwb) wireless networks. Int J Ant Propagat 2019:1–11
4. T. F. C. Commission(FCC) (2002) Revision of Part 15 of the Commission's Rules Regarding Ultra Wideband Transmission Systems; First Report and Order FCC 02-48,:The Federal Communications Commission, Washington DC USA
5. T. F. C. Commission (2007) Revision of Part 15 of the Commission's Rules Regarding Ultra Wideband Transmission Systems; First Report and Order FCC 03-33,:The Federal Communications Commission, Washington DC USA
6. Keshwal, U, Rawat S, Ray K (2019) Honeycomb shaped fractal antenna with defected ground structure for UWB applications. In: 6th international conference on signal processing and integrated networks, pp 341–345
7. Keshwala U, Rawat S, Ray K (2018) Compact half-hexagonal monopole planar antenna for UWB applications. In: Soft computing: theories and applications, Jaipur, India
8. Abolade JO, Konditi DBO, Dharmadhikary VM (2020) Bio-inspired wideband antenna for wireless applications based on perturbation technique. Heliyon 6(7)
9. Sharma N, Sharma V (2018) A design of Microstrip Patch Antenna using hybrid fractal slot for wideband applications. Ain Shams Eng J 9(4):2491–2497
10. Fujita S, Yamamoto M, Nojima T (2012) A study of a leaf-shaped bowtie slot antenna for UWB applications. In: 2012 international symposium on antennas and propagation (ISAP), pp 830-833
11. Tanyer-Tigrek FM, .Tran DP, Lager IE, Ligthart LP (2009) Wide-band tulip-loop antenna. In: 3rd European conference on antennas and propagation, Berlin
12. Mansour HM, Sharaf MH, Shams SI, Allam AMM (2012) Novel lotus shaped antenna for ultra wideband communication systems. In: 2012 loughborough antennas & propagation conference (LAPC), Loughborough
13. Samsuzzaman M, Mahmud MZ, Islam MT, Ali MM, Islam MT (2017) Compact lotus shape dual band patch antenna for Bluetooth and ultra wideband applications. Microw Opt Technol Lett 59(7):1590–1597

Designing of Metasurface for Gain Enhancement in 5G Applications

Devendra Soni, Aakarsh Mekap, Dinesh Yadav, and Manish Tiwari

Abstract In this paper, a methodology for designing a metasurface is explained and practically show this by design of unit cell rectangular shape structure. By using multiple unit cell structure can be design metasurface. Metasurface consist of a 40-unit cell structure, each unit cell length and width are 4 × 6 mm and distance from other unit cell in metasurface is 1 mm. In analysis of unit cell, we will discuss its current distribution, transmission (S_{21}) and reflection (S_{11}) coefficient of unit cell as well as metasurface. From calculation of transmission and reflection coefficient unit cell and metasurface studied in 1–30 GHz frequency band. Frequency band of proposed metasurface is shown that its applicable in 5G.

Keywords Metasurface · Transmission Coefficient · Reflection Coefficient

1 Introduction

Metasurfaces are structures that are used to change the optical characteristics of materials, such as amplitude, polarization, and refractive index [1, 2]. Metasurfaces are now being utilized without a phase gradient, which means they can only generate optical and plasmonic devices and lack numerous characteristics such as dispersive free imaging and polarization free refraction. Because of their permittivity and permeability characteristics, metamaterials affect the propagation of light [3]. Metasurfaces' two-dimensional nature makes them less bulky and allows for lower loss structures [4–6]. Metasurfaces have a number of benefits, including a planar structure and the ability to readily produce them using planar fabrication techniques.

D. Soni (✉) · A. Mekap · D. Yadav · M. Tiwari
Department of Electronics and Communication Engineering, Manipal University Jaipur, Jaipur, Rajasthan, India
e-mail: sonierdevendra6486@gmail.com

D. Yadav
e-mail: dinesh.yadav@jaipur.manipal.edu

M. Tiwari
e-mail: manish.tiwari@jaipur.manipal.edu

M. Tiwari et al. (eds.), *Optical and Wireless Technologies*, Lecture Notes in Electrical Engineering 892, https://doi.org/10.1007/978-981-19-1645-8_44

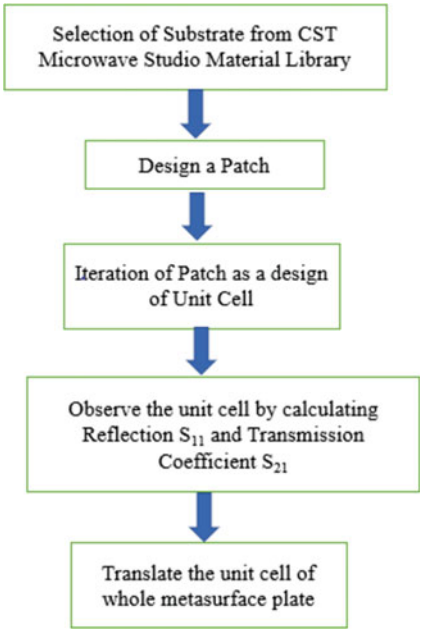

Fig. 1 Methodology of designing metasurface

In comparison to metamaterial, the cost of fabrication for metasurface is likewise extremely low [7–9].

In this paper, metasurface is designed and analysis by transmission coefficient and reflection coefficient. As well as before designing the metasurface unit cell is also analysis on basis of transmission and reflection coefficient. Results of metasurface and unit cell shown that reflection is maximum. So, gain of antenna which placing upper of metasurface is enhanced.

2 Design Methodology

(See Fig. 1).

3 Designing of Unit Cell and Metasurface with Parameters:

Designing of unit cell as well metasurface is done on CST microwave studio. RT6010LM substrate is chosen from CST substrate library those thickness is 1.27.

Length and width of chosen substrate is 4 × 6 mm. Patch is designed on substrate those length and width are 3 × 5 mm and thickness is 0.035 mm. Left hand side and right-hand side on patch a vertical strip slot is cut, those dimensions are 2 ×

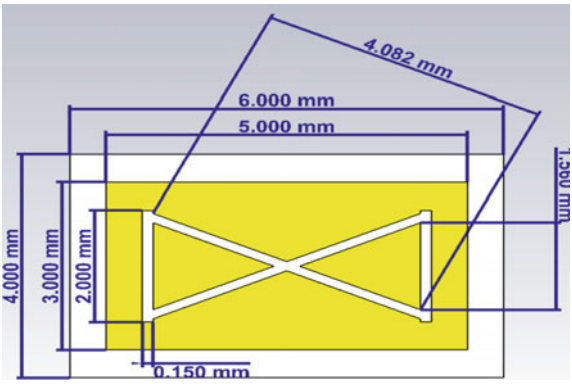

Fig. 2 Design of unit cell structure

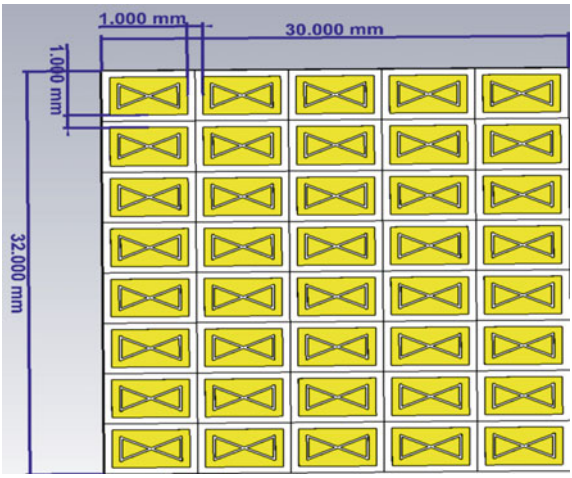

Fig. 3 Structure of 8 × 5 metasurface

0.15 mm. In same manner slot of 4.082 × 0.15 mm are cut in the middle, then copy it while rotating at 25° and 335° as shown in Fig. 2.

For designing of metasurface length and width of substrate is 32 × 30 mm. Unit cell structure is copied and replicate in whole metasurface plate. The distance between two-unit cell structure is 1 mm in column wise as same as 1 mm in row wise. In complete metasurface structure 40-unit cell is designed as shown in Fig. 3.

4 Results and Discussion

Rectangular Shape Unit Cell design is simulated between 1–30 GHz frequency band. Figure 4 shows current distribution of unit cell. Transmission coefficient (S_{21}) of unit cell is shown in Fig. 5, we observe that transmitted electric field is −40 dB on both

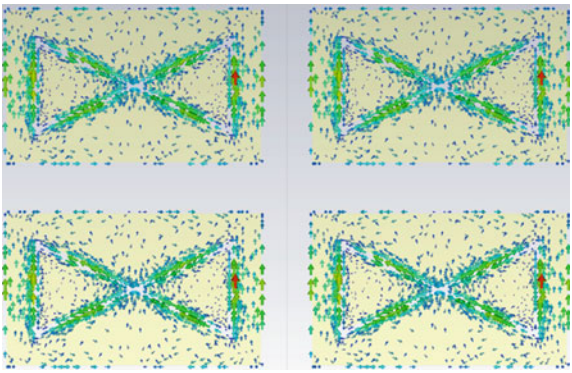

Fig. 4 Current distribution of 2 × 2 unit cell metasurface on 28.11 GHz frequency

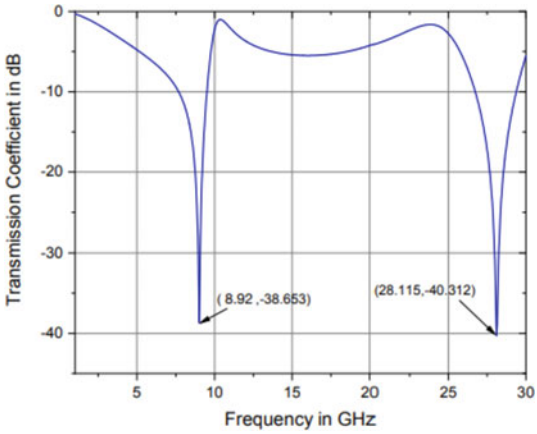

Fig. 5 Transmission coefficient (S_{21} in dB) of unit cell structure at 8.9 and 28.11 GHz

frequency (9 and 28.11 GHz) it means minimum transmission on both frequency points. Reflection coefficient (S_{11}) is –0.07 at 8.9 GHz frequency and –0.06 at 28.11 GHz frequency as shown in Fig. 6, this shows that maximum reflection take place on both frequency points.

Metasurface transmission coefficient (S_{21}) shows in Fig. 7, transmitted electric field is –49 dB on 8.9 GHz frequency point and –30 dB on 28.11 GHz shows minimum transmission on that frequency points. Reflection coefficient (S_{11}) of metasurface is –0 at 8.69 GHz and –0.51 at 28.11 GHz as shown in Fig. 8 shows that reflection is maximum.

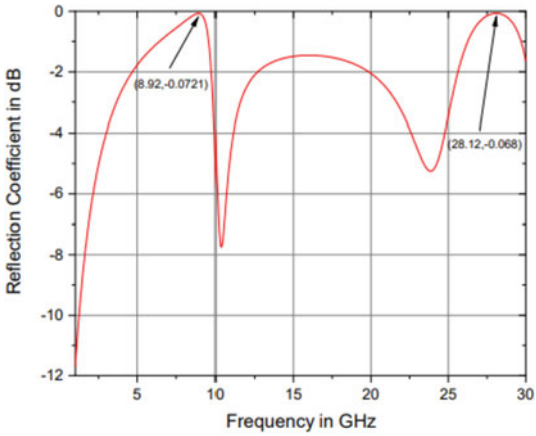

Fig. 6 Reflection coefficient (S_{11} in dB) of unit cell at 8.92 and 28.11 GHz

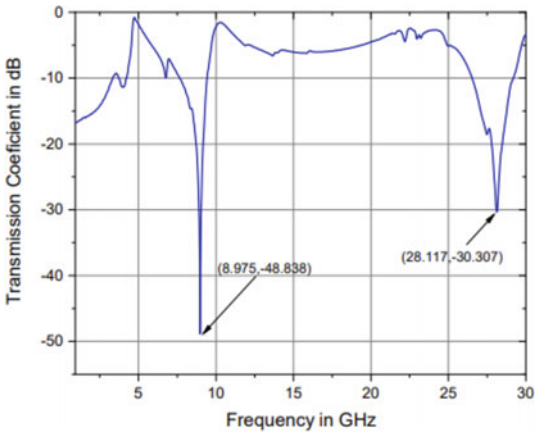

Fig. 7 Transmission coefficient (S_{21} in dB) of metasurface at 8.9 and 28.11 GHz

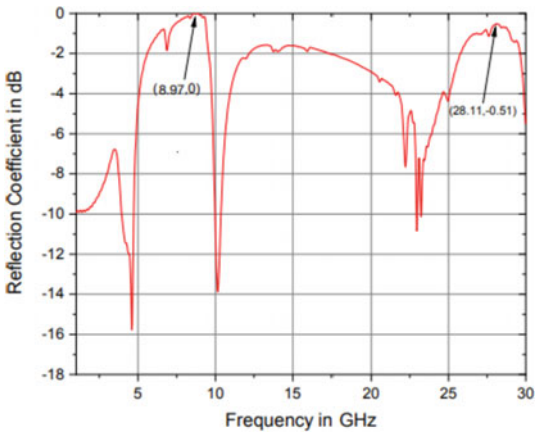

Fig. 8 Reflection coefficient (S_{11} in dB) of metasurface at 8.9 and 28.11 GHz

5 Conclusion

Designing of unit cell and metasurface are shown in this paper. Gain of any designed antenna can be enhanced by placing metasurface in back side of antenna. Designed unit cell and metasurface both studied on same frequency points that is 8.9 and 28.11 GHz. Unit Cell and Metasurface transmission and reflection coefficient shows that maximum reflection and minimum transmission on both frequency point (8.9 and 28.11 GHz), it means power is reflected back on same metasurface plate hence gain of any antenna can be enhanced. The gain from metasurface structure can be more improve by rotating the unit cells on particular angles.

References

1. Ya F, Ma HJ, Zhang J, Feng D, Geng M, Qu S (2016) In-plane feed antennas based on phase gradient metasurface. IEEE Trans Ant Propagat 64(9)
2. Yuan Y, Ding X, Zhang K, Wu Q (2017) Planer efficient metasurface for vortex beam generating and converging in microwave region. IEEE Trans Magn 53(6)
3. Zhang Y, Lyu Y, Wang H, Jin X (2018) Transforming surface wave to propagating OAM vortex wave via flat dispersive metasurface in radio frequency. IEEE Ant Wirel Propagat Lett 17(1)
4. Li HP, Wang GM, Cai T, Liang JG, Gao XJ (2018) Phase and amplitude control metasurface for antenna main-lobe and side-lobe manipulations. IEEE Trans Ant Propagat 66(10)
5. Su J, Lu Y, Lu J, Yang Y, Li Z, Song J (2018) A novel checkerboard metasurface based on optimized multielement phase cancellation for superwideband RSC reduction. IEEE Trans Ant. Propagat 66(12)
6. Modi AY, Balanis A, Birtcher CR, Shaman HN (2019) New class of RCS-reduction metasurface based on scattering cancellation using array theory. IEEE Trans Ant Propagat 67(1)
7. Katare KK, Chandravanshi S, Biswas A, Akthar MJ (2019) Beam switching of fabry–perot cavity antenna using asymmetric reflection phase response of bianisotropic metasurface. IET Microw Ant Propagat 13(13)
8. Ding X, Guan C, Wang Z, Liu S, Zhang K (2019) Metasurface for bending the reflected wave under oblique incidence. IEEE Trans Magn 55(11)
9. Yue H, Chen L, Yang Y, He L, Shi X (2019) Design and implementation of a dual frequency and bidirectional phase gradient metasurface for beam convergence. IEEE Ant Wirel Propagat Lett 18(1)

Design and Analysis of Microstrip Circular Patch Antenna with a Rectangular Slot for Bluetooth Application

Suman Sharma, Richa Sharma, Dinesh Yadav, and Mukesh Arorai

Abstract The proposed antenna is having a circular patch with ground plane and is designed on FR4 (frame sensitive) substrate having dielectric permittivity 4.4 and along with it the thickness '1.76 mm', the designed antenna resonates at a frequency of around 2.4 GHz that can be used for Bluetooth applications. It provides a directional pattern with minimum return loss of around −30 dB. Gain has been improved by inserting a rectangular slot, with an improved gain of about 2.1 dB. The design is simulated on HFSS software and is further fabricated. The testing was done on Network analyzer N9916A and the test results are closely similar to the simulated results.

Keywords Circular patch · HFSS software · Strip line feeding · FR4 substrate · VNA

1 Introduction

Antenna is a kind of transducer that converts electrical signals in the form of electromagnetic (EM) waves. Microstrip antennas are having various merits than the

S. Sharma (✉) · R. Sharma · M. Arorai
Department of Electronics and Communication, SKIT, Jaipur, Rajasthan, India
e-mail: suman.sharma.csit@skit.ac.in

R. Sharma
e-mail: sharmaricha670@gmail.com

M. Arorai
e-mail: mukesharora@skit.ac.in

R. Sharma
Department of Electronics and Communication Engineering, SKIT, Jagatpura, Jaipur, Rajasthan, India

S. Sharma · D. Yadav
Department of Electronics and Communication Engineering, Manipal University, Jaipur, Rajasthan, India
e-mail: dinesh.yadav@jaipur.manipal.edu

M. Tiwari et al. (eds.), *Optical and Wireless Technologies*, Lecture Notes in Electrical Engineering 892, https://doi.org/10.1007/978-981-19-1645-8_45

traditional microwave type of antenna, so these are usually employed in variety of applications. A radiating patch is available on one of the sides of the dielectric and a ground plane is there on another side of Microstrip patch antenna. Microstrip patch antennas are utilized in many applications of wireless transmission such as Bluetooth, WLAN etc. [2, 4–6].

The demand for Bluetooth support of the smart phone devices has encountered immense growth in the last few years. Bluetooth technology supports short distance, low data rate wireless communications. The antennas used for Bluetooth applications include planar monopole antennas and conventional patch antennas [1, 7, 9] Even a small integrated circuit can be used for implementing Bluetooth technology.

A microstrip patch antenna can be made up of a patch that is conducting and also ground plane, in between there is substrate which is a dielectric medium that is consisting of a specific dielectric constant and a certain thickness. The measurements of patch are less than that of the ground and the substrate. The value of the dielectric constant and the resonant frequency determine the dimensions of a microstrip patch antenna [3, 10].

2 Antenna Design and Designing Parameters

The purposed antenna is designed on FR4 substrate that is consisting of a dielectric constant of value 4.4 and a thickness value of 1.76 mm. The antenna has got a circular patch fed by a 50 Ω microstripline and for matching quarter wave transformer is used. The ground plane is full. The design is as shown in Fig. 1(a).

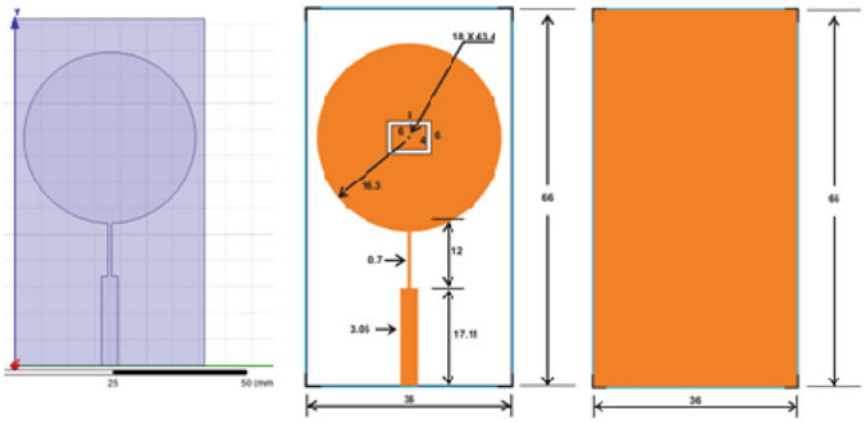

(a) Front View of Proposed design without slot (b) (a) Fron t View of Proposed design without slot (c) Back View

Fig. 1 Proposed antenna

Table 1 Dimensions of proposed antenna

Parameters	Value (mm)
Substrate length (L_s)	36
Antenna width (W_s)	66
Patch radius (R_p)	16.3
Length of feed line (L_f)	12 + 17.11
Width of feed line (W_f)	3.05
Dimension of inner slot (S_i)	6 × 4
Dimension of outer slot (S_o)	8 × 6
Length of ground(L_g)	36
Width of ground(W_g)	66

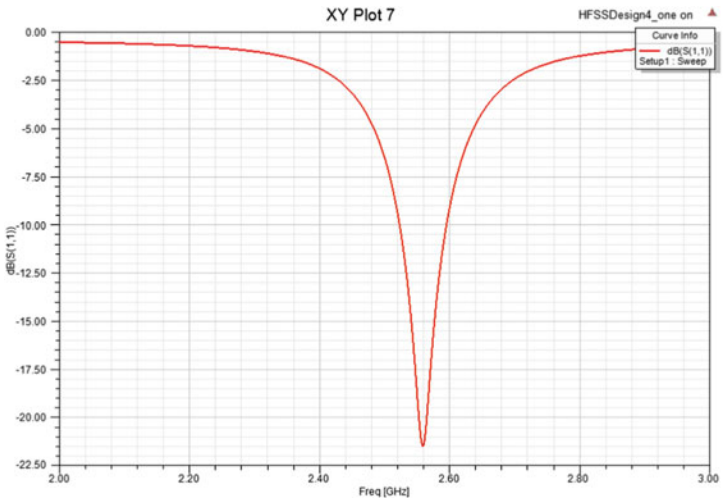

Fig. 2 Return loss (S11) vs frequency plot without slot

The gain is increased further by cutting a rectangular slot at the centre of patch as shown in Fig. 1(b) with overall dimensions. The back view with full ground plane is also shown in Fig. 1(c) (Table 1).

3 Results and Discussions

The proposed patch antenna design is simulated using the software HFSS and then fabricated on substrate FR4 with dielectric constant of value 4.4 and a thickness value of 1.76 mm. Then the testing was done using VNA N9916A.

3.1 Simulation Results

The return loss in dB is simulated for both designs without slot and with slot as shown in Fig. 2 and Fig. 3 respectively.

The simulation curves show that without slot the antenna was resonating at a frequency of 2.6 GHz and with slot the frequency shifted towards desired resonant frequency of 2.4 GHz, with a reduced return loss from −22 to −30 dB.

The radiation pattern results were also simulated for with and without slot designs at the resonating frequency as shown in Fig. 4(a) and (b) respectively. The gain improved from 2 to 2.1067 dB.

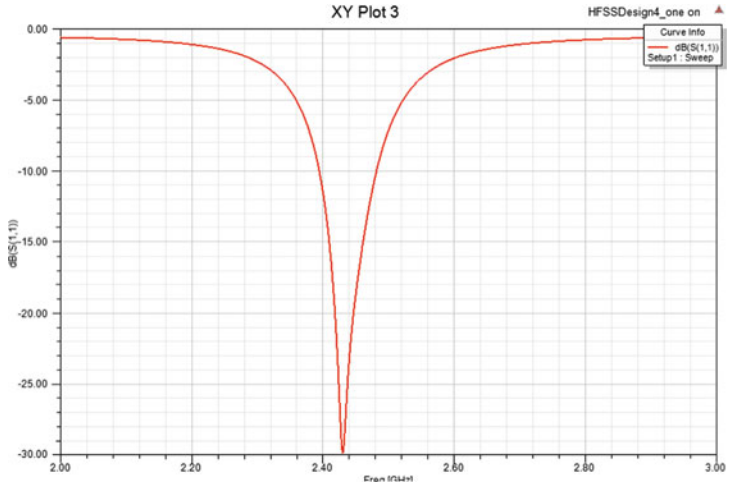

Fig. 3 Return loss (S11) vs frequency plot with slot

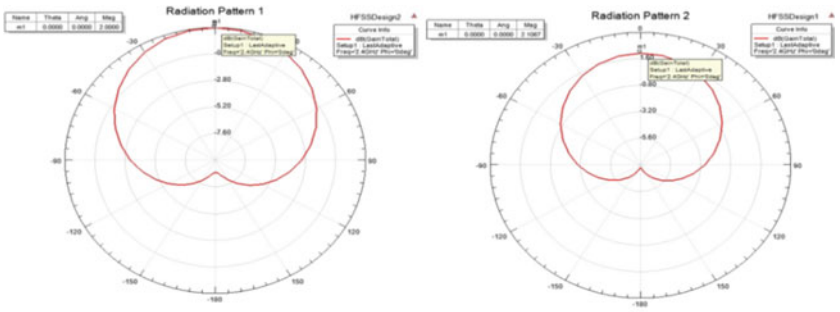

Fig. 4 Polar plot of the farfield gain of the designed antenna without slot and with slot

(a) Fabricated design-front view (b) Fabricated design-back view

Fig. 5 Front view and back view of fabricated design

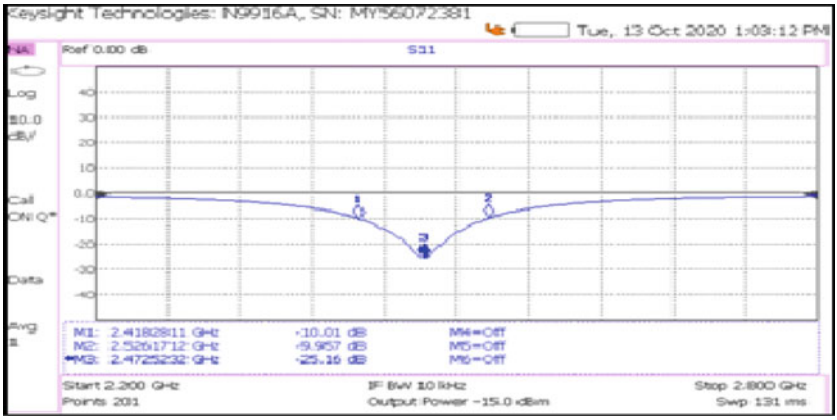

Fig. 6 VNA results- s11 parameter

4 Fabricated Design

The design was fabricated on FR4 substrate and front view and back view of design is as shown in Fig. 5(a) and (b) respectively.

The testing was done using VNA N9916A. The simulated return loss curves were verified as seen from the VNA results in Fig. 6. The resonant frequency was 2.47 GHz having a return loss of −25.16 dB which is very close to the simulated results.

5 Comparison with Other Designs

The proposed design is compared with similar designs. It can be observedDthat the proposed antenna is better than others in terms of overall size and gain and having a single element. Table 2 shows the comparison with other results.

Table 2 Comparison with other designs

	Size (mm)	Return loss (dB)	Resonant frequency (GHz)	Gain (dB)
[7]	45*35*10.5	−35	2.61	8
[8]	49*58*1.6	−26.88	2.45	2.53
Proposed design without slot	36*66*1.6	−22.5	2.67	2
Proposed design with slot	36*66*1.6	−30	2.4	2.1067

6 Conclusion

A microstrip patch antenna without and with a rectangular slot has been designed and simulated for a frequency of 2.4 GHz. The antenna covers the ISM band frequency of operation 2.4–2.48 GHz. The antenna has a directional pattern centered at the resonant frequency. The designed antenna is simulated and further fabricated and tested. The test results were very close to the simulated results. The antenna design proposed in this paper can be utilized for Bluetooth applications at a frequency of 2.4 GHz. The gain can be improved by designing an array of this single element.

References

1. Bialkowski KS, Postula A (2003) Demonstrating the effects of multipath propagation and advantages of diversity antenna techniques. In: Proceedings IEEE antennas propagation society international symposium, Columbus, OH, vol 3, pp 654–657
2. Khraisat SHY (2012) Design of 4 elements rectangular microstrip patch antenna with high gain for 2.4 GHz applications. Mod Appl Sci 6(1):68
3. Yang SLS, Kishk AA, Lee KF (2008) Frequency reconfigurable U-slot microstrip patch antenna. IEEE Ant Wirel Propag Lett 7:127–129
4. Bahal J, Bhartia P (1985) Microstrip Antennas. Artech House, Boston
5. Gupta K, Jain K, Singh P (2015) Analysis and design of circular microstrip patch antenna at 5.8 GHz. Int J Comput Sci Inf Technol 5(3):3895–3898
6. Aneesh M, Ansari JA, Singh A, Sayeed KSS (2013) Analysis of S-shape microstrip patch antenna for bluetooth application. Int J Sci Res Publ 3(11):1–4. ISSN 2250–3153
7. Sontakke M, Savairam V, Masram S, Gundewar PP (2017) Microstrip patch antenna with DGS for bluetooth application. Int J Eng Res 6(3):524–527
8. Lee SW, Sung Y (2015) Compact frequency reconfigurable antenna for LTE/WWAN mobile handset applications. IEEE Trans Ant Propag 63(10):4572–4577
9. Ilvonen J, Valkonen R, Holopainen J, Viikari V (2014) Multiband frequency reconfigurable 4G handset antenna with MIMO capability. Progr Electromagn Res 148:233–243
10. Deepak A (2017) Design of miniaturized microstrip patch antenna for low frequency mobile communication. In: 4th IEEE conference on signal processing, computing and control, Solan, India, 21–23 September 2017